Band Alignments and Interfaces in Kesterite Photovoltaics

Thesis submitted in accordance with the requirements of the

University of Liverpool

For the degree of

Doctor in Philosophy

By

James Thomas Gibbon

Stephenson Institute for Renewable Energy & Department of Physics

University of Liverpool, Peach Street

Liverpool, L69 7ZF

United Kingdom

September 2018

CONTENTS

Band Alignments and Interfaces in Kesterite Photovoltaics

James Gibbon

ABSTRACT

The kesterite materials, $Cu_2ZnSn(S,Se)_4$, represent a promising class of absorber materials, for cheap, earth-abundant, non-toxic photovoltaic cells. However, the record efficiency of a device based on these materials is only 12.6 %, compared to 15 % required for the material to be commercially viable and 22.6 % for the related chalcopyrite material, CIGS. In this thesis, we consider the architecture of a typical kesterite solar cell, from the back contact to the window layer and identify possible causes of the open-circuit voltage deficit, and how this deficit can be reduced. We begin by investigating the necessity for photovoltaics as a result of climate change, caused by our use of fossil fuels, and how the technology of photovoltaics has developed. We also consider the physical principles of photovoltaics and then discuss kesterite materials and architecture and compare them to chalcopyrites.

Thus, we begin by investigating the photoelectron spectroscopy of kesterite materials obtained from different synthetic routes, and determine, the band alignments of kesterite/buffer interfaces by the Anderson electron affinity rule and the more reliable Kraut method. Using the results, it is shown that the band offsets between CdS and the kesterite materials considered in this work are inappropriate for high-efficiency photovoltaics. In contrast, In_2S_3 shows advantageous band offsets in all cases. Simulations are then used to compare the CdS and In_2S_3 devices

Another limit on the efficiency of kesterite photovoltaics is the formation of the *n*-type $Mo(S,Se)_2$ at the back contact. The formation of this layer typically results in the formation of a reverse diode, opposed to the main photodiode, thus increasing the recombination rate of the photoholes. However, in CdTe devices, Mo is often used as a back contact, which can result in the formation of an analogous $MoTe_2$ layer which does not seem to have this effect. By considering the effects of Ar^+ ion induced defects upon single crystals or multilayers exfoliated from a single crystal, the possible reasons why $MoTe_2$ does not have the same effect as the $Mo(S,Se)_2$ layer are investigated.

We will also consider the uppermost layer of the photovoltaic cell, the window layer, which usually consists of a transparent conducting oxide (TCO). However, most of the widely-used TCOs have considerable issues, such as scarcity, cost, and self-compensating defects. Hence the final experimental chapter will consider an alternative TCO: Ga_2O_3. This material has a considerably larger band gap than that of the other TCOs, making it of interest for a wide range of applications Despite this widespread interest, fundamental properties of the material are still poorly understood. Thus, in the final chapter we begin by investigating the fundamental surface properties of a β-Ga_2O_3 single crystal with a $(\bar{2}01)$ surface termination and show that contrary to previous reports, the material exhibits surface accumulation. We also investigate the properties of several of the other polymorphs of Ga_2O_3 later in the chapter.

This thesis concludes by considering the impact of these findings upon the future of kesterite photovoltaics and describe the likely future development of the material and its prospects for commercial deployment.

ACKNOWLEDGEMENTS

A PhD undoubtedly constitutes an enormous amount of work. This is particularly so in the experimental sciences, where not only does the candidate have to read vast swathes of literature but must also deal with the trials and tribulations of experimental work. The days and weeks can often go by with the candidate feeling no further along in their experiment than when they began. Thus, a key, but often unspoken, part of doing a PhD is building a network of colleagues, friends and family to help alleviate the feelings of despair or inadequacy that can appear when experiments are showing null results or just not working at all.

One of the key people in this network is the primary academic supervisor, as a poor relationship with the primary supervisor can make and already difficult endeavour, nigh on impossible. I would, therefore like to begin by acknowledging Dr Vin Dhanak who in his role as my primary supervisor provided the platform to allow me to develop as a researcher and also for giving advice and guidance when required. I must also mention the many restaurants that we visited during my PhD where he always demonstrated his generosity.

Secondly, I have to thank Dr David Hesp and Dr Thomas Whittles, for passing on their knowledge of vacuum techniques and technologies to me and training me in the usage and applications of these, which forms the majority of this thesis.

I would also like to acknowledge Dr Mohana Rajpalke, Dr Max Birkett, Dr Tim Joyce, Dr Oliver Hutter and Dr Richard Potter for their roles in training me to use their particular experimental equipment and techniques. Professor Tim Veal must also be acknowledged for invaluable discussions. I would also like to acknowledge everyone at the Stephenson Institute for Renewable Energy who has been involved in obtaining data in this and other works of mine, for which particular thanks must go to Jack Swallow, Holly Edwards, Thomas Featherstone and Leanne Jones. I would also like to thank those at the institute who provided illuminating and interesting conversations over lunch or tea-breaks, of whom there are too many to list here. Those who passed through the lab during my time there, as visitors, master's, bachelor's or PhD students are also acknowledged. I hope you enjoyed your time in the lab as much as I did.

Outside of the University of Liverpool, I would like to acknowledge Dr Pam Dugdale and Dr Robert Lomas for their role in encouraging me to pursue my PhD.

I must also acknowledge the role that my family has played during my PhD. Not only did they provide support (and childcare!) when needed, they also kept me sane when things were not going as planned. I would like to thank Eric, Jackie and the girls (K, E & A), for their role in this work. Special mention is given to my parents for their infatigable support during my PhD and also to Joe, particularly for his role as Amelia's favourite Uncle!

Finally, I must acknowledge the two people who have had, by far, the greatest impact upon me during my time at Liverpool. My wife, Steph, and daughter, Amelia. I could not have done this without your constant love and support and would never have reached the point I have without you both. Not only, due to your support, but also due to your abilities to make me laugh, smile and otherwise encourage me to keep going, particularly towards the end. I, therefore dedicate this thesis to you both. Hopefully, now that it is done, things will settle down a little!

WORK IN CONJUNCTION WITH OTHERS

This thesis is an account of my research performed at the Stephenson Institute of Renewable Energy and the Department of Physics, University of Liverpool, between October 2014 and August 2018, under the supervision of Dr V. R. Dhanak and funded by a GTA studentship by the Department of Physics. The research here has not previously been submitted wholly or in part for admission to a higher degree at this or any other academic institution. The following list gives specifically outlines the contributions of any collaborator who has been involved in the research described in this work:

- The Ga_2O_3 thin-films described in Chapter 2 were synthesised by Joe W. Roberts[a] and Paul R. Chalker[a].
- The sputter chamber used in Chapter 3 was built by Adrian Hannah[b] and Reza Valizadeh[b].
- The CZTS and CZTSSe nanoparticle films and the In_2S_3 films in Chapter 3 were synthesised by Yongtao Qu[c], Stephen Nwankwo[c], Guillaume Zoppi[c], Neil Beattie[c] and Vincent Barrioz[c], as was the optical data presented in Figure 3.13.
- The SnS_2 thin-film described in chapter 3 was synthesised by Miika Mattinen[d], Peter. J. King[d], Leonid Khriachtchev[d] and Markku Ritala[d].
- The CZTSSe device-like stacks in chapter 4 were synthesised by Yongtao Qu[c], Guillaume Zoppi[c], Neil Beattie[c] and Vincent Barrioz[c].
- The DFT calculations in Chapter 6 were performed by Joel B. Varley[e].
- The code for solving the Poisson equation in Chapter 6 is based on code originally by Tim D. Veal[f].
- The HAXPES measurements in Chapter 6 were performed by Holly Edwards[f], Jack E. N. Swallow[f], Thomas J. Featherstone[f], Anna Regoutz[g] and David A. Duncan[h].
- The epitaxial Ga_2O_3 films described in Chapter 6 were synthesised by Joe W. Roberts[a] and Paul R. Chalker[a].
- XRD and AFM of the epitaxial Ga_2O_3 films was performed by Joe W. Roberts[a].
- TEM of the epitaxial Ga_2O_3 films was performed by Boning Ding[i], Rachel A. Oliver[i] and Fabien C-P. Massabuau[i].
- UV-Vis measurements of the epitaxial Ga_2O_3 films was performed by Jon Major[f] and Laurie J. Phillips[f].

---

[a] Centre for Materials and Structures, University of Liverpool, Liverpool, UK

[b] ASTeC, Daresbury Laboratory, Science and Technology Facilities Council, Warrington, UK

[c] Department of Physics and Electrical Engineering, Northumbria University, Newcastle upon Tyne, UK

[d] Department of Chemistry, University of Helsinki, Helsinki, Finland

[e] Lawrence Livermore National Laboratory, Livermore CA, USA

[f] Stephenson Institute for Renewable Energy and Department of Physics, University of Liverpool, Liverpool, UK

[g] Department of Materials, University College London, London, UK

[h] Diamond Light Source, Didcot, UK

[i] Department of Materials Science and Metallurgy, University of Cambridge, Cambridge, UK

LIST OF PUBLICATIONS AND PRESENTATIONS

Publications Directly Associated with this Thesis

- Gibbon, J. T.; Jones, L.; Roberts, J. W.; Althobaiti, M.; Chalker, P. R.; Mitrovic, I. Z.; Dhanak, V. R. "Band alignments at Ga_2O_3 heterojunction interfaces with Si and Ge", *AIP Advances*, **2018**, 8 (6), 065011
- Mattinen, M.; King, P. J.; Khriachtchev, L.; Meinander, K.; Gibbon, J. T., Dhanak, V. R.; Räisänen, J.; Ritala, M.; Leskelä, M. "Low-Temperature Wafer-Scale Deposition of Continuous 2D SnS_2 Films", **2018**, *Small*, 14 (21), 1800547
- Gibbon, J. T.; Qu, Y.; Beattie, N., Barrioz, V. Zoppi, G., Dhanak, V. R. "Band Alignments of CZTSSe cells measured by X-ray photoelectron spectroscopy and the effects on achievable efficiencies", **2018**, *Solar Cell Materials and Solar Cells*, manuscript in preparation
- Gibbon, J. T.; Dhanak, V. R. "Chapter 4. Properties of transition metal dichalcogenides", *Two dimensional transition metal dichalcogenides (2D TMD): Synthesis, Properties and Applications*, Ed. Sabari Arul, N.; Springer Nature Publisher, manuscript in preparation
- Swallow, J. E. N.; Varley, J. B.; Jones, L. A. H.; Gibbon, J. T.; Piper, L. F. J.; Dhanak, V. R.; Veal, T. D. "Transition from electron accumulation to depletion at β-Ga_2O_3 surfaces", Submitted to APL Materials
- Roberts, J.W.; Massabuau, F. C-P.; Chalker, P. R.; Oliver, R. A., Gibbon, J. T.; Dhanak, V. R.; Major, J.; Phillips, L. J. "Effect of Growth Temperature and Plasma Growth Parameters on Plasma Enhanced Atomic Layer Deposited α-Ga_2O_3 Grown on Sapphire", manuscript in preparation

Presentations Directly Associated with this Thesis

- Nanoenergy 2015, Manchester, UK

  Talk: Ga_2O_3: An Alternative Transparent Conducting Oxide for Energy and Other Applications

- Nanoenergy 2016, Liverpool, UK

  Talk: The Effects of Sulfurization on CZTS Surface Properties

Publications Arising from work Performed During this Thesis, but not Directly Associated with it

- Sedghi, N.; Li, H.; Brunell, I. F.; Dawson, K.; Potter, R. J.; Guo, Y.; Gibbon, J. T.; Dhanak, V. R.; Zhang, W. D.; Zhang, J. F.; Robertson, J.; Hall, S.; Chalker, P. R. "The role of nitrogen doping in ALD Ta_2O_5 and its influence on multilevel cell switching in RRAM", *Applied Physics Letters*, **2017**, 110 (10), 102902
- Sedghi, N.; Li, H.; Brunell, I. F.; Dawson, K.; Guo, Y.; Potter, R. J.; Gibbon, J. T.; Dhanak, V. R.; Zhang, W. D.; Zhang, J. F.; Hall, S.; Robertson, J.; Chalker, P. R. "Enhanced switching stability in Ta_2O_5 resistive RAM by fluorine doping", *Applied Physics Letters*, **2017**, 111 (09), 092904

- Sawangsri, K.; Das, P.; Supardan, S. N.; Mitrovic, I. Z.; Hall, S.; Mahapatra, R.; Chakraborty, A. K.; Treharne, R.; Gibbon, J.; Dhanak, V. R.; Durose, K.; Chalker, P.R. "Experimental band alignment of Ta_2O_5/GaN for MIS-HEMT applications", *Microelectronic Engineering*, **2017**, 178, 178
- Jin, J.; Wrench, J. S.; Gibbon, J. T.; Hesp, D.; Shaw, A.; Mitrovic, I. Z.; Sedghi, N.; Phillips, L. J.; Zou, J.; Dhanak, V. R.; Chalker, P. R.; Hall, S. "Schottky Diodes on ZnO Thin Films Grown by Plasma-Enhanced Atomic Layer Deposition", *IEEE Transactions on Electron Devices*, **2017**, 64 (3), 1225
- Whittles, T. J.; Veal, T. D.; Savory, C. N.; Welch, A. W; de Souza Lucas, F. W.; Gibbon, J. T.; Birkett, M.; Potter, R. J.; Scanlon, D. O.; Zakutayev, A.; Dhanak, V. R. "Core Levels, Band Alignments, and Valence-Band States in $CuSbS_2$ for Solar Cell Applications", *ACS applied materials & interfaces*, **2017**, 9 (48), 41916
- Birkett, M.; Savory, C. N.; Rajpalke, M. K.; Linhart, W. M.; Whittles, T. J.; Gibbon, J. T.; Welch, A. W.; Mitrovic, I. Z.; Zakutayev, A.; Scanlon, D. O.; Veal, T. D. "Band gap temperature dependence and exciton like state in copper antimony sulphide, $CuSbS_2$", *APL Materials*, **2018**, 6 (8), 084904

LIST OF SYMBOLS

B	Radiative Recombination Coefficient/ Background Level/Magnetic Flux Density	R_H	Hall Coefficient
$\mathbf{B}$	Magnetic Flux Density	R_S	Series/Sheet Resistance
$c_{A,e(p)}$	Auger Electron (Hole) Capture Coefficient	R_{SH}	Shunt Resistance
E	(Kinetic) Energy/Electric Field	T	Temperature
E_B/E_b	Binding Energy	T_C	Temperature of the Cold Reservoir
E_F	Fermi Energy	T_H	Temperature of the Hot Reservoir
E_f	Final Energy	V	Voltage
E_g	Band Gap	V_{BB}	Band Bending Voltage
E_i	Initial Energy	V_H	Hall Voltage
E_k	Kinetic Energy	V_{IP}	Ionisation Potential
E_P	Pass Energy	V_{OC}	Open-Circuit Voltage
$\mathbf{E}$	Electric Field	a	Lattice Constant
ΔE	Formation Energy/Energy Resolution	b	Bowing Parameter for Band Gap
$\Delta E_{C(V)}$	Conduction (Valence) Band Offset	c	Speed of Light in Vacuum
ΔE_s	Source Line Width	d	Molecular Diameter/Interplanar Separation/Thickness of a Native Oxide Layer/Thickness
ΔE_{CL}	Core-Level Natural Width	e	Elementary Charge
$\mathbf{F}$	(Lorentz) Force	h	Planck Constant
H	Hamiltonian Operator	$\hbar$	Reduced Planck Constant
I	Current/Intensity	j_{SC}	Short-Circuit Current Density
$\mathbf{J}/\mathbf{j}$	Current Density	k	Wavenumber
$N_{A(D)}$	Density of Acceptor (Donor) States	k_B	Boltzmann Constant
$N_{C(V)}$	Conduction (Valence) Band Effective Density of States	$\mathbf{k}$	Wavevector
N_{SS}	Surface State Density	m	Mass
P	Pressure	m_0	Rest Mass of a Free Electron
R	Resistance/Relaxation Energy	$m^*_{(e,h)}$	(Electron, Hole) Effective Mass
R_C	Mean Radius of the Hemispherical Plates	m^*_Γ	Effective Mass at the Γ point

n	Electron Density/Diode Ideality Factor
n_i	Intrinsic Carrier Density
n_s	Sheet Density
p	Hole Density/Momentum Operator
$\mathbf{v}$	Velocity
v	Speed
w	Slit Width
x	Composition
Δ_{SO}	Spin-Orbit Splitting
α	Auger Parameter/Absorption Coefficient
α'	Modified Auger Parameter
$\Delta\alpha$	Acceptance Angle/Auger Parameter Shift
δ	Bowing Parameter for Lattice Constant
ε_0	Permittivity of Free Space
ε_r	Relative Dielectric Constant
ε_{st}	Static Dielectric Constant
$\Delta\varepsilon$	Shift due to Initial State Effects
ζ	Conduction Band Minimum to Fermi Level Separation
η	Power Conversion Efficiency
η_C	Carnot Efficiency
η_{CN}	Chabadal-Novikov-Curzon-Ahlborn Efficiency
θ	Bragg Angle/Take-Off Angle
λ	(Inelastic) Mean Free Path/Wavelength
$\mu_{(h,e)}$	(Hole, Electron) Mobility
ν	Frequency
ξ	Valence Band Maximum to Fermi Level Separation
φ/φ	Work Function
χ	Electron Affinity
ω	Angular Frequency

LIST OF ABBREVIATIONS

AFM	Atomic Force Microscopy	**EQE**	External Quantum Efficiency
ALD	Atomic Layer Deposition	**ESCA**	Electron Spectroscopy for Chemical Analysis
ARPES	Angle-resolved Photoelectron Spectroscopy	**(MOS)FET**	(Metal-Oxide Semiconductor) Field Effect Transistor
AZO	Aluminium-doped Zinc Oxide	**FF**	Fill Factor
AZTS	Ag_2ZnSnS_4	**FL**	Fermi Level
BIS	Bremsstrahlung Isochromat Spectroscopy	**FRR**	Fixed Retardation Ratio
C-V	Capacitance-Voltage	**FTIR**	Fourier-transform Infrared Spectroscopy
CB	Conduction Band	**FTO**	Fluorine-doped Tin Dioxide
CBM	Conduction Band Minimum	**FWHM**	Full-Width at Half-Maximum
CBO	Conduction Band Offset	**HAXPES**	Hard X-ray Photoelectron Spectroscopy
CCS	Carbon-Capture and Storage	**HV**	High Vacuum
CEM	Channel Electron Multiplier	**IMFP**	Inelastic Mean-Free Path
CHA	Concentric Hemispherical Analyser	**IPA**	Isopropanol
CIGS	$CuInGaSe_2$	**IPES**	Inverse Photoemission Spectroscopy
CIS	$CuInSe_2$	**IQE**	Internal Quantum Efficiency
CNCA	Chabadal-Novikov-Curzon-Ahlborn Efficiency	**ITER**	International Thermonuclear Experimental Reactor
CNL	Charge Neutrality Level	**ITO**	Tin-doped Indium Oxide
CPE	Constant Pass Energy	**LUMO**	Lowest Unoccupied Molecular Orbit
CRR	Constant Relative Ratio	**MFP**	Mean-Free Path
CSS	Closed Space Sublimation	**MOSCAP**	Metal-Oxide Semiconductor Capacitor
CVD	Chemical Vapour Deposition	**NASA**	National Aeronautics and Space Administration
CZTS	Cu_2ZnSnS_4	**OLA**	Oleylamine
CZTSe	$Cu_2ZnSnSe_4$	**PCE**	Power Conversion Efficiency
CZTSSe	$Cu_2ZnSn(S,Se)_4$	**PEELS**	Photoelectron Loss Spectroscopy
DC	Direct Current	**PES**	Photoelectron/Photoemission spectroscopy
DEMO	Demonstrating Power Station	**PL**	Photoluminescence
DFT	Density functional theory	**PLD**	Pulsed Laser Deposition
(P), (T)DoS	(Partial), (Total) Density of States	**PV**	Photovoltaics

SCAPS	Solar Cell Capacitance Simulations
SEC	Secondary Electron Cut-off
SEM	Scanning Electron Microscopy
SLG	Soda-Lime Glass
STM	Scanning Tunnelling Microscopy
STS	Scanning Tunnelling Spectroscopy
TCO	Transparent Conducting Oxide
TEGa	Triethylgallium
TEM	Transmission Electron Microscopy
TMD	Transition Metal Dichalcogenide
UHV	Ultra-High Vacuum
UK	United Kingdom of Great Britain and Northern Ireland
UNFCC	United Nations Framework Convention on Climate Change
UPS	Ultraviolet Photoelectron Spectroscopy
UV	Ultraviolet
UV-Vis	Ultraviolet-visible Spectroscopy
VB	Valence Band
VBM	Valence Band Maximum
VBO	Valence Band Offset
XHV	Extreme Ultra-High Vacuum
XPS	X-ray Photoelectron Spectroscopy
XRD	X-ray Diffraction

LIST OF FIGURES

LIST OF TABLES

1 INTRODUCTION

1.1 ENERGY, OR WHY SOLAR?

The world currently stands at a crossroads: The global population is increasing inexorably, with some estimates predicting a global population of 12.6 billion by 2100[1]–[3]; third world countries are becoming more and more developed; whilst the energy consumption of industrialised nations continues to increase, and with the likely role of artificial intelligence in the future, energy consumption is only going to continue to increase. Predictions suggest that demand may have increased to double or triple of current demand by 2100[3]–[5]. The easily accessible fossil fuels, have been in heavy use since 1712, with the invention of the first steam engine by Thomas Newcomen, which marked the start of the industrial revolution, and are already close to peak production. This is the so-called 'peak oil' phenomenon[6]–[9]. The use of less orthodox hydrocarbon reservoirs, such as shale gas is capable of postponing the 'peak oil' phenomenon somewhat[8], [9]. These reserves are necessarily still finite and exhibit lifetimes of only months or years in comparison to the decades-long lifetimes of traditional oil fields[9]. The continued use of fossil fuels will only contribute further to the issue of climate change.

Figure 1.1 – A modern replica of the Newcomen atmospheric steam engine at the Black Country Living Museum, in sight of the location of the first completed engine at Dudley Castle. © Chris Allen and reproduced here under a Creative Commons CC BY-SA 2.0 Licence

The effects of human action upon our planet are so large in scale that it has led to some authors suggesting that our planet has now entered new geological epoch, the Anthropocene[10], [11]. Proposed starting dates for the Anthropocene epoch vary

considerably, from the start of the agricultural revolution in the fertile crescent 12,000 years ago[12], up until dates as recent as the trinity nuclear test in 1945[13], or 1964, when ^{14}C levels in the atmosphere, and hence fixed into tree-rings, were at their maximum, after the 1963 Partial Test Ban Treaty[14], [15]. This treaty limited the testing of nuclear weapons to underground sites only and as such radiocarbon reached a maximum level. Worryingly, a generalised version of the Anthropocene epoch has been proposed as a solution to the Fermi paradox[16] (i.e. why do we not observe the existence of intelligent exo-civilisations? Because they cannot survive their version of the Anthropocene.) The same work used the example of the indigenous *Rapa Nui* civilisation of Easter Island to investigate how resource-intensive civilisations interact with the feedback loops of the environment. Most concerning is their finding that it is entirely possible to make the transition from a high-impact resource to a lower-impact resource after it is too late to avoid a collapse of civilisation[16]. However, at time of writing, all member-states of the United Nations Framework Convention on Climate Change (UNFCCC) have signed the Paris Agreement[17], although the United States has signified its intentions to withdraw from the agreement. The accord aims to 'hold the increase in the global average temperature to well below 2^{o}C above the pre-industrial level and pursue efforts to keep it below 1.5^{o}C'[17]. This necessarily requires reducing the amount of greenhouse gases released into the atmosphere *per annum*, and ideally, removing greenhouse gases already present. Clearly, the development of so-called 'green' energy sources is required to reduce emissions to a level compatible with the Paris Agreement, and reduce usage of the high-environmental impact resources that are the fossil fuels. Carbon dioxide is one of the main greenhouse gases targeted, due to its role as a reaction product in the burning of fossil fuels. CO_2 concentrations are considerably above pre-industrial levels as can be seen in Figure 1.2, having recently passed the largely symbolic threshold of 400 ppm[18], [19], a level not reached since the mid-Pliocene[20], [21], over 3 million years ago when the Arctic was largely free of ice[22]–[24].

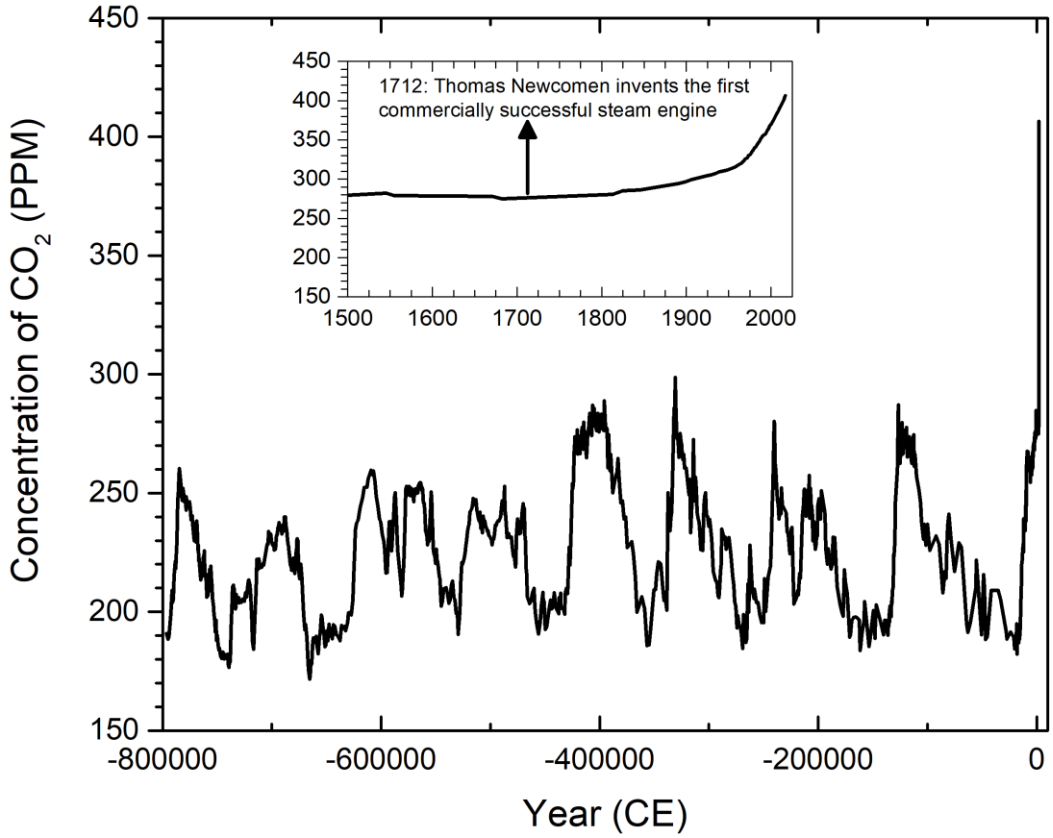

Figure 1.2 - Average CO_2 concentration in the atmosphere as a function of time. The inset shows the same data from 1500 i.e. pre-industrialisation to the present day. The industrial revolution can be considered to start in 1712, with the invention of the first commercially successful steam engine by Thomas Newcomen. The development of the steam engine resulted in fossil fuels being exploited on a much larger scale than previously occurred. Data is sourced from REFs [25]–[27]

Despite the UK government signing the Paris Agreement, the 2018 progress report for the House of Commons by the Committee for Climate Change found that the UK is likely going to miss its 2025 and 2030 carbon budgets[28], so much work still remains to be done to decarbonise the economy.

In 2019, the UK begins its next phase of power auctions, which are recommended to provide a further 45-60 TWh of low-carbon electricity generation, due to the low level of risk associated with renewables[28]. The report states that this should be 'sufficient to reach an emissions intensity below 100 gCO2/kWh by 2030'[28]. This compares to the 85 TWh of currently installed renewable energy generation capacity, and an emissions intensity of 263 gCO2/kWh[28].

Carbon capture and storage (CCS) techniques, except for those that evolved over the past 4 billion years or so[29]–[31], are still in their infancy and to date have not lived up to their initial promise[32]–[35]. The supply of fossil fuels is also limited, so even if carbon capture was suddenly working, the discussion over what to do next would still occur, just a few

decades into the future. Even so, the first CCS plant in the UK is not expected to be operational until at least 2021, and would only reach a 20MtCO_2 *per annum* by 2035[28]. However, due to the long lifetime of CO_2 in the atmosphere (approximately 10-25% of CO_2 produced by burning fossil fuels is estimated to still be in the atmosphere after 10 000 years without any human intervention[36]), CCS will likely still play a role in reducing emissions to pre-industrial levels.

If continuing to burn fossil fuels is out of the question, then how does the world meet its increasing energy demands?

Nuclear fission is likely to prove controversial due to the widespread, if unfounded, fears over safety and the very real fears over nuclear proliferation by 'rogue' states, without even considering the issue of what do you do with the spent fuel rods? In the UK, 75.4% of the nuclear provision ends up at the Sellafield nuclear site[37], with its leaky silos, crumbling buildings, and cracked concrete ponds[38]–[42]. The question of how nuclear waste is disposed is still an open question, with extra-terrestrial disposal being considered by NASA as early as the 1970s[43], [44], as an application of the space shuttle[43]–[45]. The space shuttle program was not as successful as first envisaged, with disasters destroying two of the six shuttles built. As such, plans to build a second generation of shuttles were abandoned, putting an end to the shuttle program. With the development of commercial spaceflight by companies such as SpaceX and Virgin Galactic, interest in extra-terrestrial disposal of spent fuel has been resurrected[46], however there are still several outstanding issues regarding safety, transportation to the launch site, atmospheric re-entry, orbital stability, and asteroid or micrometeoroid collisions with orbiting waste, although the risks to public health are considered to be small[47]. Contentious political and social issues also surround deep-sea and geological storage of nuclear waste[48], as such lawmakers are reluctant to back these methods with sufficient vigour to actually see the establishment of such facilities. An example of this can be seen in the UK, as although the UK and the Welsh devolved governments both, officially, support geological storage of waste, no sites has ever been chosen to host a geological disposal facility[49]. In contrast, the Scottish devolved government supports near-surface storage facilities, located as near as possible to the site where the waste is produced[49]. Additionally, many of the locations ideal for developing a geological disposal facility are currently tourism hotspots or national parks. As such, local people and tourism boards are frequently opposed to the development of these facilities due to their fears of the impact it may have on visitor numbers and hence the local economy[50]–[52]. Another potential issue for nuclear fission reactors has been highlighted

recently in France, where several nuclear reactors had to reduce their power output as the water coolant obtained from nearby rivers has been too hot to effectively cool the reactor, as a result of the recent global heatwave[53]. If extreme weather, such as said heatwave becomes more frequent as is expected as a result of climate change, then heat-engine-based fuel sources such as fission, coal and gas-fired power stations may need to reduce output to avoid overheating.

So, what about nuclear fusion? The International Thermonuclear Experimental Reactor (ITER) is not expected to achieve its first plasma until December 2025[54], and will not begin deuterium-tritium fusion until 2035[54] at the earliest. Even then, ITER is not expected to actually be commercially viable. The first commercially viable fusion reactor, currently proposed as DEMOnstrating power station (DEMO), isn't expected to be in operation until at least the early 2040s[55]. I.e. Nuclear fusion is still at least 20 years away, just as it has been for the past 60.

If nuclear fusion and fission are off the table, then we need to look at the truly renewable energies, biomass, geothermal, wind, hydroelectricity and solar power, which, with the notable exceptions of geothermal and hydroelectricity all derive their energy from the conversion of energy originating with that great nuclear fusion reactor that our planet orbits.

Geothermal power is of limited use as it requires very specific geologies that ultimately prevent it from widespread adoption. Having sufficiently hot rocks within a few kilometres of the surface of the Earth only occurs in a few geological regions, the most notable being Iceland where 30% of electricity is generated geothermally[56]. Much of the housing in Iceland is heated by geothermal water, and even pavements and roads are kept ice-free in the larger urban areas by hot water pipes laid underneath them[56]. Iceland does have a somewhat unique geology of being sat directly on top of the mid-Atlantic ridge[56], and as such is very geologically active[57], which is a considerable advantage when using geothermal power.

Biomass power is the general term for all forms of energy generation which involve burning a compound or compounds that have been generated by biological organisms[58], including but not limited to wood and its ash[59]–[61], biogas[62]–[64] and biodiesel[65]–[67]. Fossil fuels, lignite and peat are specifically excluded as these are limited resource, that arise due to specific environmental conditions. A considerable work on peatlands and their effect on the climate is available in reference [68]. A key issue with biomass power is

where do you obtain the mass from? Huge volumes of mass would be required to obtain even a small fraction of the global electricity demand, meaning that either deforestation would be required, or currently productive farmlands would need to be switched to growing crops for biofuel. Both options have large ecological, environmental and socioeconomic issues[69]–[71], which render the adoption of biofuels controversial.

Hydroelectric power similarly has huge ecological and ethical issues, whether as hydroelectric power stations or as tidal barrages[72]–[74]. A hydroelectric power station typically requires building a dam on a river far removed from the river delta, forming a new lake and potentially flooding entire settlements, including those of archaeological value[75]–[78]. A tidal barrage will also usually involve building a dam, instead on the estuary, again potentially flooding homes. Both forms of hydroelectric power can also have major impacts on any migratory fish such as salmon[79]–[83] and the European eel[83]–[87], the latter of which is considered critically endangered[88].

Onshore wind also remains controversial, due to the aesthetic effect wind turbines have on the environment and the noise that can be produced[89]–[91]. Offshore wind has issues related reliability, maintenance and other technical issues[92]–[95], particularly at deep water sites. Both forms of wind power also have critics, due to the unknown impact that the turbines can have on birds[91], [96], [97] and endangered species of bat[96].

What about solar power then? Several different forms of solar power have been proposed and the different methods are, to an extent, complimentary: Photovoltaics, whereby a photon is directly converted to a photovoltage by a photoactive diode[98]–[100]; concentrated solar-thermal, where a series of optical components concentrate light onto a high heat-capacity working fluid which is used to drive a heat engine[101]–[103]; and photocatalysis, where photons are used to drive catalytic reactions to produce hydrogen, oxygen or hydrocarbons, which can then be stored for future usage as a fuel[104]–[107]. This thesis will consider only photovoltaics henceforth.

1.2 PHOTOVOLTAICS

Photovoltaic devices are designed to take advantage of the photovoltaic effect first observed by Becquerel in 1839[108], [109], whereby a photon incident upon a material is absorbed, promoting a valence electron to a higher energy state, resulting in a photocurrent. In practice, a semiconductor diode is typically used for this purpose, as the built-in voltage of the diode aids in the separation of charges, which reduces the

recombination rate. In an operating this means absorbing photons originating from the sun, and directly converting them into an electrical current.

1.2.1 The Solar Spectrum

Since photovoltaics are dependent upon the radiation of the sun, it is worth understanding the solar spectrum in some further detail. The solar spectrum, which to a first approximation is given by a black body spectrum of temperature 5778 K[2], the specific intensity of which is described by Planck's law, given in equation (1.1)

$$B_\omega(\omega, T) = \frac{\hbar\omega^3}{4\pi^3 c^2} \frac{1}{e^{\frac{\hbar\omega}{k_B T}} - 1} \tag{1.1}$$

In actuality, absorption and re-emission processes in the chromosphere of the sun result in a spectrum that is not quite identical to a blackbody once it has passed through the chromosphere. Further broad-band absorption processes occur once the photons enter the atmosphere of the Earth. The spectra measured at the top of the atmosphere (blue), at sea-level (red) and that due to a hypothetical 5778 K blackbody (black) are given in Figure 1.3. Clearly visible are large decreases in the spectral intensities of the red data set, predominantly in the infrared part of the spectrum. These are the broad-band molecular absorptions due to gases in the atmosphere.

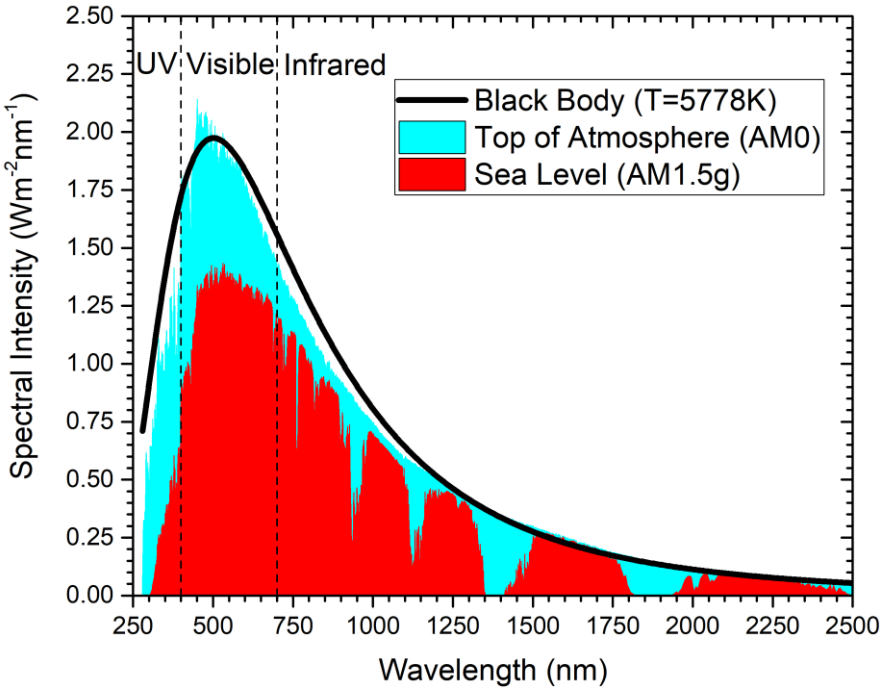

Figure 1.3 – The solar spectrum measured at the top of the atmosphere of the Earth (AM0) [111]*, at sea-level (AM1.5g)* [111] *and a synthetic blackbody spectrum for a blackbody at 5778 K.*

Naturally, the solar spectrum measured at the surface of the Earth will vary depending on many local conditions including: time of year; weather conditions; time of day; elevation; shading; and latitude. Due to this, the efficiencies reported by a photovoltaic cell that was simply sat outside would vary considerably. Instead a universal standard spectrum, the AM1.5g spectrum, is used.

The AM1.5g spectrum is calculated from the AM0 spectrum shown above in Figure 1.3, under a set of representative conditions: Firstly, the sun is at an angle of 48.19^{o} above the horizon, corresponding to an air column of 1.5x the atmospheric thickness; the receiving surface is at an angle of 37^{o} towards the equator; the atmosphere is at a standard temperature, pressure, composition and density; a total water vapour column equivalent of 1.42 cm; a total ozone column equivalent of 0.34 cm, and finally a specified surface albedo[111].

1.2.2 Electronic Properties of Semiconductors

Photovoltaic cells are dependent on the semiconducting properties of the material used as the absorber layer, as such it would be prudent to discuss the origin and nature of these properties and how they can affect the performance of a photovoltaic device.

To first understand the properties of semiconductors, we must first discuss what happens to electron energy states as crystalline materials are formed from isolated atoms. In an isolated atom, the electrons are quantised into orbitals with a particular, discrete energy value. However, as many atoms are brought together to form a crystal, the wavefunctions of the outermost electrons of neighbouring atoms begin to overlap. However, the Pauli exclusion principle forbids Fermions like the electron from having identical quantum numbers. As such, the energy levels of the states are modified such that the states are no longer exactly degenerate in energy. As many atoms are brought together, these states cover a larger and larger energy range, forming quasi-continuous bands.

Materials can therefore be classified as either (semi-)metals, insulators or semiconductors under this band theory. Metals, are materials where there is a non-zero density of states at the Fermi-level. Insulators and semiconductors are characterised by the existence of a band gap, a forbidden region where the electronic density of states is zero, around the Fermi level. The difference between a semiconductor and an insulator in this model is simply the size of the band gap. Typically, materials with band gaps $E_g \geq 4$ eV are typically considered insulators, however there are a few exceptions to this rule, most notably the transparent conducting oxides (TCOs) which will be discussed later. Examples of the band structures of

these materials are shown in Figure 1.4. Also excluded from this definition are the Mott insulators, which would be expected to be semiconductors due to their relatively small band gap, but are, in fact, insulators. For materials with band gaps below this value, electrons from the valence band can be promoted to the conduction band by thermal excitation, at room temperature, with a reasonable probability. For band gaps above this process, the thermal energy at room temperature is too small to excite the electron with a reasonable probability.

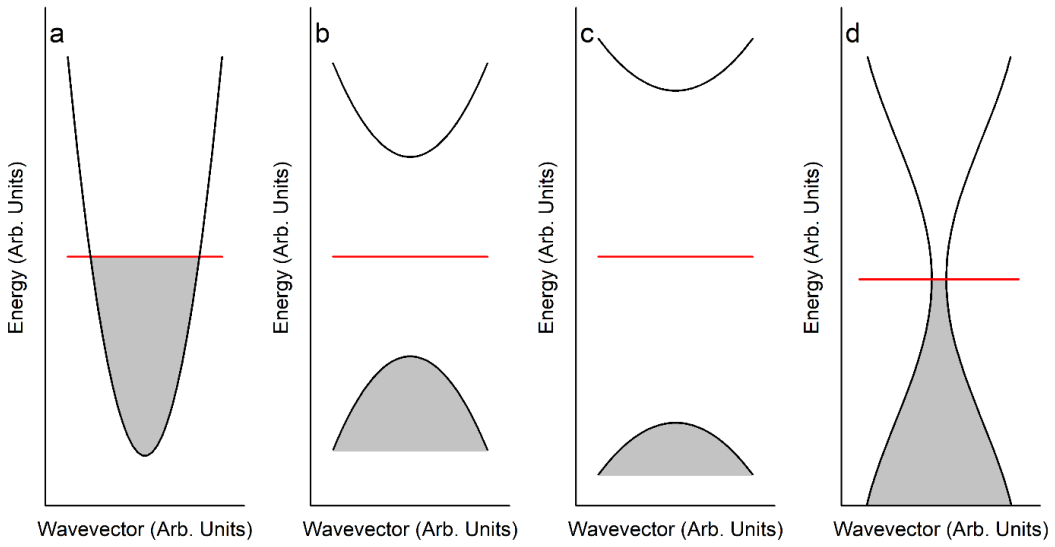

Figure 1.4 – The band structures and Fermi levels of a (a) metal, (b) semiconductor, (c) insulator and (d) semimetal. Occupied states are shaded grey whilst the Fermi level is in red.

For an intrinsic semiconductor, such as undoped silicon at equilibrium, the Fermi level occurs in the middle of the band gap, equidistant from the valence and conduction bands. When an electron is promoted to the conduction band by thermal, optical or any other excitation, a hole is left in the valence band. These holes act as if they are positive charge carriers, with a positive effective mass. Thus, for an intrinsic semiconductor at equilibrium the number of electrons in the conduction band (*n*) and the number of holes (*p*) are necessarily equal, i.e. $n = p \equiv n_i$.

Semiconductors are not usually deployed in the intrinsic state in most devices, instead the materials usually have defects or impurities deliberately introduced into them. Such action is known as doping the material. For some semiconductors, the material can be doped in such a way to have more holes in the valence band (p-type) or more electrons in the conduction band (*n*-type). For group IV semiconductors this is achieved by introducing a group IV (III) element for n-type (*p*-type) doping, as these have one more (less) valence electron. This will result in a small number of states in the band gap, close to the

conduction (valence) band due to the impurity, known as a donor (acceptor) state as the state will donate (accept) an electron. This will move the Fermi level towards the valence (conduction) band as shown in Figure 1.5, and in the case of degenerately doped semiconductors, the Fermi level can occur within the band.

By applying the law of mass action, given in equation (1.2), we can see that this results in the density of one of the charge carriers being greater than the other. The carrier with the larger density is thus known as the majority carrier, whilst that with the lower density is the minority carrier.

$$n \cdot p = n_i^2 \tag{1.2}$$

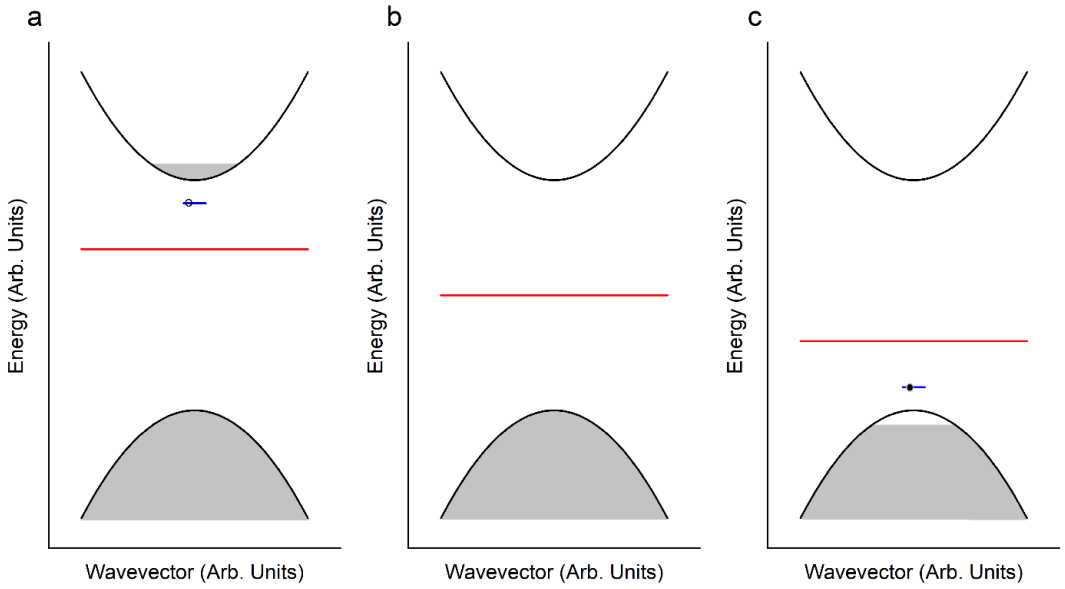

Figure 1.5 – The band structure of a (a) n-type, (b) intrinsic, (c) p-type semiconductor, with donor and acceptor states in blue. Open circles denote unoccupied states and closed circles denote occupied states.

In practice, a junction between two semiconductors with different majority carriers is usually used for a photovoltaic device, this is the *p*-*n* junction. For a silicon-based device, this typically consists of *p*-type and *n*-type doped silicon on either side of the junction. As the same material occurs on both sides of the junction, this is called a homojunction. However, many of the compound materials used in photovoltaics are ionically bonded and have native defects that naturally render the material *n*-type or *p*-type. A second material is then required to form the *p*-*n* junction, since the two semiconductors used are now different, this is called a heterojunction.

The copper-chalcogenides are an example of such materials, as many of these materials are natively *p*-type. This is usually assigned to copper-vacancies V_{Cu}, which result in shallow acceptor levels close to the valence band[112].

New semiconducting materials can be produced by isoelectronic substitution of elements from known semiconducting materials. For example, the III-V semiconductors (such as GaAs) and II-VI semiconductors (such as CdTe) are isoelectronic to the group IV semiconductors (Si, Ge). Similarly, the group II element in a II-VI semiconductor can be isoelectronically substituted with a group I and a group III element to form the I-III-VI_2 semiconductors ($CuInSe_2$), and the group III element by a group II and a group IV element, to form a I_2-II-IV-VI_4 semiconductor (Cu_2ZnSnS_4).

1.2.3 Semiconductor Junctions

When a homojunction is formed between two semiconductors of different majority carriers, a built-in voltage occurs. When the two semiconductors are brought into electrical contact, the Fermi levels of the materials align, however the relative positions of the band with respect to the Fermi level remain fixed, thus the bands are discontinuous. The majority carriers can then diffuse from one material to the other, where recombination occurs. This leaves a region at the interface with no free carriers known as the depletion region. This depletion region has only the static charged ions within causing the conduction (valence) bands on either side of the junction to bend. This static space charge bends the bands in such a way as to smooth the effects of the discontinuity, resulting in continuous bands with a built-in voltage across the interface. A schematic diagram of this process is shown in Figure 1.6.

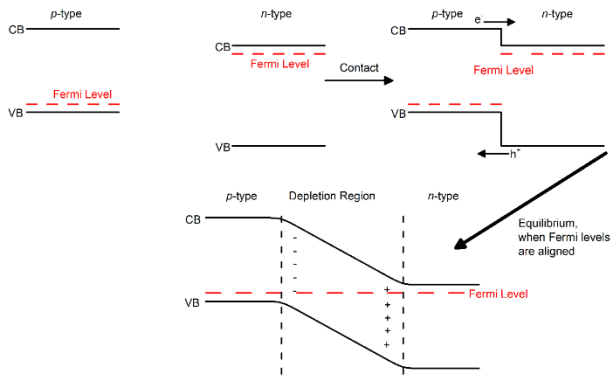

Figure 1.6 – A schematic diagram showing the formation of a junction between a p-type and an n-type doped semiconductor.

A similar process occurs when a heterojunction is formed, charge carriers flow from one side of the junction to the other and recombine, resulting in a space charge in the depletion

region. However, in a heterojunction, the band gaps on either side of the junction do not have to be the same. As such there may be discontinuous bands, because the band bending of the conduction band and valence band is only dependent on the space charge and must, therefore, be the same. Hence, if the band gaps of the two materials used are different, there will necessarily be discontinuities and therefore offsets between the bands on either side of the junction. This can result in three types of band offset, depending on the difference of the band gaps: Type I, or straddling gap; Type II, or staggered gap; and type III, or broken gap. A representation of these offsets is given in Figure 1.7.

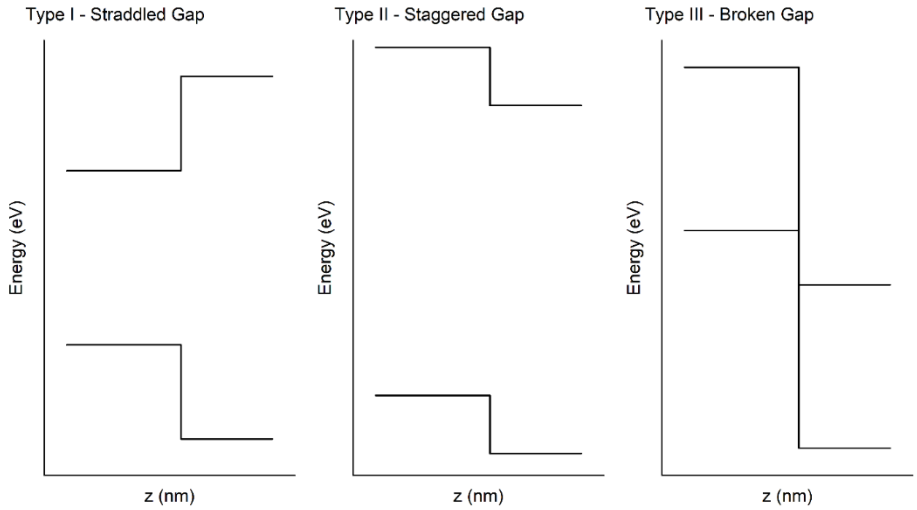

Figure 1.7 – A figure showing the three types of heterojunctions that can be formed at semiconductor-semiconductor interfaces.

1.2.4 Semiconductor Alloys

For an alloyed system $A_xB_{1-x}C$, where the two binary compounds have the same crystal structure, the variation of the crystal and electronic structures are often given by Vegard's law, shown in equations (1.3) and (1.4)[113]

$$a_{ABC} = xa_{AC} + (1-x)a_{BC} \tag{1.3}$$

$$E_{g,ABC} = xE_{g,AC} + (1-x)E_{g,BC} \tag{1.4}$$

In some cases, Vegard's law is insufficient for describing how the lattice parameters and band gap varies with composition, requiring a quadratic bowing term[114], [115]. It is not a requirement that the bowing term affect both the lattice parameter and the band gap, but rather one or both can be affected, as in the Pb chalcogenide system[116]. The bowed versions of Vegard's law are given in equations (1.5) and (1.6).

$$a_{ABC} = xa_{AC} + (1-x)a_{BC} - \delta x(1-x) \quad (1.5)$$

$$E_{g,ABC} = xE_{g,AC} + (1-x)E_{g,BC} - bx(1-x) \quad (1.6)$$

1.2.5 Semiconductors and Photovoltaics

When a photon is absorbed in a photovoltaic cell, an electron-hole pair is produced. These carriers can diffuse through the material and will either recombine or reach either the contact or the junction. However there is a fundamental thermodynamic limit on the efficiency of a single-junction photovoltaic cell, namely the Shockley-Queisser limit[117], which is dependent on the band gap of the absorber layer and the solar spectrum. The maximum obtainable efficiency for a single *p-n* junction operating at room temperature with the Sun as a light source, is thus found to be 30% with an absorber material with a band gap of 1.1 eV[117]. However, the gradient of the efficiency with respect to the absorber band gap is relatively shallow[117], so band gaps of 0.9-1.6 eV would also be capable of achieving sufficiently large efficiencies to be practicable, as shown in Figure 1.8. Figure 1.8 also shows several of the loss mechanisms and their contributions to the (in)efficiencies of the device. For photons with energy below the band gap, the photons are not absorbed, which suggests that the smaller the band gap is, the more effective the device will be. However, if too small a band gap is used, then the electron which absorbs the electron will be promoted into an excited state high in the conduction band. The electron will then rapidly undergo a thermalisation process, which typically consists of interaction with the phonons in the material. As such, the electron will rapidly lose the excess energy, which is transformed to and lost as heat. Thermalisation thus results in a preference for a large band gap material. Therefore, the size of the band gap used is a trade-off between the thermalisation and transparency of the material. Other losses can be related to parasitic resistances, defects or traps and radiative and non-radiative recombination processes.

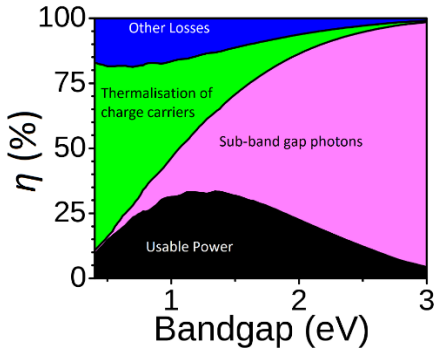

Figure 1.8 – The Shockley-Queisser limit and the loss mechanisms in each band gap region.

1.2.6 Characterisation of Photovoltaic Materials and Devices

A key question in photovoltaics is how does one quantify the quality of a photovoltaic cell? Several parameters are frequently used namely the power conversion efficiency, (PCE), under an AM1.5 spectrum, the open-circuit voltage, (V_{OC}), the short-circuit current density, (J_{SC}) and the fill-factor, (FF). The external quantum efficiency (EQE) (i.e. the current produced by the cell under a monochromatic source of a known intensity, scanning across all energies) is often also used to decide the quality of the cell.

Two other parameters which are important to the performance of a photovoltaic cell are the shunt resistance, (R_{SH}) and the series resistance, (R_S), which can be easily understood from the equivalent circuit diagram for a photovoltaic cell shown in Figure 1.9.

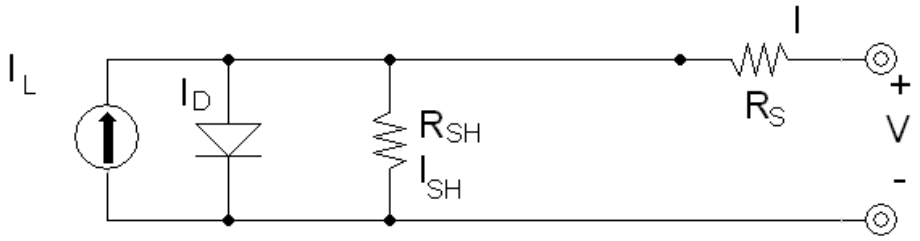

Figure 1.9 – The equivalent circuit diagram of a photovoltaic cell. Clearly shown are the shunt and series resistances.

A low shunt resistance corresponds to alternate current pathways through which the light-generated current can pass[118], which effectively reduces the voltage produced by the cell. An example of a defect that can produce a low shunt resistance would be a pinhole[119], [120] in the buffer layer, allowing charge carriers to move from the absorber, directly to the window.

In comparison, the series resistance is related to the potential differences between the various layers in the device[121]. A large series resistance reduces the fill factor and short-circuit current[122].

As a *p-n* solar cell can be approximated to a simple diode, the current-voltage relation is given by the Shockley diode equation[123] given in equation (1.7). Here, the parameter, n, is the diode ideality factor, which is another factor that can be important for a photovoltaic cell and is typically between 1 and 2[124], [125]. A value $n = 1$ corresponds to an ideal diode.

$$J = J_0\left(e^{eV/nk_BT} - 1\right) \tag{1.7}$$

When the diode is under illumination the Shockley diode can be modified to include the effect of the short circuit current density and is written as shown in equation (1.8).

$$J = J_0\left(e^{eV/nk_BT} - 1\right) - J_{SC} \tag{1.8}$$

By explicitly including the effects of the shunt and series resistances, the Shockley diode equation can be written in the form given in equation (1.9). Obtaining values for these resistances and the ideality factor is typically performed by simulating the current-voltage curve for the device and changing parameters to obtain a best fit[121], [122], [124]–[129]. This method is, however, fraught with issues as there often exist numerous local minima. As such, the resistances and ideality factors obtained are not necessarily unique solutions[128], [129].

$$J = J_0\left(e^{(eV+IR_S)/nk_BT} - 1\right) - J_{SC} + \frac{V + IR_S}{R_{SH}} \tag{1.9}$$

One issue with each of the quantities listed above is that each requires building a full device to measure, as such the reason for a decrease in one of the quantities is rarely known. One common approach in photovoltaics is to simply change one of the layers in the device in some way and see how these quantities vary. However, under this approach, understanding of the physical process causing the limitation is not gained. Instead, material science and surface science techniques should be used in conjunction with theoretical methods to understand the fundamental physical and chemical processes that are occurring and limiting the device efficiencies.

1.2.7 A Brief History of Photovoltaics

The earliest development in the history of photovoltaics was the observation of the photovoltaic effect in an electrochemical cell by Alexander Becquerel in 1839[108], [109]. Observation of the photovoltaic effect in solid-state materials would have to wait until 1873, when Willoughby Smith observed that the resistance of selenium bars varied with the intensity of light incident upon the bar[130]. Further experiments by W. G. Adams and R. E. Day confirmed this effect by measuring a current when no external voltages were applied[131], [132]. Adams also observed a similar, but much smaller effect in tellurium[131], which we can now explain as being due to the smaller band gap of tellurium relative to that of selenium.

1.2.7.1 The Zeroth Generation

The first photovoltaic cells were developed in 1883 and were deployed in 1884 by Charles Fritts. These devices were what would now be recognised as a Schottky diode, consisting of

a thin, transparent film of gold, with selenium as the absorber layer and a back contact of copper[133]–[136]. The devices were reportedly less than 1% efficient[136]. Fritts reportedly thought that his cells would eventually compete with coal-fired power plants and ultimately supplant them.

One of the supporters of the new technology was the industrialist, Werner Siemens, the founder of the Siemens engineering and technology company, who considered it "scientifically of the most far-reaching importance"[135], [137]. Unfortunately, the prevailing belief at the time was that light could not be directly converted to electricity and instead had to be converted to heat and drive a heat engine to produce electricity and so his results were largely ignored.

By the 1930s work on rectifiers had led to the observation of the photovoltaic effect in cuprous-oxide/copper rectifiers, and the development of some photovoltaic devices[138]. Bergmann reported selenium based photocells at a similar time[139], and thallous sulphide cells were also being developed[140]. However, these devices were similar in structure to those pioneered by Fritts, with little resemblance to the structure of modern photovoltaic cells. The structure of these early devices is shown in Figure 1.10, this can be compared to Figure 1.11, which shows the structure of a typical modern device. Numerous popular and academic authors also note that the photovoltaic effect was observed in either CdS or CdSe by Audobert and Stora in 1932[141]–[144], however the author has been unable to verify this.

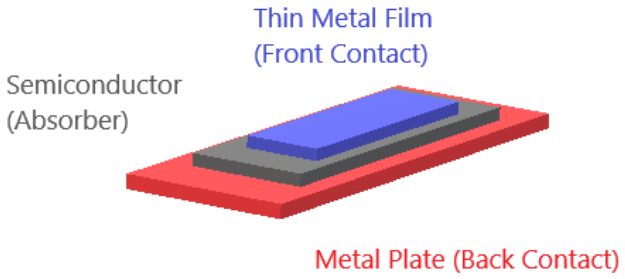

Figure 1.10 - A diagram of the structure of the early photoelectric cells. The structure of these cells is more similar to a Schottky diode than modern photovoltaic devices.

1.2.7.2 The First Generation

The first generation of photovoltaics evolved out of the work of Calvin Fuller, Gerald Pearson and Daryl Chapin at Bell Laboratories, and is entirely based on silicon[145]. After Pearson observed a considerable current when one of the *p-n* junctions he had made under the instruction of Fuller was illuminated by a desk lamp. Leading to Fuller suggesting that

Chapin use these silicon devices rather than the selenium devices he had previously been investigating. He collaborated with Fuller to try new dopants and this work culminated in the announcement by Bell Labs in 1954 of the solar battery. These solar cells had a relatively low efficiency by modern standards, at only 6% but was an order of magnitude over that of commercially available selenium photocells[136], [137], [146].

Silicon, however is an indirect band-gap material, resulting in a small absorption coefficient at between the indirect and direct gap as the absorption needs to be assisted by a phonon. Such a three-particle process has a much-reduced matrix element (i.e. has a much lower probability of occurring.) Hence silicon cells need to be very thick, of the order of hundreds of microns to achieve good absorption, resulting in (historically) costly devices. Another issue related to the use of silicon is that the grain boundaries in silicon are very active, so single-crystal silicon is required to achieve top efficiencies. However, the process of growing single-crystal silicon ingots requires large amounts of energy and time which further increases the cost of the device. Despite these issues, silicon remains the dominant photovoltaic material at present.

1.2.7.3 The Second Generation

The second generation of photovoltaics was characterised by trying to reduce the cost of photovoltaic devices, either by using a less energy intensive process for producing silicon, or by using a different material[145]. Initial work on reducing the cost of the Si solar cell was carried out by Chapin, using polycrystalline wafers, however trap sites as the grain boundaries limited the efficiencies he could obtain.

The first developments in thin-film photovoltaics was the development of the CdS solar cell, initially by Nadjakov *et al.*, with the group of D.C. Reynolds at the USAF Aerospace Research Laboratory working independently on the same material during the 1950s[147]. In contrast to the hundreds of microns of material required for a Si cell, CdS required only 1µm of absorber. The CdS cell was, however, found to be unsuitable for terrestrial application, as performance degraded rapidly upon exposure to air or water[148].

GaAs solar cell technology was also being developed during this period, but was of limited interest for terrestrial use due to the high cost of gallium[148].

Instead, interest in CdTe and copper indium selenide ($CuInSe_2$, CIS) increased. By 1975 CIS cells had achieved an efficiency of 12%[149]. At time of writing, the two most commonly used thin film technologies are CdTe and copper indium gallium diselenide ($CuIn_{1-x}Ga_xSe_2$,

CIGS) both of which are produced commercially. Both materials have considerable issues, however, Cd, Te and In are all relatively scarce in the Earth's crust, resulting in devices that are relatively costly. The relative abundancies are given in Table 1.1. Another issue for CdTe is that the commonly used $CdCl_2$ bath results in highly toxic Cd salts[150].

Element	Relative Abundance in Earth's Crust ($x10^{-4}$ % by weight)[151]
Cd	0.13
Te	0.001
In	0.25
Ga	19
Si	295000

Table 1.1 – A table showing the relative abundancies of elements commonly used in 2nd generation PV cells.

The typical architecture of a substrate-configuration thin-film solar cell, as used in CIGS and CZTS(e) devices is shown in Figure 1.11. This device consists of an, approximately 1 µm thick, *p*-type absorber deposited on top of a metallic back contact typically deposited on glass. A *p*-*n* junction is then formed with a 30nm *n*-type buffer layer. A *n*-type transparent conducting oxide is then deposited on top of the buffer layer, and a grid of metallic front contacts collects the generated electrons.

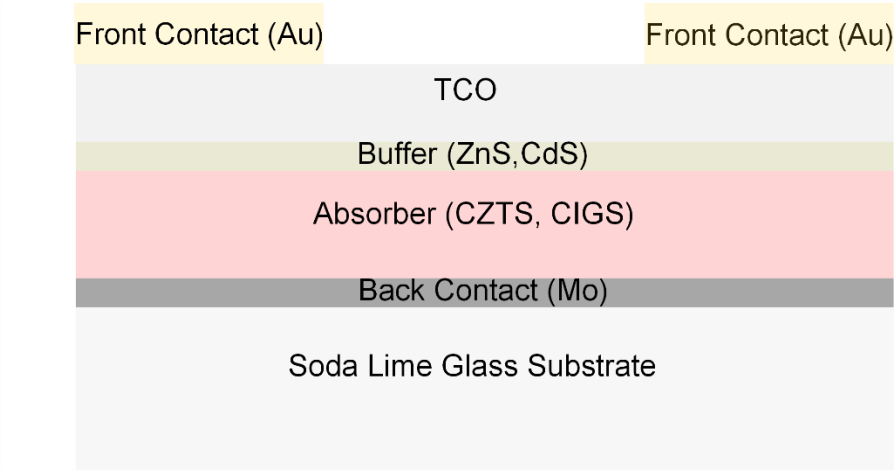

Figure 1.11 - The typical architecture of a substrate-configuration thin-film solar cell, as is typically used in CIGS and CZTS(e) devices.

For CIGS devices, the back contact is typically polycrystalline molybdenum. The typical buffer used is CdS, with alternative buffers being In_2S_3, ZnS, and $ZnO_{1-x}S_x$.

1.2.7.4 The Third Generation

The third generation of photovoltaics is characterised by the use of comparatively abundant, non-toxic materials in comparison to the second generation[152]. One such material is copper zinc tin sulphide (selenide) ($Cu_2ZnSnS(e)_4$, CZTS(e)). This material is closely related to CIGS, and is made substituting the group III elements for group II-IV elements in a 1:1 ratio. CZTSSe is not the only material of interest in this generation, many other Cu-chalcogenides are of interest, including Cu_2S[153], Cu_2SnS_3[154], [155], $CuSbS_2$[156], [157], Cu_3BiS_3[158]–[160] and $CuSbSe_2$[156]$_s$. Non-chalcogenide materials are also consideration, including the hybrid organic-inorganic halide perovskites, such as methylammonium lead iodide (MAPI)[161]–[163], SnS[164], [165], Sn_2S_3[165], $AgBiI_4$[166], $ZnSnN_2$[167] and Cu_3N[168], [169].

1.2.7.5 Beyond the Third Generation?

Extension of thin film technologies beyond the third generation to beat the Shockley-Queisser limit[117] has also been considered. One possible method to beat the limit are tandem solar cells, which are effectively a stack of solar cells with decreasing absorber band gaps, to limit loss due to charge carrier thermalisation[170], [171]. A second method is the so-called hot-carrier method, where the produced charge carriers are extracted before thermalisation occurs[172]–[176]. Either method allows for the efficiency of the photovoltaic device to approach the Chambadal-Novikov-Curzon-Ahlborn (CNCA) efficiency[177]–[179] of an endoreversible heat engine with temperatures between the surface temperature of the Earth and that of the sun. It should be noted that the CNCA efficiency, (η_{CN}), is the efficiency of an endoreversible heat engine operating at maximum power between a hot and cold reservoir of temperatures T_H and T_C and is given by the relation in equation (1.10)[177]–[181]. Higher efficiencies are possible, but only at reduced power output. In contrast, the Carnot efficiency, (η_C) is given by the relation in equation (1.11)

$$\eta_{CN} = 1 - \left(\frac{T_C}{T_H}\right)^{1/2} \tag{1.10}$$

$$\eta_C = 1 - \frac{T_C}{T_H} \tag{1.11}$$

As the temperature of the hot reservoir is necessarily larger than that the of the cold reservoir, the CNCA efficiency is always lower than that of the Carnot efficiency operating between the same temperatures. As a solar cell operates due to radiation rather than

conduction of heat, the CNCA efficiency is modified by the Stefan-Boltzmann law in a non-trivial manner, beyond the scope of this thesis.

Engine Type	Thermodynamic Efficiency Limit (%)
Carnot	94.8
Endoreversible	85.4[182]–[184]

Table 1.2 – A table showing the efficiencies of a Carnot engine and an endoreversible engine operating at maximum power.

However, the final result is still considerably less than that of a Carnot engine operating between the same temperature reservoirs, as can be seen in Table 1.2. Full treatments of the thermodynamics of a photovoltaic cell can be found in Chapter 3 of Ref [182] and Refs [180], [183], [184].

1.3 WHY CZTS(SE)?

If CIGS is already a commercially-viable technology, why should we be interested in going beyond the second generation of photovoltaics? The key issue is the relative scarcity of indium, which is already in large demand for III-V semiconductors, and transparent conducting applications. Thus, deployment of CIGS is limited due to the cost of the material required to actually produce the cell.

Element	Relative Abundance in Earth's Crust ($x10^{-4}$ % by weight)[151]
In	0.25
Ga	19
Zn	83
Sn	2.5
Si	295000

Table 1.3 - This table shows the relative abundance of the scarce elements used in CIGS devices, in contrast to those used to replace them in CZTS.

The key advantage of CZTS(Se) over CIGS is that the elements are considerably more abundant than indium and hence will be cheaper. Even if the efficiency of CZTS(Se) cells does not reach the same efficiency as CIGS, if the cost per KWh is cheaper, it is more likely that widespread adoption may occur. The estimated efficiency required for CZTS(Se) to be commercially viable is estimated to be approximately 15 %[185], in comparison, the current record efficiencies for CZTS and CZTSSe cells are 11.0±0.2 % and 12.6±0.3 % respectively[186].

1.4 CZTS(Se)

1.4.1 Structural and Electronic Properties of CZTS(Se)

CZTSSe is closely related to CIGS, and has a similar crystal structure to the chalcopyrite structure of CIGS, namely the kesterite structure. The kesterite structure is produced from the chalcopyrite structure, simply by replacing the trivalent In/Ga ions, with bivalent Zn and IV-valent Sn ions. CZTSSe is also known to take the closely related stannite structure[187]–[191], and a metastable wurtzite structure[192]–[194]. A diagram of the kesterite and stannite structures of CZTSSe is shown in Figure 1.12 alongside the chalcopyrite structure adopted by CIGS.

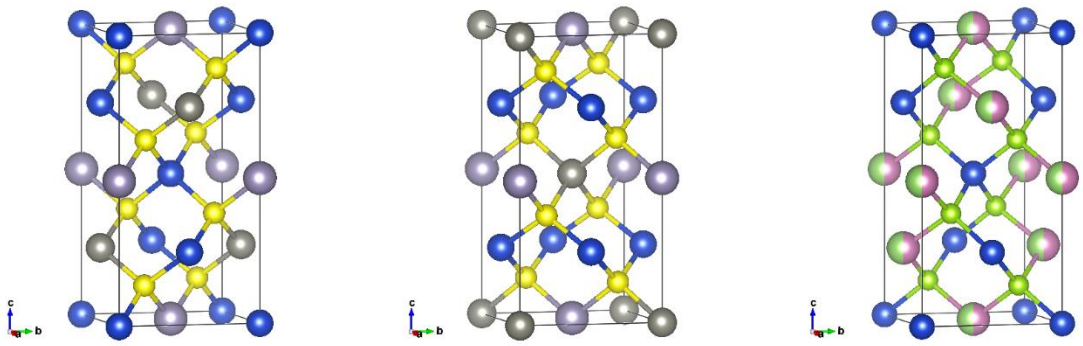

Figure 1.12 – Crystal structures of kesterite CZTS[195], [196]*, Stannite CZTS*[197] *and CIGS*[198]*, showing the individual Cu (blue), Zn (dark grey), Sn (light grey), S (yellow), In (dark green), Ga (pink) and Se (light green) atoms.*

In the kesterite structure the cations each exhibit tetrahedral co-ordination with four sulphur anions, whilst each sulphur atom is co-ordinated with two copper, one zinc and one tin atoms. The unit cell thus has the $I\bar{4}$ space group. The cations occupy lattice planes alternating between Cu-Zn and Cu-Zn planes, each in a 1:1 ratio. The stannite structure is similar to the kesterite structure, with the major difference being in the cation ordering. In contrast to the mixed cation lattice planes seen in the kesterite structure, the stannite structure has 1:1 Zn-Sn planes alternating with Cu-only cation planes. As such the symmetry of the stannite unit cell is different, resulting in a different space group, namely the $I\bar{4}2m$ space group. The chalcopyrite structure of CIGS is similar to both, where the cation lattice planes only consist of 1:1 mixtures of Cu and (In/Ga).

As the cation ordering is not symmetric about the anion planes, in either the kesterite or stannite phases, the tetrahedra are distorted due to the differences in the atomic radii. The bond lengths and therefore the electronic structures are likely to be different to CIGS.

Material	a (Å)	ΔE (meV/atom)	E_g (eV)
Kesterite CZTS	5.467	0	1.50
Stannite CZTS	5.458	2.86	1.38
Kesterite CZTSe	5.763	0	0.96
Stannite CZTSe	5.763	3.79	0.82

Table 1.4 – This table shows the structural, thermodynamic and electronic properties of kesterite and stannite CZTS and CZTSe. The data is reproduced from Ref. [199].

The stannite phase of CZTSSe is slightly less stable than the kesterite phases, with the energy difference being only a few meV per atom[199]. The band gaps of both kesterite CZTS (1.50 eV[199]) and CZTSe (0.96 eV[199]) compare favourably with that required to achieve maximum efficiency, however usually an alloy of the material is used for devices, $Cu_2ZnSn(S_xSe_{1-x})_4$. This material shows relatively small band bowing with a bowing parameter $b \approx 0.10$ eV[200]. This is similar to the $CuGa(S_x,Se_{1-x})_2$[201] and $CuIn(S_x,Se_{1-x})_2$[202], which also exhibit small bowing with composition. This is likely due to the small differences in ionic size and chemistry of the S and Se anions[199], [202].

In contrast to many of the Cu-based chalcogens, copper vacancies are not thought to be the dominant acceptor level in kesterite-based materials. Instead, the dominant shallow acceptor is thought to be Cu_{Zn}[112].

1.4.2 CZTSSe Issues

The current record efficiencies recorded for CZTS and CZTSSe cells are 11.0±0.2% and 12.6±0.3%, well short of those record for CIGS (22.6±0.5%) and CdTe (22.1±0.5%)[186], despite CZTS and CZTSSe being closely related to CIGS. The parameter that seems to be causing the low efficiency is the open-circuit voltage, which almost universally shows a large open-circuit voltage deficit[203]–[206]. Numerous reasons have been given for this deficit, including the formation of a detrimental layer at the back contact, the presence of binary and tertiary secondary phases within the absorber, poor band alignments, grain boundaries, defect sites caused by Cu_{Zn} and Zn_{Cu} due to the small differences in their ionic radii and the presence of intermixed stannite and kesterite phases. Each of these will be addressed in its own right in this section.

1.4.2.1 Detrimental Phases at the Back Contact

Another considerable issue is the formation of a MoX_2 layer (X=S, Se) at the interface between the absorber and the back contact[207]–[209], an example of which can be seen in Figure 1.13. Experimentally, a Schottky contact at the back contact is observed in low-

carrier density devices, which has been suggested to be due to the formation of the MoX_2 layer[210], [211]. However, in higher carrier density devices, the contact is observed to be Ohmic[210], [211].

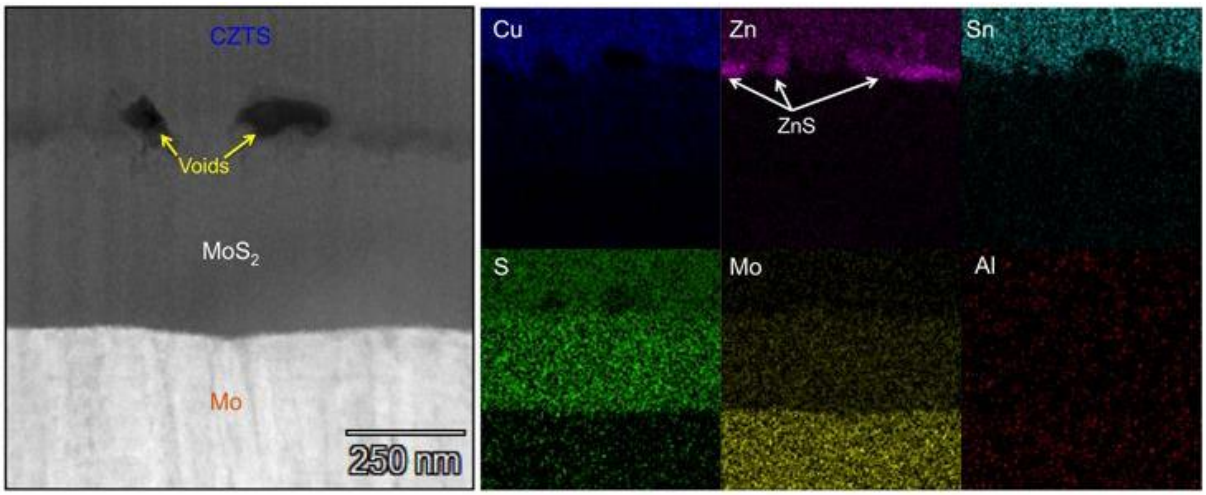

Figure 1.13 – Cross-sectional transmission electron microscopy (TEM) image showing the CZTS absorber layer, the Mo back contact and the detrimental MoS_2 layer. Also shown are energy dispersive x-ray spectroscopy (EDX) images, mapping the elemental distributions in the corresponding region. Reproduced from Liu et al.[212] *under a Creative Commons Attribution 4.0 International License*

The presence of the MoX_2 layer is thought to lead to considerable series resistance[212], and since the CZTSSe/Mo interface is thermodynamically unstable[208], [213], decomposition of the CZTSSe into secondary phases at the back contact is common. An example of such a decomposition pathway is seen in equation (1.12)[208], [213].

$$2Cu_2ZnSnX_4 + Mo \leftrightharpoons 2Cu_2X + 2ZnX + 2SnX + MoX_2 \qquad (1.12)$$

Three main methods to limit the formation of this layer have been investigated: firstly, the use of an alternative metallic contact; the introduction of an ultra-thin chalcogen diffusion barrier between the absorber and back contact; and the use of a rapid thermal annealing process.

Alternative back contacts have been considered to avoid the formation of the MoX_2 layer. These can generally be split into two methods: either an alternative metallic contact can be used[214]–[216]; or alternatively a transparent conducting contact, such as a transparent conducting oxide[217], [218], [227]–[233], [219]–[226] or graphene[234], [235] can be used to produce a bifacial photovoltaic cell. Work on bifacial kesterite-based solar cells are, however, limited by the lack of high performance *p*-type TCOs[236], [237], as native donors, such as oxygen vacancies, often compensate for the acceptors[236], [237].

Numerous authors have reported using different chalcogen diffusion barrier layers, including Al_2O_3[212], TiN[208], [213], [215], [238]–[240] and others[215], [241], [250]–[254], [242]–[249] which will be discussed here. Liu *et al.*[212] have fabricated an ultra-thin CZTS photovoltaic cell with and without an intermediate Al_2O_3 diffusion barrier layer to inhibit the formation of MoS_2. They observe an increase in the photo-conversion efficiency from 7.34 % to 8.56 %.

Rapid thermal annealing (RTA) processes have also been investigated, showing increased device statistics with respect to a slower annealing process[254]–[257]. Some studies show that an RTA process can inhibit the formation of the MoX_2 layer, due to either the formation of a thin MoO_2 layer[254], or by densifying the Mo films, making chalcogen diffusion more difficult[255]. In contrast, other authors have found that the RTA process has no effect on the thickness of the MoX_2 layer[258]. Further work is therefore required to establish the effects of the RTA process and distinguish these from other effects that may be occurring during device fabrication.

1.4.2.2 Secondary Phases

The presence of binary and tertiary secondary phases is also problematic within the CZTSSe system. Due to the complex quaternary or quintenary nature of the material, the region of the phase diagram where kesterite CZTSSe is formed is particularly small[259]. A representative phase diagram of the Cu_2S-ZnS-SnS_2 quasi-ternary system is shown in Figure 1.14.

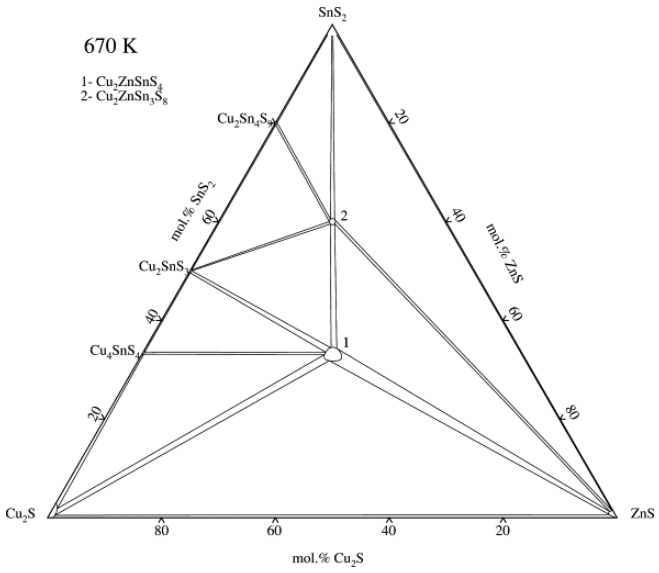

Figure 1.14 – The phase diagram of the quasi-ternary Cu_2S-ZnS-SnS_2 system at 670K. The region labelled 1 is the region where Cu_2ZnSnS_4 is the preferred phase. Reprinted from Olekseyuk et al.[259] *Copyright 2004, with permission from Elsevier.*

Particularly problematic is the SnS binary sulphide phase, as the CBM of CZTS occurs at a similar energy relative to the vacuum level as the VBM of SnS[165], [260]. Thus, the SnS secondary phase will, in effect, act as a short-circuit and lead to considerable recombination. Also problematic is the stannite phases of CZTS. As the energy difference per atom is only a few meV greater than that of the kesterite phase, there will often be intermixed stannite and kesterite phases in the absorber layer. This is particularly problematic due to the reduced band gap of the stannite phases, which results in stannite regions acting as potential trap sites and can cause band tailing.

Although the secondary phases are known to be a considerable issue in CZTSSe photovoltaics, identifying secondary phases in the material is not simple. X-ray diffraction, which is commonly used in material science for phase identification, is hindered as many of the secondary phases have peaks at similar angles to CZTSSe.

Instead, XRD is commonly used in conjunction with Raman spectroscopy to identify secondary phases, however Raman spectroscopy also has some issues identifying phases, as the spectrometers are in many cases not correctly calibrated.

1.4.2.3 Detrimental Band Alignments

Due to the similarities with CIGS, the CIGS device architecture is simply reproduced in most cases, and only the absorber layer is changed. Such naïve adoption of the CIGS structure is one possible reason for the relatively poor efficiencies obtained from CZTSSe devices. Numerous authors have suggested that the band alignment of CZTSSe with CdS is inappropriate[261]–[269], although some results have contradicted this[270], [271], instead suggesting numerous other materials including $CdS_{1-x}O_x$[272] ZnO[273], [274], ZnS[273], [275]–[277], $Zn_xCd_{1-x}S$[278], ZnSe[275], ZnO_xS_{1-x}[264], [279]–[284], $Zn_xSn_{1-x}O_y$[285]–[287], CeO_2[288], TiO_2[289]–[291] and In_2S_3[264], [273], [292], [293]. Another interesting buffer layer is the Ag-based material Ag_2ZnSnS_4, which has recently been reported as a buffer layer for the first time[294]. Alternatively, band gap narrowing due to interface states, between the CdS and CZTS(Se) layer, may also render CdS unfit[295].

Contrary to expectation, theoretical models predict that a potential step up of $0 < \Delta E_c < 0.4$ eV from the absorber to the buffer layer is advantageous[161], [296], [297], as a cliff-like band offset at the interface results in considerable recombination.

An alternative approach to using a different buffer layer, is to alloy the CZTS(Se) with another material, to modify the band positions and reduce secondary phase

formation[298]. $(Ag,Cu)_2ZnSn(S,Se)_4$[299]–[302], $Cu_2Zn(Ge,Sn)(S,Se)_4$[303]–[307], $Cu_2(Zn,Fe)Sn(S,Se)_4$[298], [308]–[311], $Cu_2(Zn,Ni)Sn(S,Se)_4$[312]–[314], $Cu_2MgSn(S,Se)_4$[315], [316], and other alloys[272], [298], [325], [326], [317]–[324] have been attempted to date.

1.4.2.4 Defects and Disorder

Defects have also been identified as a possible explanation for why kesterite photovoltaics do not reach comparable efficiencies to that of CIGS. However, experimental work investigating defects is challenging, particularly due to the similarities in ionic mass and radius of the Cu and Zn cations. Experimentally most work investigating the defects of the kesterite system have been by photoluminescence, Raman spectroscopy[327] and neutron and synchrotron x-ray diffraction[328].

A particularly problematic defect for the pure sulphide phase of CZTS is the tin-on-zinc (Sn_{Zn}) antisites, which has been identified recently[329]. These antisites are suggested as the origin of the persistent electron traps identified by time-resolved photoluminescence[330]. These defects are more stable in the pure sulphide phases, and have been proposed as the reason why alloyed and pure-selenide kesterite materials have a higher efficiency than the pure sulphide phase[329].

Other problematic defects are the zinc-on-copper (Zn_{Cu}) antisites, which are found to be extremely common from first-principles calculations, due to the low formation energy of the Cu_{Zn}-Zn_{Cu} defect clusters, which can be as low as a few meV[331], [332]. The Zn_{Cu} defects are identified as donors[331], [333], [334], thus Cu_{Zn}-Zn_{Cu} clusters are in fact compensating defects[331]. Cu_{Zn} defects have in fact been proposed as the dominant acceptor in kesterite material[112], and the fact that high performance cells are grown in Cu-poor and Zn-rich conditions[335], [336], when Cu_{Zn} defects are less likely to form and V_{Cu} more likely, would suggest that the compensating Cu_{Zn}-Zn_{Cu} defect clusters do have a detrimental effect upon the performance of the devices[331], [337]. V_{Cu} are predicted to be the most common neutral defect in both the pure sulphide and pure selenide phases[191]. Large densities of defects have also been suggested to cause the band gap of the material to vary from the expected gap, which will naturally also affect the band alignment[332], [337], [338]. Band tailing is widely seen across kesterite materials, recently, the [$2Cu_{Zn}^{-}$ + Sn_{Zn}^{2+}] defect cluster has been proposed as the main origin band tailing in the kesterite family of materials[339].

1.5 Overview of this Thesis

In the next chapter we will consider the main characterisation techniques used for the work described in this thesis. We will begin b considering ultra-high vacuum and why UHV techniques are necessary for understanding the properties of materials.

We will then discuss photoelectron spectroscopy techniques and their application to determine the chemical and electronic properties of materials. A particular focus will be on x-ray photoemission spectroscopy (XPS) and its use in determining the band offsets at heterojunction interfaces, and the combination of XPS measurements of the valence band and inverse photoemission spectroscopy to determine the band gap of materials.

After this, there will be a discussion on the identification of secondary phases within kesterite materials and how x-ray diffraction and Raman spectroscopy can be used to identify these secondary phases. A short discussion on the Hall effect focussing on the van der Pauw method to determine carrier densities and mobility will follow. Finally, the chapter will conclude with a short discussion on how theoretical methods such as density functional theory or $\boldsymbol{k} \cdot \boldsymbol{p}$ perturbation theory can be used by the experimentalist to elucidate further information from a given material system.

Chapter 3 considers the photoelectron spectroscopy of kesterite materials deposited by sputtering and by spin-coating of nanoparticle inks. The band alignments with respect to the vacuum level for the synthesised layers are found by XPS and optical techniques and compared with those determined for alternative buffer layers to CdS using the Anderson electron affinity rule.

Chapter 4 builds on the results of chapter 3 by considering the band alignments of ZnO/CdS/CZTSSe and ZnO/In_2S_3/CZTSSe stacks, found by the Kraut method and carefully Ar^+ ion etching the stacks. The experimentally determined band alignments are then used in simulated solar cells to determine the device characteristics, which are then compared to experimental solar cells from literature. The requirement for a small, positive conduction band offset is therefore seen.

Chapter 5 moves from considering the absorber-buffer interface, to the absorber-back contact interface. This interface is particularly problematic in kesterite materials due to the formation of *n*-type molybdenum-dichalcogenides, resulting in a diode opposed to the main photodiode of the device. By Ar^+ ion etching single crystals of the molybdenum-dichalcogenides, the roles of chalcogen vacancies in the MoX_2 materials is investigated, and

thus the requirements placed on device synthesis for kesterite and CdTe to avoid the formation of detrimental layers at the back contact.

Chapter 6 considers the uppermost layer of the device; the window layer. The window layer is typically a transparent conducting oxide (TCO), the most common of which is tin-doped indium oxide (ITO). Indium is particularly scarce and expensive due to its use in touch screens and III-V materials, thus alternative TCOs are likely to be required. We discuss why ZnO and SnO_2 are not suitable for this task and suggest Ga_2O_3 as an alternative to In_2O_3.

The properties of β-Ga_2O_3 single crystals are therefore investigated to determine whether Ga_2O_3 could be suitable as a window layer in photovoltaics and whether Ga_2O_3 exhibits charge accumulation or depletion at the vacuum interface. Previous literature reports suggest that only depletion is observed in contrast to this work.

The properties of alternative polymorphs to the β-phase of Ga_2O_3 synthesised on sapphire substrates are then investigated by photoemission, and the Auger parameters for each, evaluated.

The thesis will conclude with a summary of the findings of this work before presenting an outlook for the future development of the architecture of kesterite photovoltaic devices.

2 EXPERIMENTAL METHODS

2.1 ULTRA-HIGH VACUUM

In surface science, ultra-high vacuum (UHV) is ubiquitous, however as surface science techniques are becoming more widely applied to less ideal, more realistic materials, vacuum technology has become more widespread.

There are several regimes of vacuum, starting from a poor or rough vacuum, up to extreme ultra-high vacuum (XHV). These regimes and the corresponding pressure ranges are tabulated in Table 2.1. The division between rough or low vacuum and high vacuum occurs at the point in a typical vacuum chamber, where the nature of gas flow changes from a viscous flow, where scattering is primarily from other gas molecules; to molecular flow, where interactions are primarily with the chamber walls[340].

In the application of surface science techniques, two main reasons are given for the requirement of UHV: the first reason is that many surface science techniques involve the detection of or a knowledge of the kinetic energy of a charged particle, however at atmospheric pressure the mean free path (MFP) at room temperature is approximately 100 nm. The equation for the MFP of a neutral molecule is given by equation (2.1)[341], where *d* is the molecular diameter. From this equation, the MFP of a hydrogen molecule in the various pressure regimes are calculated and are presented in Table 2.1. In comparison, to the 100 nm MFP in atmospheric conditions in UHV conditions the MFP is of the order of kilometres, hence UHV allows for the detection of these charged particles.

$$\lambda = \frac{k_B T}{(\sqrt{2})\pi d^2 P} \qquad (2.1)$$

Secondly, UHV techniques are typically sensitive to the sample surface, however at 1×10^{-6}mbar it takes approximately 1 second to form a monolayer of residual gas upon the sample. Typically, surface science measurements are measured on a timescale of hours, so the experimentalist would want the sample to stay clean for at least one hour. To achieve this, UHV is required. A pressure of 1×10^{-9} mbar is required to obtain a monolayer

deposition time of 1 hour[342]. The time required for a monolayer of residual gas to be deposited upon the sample in the pressure regimes is also given in Table 2.1.

Level of Vacuum	Pressure Range (mbar)[340]	H_2 Mean Free Path (m)	Monolayer Deposition Time (s)[342]
Atmosphere	1000	$1x10^{-7}$	$<1x10^{-6}$
Rough/Low	$1000>p\geq1x10^{-3}$	$1x10^{-5}$	$1x10^{-6}$
High Vacuum (HV)	$1x10^{-3}>p>1x10^{-9}$	$1x10^{2}$	1
Ultra-High Vacuum (UHV)	$1x10^{-9}>p>1x10^{-12}$	$1x10^{5}$	3600
Extreme-Ultra-High Vacuum (XHV)	$p<1x10^{-12}$	$>1x10^{5}$	>3600

Table 2.1 - This table shows the pressure ranges for the respective vacuum regimes and the calculated mean free paths.

2.2 Sample Preparation

Materials of interest inevitably need to be prepared in some way prior to being inserted into a vacuum chamber. Usually, this consists of being mounted upon a sample plate, allowing for the sample to be moved to different positions in the chamber; and making an electrical connection to the chamber, via the sample plate, through which any accumulated charge is depleted or replenished. In this work, samples were mounted upon Omicron-style sample plates. For most of the work presented in this thesis, the sample plate was simply a flat steel Omicron plate. However, for section 6.1, the sample was mounted on an Omicron direct heating sample plate, allowing for a better, more secure electrical contact. A schematic diagram of this plate is shown in Figure 2.1.

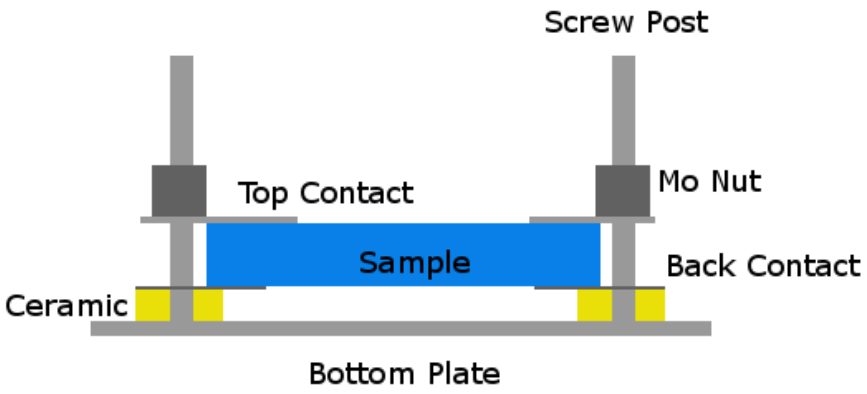

Figure 2.1 – A schematic diagram showing the Omicron-style direct heating plate, as used for grounding a sample.

One method of mounting the sample and making electrical contact is the use of conductive double-sided carbon tape. The tape is placed on the sample plate and makes an electrical contact through the back face of the sample. However, if the substrate is insulating, as is commonly the casein photovoltaic materials, or if the conductivity of the sample is too low, this can still lead to considerable charging effects, particularly if measured by monochromatic XPS. As such, electrical contacts are usually also made with the front face of the sample, using one or more metallic strips across part of the face of the surface. For this work, Ta foil was cut into strips, and spot welded on either side of the sample, to make electrical contact with the top surface. This approach is used in chapters 3 and 4 and section 6.2. For the work presented in chapter 5, samples were mounted using only carbon tape, due to the thin nature of the samples considered.

In the previous section, how UHV conditions aid in keeping samples clean was discussed, however the methods by which samples are, in fact, cleaned was not. After all, samples will pass through air and rough vacuum before reaching the UHV chamber, so will already have multiple layers of contamination prior to measurement.

In this work, two methods were used for sample cleaning, namely Ar^+ ion etching or sputtering, and thermal annealing, both of which will be discussed in this section.

2.2.1 Ion Etching/Sputtering

In general, ion etching is performed by leaking an inert gas into the vacuum chamber, the inert gas is then ionised and accelerated towards the target by an anode. The ions then collide with the target surface, transferring momentum and energy. Depending on the accelerating voltage used, this scattering process may provide sufficient energy to liberate the top-most atoms of the sample surface. In practice this often results in a damaged sample which may require annealing to remove the defects introduced by the sputtering process[341].

The ion source used for this work was the PSP Vacuum Ltd. ISIS 3000 ion source, which is an oscillating electron discharge source[a], a schematic diagram of which can be seen in Figure 2.2. The oscillating electron discharge source, in this case, consists of a thoriated-tungsten filament which thermionically emits electrons between a pair of positively biased electrodes, which are surrounded by a conducting cylinder. The electrodes will then cause

[a] Manufacturer's website.

the emitted electrons to follow a long, oscillatory path, which will always pass between the two electrodes[343]–[345].

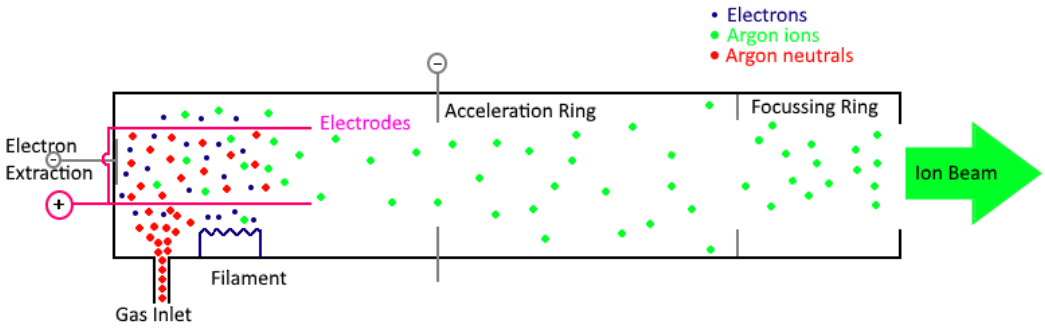

Figure 2.2 – A schematic diagram of the PSP Vacuum Ltd. ISIS 3000 oscillating electron discharge ion source used in this work.

The inert gas can then be injected close to the orbiting electrons. Each electron can then generate a large number of ions, due to their long path length. Injecting the gas close to the electron source will result in a greater local pressure, allowing for a lower chamber pressure to be used for the same beam current density in comparison to other designs[343]–[346].

The newly-formed ions are then accelerated by an anode towards the sample, passing through an electrostatic focussing ring to maximise the beam current density. The diameter of the ion beam is estimated to be 10mm[b]. The accelerating voltage of the source has a range of 0.1-3kV, however for this work, low-energy ions (0.25-1.00 kV accelerating voltages) were typically used to prevent the preferential sputtering that can occur at high ion energies[347], [348].

To avoid Ar^+ ion implantation, samples were oriented such that the sample normal was at an angle of 45° to the beam current density vector.

2.2.2 Thermal Annealing

Whilst the ion etch described previously is appropriate for most samples, some require a more careful cleaning method, as sputtering of highly-mismatched cation-anion systems can result in the preferential sputtering of the lighter element. The metal-oxides are more commonly cleaned *via* a thermal anneal for this reason[349].

[b] Manufacturer's website.

By heating the sample to a sufficiently high temperature, the constituent atoms gain enough thermal energy that they are free to move about within the sample, thus point defects, such as vacancies or antisites can be removed.

Samples requiring annealing were heated radiatively by a tungsten filament, capable of currents up to 7A. Two methods of temperature measurement were used, Cu-Ni thermocouple cable, and an infra-red pyrometer.

2.3 Photoelectron Spectroscopy

Photoelectron spectroscopy (PES) naturally arises from the photoelectric effect first successfully explained by Einstein in his 1905 work "On a Heuristic Point of View about the Creation and Conversion of Light"[350] (an English language translation of which can be found in Ref [351]). The 1921 award of the Nobel Prize in Physics to Einstein was "especially for his discovery of the law of the photoelectric effect"[352]. After Einstein's explanation of the photoelectric effect, some experimental work was performed investigating the photoelectric effect of different materials, however the development of PES would wait until after the second world war, due to a lack of technology.

The next stages in the development of PES occurred in Uppsala, Sweden during the 1950s in the group of Kai Siegbahn[353], [354]. At the time it was more commonly known as electron spectroscopy for chemical analysis (ESCA) as the shift in the core-level binding energies of a particular element were observed to shift depending on the chemical environment. Half of the 1981 Nobel Prize in Physics was awarded to Kai Siegbahn for "his contribution to the development of high-resolution electron spectroscopy"[355].

2.3.1 X-ray Photoelectron Spectroscopy

X-ray photoelectron spectroscopy (XPS) is the form of PES which uses x-rays to produce photoelectrons, and is commonly used to probe the chemical and electronic structure of materials.

Despite the fact that the x-rays probe the bulk of the sample in question, XPS is a surface-sensitive technique. This is due to the inelastic mean-free-path of the photoelectrons, which obeys a 'universal curve' given in equation (2.2), where λ is in Ångstroms and E is in electron volts[356], [357].

$$\lambda = \frac{1430}{E^2} + 0.54\sqrt{E} \qquad (2.2)$$

This relationship is also plotted in Figure 2.3.

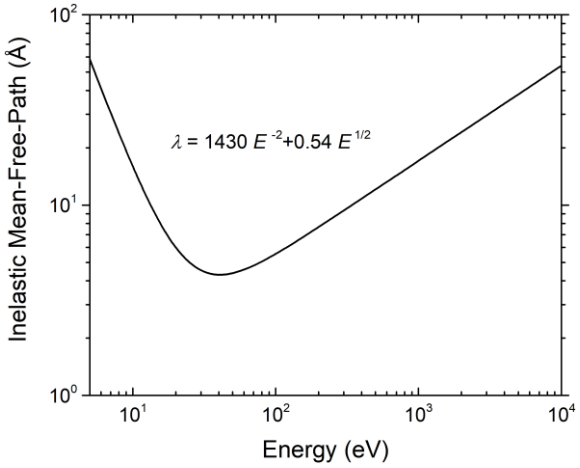

Figure 2.3 - The universal curve for the inelastic mean-free-path of the electron in a solid

The intensity of electrons from a particular depth, *d* and an energy, *E* that reach the sample surface is then given by the Beer-Lambert law, given in equation (2.3).

$$I(d,E) = I_0(E)e^{-\frac{d}{\lambda}} \qquad (2.3)$$

Thus, 86.5% of all photoelectrons that reach the surface originate from within two IMFP of the surface. A table of the percentages of the electrons originating up to a particular depth is given in *Table* 2.2.

d/λ	**PERCENTAGE OF ELECTRONS ORIGINATING UP TO THIS DEPTH (%)**
1	63.3
2	86.5
3	95.0
4	98.2
5	99.3

Table 2.2 - A table showing the percentage of electrons with their origin up to a particular depth

Hence, for a lab x-ray source ($h\nu \approx 1000$ eV), the IMFP is of the order of 1-2 nm, whereas for ultraviolet photoemission spectroscopy (UPS) ($h\nu \approx 20$ eV) the IMFP is of the order of 5 Å. Hence UPS is more sensitive to any surface contamination of the sample. Hard XPS (HAXPES) ($h\nu \approx 6000$ eV) is less surface sensitive again, with an IMFP of around 4-5 nm.

2.3.1.1 X-ray Generation

Two different x-ray sources were used in the work presented in this thesis, the first is a dual-anode laboratory source capable of producing non-monochromatic Al K_α and Mg K_α x-rays. The second x-ray source is a monochromatic Al K_α source, consisting of the x-ray source itself shown in Figure 2.5, and the monochromator a diagram of which is given in Figure 2.4. For the monochromatic source, the sample, source and crystalline mirror are placed such that each is located on the edge of a Rowland circle, the reasons for which will be discussed later.

In both x-ray sources, the principles of generating the x-rays are the same. A large current, typically 2-3 A is passed through a thoriated tungsten filament resulting in thermionic emission of electrons and accelerated towards the anode by a large voltage, typically 12.5 kV as this is where the maximum quantum yield is for an Al anode. The electrons then interact with the anode material, resulting in the emission of x-rays of the characteristic energies superimposed upon the bremsstrahlung spectrum. Bremsstrahlung occurs due to the deceleration of the electrons caused by interactions with the positively charged atomic nuclei. The characteristic x-rays occur due to the emission of secondary electrons from the core-levels of the sample, electrons in higher energy states can then relax into the unoccupied state by emitting a high energy photon of a characteristic energy. The fundamental resolution of the source is thus limited by the lifetime of the unoccupied state.

The monochromator uses the Bragg diffraction of the x-rays from a curved Quartz $(10\bar{1}0)$ single crystal mirror with a radial curvature of 250 mm to obtain monochromatic light. The diffraction conditions are given by the well-known form of the Bragg condition given in equation (2.4).

$$n\lambda = 2d\sin\theta \tag{2.4}$$

Thus, the non-monochromatic light generated by the source is monochromated, as only the radiation with a wavelength satisfying the Bragg condition will be diffracted and hence incident upon the sample. The x-rays generated by the source are innately dispersive, i.e. they are not travelling in the same direction, which limits the maximum possible intensity that can be achieved. To increase the intensity obtained the x-ray anode, the sample and the crystal mirror are all placed on the edge of a Rowland circle. As can be seen in the ray diagram in Figure 2.4,the geometry results in the x-rays being focused onto a point equidistant from the axis of the crystal as the source.

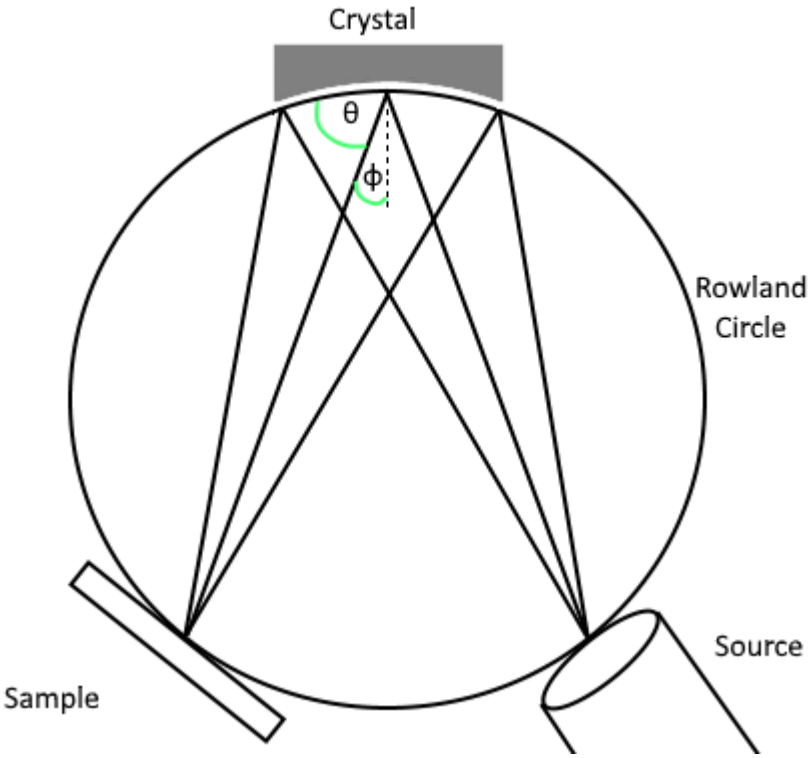

Figure 2.4 – The ray diagram for a monochromatic X-ray system.

Likewise, by using a curved crystal with the same radius of curvature as the Rowland circle, a greater intensity can be achieved, as all the x-rays of the correct energy incident upon the mirror will be focussed onto the sample. Thus, the bremsstrahlung and the lower energy characteristic x-ray (i.e. those that do not obey the Bragg condition) are removed contributing to a lower background signal.

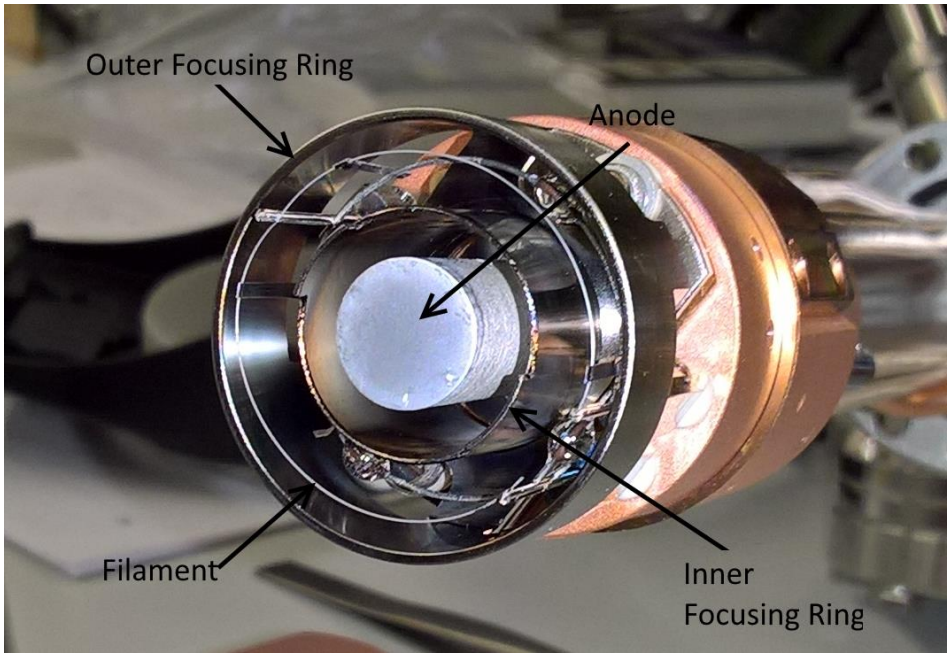

Figure 2.5 – A labelled photograph of the x-ray source used to obtain monochromatic Al K_α spectra.

In contrast, the dual anode source, does not remove the lower energy characteristic x-rays, however some of the bremsstrahlung radiation is removed by the Al foil window at the end of the source. The absorption of the bremsstrahlung by the window also leads to the emission of secondary electrons which can aid in neutralising the sample for less conductive samples.

An alternative way of generating x-rays is to use a synchrotron, which accelerates electrons around a storage ring using a series of bending magnets. The acceleration of the electrons around the ring results in the emission of synchrotron radiation. In modern synchrotrons, the radiation generated by bending magnets alone is not brilliant enough for most uses. Instead an insertion device, (an undulator or a wiggler) is used to obtain a higher brilliance. These insertion devices consist of a periodic, alternating magnetic field, which causes the electron beam to be deflected periodically in the transverse direction. The acceleration causing the electron to follow the deflected trajectory causes the electrons to radiate across a relatively-broad spectrum. By varying the distance of the magnets from the electron beam (the gap height) of the strength of the magnetic field, the critical photon energy can be changed, allowing for a range of photon energies to be produced[101].

A series of monochromator crystals using either or both of the Bragg-Brentano and the Laue geometries can then be deployed to obtain a monochromatic beam[359]–[362], which can then be focussed on to the sample using a series of curved mirrors[359]. As the positions of the various optical components can drift over time, resulting in slightly different photon energies, correct calibration of the spectrometer is vital. This is often performed using the Au 4f core-levels and its Fermi-level. Convention dictates that in photoemission experiments, the binding energies and band edge positions obtained are stated with respect to the sample Fermi-level, thus that convention is followed throughout this thesis.

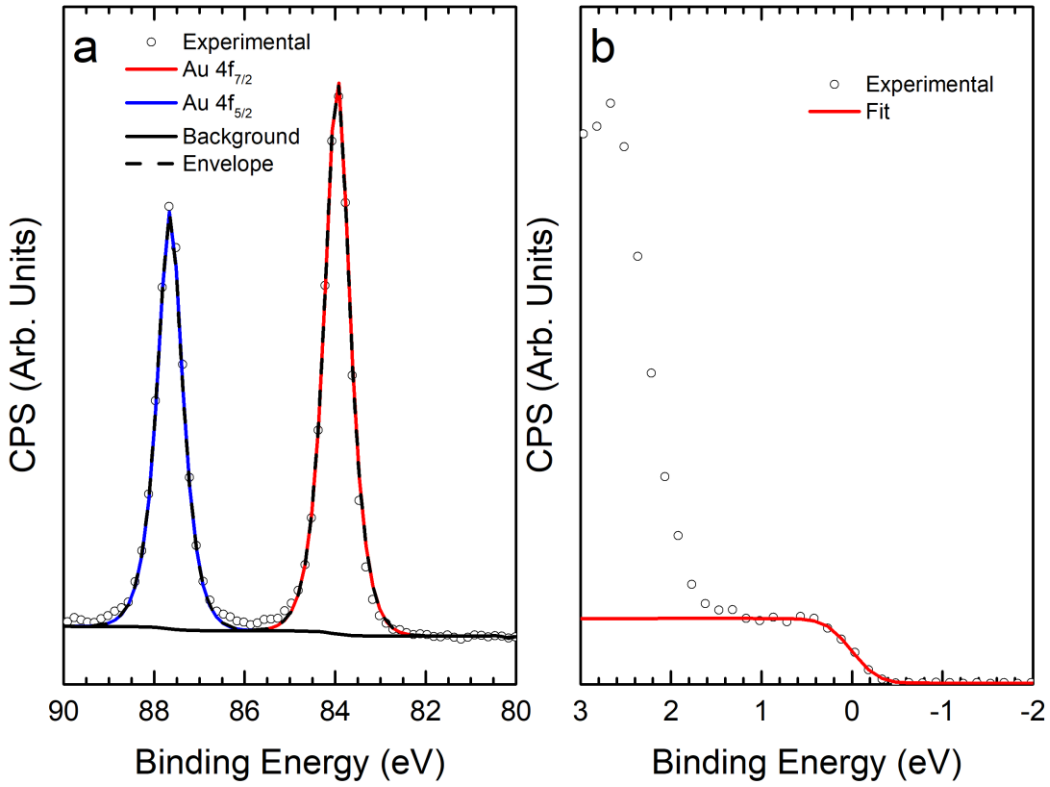

Figure 2.6 – Calibration of HAXPES results. (a)shows the Au 4f core-levels measured on the I09 beamline at Diamond Light Source with a nominal photon energy of 6450 eV. The Au $4f_{7/2}$ core-level occurs at 83.95 eV (b) shows the corresponding Fermi-level, which is found to occur at 0 eV.

Monochromatic and synchrotron sources do not have a built-in charge neutralisation mechanism, so samples under monochromatic x-rays will be more prone to charging effects. These charging effects can lead to the distortion of the line shape of the core-levels, so a low-energy electron flood gun is typically used to neutralise the charge build-up.

The flood gun used in this work consists a tungsten filament, through which a current is passed, resulting the thermionic emission of electrons. These electrons are focussed by a negatively biased Wehnelt cylinder and are accelerated towards the extractor electrode, which further focuses the beam to increase the beam current. The electrons are then decelerated to the set energy by the anode. A schematic diagram of the flood gun is given in Figure 2.7.

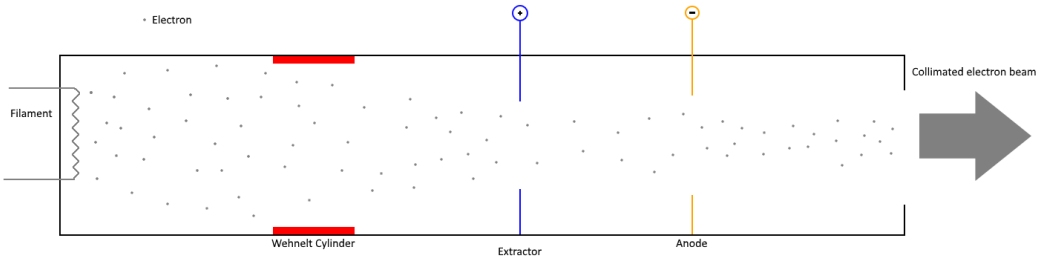

Figure 2.7 – Schematic diagram of the low-energy electron flood-gun used in this work.

2.3.1.2 Electron Collection

An electron spectrometer can generally be split into two parts: firstly, the electron energy analyser, which allows only electrons of certain energies to pass; secondly, the electron detector, which counts the number of electrons that pass through the analyser. Thus, by scanning over the range of energies that the analyser will allow to pass, a photoelectron spectrum can be constructed.

The most common type of analyser used in a PES system is the concentric hemispherical analyser (CHA). The CHA consists of two concentric, hemispherical metal plates. An electrostatic potential difference is applied between the two plates (i.e. the potential difference varies radially), thus deflecting the electrons.

An electron will pass through the analyser to reach the detector if the kinetic energy of the electron is such that the deflecting potential difference keeps the electron on a concentric course with respect to the hemispherical plates. If the kinetic energy is too large, then the electron will collide with the outer plate. Likewise, if the kinetic energy is too small, then the electron will hit the inner plate before reaching the detector. The energy for which the electron is transmitted through the analyser is thus known as the 'pass energy' (E_P).

As the entrance slits and the physical size of the analyser are finite, a small energy range of electrons about the pass energy can, in fact, traverse the analyser by taking slightly different trajectories. Thus, an uncertainty in the energy of the electrons arises, and is given by equation (2.5). This is equivalent to the energy resolution of the analyser.

$$\Delta E_A = \frac{E_P}{E_k}\left(\frac{w}{2R_c} + (\Delta\alpha)^2\right) \tag{2.5}$$

Here, R_c is the mean radius of the inner and outer plates and corresponds to the radius of the trajectory of an electron with a kinetic energy exactly equal to the pass energy. w, is the slit width used in the analyser and $\Delta\alpha$ is the acceptance angle of the analyser.

Equation (2.5) can equally be re-written into a form to determine the mean radius that one would need to obtain a particular resolution with a particular pass energy. For a lab source, the highest energy photon commonly used is the Al K_α which has photon energy $h\nu = 1486.7$ eV. Thus, to obtain an energy resolution of 1 eV, with a slit width of 10mm, an analyser of radius $R_c = 3.7$ m is required, which is clearly too large to be of any practical use. The calculation of this result is shown in equation (2.6)(2.6).

$$R_c = \frac{1486.7 \text{ eV}}{1 \text{ eV}} \frac{5 \text{ mm}}{2} = 3.7 \text{ m} \tag{2.6}$$

For a synchrotron source, photon energies upwards of 6000 eV are regularly used, corresponding to typical kinetic energies of 5000 eV, which would require even larger analysers. Similarly, when obtaining a spectrum over the range of kinetic energies available, the resolution of the analyser would vary as different kinetic energies would require different pass energies, giving a different resolution.

Instead of using such large, impractical analysers, a series of retarding lenses are used to reduce the kinetic energy of the electrons incident upon the analyser by the same amount in normal operation. In this case a constant pass energy is used, and the retardation voltage is varied, such that the analyser resolution is independent of the initial kinetic energy of the electron. This mode of operation is the constant pass energy (CPE) mode and is most commonly used. The other mode of operation used is the constant relative ratio (CRR) or fixed retardation ratio (FRR) mode. Analysers operating in this mode have a more uniform sensitivity across the kinetic energy range, however the resolution will be worse at higher kinetic energies.

In this work, the electrons are collected by a channel electron multiplier (CEM), consisting of a metal cone, a ceramic semiconducting spiral and a separate metallic anode. A potential difference on the order of 2kV is applied between the cone and the end closest to the anode, whereby the cone is given a large negative bias relative to the spiral. Thus, electrons are accelerated from the cone towards the anode. Due to the curved shape of the multiplier, the incident electron will impact the semiconducting surface, resulting in the emission of secondary electrons from the surface. The resulting electrons are then accelerated and impact further down the dynode spiral generating more electrons until the multiplied electrons reach the anode where the signal is collected. A photograph of a CEM is given in Figure 2.8.

Figure 2.8 – A photograph of a single channel electron multiplier. Clearly visible is the continuous-dynode spiral structure, as are the electrical connections for providing the bias across the multiplier.

The analyser used in this thesis is equipped with an array of 5 CEMs separated in energy by 0.025 eV per CEM, resulting in a higher count rate. Photographs of this array are shown in Figure 2.9.

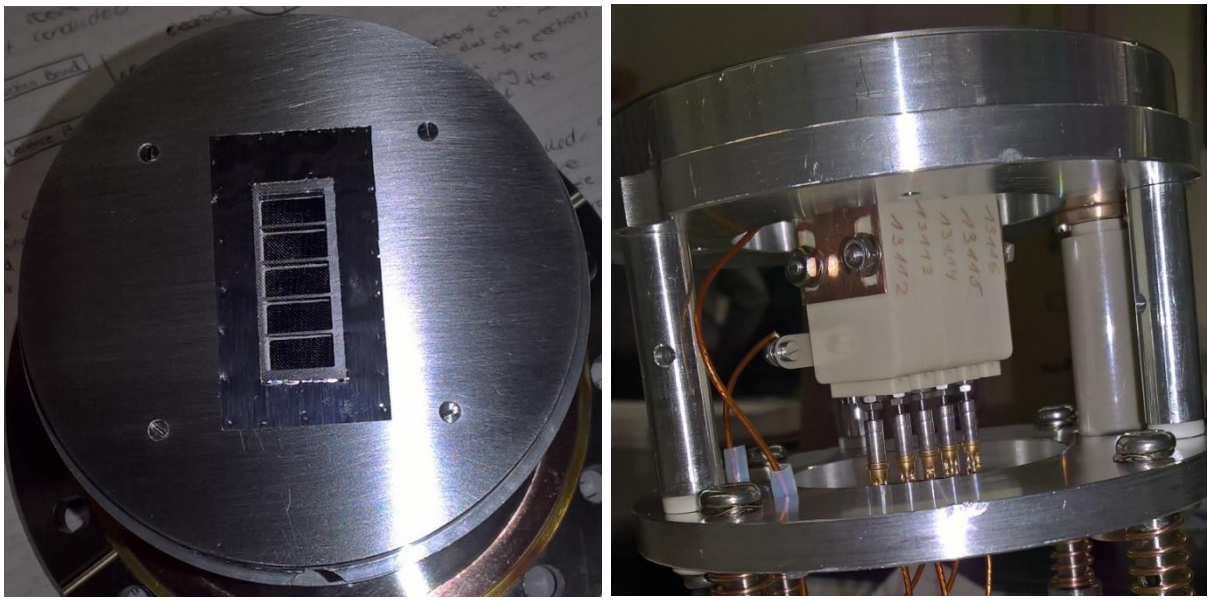

Figure 2.9 – Photographs of the array of 5 channel electron multipliers used in this work from the top and side perspectives.

2.3.1.3 Angle-Dependent Photoelectron Spectroscopy

As XPS is a surface-sensitive technique, varying the take-off angle will change the effective probing depth for a particular photon energy, where the take-off angle is defined as shown in (2.7).

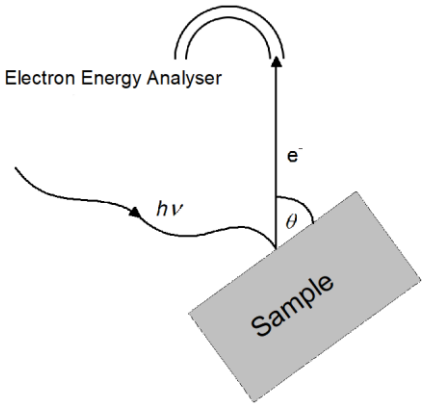

Figure 2.10 - A schematic diagram of an angle-dependent photoemission experiment. Here θ is the take-off angle, defined as the angle of emission of the photoelectrons relative to the sample surface.

The dependence of the mean-free-path of the photoelectrons in the material on the take-off angle is then given by equation (2.7).

$$\lambda = \lambda_0 \sin\theta \qquad (2.7)$$

Where λ_0 is the inelastic mean-free-path (IMFP) of an electron with the same kinetic energy, *E*, with a take-off angle normal to the sample surface, and is calculated from equation (2.2).

Thus, by reducing the take-off angle, θ, the depth probed by XPS is reduced, and the surface sensitivity is increased. This can be of use when looking at the interfaces between two materials as depth-dependent band bending can occur at some interfaces.

2.3.1.4 Analysis of Photoelectron Spectroscopy

Without any analysis, a simple photoemission spectrum will give the experimentalist relatively little information, primarily, 'what elements occur at the surface of the material?', with little input on questions such as: What oxidation state are the elements in? What are the relative concentrations of the elements? To determine any further information, the spectra obtained by the experimentalist must be analysed.

In practice, there are multiple levels at which researchers analyse photoemission spectra, from the comparatively simple, ‘our peaks occur at these energies’, to the more complex, such as band comparisons with density functional theory (DFT).

The first step in analysing a photoemission spectrum is usually checking for and correcting for any charging effects. As electrons are removed from the sample by the photoelectric effect, a positive space charge can occur at the sample surface. This positive space charge results in the deceleration of the emitted photoelectrons due to the attractive Coulomb potential. Thus, the presence of sample charging manifests as a spectrum at an increased binding energy for all the core-level and valence electrons from the sample (i.e. a lower kinetic energy). In some cases, the charge being removed from the sample can be replaced either by low-energy free electrons from a flood gun or emitted from the chamber due to interactions with the bremsstrahlung, or by conduction of electrons from the system through electrical contacts either at the bottom or top surface of the material. These are known as charge-compensation techniques

The issue with charge-compensation techniques is that it is difficult to determine whether or not the sample charge is fully neutralised, or if the sample charge has only been reduced somewhat. It is therefore common to use a reference energy and correct the entire spectrum to the binding energy of this reference peak. Historically, the evaporation of a thin layer of the noble metals (Ag, Au) onto the sample was commonly used to provide a standardised binding energy scale. Alternatively, Ar^+ ions could be implanted into the surface by using an ion gun, however both of these methods require modifying the sample in some way, which may result in a sample that is not identical to that which was initially entered. In the case of evaporated metals, Schottky diodes can be formed, resulting in potential differences between the sample and the metal which can also alter the energy of the photoelectrons.

However, one minor advantage (for photoemission spectroscopists) of the industrialised nature of our society, is the ubiquitous presence of small hydrocarbon molecules in the atmosphere. The presence of these hydrocarbon molecules results in a layer of hydrocarbon contamination on any sample that has transited through atmosphere. The binding energy of the C 1s core-level due to this contamination species can then be used to reference the energy scale. Values from anywhere between 287 eV to 284 eV have been used, most commonly between 285 and 284.5 eV, for this contamination level and there is some evidence to suggest that the binding energy that should be used is dependent on the

material being investigated. As a result, spectroscopists should always be careful in checking the charge-correction method used in the literature, as a result that appears to be in complete contradiction, may in fact simply have used a different or incorrect charge-correction method.

The next stage in analysing a photoemission spectrum is to identify and analyse the various peaks present. Identification can usually be made with relative ease, by comparing the peak energies of the charge-corrected spectrum with those tabulated in the many XPS handbooks and data banks. Examples of such handbooks and databases are given in references [363]–[365]. It is quite common in the literature for authors to simply quote the maximum of the peak as the binding energy of the core-level for that particular chemical species. This approach is problematic for a number of reasons: firstly, for some core-levels, the peaks can be quite broad and often mask the presence of a second, smaller peak; secondly, for some core-levels the spin-orbit splitting of the components is small, resulting in an asymmetric peak, the maximum of which is not necessarily directly related to either component. This issue is particularly prominent for the S 2p and Se 3d core-levels, where the binding energy of the whole core-level is often given, instead of that of the $2p_{3/2}$ or the $3d_{5/2}$ respectively.

To properly analyse core-levels, they must be modelled mathematically and compared to the experimental data. The core-levels are superimposed upon a background of secondary electrons, which must also be accounted for during the modelling process.

The most basic form of background is a simple linear background, consisting of a straight line joining the start and end points of the region under investigation, however there is no physical justification for the use of such a background and as such its usage should be limited to regions where the intensity of the background changes only very slowly.

There are two background models that have been derived for the inelastic scattering of electrons for specific use in photoemission spectroscopy, namely the Shirley[366] and the Tougaard backgrounds. The Shirley background is an iterative background, composed of a set of *k* points, each separated by an energy *h*. The intensity of the background at some point *x*, is then given by equation (2.8).

$$B(x) = \frac{(a-b)Q}{(P+Q)} + b \qquad (2.8)$$

Where *a* is the average starting point, *b* is the average endpoint, *P+Q* is the total background subtracted peak area, and *Q* is the background subtracted peak area from

point *x* to point *k*. This area is found by applying the trapezium rule as given in equation (2.9).

$$Q = h\left[\left(\sum_{i=x}^{k} y_i\right) - 0.5(y_x + y_k)\right] \quad (2.9)$$

Initially, a constant linear background is chosen and substituted into equation (2.8), and a new background is generated. The process can then be repeated until, the sum *P+Q* is identical within some margin of error upon successive iterations[366]–[368]. The ease of implementation of the Shirley background along with its semi-physical nature have made it the go-to background type for photoemission studies, however some caution should be practiced. The Shirley background fails to account for asymmetric line shapes, which can lead to some researchers applying the background in an inappropriate fashion[368].

The Tougaard background is more rigorous theoretically, and accounts for the full kinetic energy range of the inelastically scattered electrons[369]. However, this typically requires large energy range (at least 50 eV) on the high binding energy side of a peak, which often is not practical or indeed possible. As the Shirley background has, at least, some theoretical basis, albeit one developed after the fact, it has become the *de facto* standard background used in XPS analysis as it is much easier to implement than the Tougaard background.

Once the background is accounted for, the spectroscopist can begin to consider peak fitting. The minimum broadening achievable in a photoemission spectrum is limited by a number of sources: Firstly, the natural line width of the feature (ΔE_{CL}); secondly, the line width of the source (ΔE_S); and thirdly, the analyser response (ΔE_A). These sources can to a first approximation add in quadrature to estimate the broadening of a given feature, this is shown in equation (2.10).

$$\Delta E \approx \sqrt{(\Delta E_{CL})^2 + (\Delta E_S)^2 + (\Delta E_A)^2} \quad (2.10)$$

The lifetime broadening effects are Lorentzian in nature, whilst the broadening due to the analyser is Gaussian in nature. As such, Gaussian-Lorentzian functions are typically used for the fitting of core-levels in photoelectron spectroscopy.

A notable exception to this rule is in the case where there is a considerable density of free electrons, in which case the photoelectrons can leave a hole and the Fermi sea in an excited state. This electron can then form a pair with a free electron. Doniach and Šunjić, demonstrated that it was favourable to produce many low energy pairs, resulting in an

asymmetric tail in photoemission spectra observed for metallic (or metal-like) samples. The line shape describing this is known as the Doniach-Sunjic line shape[370].

Other processes can also transfer some kinetic energy to the Fermi sea in less conducting samples. This energy can either be transferred to the bulk electron plasma resulting in a (bulk) plasmon, or the surface electrons (a surface plasmon). These processes result in photoemission peaks occurring at higher binding energies from the main photoemission peak, separated by the plasmon energy. An example of the plasmon peaks in *n*-type Si is shown in Figure 2.11.

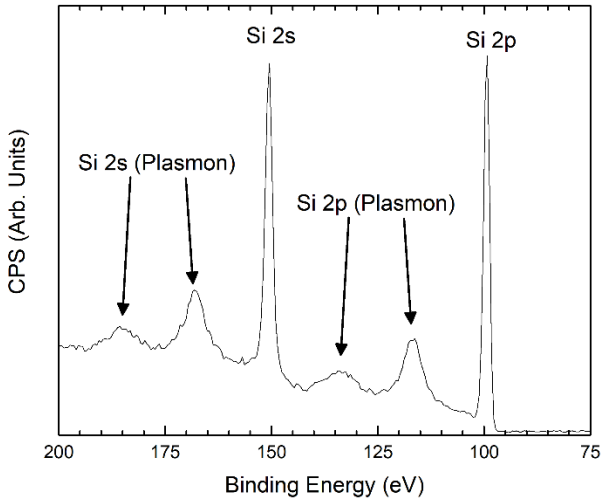

Figure 2.11 – XPS spectrum of the region near to the Si 2p and Si 2s core-levels. At higher binding energies, two plasmon resonances are seen, separated by approximately 15 eV and 30 eV respectively. This also shows why the Tougaard background is not usable in many cases.

A second source of peaks in photoemission spectra are the Auger processes. When a core-electron is emitted from the sample by a photoionisation process, a hole is left occupying the core-level. An electron from a higher energy-level can then decay into the core-level. Usually such a process results in the emission of a photon with energy equal to the difference between the two levels. However, in some cases, the electron undergoing the transition instead transfers the energy to another outer shell electron. In contrast to the photoelectrons, the Auger electron is emitted with a constant kinetic energy, equal to the difference between the initial and final state of the decaying electron, subtracted by the binding energy of the initial state of the Auger electron. A schematic diagram of a single Auger process is shown in Figure 2.12.

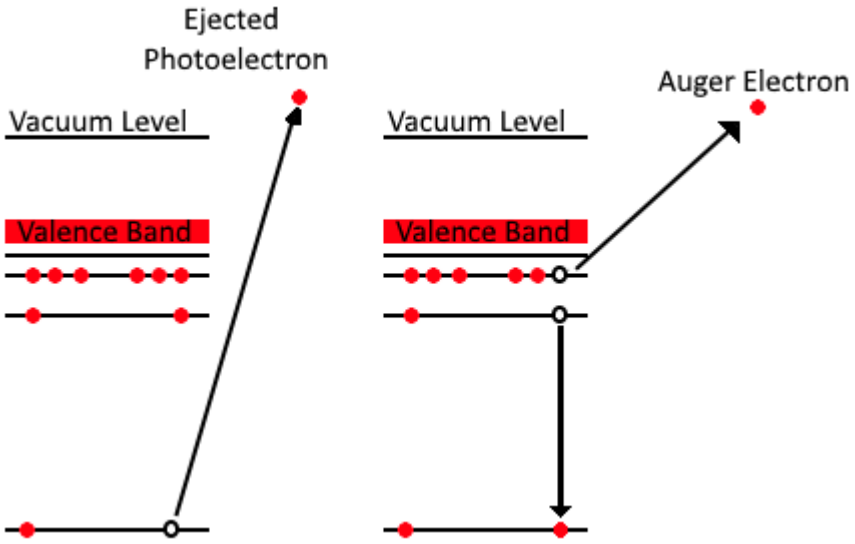

Figure 2.12 - A schematic diagram showing a single Auger process.

The fact that the kinetic energy of the Auger electron is fixed means that its position on the binding energy scale typically used for photoemission measurements varies with the photon energy. Hence if an Auger peak coincides with a core-level of interest with one photon source, changing the photon energy (e.g. changing from an Al to a Mg anode) allows for the Auger peak to be shifted away from the core-level peak. An example of this would be in GaN. The N 1s peak occurs at 400eV, using an Al x-ray source, however the Ga LMM Auger feature also has a peak in the same energy range, making analysis of the peak challenging. However, by changing to a Mg x-ray source, the Ga LMM Auger is shifted away from the N 1s, and instead occurs at 280eV. However, this makes using the C 1s for charge-correction difficult. As a result, the spectroscopist would want to use both a Mg and an Al source. This can be seen in Figure 2.13.

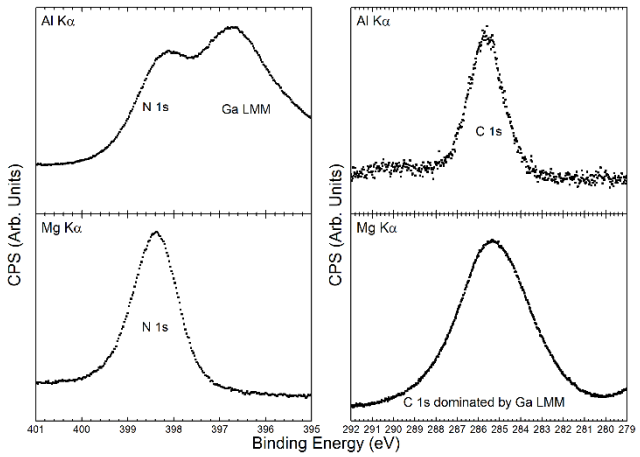

Figure 2.13 – The N 1s and C 1s regions of an as-entered GaN sample as measured with an Al K_α and Mg K_α x-ray source, showing how the Auger peaks can be moved by changing the x-ray source used.

In the previous section, it has been assumed that only single Auger processes, resulting in a doubly charged ion are possible. In fact, double and triple Auger processes have also been observed experimentally, however the cross-sections for these processes are 10^{-2} and 10^{-4} times that of the single Auger process, and so can be neglected in photoemission experiments[371]–[373].

Although in many cases, the Auger processes complicate matters for the spectroscopist, the Auger electrons can, in fact, be useful. The Auger parameter is defined as the difference of the kinetic energy of the Auger electron, $\left(E_k^A\right)$, and the kinetic energy of the photoelectron, $\left(E_k^C\right)$, as shown in equation (2.11)[374].

$$\alpha = E_k^A + E_k^C \tag{2.11}$$

However, as the kinetic energy of the photoelectron is dependent on the photon energy of the x-ray source, this leads to an Auger parameter which varies with the source. Instead, the modified Auger parameter, α', is used, which is given by the sum of the binding energy of the photoelectron, $\left(E_B^C\right)$, and the kinetic energy of the Auger electron as shown in equation (2.12)[375]. In some cases, the 'modified' part of the name is dropped, however in this work the full name will be used for the sake of clarity. As both variables are independent of the photon energy used, the modified Auger parameter is also independent of the photon energy. The parameter is also independent of charge-correction as it is only based on the energies of two points on the same scale.

$$\alpha' = E_k^A + E_B^C \tag{2.12}$$

This parameter is of interest, as it allows for the comparison of the chemical state of the same element in multiple different samples and attribute the origin of the chemical shift, to initial and final state contributions due to the differing effect each has on the Auger and photoelectron[376].

When comparing the modified Auger parameter between two samples, the relaxation energy, or the polarisation energy can be written as in equation (2.13) as derived by Moretti[377].

$$\Delta\alpha' = 2\Delta R \tag{2.13}$$

If one of the samples being compared is the elemental form of the atom, then this is necessarily equal to $\Delta\alpha' = 2\Delta R = 2R$, as the relaxation energy for the elemental form is necessarily zero[377]. The initial state effect is then $\Delta\varepsilon$, and the two parameters are related

to the change in the Auger kinetic energy and the photoelectron binding energy by the relations given in equations (2.14) and (2.15)[378]–[381].

$$\Delta E_k = \Delta\varepsilon + 3\Delta R \quad (2.14)$$

$$\Delta E_b = -\Delta\varepsilon - \Delta R \quad (2.15)$$

Where positive values of $\Delta\varepsilon$ and ΔR correspond to a shift to a lower binding energy. The initial state contributions, $\Delta\varepsilon$, are therefore due to the ground-state electronic structure of the atom emitting the photoelectron, which is dependent on the local electronic and lattice parameters, corresponding to what is normally called the 'chemical shift'. Thus, the different contributions to the binding energy shift can be investigated and hence further information about the chemical bonding of the sample can be obtained by simply measuring an extra parameter. In contrast, the relaxation energy is only dependent on final state effects, i.e. interactions between the photo and Auger holes and the electronic structure of the atom.

2.3.2 Inverse Photoemission Spectroscopy

Inverse photoemission spectroscopy (IPES) is a closely related technique to standard photoemission spectroscopy, and is to a first approximation, the time-reversed process (although in reality it is more complex than that)[382], [383], whereby an electron is absorbed by a material, resulting in the emission of bremsstrahlung photons as the electron travels through the material, hence giving the alternative name of bremsstrahlung isochromat spectroscopy (BIS). As such, IPES is sensitive to the *unoccupied* states of the conduction band in contrast to standard PES which measures the occupied states of the core-levels and valence band[384], [385].

Two modes are commonly used in IPES, the isochromatic mode and the spectrographic mode[386]. The spectrographic mode uses a fixed kinetic energy of the electron and measures all photon energies are measured simultaneously, usually using a diffraction grating to separate the various photon energies[387]. The spectrographic mode also allows for resonant inverse photoemission, where the kinetic energy of the electron is resonant with a particular unoccupied state in the conduction band of the material being investigated.

In contrast, the isochromatic mode uses a variable electron kinetic energy, measuring a fixed photon energy[388], [389]. The detector in this case is a bandpass detector, designed to detect photons of energy $h\nu \approx 9.5$ eV, as originally pioneered by Dose in the late 1970s[388]. The detector consists of a SrF_2 window which is transparent to photons with

energy $h\nu \leq 9.7$ eV, with a Mo mesh on the side of the window facing the sample to prevent charging effects. The transmitted photons are then incident upon a photocathode consisting of a NaCl-coated Ta cone, which produces electrons by the photoelectric effect when photons of energy $h\nu \geq 9.0$ eV are incident upon it. Thus, the energy range of the photons collected by the detector gives a resolution of 0.70±0.10 eV. The photoelectrons generated from the cone are then collected by a channel electron multiplier similar to that described previously in section 2.3.1.2. A schematic diagram of the detector used for the work in this thesis is shown in Figure 2.14.

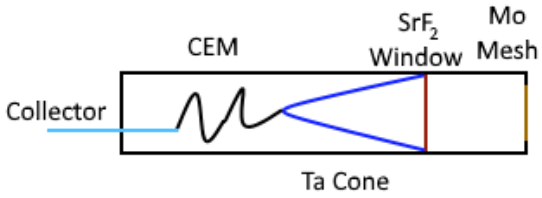

Figure 2.14 – A schematic diagram of the isochromatic bandpass detector used for IPES.

For operation, the detector is wound into its operating position, approximately 40 mm away from the sample. The acceptance angle of the detector can, thus be estimated from the size of the window (approximately 25 mm) to be 30˚. Hence, the isochromatic detector described probes the entirety of the Brillouin zone. All IPES measurements presented in this work therefore consist of an average across the Brillouin zone.

An isochromatic IPES system is cheaper and easier to maintain than a spectrographic IPES system, and as only a small range of photon energies are collected, the detector can be designed to achieve a much more efficient collection rate and thus a much higher count rate albeit at the loss of some resolution.

IPES spectra need to be calibrated to a known energy, as the kinetic energy of the free electron is not obviously related to the energy of the bound electron in the sample. In practice, several methods are used to do this, for instance calibration to the Fermi level of a clean metal foil (usually silver or gold) however the density of states close to the Fermi level is often quite low resulting in a low number of counts. Alternatively, the lowest unoccupied molecular orbit (LUMO) of a well-known molecule can be used, as the LUMO position will occur at a particular energy above the Fermi level.

To calibrate the IPES spectra shown in this work, both Fermi level from a clean polycrystalline Ag foil and the LUMO of C60 molecules evaporated in situ onto the same foil were used to calibrate the spectra. The LUMO of a thick film of C60 (i.e. a film thick enough that interactions between the surface molecules and the metal foil can be neglected) is

known to occur at 1.5eV above the Fermi level[390]–[392]. An example of the spectra obtained from evaporated C60 is shown in Figure 2.15. As the sample and the electron source are in electronic contact, the Fermi level of the entire system will be equilibrated, and thus the energy of the bound electrons can be defined relative to this joint Fermi level as in standard PES experiments.

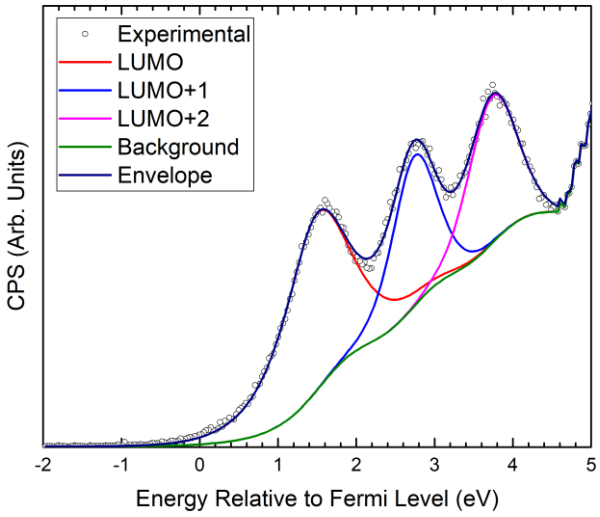

Figure 2.15 – The inverse photoemission spectrum showing the first three LUMOs of an in situ evaporated thin film of C60 on Ag foil

2.3.3 Band Alignment Determination

In a homojunction interface (i.e. an interface where the same material is present on either side of the interface, such as a silicon diode) the band alignment can simply be understood by the alignment of the Fermi level on either side of the interface. However, for heterojunctions, the density of states close to the band edges do not have to be the same, thus the alignment of the Fermi level will not necessarily occur at the same position as in the homojunction case. Other possible issues relate to the formation of defects in the gaps of the semiconductors that are at the semiconductor-vacuum interface prior to forming the junction (surface states), or induced states due to chemical bonding between the two materials (e.g. metal-induced gap states). The presence of such states can lead to Fermi-level pinning at the interface.

2.3.3.1 Anderson's Electron Affinity Rule

The first method of describing the band alignments of two materials are the closely related methods of the Anderson rule and the Schottky-Mott rule, which apply to semiconductor-semiconductor and semiconductor-metal interfaces respectively. The Anderson rule was first described by R. L. Anderson in 1960[393], whereby he used the built-in voltage determined by I-V measurements to determine the conduction band offset (CBO). From the

CBO, the valence band offset (VBO) could be determined using the band gaps of the materials on either side of the junction. The equations for the CBO and VBO are given in equations (2.16) and (2.17) respectively.

$$\Delta E_c = \chi_1 - \chi_2 \tag{2.16}$$

$$\Delta E_v = (\chi_1 + E_{g1}) - (\chi_2 + E_{g2}) \tag{2.17}$$

As the electron affinity cannot be determined directly by photoemission it is more common that the ionisation potential V_{IP} is used as the V_{IP} can be measured directly. This corresponds to the difference between the valence band maximum and the vacuum level for a semiconductor in contrast to the electron affinity, which is the difference between the conduction band minimum and the vacuum level. The relations between V_{IP}, φ, E_g and χ are shown in Figure 2.16.

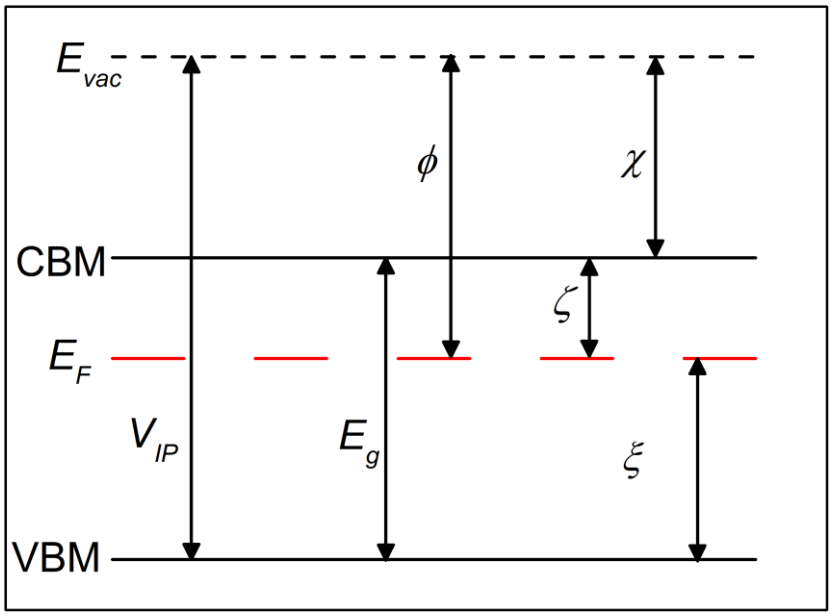

Figure 2.16 - Definitions of the various parameters used to describe band positions relative to the Fermi and vacuum levels.

Determination of the ionisation potential is made firstly be measuring the valence band and finding the position of the VBM by an appropriate method. Secondly the secondary electron cut-off (SEC), needs to be determined. This corresponds to the minimum kinetic energy an electron needs to be able to escape the sample, i.e. the work function. However, the analyser itself also emits secondary electrons, henceforth a negative bias (typically 5-20 V) is usually applied to the sample with respect to the analyser. The secondary electrons from the sample are then shifted by the bias voltage to a lower binding energy, which can be corrected for after the measurement, but prior to data analysis. The ionisation potential is then given by equation (2.18). An example of this process is presented in Figure 2.17.

Once the ionisation potential is found, knowledge of the band gap allows the electron affinity to be determined also, giving a full band alignment with respect to the vacuum level.

$$V_{IP} = h\nu - (SEC - \xi) \qquad (2.18)$$

Due to the large number of low-energy secondary electrons, a reduced nominal power is usually used for these measurement, between 9 W (3 kV, 3 mA) and 25 W (5 kV, 5 mA). If necessary, the smaller entrance and exit slits can be used, and the pass energy also reduced.

However the Anderson rule does have several notable issues associated with it: firstly it neglects the existence of interfacial states such as surface or induced gap states as the interface is assumed to be neutrally charged[393]; secondly the actual alignment will depend on the flow of charge across the junction during formation and thus depend on the density of states on either side of the junction.

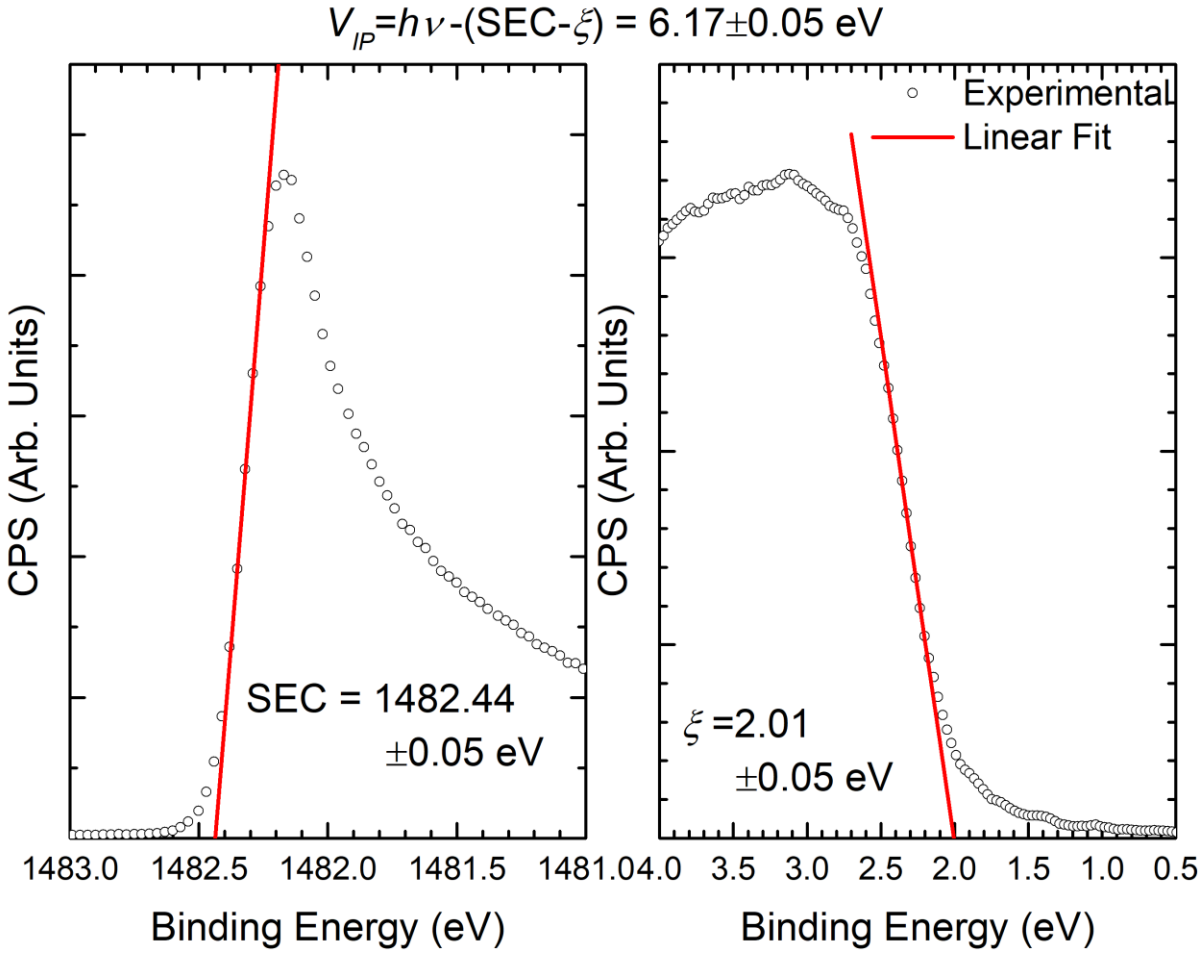

Figure 2.17 – An example of the determination of the ionisation potential of a semiconductor from measurements of the secondary electron cut-off and the valence band maximum.

2.3.3.2 The Kraut Method

Due to the failures of the Anderson rule for all but the simplest systems, considerable effort was spent in search of a better method for finding the band alignments between two semiconducting materials. In 1980 E. A. Kraut proposed his method for using the core-level to valence-band separation measured by XPS to determine the band bending at a generalised interface[394]. This led to the development of the so-called Kraut method.

The modern variant of the Kraut method requires the use of three samples: a thick overlayer, typically >20 nm; a thin overlayer on the substrate, typically 2-3 nm such that the core-levels of the substrate are visible alongside the core-levels of the overlayer; and a clean substrate, with no overlayer. These 3 samples can either be produced separately during the growth process, or otherwise can be produced by Ar^+ ion etching the thick overlayer until the core-levels of the substrate are present, and then until the overlayer is removed.

The VBO is then determined by equation (2.19) from the separations of the core-levels and the valence band maximum (VBM, ξ) of the thick overlayer and the substrate, and the relative difference between the same core-levels in the thin overlayer sample. From this the CBO is easily determined by simply considering the band gaps of the substrate and the overlayer, as given in equation (2.20).

$$\Delta E_v = (E_B - \xi)_{over} - (E_B - \xi)_{sub} - \left(E_B^{over} - E_B^{sub}\right) \quad (2.19)$$

$$\Delta E_c = \Delta E_v + E_g^{over} - E_g^{sub} \quad (2.20)$$

Thus, the Kraut method avoids the limitations of the Anderson rule, as the surface states will implicitly be accounted for in the measurement process, because the binding energies determined in XPS are given with respect to the joint sample-system Fermi level.

To demonstrate the application of the Kraut method, we will consider the example of amorphous Ga_2O_3 thin-films deposited on Si and Ge wafers, adapted from reference [395].

Ga_2O_3 is a wide band gap material with the largest band gap of the transparent conducting oxides, at ≈4.8 eV. The large band gap, combined with the excellent thermal and chemical stabilities of the material have led to considerable recent interest in the material, for applications as wide ranging as gas-sensing[396]–[398], high-power electronics[399], photovoltaics[400], [401] and UV optoelectronics[402]–[404]. A Ga_2O_3 metal-oxide-semiconductor capacitor has also recently been reported on silicon[405], as has the use of ALD-grown Ga_2O_3 as an ultrathin passivation layer for silicon-based photovoltaics[401].

To understand the behaviour of these devices, the band alignments with commonly used semiconductor substrates need to be investigated. The band alignment of β-Ga_2O_3 with Si has previously been reported by Guo *et al.*[404] using the electron affinity rule[393], however this disagrees with the alignment obtained by Chen *et al.*[406], where the alignment is measured by photoelectron spectroscopy. The interpretation of the alignment obtained by Chen *et al.* is complicated by a number of issues: Firstly, the authors use a non-monochromatic x-ray source, resulting in the presence of x-ray satellites, which are particularly problematic for finding the valence band maximum (VBM) of the Ga_2O_3 sample; secondly, the interfacial sample is produced by Ar^+ ion etching, however, the interfacial sample clearly shows two Ga species in the Ga 2p spectrum, indicative of the preferential removal of oxygen, thus leaving a sub-stoichiometric oxide or elemental Ga; finally, their discussion on the formation of an interfacial SiO_{2-x} layer is limited by the issues raised above.

The band offsets of Ga_2O_3 with Ge have not been reported previously, with only that found for Ga_2O_3(Gd_2O_3) having been reported, where ΔE_v = 2.35±0.1 eV[407], however in this case the Kraut method is used incorrectly, as the thickest sample used is only 3 nm and therefore still sensitive to the interface. Previous reports of photoelectron spectroscopy on Ga_2O_3(Gd_2O_3) on Ge have found evidence of an interfacial oxide layer formed upon deposition of the dielectric layer[408], [409], with the notable exception of Chu *et al.*[407], however the binding energy reported is considerably larger (at a binding energy of approximately 30 eV) than that expected for elemental Ge. Such an energy suggests that the wafer may in fact be oxidized, however accurate determination of the oxidation state is rendered impossible since the data had not been deconvoluted.

In this work, we describe the use of the Kraut method[394] to investigate the band alignments of Ga_2O_3 with Si(111), Si(100) and Ge(100) substrates. As the Kraut method requires a thick, bulk-like sample, a thin, interfacial sample, where the core-levels of the substrate can be observed and a clean substrate, thick (31 nm) and thin (3 nm) Ga_2O_3 layers were synthesized on the aforementioned substrates. Regarding the thickness, the Debye length is characteristic of the length scale over which the effect of the interfacial potential is felt. For crystalline β-Ga_2O_3 nanowires, the Debye length is found to be 40.5 nm[410]. However, as the Debye length is proportional to the defect density[411], the Debye length of the films described here will be considerably smaller, as the films described in this work are amorphous and hence defect-rich. Similar behaviour has been observed in a-IGZO thin

film transistors[411], where the defect density is approximately $2 \times 10^{17} \mathrm{cm}^{-3}$. Hence, the thickness of the 31 nm samples used in this work is considered adequate.

The use of a thin sample also allows for the quality of the interface to be investigated in a non-destructive manner. In contrast to Chen *et al.*[406], we use a monochromatic x-ray source, thus avoiding the issue of x-ray satellites.

Ga_2O_3 layers were deposited by atomic layer deposition (ALD) on clean p-type Si(111) and Ge(100) wafers in an Oxford Instruments Plasma-OpAL reactor. The precursors used for deposition were triethylgallium (TEGa) and O_2 plasma and with a substrate temperature of 250˚C. 58 ALD cycles were used to obtain thin samples, and 580 cycles for the thick samples.

Prior to deposition, the Si substrates were cleaned by 10 minutes immersed in methanol in a sonic bath, followed by 10 minutes immersed in acetone in a sonic bath. The Si substrates were then immersed in 5% HF for 5 minutes with agitation before being rinsed with distilled water and dried by N_2 gas. The Ge substrates were cleaned by 10 minutes immersed in methanol in a sonic bath, followed by 10 minutes immersed in acetone in a sonic bath and dried by N_2 gas.

The deposited films were confirmed to be amorphous by x-ray diffraction with a Rigaku SmartLab x-ray diffractometer ($h\nu = 8047.8$ eV). Spectroscopic ellipsometry was used to determine the thicknesses of the deposited films with a Horbia Jobin Yvon MM-16 spectrometer with a range of 430 – 850 nm. The thicknesses of the deposited films were found to be 30.05±0.18 nm and 3.05±0.10 nm for the thick and thin layers respectively. Ellipsometry spectra were fitted using a Cauchy model adopted from reference [412].

Prior to measurement, the Si and Ge substrate samples were lightly sputter-etched (0.25 kV, 1 mA) in 5 minute intervals to remove oxygen and carbon contamination, until the O 1s peak was no longer visible in XPS. Since the mean-free-path of the photoelectrons is dependent on the kinetic energy of the emitted photoelectron, core-levels with large separations in kinetic energy will have different probing depths and hence different sensitivities to the interface potential. The Ga 3p, Ge 3p and Si 2p core-levels were therefore used for Kraut method analysis as these peaks occur in a narrow range of binding energies, ensuring that the photoelectrons originated from similar depths.

The Kraut method, uses the binding energies of the core levels and the VBM of the three samples to determine the valence band offset, ΔE_v, as shown in equation (2.19)

$$\Delta E_v = (E_B - \xi)_{over} - (E_B - \xi)_{sub} - E_B^{over} - E_B^{sub} \quad (2.19)$$

.

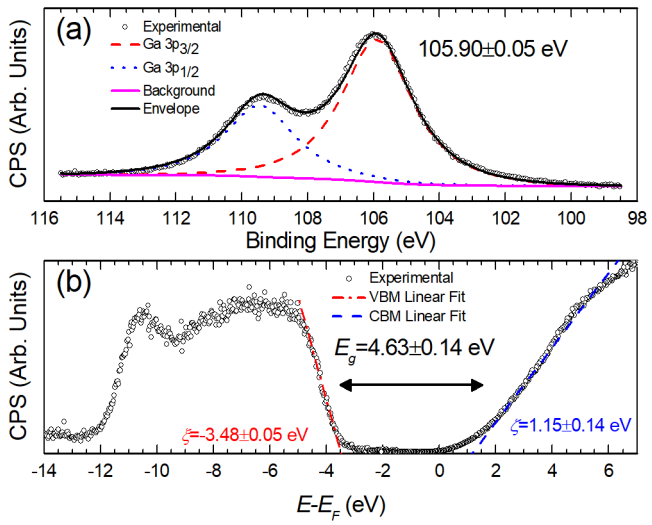

Figure 2.18 – This figure shows (a) the Ga 3p core levels, and (b) the valence band obtained by XPS and the conduction band edge obtained by IPES for the 30nm Ga_2O_3 sample.

Figure 2.18(a) show the Ga 3p region for the thick, 30 nm Ga_2O_3 sample. Figure 2.18(b) shows the valence band measured by XPS and the conduction band, as measured by IPES. The VBM was found at -3.48±0.05 eV, whilst the CBM occurred at 1.15±0.14 eV relative to the Fermi level. By combining these values, the bandgap of the 30 nm Ga_2O_3 film was determined to be 4.63±0.14 eV, consistent with the 4.4-4.9 eV band gap range previously reported for amorphous Ga_2O_3 films[413]–[416].

Figure 2.19(a) and Figure 2.19(b) shows the Si 2p region and valence band respectively for the clean Si(111) substrate. Figure 2.19(c) and Figure 2.19(d) show the Ge 3p region and valence band for the clean Ge(100) substrate. The data show that the surfaces of the substrates were clean of any contamination. The binding energies and their differences from the VBM obtained from these figures are given in table I. The binding energy of the Si $2p_{3/2}$ core-level is consistent with values reported in the literature for p-type Si wafers[417]–[420]. The separation between the Si $2p_{3/2}$ and the VBM is found to be 98.83±0.08 eV, consistent with that reported previously[420]–[423].

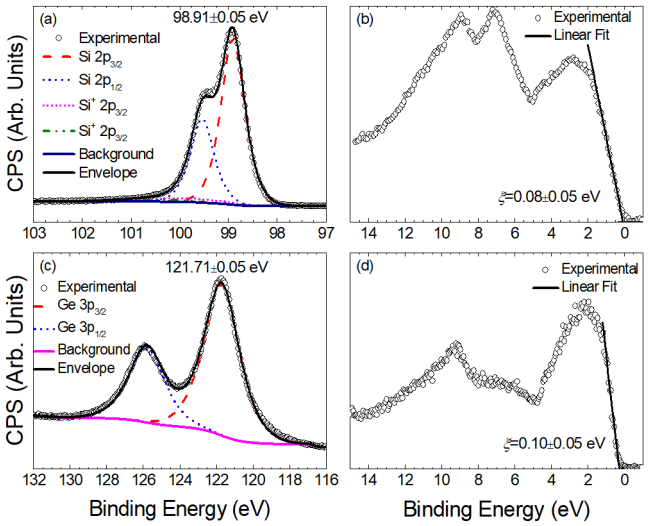

Figure 2.19 – (a) shows the Si 2p region for the clean Si(111) substrate (b) shows the corresponding valence band. (c) shows the clean Ge 3p for the Ge(100) substrate and (d) shows the valence band for the same sample.

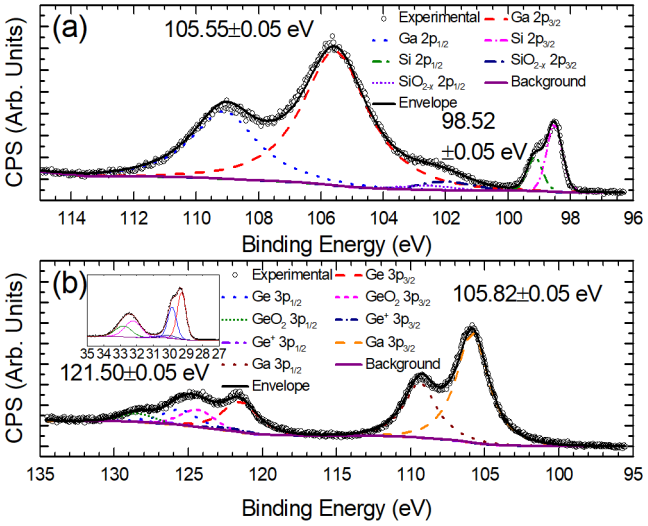

Figure 2.20 – (a) shows the Si 2p and Ga 3p region for the interfacial Ga¬2O3/Si(111) sample. (b) shows the Ge 3p and Ga 3p region for the interfacial Ga2O3/Ge(100) sample. Inset is the Ge 3d spectrum as measured by XPS.

Figure 2.20(a) shows the Si 2p and Ga 3p region for the 3 nm Ga_2O_3/Si(111) sample, whilst Figure 2.20(b) shows the Ge 3p and Ga 3p region for the 3 nm Ga_2O_3/Ge(100) sample.

As XPS is a surface-sensitive technique, varying the take-off angle will change the effective probing depth for a particular photon energy. The dependence of the mean-free-path of the photoelectrons in the material on the take-off angle is given by $\lambda = \lambda_0 \sin\theta$, where λ_0 is the inelastic mean-free-path (IMFP) of an electron with the same kinetic energy, *E*, with a take-off angle normal to the sample surface, and is calculated from $\lambda_0 = \frac{1430}{E^2} + 0.54\sqrt{E}$,[356], [357] where *E* is in eV and λ_0 is in Å. Using this relation, the IMFP is calculated to be 2.0 nm. By measuring the core levels at multiple take-off angles, the presence of any band-bending close to the interface can be determined. The Ga $3p_{3/2}$, Si

$2p_{3/2}$ and Ge $3p_{3/2}$ binding energies were determined for 30˚, 60˚ and 90˚ take-off angles. If band-bending were present at the interface, it would be expected that the difference in the core-level binding energies, ΔE_{CL} would vary with different take off angles. In fact, no such angular dependence is seen, as shown in Figure 2.21(a)-(c). It can, therefore, be concluded that band bending at the interface is negligible for these systems. If band-bending were present, then the FWHM of the core-levels would also be expected to broaden[424], [425], in fact, no changes in the FWHM are observed, further confirming the absence of band-bending.

Substrate	E_B (eV)	ξ (eV)	E_g (eV)	E_B-ξ (eV)	ΔE_{CL} (eV)	ΔE_v (eV)	ΔE_c (eV)
Ge(100)	121.71	0.10	0.67	121.61	-15.68	-3.51	0.45
Si(111)	98.91	0.08	1.11	98.83	7.03	-3.49	0.03
Si(100)	98.92	0.13	1.11	98.79	7.10	-3.47	0.05
30 nm Ga_2O_3	105.90	3.48	4.63	102.42	-	-	-

Table 2.3 – The binding energies positions of the core-levels and valence band minima and band gaps for each substrate and the bulk like Ga_2O_3. Also shown are the calculated valence band and conduction band offsets.

By applying equation (1), the VBO for the amorphous Ga_2O_3 film on Si(111) was determined to be 3.49±0.08 eV consistent with that found for β-Ga_2O_3 on Si(111) by Chen *et al.* [406] and contrasting to that reported by Guo *et al*. [404]. The VBO for the amorphous Ga_2O_3 film on Ge(100) is likewise determined to be 3.51±0.08 eV.

Using the bandgap determined in Figure 2.18(b) combined with literature bandgaps for Si(1.11 eV) and Ge (0.67 eV), the conduction band offsets (CBO) are found to be 0.03±0.14 eV and 0.45±0.14 eV for the Si(111) and Ge(100) samples respectively. The core-level energies, valence band maxima, band gaps and band offsets are summarised in Table 2.3. A schematic diagram of the band alignments is given in Figure 2.21.

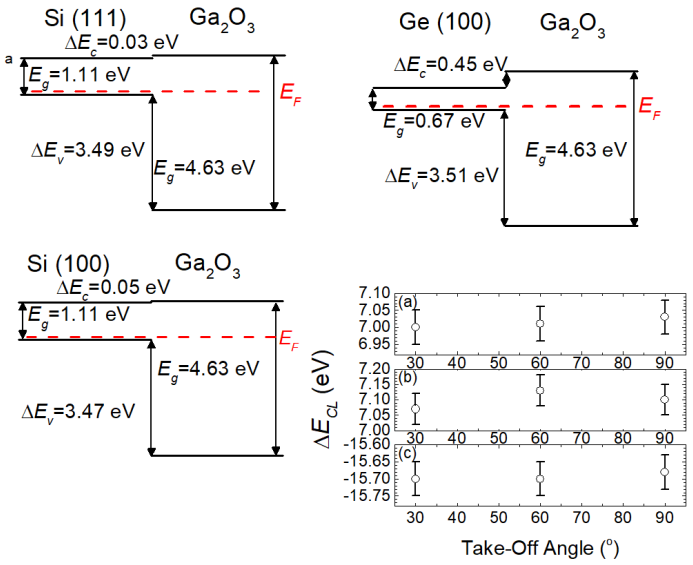

Figure 2.21 – A schematic band alignment diagram showing the XPS determined band alignments for ALD-grown Ga_2O_3 on a variety of common semiconductor substrates. (a)-(c) show the difference in the core-level binding energies against the take-off angle for the Si(111), Si(100) and Ge(100) samples respectively. No difference above the error is observed, thus ruling out significant band-bending.

Similar measurements were also performed on a Si(100) substrate, the results of which are shown in Table 2.3 and Figure 2.21. The differences in the VBOs for the Si substrates are within the experimental error of the XPS system. The VBOs obtained from both the Si(111) and Si(100) samples are consistent with that found by Chen *et al.*[406]. The CBOs obtained from the Si(111) and (100) are different to those obtained by Chen *et al.*[406], these differences are likely due to the different methods of evaluating the band gap. Chen *et al.* use the photoelectron energy loss spectrum (PEELS) from the O 1s peak, rather than the combined VBM-CBM separation used in this work. The error on the PEELS method can be estimated to be of the order of 0.6-1.0 eV from Figure 1b of Chen *et al.*[406]. An interesting question would be whether the doping level affects the band alignment. By considering the position of the VBM with respect to the Fermi level, we can conclude that the Si wafers used in this work are more heavily p-type doped than those used by Chen *et al.*[406], however the VBOs found are consistent, suggesting that the doping density has little effect on the band offsets.

Another important variable in the performance of semiconductor devices is the quality of the interface and the existence of any interfacial layers between the substrate and the deposited film. The substrate is frequently observed to be partially oxidized after deposition of a binary metal-oxide upon Si or Ge [422], [426]–[434], but is typically less than 3 nm in thickness[405]. Figure 2.20(a) shows the interfacial Si 2p and Ga 3p spectra. A second set of peaks attributed to silicon occur at 3.5 eV above the Si^0 $2p_{3/2}$, consistent with

that expected for the Si^{4+} oxidation state of SiO_2[435]–[438]. A similar layer was also observed for 3 nm Ga_2O_3/Si(100). Paskaleva *et al.*[405] have likewise observed the formation of an interfacial SiO_2 layer by ellipsometry and C-V measurements when depositing β-Ga_2O_3 on Si(100) by the closely related chemical vapour deposition technique. Chen *et al*[406]. do not observe this oxide formation, however the interpretation of their data is limited as the spectra presented are at low resolution and are not deconvoluted. The interpretation of their data is further complicated by the Ar^+ ion etching process used to produce the interfacial dataset. Here, the Ga 2p peaks are clearly asymmetric, suggesting the formation of either a non-stoichiometric oxide (Ga_2O_{3-x}, GaO), or possibly metallic Ga^0. These features would obscure the signal from the Si 2p for the interfacial oxide, as the Ga 3p peaks would be shifted to a similar binding energy as Si 2p from SiO_2. Interpretation of the spectra in Chen *et al.*[406] is further complicated by their use of a non-monochromatic x-ray source, resulting in x-ray satellite features. For a Mg source such as the one they used, these occur 8.4 eV and 10.1 eV away from the main peak on the low binding energy side[363]. An alternative explanation could be in the differences between the growth techniques as Chen *et al.*[406] used pulsed laser deposition to deposit their films, rather than the chemical techniques described here and by Paskaleva *et al.*[405].

Similarly, Figure 2.20(b) shows the XPS spectrum for the interfacial Ga_2O_3/Ge(100) sample in the Ge 3p and Ga 3p region. Here, the formation of GeO_2 occurs analogous to the formation of SiO_2 above. The inset in Figure 2.20(b) shows the Ge 3d region. As well as the GeO_2 previously mentioned, there is also a doublet shifted from the elemental Ge peaks by 0.80 eV. This corresponds to an oxidation state of Ge^+ [438].

The thickness of the interfacial oxide can be estimated by the process established by Hill *et al.*[439]–[441], where the thickness of the native oxide, *d*, is given by equation (2.21). I_o is the native oxide peak intensity, and I_s is the substrate peak intensity.

$$d = \lambda_0 \sin\theta \ln\left(1 + \frac{I_o}{I_s}\right) \qquad (2.21)$$

Hence, by using equation (2.21), the native oxide thickness is found to be 0.73 nm, 0.75 nm, and 0.89 nm for the Si(111), Si(100) and Ge(100) substrates respectively. It should be noted that as this analysis neglects the 3 nm Ga_2O_3 overlayer, the signal from the bulk Si/Ge is reduced relative to that of the native oxide, the calculated thicknesses are an upper limit, and the actual thickness of the native oxide will be less than this. Whilst, it would be expected that the interfacial oxide may have an effect on the band alignment, the band

offsets reported here are consistent with those reported by Chen *et al.*[406] who do not observe the interfacial native oxide. This would suggest that a thin interfacial oxide, as observed here, has little effect on the band alignment, and hence the device performance.

To summarize, amorphous Ga_2O_3 films are grown on Si and Ge substrates by ALD. The valence band offsets are determined by XPS to be 3.49±0.08 eV, 3.47±0.08 eV and 3.51±0.08 eV for the Si(111), Si(100) and Ge(100) substrates respectively. IPES is also used to investigate the conduction band of a thick Ga_2O_3 film, by combining the IPES with VB-XPS, the band gap is found to be 4.63±0.14 eV. The resulting conduction band offsets are found to be 0.03, 0.05 and 0.45 eV respectively, resulting in a type I heterojunction in all cases. In all cases a thin, native oxide is observed after deposition. The determination of the band alignments to this accuracy, has important implications for devices based on Ga_2O_3/Si and Ga_2O_3/Ge heterojunctions, including MOSFET and MOSCAP type devices.

Here, we can see the advantage of using the Kraut method to determine the band alignments of semiconductor heterojunctions, as this allows for the properties of devices to be explained easily.

2.4 Phase Identification

Due to the complex nature of the kesterite structure and the many secondary phases that may be present in CZTS(Se). Several techniques are commonly used to identify the phase of the deposited films and determine the presence of any secondary phases. The two most commonly used techniques are x-ray diffraction and Raman spectroscopy.

2.4.1 X-Ray Diffraction

Consider an infinite square lattice of atoms of spacing, d. X-rays of wavelength, λ, are incident upon the sample at an angle, θ, to the sample surface such that $\theta = 90°$ corresponds to the sample normal. The geometric derivation of this result is shown in Figure 2.22.

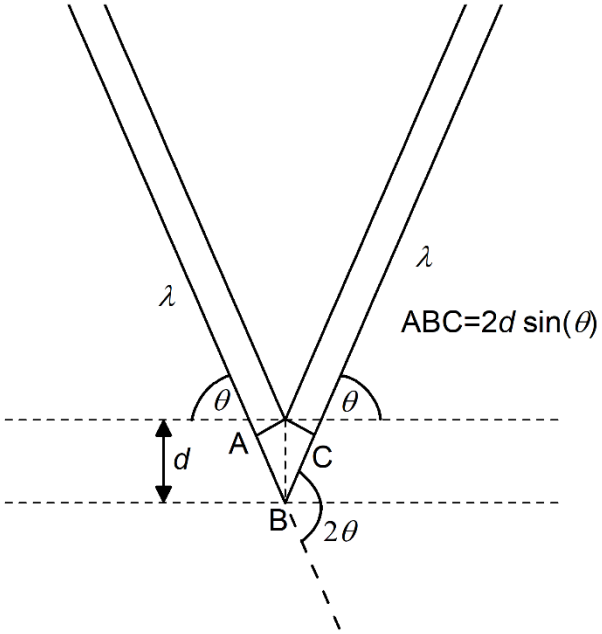

Figure 2.22 – A geometric derivation of Bragg's Law.

The x-ray wave-fronts can diffract off any of the planes parallel to the sample surface. By considering the path difference of the wave-fronts diffracting from neighbouring planes and stating that this must be equal to an integer number of wavelengths, the condition for constructive interference can be found. This is Bragg's law, as given in equation (2.22).

$$n\lambda = 2d \sin\theta \tag{2.22}$$

The interplanar spacing of the (hkl) plane, d_{hkl}, can then be related to the lattice parameters by the Miller indices of the plane. In the case of a simple cubic structure this is given by equation (2.23).

$$d_{hkl} = \frac{a}{\sqrt{h^2 + k^2 + l^2}} \tag{2.23}$$

For crystals with a non-cubic lattice, the equation for the interplanar spacing is more complex due to the reduced symmetry of the lattice. For instance, for a tetragonal lattice, such as that of the kesterite or stannite structures, the interplanar spacing is given by equation (2.24).

$$\frac{1}{d_{hkl}^2} = \frac{h^2 + k^2}{a^2} + \frac{l^2}{c^2} \tag{2.24}$$

The lattice parameters of many of the secondary phases that can be present in kesterite thin films are comparable to that of the kesterite phase itself. Thus, many secondary phases exhibit diffraction maxima at similar values of 2θ as the kesterite phase, making the identification of secondary phases by XRD alone difficult. A representative x-ray

diffractogram of CZTS nanoparticles is shown in Figure 2.23(a), from which it is difficult to distinguish the phases present. Typically, Raman spectroscopy is used in conjunction with XRD to identify secondary phases. Figure 2.23(b) shows the Raman spectrum from the same sample, where considerably more secondary phases can be observed than in the diffractogram shown in Figure 2.23(a).

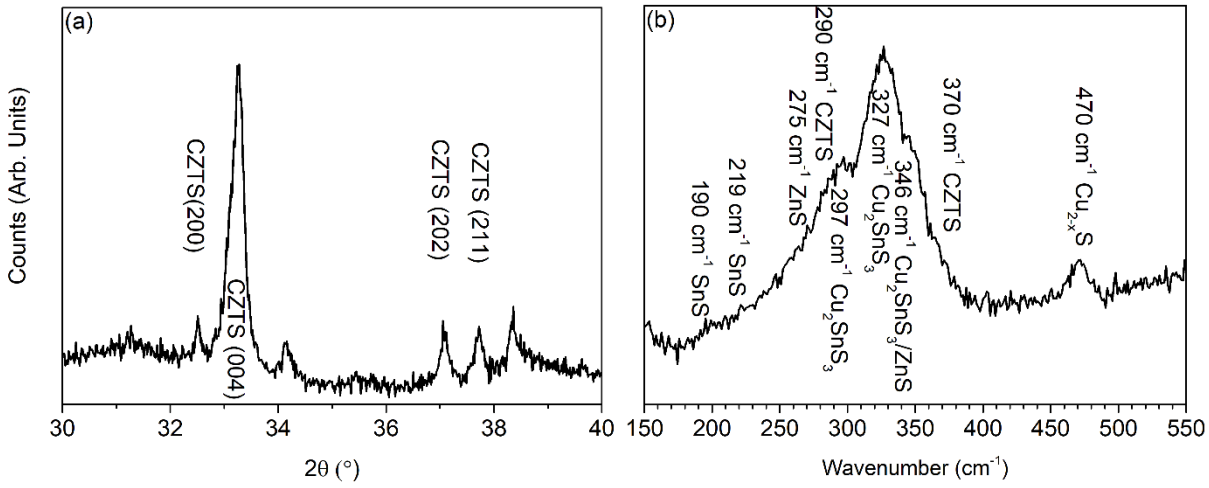

Figure 2.23 - (a) shows the powder x-ray diffractogram of CZTS nanoparticles, with several peaks labelled. (b) shows the Raman spectrum of the nanoparticles, which show considerable amounts of secondary phases.

2.4.2 Raman Spectroscopy

Raman spectroscopy is another technique commonly used for determining the phases present in thin films of kesterite materials and can also be used for determining the number of layers in a sample of 2-D material, such as the transition-metal dichalcogenides (TMDs).

The technique uses the inelastic scattering of photons to observe rotational and vibrational modes of a system. In solid-state materials, only the vibrational modes occur and these usually correspond to the phonons (i.e. the quantised lattice vibrations.) of the crystal.

In Raman spectroscopy, a light source, typically a laser with a photon energy in the near-infrared, visible or near-ultraviolet range, is incident upon the sample, exciting the sample into an unstable, virtual state. A photon is then re-emitted by the sample with a particular energy, which can be the same as the incident photon energy, corresponding to elastic, Rayleigh scattering, or higher or lower than the incident photon energy, corresponding to inelastic scattering. If the emitted energy is larger than the incident energy, then the process is known as Anti-Stokes (Raman) scattering, otherwise if the photon energy is lower than the initial energy, the process is called Stokes (Raman) scattering. Stokes scattering results in a ground state system being excited into a higher vibrational state, and

the difference in the photon energies thus corresponds to the energy difference between the ground and the first excited vibrational state. The energy-level diagram of the different scattering mechanisms is given in Figure 2.24. Vibrational modes can also be probed by infrared absorption techniques, such as Fourier-transform infrared spectroscopy (FTIR). The techniques are, in many cases, complimentary, as some modes that are inactive in Raman spectroscopy are active in absorption spectroscopy and *vice versa*.

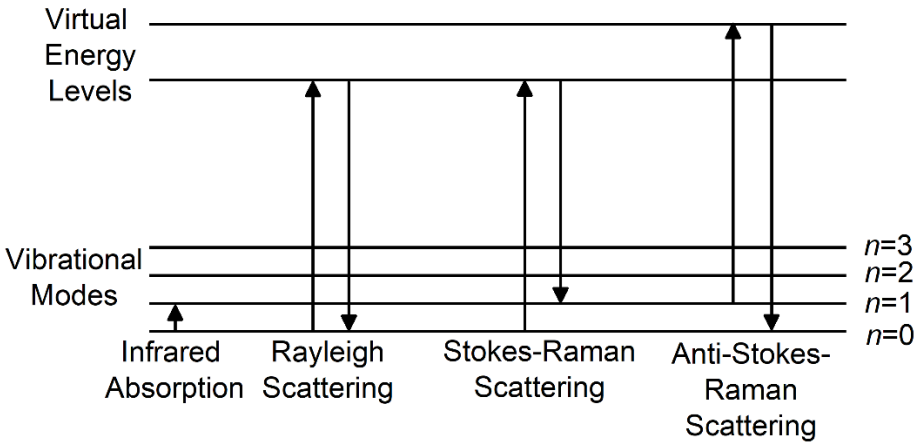

Figure 2.24 – A schematic diagram showing infrared absorption, and the Rayleigh, Stokes and anti-Stokes scattering mechanisms.

For historical reasons, the energy unit most commonly used in Raman spectroscopy is the relative wavenumber, which is defined as the difference between the reciprocals of the incident and the final wavelengths. This definition is given equation (2.25). Typically, the wavenumber is given in units of inverse cm, i.e. cm^{-1}.

$$\Delta w = \frac{1}{\lambda_0} - \frac{1}{\lambda_1} \qquad (2.25)$$

A list of the most commonly observed Raman peaks in kesterite materials and the secondary phases thereof is given in Table 2.4.

Phase	*Raman Scattering Peak (cm^{-1})*	*References*
CZTS	289, **339**, 350, 370	[188], [327], [442], [443]
CZTSe	168, **191**, 231, 243, 383	[444], [445]
Tetragonal Cu_2SnS_3	297, **337**, 352	[188], [446], [447]
Cubic Cu_2SnS_3	267, **303**, **356**	[188], [446], [447]
Cu_3SnS_4	275, **318**	[188], [446], [447]
ZnS	275, **352**	[188], [448], [449]
SnS	160, **190**, 219	[188], [450], [451]
SnS_2	215, **312**	[188], [450], [451]
Sn_2S_3	183, 234, 251, **307**	[450], [451]
Hexagonal $Cu_{2-x}S$	**475**	[188], [452], [453]
MoS_2	288, 384, **410**	[188], [454]–[458]
$MoSe_2$	**242**, 285	[457]–[460]

Table 2.4 - This table gives a summary of the main peaks observed for kesterite materials and their common secondary phases. The strongest peaks are indicated in bold font.

2.5 The Hall Effect

2.5.1 The Standard Hall Effect

When a free charge is moving in a magnetic field, its motion is affected by the Lorentz force, which is given by equation (2.26).

$$\boldsymbol{F} = q(\boldsymbol{E} + \boldsymbol{v} \times \boldsymbol{B}) \tag{2.26}$$

Where $\boldsymbol{F}$ is the Lorentz force, q is the electronic charge, $\boldsymbol{E}$ is the electric field, $\boldsymbol{v}$ is the velocity vector of the charge carrier and $\boldsymbol{B}$ is the magnetic field.

When a (semi-)conductor is placed in a magnetic field and a current passed through it, the charge carriers composing the current are affected by the same force as in equation (2.26). However, for the current to still be measured there must be no net resultant force upon the charge carriers (i.e. $\boldsymbol{F} = 0$). Thus, there must be some electric force equal in magnitude and opposite in direction to the magnetic field, as in equation (2.27).

$$E_y = -v_x B_z \tag{2.27}$$

This electric field is caused by charge carriers accumulating on one side of the probed material, leaving the opposite side with an equal and opposite charge, thus generating an electric field. Since the width of the conductor, w, would typically be known, this field can instead be written as the potential difference between the two charged faces, which is the Hall voltage, V_H. This is shown as a schematic diagram in Figure 2.25.

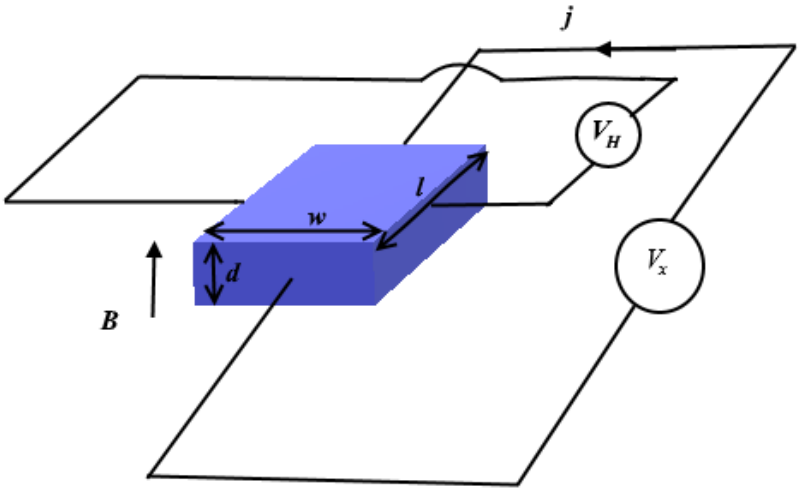

Figure 2.25 – A schematic diagram showing the experimental set-up of the standard Hall effect.

The Hall voltage can itself then be related to the sheet carrier density, n_s by the relation shown in equation (2.28).

$$n_s = \frac{IB}{e|V_H|} \tag{2.28}$$

Where e is the elementary charge. The sheet density is then related to the bulk carrier density, n by equation (2.29), where d is the thickness of the sample.

$$n_s = nd \tag{2.29}$$

Equivalently, the Hall coefficient, R_H, can be considered where R_H is given by equation (2.30).

$$R_H = \frac{V_H d}{IB} = -\frac{1}{ne} \tag{2.30}$$

A key advantage of the Hall effect is that it is able to distinguish between positively charged and negatively charged carriers by the sign of the Hall coefficient. Thus, the Hall effect can be used to distinguish between p-type and n-type semiconductors.

For a semiconducting material, there will necessarily be contributions from both electrons and holes, in which case the Hall coefficient is modified to the form shown in equation (2.31).

$$R_H = \frac{p\mu_h^2 - n\mu_e^2}{e(p\mu_h - n\mu_e)^2} \tag{2.31}$$

For the cases where $n \gg p$ or $p \gg n$ (i.e. for doped semiconductors) equation (2.30) is recovered.

2.5.2 The van der Pauw Method

The van der Pauw method, first proposed by L. J. van der Pauw[461], also allows for the determination of the resistivity of any flat arbitrarily shaped sample, and hence the mobility of the majority charge carrier using the same apparatus. A series of four contacts are used to determine these properties, as shown in Figure 2.26.

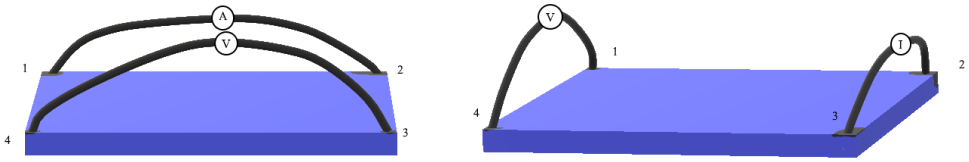

Figure 2.26 – A schematic diagram showing the contact set-ups used in the van der Pauw method.

The following four requirements were proposed by van der Pauw: Firstly, the contacts must be at or close to the edge of the sample; secondly, the contacts are small (i.e. contact size is much smaller than the sample size); thirdly, the sample is of uniform thickness, and finally, the sample is singly connected such that there are no isolated holes in it.

The mobility, μ, is then related to the sheet resistance, R_s, by equation (2.32).

$$\mu = \frac{|V_H|}{IBR_s} = \frac{1}{en_sR_s} \tag{2.32}$$

Where R_s is given by the van der Pauw formula in equation (2.33).

$$e^{-\pi R_A/R_S} + e^{-\pi R_B/R_S} = 1 \tag{2.33}$$

Here, R_A and R_B are characteristic resistance between sets of contacts. $R_{ij,kl}$ is defined by equation (2.34), where V_{kl} is the voltage difference between the kth and lth contact whilst I_{ij} is current between the ith and jth contact.

$$R_{ij,kl} = \frac{V_{kl}}{I_{ij}} \tag{2.34}$$

The reciprocity theorem requires that equation (2.35) holds, such that the resistances are consistent when the current is reversed.

$$R_{ij,kl} + R_{ji,lk} = R_{kl,ij} + R_{lk,ji} \tag{2.35}$$

Thus, the resistances R_A and R_B are given by equations (2.36) and (2.37) .

$$R_A = \frac{R_{12,43} + R_{21,34} + R_{34,21} + R_{43,12}}{4} \quad (2.36)$$

$$R_B = \frac{R_{23,14} + R_{32,41} + R_{41,32} + R_{14,23}}{4} \quad (2.37)$$

Hence, equation (2.33) can be solved numerically to obtain the sheet resistance.

Hall measurements in the van der Pauw geometry are also somewhat more complicated than in the simple Hall effect described earlier. Instead of a single measurement being made, a minimum of 8 voltages are measured between the diagonal contacts. The Hall voltage is then given by equation (2.38).

$$V_H = \frac{V_{13}^+ + V_{13}^- + V_{31}^+ + V_{31}^- + V_{24}^+ + V_{24}^- + V_{42}^+ + V_{42}^-}{8} \quad (2.38)$$

Where $V_{ij}^{\pm}$ denotes the potential difference between the ith and jth contact under a positive and negative current respectively.

2.5.3 Hall Effect Apparatus

Hall effect measurements described in this thesis were performed with a homebuilt Hall effect station in the van der Pauw at room temperature in ambient conditions and a magnetic field strength of 0.8 T[462]. Ohmic contacts were made by drop casting liquid gallium onto the top surface of the sample, which was then contacted by gold probes.

2.6 Band Structure Calculations

2.6.1 Density Functional Theory

Although density functional theory (DFT) is not the main topic of this thesis, and as such will not consider it as thoroughly as a theorist would, it does have some practical usage for the spectroscopist. Comparisons of the electronic densities of states in the valence band predicted by DFT can be useful in predicting and explaining some properties of semiconductors and insulators.

The theoretical underpinning of DFT was pioneered in the 1960s, by Hohenberg, Kohn and Sham[463], [464]. Kohn's role in the development of DFT led to his award of half of the 1998 Nobel prize in Chemistry[465].

DFT can effectively be considered a numerical method of attempting to solve the Schrödinger equation for a many-body system. To simplify matters, the Born-Oppenheimer

approximation, that the kinetic energy of the positively charge nuclei can be ignored is used. As nuclear masses are approximately 6 orders of magnitude greater than that of a free electron. Such an approximation is clearly valid, as the speed of the nuclei will be considerably smaller than that of the electrons, due to this huge difference in mass. Henceforth the nuclei can be treated as a potential in which the electrons move. A wavefunction can then be guessed, and refined to minimise the energy of the system, which acts as an upper limit of the ground state of the system.

However, in a many-body system of N electrons, the nature of the wavefunction will itself be complicated and is dependent on 4N variables. Equally, the wavefunction itself cannot be probed directly by experiment. Fermi and Thomas independently developed an alternative method, instead of considering the wavefunction, the electron density is considered[466], [467]. The electron density, can at least in principle, be measured experimentally, by low-energy electron diffraction and PES for instance, thus allowing for experimental verification of the results.

In practice, DFT is regularly used to predict the crystal structures that a particular system may take under equilibrium conditions, as well as the formation energies of defects, and the electronic band structure of materials. Several issues remain, however, namely the prediction of the band gap, and band alignments in heterojunctions. These problems can be overcome to some extent by using different approximations and functional forms[468]–[471].

The electronic band structures that DFT programs obtain can then be projected, resulting in an orbital-resolved density of states that can be directly compared with photoemission measurement of the bands. Prior to comparison, some corrections need to be made to the theoretical density of states: firstly, the orbitals need to be corrected for the cross-section of the photoemission process. Numerous tables of the cross-sections and the corresponding asymmetry parameters exist for various photon energies, including references [472]–[477].

After cross-section correction, the partial densities of states (PDoS) can be summed to obtain a total density of states (TDoS) which should then be convoluted with functions representing the experimental broadening. In practice this usually consists of evaluating the analyser resolution by convoluting the Fermi-Dirac distribution, with a Gaussian of variable FWHM, and minimising the residual. By this method, the resolution of the analyser

described in section 2.3.1.4 is found to be 0.38±0.03 eV. Figure 2.27 shows the comparison between the experimentally measured Fermi level and the broadened synthetic function.

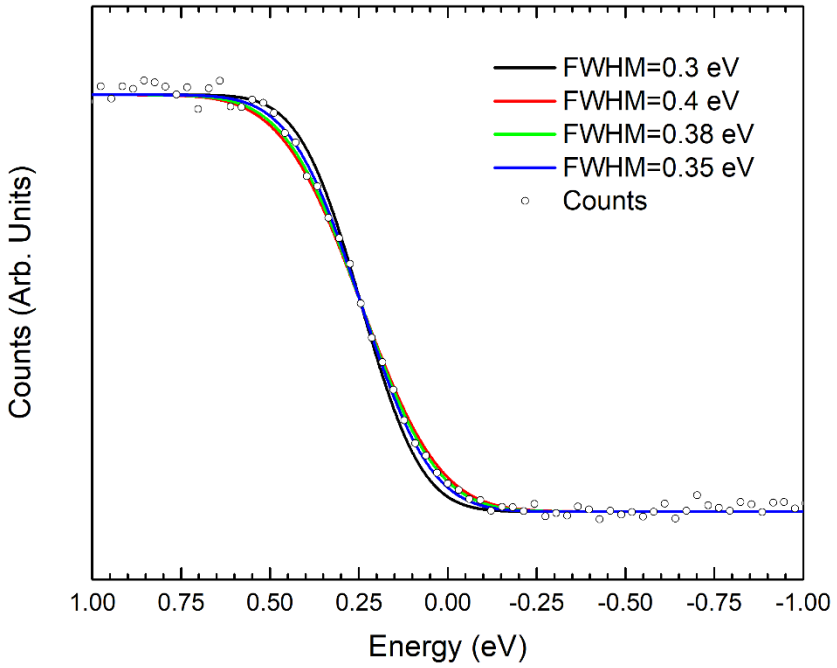

Figure 2.27 - Experimental Ag Fermi level from a clean polycrystalline Ag foil and several synthetic Fermi-Dirac functions at 300K which are broadened by convoluting with a Gaussian function of the stated FWHMs. The Gaussian with a FWHM of 0.38 eV provides the best fit.

Once the resolution is found, the TDoS should be convoluted with the Gaussian function found to best describe this broadening. Finally, a Lorentzian function, accounting for lifetime broadening effects, should also be convoluted with the Gaussian-broadened TDoS. The FWHM of the Lorentzian should be allowed to vary, to best fit the valence band maximum.

After the convolution with the Lorentzian function is applied, the experimentally corrected density of states (EDoS) can be normalised to the intensity of a feature in the PES valence band and aligned allowing for comparison between the theoretical results and the experimental spectrum. By also displaying the PDoS on the same figure, the origin of features within the valence band can be ascertained.

2.6.2 $\boldsymbol{k} \cdot \boldsymbol{p}$ Perturbation Theory

An alternative approach for calculating the band structure of a material is $\boldsymbol{k} \cdot \boldsymbol{p}$ perturbation theory, this is based on a perturbation of the familiar parabolic band approximation. As $\boldsymbol{k} \cdot \boldsymbol{p}$ perturbation theory is not the main topic of this thesis, we will only cover the key points of the derivation. In the parabolic band approximation, the region

close to the band extrema are responsible for the transport, electronic and optical properties of the material, as it is these states that are first occupied by charge carriers.

In many cases the extrema occur at the Γ point (i.e. the centre of the Brillouin zone, where $\boldsymbol{k} = 0$). Thus, the dispersion relation close to the band extrema can be approximated by equation (2.39), which can be understood simply as the Taylor series expansion of the band structure close to the Γ point.

$$E_{e,h}(\boldsymbol{k}) = E_{e,h}(0) \pm \frac{\hbar|\boldsymbol{k}|^2}{2m^*_{e,h}} \tag{2.39}$$

However, for materials where there are defect levels present or a large carrier density in either band, the excitation of carriers will no longer be primarily to states close to the band extrema. Thus, the carriers in the two bands can interact resulting in a non-parabolic dispersion. This effect is more pronounced in small band-gap materials, due to the smaller difference in energy between the carriers in each band.

Instead, the dispersion relation within the one-electron approximation can be calculated by considering $\boldsymbol{k} \cdot \boldsymbol{p}$ interactions. Thus, the Schrödinger equation can be written as in equation (2.40).

$$H_{\boldsymbol{k}} u_{n,\boldsymbol{k}} = \left[-\frac{\hbar^2}{2m_0}\nabla^2 + V(\boldsymbol{r}) + H_1 + H_2 + H_{SO} \right] u_{n,\boldsymbol{k}} = E_{n,\boldsymbol{k}} u_{n,\boldsymbol{k}} \tag{2.40}$$

$$H_1 = \left(\frac{\hbar}{m_0}\right) \boldsymbol{k} \cdot \boldsymbol{p} \tag{2.41}$$

$$H_2 = \frac{\hbar^2|\boldsymbol{k}|^2}{2m_0} \tag{2.42}$$

Here, $\boldsymbol{k}$ denotes the wave vector of the lattice and $\boldsymbol{p}$ is the momentum operator of the particle. $V(\boldsymbol{r})$ is the periodic potential of the lattice and H_{SO} is the part of the Hamiltonian which accounts for spin-orbit interactions. Here, H_1 and H_2 are the first and second order terms of the perturbation.

By substituting $u_{n,\boldsymbol{k}}$ for the sum of the Bloch functions over all bands and considering only spin orbit interactions that are $\boldsymbol{k}$-independent by assuming that the $\boldsymbol{k}$-dependent spin-orbit interactions are negligible, the Hamiltonian matrix can be written as the diagonal matrix in equation (2.43).

$$H = \begin{bmatrix} \widetilde{H} & 0 \\ 0 & \widetilde{H} \end{bmatrix} \tag{2.43}$$

Where $\widetilde{H}$ is given by equation (2.44).

$$\widetilde{H} = \begin{bmatrix} E_s & 0 & kP & 0 \\ 0 & E_p - \Delta_{SO}/3 & \sqrt{2}\,\Delta_{SO}/3 & 0 \\ kP & \sqrt{2}\,\Delta_{SO}/3 & E_p & 0 \\ 0 & 0 & 0 & E_p + \Delta_{SO}/3 \end{bmatrix} \tag{2.44}$$

Where E_s and E_p are the energy eigenvalues of the conduction and valence bands under the parabolic approximation respectively. Δ_{SO} is the spin-orbit splitting of the valence band given in equation (2.45) and P is the momentum matrix element given in equation (2.46).

$$\Delta_{SO} = i\frac{3\hbar}{4m_0^2c^2}\langle X|\boldsymbol{\nabla} V \times \boldsymbol{p}|Y\rangle \tag{2.45}$$

$$P = -\frac{i\hbar}{m_0}\langle S|p_z|Z\rangle \tag{2.46}$$

Where $|S\rangle$ is the *s*-like basis function corresponding to the conduction band, whilst $|X\rangle$, $|Y\rangle$, and $|Z\rangle$ are the equivalent *p*-like basis functions of the valence band. The eigenvalue equation can hence be found to have the form given in equation (2.47).

$$(E - E_s)\big(E - E_p\big)\big(E - E_p + \Delta_{SO}\big) - k^2p^2\big(E - E_p + 2\,\Delta_{SO}/3\big) = 0 \tag{2.47}$$

By assuming that the eigenvalues are small (i.e. much less than the band gap) and by expressing the momentum matrix element as a function of the effective mass of the band edge, the dispersion relation can be written as in equation (2.48).

$$E(1 + \alpha E) = \frac{\hbar^2k^2}{2m_0^*} \tag{2.48}$$

Where the energy, E, is measured with respect to the conduction band minimum. In the case where the effective mass is considerably less than the rest mass of a free electron, and the spin-orbit splitting of the valence band is not comparable to the band gap of the material, α can be approximated by the form shown in equation (2.49). This is the α-approximation.

$$\alpha = \frac{1}{E_g} \tag{2.49}$$

Figure 2.28 shows the dispersion relations, the density of states and carrier densities of the conduction band within the parabolic and α-approximation regimes. The code used to produce Figure 2.28 is given in Appendix A. The effective masses and the band gap used to produce the figures were $m^* = 0.28m_0$ and $E_g = 4.63$ eV respectively.

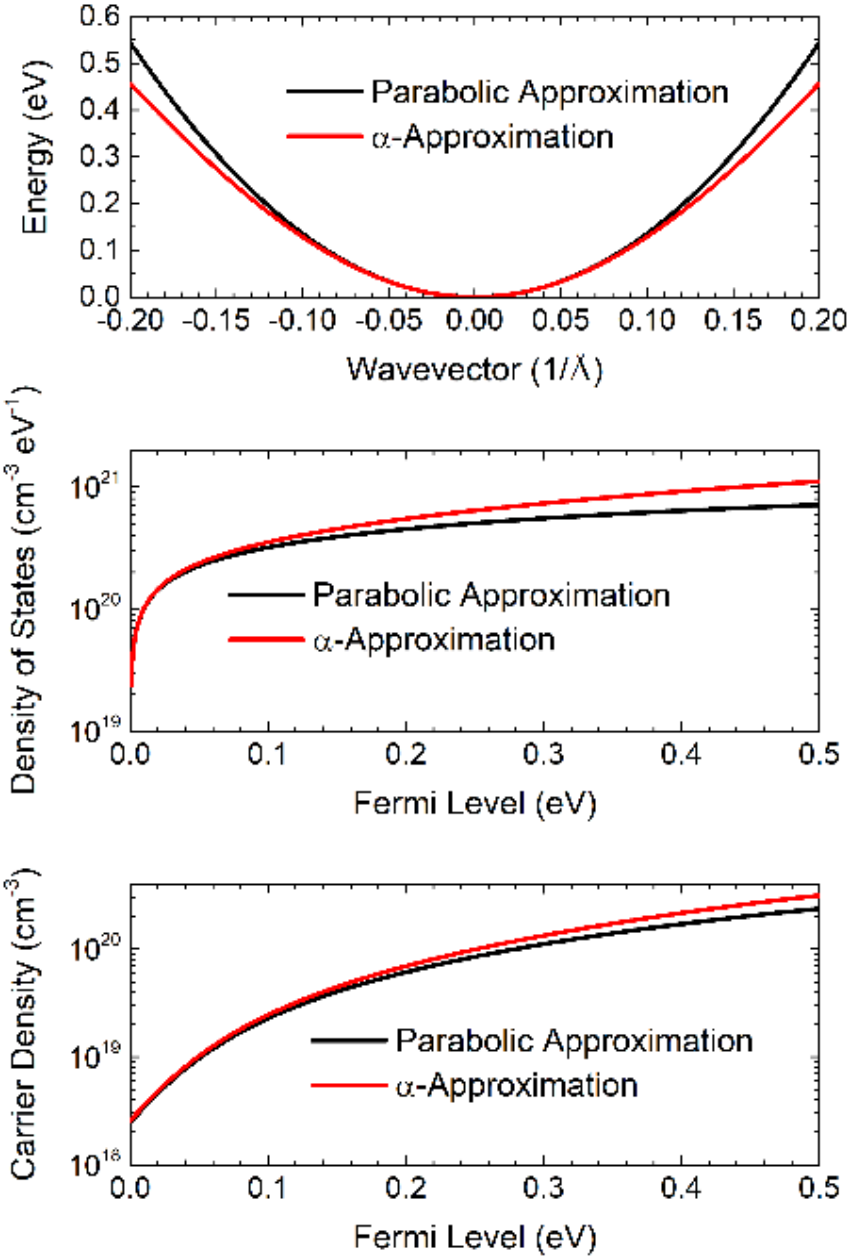

Figure 2.28 – The dispersion relation, density of states and carrier densities of the conduction band calculated within the parabolic and ∝-approximation for Ga_2O_3.

2.7 Thin Film Synthesis Methods

The thin films investigated during this thesis were deposited in several different modes, by the author and by collaborators. In this section we will briefly consider the different synthesis routes and the advantages and disadvantages thereof. Synthetic routes can generally be split into two categories: chemical synthesis, where precursors undergo a chemical reaction at the substrate interface, to form a thin, solid film; and physical synthesis, where films are produced by mechanical or thermodynamic processes. The next part of this work will consider the physical and chemical synthetic routes separately and discuss the examples of each that have been deployed in the work described in this thesis.

2.7.1 Chemical Synthesis Techniques

Chemical synthesis techniques typically consist of a number of precursors chemicals, containing the elements that form the compound of interest. In solution-based synthetic routes these are usually dissolved in a solvent. When the solution comes into contact with the solid substrate, the precursors react, forming a solid thin-film on the substrate. Alternatively, precursor vapours may be carried by an inert carrier gas, usually dry N_2 or Ar gas, and carried to the target, where the different precursors react to form a solid thin-film once again.

2.7.1.1 Atomic Layer Deposition

Atomic layer deposition (ALD) is closely related to the widely-known chemical vapour deposition (CVD), which is frequently used for the synthesis of III-V and II-VI semiconductors, as both use the vapours of, usually organic precursors, in vacuum to deposit thin-films. A key difference between the two techniques is that ALD uses a self-terminating reaction to deposit a monolayer of the precursor under ideal conditions. Another major difference is that the substrate temperature in ALD is usually considerably lower than that used in CVD. ALD processes typically self-saturate at temperatures that are less than 400^{o}C[478], [479], whereas CVD typically requires temperatures of approximately 1000^{o}C, due to the stronger bonds of the precursors used.

The use of such low temperatures in ALD processes usually results in amorphous or polycrystalline rather than epitaxial thin films in most cases. For dielectric applications in electronics and as a diffusion barrier, amorphous films are usually preferred, as this effectively reduces the number of pinholes and grain boundaries, and hence the number of sites through which charge carriers or atoms can leak or diffuse[480], [481].

Initially, the substrate is cleaned either *ex situ* prior to entering the ALD chamber or by an etch *in situ*, typically using an ozone or nitrogen plasma. After cleaning, the substrate is then heated to a temperature within the so-called ALD window, which is the range of temperatures for which the reaction is self-saturating[479], [481]. The first precursor is then allowed into the chamber in a 'pulse', for a set amount of time which corresponds to complete coverage of the substrate. Any remaining precursor and any reaction by-products are then purged with an inert carrier gas. The length of the purge depends on the desorption time of the unreacted precursor, to ensure that no excess precursor is left on the sample surface. After the purge, the second precursor is allowed into the reaction chamber and reacts with the remaining dangling ligands at the sample surface to form a second layer upon the first. The chamber is then once again purged, and the cycle repeated until the film has the thickness desired.

As the deposition of the film is layer-by-layer, ALD allows for a very-fine control over the thickness of the deposited films. By choosing sufficiently long pulse times, uniform coatings over very-high aspect ratio surfaces can also be achieved[482]–[484].

2.7.1.2 Sol-Gel Deposition

In contrast to ALD sol-gel deposition uses precursor chemicals dissolved in a liquid solvent. The substrate can then be immersed in the solution for some time, and the solution heated to promote the reaction. Alternatively, the solution may be cast onto the substrate, by a wide variety of techniques, such as drop casting, spray pyrolysis or spin coating and heated until the reaction is complete.

2.7.1.3 Nanoparticle Inks

An alternative solvent-based method of deposition is the formation of nanoparticles dispersed in a volatile solvent. Typically, nanoparticles can be formed by injecting the precursor chemicals into the hot solvent. This is known as the hot-injection method and typically occurs under an inert atmosphere.

2.7.2 Physical Synthesis Techniques

Physical synthesis techniques typically use mechanical or thermodynamic processes to remove material from a target, and subsequently deposit the material upon a substrate. Examples include pulsed laser deposition, molecular beam epitaxy and sputter deposition.

2.7.2.1 Pulsed Laser Deposition

In pulsed laser deposition (PLD), a high-power, pulsed laser is incident upon a target of the material to be deposited. Often these targets are stoichiometric powders, pressed to form a target. The coherent light from the laser is absorbed by the target, heating it rapidly thus vaporising material close to the surface of the target. Some of the ablated material is then ionised by multiphoton ionisation processes, producing a plasma plume close to the target[485]–[488].

Material from the target is then incident upon the substrate, which is at an elevated temperature to promote epitaxial growth[485], albeit at temperatures lower than those required for molecular beam epitaxy (MBE)[487].

2.7.2.2 Sputter Deposition

Sputter deposition is similarly a physical deposition method. The process is similar to that described for ion etching material described in section 2.2.1. An inert gas, typically Ar, is leaked into a vacuum chamber. The Ar atoms are ionised, and then accelerated by a voltage towards one or more targets[489]–[492]. Depending on the material being deposited, reactive gases can also sometimes be used, for instance O_2 is often used as the sputter gas for the deposition of oxides, as this naturally resolves the issue of differential sputtering of the target material[493].

As in sputter etching, material from the target is then liberated. This material is then free to move within the vacuum chamber and will be deposited upon any free surface. Typically, the substrate is placed directly beneath the target and may be heated to allow for greater crystallinity and larger crystallites.

In many cases the sputter target may need to be cooled, typically by water as the sputter process can impart a large amount of thermal energy. Without cooling, the heat of the target can result in radiative heating of the substrate and as such can unintentionally change the properties of the deposited film[493].

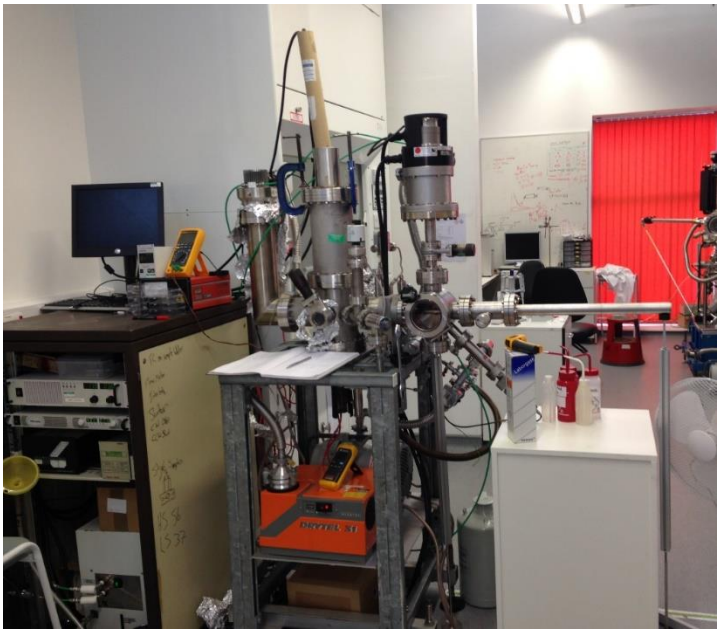

Figure 2.29 – A photograph of the homebuilt DC magnetron sputtering system used in this work for sputtering CZTS from a single, near stoichiometric quaternary target.

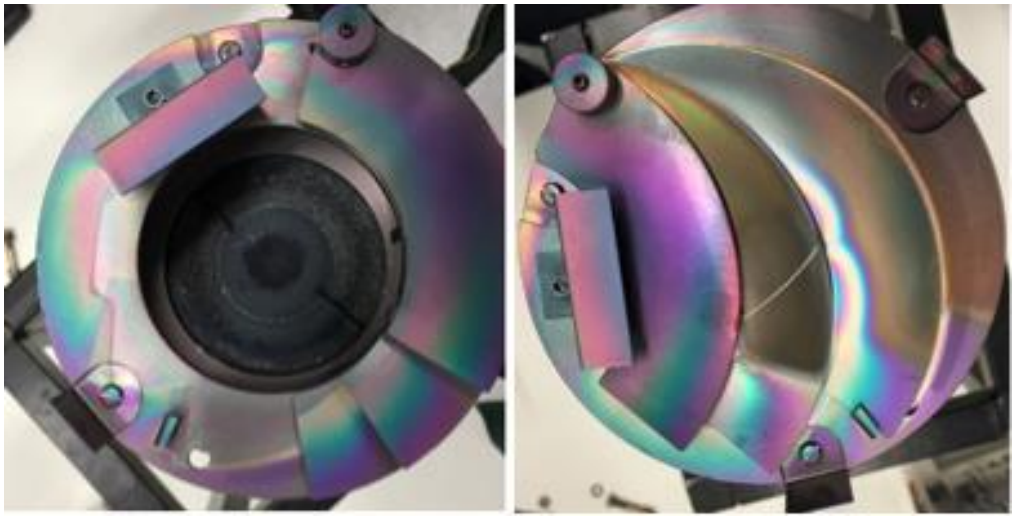

Figure 2.30 – Left, shows the DC magnetron sputter chamber with the shutter open, such that the single, near-stoichiometric quaternary target can be seen in the centre. Also visible is that characteristic doughnut shape etched into the target. Right, shows the same chamber but with the shutter closed. In both images thin film coating of the vacuum chamber can be seen as a rainbow-like pattern covering exposed parts of the system.

In the next chapter of this thesis, we will consider the deposition of kesterite thin-films by sputtering and nanoparticle spin-coating. The characterisation of the sputtered films will then be described, and the photoemission spectra investigated. Finally, the band alignments with several potential buffer materials will be investigated using the Anderson electron affinity rule.

3 PHOTOELECTRON SPECTROSCOPY OF KESTERITE THIN FILMS

This chapter is partially based on the following paper:

Mattinen, M.; King, P. J.; Khriachtchev, L.; Meinander, K.; Gibbon, J. T., Dhanak, V. R.; Räisänen, J.; Ritala, M.; Leskelä, M. "Low-Temperature Wafer-Scale Deposition of Continuous 2D SnS_2 Films", **2018**, *Small*, 14 (21), 1800547

This chapter will open with a summary of the published literature on photoemission of CZTSSe which will be analysed critically. Much of the literature for the material is of a low quality, in many cases, using inappropriate backgrounds and peak-fitting. The PES of a number of CZTS, CZTSe and CZTSSe samples from numerous sources and growth techniques are described and analysed.

The band alignments with CdS, ZnS, ZnO, ZnSe, SnS_2 and In_2S_3 by the Anderson rule are determined and the implications of the results discussed.

Extensive literature exists for the XPS of CZTS and CZTSe based materials, however the quality of the research is generally poor and contains poor quality data, significant errors and misconceptions, up to the point of outright plagiarism of paragraphs relating to the XPS work.

A commonly used phrasing of the analysis of photoelectron spectra of CZTS thin films is that:

"the copper HR-XPS spectrum shows two narrow and symmetric peaks at 932 and 952 eV, indicative of Cu(I) with a peak splitting of 19.8 eV. The zinc 2p peaks located at 1022 and 1045 eV show a peak separation of 23 eV, consistent with the standard splitting of 22.97 eV, suggesting zinc(II). The tin 3d5/2 peaks located at 486.2 and 494.9 eV, and a peak splitting of 8.4 eV indicates Sn(IV). The S 2p3/2 peak for sulphides lies between 160 and 164 eV with a peak splitting of 1.18 eV. The sulphur 2p3/2 and 2p1/2 peaks in the spectra are located at 161.3 and 162.45 eV, which are consistent with the 160-164 eV range expected for S in sulphide phases."

This phrasing occurs originally by Riha *et al.* in the caption of figure S5 of ref [494] and later in the thesis of the aforementioned author[495]. Similar phrasing appears throughout the literature when referring to the photoelectron spectroscopy of CZTS and related compounds, a non-exhaustive list of which can be found in references[193], [496], [505]–[514], [497], [515]–[524], [498], [525]–[534], [499], [535]–[544], [500], [545], [501]–[504].

This has led to the propagation of key misunderstandings such as the identification of the chemical state is based on the energy splitting of components of the same core-level with different total angular momentum values, ***j***.

In many cases, the spectra that are presented are not deconvoluted and the binding energy is only given in the text, or with a line to the horizontal axis denoting the binding energy position of the peak. Likewise, in some cases XPS is used to obtain compositions, but no spectra are presented[546]–[550].

Where deconvoluted peaks are presented, the fitted peaks are in many cases obviously not correct: Backgrounds are often sat above the experimental data[505], [514], [515];the spin-orbit splitting is treated as a variable which indicates the chemical state[514], [518], [532], [551], [520], [523]–[525], [528]–[531]; FWHM vary considerably between spin-orbit split components[503], [538], [552], where the Coster-Kronig effect is not present[553], [554]; spin-orbit splitting of the S 2p is often neglected, and instead only fitted as a singlet[505]; asymmetric peaks due to impurities or secondary phases are ignored[515], [538], [541], [545], [555]–[557]; spin-orbit splitting is not used as a constraint on the peak positions; and synthetic peaks simply do not match the experimental data[193]; branching ratios for spin-orbit split components are not obeyed[537]; or only survey spectra are presented[558]–[561]; the spin-orbit splitting of the Sn 3d core-level being due to 'final-state' effects[540].

In some cases, features are misidentified as being different peaks[531], [542]. Another common issue, particularly when considering chemical synthetic methods is that impurities due to the precursors are described as negligible as the peak intensity is small[562], [563]. However, the impurities from commonly-used precursors, such as C, O, N and Cl, all have small photoionisation cross-sections. As such, the fact that the impurities are obviously visible in the photoemission spectra suggests that, in fact, considerable contamination is present in the sample.

Using the Anderson model, Yu *et al.*[564] find that In_2S_3 is likely to provide a beneficial band alignment with pure-sulphide CZTS. In contrast, Guo *et al.*[294] find that the band alignment of a device using the related n-type material Ag_2ZnSnS_4 (AZTS) as the buffer layer with CZTS, is detrimental, with a cliff-like CBO of 0.07eV.

CZTS and CZTSSe samples were synthesised by several methods namely physical vapour deposition and spin-coating of nanoparticle inks, and the chemical and electronic properties investigated by photoelectron spectroscopy. The band alignments with multiple

potential buffer layers are investigated using the Anderson method and the resulting band alignments are discussed.

3.1 Effects of Sulphurisation on the Surface Properties of CZTS Films Synthesised by DC Magnetron Sputtering From a Single, Quaternary Target

3.1.1 Film Synthesis

Prior to deposition, uncoated soda-lime glass (SLG) was cleaned *via* immersion in lab detergent and agitated by a sonic bath for 5 mins. The SLG was then rinsed with deionised water and dried with nitrogen. To remove any remaining detergent, the SLG was then agitated for a further 5 mins in acetone and rinsed and dried once more. To remove any remaining acetone, the SLG was agitated for a further 5 mins in propanol and blown dry using dry nitrogen. The SLG was clamped by the sample holder and transferred into the load-lock chamber. The load-lock chamber was evacuated until a pressure of 1×10^{-6} mbar was obtained, at which point the gate valve separating the load lock and the deposition chamber was opened and the sample transferred for deposition.

Deposition was performed using a DC-magnetron, sputtering a water-cooled, single, near-stoichiometric quaternary target, using Ar (99.999%, CK Gas) as the working gas. Prior to deposition, the Ar gas lines were evacuated and flushed a minimum of three times, to ensure the gas supply reaching the deposition chamber was clean. The substrate was placed under no external heating during deposition, heating due to plasma exposure resulted in a substrate temperature of approximately 80 ℃ as measure by an Al-Ni thermocouple in thermal contact with the sample holder and substrate.

After deposition, the Ar gas line was closed off, allowing the pressure to return to the baseline and the sample allowed to cool naturally to room temperature, at which point it was returned to the load-lock chamber. The load-lock was then vented with liquid nitrogen and the sample removed.

Sulphurisation was performed by placing the sample in a small graphite box of approximately $10 \times 1 \times 1$ cm alongside 50 mg of sulphur powder in a closed-space sublimation (CSS) chamber. The CSS chamber was then evacuated to 1 mbar before being backfilled to 300 mbar of nitrogen gas. The sample was then heated by ceramic heaters to between 400 ℃ and 600 ℃ and then left for 30 mins at the desired temperature, after

which the heaters were turned off and the sample allowed to cool naturally to room temperature. The resulting samples were then investigated by XRD, Raman spectroscopy, atomic force microscopy and Fourier-transform infrared spectroscopy and photoemission techniques.

3.1.2 Characterisation of DC-Magnetron Sputtered CZTS from a Single, Quaternary Target

Characterisation of the synthesised material required the usage of several techniques.

Figure 3.1 shows the x-ray diffractograms of the sputtered CZTS samples, with the prominent features labelled. The as deposited film and the film sulphurised at 400 ℃ show no significant peaks in the region of interest, suggesting that the films are amorphous in nature. At sulphurisation temperatures of 500 ℃ or greater, the CZTS (112) becomes apparent. However, at sulphurisation temperatures of 550 ℃ or greater, XRD peaks due to CuS secondary phases also become apparent. At 550 ℃ the CuS (101) is comparable in magnitude to the CZTS (112), whilst at 600 ℃ the CuS (101) and CZTS (112) are barely visible above the background, however the CuS (100) is considerably larger.

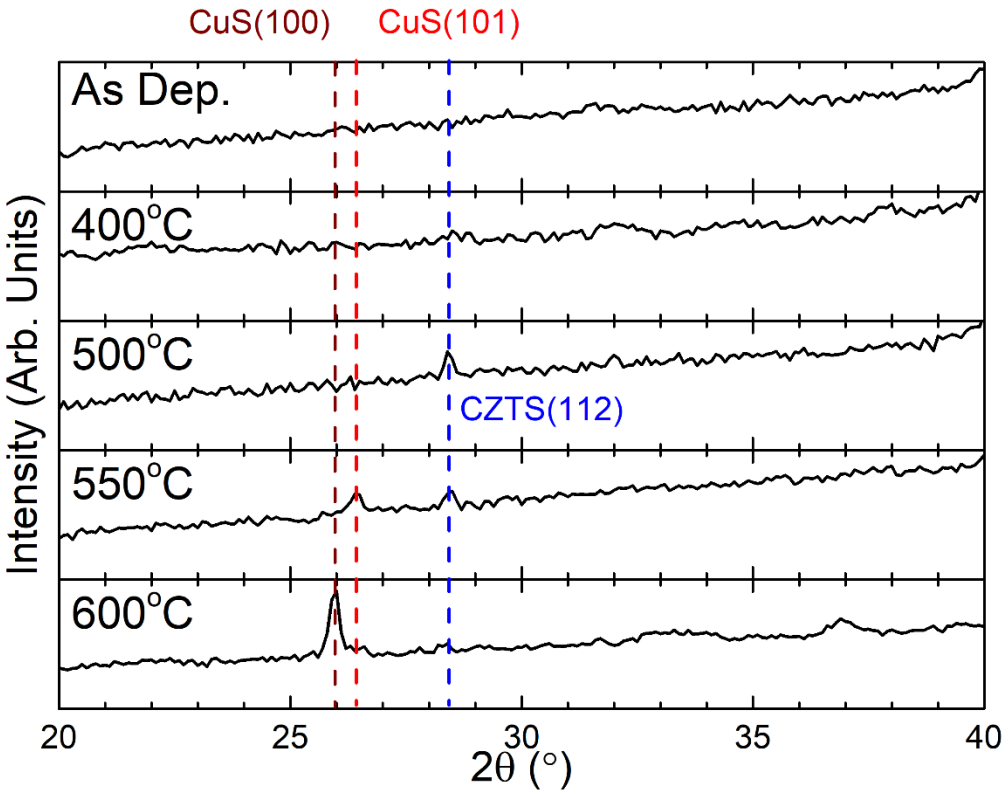

Figure 3.1 – X-ray diffractogram of sputtered CZTS samples. Also labelled are the main features in each diffractogram.

Raman spectroscopy was used to determine if any secondary phases were present, the resulting spectra are shown in Figure 3.2. The as deposited sample shows a single broad

peak, centred on $340\ \mathrm{cm}^{-1}$, corresponding to the strongest Raman mode of kesterite CZTS. The broadness of the peak indicates that the sample is amorphous in nature and has many secondary phases present. After sulphurisation at $400\ ^{\circ}\mathrm{C}$, the central peak is reduced in width, showing a clearer peak at approximately $340\ \mathrm{cm}^{-1}$, the reduced width suggests that the sample is more crystalline and has reduced quantities of secondary phases present. At $500\ ^{\circ}\mathrm{C}$, the Raman spectrum consists of several sharp peaks that can be assigned to kesterite CZTS or MoS_2 only. The presence of the MoS_2 peak is due to the chemical reaction of sulphur from the absorber with the Mo back contact. The main CZTS peak occurs at approximately $340\ \mathrm{cm}^{-1}$, whilst the main MoS_2 peak occurs at approximately $410\ \mathrm{cm}^{-1}$. When sulphurised at $550\ ^{\circ}\mathrm{C}$, the CZTS peak is reduced in size, and is becoming broader once again, indicating that the crystal quality is degrading at this high a temperature, the MoS_2 peak has increased in size and narrowed, suggesting a better quality MoS_2 layer. Finally, at $600\ ^{\circ}\mathrm{C}$, the CZTS Raman signal is barely visible, and the MoS_2 is by far the dominant peak, suggesting that by annealing at such high temperatures, the CZTS films has, in fact, delaminated from the substrate. Hence, by considering the diffractograms and spectrographs presented in Figure 3.1 and Figure 3.2, sulphurisation at $500\ ^{\circ}\mathrm{C}$ appears to produce the best quality CZTS films.

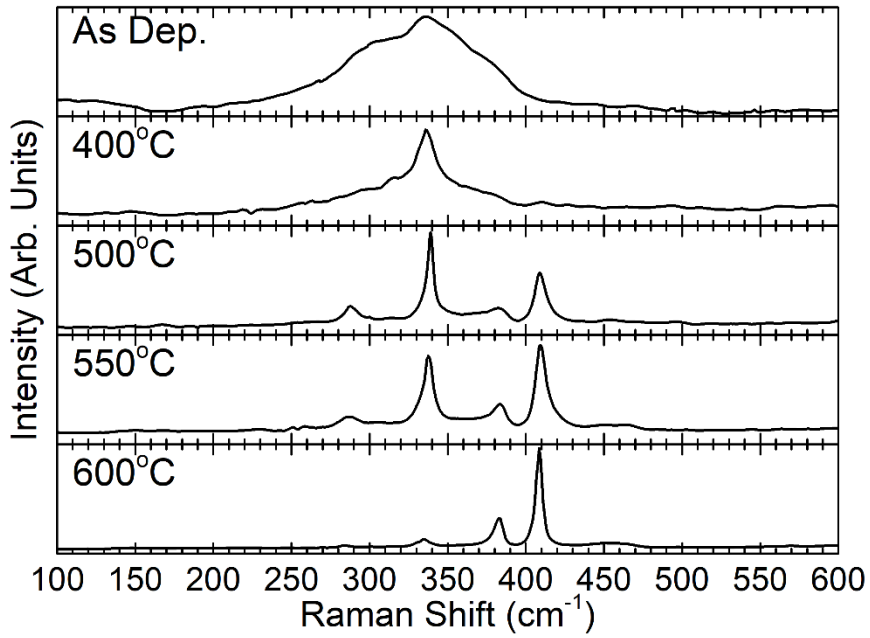

Figure 3.2 – Raman Spectra from the sputtered CZTS samples.

Atomic force micrographs of the samples are shown in Figure 3.3. It is clear that the as deposited film is formed of small densely-packed crystallites with an average size of approximately 50 nm, rendering the film amorphous-like in nature. After sulphurisation between $400\ ^{\circ}\mathrm{C}$ and $550\ ^{\circ}\mathrm{C}$, the crystallites more than double in size to approximately 130

nm. However, the film sulphurised at 400 °C also has many smaller grains as can be seen in Figure 3.3, which may mean that the film is still mostly amorphous, as would be consistent with the Raman spectra and XRD results above. At 600 °C, the apparent crystallite size is considerably larger at around 500 nm, however as has already been seen, the CZTS crystals have delaminated, and so the increased crystallite size is due to the MoS_2 layer, rather than the CZTS. The 600 °C, will henceforth not be considered any further. The average and RMS roughnesses also follow similar trends to the crystallite size, as can be seen in Table 3.1.

Sulphurisation Temperature (°C)	**Average Roughness (nm) (1 µm x 1 µm)**	**RMS Roughness (nm) (1 µm x 1 µm)**	**Average Crystallite Size (nm)**
As Dep.	0.62	0.81	50±10
400	2.5	3.1	141±20
500	4.9	6.3	136±20
550	4.7	5.9	122±20
600	5.9[c]	9.2[c]	524±20

Table 3.1 – Table showing the parameters characterising the surface topology of the CZTS samples as determined by AFM.

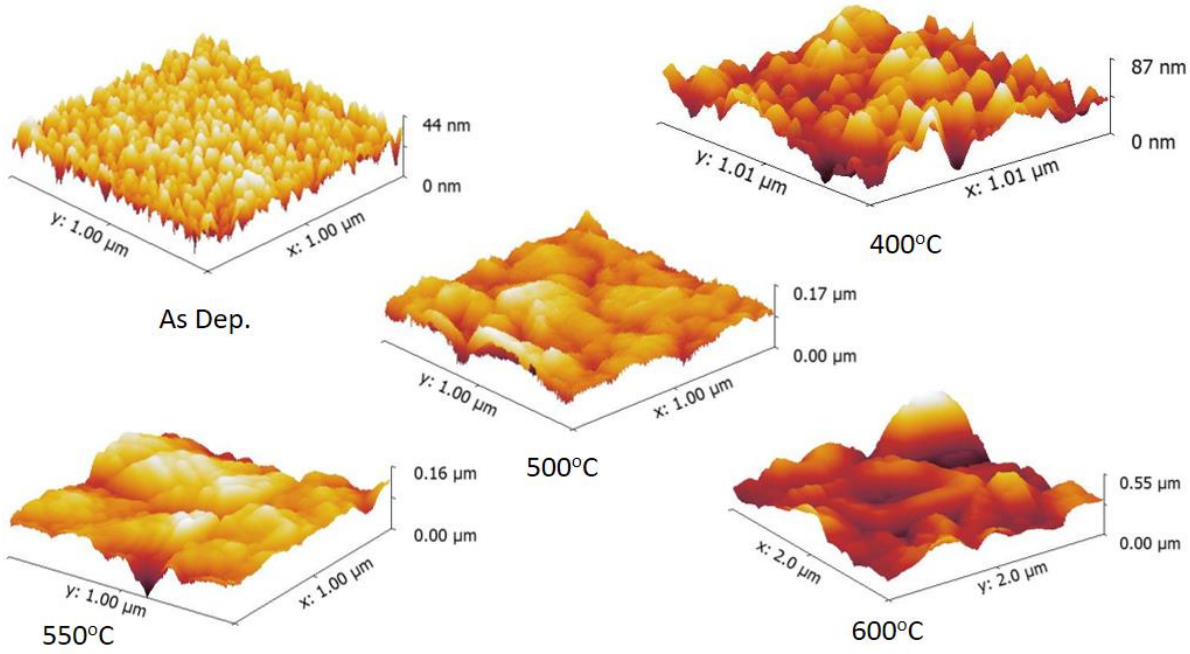

Figure 3.3 – Atomic force micrographs of the sputtered CZTS samples before and after sulphurisation at temperatures up to 600 °C.

[c] Over a 2 µm x 2 µm region.

The band gap is a crucial property for a photovoltaic absorber, thus Fourier-transform infrared spectroscopy was used to determine the band gaps of the deposited material, the resulting spectrographs can be seen in Figure 3.4. The lower quality materials synthesised at low temperatures have a band gap larger than that of the bulk material, as is frequently observed in amorphous materials. At 500 °C and 550 °C, the band gap is reduced to 1.41 ± 0.12 eV and 1.49 ± 0.08 eV respectively, in line with what would be expected from bulk CZTS. Also visible at these temperatures is a second band gap at approximately 1.7 eV. This band gap is consistent with the direct band gap of bulk MoS_2, which is prominent in the Raman spectrum of both samples.

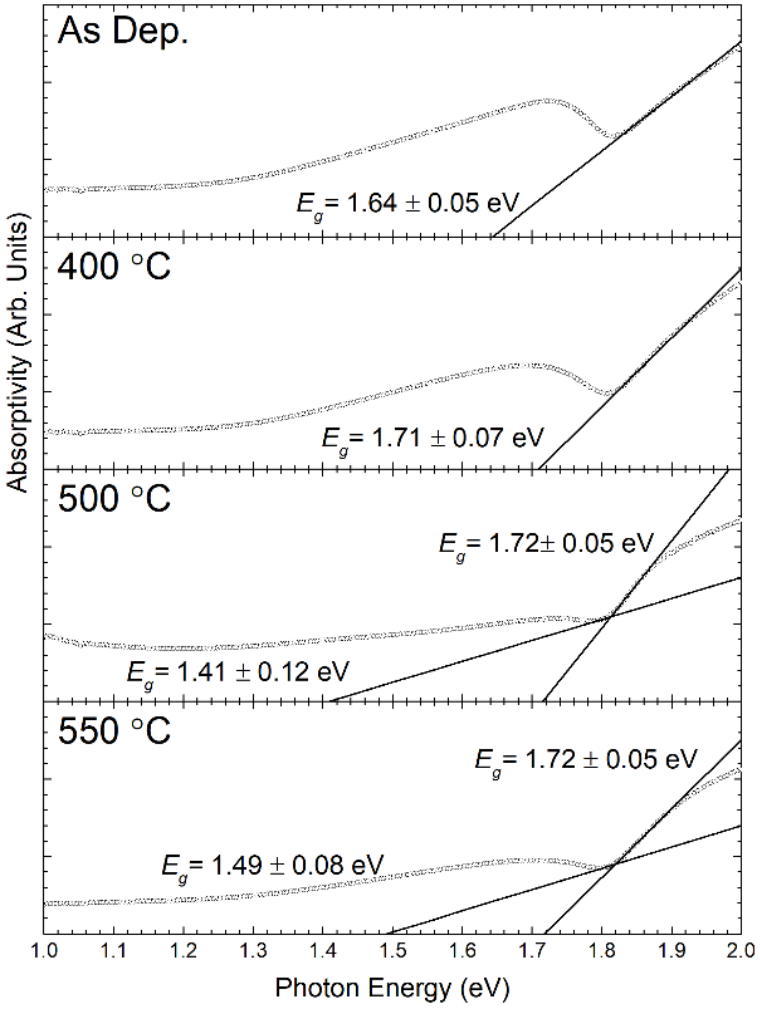

Figure 3.4 – Fourier-transform infrared spectra from the sputtered CZTS samples.

3.1.3 Photoelectron Spectroscopy of Sputtered CZTS

As outlined above, sulphurisation of CZTS precursor material at 500 °C appears to produce the highest quality CZTS samples. Hence, we will consider the PES spectra of this sample and compare it with that of the amorphous, as-deposited material and that of the film sulphurised at 550 °C.

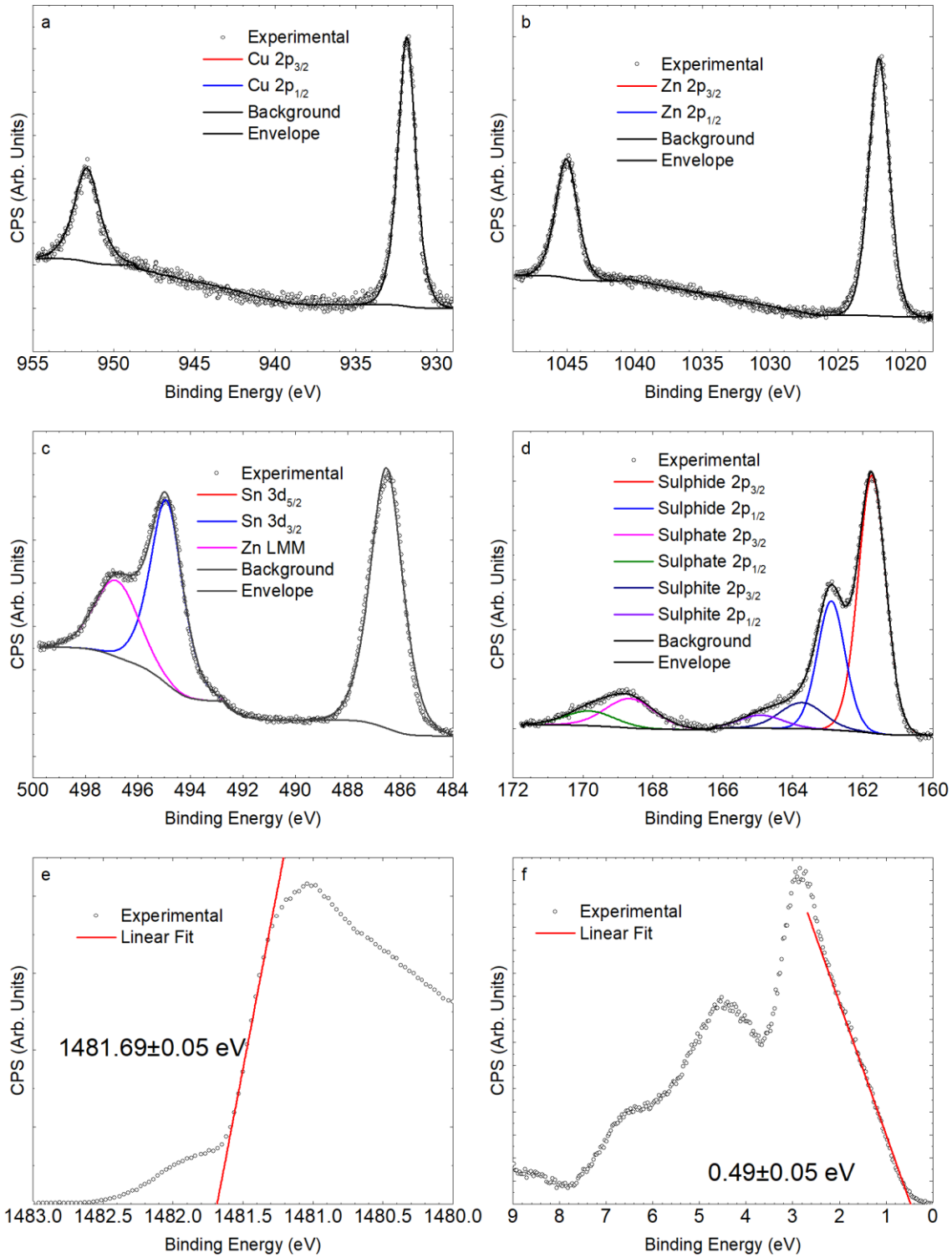

Figure 3.5 – PES spectra of the sputtered CZTS film after sulphurisation at 500 ℃. (a), (b), (c) and (d) show the Cu 2p, Zn 2p, Sn 3d and S 2p core-levels respectively. Also shown in (c) is the Zn LMM Auger level. (e) and (f) show the secondary electron cut-off and valence band regions respectively.

Figure 3.5 shows the resulting PES spectra from the sputtered sample after sulphurisation at 500 ℃. Figure 3.5(a) and (b) show the Cu 2p and Zn 2p core-level regions respectively, which are both fitted with a single set of peaks. Figure 3.5(c) shows the Sn 3d region with the Zn LMM superimposed upon it. Figure 3.5(d) shows the S 2p region, which shows

numerous S-O type species alongside that of the main sulphide doublet. The binding energy positions of the main core-levels are tabulated in Table 3.2. Figure 3.5(e) and (f) show the secondary electron cut-off and valence band regions respectively. The SEC is found to occur at 1481.69 ± 0.05 eV, whilst the VBM occurs at a binding energy of 0.49 ± 0.05 eV, thus the ionisation potential is found to be $V_{IP} = 5.39 \pm 0.05$ eV, which is comparable with reported literature values [499], [565], [566] and that previously obtained from a CZTS (112) single crystal, where the ionization potential is found to be 5.28 eV[567]. By considering the band gap of the sample presented in Figure 3.4, the electron affinity of this sample is found to be 3.98 ± 0.12 eV.

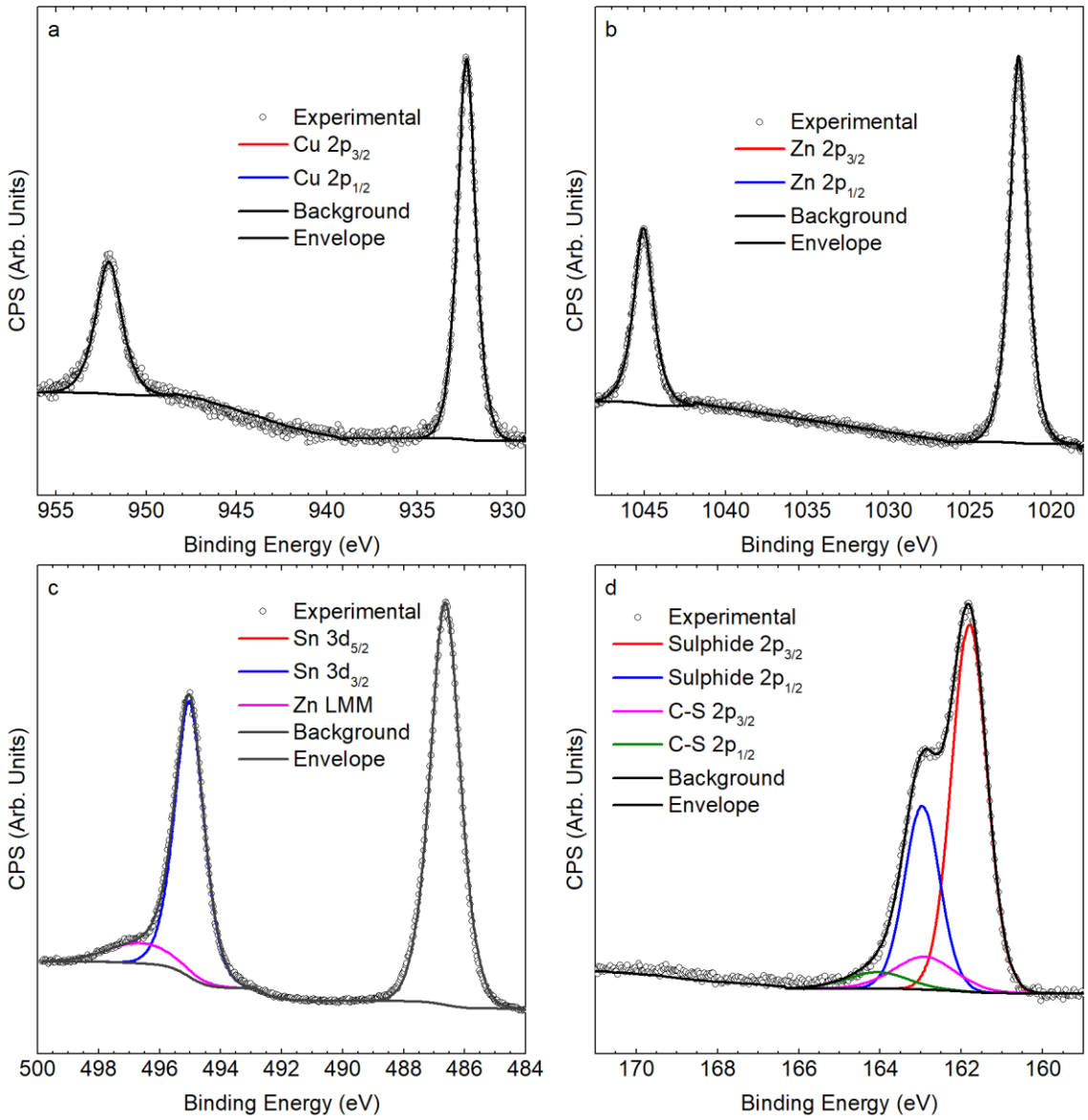

Figure 3.6 – PES spectra of the as-deposited sputtered sample, showing the (a) Cu 2p, (b) Zn 2p, (c) Sn 3d and (d) S 2p regions respectively.

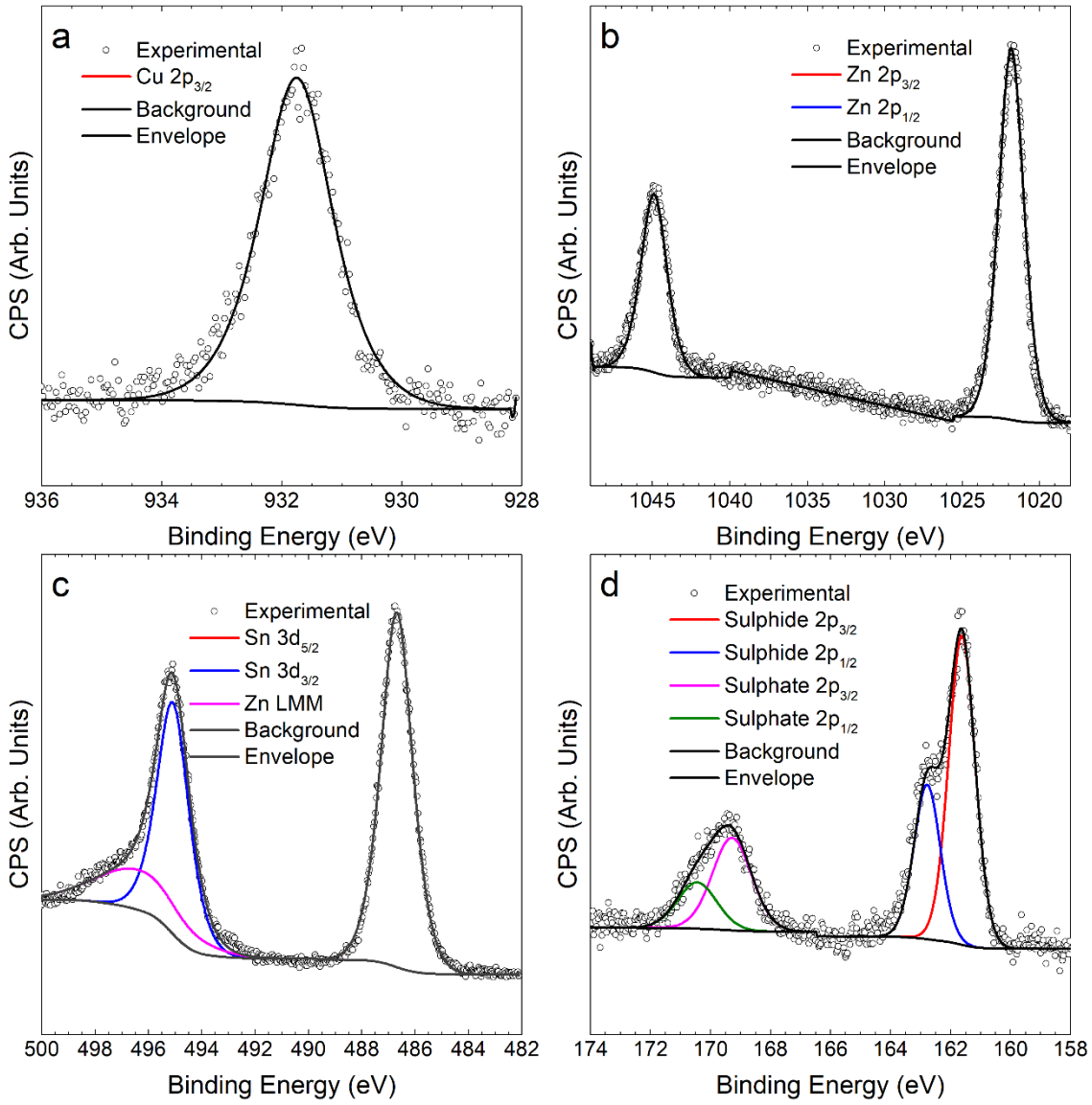

Figure 3.7 – PES spectra of the sputtered sample after sulphurisation at 550 °C, showing the (a) Cu $2p_{3/2}$, (b) Zn 2p, (c) Sn 3d and (d) S 2p regions respectively.

Figure 3.6 and Figure 3.7 shows the equivalent PES spectra from the as-deposited and 550 °C sulphurised sample respectively. In each (a) shows the Cu 2p region, (b) shows the Zn 2p region, (c) shows the Sn 3d region and (d) shows the S 2p region. The binding energies of the main features are similarly presented in Table 3.2. The S 2p region of the as-deposited sample, shown in Figure 3.6(d) does not show any presence of S-O bonds, likely due to the low deposition temperature. Instead, the only secondary peaks are assigned to S-C bonds, which are likely due to the incorporation of carbon into the film. The source of the carbon is likely to be the insulating polymer used to isolate the Ar plasma from the chamber wall. In contrast, the S 2p regions of the samples sulphurised at 500 °C and 550 °C shown in Figure 3.5(d) and Figure 3.7(d) respectively show S-O species. In the case of the sample sulphurised at 500 °C, these S-O species are sulphate (SO_4) and sulphite (SO_3). In

contrast, after sulphurisation at 550 ℃ only sulphate species are present, however the relative intensity of the sulphate peak is about double that of the sulphate peak at 500 ℃. The total relative intensity of S-O species, does however, remain the same, suggesting that the less thermodynamically stable sulphite species are fully oxidised to sulphates when the sample is sulphurised at 550 ℃. The presence of these S-O species appears to be linked to the sulphurisation process, in which case their presence may be linked to reactions with any remaining traces of air in the CCS chamber, or alternatively may be due to out-diffusion of sodium compounds from the glass, as the Na 1s core-level is detected only after sulphurisation. A similar process is seen in the deposition of MoS_2 thin-films on SLG, where sulphate species are also seen[546].

Sulphurisation Temperature (ºC)	**Binding Energy (eV)**			
	Cu $2p_{3/2}$	Zn $2p_{3/2}$	Sn $3d_{5/2}$	S $2p_{3/2}$
As Dep.	932.28	1021.98	486.64	161.80
500	931.86	1021.96	486.53	161.74
550	931.75	1021.82	486.68	161.62

Table 3.2 – Binding energies for the core-levels of the sputter-deposited samples before and after sulphurisation.

PES can also be used to determine the surface stoichiometry of the samples by using the photoelectron ionisation cross sections to correct the peak areas from PES. The stoichiometries of the samples have been determined from the main core-level peaks shown above and are presented in Table 3.3.

Sulphurisation Temperature (ºC)	**Atomic Percentage (%)**			
	Cu	Zn	Sn	S
As Dep.	12.6	21.0	22.0	44.3
500	12.4	36.3	13.0	38.3
550	8.9	21.7	27.4	42.0
Nominal Stoichiometry	25.0	12.5	12.5	50.0

Table 3.3 – XPS atomic compositions of the sputtered CZTS films before and after sulphurisation. Errors are ±5%.

The as-deposited film is found to be Cu- and S- poor and heavily enriched in Zn and Sn. In contrast, the film sulphurised at 500 ℃, is similarly Cu- and S-poor and even more Zn-rich than the as-deposited film, however Sn occurs in approximately the expected percentage. After sulphurisation at 550 ℃, the film becomes further depleted in Cu and remains

similarly S-poor. However, the amount of Zn is reduced once more, to a level comparable to the as-deposited film. The S-poor nature of the films can be easily explained by the high volatility of sulphur; hence sulphur will be more easily lost than the metal cations. Similar sulphur-poor concentrations have been observed in depth-profiled CZTS films[508], [568], [569], the same works also found that the surfaces that were Cu-poor[508], [568]–[570]. The behaviour of the Zn atomic percentage can similarly be understood by the volatility of Zn. At 500 ℃, the Zn migrates from deeper in the material towards the top contact, due to its high volatility, as is frequently observed[508], [570], [571]. At 550 ℃, some of the excess Zn is lost as vapour to the CCS chamber. The vapour pressure of Zn at 500 ℃ is approximately 1.8 ± 0.18 mbar, whilst at 550 ℃ it has more than trebled to 5.6 ± 0.6 mbar [572]. The vapour pressures for Cu, Zn, Sn and S are given in Table 3.4.

Temperature (ºC)	**Vapour Pressure (mbar)**			
	Cu	Zn	Sn	S
80	-	$8\text{x}10^{-11}$	-	$1\text{x}10^{-2}$
500	$1\text{x}10^{-13}$	1.8	$3\text{x}10^{-12}$	$22\text{x}10^{2}$
550	$3\text{x}10^{-12}$	5.6	$4\text{x}10^{-11}$	$36\text{x}10^{2}$

Table 3.4 – Vapour pressures of the elements in CZTS. Vapour pressures for the metallic elements are calculated using the vapor pressure calculator applet from Institut für Angewandte Physik at der Techniscien Universität Wien[572]*. Vapor pressures for S are adapted from West and Menzies*[573]*.*

3.2 Films Synthesised From Nanoparticle Inks

Chemical techniques are also used for synthesising kesterite photovoltaic materials, and in fact, many of the previous record kesterite devices have been deposited by chemical rather physical deposition techniques. As such, the electronic properties of chemically-grown kesterite films will also be investigated in this next section.

3.2.1 Film Synthesis

The samples characterised in this section were deposited by spin-coating of nanoparticle inks. The inks were produced by the hot-injection method, whereby copper acetylacetonate, zinc acetylacetonate, tin bis(acetylacetonate) dibromide are dissolved in oleylamine (OLA), or formamide[574]. The samples produced from each solution are subsequently referred to as high-carbon and low-carbon respectively, due to the carbon densities of the solvent used. The solution is placed into a three-neck flask connected to a Schlenk line and placed under vacuum, with a residual pressure of below $1\text{x}10^{-1}$ mbar. The flask is then purged twice with N_2 gas to remove any remaining water or O_2. The temperature of the reaction vessel was then increased to 225 ˚C and 1 M of sulphur-OLA

solution is injected into the vessel. The temperature was held at the reaction temperature for 30 mins, before being cooled to room temperature at a rate of approximately 5 ˚C/min.

Once the mixture reached room temperature, 5 ml of toluene and 40 ml of isopropanol (IPA) was added to the reaction mixture. The nanoparticles are then collected using a centrifuge operated at 8450 rpm for 10 mins. The resulting precipitate was washed twice with toluene and IPA. Larger particles and nanoparticle agglomerates were removed using a size selection process, consisting of centrifuging at 7000 rpm for 3 mins and re-dispersed in hexanethiol.

The inks were then spin-coated on Mo-coated soda-lime glass at 1200 rpm for 5 seconds, and then dried in air at 150 ˚C for 30 seconds followed by 300 ˚C for a further 30 seconds. Repeated spin-coatings allowed for film thicknesses up to 1 µm to be achieved. For the sulphur-selenium alloy samples, the films were placed in a graphite box with 300 mg of selenium powder. The graphite box was placed in a tube furnace, which was then evacuated to $6x10^{-3}$ mbar and backfilled to 10 mbar with argon. The temperature of the box was increased to 500 ˚C at a rate of approximately 20 ˚C/min, and left at the selenisation temperature for 20 mins, before being allowed to cool to 300 ˚C naturally, with assistance from a fan. After this it was left to cool naturally to room temperature over 60 mins.

3.2.2 Photoelectron Spectroscopy of Films grown from Nanoparticle Inks

The surface electronic structure of the CZTS(Se) samples described above was then investigated by x-ray photoelectron spectroscopy. Figure 3.8 shows the background-subtracted valence band spectra measured by XPS for the high and low carbon samples after selenisation, normalised to the same peak height. By comparing the valence band features in Figure 3.8 to orbital-projected densities of states (DoS) obtained by theoretical works, the dominant orbitals contributing to each feature can be determined. Examples of the projected DoS for CZTS are shown in by Paier *et al.* in figure 3 of reference [575] and for CZTSe by Mortazavi Amiri *et al.* in figure 2 of reference [576].

By comparing these projected DoS, with the valence bands in Figure 3.8, we can deduce that regions I and II are dominated by Cu 3d states, with some limited contributions from the S 3p and Se 4p orbitals. However due to the smaller comparative cross sections of these orbitals[473], the XPS spectrum will be heavily dominated by Cu 3d in these regions. Region III is similarly dominated by the Cu 3d orbital, but with a comparatively large

contribution from the anion states. Region IV is predominantly Sn 5s and anion p states which have comparable cross sections, with some contribution from the Cu 3d states.

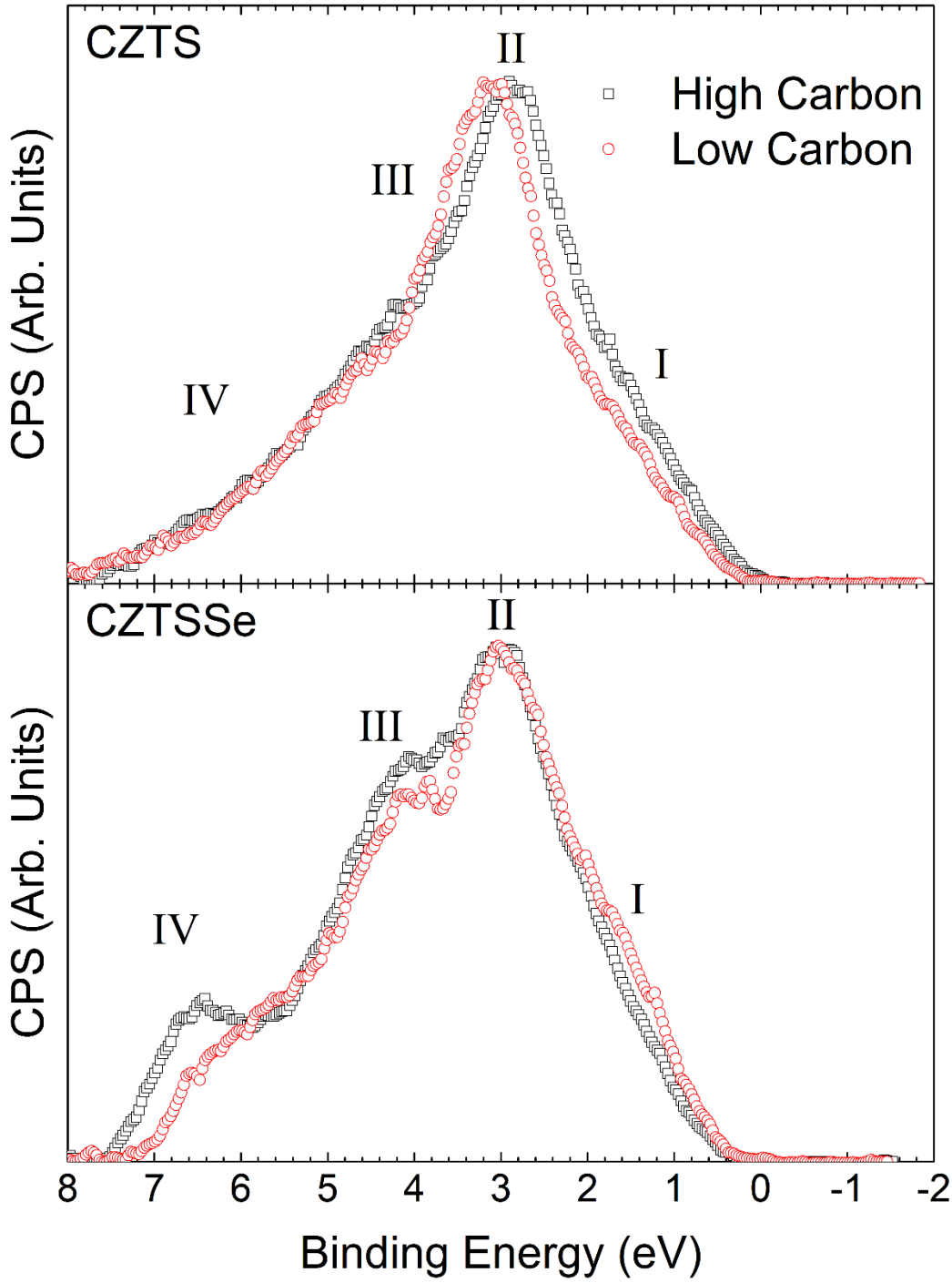

Figure 3.8 - This figure shows the valence band spectra as measured by XPS for the high and low carbon samples before and after selenisation. Features of interest are labelled as I, II, III and IV.

The XPS core-level spectra after selenisation are shown in Figure 3.10 and Figure 3.11. in Figure 3.10(a) and Figure 3.11(a) show the Cu $2p_{3/2}$ spectra for the two samples. The spectra both show a large peak at approximated 932.4eV, (932.47 ± 0.05 eV for the low carbon sample and 932.39 ± 0.05 eV for the high carbon sample), which is consistent with

an oxidation state of 1+ as is expected for CZTSSe and is consistent with literature values for the material[568], [569], [577], [578].

Figure 3.10(b) and (c) and Figure 3.11(b) and (c) show the Zn $2p_{3/2}$ and $Sn3d_{5/2}$ respectively for the two samples. Here the data are fitted with a single Voigt function, at binding energies consistent with those previously measured in the literature[568], [569], [577], [578]. These binding energies are consistent with oxidation states of Zn^{2+} and Sn^{4+} respectively.

Figure 3.10(d) and Figure 3.11(d) show the selenium 3d core level for their respective samples. In both cases, there is a doublet, with a Se $3d_{5/2}$ component at approximately 54.3 eV. Also present in both is a small peak on the high binding energy side of the main peaks. The binding energy position of this peak is not sufficiently high enough to be SeO_2, and is consistent with binding energies given for C-Se bond networks[579]. Intriguingly, the relative area of peaks assigned to C-Se bonds in the low carbon sample is greater than that of the high carbon sample. The C:Se ratios are found from the Se 3d region to be 1:49 and 1:7 for the high-carbon and low-carbon samples. This is consistent with SIMS data which showed for the high carbon sample, the carbon tended to segregate at the back contact, whereas for the low carbon sample the carbon remained uniform throughout[574].

The presence of only single peaks for the metal core-levels, suggests any secondary phases present are below the detection limit of XPS, typically considered to be 0.1-1 at%[580].

Figure 3.10(e) and (f) and Figure 3.11(e) and (f) show the SEC and VBM for the high and low carbon samples respectively. By applying a linear fit to the leading edge of the SEC and VBM, the position of each can be determined. The positions for the high carbon sample are determined to be 1482.11 ± 0.05 eV and 0.49 ± 0.05 eV, whilst for the low carbon sample they are determined to be 1482.09 ± 0.05 eV and 0.53 ± 0.05 eV. These values correspond to ionization potentials $V_{IP} = 5.02 \pm 0.05$ eV and $V_{IP} = 5.04 \pm 0.05$ eV. The band alignments with respect to the vacuum level are shown in Figure 3.21.

	Binding Energy (eV)						
Sample	Cu $2p_{3/2}$	Zn $2p_{3/2}$	Sn $3d_{5/2}$	S $2p_{3/2}$	Se $3d_{5/2}$	SEC	VBM
LC CZTS	932.44	1022.20	486.91	161.84	-	1481.83	0.55
LC CZTSSe	932.45	1022.12	486.57	161.77	54.26	1482.11	0.49
HC CZTS	932.50	1022.33	486.86	161.74	-	1481.65	0.32
HC CZTSSe	932.39	1022.20	486.59	161.78	54.32	1482.09	0.53

Table 3.5- This table shows the binding energies of each element as determined by XPS. Binding energies are calibrated to the adventitious C 1s peak at 285.0 eV. Errors on each measurement are ±0.05 eV

Also of interest is the S:Se ratios of the samples after selenisation. For this purpose the S 2p region is also measured as seen in Figure 3.9(a) and (b), which show the region for the high-carbon and low-carbon samples respectively. However, considerable overlap occurs with the Se 3p core-level. As these core-levels occur at similar kinetic energy, they necessarily probe a similar depth of material. Thus to evaluate the S:Se ratio the S 2p and Se 3p are used rather than the S 2p and the Se 3d, as this removes any variation due to a change of ratio with depth. Hence the S:Se ratios are found to be 16:84 for the high-carbon sample and 27:73 for the low-carbon sample.

Similar spectra to Figure 3.10 and Figure 3.11 are shown for the unselenised precursor materials in Figure 3.12 and Figure 3.13. The main difference in these figures are that (d) of each shows the S 2p rather than the Se 3d core-levels.

The metal core-levels are similarly fitted with only single, spin-orbit split doublets, showing the lack of secondary phases. The S 2p core-level requires numerous doublets, which are assigned to various S-O and S-C species respectively, as well as the main sulphide species. These species are likely due to impurities from the precursor and solvent materials, which are rich in carbon and oxygen remaining in the absorber layers after synthesis. The C:S ratio for the low-carbon sample is found to be 1:3, whilst for the high-carbon sample, it is 1:5, this is consistent with SIMS data, where the carbon in the high-carbon sample is found to be segregated at the back contact and depleted in the surface and bulk regions, whereas for the low-carbon sample it is uniformly distributed[574].

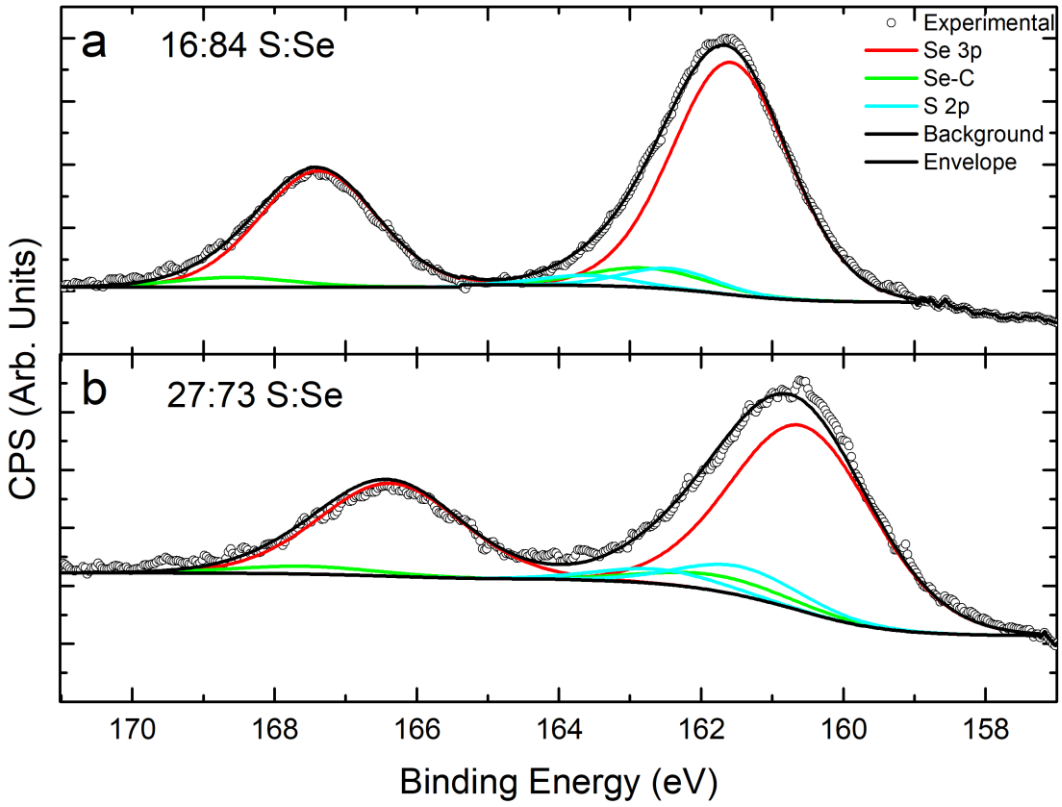

Figure 3.9 – The S 2p region for the (a) high-carbon sample after selenisation and the (b) low-carbon sample after selenisation. Considerable overlap between the S 2p and Se 3p is observed. However by deconvoluting the spectra the S:Se ratios are found to be 16:84 and 27:73 respectively.

After selenisation, the oxygen species are lost leaving only S-C and Se-C species behind. The ionization potential of these samples is thus determined to be $V_{IP} = 5.32 \pm 0.05$ eV and $V_{IP} = 5.24 \pm 0.05$ eV for the low and high carbon samples respectively. These measurements of the ionization potentials are consistent with reported literature values [499], [565], [566] and that previously obtained from a CZTS (112) single crystal measured on the same system, where the ionization potential is found to be 5.28 eV[567].

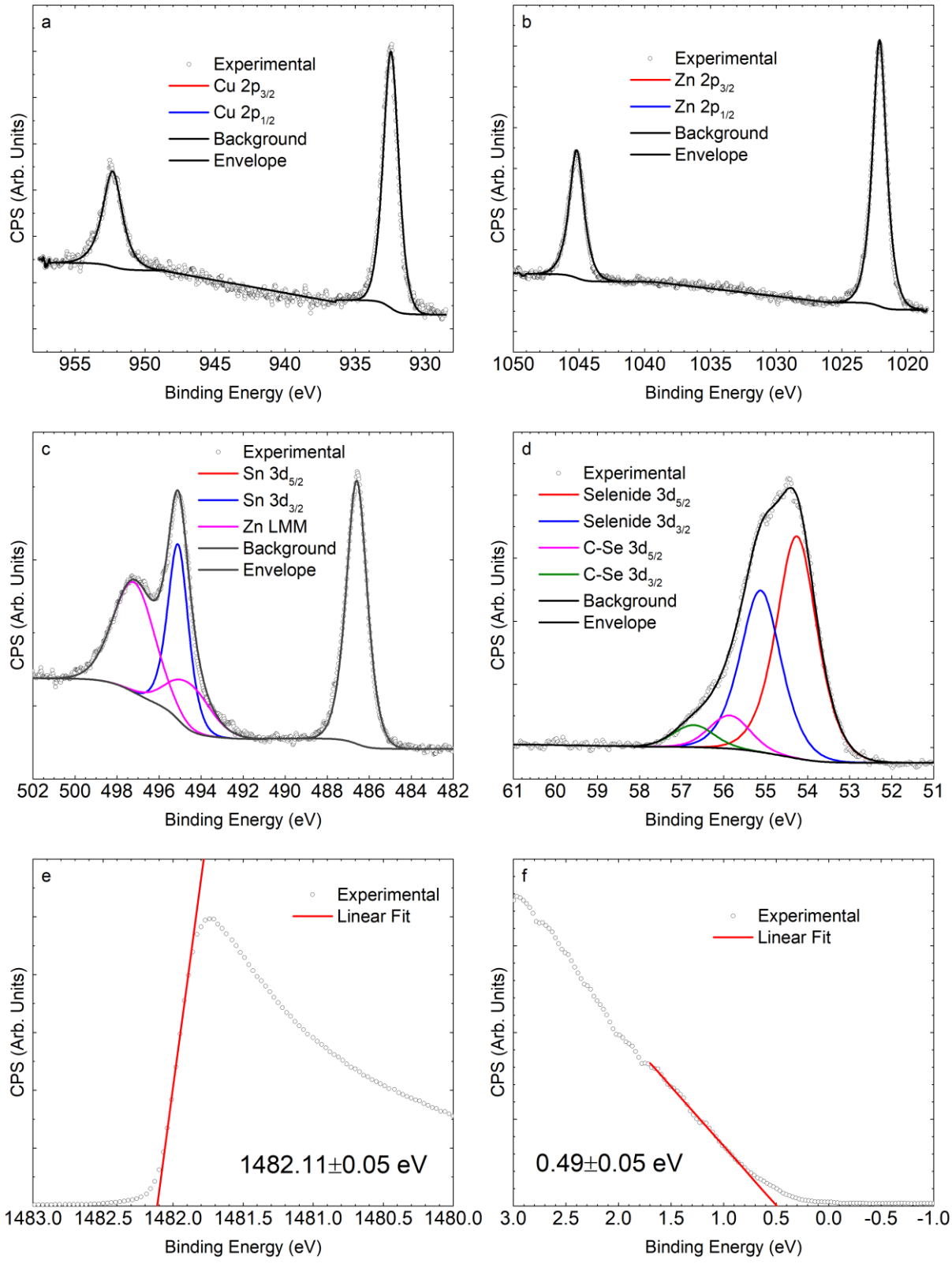

Figure 3.10 - This figure shows the deconvoluted XPS spectra for the (a) Cu $2p_{3/2}$, (b) Zn $2p_{3/2}$ (c) Sn $3d_{5/2}$ (d) Se 3d core levels and the (e) secondary electron cut-off and (f) valence band maximum for the low-carbon sample after selenisation. No metal oxides are observed in the metal core-levels. The Se 3d spectrum also shows a shoulder at the high binding energy side of the main peak, this is assigned to C-Se bonds.

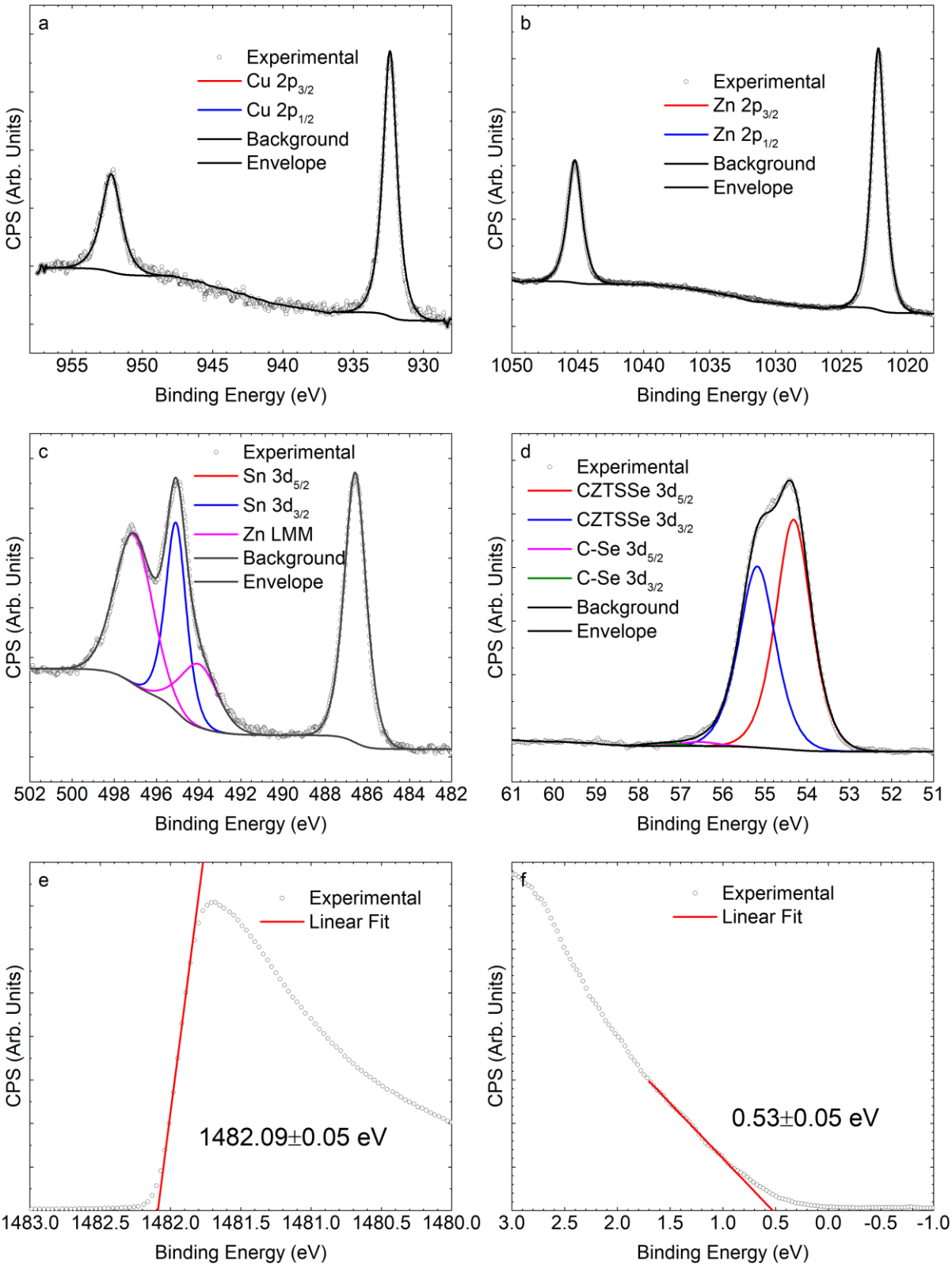

Figure 3.11 - This figure shows the deconvoluted XPS spectra for the (a) Cu $2p_{3/2}$, (b) Zn $2p_{3/2}$ (c) Sn $3d_{5/2}$ (d) Se 3d core levels and the (e) secondary electron cut-off and (f) valence band maximum for the high-carbon sample after selenisation. No metal oxides are observed in the metal core-levels. The Se 3d spectrum also shows a shoulder at the high binding energy side of the main peak, this is assigned to C-Se bonds, at a reduced level compared to the low-carbon sample.

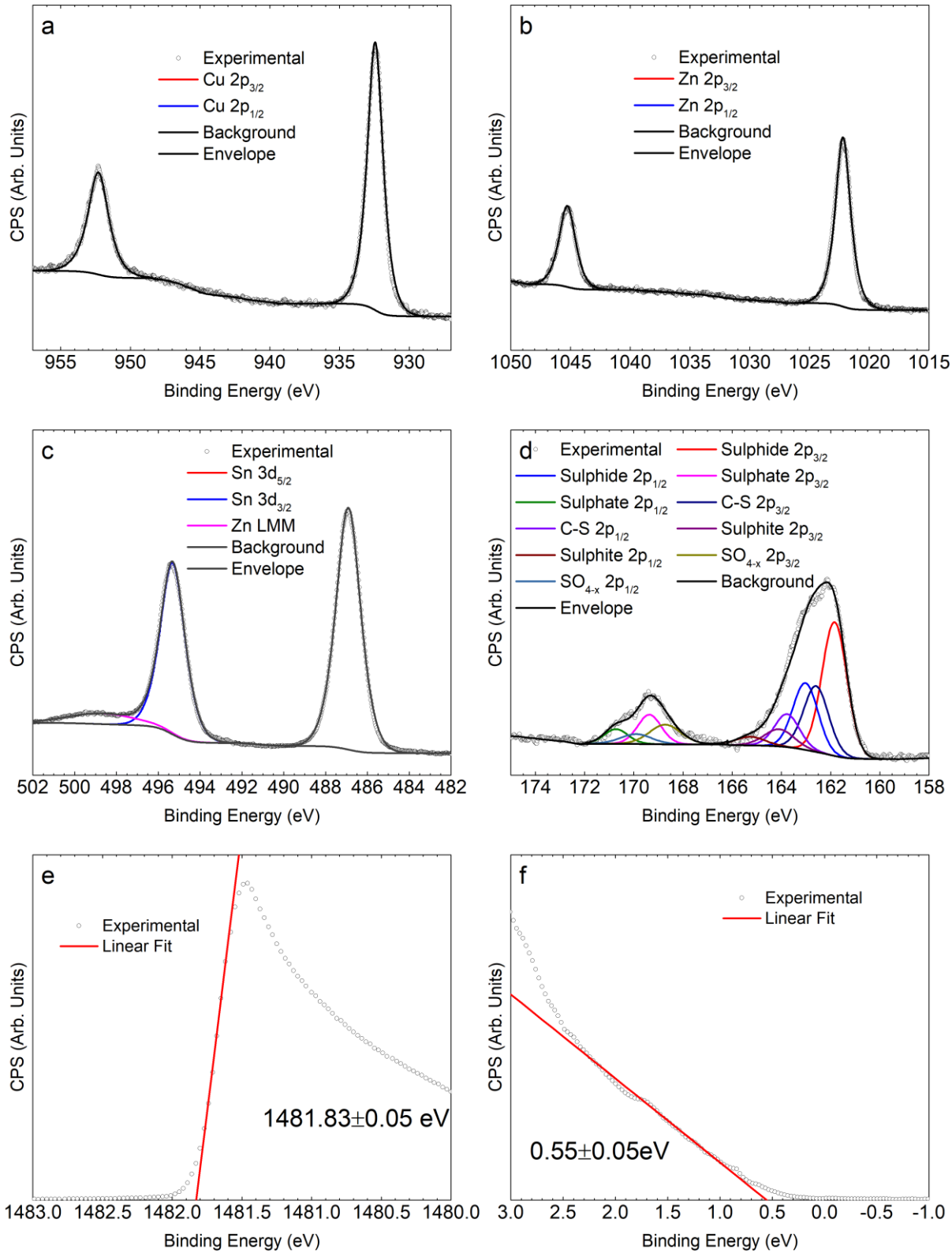

Figure 3.12 – PES spectra from CZTS thin-films from the low-carbon nanoparticle synthetic route. (a) and (b) show the Cu 2p and Zn 2p core-levels respectively. (c) shows the Sn 3d core-level and the Zn LMM Auger level. (d) shows the S 2p region. (e) and (f) show the secondary electron cut-off and valence band maximum respectively.

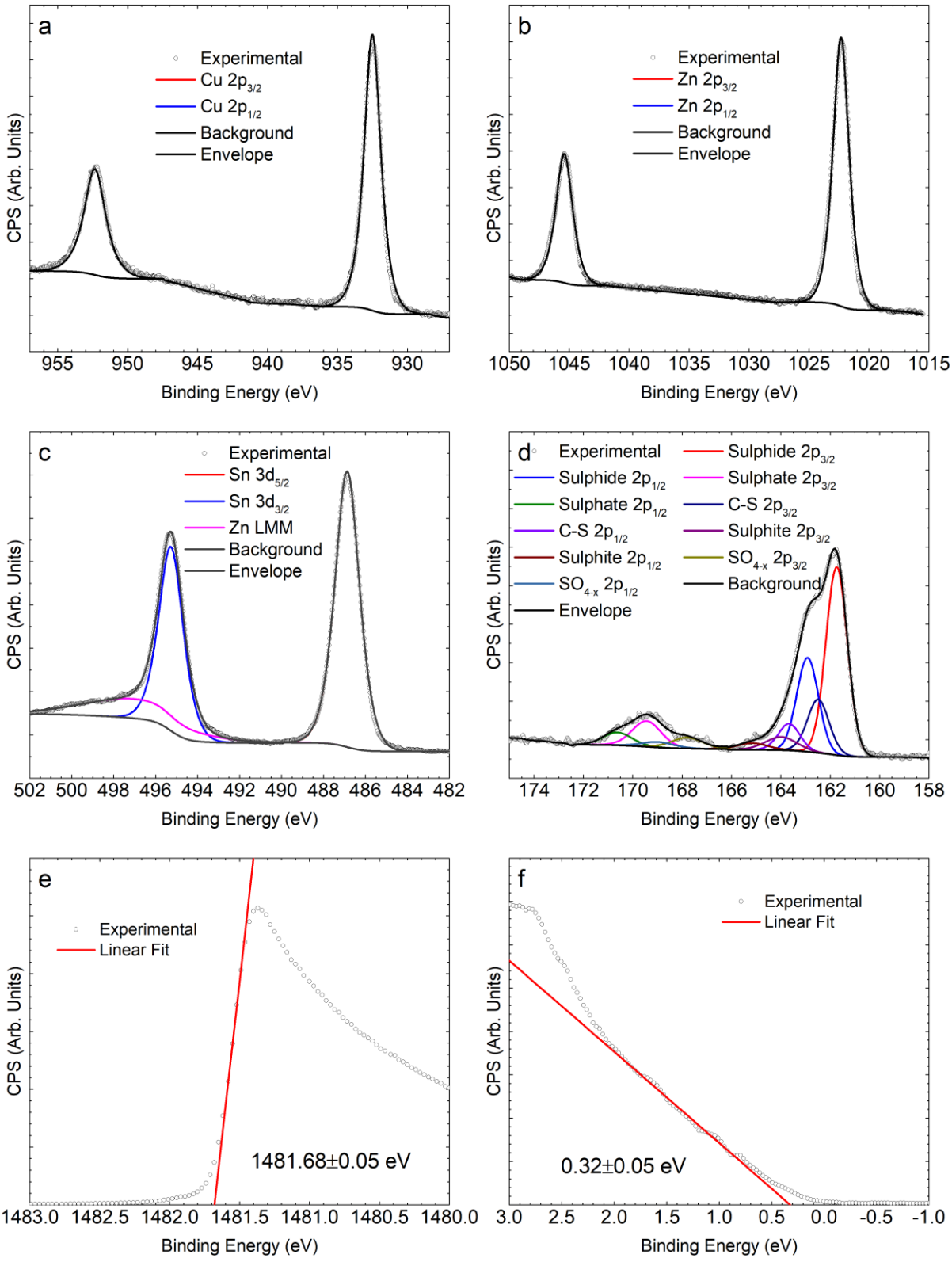

Figure 3.13 – PES spectra from CZTS thin-films from the high-carbon nanoparticle synthetic route. (a) and (b) show the Cu 2p and Zn 2p core-levels respectively. (c) shows the Sn 3d core-level and the Zn LMM Auger level. (d) shows the S 2p region. (e) and (f) show the secondary electron cut-off and valence band maximum respectively.

To determine the electron affinity of each sample, the band gap is required. Figure 3.14 shows UV-Vis spectra from each sample. By linear extrapolation, the band gaps are found

to be 1.60, 1.34, 1.50 and 1.15 eV for the LC-CZTS, LC-CZTSSe, HC-CZTS and HC-CZTSe samples respectively

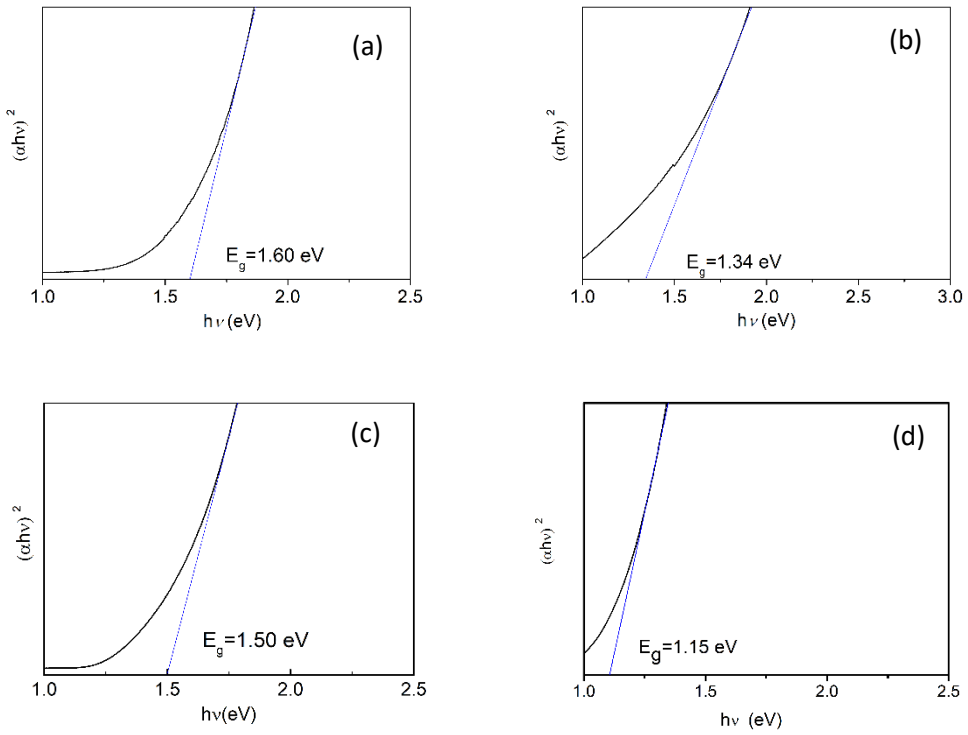

Figure 3.14 – UV-Vis spectra of (a) the unselenised low-carbon CZTS sample, (b) the selenised low-carbon CZTSSe sample, (c) the unselenised CZTS sample and (d) the selenised CZTSSe sample. The band gaps are found to be 1.60, 1.34, 1.50 and 1.15 eV respectively.

Hence the electron affinities are calculated to be $\chi = 3.72 \pm 0.05$ eV, $\chi = 3.68 \pm 0.05$ eV, $\chi = 3.74 \pm 0.05$ eV and $\chi = 3.89 \pm 0.05$ eV.

3.3 Natural Band Alignments with Common and Potential Buffer Layers

Next, we shall investigate the natural band alignments that would be expected with commonly used and alternative buffer layers and the kesterite absorber layers discussed above.

3.3.1 SnS_2

SnS_2 is an indirect gap semiconductor, which crystallises in the 2H crystal structure[581]. Neighbouring layers of atoms are bonded weakly *via* the van der Waals force, allowing for the deposition and foliation of layers from multilayers down to monolayers[581]. SnS_2 typically forms as a *n*-type material[582]–[585]. Since Sn and S are both already contained within the CZTSSe structure, the material has a sufficiently large band gap and the material is typically *n*-type, SnS_2 is of interest as an alternative buffer layer for kesterite materials.

Thin films of SnS_2 were deposited on $5 \times 5\ \mathrm{cm}^2$ silicon wafers by atomic layer deposition (ALD) at 150 ˚C using tin (IV) acetate ($Sn(OAc)_4$) and H_2S as precursors[586]. The pulse times for the precursors were 1 s for the $Sn(OAc)_4$, 4 s for H_2S, with purge times of 2 s separating each pulse[586]. The growth rate of the films was found to be 0.17 Å per cycle[586]. The as-deposited films were found to be amorphous. To produce crystalline SnS_2 films, the as-deposited films were annealed at 250 ˚C in a N_2/H_2S atmosphere[586].

X-ray photoelectron spectroscopy (XPS) measurements of the Sn $3d_{5/2}$ and S 2p core-levels, shown in Figure 3.15(a) and Figure 3.15(b) respectively, showed features in agreement with previous reports on SnS_2 single crystals[165], [587] and ALD thin films[582] with binding energies of 486.5 and 161.5 eV for the Sn $3d_{5/2}$ and S $2p_{3/2}$ peaks, respectively. The absence of notable SnO_2 any component at 487.2 eV[165] in the unsputtered, air-exposed sample highlights the stability of the films toward oxidation. The bandgap was determined to be 2.35±0.14 eV using a combination of VB-XPS and IPES measurements. The bandgap is given by the energy difference between the VBM and CBM, which were determined by a linear extrapolation of the edges of the valence band and the conduction band, respectively, to the background level as shown in Figure 3.15(c). The obtained value is between those reported for the indirect bandgap of bulk (2.2 eV)[165], [260], [581], [582], [587]–[589] and monolayer (2.6 eV)[583], [590], [591] SnS_2, which is reasonable considering the film thickness is approximately 10 monolayers. Furthermore, the position of the Fermi level, which lies closer to the CB than the VB, is in line with the expected n-type nature of SnS_2 films[582]–[585], and the band structure probed by VB-XPS was comparable to that previously measured from a SnS_2 single crystal[165].

Figure 3.15(d) shows the secondary electron cut-off of the SnS_2 sample. Using the binding energy of the SEC and the VBM, the ionisation potential is thus determined to be $V_{IP} = 6.37 \pm 0.05\ \mathrm{eV}$, consistent with that reported by Burton *et al.*[581] and Whittles *et al.*[165] for SnS_2 single crystals. The electron affinity is, thus, found to be $\chi = 4.02 \pm 0.14\ \mathrm{eV}$.

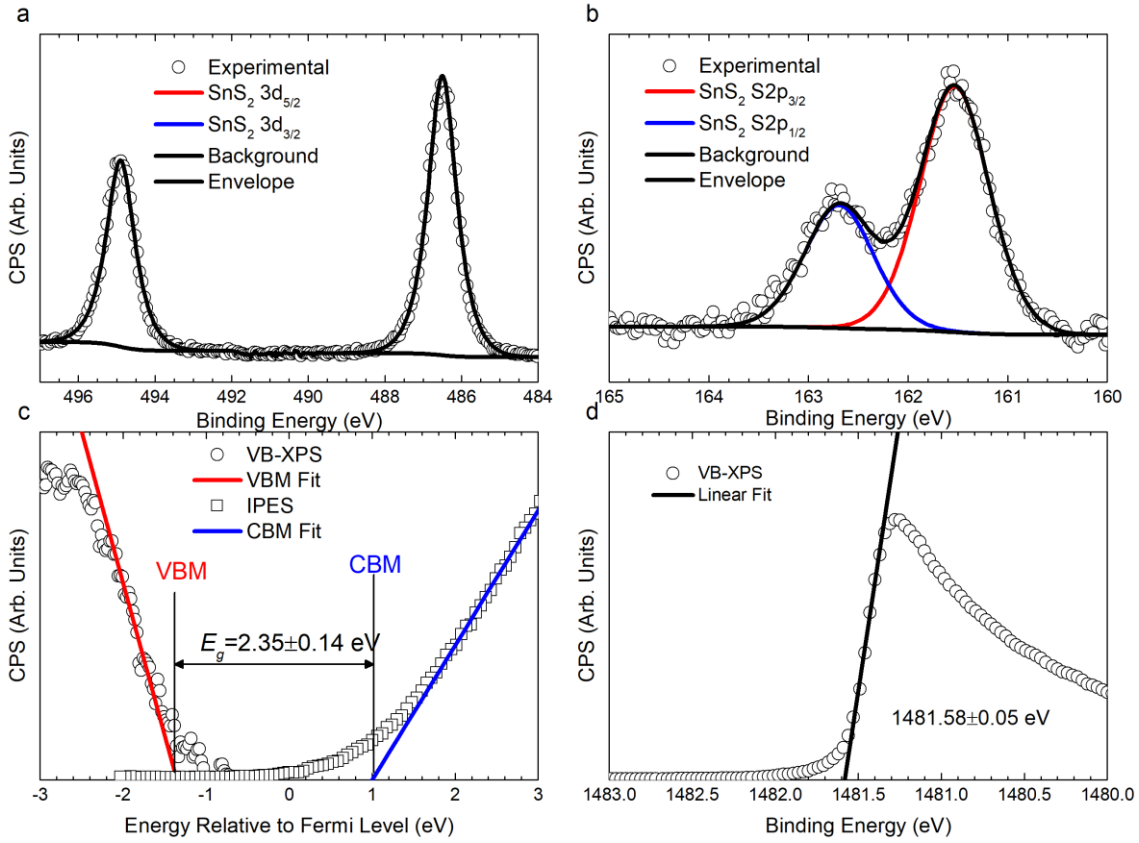

Figure 3.15 – PES spectra of a SnS_2 sample. (a) shows the Sn 3d core-level. (b) shows the S 2p core level. (c) shows the combined VB-XPS and IPES to determine the band gap. (d) shows the secondary electron cut-off.

3.3.2 Zn-Chalcogenides

Other buffer layers that may be of interest include ZnS, ZnSe and ZnO. In kesterite materials, the interface with the buffer material is often Cu-poor and Zn-rich, due to the high volatility of Zn. Thus, Zn-based buffer layers are natural materials to consider using as buffer layers, as this may reduce the band offsets further.

3.3.2.1 ZnS

The first of these Zn-based chalcogenides to consider is ZnS, which typically adopts the zincblende cubic structure (space-group $\mathrm{F\bar{4}3m}$), which gives a band gap of 3.54 eV. Alternatively, it may adopt the less stable hexagonal wurtzite structure, which has a band gap of 3.91 eV. Since the zinc-blende form of the material is most stable, it is this form we shall consider in the next section.

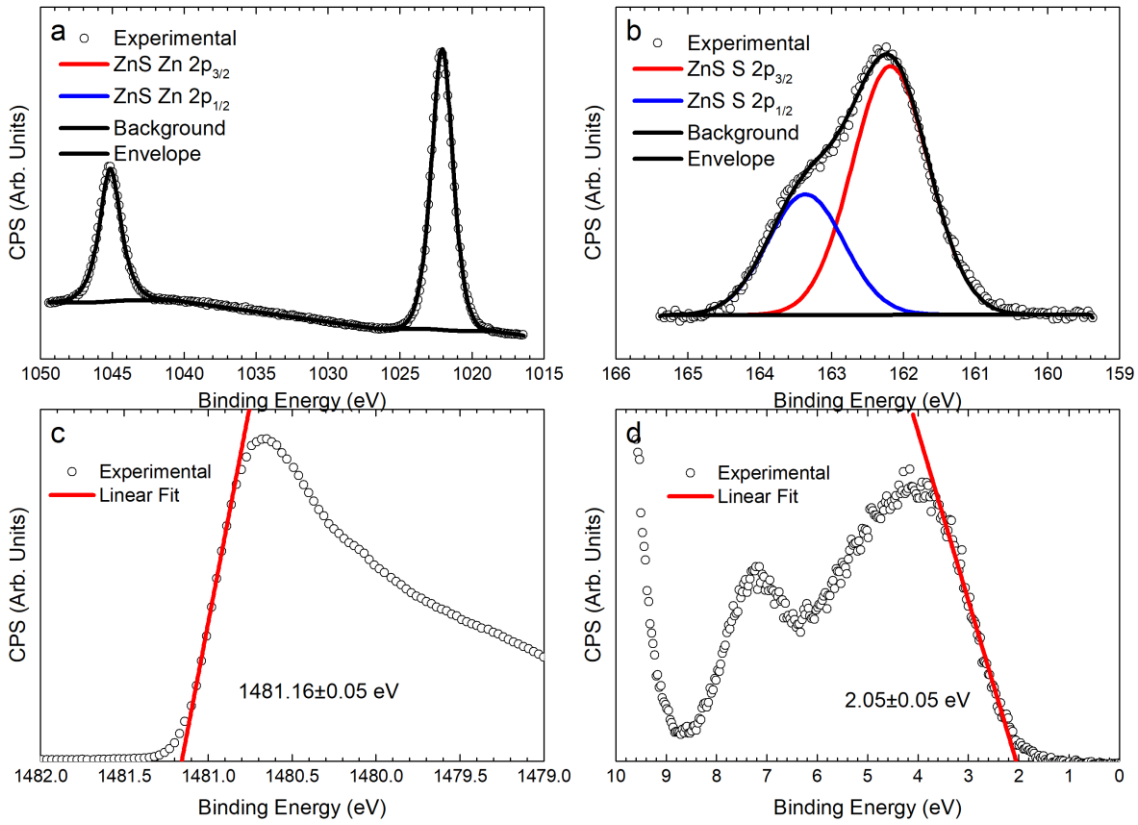

Figure 3.16 – PES spectra from a zincblende (100) ZnS single-crystal. (a) shows the Zn 2p core-levels and (b) shows the S 2p core-level. (c) and (d) show the secondary electron cut-off and valence band respectively. From this the ionisation potential is determined to be 7.49 ± 0.05 *eV.*

For this purpose, the photoemission spectra of a commercial ZnS (100) single crystal was measured, the results of which are shown in Figure 3.16. Figure 3.16(a) shows the Zn 2p region which is fitted with a single pair of spin-orbit split peaks. The Zn $2p_{3/2}$ core-level is found to occur at 1022.06 ± 0.05 eV, in agreement with values previously reported in the literature[375], [592]–[597]. The S 2p regions is shown in Figure 3.16(b), where the binding energy of the S $2p_{3/2}$ core-level is found to be 162.2, in agreement with that found by Strohmeier *et al*.[597]. By combining the results of Figure 3.16 (c) and Figure 3.16 (d), the ionisation potential of the ZnS (100) face is found to be $V_{IP} = 7.49 \pm 0.05$ eV, which when combined with the literature band gap of ZnS (3.54 eV), gives an electron affinity of $\chi = 3.95 \pm 0.05$ eV, which is comparable to that previously reported in the literature[598].

3.3.2.2 ZnSe

ZnSe is similar to ZnS, in that the ground state crystal structure adopted is the zincblende structure. ZnSe is also a direct gap semiconductor with a somewhat reduced band gap of 2.70 eV[599]–[601] compared to the 3.54 eV band gap of zincblende ZnS. The size of the band gap, and the fact that is direct in nature has led to interest for optoelectronic applications such as blue-green lasers[602], [603] and LEDs[604], [605]. ZnSe typically

forms as an *n*-type material even when not deliberately doped, which combined with the band gap of the material suggests that it may be an ideal buffer layer for kesterite photovoltaic devices. ZnSe has also previously been investigated as an alternative buffer layer for CIGS[606]–[610], so growth methods that could be used for depositing the material on kesterites have already been developed.

Thus, to determine the band alignments of ZnSe with the kesterite materials described previously XPS measurements were made on a commercial ZnSe (100) single crystal, the results of which are shown in Figure 3.17.

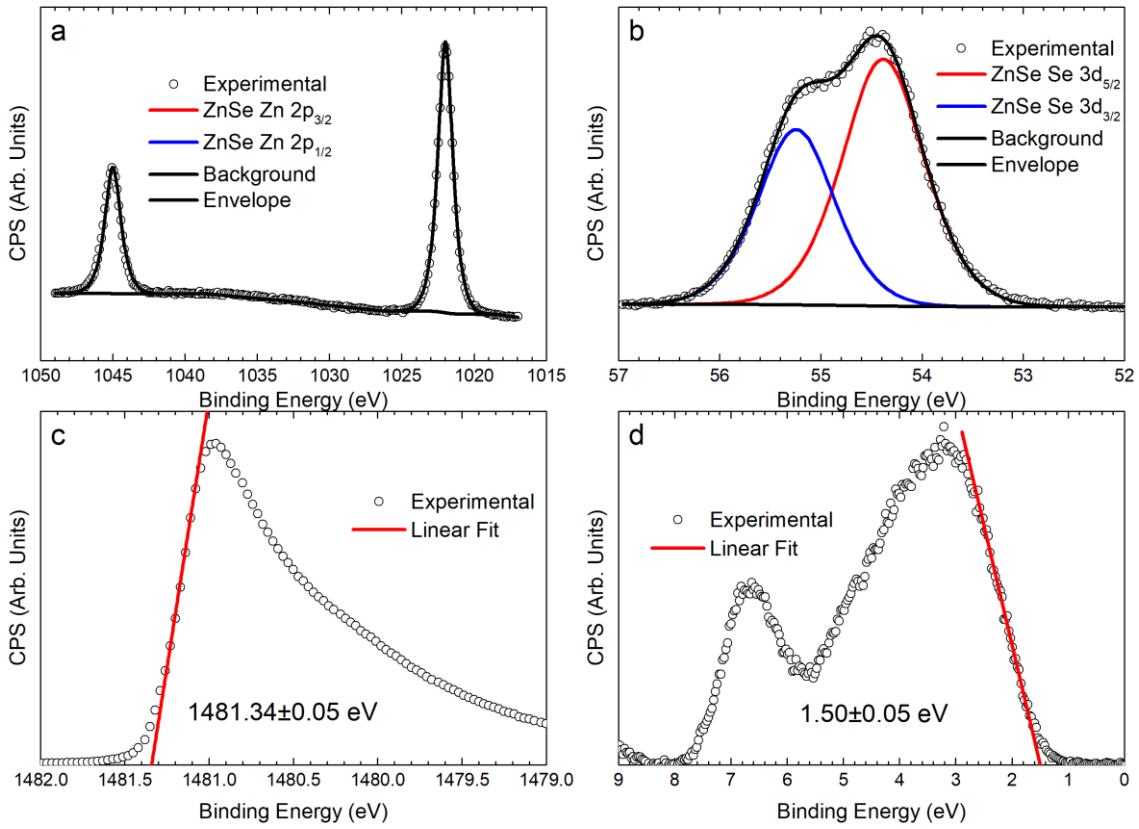

Figure 3.17 – PES Spectra from a zincblende (100) ZnSe single crystal. (a) shows the Zn 2p core-levels, (b) shows the Se 3d, (c) shows the secondary electron cut-off and (d) shows the valence band regions (excluding the Zn 3d semi-core level)

Figure 3.17(a) shows the Zn 2p region, which is fitted with a single pair of spin-orbit split peaks. The Zn $2p_{3/2}$ is found to occur at 1021.98 ± 0.05 eV, similar to that of the ZnS above and consistent with previously reported values[592], [600], [618], [601], [611]–[617]. The similarity of the binding energy to that of ZnS in the same structure is to be expected as the oxidation state of the Zn ions is 2+ in both cases, and the difference in the electron affinity between S and Se is small. Figure 3.17(b) shows the corresponding Se 3d region which is similarly fitted with only a single pair of peaks. The Se $3d_{5/2}$ is found to occur at a binding energy of 54.38 ± 0.05 eV. In the literature, reports of ZnSe use non-monochromatic

sources and hence do not resolve the spin-orbit splitting of the components[592], [600], [621], [601], [611], [613]–[616], [619], [620]. Where spin-orbit splitting is ascribed, it is often done mistakenly, where the peak due to SeO_2, at approximately $59\ \mathrm{eV}$, is assumed to be the Se $3d_{3/2}$[600], [601], [616], [620]. In fact, references [600], [601] and [616] share the same first author and appear to reproduce the same XPS spectra despite different nominal growth techniques. In fact, AFM images from figure 4(a)-(c) of reference [601] have been reproduced as figure 4(a)-(c) in reference [616], with a caption claiming different growth conditions to that in the original reference. Figure 5 of reference [600] also reappears as figure 7 of reference [601], and the Raman spectra presented in references [601] and [616] are similarly duplicated.

The binding energy of the Se $3d_{3/2}$ obtained in this work is comparable with many of the reports of the binding energy of the centroid given for the entire Se 3d core-level. Where the spin-orbit splitting of the Se 3d has been reported correctly, the Se $3d_{5/2}$ is found to occur at a comparable binding energy as in this work[618].

Figure 3.17(c) and Figure 3.17(d) show the secondary electron cut-off and valence band respectively. From Figure 3.17(c), the cut-off is found to occur at $1481.34 \pm 0.05\ \mathrm{eV}$ and the VBM is found to occur at a binding energy of $1.50 \pm 0.05\ \mathrm{eV}$ from Figure 3.17(d). Thus, the ionisation potential of the ZnSe (100) single crystal was found to be $V_{IP} = 6.76 \pm 0.05\ \mathrm{eV}$, which when combined with a literature band gap of $2.70\ \mathrm{eV}$, gives an electron affinity of $\chi = 4.06 \pm 0.05\ \mathrm{eV}$, comparable to the value, $\chi = 4.09\ \mathrm{eV}$, which was previously reported in the literature[622].

3.3.2.3 ZnO

In contrast to ZnS and ZnSe, ZnO is most stable in the hexagonal wurtzite structure under ambient conditions. ZnO has a large, direct band gap of approximately 3.37 eV[623]–[625], considerably larger than that of ZnSe and comparable to that of zincblende ZnS, and is typically conducting, even when not intentionally doped. Thus, ZnO is one of the family of materials known as the transparent conducting oxides or TCOs. ZnO is therefore often doped with Al to produce Al:ZnO or AZO[626], which is frequently used as the top transparent contact in photovoltaics[627], [628] and liquid crystal displays[629]. ZnO has also been deployed in thin-film transistors (TFTs)[630] and Schottky diodes[631], and other applications[632].

Figure 3.18 shows the resulting XPS spectra from a commercial ZnO single crystal. Figure 3.18(a) shows the Zn 2p region which is fitted with only a single, spin-orbit split doublet.

The binding energy of the Zn $2p_{3/2}$ is found to occur at 1021.71 ± 0.05 eV. Figure 3.18(b) shows the O 1s region, which requires two peaks to account for the shape of the spectrum. The larger peak, at lower binding energy is due to Zn-O bonds and occurs at 530.71 ± 0.05 eV. The second, smaller features occurs 1.5 eV above the Zn-O peak, and is assigned to surface-adsorbed O-H[625], [633]–[635], which remains even after annealing.

Figure 3.18(d) shows the valence band region of the ZnO single crystal. Since the wurtzite crystal structure has polar surfaces, the electronic structure of the valence band of ZnO is dependent on the face and termination of surface[625]. By comparison of the relative intensities of the features labelled I and II in Figure 3.18(d), the surface is found to be the Zn-polar (0001) face[624], [625]. The valence band maximum is thus found to occur at 3.50 ± 0.05 eV.

Figure 3.18(c) shows the secondary electron cut-off, which is found to occur at 1482.60 ± 0.05 eV. Thus, the ionisation potential of the ZnO single crystal is found to be $V_{IP} = 7.50 \pm 0.05$ eV. By using the literature value of the band gap, the electron affinity is found to be $\chi = 4.13 \pm 0.05$ eV, consistent with values previously reported for the equivalent O-polar $(000\bar{1})$ face[636], [637].

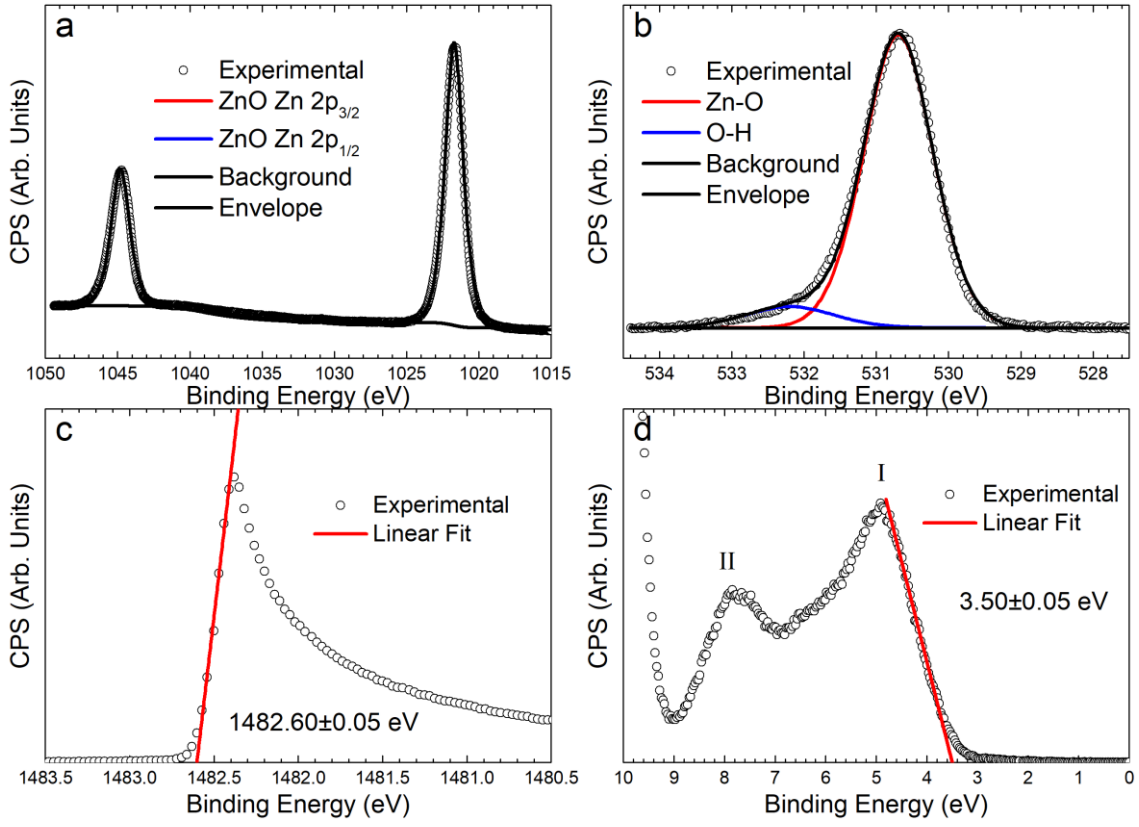

Figure 3.18 – The PES spectra from a wurtzite-hexagonal ZnO single crystal. (a) and (b) show the Zn 2p and O 1s regions respectively, whilst (c) and (d) show the secondary electron cut-off and valence bands respectively.

3.3.3 In_2S_3

In_2S_3 buffer layers were deposited through thermal evaporation (using a UNIVEX 250) of 4N purity In_2S_3 powder. The layers were deposited under high vacuum conditions (<3.7x10^{-6} mbar) at a substrate temperature of 250 ˚C with thicknesses of 60 ± 5 nm. The films were grown at deposition rate of 1.4 ± 0.2 Å/s in 13 minutes.

XPS characterisation of the In_2S_3 sample was performed, the resulting spectra are shown in Figure 3.19. Figure 3.19(a) shows the In $3d_{5/2}$ core level, which is fitted with a single Voigt function, at a binding energy of 445.34±0.05 eV. Figure 3.19(b) shows the S 2p spectrum, these are fitted with two Voigt functions, which are separated with a spin-orbit splitting of 1.16 eV, with an intensity ratio of 2:1. The binding energy of the S $2p_{3/2}$ peak is thus found to be 161.97 ± 0.05 eV. Figure 3.19(c) shows the SEC, the position of which is found to be 1482.44 ± 0.05 eV by linear extrapolation. Figure 3.19(d) shows the valence band maximum of the In_2S_3 sample. The valence band maximum is found to occur at 2.01 ± 0.05 eV. The ionization potential of In_2S_3 is thus found to be $V_{IP} = 6.17 \pm 0.05$ eV.

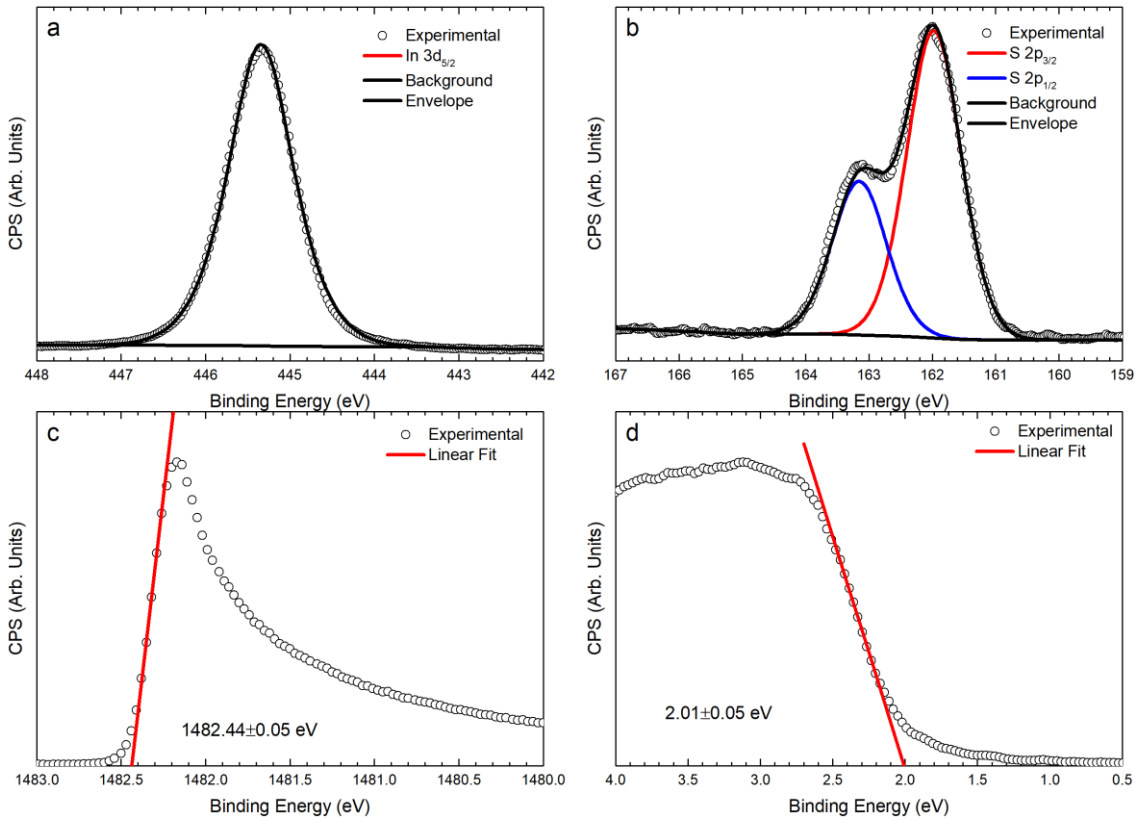

Figure 3.19 - This figure shows the XPS spectra for the (a) In $3d_{5/2}$, (b) S 2p, (c) secondary electron cut off and (d) valence band maximum for an In_2S_3 sample.

To fully construct the natural band alignment of In_2S_3 with the CZT(S,Se) samples, the band gap of the In_2S_3 sample is required. UV-Vis spectrometry was carried out in transmission mode. The resulting Tauc plot is shown in Figure 3.20. The band gap of the In_2S_3 sample is found to be 2.69 ± 0.10 eV. Literature values of the band gap of In_2S_3 vary from 2.00[638]–[640] to 2.7 eV [641], [642] and are heavily dependent on the growth method.

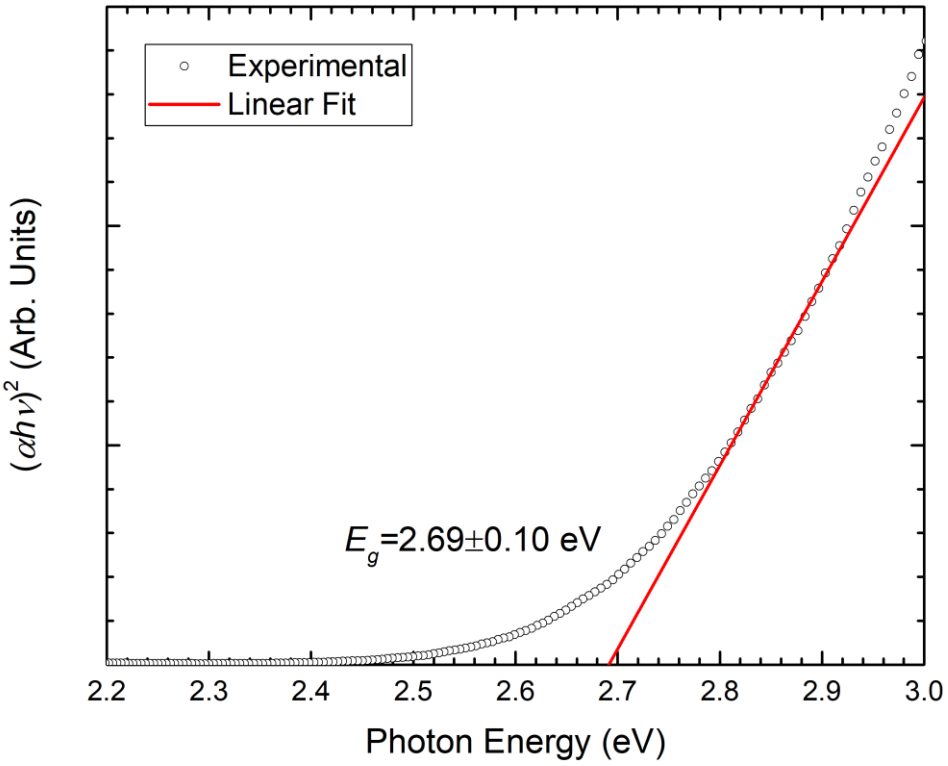

Figure 3.20 - This figure shows the Tauc plot for the In_2S_3 sample. The band gap is determined to be direct, with a value E_g=2.69±0.10 eV.

When combined with the electronic band gap, this allows for the determination of the electron affinity which is found to be $\chi = 3.48 \pm 0.10$ eV.

3.3.4 Band Diagram of CZTS(Se) with Various Potential Buffer Layers

As has been outlined previously, photoemission spectroscopy allows for the determination of the band positions of a particular material with respect to the vacuum level, and hence the natural band alignments of different materials, assuming the absence of interface defects or states. Such a diagram is shown in Figure 3.21 using the values obtained above alongside the literature values for CdS[499], [260], [643], [644].

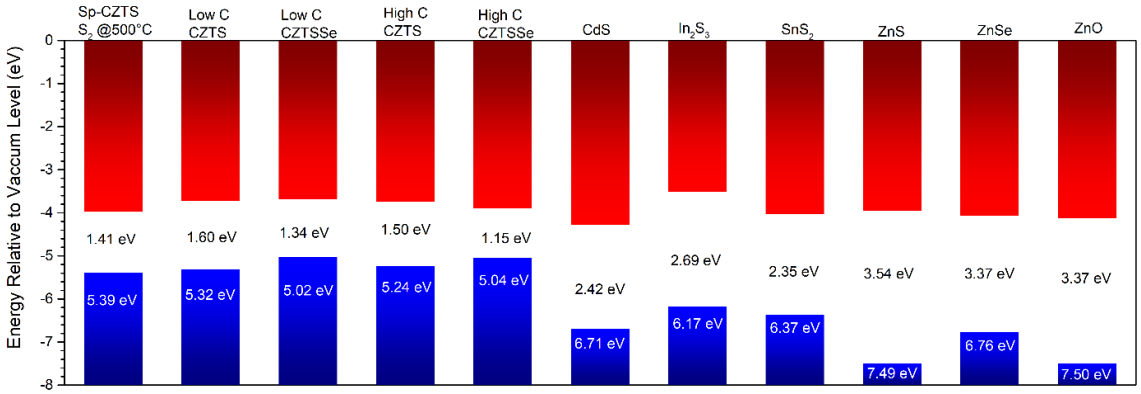

Figure 3.21 - This figure shows the band alignments relative to the vacuum level as measured by XPS for the CZTS and CZTSSe samples. Also shown is that measured for In_2S_3 and SnS_2 and literature values for CdS.

From the data shown in Figure 3.21, it is possible to estimate the CBOs and VBOs between the samples and the buffer layers presented, using the Anderson rule[393]. These offsets are shown in Table 3.6.

Buffer Material	Offset (eV)	Absorber Material				
		Sp CZTS S_2 @ 500˚C	Low C CZTS	Low C CZTSSe	High C CZTS	High C CZTSSe
In_2S_3	ΔE_C	0.47	0.24	0.20	0.26	0.43
	ΔE_V	-0.78	-0.85	-1.15	-0.93	-1.13
CdS	ΔE_C	-0.3	-0.56	-0.6	-0.54	-0.38
	ΔE_V	-1.31	-1.38	-1.68	-1.46	-1.66
SnS_2	ΔE_C	-0.04	-0.30	-0.34	-0.28	-0.13
	ΔE_V	-0.98	-1.05	-1.35	-1.13	-1.33
ZnS	ΔE_C	0.03	-0.23	-0.27	-0.21	-0.06
	ΔE_V	-2.10	-2.17	-2.47	-2.25	-2.45
ZnSe	ΔE_C	-0.08	-0.34	-0.38	-0.32	-0.17
	ΔE_V	-1.37	-1.44	-1.74	-1.52	-1.72
ZnO	ΔE_C	-0.15	-0.41	-0.45	-0.39	-0.24
	ΔE_V	-2.11	-2.18	-3.48	-2.26	-2.46

Table 3.6- This table shows the calculated band offsets determined by Anderson's rule for the samples with In_2S_3, SnS_2, ZnS, ZnSe and ZnO and CdS.

For all samples, the CBO with CdS is large and negative. Such a CBO is thought to be detrimental to the performance of a photovoltaic device, leading to increased interfacial recombination and a reduced V_{OC}[296] [164][645]. Here, we see that the selenised, high carbon sample has the smallest CBO with CdS, suggesting that this sample should result in

the best efficiency and highest V_{OC}. In fact, the CBO considered to be least detrimental is a positive CBO, between 0 to 0.4eV[161], [296], [297], as thermionic emission of electrons from the absorber into the buffer layer allows for a sufficiently large current to prevent recombination, whereas a cliff-like negative CBO results in increased recombination[645], [23]. These results would therefore suggest that In_2S_3 would be a more ideal buffer layer for CZTSSe than CdS. SnS_2 would also appear to be a more ideal buffer layer the CZTSSe, particularly for the high carbon sample, where $\Delta E_C = -0.13$ eV. Although the band offset is negative, it is considerably smaller than the equivalent offset for a CdS buffer. Although Sn is not formally a transition metal, it is worth noting that the SnX_2 (X=S,Se,Te) compounds also exhibit layered structures and have similar properties to the group 6 TMDs, which have a similar layered structure. The band gap of SnS_2 is known to be layer dependent, reaching a maximum of 2.6 eV[583], [590], [591] in the monolayer limit, so by further reducing the thickness of the SnS_2 layer, it may be possible to induce a small, positive CBO of up to approximately 0.10 eV. Intriguingly, the band gap of SnS_2 is expected to remain indirect from the bulk to the monolayer limit[588], [591]. The bulk gap occurs at 0.2-0.4 eV above the indirect gap according to calculations from first principles[588], [591]. Significant absorption due to the buffer layer may, therefore, only occur for photon energies of greater than 2.8 eV, which should result in an improved external quantum efficiency at high photon energies. Hence, SnS_2 may be of interest as an absorber layer for kesterite photovoltaics, however the formation of other Sn-chalcogenides will need to be supressed.

We can also see Table 3.6 that in some cases ZnS may also provide a sufficient conduction band offset to enable high efficiency kesterite devices, however ZnSe and ZnO always provide a negative CBO.

3.4 Summary and Discussion

In this chapter, we have considered the photoelectron spectroscopy of kesterite-structure absorber materials grown by several different methods, some selenised and some in the pure sulphide phase. The XPS spectra of several alternative materials for use as the buffer layer in kesterite photovoltaics cells have been measured, and the band alignments with the PES data described previously have been investigated by the Anderson electron affinity rule.

We have shown that CdS is likely a poor choice of material for the buffer layer in kesterite-based devices, due to the large ionisation potential of the material. In_2S_3 is a particularly

promising material for use as the buffer layer as the conduction band offset is less than 0.5 eV for each absorber considered. However, the material properties of In_2S_3 have not been investigated thoroughly. Properties as fundamental as the band gap and its nature are unknown. Hence further investigation of the properties of In_2S_3 will be required to realise a device with an In_2S_3 buffer layer capable of matching and exceeding the efficiencies of devices using well-established CdS methods.

Another material of interest is SnS_2, which has an intriguing layered structure, similar to that adopted by the group VI transition metal dichalcogenides. The similarity of the structure also results in some properties which are also similar: namely the indirect nature of the band gap (in this case down to the monolayer level); and a band gap that varies with layer number. Of the Zn monochalcogenides, only ZnS provides a positive conduction band offset, and only then in some cases. ZnSe and ZnO each produce negative conduction band offsets only.

In the next chapter we will consider the band alignments of In_2S_3 and CdS with CZTSSe by the Kraut method, to test whether or not the findings in this chapter hold in device-like structures. We will then use the SCAPS software to simulate devices and investigate the effect of the band alignments upon the device statistics.

4 CZTSSe Device Band Alignments

One of the key parameters in deciding the efficiency of a photovoltaic device is how the bands align at the photoactive region. Despite this, experimental determination of the band alignments is relatively rare. Instead, device simulations such as solar cell capacitance simulations (SCAPS)[646] are more frequently used, which usually naively assume the Anderson rule to evaluate the band alignment.

The previous chapter has established that the Anderson rule suggests that CdS is inappropriate as a buffer layer for CZTSSe based photovoltaic devices and that In_2S_3, may in fact, be a better buffer layer for this application. However, as was discussed previously in section 2.3.3, the Anderson rule fails, when interfacial states (i.e. Fermi pinning) or band bending occur at the interface. In this chapter we consider two device-like samples consisting of ZnO/CdS/CZTSSe/Mo and ZnO/In_2S_3/CZTSSe/Mo stacks. By carefully etching the samples using the Ar^+ ion gun previously described in section 2.2.1, the band alignments of the stacks are found using the Kraut method. The implications of the results are then discussed.

Both theoretical and experimental work agrees with the findings of the previous chapter. Xiao *et al.* use DFT to calculate the band alignment at the interface of a CZTS/CdS cell, finding a cliff-like CBO of 0.05eV[267]. Bao *et al.* also investigated similar interfaces of CZTS/CdS structures by DFT, considering how the kesterite and stannite crystal structures and termination may affect the band alignments, finding, in each case, a cliff-like CBO of between 0.1-0.4 eV[268]. Dong *et al.* also considered the band alignment of CZTS/CdS heterojunction and also obtained a cliff-like CBO of 0.05eV using DFT and a cliff-like CBO of 0.13eV using XPS[265]. Hiroi *et al*. used UPS to determine the band alignments of In_2S_3/CdS/CZTS and CdS/CZTS stacks, showing that the CBO is cliff-like in both cases[647].

Udaka *et al*. find that the CBO at the interface of a CZT$(S_xSe_{1-x})_4$/CdS heterojunction is 0.55eV and -0.15eV for x=0 and x=1, corresponding to the pure-selenide and pure-sulphide phases, respectively[648]. The changeover from a positive, to a negative CBO suggests that for some intermediate value of x, that CdS may produce a favourable band alignment with CZTSSe, which the authors suggest to occur at around x=0.3-0.4[648]. The same group have previously reported that for x=0.28, the CBO is of the order of 0.23eV[649], which would appear to agree with the above hypothesis. A separate report from the same group also finds that the alignment of CZTSe/CdS produces a spike-like CBO of 0.56eV[650].

In contrast to the above results, Rondiya *et al*. obtained a spike-like CBO of 0.55 for a CZTS/CdS heterojunction using cyclic voltammetry[270], the authors fail to discuss the discrepancy and as such it is possible that the difference is due to the differences in the experimental techniques rather than some fundamental property of the interfaces.

Previous work by Yu *et al.*[564] has indicated that the for In_2S_3 films on the pure-sulphur CZTS, the conduction band shows a potential barrier from the CZTS to the In_2S_3 layer with a CBO between 0.01-0.41 depending on growth conditions. This is consistent with values obtained from the Anderson rule in the same reference[564].

Partial oxidation of the CdS buffer layer has been considered as an alternative to changing the barrier layer entirely. Oxidation of the buffer layers, results in a widening of the band gap relative to that of pure CdS, resulting in a CBO that may be positive. Such work has been performed by Ge *et al.*[272], who investigated the band alignments of CdO_xS_{1-x} ($0.05 \geq x \geq 0.01$) buffer layers with Cu_2BaSnS_4, finding that at $x \geq 0.03$, the CBO became positive, allowing for effective charge transport between the layers. Caution must, however be kept for applying the same results to CZTSSe, as the band gap of Cu_2BaSnS_4 is considerably larger, at 2.05eV.

An alternative II-VI alloy that has been considered in $Zn_{1-x}Cd_xS$. Sun *et al*. investigated the alignment of $Zn_{0.35}Cd_{0.65}S$ on CZTS, finding a CBO of 0.37eV[278].

CZTSSe samples were grown on molybdenum coated soda-lime glass from CZTS nanoparticle inks similar those described in chapter 3. The In_2S_3 layer was also grown in a similar fashion to that in the previous chapter.

CdS was grown on the CZTSSe layer by chemical bath deposition. Deionised water was added to a double walled beaker, in thermal contact with a circulating water bath. Once the temperature of the water had stabilised at 70 ˚C, 2mM of $CdSO_4$ was added to the water, followed by 1.5M of ammonia under continuous magnetic agitation, until dissolved.

The CZTSSe films were then immersed in the resulting solution for 2 mins, after which 12 mM of thiourea was mixed into the solution. The addition of which resulted in the formation of the CdS buffer layer. The samples were then rinsed with deionised water, and dried under a N_2 stream, before being annealed for 10 mins at 200 ˚C in air. 60 nm of *i*-ZnO could then be deposited by magnetron sputtering.

4.1 Experimental Band alignments for ZnO/CdS/CZTSSe/Mo and ZnO/In_2S_3/CZTSSe/Mo using the Kraut Method

To investigate the validity of the Anderson electron affinity rule deployed to construct Figure 3.21 in the previous chapter, substrate-architecture cell-like stacks were prepared to allow for the determination of the band alignments by the Kraut method. Two architectures were used, with different buffer layers, to investigate the band alignments at the interface with the absorber and window layers respectively. The window layer used in each case was a polycrystalline ZnO film, the buffers layers deployed were CdS and In_2S_3 respectively on a CZTSSe layer comparable to the high carbon CZTSSe described in chapter 3.

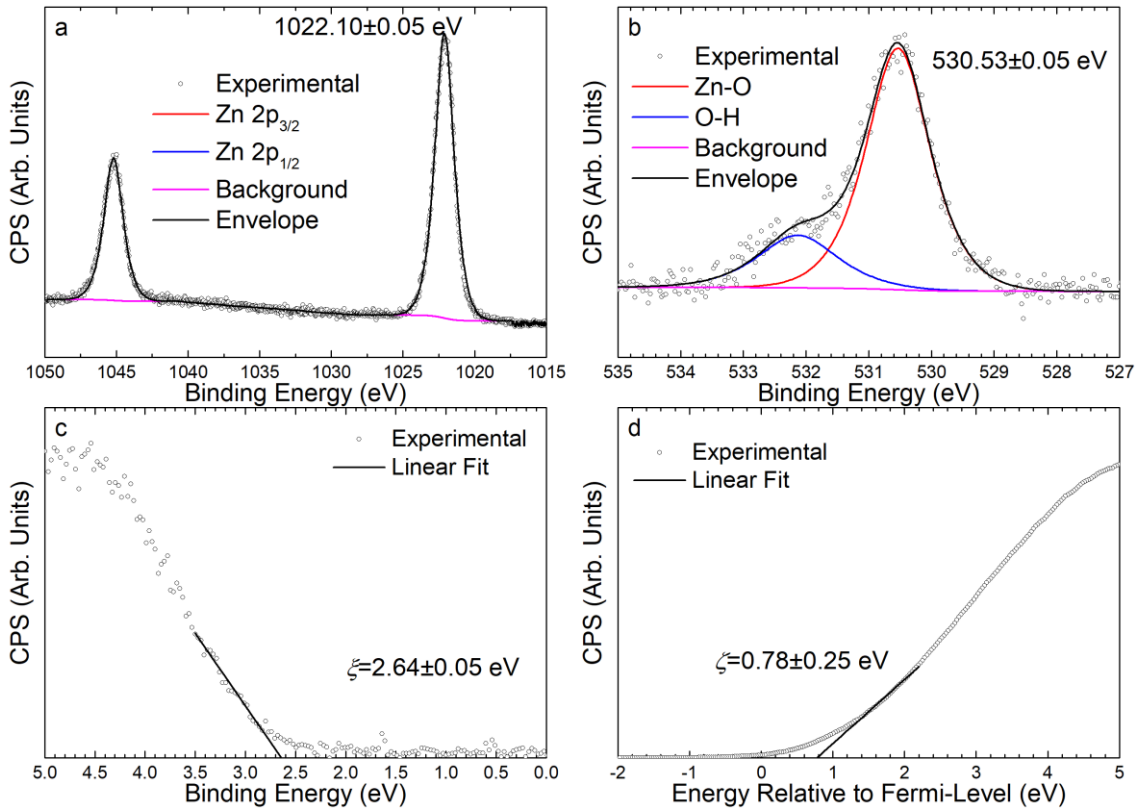

Figure 4.1 - shows (a) the Zn 2p region (b) the O 1s region (c) the valence band minimum as measured by XPS for the thick ZnO sample. (d) shows the conduction band minimum as measured by IPES. By comibining the VBM and CBM values, the band gap of the ZnO film is found to be 3.42±0.25 eV, consistent with the 3.30-3.37 eV gap reported in the literature[623], [651]–[653].

Figure 4.1 shows the XPS and IPES spectra obtained for the thick ZnO sample. (a) shows the Zn 2p core-levels which are fitted with a single doublet, constrained by the spin-orbit splitting of the level. No further peaks are required to fit the data. (b) shows the O 1s region for the sample, which is fitted with two peaks, the larger of which is due to Zn-O bonds. The shoulder at high binding energy is fitted with a second peak, 1.6 eV above that

assigned to Zn-O bonds. The second smaller peak is assigned to the presence of O-H bonds[625], [631], [633], [634], due to the adsorption and incorporation of water vapour into the ZnO layer during deposition. (c) and (d) shows the valence band maximum and conduction band minimum as measured by XPS and IPES respectively. The band edges are found by linearly extrapolation of the leading edge to the baseline. By this method, the band gap of the thick ZnO sample is found to be 3.42±0.25 eV, which is consistent with the 3.30-3.37 eV gap previously reported[623], [651]–[653]. Theoretical works frequently find the conduction band edge of ZnO to be non-linear in nature[654]–[656]. Instead, there is a local maximum in the DoS at about 1 eV from the CBM. The band is typically then found to decrease before reaching a larger maximum. As the resolution of IPES is relatively low, this larger maximum is broadened into the region where the decrease ought to be. Thus only a relatively small amount of the IPES data is used to find the CBM. As the obtained band gap is comparable to that reported elsewhere, the decision to use only a small region is therefore justified.

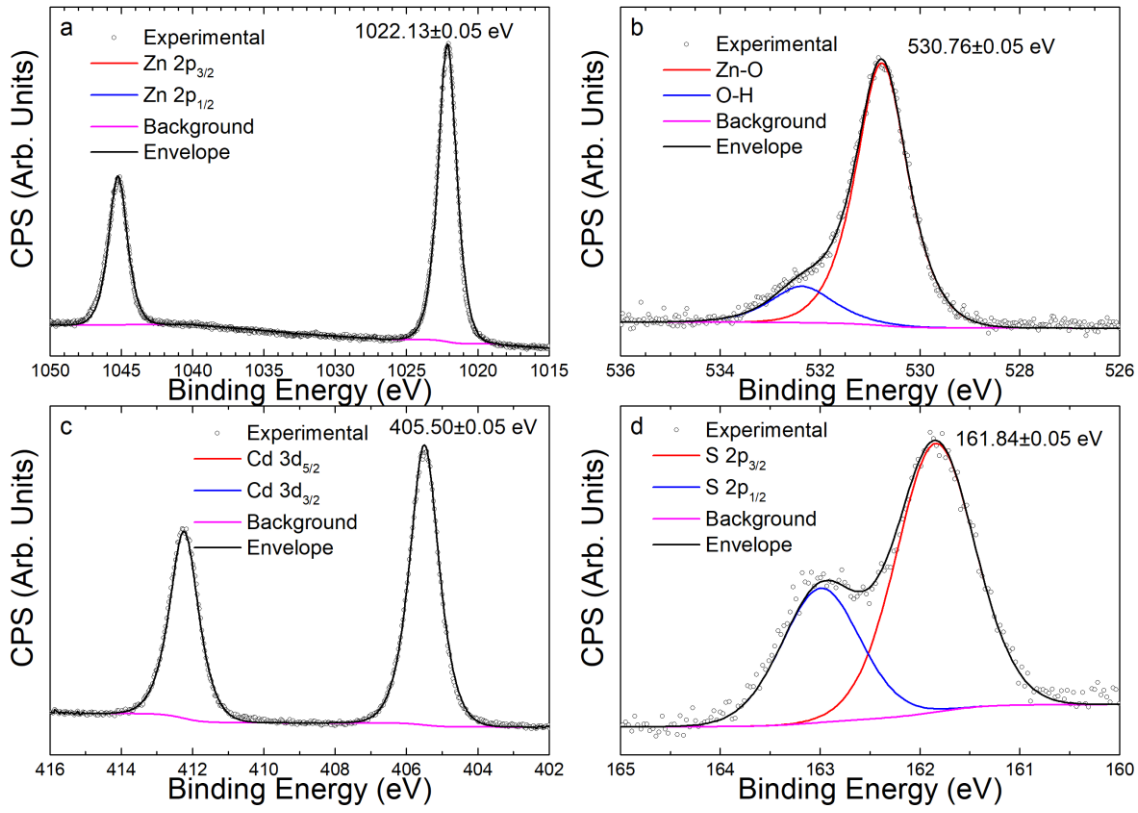

Figure 4.2 – shows the (a) Zn 2p region, (b) the O 1s region, (c) Cd 3d region and (d) the S 2p region, after Ar^+ ion etching until the ZnO/CdS interface was visible.

To obtain an interfacial ZnO/CdS sample the thick Zn/CdS was Ar^+ ion etched with low energy Ar^+ ions (E_k=0.25 keV) with a flux of 6.25×10^{13} ions cm^{-2} s^{-1}, until the Cd 3d and S 2p peaks were visible. The resulting spectra are shown in Figure 4.2. (a) shows the Zn 2p

regions, which is fitted using a single spin-orbit split doublet, (b) shows the O 1s region which is fitted with two peaks, corresponding to Zn-O and O-H bonds, as in the case of the thick ZnO film. (c) and (d) show the Cd 3d and S 2p regions respectively, both of which are fitted with only a single doublet each. The presence of only a single set of peaks in the Zn 2p, Cd 3d and S 2p regions are suggestive of the phase purity of the interface, implying that any intermixing between the two layers is necessarily below the detection limit of XPS.

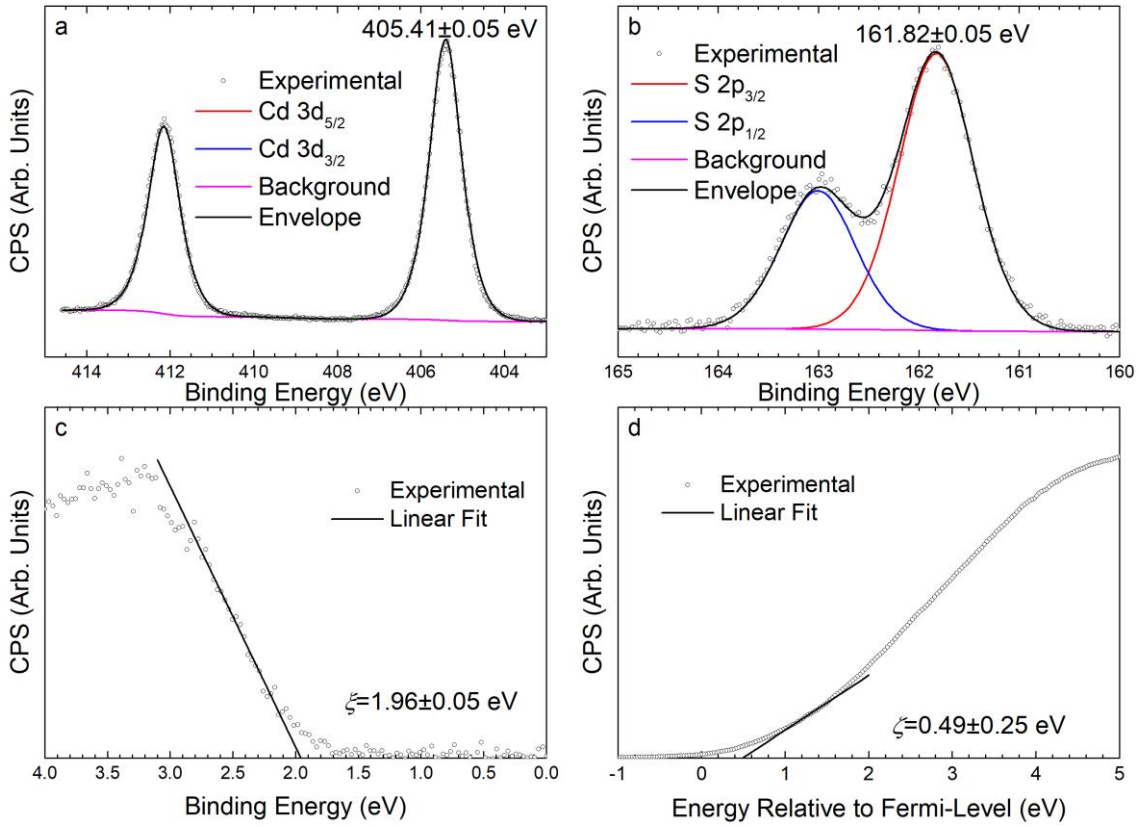

Figure 4.3 – shows the (a) Cd 3d, (b) S 2p and (c) valence band maximum regions as measured by XPS from a thick CdS sample. (d) shows the conduction band minimum as measured by IPES from the same sample. By combining the results from (c) and (d), the band gap is found to be 2.45±0.25 eV, consistent with the 2.42 eV gap determined from single crystal CdS[657]–[659].

Figure 4.3 shows the XPS and IPES spectra measured from a clean CdS film deposited on CZTSSe. (a) and (b) show the Cd 3d and S 2p regions respectively, both of which require only a single set of peaks to fit, indicating that the film is phase-pure within the detection limits of XPS. (c) and (d) shows the valence band maximum and conduction band minimum as measured by XPS and IPES respectively. Also shown in (c) and (d) are the linear extrapolations used to determine the band positions. Similar to ZnO the conduction band edge of CdS is found to be decidedly non-linear in theoretical works[660], [661] and the relatively low resolution of IPES (which leads to a broadening of the higher energy, more-intense features), only a small section of the IPES data is used to find the CBM. Using the

values obtained from the linear extrapolations, a band gap of 2.45±0.25 eV is found, consistent with the 2.42 eV gap reported for single crystals and polycrystalline films of CdS[657]–[659], and comparable to band gaps obtained by combined UPS/IPES methods[271], [648]–[650], [662]. Using equations (2.19) and (2.20), the band alignments of the ZnO/CdS interface can be determined. The results are summarised in Table 4.1. By averaging the two values given in Table 4.1, the VBO is found to be $\Delta E_v = 0.66 \pm 0.10$ eV and the CBO is found to be $\Delta E_c = 0.31 \pm 0.3$ eV.

Sample		E_B (eV)	ξ (eV)	E_g (eV)	E_B-ξ (eV)	ΔE_{CL} (eV)	ΔE_v (eV)	ΔE_c (eV)
CdS	Cd $3d_{5/2}$	405.41	1.96	2.45	403.45	616.63	-0.62	0.35
	S $2p_{3/2}$	161.82	1.96	2.45	159.86	860.29	-0.69	0.28
ZnO	Zn $2p_{3/2}$	1022.1	2.64	3.42	1019.46	-	-	-

Table 4.1 - A summary of the parameters used to determine the band alignment at the ZnO/CdS interface by the Kraut method.

The thick CdS/CZTSSe sample was then etched by low energy Ar^+ ions (E_k=0.25 keV) and an ion flux of 6.25×10^{13} ions cm^{-2} s^{-1}, until the core-levels of the CZTSSe layer were visible and comparable in intensity to the Cd 3d core-levels. Figure 4.4 shows the resulting XPS spectra from the CdS/CZTSSe interface. (a) and (b) show the Cd 3d and S 2p regions respectively/. For the Cd 3d, only a single doublet is required, whilst for the S 2p a doublet is used to fit the S 2p, however the Se $3p_{3/2}$ is also present at lower binding energy. (c) and (d) show the Cu 2p and Zn 2p core-levels respectively, each is fitted with only a single spin-orbit split doublet. (e) shows the Sn 3d region, however for an Al-anode, the Zn $L_3M_{45}M_{45}$ Auger peak occurs at a similar kinetic energy to the Sn $3d_{3/2}$ peak. To fit the Sn $3d_{3/2}$, the Zn $L_3M_{45}M_{45}$ peak from the thick ZnO sample is fitted with two peaks, the separations and relative intensities of which are allowed to vary to best fit the peak. These are then used to constrain the same two Zn $L_3M_{45}M_{45}$ peaks due to the CZTSSe. The Sn $3d_{3/2}$ is then fixed to have the same FWHM as the Sn $3d_{5/2}$, a relative intensity of $^2/_3$ of the Sn $3d_{5/2}$ and a separation equal to the spin-orbit splitting energy for the Sn 3d core-level. Any remaining intensity is then necessarily due to the Zn $L_3M_{45}M_{45}$ which can then be accounted for by the fitted Auger levels. (f) shows the Se 3d region, which is fitted with only a single set of doublets.

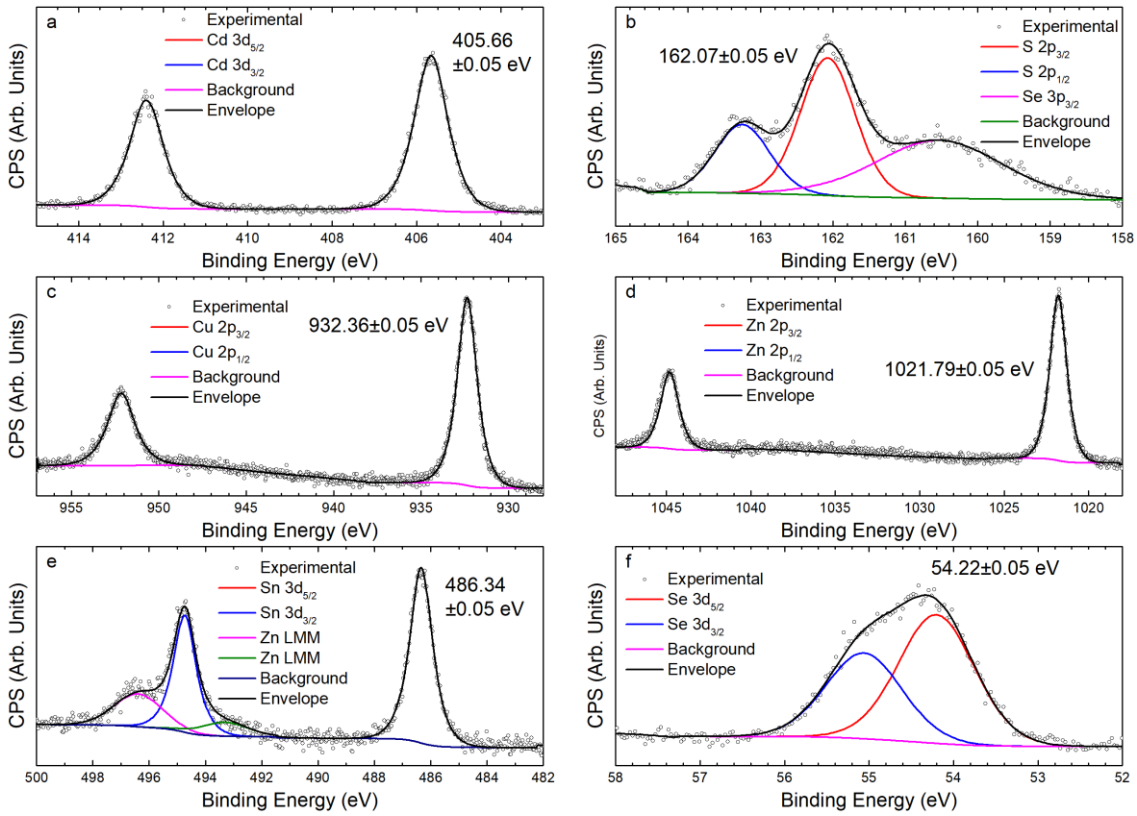

Figure 4.4 – shows the (a) Cd 3d, (b) S 2p and Se 3p, (c) Cu 2p, (d) Zn 2p, (e) Sn 3d and Zn LMM, (f) Se 3d regions measured by XPS after Ar^+ ion etching until the CdS/CZTSSe interface was visible.

The sample was then further etched using the same conditions until the Cd 3d peaks were no longer present, thus obtaining a clean CZTSSe surface. The resulting XPS spectra are shown in Figure 4.5. In each case, the core-levels are fitted with only a single set of doublets. The Sn $3d_{3/2}$ core-level is fitted in the same way as that described previously for Figure 4.4. (e) and (f) shows the valence band maximum and conduction band minimum as determined by XPS and IPES respectively. Also shown are the linear extrapolations of the leading edges to determine the band edge positions. By combining these, the band gap of the film is determined to be 1.15±0.14, consistent with that determined for a similar film in chapter 3.

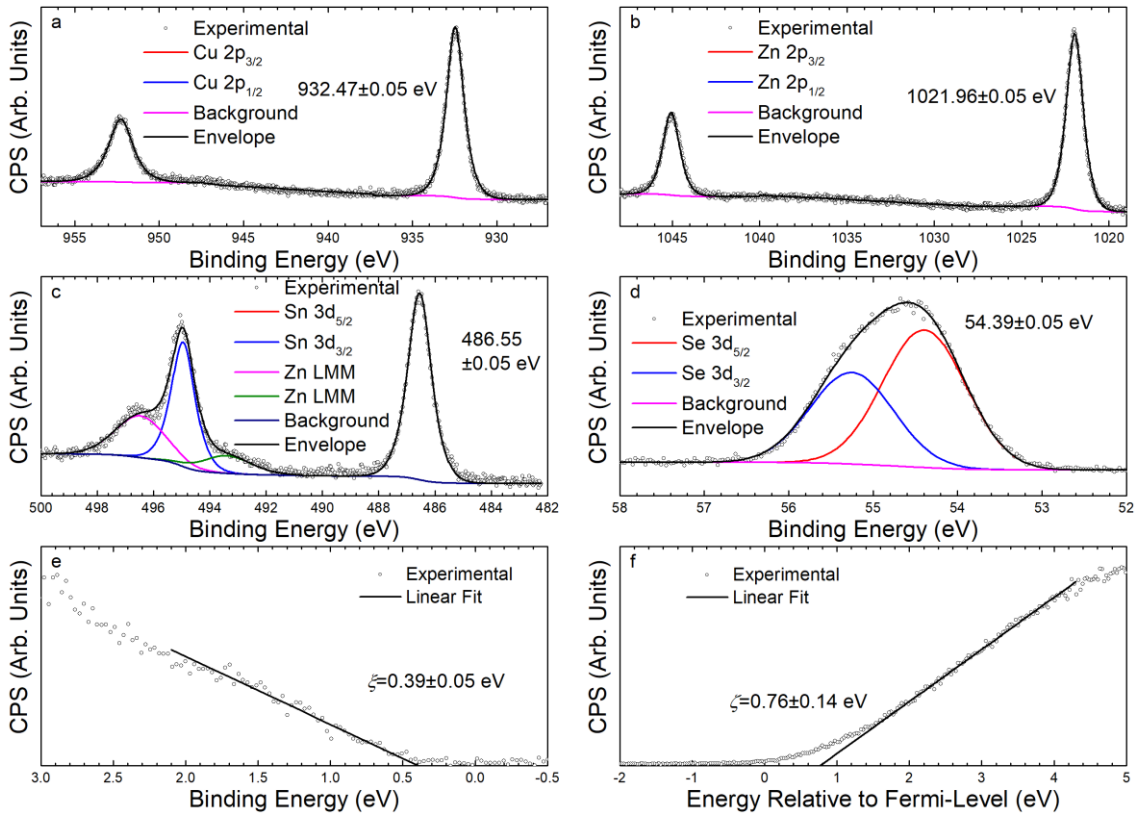

Figure 4.5 – shows the (a) Cu 2p, (b) Zn 2p, (c) Sn 3d and Zn LMM, (d) Se 3d and (e) valence band maximum regions from a CZTSSe thin-film as measured by XPS. (f) shows the conduction band minimum as measured by IPES. By combining the results of (e) and (f), the band gap of the film is found to be 1.15±0.14 eV, consistent with that measured in chapter 3.

By combining the results of Figure 4.3, Figure 4.4 and Figure 4.5, the band alignment at the CdS/CZTSSe interface can be determined by the Kraut method. The parameters used and the resulting band offsets are given in Table 4.2. To find the final value of the valence band and conduction band offsets, the mean of the VBO and CBOs obtained for each core-level is taken. Thus, the VBO is determined to be $\Delta E_v = -1.98 \pm 0.10$ eV, whilst the CBO is found to be $\Delta E_c = -0.68 \pm 0.14$ eV.

Sample Core-Level		E_B (eV)	ξ (eV)	E_g (eV)	E_B-ξ (eV)	ΔE_v Cd (eV)	ΔE_v S (eV)	ΔE_c Cd (eV)	ΔE_c S (eV)
CdS	Cd $3d_{5/2}$	405.41	1.96	2.45	403.45	-	-	-	-
	S $2p_{3/2}$	161.82	1.96	2.45	159.86	-	-	-	-
CZTSSe	Cu $2p_{3/2}$	932.47	0.39	1.15	932.08	-1.92	-1.93	-0.62	-0.63
	Zn $2p_{3/2}$	1021.96	0.39	1.15	1021.57	-1.98	-1.99	-0.68	-0.69
	Sn $3d_{5/2}$	486.55	0.39	1.15	486.16	-2.02	-2.03	-0.72	-0.73
	Se $3d_{5/2}$	54.39	0.39	1.15	54.00	-1.98	-1.99	-0.68	-0.69

Table 4.2 – A summary of the parameters used to determine the band offsets using the Kraut method for the CdS/CZTSSe interface

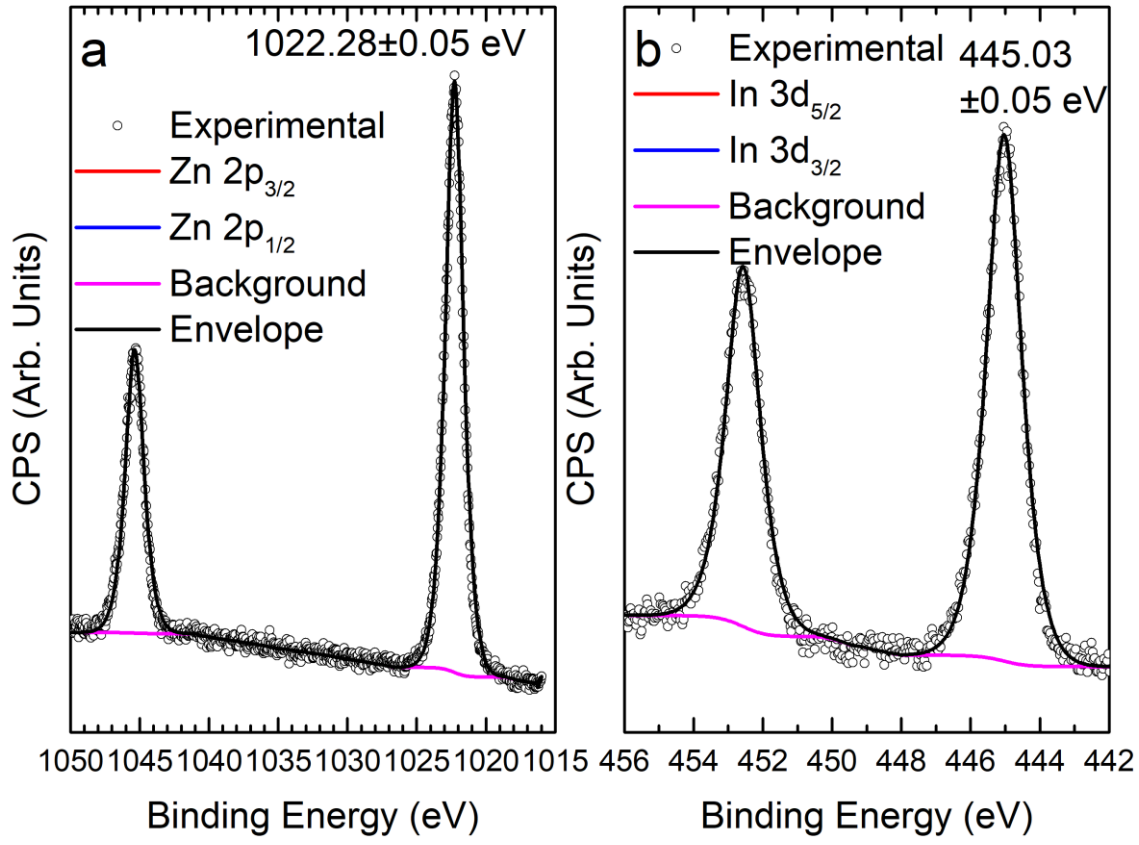

Figure 4.6 – shows the (a) Zn 2p and (b) the In 3d regions as measured by XPS. A thick ZnO/In_2S_3 sample was etched by Ar^+ ions until the In 3d peaks were visible to obtain the interfacial sample.

To determine the band alignment of the ZnO-In_2S_3-CZTSSe stack, a similar experiment to that described previously was performed. As the thick ZnO samples was sufficiently thick so that its properties were not dependent on the buffer layer, the values for the thick ZnO sample can be used here. The sample was initially etched with Ar^+ ions until the In 3d peaks were visible, then high-resolution scans were made of the Zn 2p and In 3d regions, which

can be seen in Figure 4.6. As with the previous experiments, both spectra are fitted using only two components corresponding to the Zn $2p_{3/2}$, Zn $2p_{1/2}$ and the In $3d_{5/2}$ and In $3d_{3/2}$ core-levels respectively. The absence of any secondary peaks is indicative of the phase purity of the materials, suggesting that any intermixing at the interface is below the detection limit of XPS.

An In_2S_3 sample was then used to determine the band alignments of the ZnO/In_2S_3 heterointerface. Figure 4.7 shows the XPS [(a), (b), (c)] and IPES [(d)] spectra from the film. Both the In 3d and S 2p, in (a) and (b) respectively, require only two peaks to fit the data, constrained by the spin-orbit splitting of the core-levels. This indicates that the In_2S_3 does not have large levels of contamination in the materials. (c) and (d) can also be used to determine the band gap of the film, which is found to be 2.75±0.14 eV, which is consistent with the band gap obtained by UV-Vis spectrometry, shown in Figure 3.20.

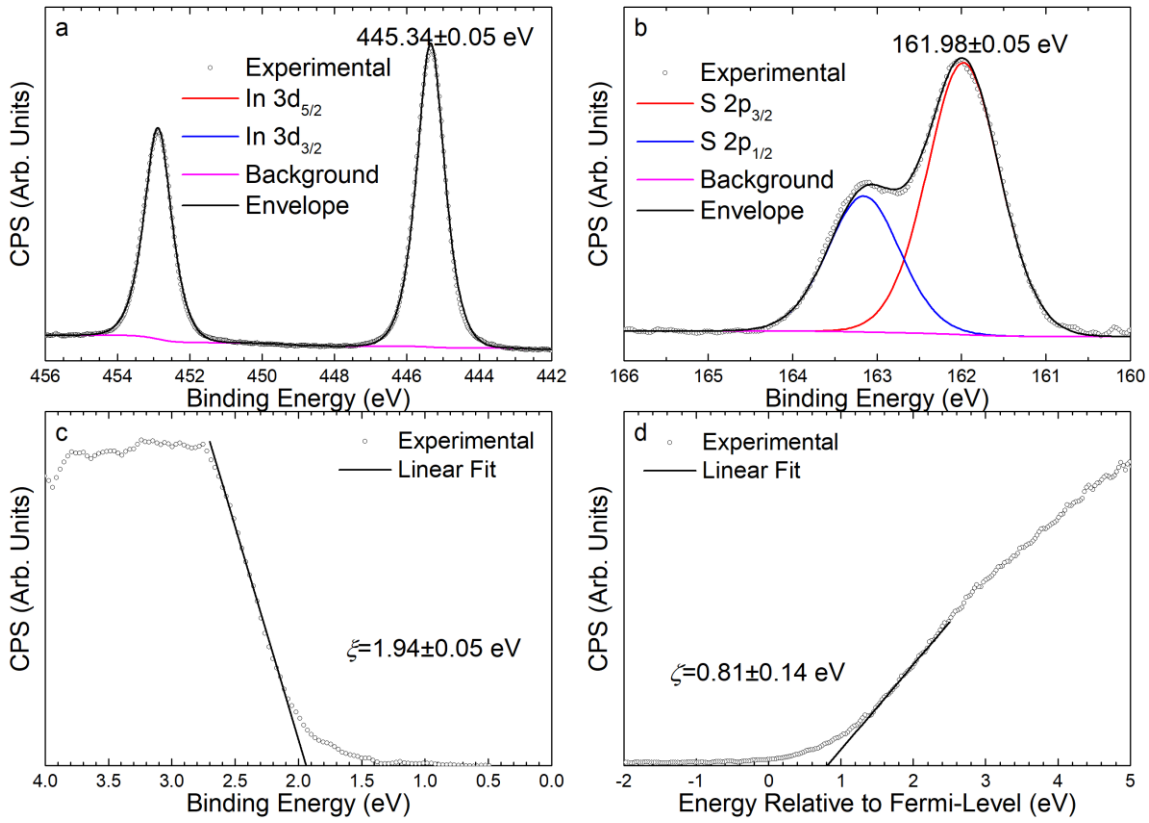

Figure 4.7 – shows the (a) In 3d, (b), S 2p and (c) valence band maximum regions for a thick polycrystalline In_2S_3 sample as measured by XPS. (d) shows the IPES spectrum measured from the same sample. By combining the results of (c) and (d), the band gap is found to be 2.75±0.14 eV, consistent with that found by UV-Vis spectroscopy in Figure 3.20.

To determine the band alignment at the ZnO/In_2S_3 interface, the Kraut method is used once more to determine the band offsets. The parameters used and the resulting band offsets

are summarised in Table 4.3. For the ZnO/In_2S_3 interface, the VBO is found to be $\Delta E_v = -1.19 \pm 0.10$ eV, whilst a value of $\Delta E_c = -0.52 \pm 0.14$ eV for the CBO.

Sample	E_B (eV)	ξ (eV)	E_g (eV)	E_B-ξ (eV)	ΔE_{CL} (eV)	ΔE_v (eV)	ΔE_c (eV)
ZnO	1022.1	2.64	3.42	1019.46	-	-	-
In_2S_3	445.34	1.94	2.75	443.40	577.25	-1.19	-0.52

Table 4.3 - A summary of the parameters used to obtain the band offsets for the ZnO/In_2S_3 interface using the Kraut method.

The thick In_2S_3 sample was then further etched using Ar^+ ions, until the In_2S_3/CZTSSe interface was visible by XPS. High-resolution XPS spectra were then measured of the In 3d, Cu 2p, Zn 2p, Sn 3d and Se 3d core-levels, which are shown in Figure 4.8. In each case the core-levels are fitted with only two peaks, separated by their respective spin-orbit splitting energy. Combining the results from Figure 4.8 with those from Figure 4.5 and Figure 4.7 allows for the band alignment of the CZTSSe interface to be determined. The parameters and results of which are summarised in Table 4.4. To obtain the VBO, the mean of the values given in Table 4.4 is determined, thus the VBO is found to be $\Delta E_v = -1.21 \pm 0.10$ eV. Likewise, the CBO is found to be $\Delta E_c = 0.39 \pm 0.14$ eV.

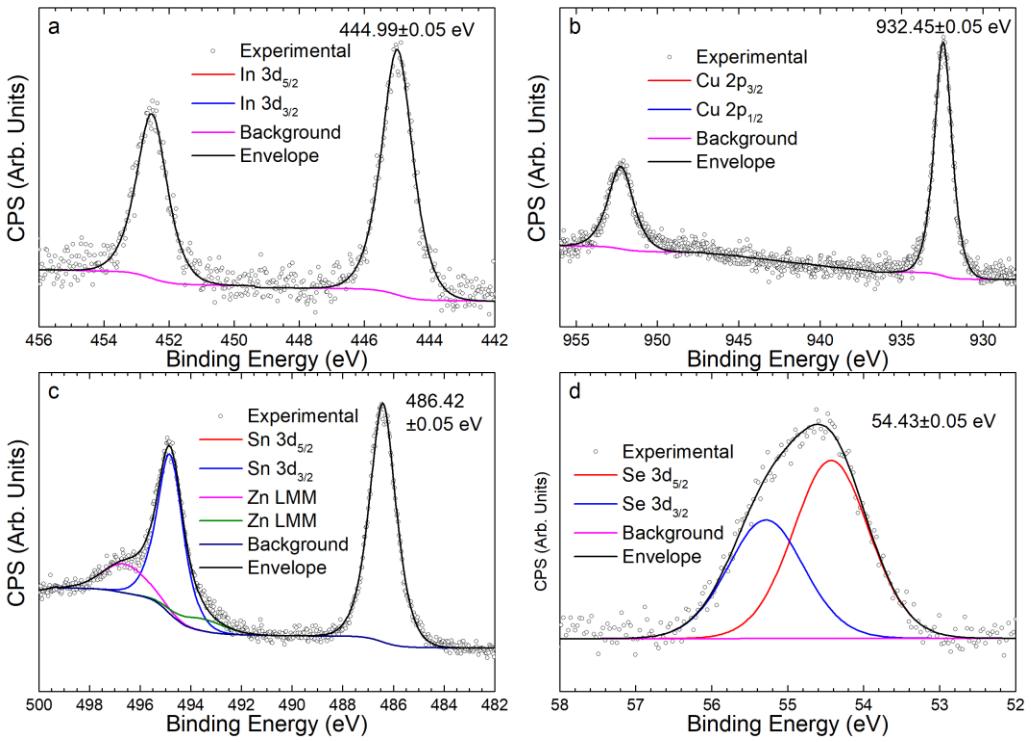

Figure 4.8 – shows the (a) In 3d, (b) Cu 2p, (c) Sn 3d and Zn LMM and (d) the Se 3d regions for the interfacial In_2S_3/CZTSSe sample after Ar^+ ion etching.

Sample(Core-Level)		E_B (eV)	ξ (eV)	E_g (eV)	E_B-ξ (eV)	ΔE_{CL} (eV)	ΔE_v(eV)	ΔE_c (eV)
In_2S_3	In $3d_{5/2}$	445.34	1.94	2.75	443.40	-	-	-
CZTSSe	Cu $2p_{3/2}$	932.47	0.39	1.15	932.08	-487.46	-1.22	0.38
	Zn $2p_{3/2}$	1021.96	0.39	1.15	1021.57	-577.05	-1.12	0.48
	Sn $3d_{5/2}$	486.55	0.39	1.15	486.16	-41.43	-1.33	0.27
	Se $3d_{5/2}$	54.39	0.39	1.15	54	390.56	-1.16	0.44

Table 4.4 - A summary of the parameters used to obtain the band offsets at the In_2S_3/CZTSSe interface using the Kraut method.

Figure 4.9 shows the band alignments determined by the Kraut method from XPS. The alignment of the ZnO window layer with the CdS buffer layer is spike-like, which for this interface may be detrimental to the efficiency of the device, as electrons would require thermal excitation to leave *via* the front contact. In contrast, the ZnO/In_2S_3 interface is cliff-like, which should aid in removing electrons from the In_2S_3 layer. Note that this is the opposite for the CZTSSe/In_2S_3 and CZTSSe/CdS interfaces which are spike-like and cliff-like respectively. Previous reports of the band alignments of CZTS(Se)/In_2S_3 interfaces have suggested a small (0-0.5 eV) spike-like alignment[264], [273], [564], comparable to what is found here. A similar spike-like alignment has also been found for the closely related Cu_2SnS_3 absorber layer with In_2S_3[154].

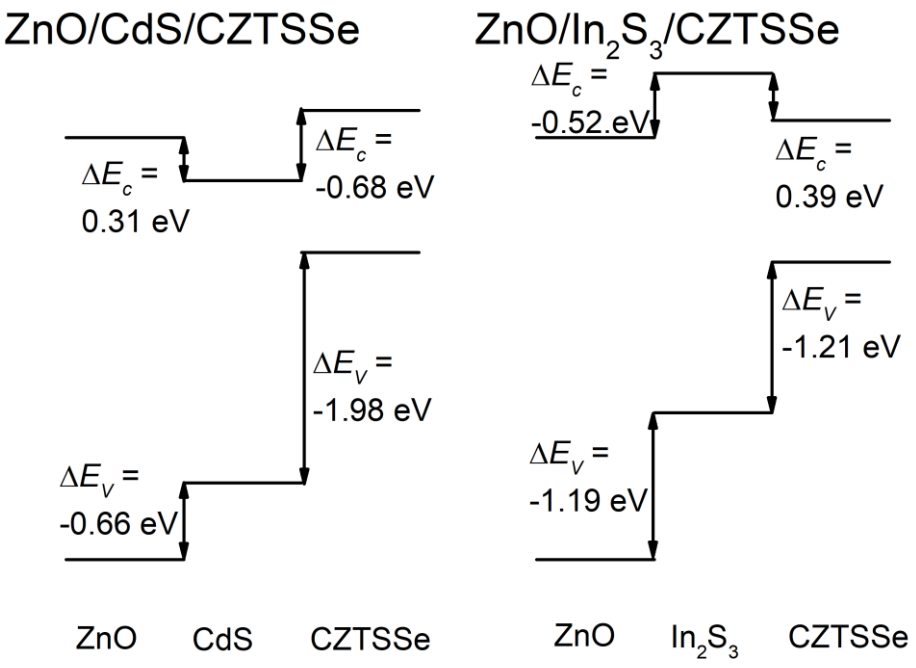

Figure 4.9 – Shows the band alignments of the ZnO/CdS/CZTSSe and ZnO/In_2S_3/CZTSSe stacks.

4.2 SCAPS SIMULATIONS OF DEVICES

Once the full band alignments of the device-like stacks are known, it is possible to use solar cell capacitance simulations (SCAPS)[646] to estimate the maximum achievable efficiencies, J_{SC} and V_{OC} based on the properties of the materials used. The values used for the simulations are given in Table 4.5.

The intrinsic concentration of any undoped semiconductor is necessarily related to the effective densities of states in the conduction and valence bands by equation (4.1). By considering detailed balance, i.e. the conservation of charge, it necessarily follows that $n_i^2 = np$.

$$n_i^2 = N_C N_V e^{-\frac{E_g}{k_B T}} = np \tag{4.1}$$

Where N_c and N_v are given by equations (4.2) and (4.3)[663], [664].

$$N_C = 2\left(\frac{2\pi m_e^* k_B T}{h^2}\right)^{3/2} \tag{4.2}$$

$$N_V = 2\left(\frac{2\pi m_h^* k_B T}{h^2}\right)^{3/2} \tag{4.3}$$

Where $m_{h(e)}^*$ are the density-of-states effective masses, for the valence (conduction) bands. If the effective masses of the charge carriers are known, then the values of N_C and N_V can thus be calculated.

The properties of the alloyed CZTSSe system are generated by application of Vegard's law to the properties of the pure CZTS and CZTSe phases given in Table 4.5. As the band bowing parameter for the CZTS/CZTSe alloy system is only small ($b \approx 0.07$ eV)[200], we have neglected the non-linear corrections to Vegard's law for simplicity. The band gap obtained from photoemission is then used to estimate the composition of the materials by solving the linear form of Vegard's law for the composition, x, as shown in equations (4.4) and (4.5).

$$1.00x + 1.58(1 - x) = 1.15 \text{ eV} \tag{4.4}$$

$$x = \frac{1.15 - 1.58}{1.00 - 1.58} = 0.75 \tag{4.5}$$

	CZTSe	CZTS	CdS	In_2S_3	i-ZnO	Al:ZnO
Thickness (μm)	1.00	1.00	0.05	0.05	0.10	0.10
E_g (eV)	1.00[665]	1.58[338], [666], [667]	2.45	2.75	3.42	3.42
χ (eV)	3.89	3.89	4.57	3.50	4.26[a], 4.02[b]	4.26[a], 4.02[b]
ε_r	9.1[668], [669]	7.0[670], [671]	8.73[672]	6.25[673]	8.75[674]	8.75[674]
N_V (cm^{-3})	$4.75x10^{18}$	$1.50x10^{19}$	$1.47x10^{19}$	$8.08x10^{19}$	$1.14x10^{19}$	$1.14x10^{19}$
N_C (cm^{-3})	$5.67x10^{17}$	$1.92x10^{18}$	$3.13x10^{18}$	$1.64x10^{18}$	$2.95x10^{18}$	$2.95x10^{18}$
v_e ($cm\ s^{-1}$)	$1x10^7$	$1x10^7$	$1x10^7$	$1x10^7$	$1x10^7$	$1x10^7$
V_h ($cm\ s^{-1}$)	$1x10^7$	$1x10^7$	$1x10^7$	$1x10^7$	$1x10^7$	$1x10^7$
μ_e ($cm^2\ V^{-1}\ s^{-1}$)	690[665]	5[675]	300[676]	90[677]	440[678]	136[679]
μ_h ($cm^2\ V^{-1}\ s^{-1}$)	105[680]	30[675]	200[681]	0.5[682]	20[683], [684]	20[683], [684]
m_e^*	0.08[685]	0.18[685]	0.25[686]	0.162[687]	0.24[688]	0.24[688]
m_h^*	0.33[685]	0.71[685]	0.70[686]	0.470[687]	0.59[688]	0.59[688]
N_D (cm^{-3})	0	0	$1.19x10^{19}$[689]	$6.56x10^{18}$[690]	$1x10^6$[688]	$9.03x10^{18}$[691]
N_A (cm^{-3})	$2x10^{15}$	$7.9x10^{19}$[692]	0	0	0	0
α ($eV^{1/2}\ cm^{-1}$)						
B ($cm^3\ s^{-1}$)	$1.0X10^{-10}$	$1.0X10^{-10}$	$1.0X10^{-10}$	$1.0X10^{-10}$	$1.0X10^{-10}$	$1.0X10^{-10}$

Table 4.5 - This table lists the parameters used for SCAPS simulations of the ZnO-CdS-CZTSSe and ZnO-In_2S_3-CZTSSe stacks characterised in section 4.1. [a] for ZnO-CdS-CZTSSe, [b] for ZnO-In_2S_3-CZTSSe.

Thus, the sulphur: selenium ratio is estimated to be 1:3. Figure 4.10 shows the resulting external quantum efficiency (EQE) and current density-voltage curves for the simulated devices. By examining the EQE curves for the two devices, it is clear that the CdS-based device has a much lower EQE across all photon energies. At approximately 2.4 eV, and 2.7 eV for the CdS and In_2S_3-based device, the EQE is observed to decrease by approximately 2% and 20% respectively. This decrease corresponds to the band gap of the buffer layers and hence is due to absorption within the buffer. At photon energies above approximately 3.4 eV, the EQE further decreases to near zero, this corresponds to absorption in the ZnO

layers. Here the hole is extremely unlikely to be collected by the back contact and is much more likely to undergo a recombination process, resulting in a very low EQE in this region.

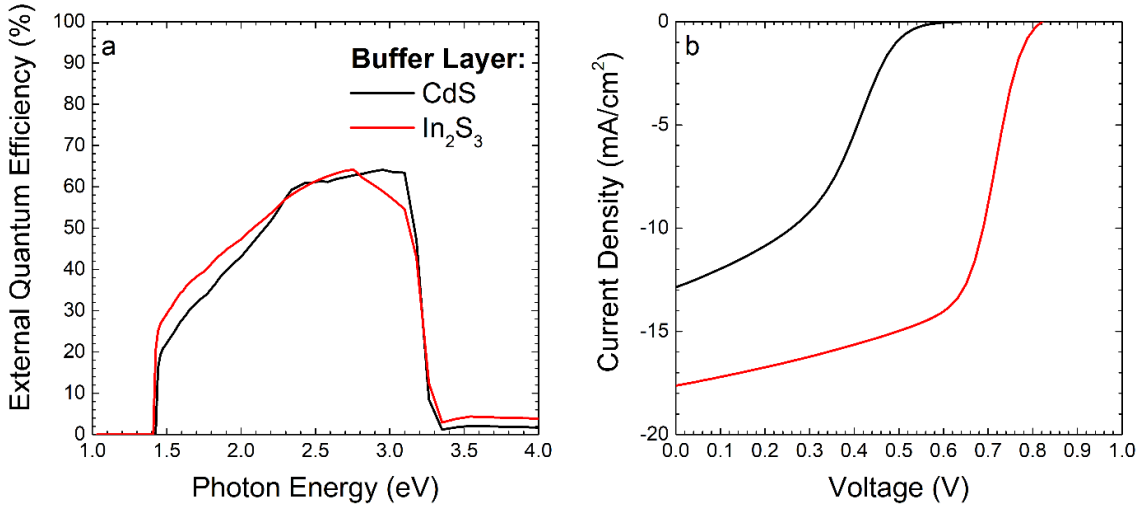

Figure 4.10 – This shows the simulated external quantum efficiency and current density-voltage curves obtained for the ZnO/CdS/CZTSSe and ZnO/In_2S_3/CZTSSe device-like stacks.

Table 4.6 shows the photo-conversion efficiency (η), open-circuit voltage (V_{OC}), short-circuit current (J_{SC}) and fill factor (FF) for the simulated devices. Also shown are the same device statistics for the record CZTSSe[693] and CIGS[694] devices. The differences in the device statistics between the devices with CdS and In_2S_3 buffer layers are intriguing. Each statistic is considerably lower for the device with a CdS buffer layer compared to that of the device with In_2S_3 layer. The open-circuit voltage for both simulated devices is larger than that of the record CZTSSe device but shows a reduced short-circuit current and FF. This is likely due to recombination in the simulated device, possibly at either the Buffer/CZTSSe or the ZnO/Buffer interface. Intriguingly the open-circuit voltage for the device with an In_2S_3 buffer layer is larger than that of the record CIGS device[694].

Device	η (%)	V_{OC} (V)	J_{SC} (mA/cm^2)	FF (%)
ZnO/CdS/CZTSSe	2.79	0.65	12.9	33.2
ZnO/In_2S_3/CZTSSe	8.48	0.82	17.6	59.3
CZTSSe Record[693]	12.6	0.51	35.2	69.8
CIGS Record[694]	22.6	0.74	37.8	80.6

Table 4.6 – This table shows the device statistics of the simulated CZTSSe devices described above. Also shown are the same device statistics for the record CZTSSe and CIGS devices.

The record CZTSSe device, however has a device structure incorporating ZnO and CdS layers, as shown in Figure 4.11[693], [695]. This begs the question, why our simulated CdS devices are so different in behaviour to the real devices? The band gap of the CZTSSe layer

used for the record device is 1.13 eV, which is consistent with the 1.15 eV band gap obtained in this work, so the band offsets should not be too dissimilar as a result of variation in the band gap.

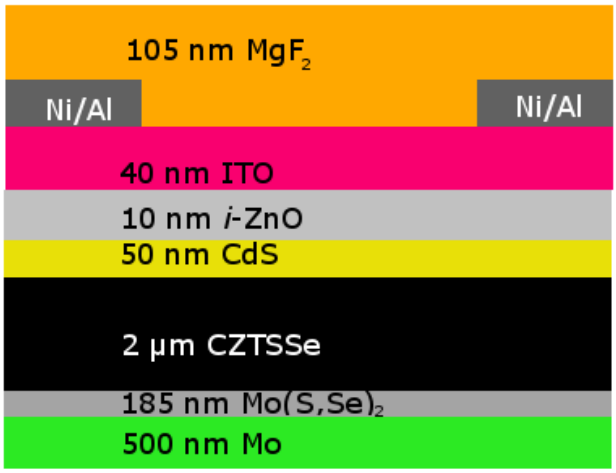

Figure 4.11 – A schematic diagram showing the device architecture of the current record CZTSSe device[513], [515].

Instead, it seems more probable that due to the small thickness of ZnO used (i.e. 10 nm), the charge carriers are not particularly affected by the presence of the ZnO, and the improvements in efficiency that are seen when using a ZnO layer are due to the prevention of diffusion between the ITO and CdS layers, and also its properties as a reflective coating. In CdTe-based substrate architecture devices, the inclusion of an intermediate ZnO layer between the CdS and ITO layers is shown to increase the efficiency[696]. The mechanism proposed for this is that the ZnO layer acts as a passivating layer, removing shunting paths and passivating pinholes in the CdS layer, thus preventing the formation of diodes between the CdTe and ITO layers[696].

An alternative explanation proposed by Liu *et al.*[697], [698] is that the ZnO intermediate layer reduces the effective size of the potential barrier between the ITO and CdS layers, as the probability of excitation above a potential barrier shows and exponential dependency on the barrier height, which they show *via* the Kraut method. However, their argument is somewhat weakened by the fact that the band gap they use for the ITO layer is the *optical gap* of the ITO, rather than the electronic gap. Direct excitation from the VBM to the CBM is dipole forbidden due to the symmetry of the bixbyite structure In_2O_3 adopts[699], [700]. The actual dipole-forbidden band gap is approximately 2.93 eV, whilst the allowed direct gap occurs at around 3.55 eV[699]–[701].

Another factor is that as ITO is typically degenerately doped semiconductor, there are large numbers of electrons in the conduction band. Therefore, when the band gap is measured by optical methods, the band gap is considerably over-estimated, as the photons need to have sufficient energy to excite the electrons into unoccupied states higher in the conduction band. This is the Moss-Burstein effect[702], [703], which is commonly seen in degenerately-doped semiconductors[704]–[710], including In_2O_3[701], [711]–[713].

Whilst it is the optical gap that determines the optical properties of the material, it is the electronic gap that determines the band offsets. If the electronic gap of 2.9 eV is used in place of the optical gap of 3.72 eV determined by Liu *et al*.[697], [698], then the resulting electron affinity is found to be $\chi = 4.39\ \mathrm{eV}$, which is consistent with values obtained in literature when the appropriate band gap is used[711], [714]–[717]. In contrast, numerous older reports give an electron affinity, $\chi \approx 3.5\ \mathrm{eV}$ when a band gap of 3.6 eV is used[718]–[721]. However, most reports give the ionisation potential to be 7-8 eV[711], [714], [723]–[727], [715]–[722] which is consistent with the ionisation potential in the work of Liu *et al*.[697]and work by the author of this work, presented in chapter 6.

The results are also complicated by the fact that although they are using the Kraut method, the valence bands maxima positions are determined from UPS, whilst the core-level binding energies are necessarily determined from XPS. As such, the core-level to valence band separations given are not reliable, as the charge corrections are not necessarily the same. Thus, neither the conduction band or valence band offsets and hence the conclusions, are reliable.

The band offsets at ZnO/In_2O_3 heterojunctions have also been reported by Song *et al.*[728] and Kaspar *et al.*[729], [730]. In the case of Kaspar *et* .[729], [730], the shallow Zn 3d and In 4d energy-levels are used to evaluate the core-level to valence band separations, however these energy-levels are hybridised with oxygen states to form the valence band, and hence the validity of using these shallow energy-levels is questionable.

In the case of Song *et al.*[728], the In 3d and Zn 2p core-levels are used, which occur at energies far away from the valence band. However, the authors use the linear extrapolation method to evaluate the binding energy of the valence band maximum. This method was shown to be invalid for In_2O_3, by King *et al.*[699] due to the high density of states close to the VBM. As such, the onset of the VBM is rapid, and the broadening of the VBM is dominated by the instrumental resolution. Thus the VBM binding energy may be underestimated by up to 0.60 eV as seen in fig. 5 of King *et al*.[699].

The core-level to valence band separation found by Song *et al.*[728], is therefore overestimated by up to 0.60 eV, which when propagated through results in the In_2O_3 valence band being 0.11 eV below that of the ZnO, which, surprisingly, is similar to that obtained by Kaspar *et al.*[729], [730]. The re-calculated VBO is comparable to that predicted by Walsh *et al.*[731] by hybrid density functional theory calculations. By using the re-calculated valence band offset, the In_2O_3 conduction band is found to occur 0.33 eV below the ZnO conduction band, which is consistent with the performance of ZnO/In_2O_3 transistors[732]. It is, thus, unlikely that ZnO acts as an intermediate layer between the CdS and ITO layers. This hypothesis is further weakened, as the band alignments at a CdS/ITO heterojunction were investigated by Krishnakumar *et al.*[733], who found the In_2O_3 conduction band to occur at 0.70 eV below that of CdS, in clear contrast to the 0.90 eV above found by Liu *et al*.[697], [698].

In which case, if instead of the *i*-ZnO/Al:ZnO window layer used above, what happens to the simulated device parameters if a *i*-ZnO/ITO or a simple buffer/ITO layer is used in simulations with the two buffer layers considered here? Since, the VBOs of these interfaces have not been measured in this work, the simulations will use the valence band offsets determined in literature, with corrections for the In_2O_3 valence band edge position where required. Conduction band offsets will then be calculated from the band gaps of the materials in question.

Interface	ΔE_v (eV)	ΔE_c (eV)
i-ZnO/ITO	-0.11[728]	-0.33
CdS/ITO	-1.25[733]	-0.70

Table 4.7 – Valence band offsets from the literature for the i*-ZnO/ITO and CdS/ITO interfaces after corrections for the extrapolation of the In_2O_3 valence band edge. Conduction band offsets are then recalculated using the correct electronic gaps for the materials.*

Table 4.7 shows the band offsets used for these simulations, alongside the literature reference. The resulting EQE and $J-V$ curves for CdS/ITO, CdS/*i*-ZnO/ITO and In_2S_3/*i*-ZnO/ITO devices are shown in Figure 4.12. The statistics for these simulated devices are also presented in Table 4.8.

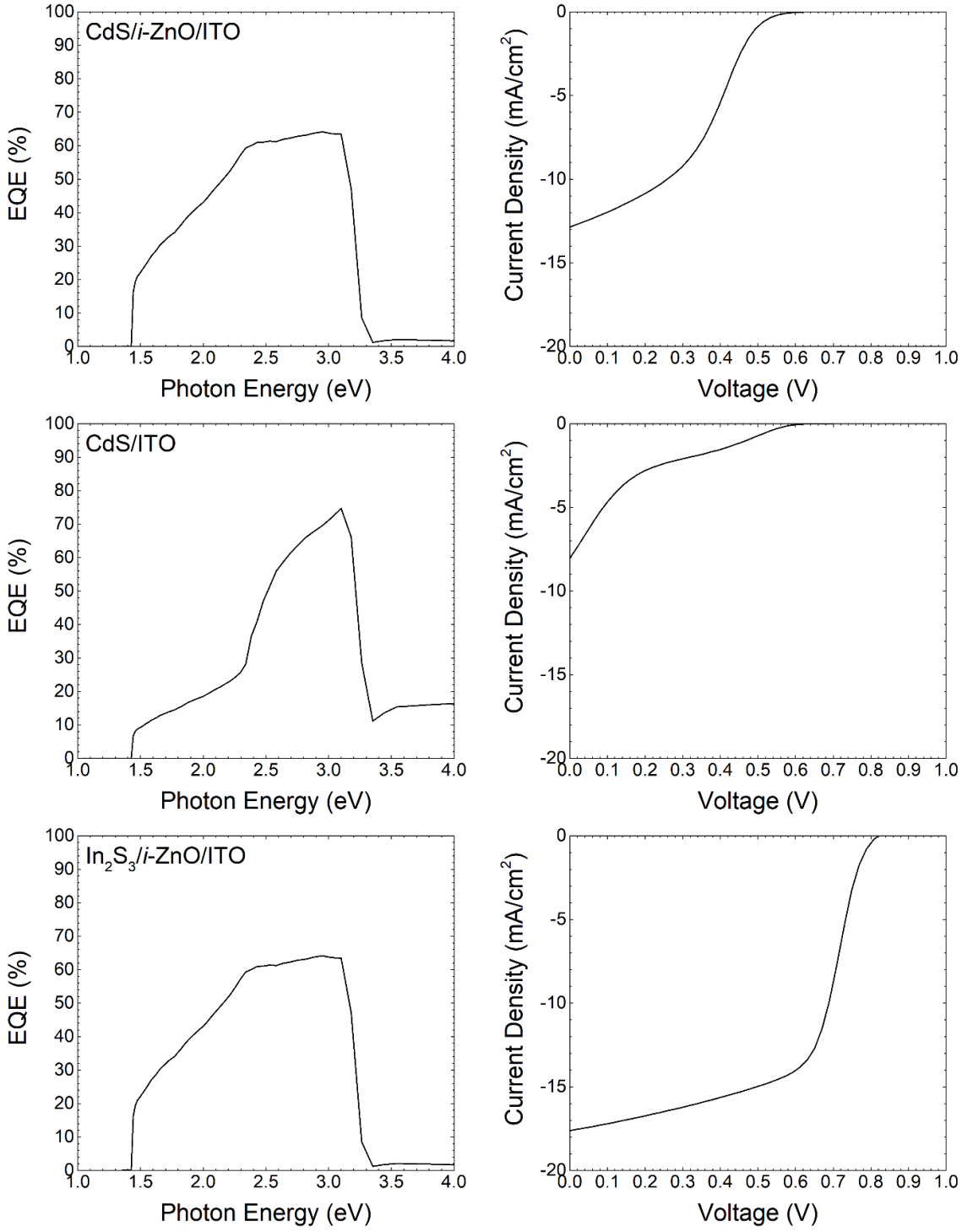

Figure 4.12 – Simulated EQE and J-V curves for the devices using ITO as an alternative to (Al:)ZnO.

In the case of the CdS/*i*-ZnO/ITO and the In_2S_3/*i*-ZnO/ITO simulated devices, there is little to no difference in the shape of either the EQE or $J-V$ curves, and no appreciable differences in the device statistics given in Table 4.8, suggesting that the band offset between intrinsic ZnO layer and the window has little effect on the device performance. However, in these simulations, only the band offsets and the band gaps of the TCO are varied, whereas in reality other properties will also change. Therefore, here, we are only

stating that the band offset between the *i*-ZnO and window layers has little effect as long as the band offset is negative. Other properties such as the mobility of electrons and the defects within the TCO will affect device performance, however these are outside the scope of this work, and hence are neglected.

Device	η (%)	V_{OC} (V)	J_{SC} (mA/cm^2)	FF (%)
CdS/*i*-ZnO/ITO	2.79	0.65	12.9	33.2
CdS/ITO	0.64	0.65	8.0	12.3
In_2S_3/*i*-ZnO/ITO	8.48	0.82	17.6	58.7

Table 4.8 – This table shows the device statistics for devices using ITO in place of (Al:)ZnO as the window layer.

In contrast, the performance of the CdS/ITO device is significantly degraded. The EQE between $1.5 - 2.5$ eV is reduced considerably, likely due to recombination at the ZnO/ITO interface. The EQE at approximately 3.3 eV and above is increased due to the absence of the ZnO layer, thus more of the photons in this range are reaching the absorber and contributing to the photocurrent. The $J - V$ curve no longer has the typical shape of a diode, again, likely due to recombination at the ZnO/ITO interface. In terms of the device statistics, V_{OC} is unaffected by the change in the window layer, but the J_{SC} is reduced by nearly 5 mA, due to the aforementioned recombination, this also has a knock-on effect on the FF and the efficiency of the device.

If this is not the cause of the increased efficiency of real CZTSSe devices compared to that simulated here, then what is? Another possibility is that the band gap is reduced at the interface. One possible cause of this is the reported band gap tailing and narrowing of CZTSSe at the interface with CdS. In this, the band gap is reduced by up to approximately 0.15 eV by tailing, and 0.2 eV by narrowing[295]. Thus, the band offsets could be reduced by up to 0.35 eV by this method, which would considerably reduce the interface recombination. Alternatively, CdS deposition is usually carried out at an elevated temperature. Thus, there will be intermixing of the CZTSSe and CdS close to the interface. Theoretical and experimental studies of deliberate Cd-doping of CZTSSe have shown that the introduction of Cd into the CZTSSe lattice results in the band gap being reduced by up to 0.5 eV[734]–[736]. As such, any intermixing at the interface may result in a reduced band gap and as such a reduced CBO, giving a higher efficiency. Hence, a further simulation of the CZTSSe/CdS/*i*-ZnO/Al:ZnO was performed, this time with a 50 nm thick interfacial layer of CZTSSe with the band gap and electron affinity reducing and increasing respectively by 0.35 eV in a linear fashion over the 50 nm, as a representative mix of band-narrowing, band-tailing and Cd-doping.

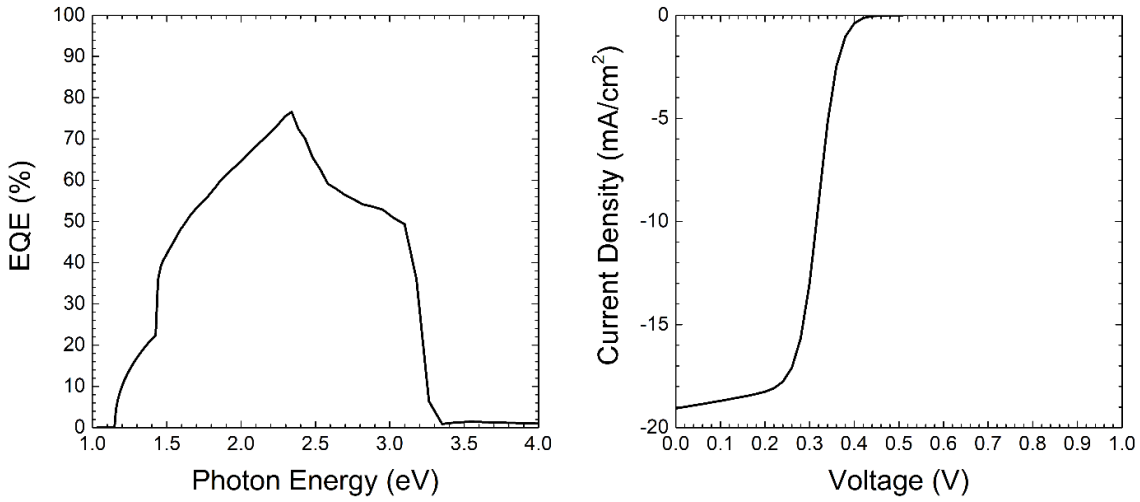

Figure 4.13 – EQE and J-V curves of a CZTSSe/CdS-based device with a 50 nm layer with a linearly reducing band gap and increasing electron affinity by a maximum of $0.35\ eV$.

Figure 4.13 shows the simulated EQE and $J-V$ curves for this device. At low photon energies, the EQE is higher, as the reduced band gap material can absorb photons with energies below the gap of the bulk CZTSSe material. At higher photon energies the EQE is similarly larger, due to the reduced interface recombination, caused by the reduction in the conduction band offset. This manifests as a short-circuit current density that is $6.2\ \mathrm{mA}$ greater than the layer without the interfacial layer, as can be seen in Table 4.9. The increase in J_{SC} results in an increase in the power conversion efficiency and the FF. In contrast, the open-circuit voltage is reduced to a value comparable with that of the CZTSSe record device[693].

	η (%)	V_{OC} (V)	J_{SC} (mA/cm^2)	FF (%)
CZTSSe with interfacial layer	4.5	0.47	19.1	49.9

Table 4.9 – The statistics of a CZTSSe/CdS-based device with a 50 nm layer with a linearly reducing band gap and increasing electron affinity by a maximum of $0.35\ eV$.

Hence, it appears that the reduced band gap of the CZTSSe close to the interface, is, at least partially responsible, for the improved efficiencies of real devices compared to those simulated here.

4.3 Summary and Discussion

This chapter described the determination of the band alignments of device-like stacks of ZnO/CdS/CZTSSe and ZnO/In_2S_3/CZTSSe to investigate the effect of changing the buffer layer. The results of the band alignments between the buffer and absorber layers are somewhat consistent with the results from the previous chapter, typically showing the

same sign for the band offsets, although the numerical values may be inconsistent. In the previous section the conduction band offset between In_2S_3 and the high-carbon CZTSSe was estimated to be 0.43 ± 0.14 eV, which is consistent with the CBO found in this chapter (0.39 ± 0.14 eV), suggesting that there any interface states are limited in number, as there is no evidence to suggest that the Fermi level is pinned in this system.

In contrast the band alignment determined for the CdS/CZTSSe interface was estimated to be -0.38 ± 0.05 eV from the Anderson electron affinity rule, whereas in this chapter it was found to be -0.68 ± 0.14 eV. Several possible explanations are considered for this disagreement: Firstly, it may be that there are considerably more interfacial states; secondly, there may be intermixing of the layers up to some depth, however this is not seen in the PES measurements; finally, there have been some reports of band gap narrowing at the CdS/CZTSSe interface, which may result in the band offsets being modified considerably.

Using the band offsets determined in this section, devices are modelled using the SCAPS software to investigate the effects of changing the buffer layer. Considerable improvements in the efficiency and external quantum efficiency are observed in the device with an In_2S_3 buffer layer, compared to that with a CdS layer, obtaining open-circuit voltages larger than both the record CZTSSe and CIGS achieved.

Simulations of alternate device structures using band offsets from the literature are also investigated to identify other potential window layers for these device structures. It is suggested that the CZTSSe interfacial layer has a reduced band gap and electron affinity compared to the bulk, due to band tailing, band narrowing and inter-diffusion of Cd. The reduced band gap can account for some of the increased efficiency of real CZTSSe/CdS devices, compared to the results of the simulations described here. In the next chapter, we will move away from the absorber/buffer and buffer/window interfaces, and instead investigate the back-contact of kesterite photovoltaics.

5 DEFECT ENGINEERING IN MOLYBDENUM DICHALCOGENIDES

The work in this chapter is partially based upon the work presented in the following book chapter:

Gibbon, J.T.; Dhanak, V. R. "Chapter 4. Properties of transition metal dichalcogenides", *Two dimensional transition metal dichalcogenides (2D TMD): Synthesis, Properties and Applications*, Ed. Sabari Arul, N.; Springer Nature Publisher, manuscript in print

The transition-metal dichalcogenides (TMDs) are materials of particular interest currently. Many of the TMDs exhibit layered crystal structures. Each successive layer is only bound to the layers above and below by Van der Waal's forces, allowing the layers to slide along one another. It is for this reason that graphite is used in pencils, and MoS_2 (a TMD) is used as a grease-free lubricant.

As the crystal structure is layered, it is possible to obtain only a few or even a single layer of these materials. The reduction in the number of layers can lead to the development of new properties, such as the band gap changing from an indirect to a direct gap, increased carrier mobility and enhanced excitons and trions[737], [738].

Numerous crystal structures have been reported for the 2D TMDs, including the 2H, 1T and the (distorted) 1T' structures. Such a range of crystal structures, inevitably results in many varied electronic phases. For the group VI TMDs (MX_2, M=Mo, W), the 2H phase is the lowest energy state[739], [740] and corresponds to semiconducting behaviour[739], [741]. In contrast, the 1T structure is a metastable state for the group VI TMDs[740], corresponding to a metallic state[739], [741], [742]. The optical and structural properties of the semiconducting 2H-MoX_2 TMDs are presented in Table 5.1.

	***a* (Å)**	***c* (Å)**	**Bulk E_g (eV)**	**Direct E_g (eV)**	**1L E_g (eV)**
MoS_2	3.160[743]	12.294[743]	1.29[743]	1.78[743]	1.9[744]
$MoSe_2$	3.299[743]	12.938[743]	1.10[743]	1.42[743]	1.55[745]
$MoTe_2$	3.522[743]	13.968[743]	1.00[743]	1.10[743]	1.10[746]

Table 5.1 - A summary of the structural and electronic properties of the molybdenum dichalcogenides in the 2H structure.

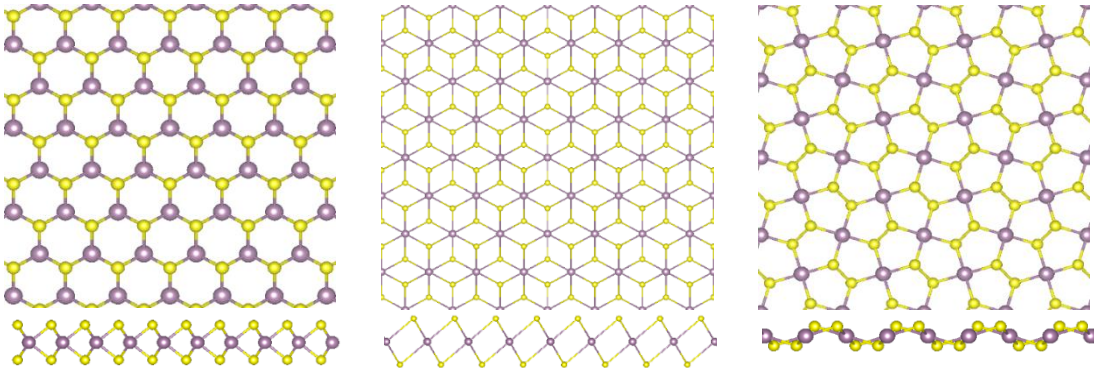

Figure 5.1 – Common crystal structures of the TMDs. Metal atoms are purple, chalcogen atoms are in yellow. Left shows the top and side views of the 2H structure[752]*. Centre shows the top and side views of the 1T structure*[753]*. Right shows the PdX_2 type structure*[748]*. This structure is unusual as it is pentagonal as can be seen in the top view. In the side view, it is clear that the structure follows a puckered-type structure.*

In the case of the Pd-based TMDs, the unit cell of the bulk material is orthorhombic[747], [748], with neighbouring sheets bonded *via* van der Waals forces. Recent density functional theory (DFT) results suggest that the most stable phase of PdS_2 has the corresponding 2D rectangular unit cell, with a pentagonal configuration of atoms[749], similar results have been shown experimentally for $PdSe_2$[750]. Experimental verification of the properties of monolayer PdX_2 is rendered difficult as competing Pd_2X_3 phases are frequently formed upon exfoliation[751]. Top and side views of the 2H, 1T and PdX_2 structures are presented in Figure 5.1. The crystallographic information presented in Figure 5.1 was obtained from [752] for the 2H structure, [753] for the 1T structure and [748] for PdX_2 type structure. A final phase of note is the Haeckelite phase predicted for numerous TMDs. In the case of the group VI TMD monolayers, the Haeckelite phases exhibit semi-metallic behaviour, whilst for group V TMD monolayers, a band gap opens resulting in semiconducting behaviour[754].

Generally, the semiconducting group 6 TMDs, MX_2 (M=Mo, W) have an indirect band gap when in the bulk phase. As the number of layers is reduced, there exists a point at which the band gap transitions from an indirect to a direct gap. The transition of the band gap has been studied theoretically and experimentally in the archetypal TMD, MoS_2, by DFT[755], [756] and angle-resolved photoelectron spectroscopy (ARPES)[757] respectively. Early experimental evidence of the transition from an indirect to a direct gap came from observing the increased photoluminescence yield, as the number of layers decreased[744], [758]. Direct observation of the changing value of the band gap with the number of layers has also been made by spatially-resolved optical absorption spectroscopy of MoS_2 flakes[759].

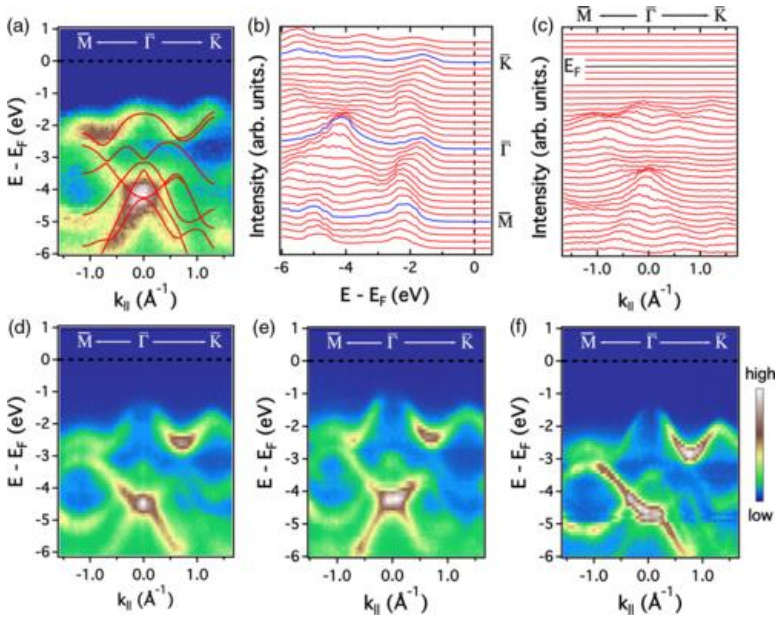

Figure 5.2 – ARPES valence band structure of MoS2 for varying numbers of layers. (a) Monolayer MoS2 ARPES valence band spectra, overlaid with DFT calculated band structure. (b) and (c) are the corresponding energy and momentum distribution curves respectively. (d)-(f) ARPES band structure of bilayer, trilayer and bulk-like MoS2. Reprinted figure with permission from REF [757] *Copyright 2013 by the American Physical Society.*

Figure 5.2 shows the ARPES band structure for monolayer, bilayer, trilayer and bulk-like MoS_2. For the bulk-like MoS_2 layer, the valence band maximum is at $\bar{\Gamma}$, whilst the conduction band minimum is known to be at $\bar{K}$. As the number of layers is reduced, the states at $\bar{K}$, move upwards in energy towards the VBM at $\bar{\Gamma}$, and finally move above the states at $\bar{\Gamma}$ when the MoS_2 is monolayer in nature. The evolution of the band structure in this way is explained by considering the quantum confinement of the electrons at $\bar{K}$ and $\bar{\Gamma}$. The electrons at $\bar{K}$, are derived from in-plane Mo $d_{x^2-y^2}/d_{xy}$ orbitals, which are unaffected by the confinement in the z-direction[757]. In contrast, the states at $\bar{\Gamma}$, are derived from Mo d_{z^2} and S p_z contributions[757]. As the number of layers is reduced, the interplane contributions at $\bar{\Gamma}$, are necessarily, reduced. Thus, the energy of the VBM at $\bar{\Gamma}$, is reduced relative to $\bar{K}$ as the number of layers is reduced. Similar behaviour is predicted for many other TMDs including $MoSe_2$, $MoTe_2$ and the tungsten dichalcogenides[755], [756] and has been confirmed experimentally in $MoSe_2$[745], WS_2[760] and WSe_2[760]. Similar behaviour has been seen for $MoTe_2$[761], however verification of this behaviour in WTe_2 has been complicated by the existence of a thermodynamically-preferred type II Weyl semi-metallic phase[762], [763]. As the increasing band gap with reduced layer number is due to the reduced interactions between neighbouring atomic layers, it is likely that this behaviour, in fact, holds for all of the semiconducting 2D TMDs in the 2H crystal structure.

Figure 5.3(a) and (b) shows the photo-luminescent behaviour of monolayers, bilayers and multilayers of WS_2 and WSe_2, after normalisation[760]. In the multilayer regime, a small feature is seen due to photoluminescence cross the direct gap (A), with a larger feature occurring for the indirect gap (I). Also present are hot electron peaks A' and B, corresponding to direct transitions from excited states in the conduction band. As the layer number is reduced, the indirect PL peak moves to higher energy (i.e. lower wavelength), indicating the increasing band gap, whilst the direct gap does not change[760]. The direct PL peak also becomes more intense with decreasing layer number[760] as can be seen in Figure 5.3(c) and (d), which show the relative PL quantum yield. Similar behaviour is observed in the other group VI TMDs[744], [758].

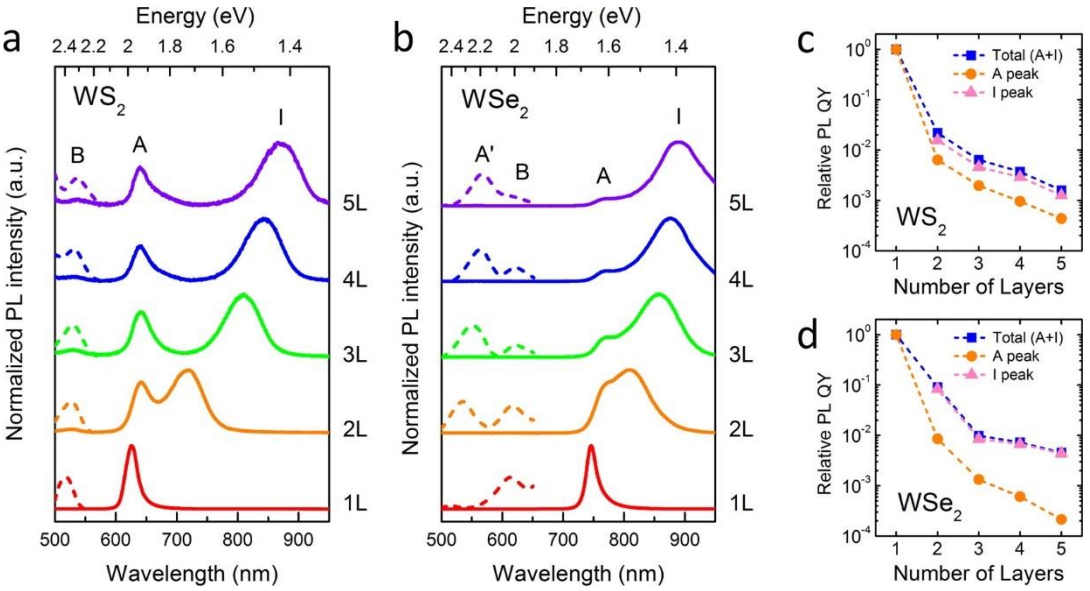

Figure 5.3 – (a) and (b) show the normalised photoluminescence of WS_2 and WSe_2 layers respectively. (c) and (d) show the relative photoluminescence quantum yield as a function of layer number for the direct and indirect transition of the WS_2 and WSe_2 respectively. Reprinted with permission from REF [760]*. Copyright 2012 American Chemical Society.*

The molybdenum dichalcogenides, MoX_2 (X= S, Se, Te) are also of interest in photovoltaics, as molybdenum is often used as the back contact for thin film technologies, particularly in CIGS and CZTSSe devices. In the case of CZTSSe, it is sometimes considered to be one of the causes of the reduced efficiencies of CZTSSe, compared to CIGS[207], [208]. Hence, understanding the electronic properties of these dichalcogenides is important for increasing the efficiencies. However experiments to understand the electronic properties, and in particular the effects of defects on the electronic properties are limited, with only MoS_2 having been studied in detail[546], [764]. Engineering defects in the TMDs is known to affect the barrier properties in Schottky diode-like devices [765]–[768] and has, in some cases, been studied by theoretical methods and STM.

Monolayer MoS_2 has also been used as part of photovoltaic device in its own right, as part of a hot-carrier solar cell[176].

$MoTe_2$ is also of interest for CdTe photovoltaics, where Mo is sometimes used in place of Cu as the back contact. Without an intermediate layer, some intermixing is likely at the interface between the Mo and CdTe layers, resulting in a thin $MoTe_2$ layer at the interface[769]–[774]. In some cases, a $MoTe_2$ layer is deliberately inserted between the two layers.

As outlined above, defects also play a key role in determining the electronic properties of the TMDs. MoS_2 has been shown to exhibit both *n*-type[775]–[778] and *p*-type behaviour[546], [778]–[781]. Different conductivity behaviours have, in fact, be observed within the same sample, over the scale of nanometres and appear to be heavily dependent on the local defect density[765], as can be seen in Figure 5.4.

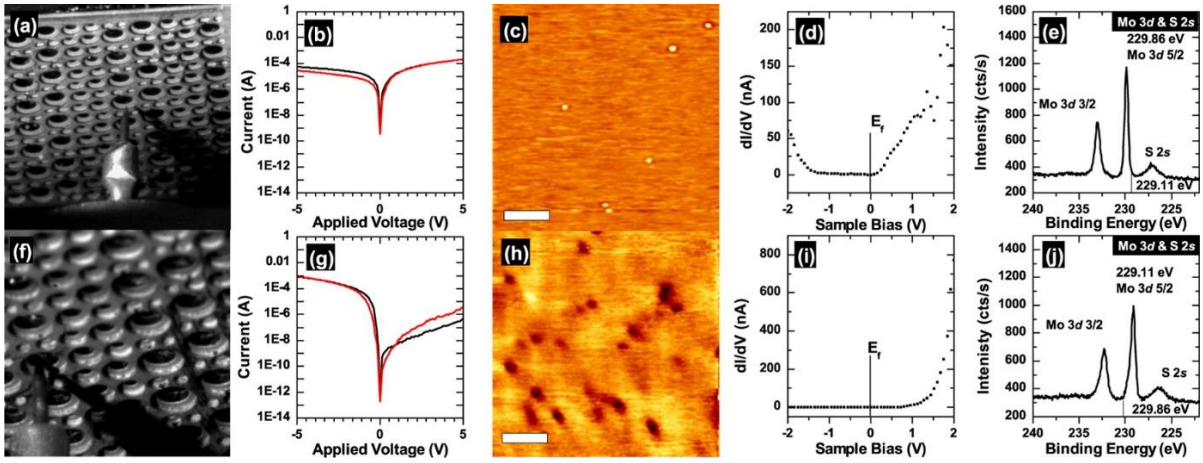

Figure 5.4 – Correlated I-V characteristics of MoS_2 crystals with STM, STS and XPS (a) STM tip position above an aperture in a shadow mask. (b) I-V characteristics of the MoS_2 crystal measured from a particular aperture, indicative of n-type behaviour. Measurements shown in (c)-(f) were made on the same aperture as (b). (c) STM image showing light and dark defects. (d) STS from the aperture used for (b), showing the Fermi-level close to the conduction band, indicating n-type behaviour. (e) XPS spectrum of the Mo 3d and S 2s core-levels, consistent with n-type MoS_2. (f) shows a different aperture in the shadow mask (g) I-V characteristics from the second aperture. The asymmetry on the positive voltage side is indicative of p-type behaviour. (h)-(j) were measured from the same aperture. (h) STM image showing a high concentration of dark defects (i) STS results showing that the Fermi-level is much further away from the conduction band than for (d), suggesting p-type behaviour (j) XPS spectrum of the Mo 3d and S 2s regions. The shift in the core-levels relative to those in (e) is indicative of p-type behaviour. Reprinted with permission from REF [765]*, Copyright 2014 American Chemical Society.*

The presence of defects, has also been shown to significantly affect the height of the Schottky barrier between the TMDs and metallic contacts[766], [768], [782]. Considerations of the defects in TMDs are therefore critical for applications in electronic devices. It is reasonable to assume that this behaviour will likely extend to further TMDs, and in fact, both *n*-type and *p*-type conductivity have also been demonstrated in other TMDs[783]–[785].

In both WSe_2 and MoS_2 single crystals, irradiation with Ar^+ results in chalcogen vacancies and cause the Fermi level of the crystal to move towards the valence band edge[768], [786], suggesting that the crystal surface becomes more *s*-type in nature, or alternatively that the bands are bent upwards by the surface defects. In contrast, when polycrystalline films or naturally-occurring molybdenite are etched in the same manner, chalcogen vacancies are still produced, but the Fermi level of the sample is not observed to change, presumably due to pinning of the Fermi level by surface defects[546], [786], [787].

In the work of Santoni *et al*.[546] polycrystalline thin-films of MoS_2, formed by the sulfurization of Mo films on glass, are exposed to Ar^+ ion irradiation with increasing ion dosage and the changes in the chemical and electronic structures are observed using XPS and IPES. The XPS spectra of the Mo 3d regions are shown in Figure 5.5. In this work, it is found that the surface region can become heavily depleted of sulphur, with the Mo 3d component due to the MoS_2 having much less area than the area of the metallic Mo^0 species, i.e. the metal: sulphide ratio reaches a value of greater than 1.5:1. An equilibrium state is found to occur at $2.49 \times 10^{17}\ \mathrm{ions/cm^2}$.

Although not expected to natively exhibit magnetic properties, ferromagnetism is exhibited in both bulk, nanosheet and exfoliated MoS_2 and WS_2[788]–[790]. Theoretical models based on MoS_2 nanoribbons suggest that these are due to the presence of zigzag edges, which are (half-)metallic, which have a non-zero magnetic moment, in contrast to armchair edges, which are semiconducting and non-magnetic[791]–[794]. The zigzag edges are more chemically stable and are energetically favourable and hence would be expected at the edges of crystals and atomic-scale layers[789], [791], [794], [795]. An example of this ferromagnetic behaviour can be seen in Figure 5.6.

In nanosheets and exfoliated MoS_2 and WS_2, the layers exhibiting ferromagnetism are found to have a high density of point defects[788], [790]. Theoretical modelling, suggests that molybdenum and sulphur vacancies can both produce magnetic moments comparable to μ_B[788], [793], [795]. An alternative explanation is that wrinkles are observed by TEM in exfoliated samples[790], which has also been seen in ferromagnetic $ReSe_2$ nanosheets[796]. Finally, unsaturated bonds at the edges of the sample may be responsible[788]. Intriguingly, the Curie temperature observed for nanosheet MoS_2 is 685K, higher than that of other dilute magnetic semiconductors[788].

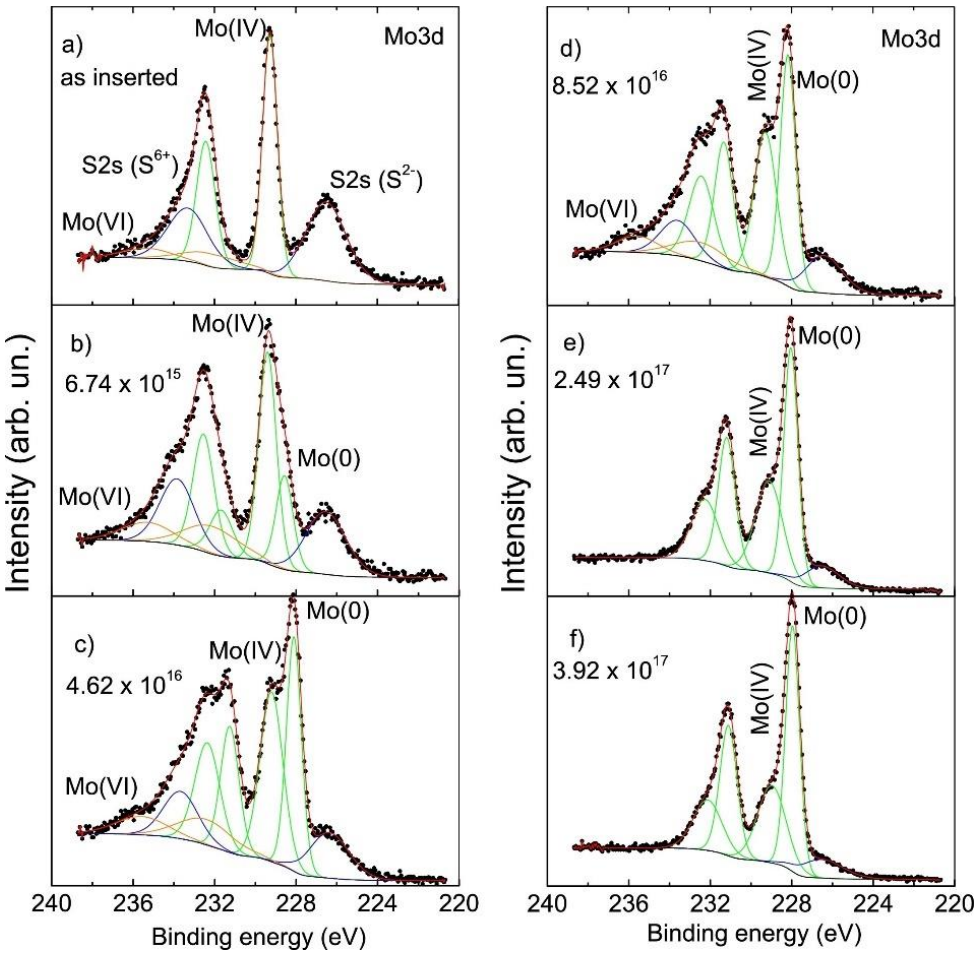

Figure 5.5 – Mo 3d X-ray photoelectron spectra from polycrystalline MoS_2 thin-films grown on glass at increasing Ar^+ ion doses. Ion doses are indicated on the graphs, in units of ions/cm^2. Reprinted from REF[546] *Copyright 2017, with permission from Elsevier*

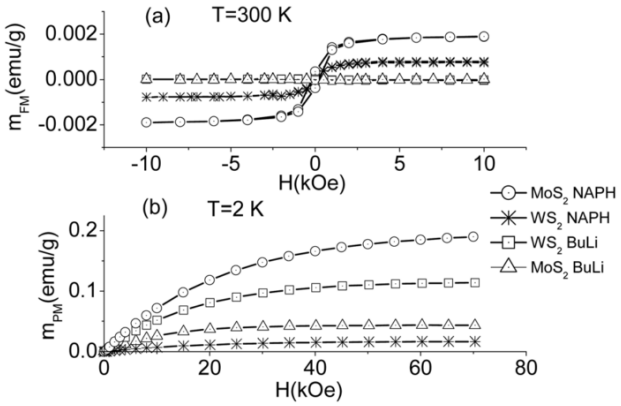

Figure 5.6 – (a) shows the ferromagnetic hysteresis loops of monolayers of MoS_2 and WS_2 exfoliated by two different chemical methods, measured at room temperature. (b) shows the magnetisation curves for the same samples measured at 2 K. Figure reprinted from REF [790]*, Published by The Royal Society of Chemistry, under a Creative Commons Attribution 3.0 Unported Licence*

An alternative approach to inducing magnetism in the 2D-TMDs is to introduce magnetic defects by doping the material with metals[797]–[800] or other elements, introducing defects[801], [802], applying strain[801]–[803] or irradiation by charged particles[804].

This chapter will describe the deliberate engineering of vacancies into commercially grown MoS_2, $MoSe_2$, and $MoTe_2$ single crystals by Ar^+ ion etching as previously described in section 2.2.1 and consider the effects of these defects on the chemical and electronic structures.

5.1 MoS_2

MoS_2 is the archetypal TMD material and is by far the most-studied of this class of material. Angle-resolved photoemission spectroscopy (ARPES) has been used to directly observe the changing nature of the band gap, from indirect for bulk and multilayer films, to a direct gap at the *K*-point for a monolayer[757]. For bulk and multilayer films, the VBM is found to occur at the *Γ*-point, whereas the CBM is at the *K*-point. However, once the film only consists of a monolayer, the VBM also occurs at the *K*-point, thus rendering the monolayer a direct gap material, verifying previous theoretical predictions of such properties[755], [756]. The same theoretical studies also predicted the same indirect-direct transition for $MoSe_2$[755], [756], $MoTe_2$ and the Tungsten dichalcogenides WS_2, WSe_2 and WTe_2. These predictions have been verified for $MoSe_2$[745], WS_2[760], WSe_2[760] and partially verified for $MoTe_2$[761]. Experimental verification for WTe_2 is hindered by the existence of a thermodynamically-preferable type II Weyl semi-metal phase[762], [763].

A 10 mm x 10 mm multilayer was mechanically exfoliated from a bulk 2H-MoS_2 single crystal (2-D Semiconductors, Scottsdale, AZ, USA) with double sided carbon tape and mounted upon an Omicron-style sample plate. To confirm that the bulk material in nature, XRD measurements were performed. The resulting diffractograms can be seen in Figure 5.7, alongside the calculated powder diffraction pattern[805], [806]. Only even reflections of the (001) lattice plane are observed due to the symmetry of the hexagonal crystal structure of the material. The absence of other peaks confirms the crystal to be monocrystalline in nature.

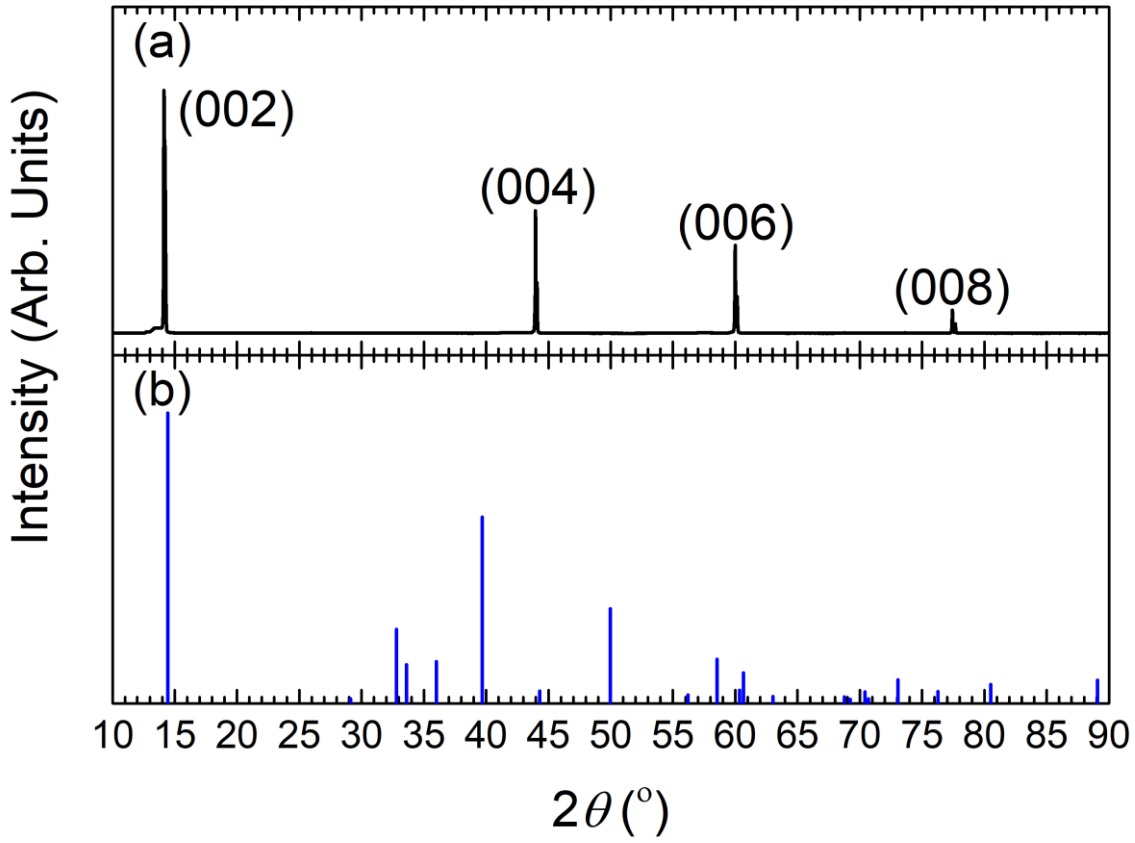

Figure 5.7 – An X-ray diffractogram of the MoS_2 single crystal. (a) shows the diffractogram of the single-crystal, whilst (b) shows the calculated powder diffractogram of the material[805], [806].

As the number of layers in MoS_2 multilayers is strongly correlated with the band gap, as shown in Table 5.2, we can use the band gap to estimate the number of layers in the material. Figure 5.8 shows combined valence band XPS and IPES measurements, allowing for the determination of the band gap, which is found to be 1.53±0.14 eV. This band gap is consistent with between 2 and 4 layers of MoS_2, as can be seen in Table 5.2.

Number of Layers	Band Gap (eV)	Direct/Indirect
1	1.90[744], 1.82[807], 2.22[808]	Direct
2	1.60[744], 1.53[807], 1.70[808]	Indirect
3	1.45[744], 1.57[808]	Indirect
4	1.40[744], 1.52[808]	Indirect
5	1.38[744], 1.50[808]	Indirect
6	1.35[744], 1.48[808]	Indirect
Bulk	1.29[744], 1.44[808]	Indirect

Table 5.2 – The relationship between the number of layers in an MoS_2 multilayer, and the band gap.

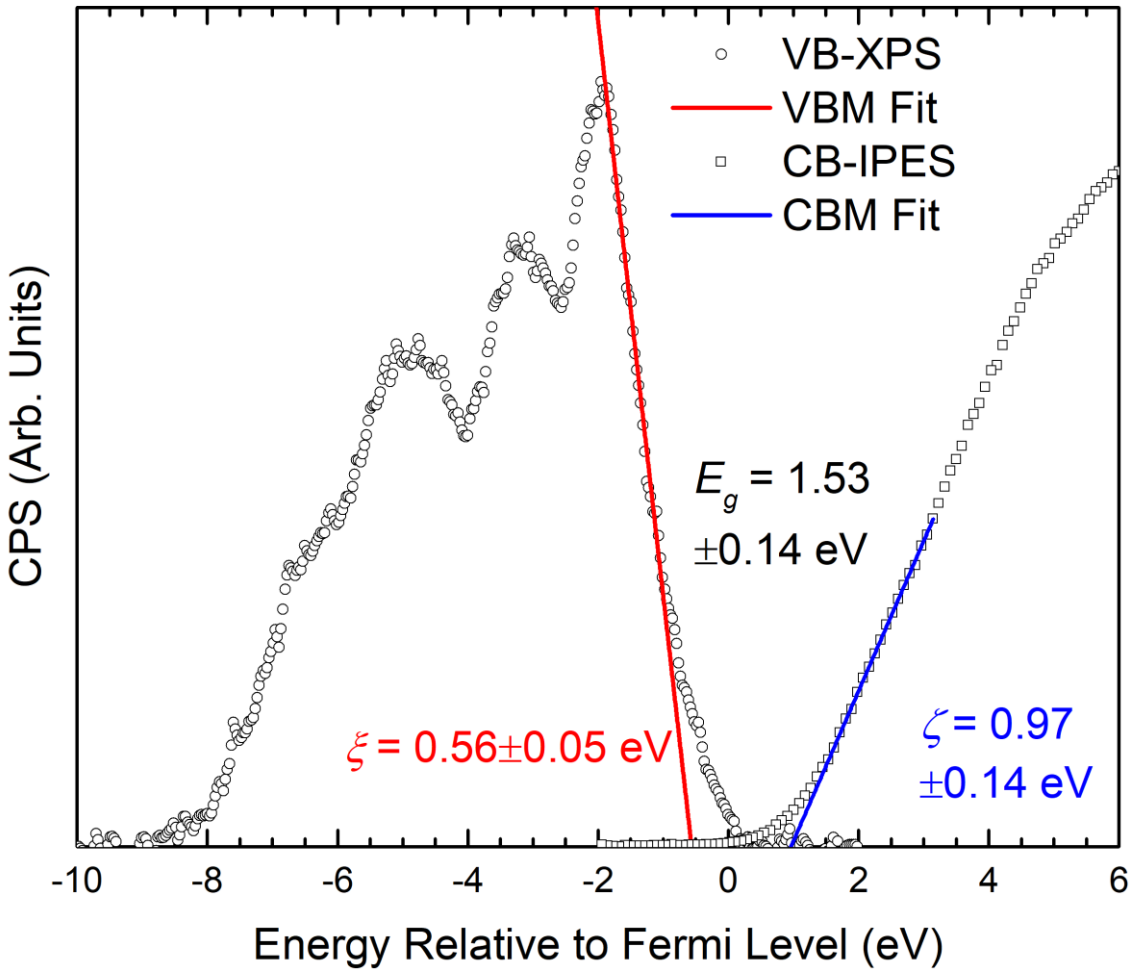

Figure 5.8 – Combined VB-XPS and IPES to obtain the band gap of the exfoliated MoS_2 layer.

Figure 5.9 shows the XPS spectra prior to and after Ar^+ ion bombardment, (a) and (b) show the Mo 3d and S 2p core-levels respectively. In both spectra, there is an extra doublet which can be assigned to surface contamination. The binding energy of the Mo $3d_{5/2}$ component due to the surface contamination occurs at 229.63±0.05 eV, consistent with the binding energy of molybdenum dioxide, MoO_2, rather than the more stable trioxide, MoO_3, which occurs at an approximate binding energy of 232.75 eV. This is likely due to the trioxide requiring a change in oxidation state of the molybdenum, whereas the dioxide results in the same formal oxidation state as the disulphide. A similar phenomenon is seen in the layered SnS and SnS_2 compounds, where native oxide on SnS occurs as SnO, rather than the more stable SnO_2[165]. Alternatively, it may be that the MoS_2 sample had insufficient time to oxidise fully, because the sample was exfoliated and transferred into the vacuum chamber within minutes. This seems probable, as most other reports of the native oxide on MoS_2 find a Mo^{6+} oxidation state, corresponding to MoO_3[546], [619], [809]–[816], in contrast to the results here. A second doublet also appears in the S 2p spectrum, at a separation of 0.60 eV on the higher binding energy side of the peaks due to

stoichiometric MoS_2. This does not correspond to a molybdenum sulphate ($MoSO_4$), as the binding energy of the sulphate occurs at a much higher binding energy of around 168.80 eV[810].

The multilayers reach an equilibrium state at considerably lower dosages ($6.0 \times 10^{15}\,\mathrm{ions/cm^2}$) than in the work of Santoni *et al*.[546] and have a much smaller metal: sulphide ratio (0.74:1) than reported elsewhere, as can be seen by comparing Figure 5.5(f) and Figure 5.9(e). This is likely due to the reduced dimensionality of the multilayer system, as in bulk-like systems, both preferential sputtering and ion implantation can occur. Implantation of lighter ions from the surface region into the bulk is known to occur, even at low ion energies. This is known as recoil implantation[492], [817]–[820]. Clearly this process cannot happen in a multilayer system such as that investigated, due to the reduced dimensionality of the system, as such this may explain the different ratio at which the steady state occurs. Similarly, the reduced dimensionality is likely the reason for the equilibrium state occurring at reduced dosage in the case of MoS_2 multilayers.

Table 5.3 shows the binding energies of the features shown in Figure 5.9. The binding energy position of the low ion-dose sample is consistent with the exfoliated layers being p-type in nature[821][546], [765]. With increasing ion dose, the binding energies of the core-levels due to the stoichiometric MoS_2 are shifted to lower binding energy by 0.10±0.05 eV. In contrast, metallic Mo^0 species starts at 0.70 eV below the MoS_2 peak but moves to be approximately 0.90 eV below the stoichiometric species. This is consistent with Santoni *et al*[546], who found that the metallic species was initially 0.70 eV below the MoS_2 species, before moving to approximately 1.00 eV below the MoS_2 species once the sample was equilibrated.

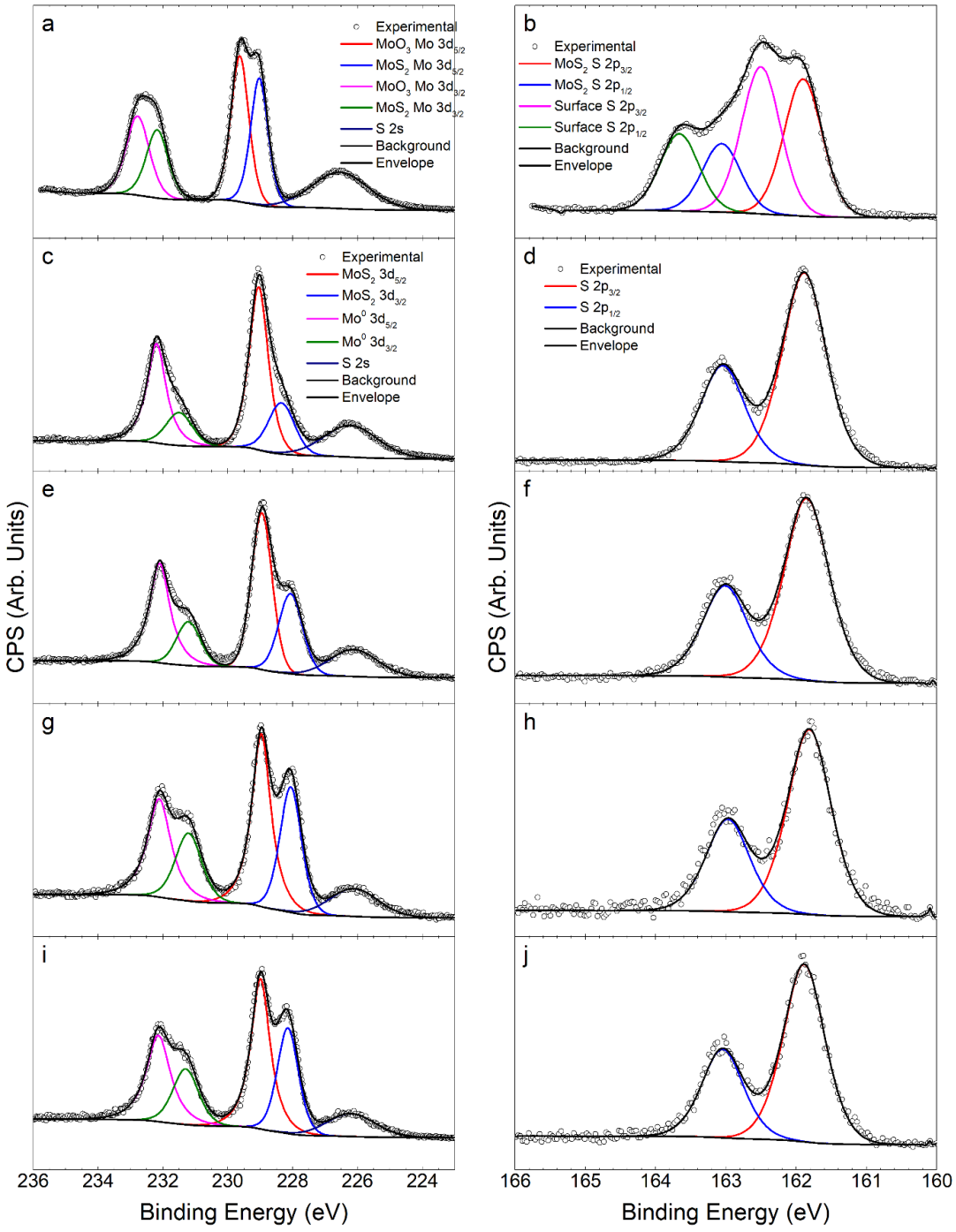

Figure 5.9 – XPS spectra of MoS_2 multilayers after Ar^+ ion etching. (a) and (b) show the Mo 3d and S 2p regions prior to any etching. (c) and (d), (e) and (f), (g) and (h) and (i) and (j) shows the same regions after 1 minute, 5 mins, 10 mins and 15 mins of ion exposure respectively.

An alternative explanation for what is labelled the metallic species here, is that it, in fact, corresponds to the 1T, rather than the 2H crystal structure of MoS_2, following the work of Zhu *et al*.[822], in which a 2H-MoS_2 sample is bombarded with Ar^+ ions in a plasma of 'certain kinetic energies'[822]. Unfortunately, the authors did not disclose what value these 'certain kinetic energies' claiming only that the kinetic energy of the Ar ions was 'well below the level that etching… could occur'[822]. The presence of the 1T phase, would also

explain the presence of the Fermi-edge that can be seen in Figure 5.10, as the 1T phase is metallic rather than semiconducting.

Dose Time (mins)	**Ion Dose (ions/cm^2)**	**Binding Energy (eV)**					**Mo^0/MoS$_2$**
		MoS$_2$ 3d$_{5/2}$	Mo^0 3d$_{5/2}$	S 2p$_{3/2}$	SEC	VBM, ξ	
0	0	229.03	-	161.90			-
1	6x10^{14}	229.05	228.35	161.88	1482.63	0.56	0.40
5	3x10^{15}	228.95	228.06	16.85			0.59
10	6x10^{15}	228.97	228.05	161.81	1482.02	0.24	0.74
15	9x10^{15}	228.99	228.06	161.89			0.78

Table 5.3 – A summary of the binding energies of features shown in Figure 5.9 and Figure 5.10. Also given is the area ratio of the metallic Mo^0 species to that of the MoS$_2$ species.

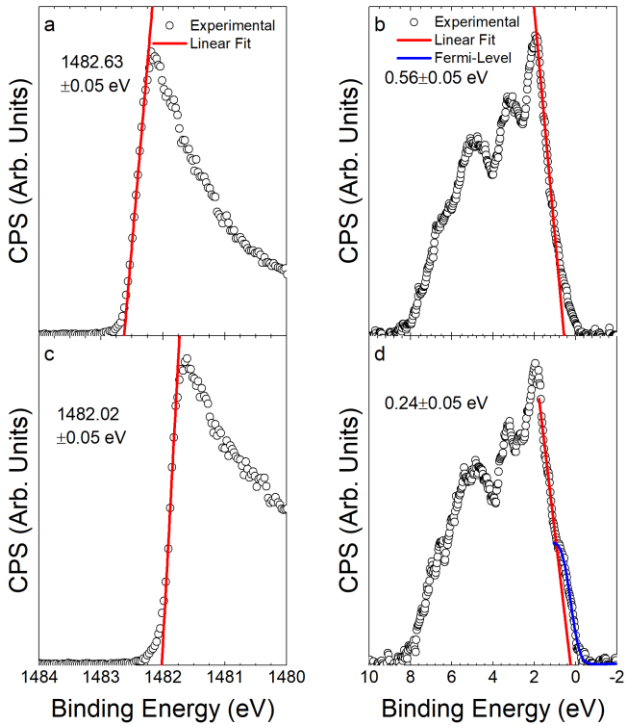

Figure 5.10 – PES Spectra of the dosed MoS$_2$ multilayers. (a) and (b) show the secondary electron cut-off and valence band respectively after 1 min exposure to Ar$^+$ ions. (c) and (d) show the same regions after 10 mins exposure.

Figure 5.10 (b) and (d) shows the valence bands of the dosed material. At low ion dose, the valence band maximum occurs 0.56 ± 0.05 eV from the Fermi level. With increasing ion dose, the valence band maximum approaches the Fermi level, until a steady state is reached, at which point the valence band maximum is only 0.24 ± 0.05 eV away from the Fermi level. Intriguingly, there is little variation in the relative intensities of the features in

the valence band, suggesting that at the photon energy used ($\hbar\omega = 1486.6$ eV), the valence band is dominated by Mo states. Also present in (b) and (d) are intensities at the Fermi level. This is likely due to the presence of the metallic Mo^0 states but may be due to the presence of 1T-MoS_2 as described above. Also, of interest is the secondary electron cut-off, which moves to approximately 0.61 ± 0.05 eV lower binding energy. This is of interest as the ionisation potential is given by the relation $V_{IP} = \hbar\omega - (SEC - \xi)$, thus as the relative shifts of the VBM and the SEC differ, there appears to be some tunability in the ionisation potential and electron affinity of the material.

5.2 $MoSe_2$

An 8 mm x 5 mm single-crystal flake of $MoSe_2$ (2-D Semiconductors, Scottsdale, AZ, USA) was mounted upon an Omicron-style sample plate using double sided carbon tape. To confirm the monocrystalline nature of the sample, x-ray diffraction was performed prior to mounting the sample on the sample plate. The resulting diffractogram is shown in Figure 5.11, alongside the simulated powder diffraction pattern. The simulated powder diffraction pattern was generated using the ReciprOgraph software[823] using a crystallographic information file (entry 2310945, produced from the work of James and Lavik[824]) from the crystallography open database[825]–[829]. As only even indexed reflections of the (001) lattice plane are observed, the crystal can be confirmed as monocrystalline in nature, as expected.

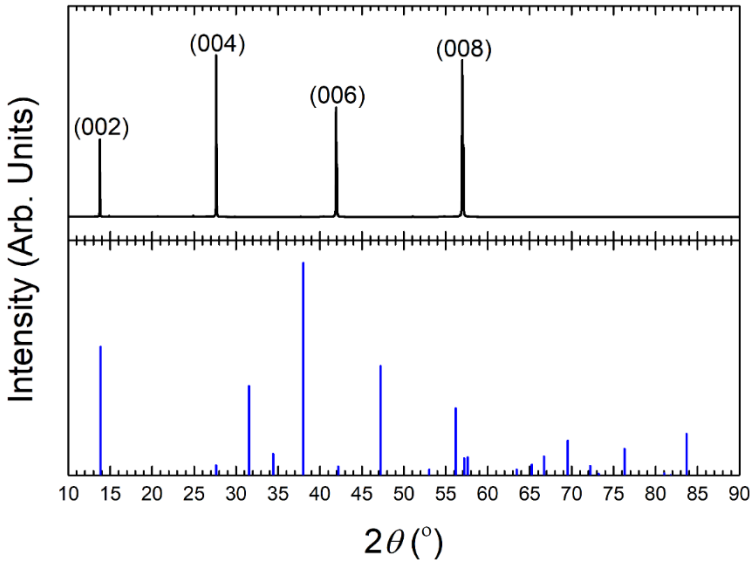

Figure 5.11 – X-ray diffractogram of a $MoSe_2$ single crystal, compared with the simulated powder diffraction pattern.

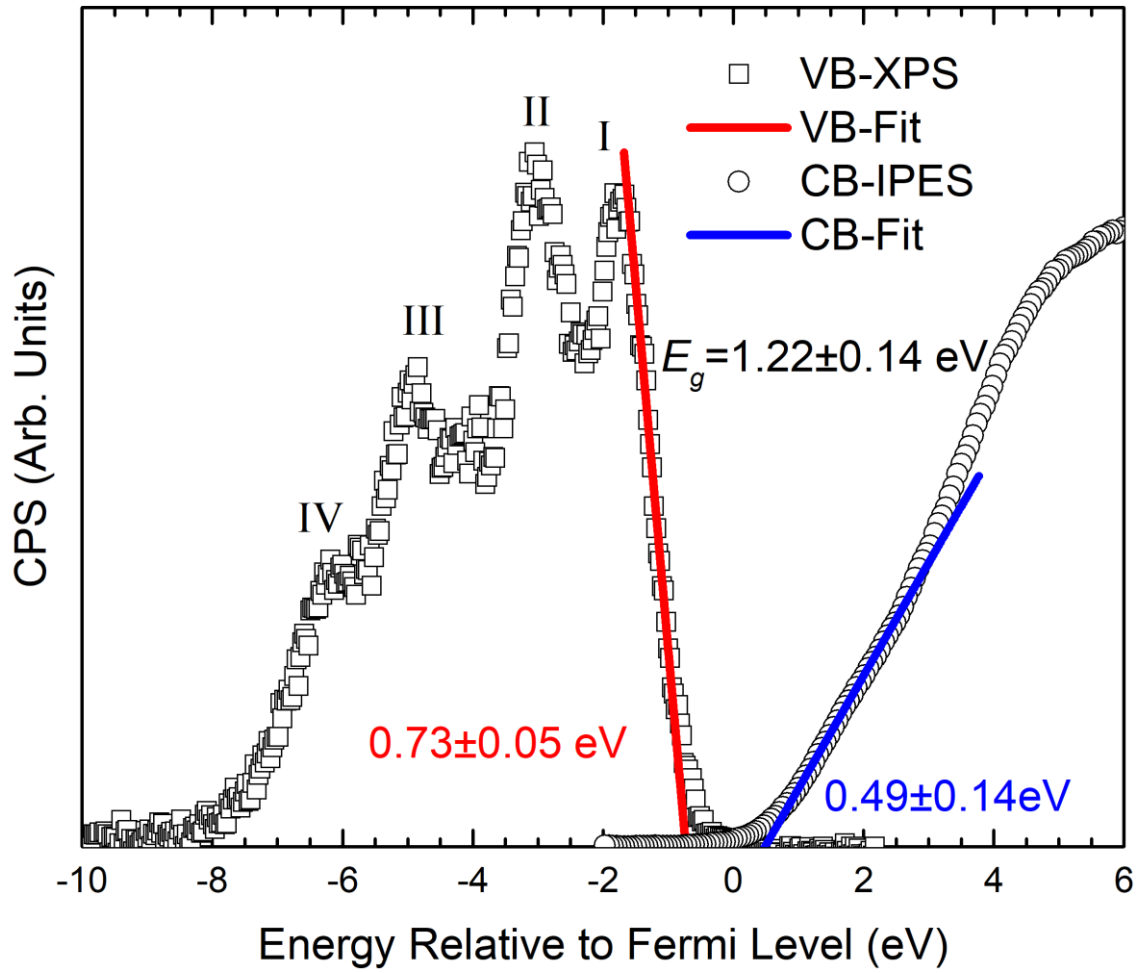

Figure 5.12 – PES Spectra of the $MoSe_2$ single crystal. VB-XPS and IPES are used to determine the band gap of the sample, which is found to be $E_g = 1.22 \pm 0.14\ eV$.

Figure 5.12 shows the VB-XPS and IPES spectra of the MoS_2 single crystal, prior to exposure to the Ar^+ ions. By way of linear extrapolation of the band edges, the band gap is found to be 1.22 ± 0.14 eV, consistent with the bulk band gap of $MoSe_2$[743] as would be expected. The position of the valence band is consistent with native *n*-type doping of the crystal.

The valence band consists of 4 major features labelled I-IV. By comparing the valence band structure in Figure 5.12 with the orbital-resolved densities of states produced by theorists, the nature of each feature can be determined. These 4 features correspond to the four valence bands predicted by Bromley *et al*.[830], who found that this four-valence band was shared with MoS_2 and $MoTe_2$, which can be seen in this work by comparing with Figure 5.8 and Figure 5.17 respectively. Bromley *et al*.[830] also predicted that the bands of $MoSe_2$ would be the narrowest, due to the similarities in the atomic energy levels. This is also observed here where the $MoSe_2$ features labelled I-IV are narrower and sharper than the equivalent features for MoS_2 and $MoTe_2$.

The origin of the features labelled I-IV is determined by comparison to the DFT partial density of states presented by Reshak *et al.* [831]. In each case, the features are found to be dominated by Mo *d*-states hybridised with Se *p*-states, however the contribution from each varies across the valence band. Feature I is predominantly Mo *d*-states with only a small contribution of Se *p*-states, whereas II and III are roughly equal mixes of Mo *d*- and Se *p*-states, whilst IV is mostly Se *p*-states with a smaller contribution from Mo *d*-states. A Se *s*-band is found at approximately 12 eV below the VBM, which is beyond the spectra measured here, however a very small contribution of Se *s*-like states is found throughout the rest of the valence band.

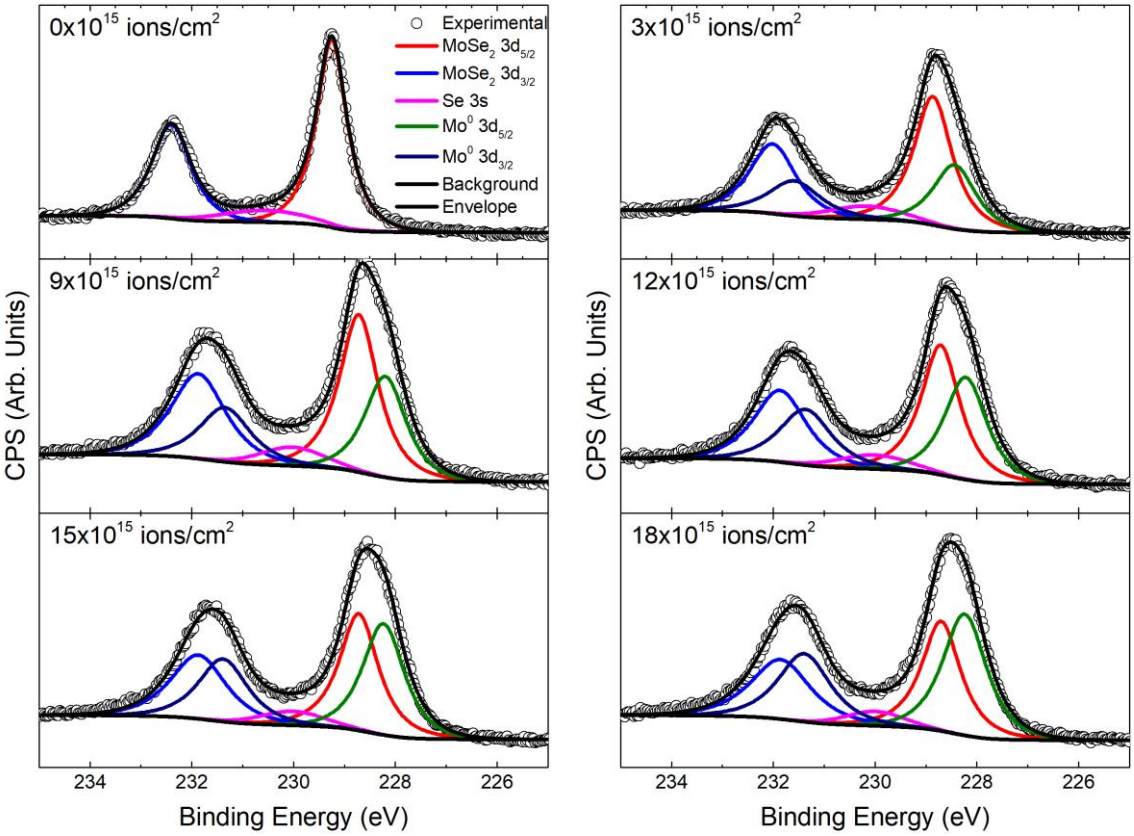

Figure 5.13– The Mo 3d core-levels for a $MoSe_2$ multilayer exposed to increasing Ar^+ ion doses. As the dosage increases, the area of the Mo^0 component increases up to a dosage of $18x10^{15}$ ions/cm^2, at which point a steady state is reached.

In contrast to MoS_2, $MoSe_2$ single crystals were found to require a considerably larger ion dose of 18×10^{15} ions cm^2 to reach a steady state. Figure 5.13 shows the Mo 3d core-levels for various ion dosages, the binding energies of which are presented in Table 5.4.

Figure 5.14 shows the Se 3d core-level under varying Ar^+ ion dosages. Similar to the Mo 3d core-level, the Se 3d moves to lower binding energy with increasing ion dose. Prior to ion exposure the FWHM of the Se 3d core-level was observed to be 0.75±0.05 eV, however

after ion dosing the surface, the FWHM increases to 0.92±0.05 eV, where it remained up to the maximum ion dosage. This is commonly observed in sputter-damaged material due to the loss of ordering.

Native oxides do not appear in the spectra of either the Mo 3d or Se 3d core-levels shown in Figure 5.13 and Figure 5.14, despite the material being stored and transported in ambient conditions, suggesting that $MoSe_2$ may be relatively immune to surface oxidation.

It should be noted that as these results are from a bulk single-crystal the sputtered atoms can be implanted into the bulk material, allowing for a larger Mo^0/MoX_2 ratio than was possible for the MoS_2 above. However, the final Mo^0/MoX_2 ratio is smaller than that obtained for bulk MoS_2 by Santoni *et al.*[546]. This is reasonable, as the atomic mass of Se is much closer to that of Mo, than the atomic mass of S is. As such, preferential sputtering processes are considerably less likely, resulting in a higher X/Mo ratio and hence a smaller $Mo^0/MoSe_2$ ratio.

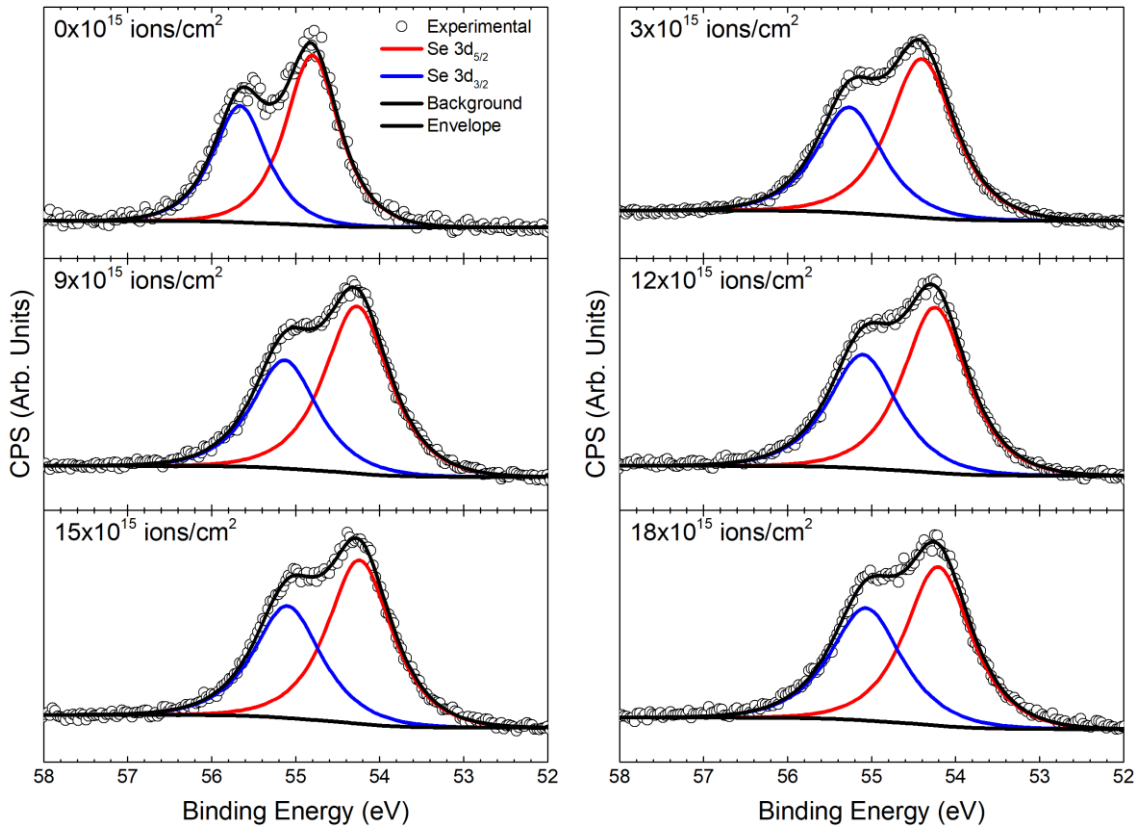

Figure 5.14 - XPS spectra of the Se 3d core-level under increasing Ar^+ ion dosages.

The binding energies presented in Table 5.4 are consistent with those of Abdallah *et al.*[832] both before and after Ar^+ ion etching. Similarly, the final Se/Mo ratio obtained is consistent with that found by Bernede[833].

Ion Dosage ($x10^{15}$ ions/cm^2)	Binding Energy (eV)				$Mo^0/MoSe_2$	Se/Mo
	$MoSe_2$ $3d_{5/2}$	Mo^0 $3d_{5/2}$	Se 3s	Se $3d_{5/2}$		
0	229.25	N/A	230.55	54.80	0.00	2.00
3	228.86	228.43	230.16	54.40	0.52	1.43
9	228.72	228.20	230.02	54.27	0.64	1.28
12	228.71	228.22	230.01	54.24	0.81	1.16
15	228.72	228.23	230.02	54.24	0.96	1.03
18	228.72	228.24	230.00	54.21	1.17	0.96

Table 5.4 – A summary of the binding energies of core-levels in the Ar^+ ion dosed $MoSe_2$ single crystal at different dosages. Also given is the ratio of the area of the metallic Mo^0 species to that of the $MoSe_2$ species and the Se/Mo ratio.

5.3 $MoTe_2$

To investigate the effects of Ar^+ ion-induced defects on $MoTe_2$, a bulk single-crystal of $MoTe_2$(HQ Graphene, Groningen, The Netherlands) was acquired. To confirm the monocrystalline nature of the bulk material, x-ray diffraction was performed, the resulting diagram is shown in Figure 5.15, alongside the synthetic powder diffraction pattern for comparison. The powder diffraction pattern was simulated in a manner similar to that of the $MoSe_2$ pattern in Figure 5.11. Here, the crystallographic information file of entry 9009147 in the Crystallography Open Database[825]–[829], created from data originally published by Wyckhoff[834], was used with the ReciprOgraph software[823] to simulate the powder diffraction pattern.

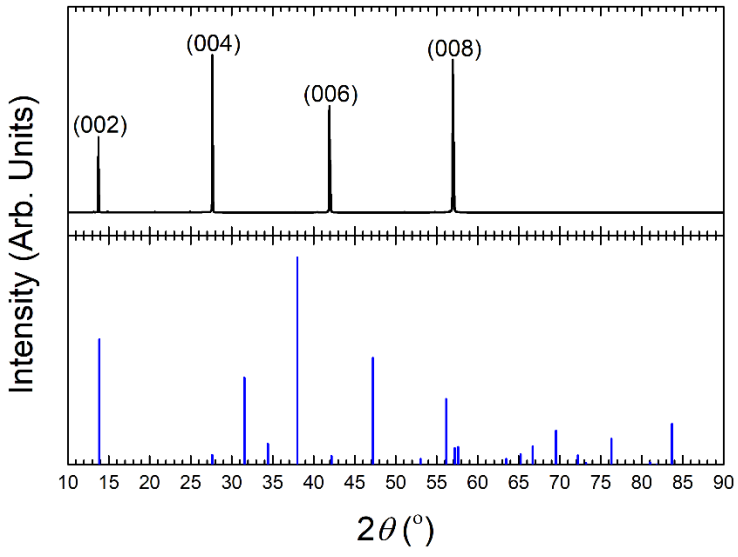

Figure 5.15 – The X-ray diffractogram obtained from a $MoTe_2$ bulk single crystal, alongside a simulated powder diffraction pattern for comparison.

Multilayers were then mechanically exfoliated from the bulk $MoTe_2$ single crystal using double sided carbon tape and entered into the fast-entry lock of the vacuum system. Photoemission spectra were measured prior to exposure to the Ar^+ ions, the results of which are shown in Figure 5.16. Figure 5.16(a) shows the Mo 3d core-level which is fitted with a single, spin-orbit split doublet. The Mo $3d_{5/2}$ is found to occur at a binding energy of 228.31 ± 0.05 eV. Figure 5.16(b) shows the Te 3d region, which is similarly fitted with only a single, spin-orbit split doublet. The Te $3d_{5/2}$ is found to have a binding energy of 572.92 ± 0.05 eV. Both the Mo $3d_{5/2}$ and Te $3d_{5/2}$ core-level binding energies are consistent with values previously reported for bulk crystalline and CVD thin films of $MoTe_2$[835], and comparable to those obtained by Bernède *et al*. for thin-films and a single crystal[771]. The absence of extra components on the high binding energy side indicates that there is no oxidation of the surface, likely due to the short duration of time during which the exfoliated $MoTe_2$ layers were exposed to air. The binding energies obtained from Figure 5.15 are tabulated in Table 5.5.

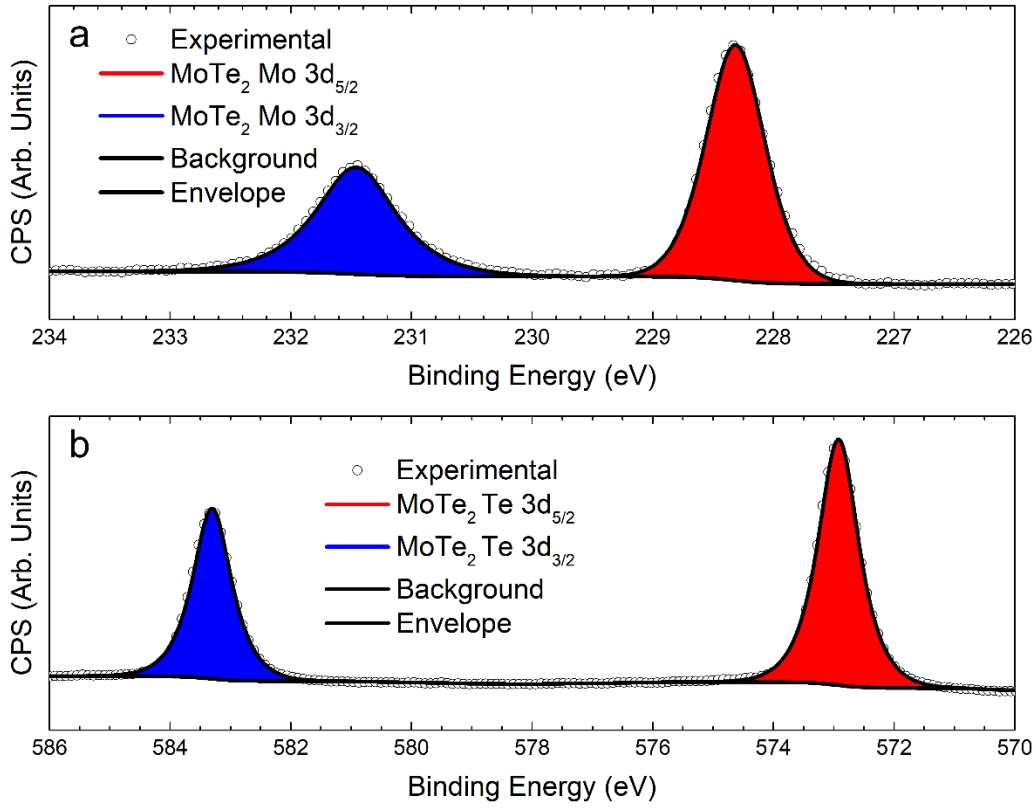

Figure 5.16 – PES spectra of the freshly exfoliated $MoTe_2$ sample. (a) shows the Mo 3d core-level whilst (b) shows the Te 3d core-level.

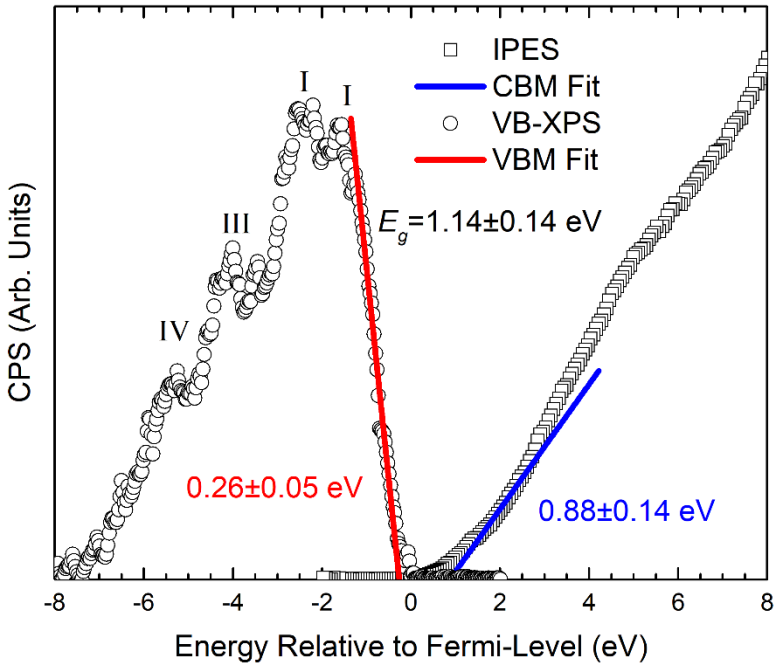

Figure 5.17 – Combined VB-XPS and IPES spectra of the exfoliated $MoTe_2$ layers. By linear extrapolation of the band edges, the band gap is found to be $E_g = 1.14 \pm 0.14\ eV$.

To determine the band gap of the $MoTe_2$ multilayers, VB-XPS and IPES were used to find the energy positions of the band edges, as can be seen in Figure 5.17. The VBM is found at 0.26 ± 0.05 eV below the Fermi level, whilst the CBM is found at 0.88 ± 0.05 eV above it. Thus, the band gap is found to be $E_g = 1.14 \pm 0.14$ eV. Due to the small variation in the band gap with the number of layers, as seen in Table 5.1, the number of layers cannot be uniquely determined. The position of the VBM with respect to the Fermi level is consistent with the $MoTe_2$ sample being *p*-type in nature. The electronic structure is consistent with previous measurements from α-$MoTe_2$ single crystals[836]–[838]. Features of interest in the valence band are labelled I, II, III and IV, which occur at approximately 1 eV, 2 eV, 4 eV and 5 eV below the VBM. I is found to be due to electrons with *d*-symmetry wavefunctions, whilst II, III and IV are *p*-like in nature, primarily due to contributions from Te atoms[836]–[838]. *S*-type states are also found throughout the valence band[839].

More recent work has found that I and II are dominated by Mo *d*-states with only small contributions due to Te *p*-states, whilst III and IV are composed of roughly equal numbers of Te *p*- and Mo *d*-states[831]. In the same work, a small number of Te *s*-states are also found throughout the valence band[831].

Exposure Time (mins)	Ion Dosage (x10^{15} ions/cm^2)	Binding Energy (eV)		$Mo/MoTe_2$ Mo 3d	$Te/MoTe_2$ Te 3d	Te/Mo
		Mo $3d_{5/2}$	Te $3d_{5/2}$			
0	0	228.31	572.92	-	-	0.60
2	12x10^{14}	228.45	573.00	0.25	0.28	0.49
4	24x10^{14}	228.64	573.07	0.35	0.34	0.58
6	36x10^{14}	228.50	573.00	0.40	0.40	0.67
10	60x10^{14}	228.73	573.12	0.40	0.40	0.60

Table 5.5 – This table shows the binding energies of the stoichiometric peak components of the $MoTe_2$ multilayers shown in Figure 5.18. Also shown are the peak-area ratios of the elemental and $MoTe_2$ components calculated from both the Mo 3d and Te 3d core-levels and the total Te/Mo ratio.

Figure 5.18 shows the Mo and Te 3d core-levels after Ar^+ ion irradiation. The binding energies of the stoichiometric components are tabulated in Table 5.5. As the ion dosage is increased, the binding energy of the stoichiometric component moves to higher binding energy, reaching $0.4\ \mathrm{eV}$ above the initial position after receiving an ion dosage of $6 \times 10^{15}\ \mathrm{ions/cm^2}$. The direction of this drift is opposite in direction to that observed for MoS_2 and $MoSe_2$ above and corresponds to the sample becoming more *n*-type (or less *p*-type).

A second set of peaks is required to satisfactorily fit the experimental data, for the Mo 3d region this is $0.37\ \mathrm{eV}$ to lower binding energy from the stoichiometric $MoTe_2$ peak, whereas for the Te 3d region, the second peak occurs $0.31\ \mathrm{eV}$ to higher binding energy. The extra peak on the Mo 3d core-level can easily be explained as metallic Mo^0, by analogy with MoS_2 and $MoSe_2$. In contrast, the extra feature in the Te 3d spectra is more difficult to explain. One possible cause is the formation of Mo_6Te_6 nanowires, which have previously been reported when annealing in vacuum[840]–[843], however, *in situ* photoemission measurements indicate that the resulting Te 3d species occurs at lower binding energy[842], [843], rather than the higher binding energy observed here. An STM study by Zhu *et al.* has also shown that under Te-poor conditions, pits are also frequently formed[841]. The same work has also shown that Te atoms have a high mobility even under low-temperatures, thus the heating effect of the sputtering process, may in fact be sufficient to allow the Te to out-diffuse and segregate in these pits. If this were the case, then it would also explain why the stoichiometry varies very little during the sputtering

process, as can be seen in Table 5.5. The sample investigated by Zhu *et al.* was heavily *n*-type, with the Fermi level being found approximately 0.3 eV below the CBM. The main defect detected was Te adatoms, hence the increasing concentration of elemental Te would also explain why the core-levels in $MoTe_2$ move in the opposite direction to MoS_2 and $MoTe_2$. Hence, for these reasons the extra peak in the Te 3d spectrum is assigned to isolated pockets of elemental Te. Elemental Te has, likewise, been reported at binding energies comparable to those observed in this work[376], [844], further strengthening the identification of the peak.

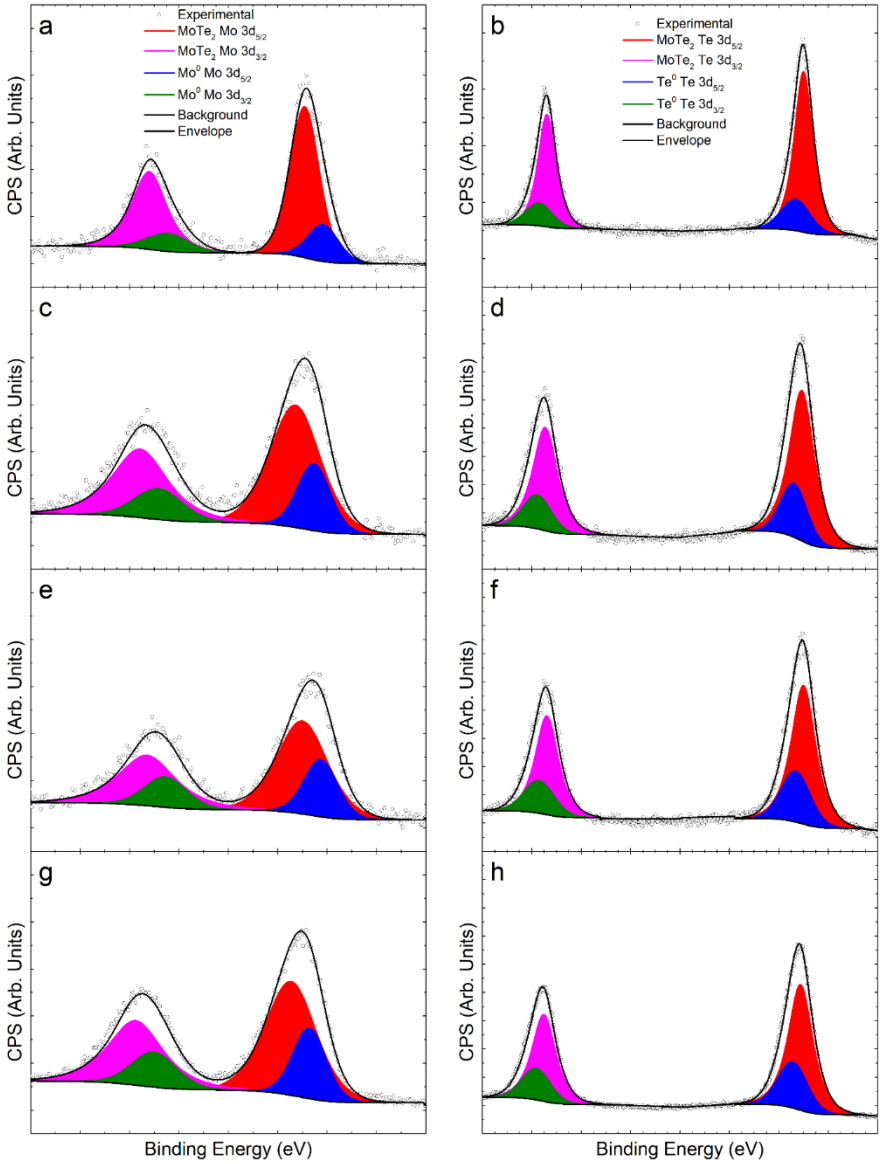

Figure 5.18 – PES spectra of the $MoTe_2$ under Ar^+ ion irradiation. (a), (c) (e) and (g) show the Mo 3d core-levels after 2, 4, 6 and 10 mins exposure respectively, whilst (b), (d), (f) and (h) show the Te 3d core-levels after the same durations.

5.4 Summary and Conclusions

In this chapter, the effects of defects upon the molybdenum dichalcogenides were considered. Chalcogenide vacancies were deliberately introduced by Ar^+ ion etching monocrystalline samples, and the effects upon the electronic and chemical structure of the material were probed by photoelectron spectroscopy.

For MoS_2 it was found that the multilayers saturated at a considerably higher sulphur content than that previously reported for polycrystalline and bulk single-crystal samples. This is likely due to the reduced dimensionality of the multilayer system, which prevents sulphur from being implanted into the vacancy positions between the van der Waals layers. The band gap of the MoS_2 multilayer sample is consistent with between 2-4 layers and the crystal was determined to be *p*-type by the position of the valence with respect to the Fermi level. After Ar^+ ion etching, the binding energies of the core-levels shift to lower binding energy, consistent with increased *p*-type doping of the material.

In the case of a bulk $MoSe_2$ single crystal, the binding energies of the core-levels are found to move towards lower binding energy, suggesting that the material is becoming more *p*-type in nature after irradiation. The final Se/Mo ratio obtained is consistent with that found by Bernede[833] for a $MoSe_2$ single crystal. The Se/Mo ratio is smaller than the equivalent ratio found for the MoS_2 sample, which is likely due to the bulk nature of this sample, where Se atoms can be implanted deeper into the crystal, occupying vacancies between the van der Waals sheets. In contrast, the MoS_2 sample is two-dimensional in nature, as such there are far fewer vacancy sites for the S to occupy, resulting in an increased S/Mo ratio.

Intriguingly, for a $MoTe_2$ the composition was found to vary little after Ar^+ ion irradiation, instead Te and Mo were found to partially segregate out from the lattice, possibly into pinholes or pits. In contrast to the results obtained for the MoS_2 and $MoSe_2$ samples, the core-levels moved to higher rather than lower binding energies after irradiation, suggesting that the samples were becoming more *n*-type in nature. This is due to the segregation of the Te from the lattice by comparison with Te-rich *n*-type materials as Te adatoms appear to act as electron donors.

Thus, for growing kesterite materials on Mo substrates, the nature of the chalcogen vacancies found in this work suggest that the kesterite layer should be deposited in

chalcogen-poor conditions, to prevent the formation of chalcogen-rich MoX_2 layers which are more *n*-type than vacancy-rich layers. This is made difficult by the two-stage deposition process usually used for kesterite deposition, as the second stage is invariably a high temperature anneal in a chalcogen-rich environment. Thus, the MoX_2 layer is typically *n*-type, and hence produces a diode opposed to the man diode of the photovoltaic cell. However, STM studies of the defects in MoS_2 show that contrary to the results here and in Santoni *et al*.[546], highly-defective, sulphur-poor surfaces are *n*-type in nature[765]. In contrast, Addou *et al*. find that defective surfaces in natural MoS_2 are typically *p*-type, whilst pristine samples are more typically *n*-type[764]. Electron paramagnetic response has also been used to show that sulphur vacancies are acceptors in MoS_2[845]. Theoretical works also find contradictory results as to the nature of sulphur vacancies in MoS_2, with different theorists finding the vacancies to be acceptors[846], [847] and donors[848]–[850]. Thus, further theoretical and experimental work is required to truly understand the nature of vacancies in the TMDs.

Similarly, for the growth of substrate-configuration CdTe photovoltaic cells using Mo as the substrate, the CdTe should be deposited in Te-poor conditions to limit the presence of Te adatoms on the $MoTe_2$ layer. In practice, this is usually less of an issue for CdTe than it is for kesterites as CdTe deposition does not usually require a second, annealing stage in a Te-rich atmosphere unlike kesterites.

In the next chapter, we will investigate the properties of an alternative window layer: Ga_2O_3, by photoemission.

6 Ga_2O_3, An Alternative TCO?

This chapter is based upon unpublished work, which is the basis of several papers which are currently in preparation or submission. These papers are as follows:

- Swallow, J. E. N.; Varley, J. B.; Jones, L. A. H.; Gibbon, J. T.; Piper, L. F. J.; Dhanak, V. R.; Veal, T. D. "Transition from electron accumulation to depletion at β-Ga_2O_3 surfaces", Submitted to APL Materials
- Roberts, J.W.; Massabuau, F. C-P.; Chalker, P. R.; Oliver, R. A., Gibbon, J. T.; Dhanak, V. R.; Major, J.; Phillips, L. J. "Effect of Growth Temperature and Plasma Growth Parameters on Plasma Enhanced Atomic Layer Deposited α-Ga_2O_3 Grown on Sapphire", manuscript in preparation

The transparent conducting oxides (TCOs) are an unusual class of material, in that they combine several properties that are usually mutually exclusive. Namely that they are transparent ($E_g \geq 3$eV) and conducting. This combination of properties has led to the widespread adoption of TCOs for any application where a transparent conductor is required. Examples of applications include, touch screens, window layers in photovoltaics, smart or self-cleaning windows and optoelectronics.

The TCOs are usually post-transition metal oxides (In, Sn, Zn, Cd, Ga), and are generally n-type. Work on developing p-type TCOs are ongoing, however this is limited as the materials are natively n-type, thus dopant need to first compensate for the native doping. Another unusual property of the TCOs is that they often exhibit charge accumulation at the surface, in contrast to most materials, which exhibit charge depletion. This property has allowed for the development of highly-sensitive gas sensors based on In_2O_3, ZnO, SnO_2 and Ga_2O_3.

The industry standard TCO is tin-doped indium (pent)oxide (Sn:In_2O_3, ITO). Due to the scarcity of indium, as outlined in Table 1.1, and the resulting cost of the material, and the demands for indium for III-V semiconductor devices, industry is interested in developing alternative TCOs which use more abundant elements. The second most common commercial TCO is fluorine-doped tin (di)oxide (F:SnO_2, FTO), however the conductivity of this material is limited by self-compensating doping[462]. In any rate, the relative abundance of tin is only a factor of 10 greater than that of indium, as shown in Table 1.3. Some researchers have proposed indium-doped cadmium oxide (In:CdO, ICO) as this would use comparatively little indium, however cadmium is about half as abundant as indium in the crust of the Earth, which would rather defeat the point. Other work has proposed

doped ZnO as an alternative. At first look, this would be quite reasonable as zinc is approximately 300 times more abundant than indium, however reliably making Ohmic contacts with ZnO is surprisingly difficult to achieve[851]–[856]. In any rate, industry is not interested in ZnO due to the unusual chemical properties of zinc (private communications with Paul Warren, Principal Technologist, NSG).

Gallium pentoxide (Ga_2O_3) is an alternative material that could be used. Gallium is chemically similar to indium, meaning that industrial CVD processes should not require much change to switch over. It is also considerably more abundant than indium (approximately 80 times more so), although there is also heavy demand for gallium for III-V semiconductor applications as with indium.

Ga_2O_3 also has the largest band gap of any of the TCOs, which is frequently quoted as being in the range of 4.5 to 5 eV, and has excellent chemical and thermal stability. These properties have led to interest in the material for many applications, including optoelectronics, solar-blind UV detectors, high-power electronics, high-temperature gas sensing for industry, photovoltaics, photocatalytic water splitting and as a UV-TCO.

A number of polymorphs of Ga_2O_3 are known, the most stable of which is the β-Ga_2O_3 phase, which has a monoclinic crystal structure, with space group C2/m. The unit cell of this structure is shown iand contains 30 atoms, with two inequivalent Ga sites and 3 inequivalent oxygen sites[857]–[859].

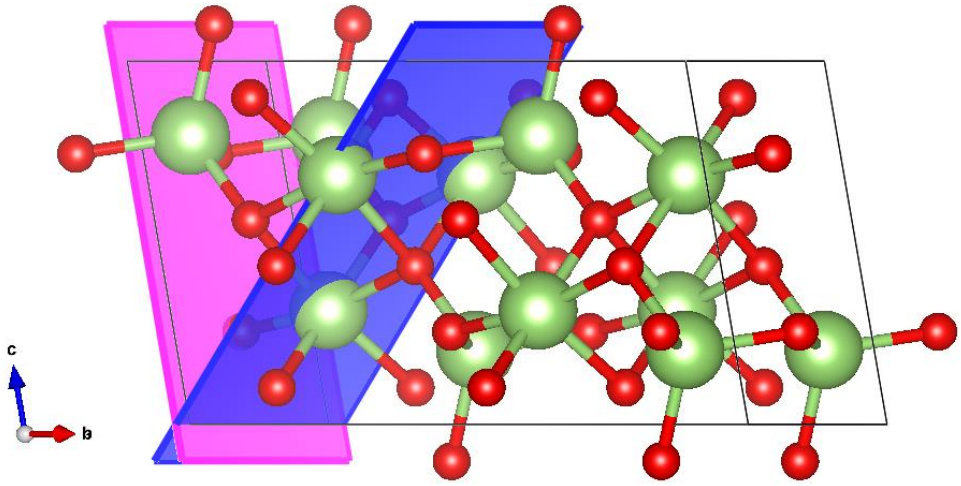

Figure 6.1 – The unit cell of β-Ga_2O_3. The plane in pink marks the (100) lattice plane whilst blue denotes the $(\bar{2}01)$ plane. Ga atoms are represented by green spheres, whilst oxygen atoms are represented by red spheres.

Another polymorph of Ga_2O_3 is the α-Ga_2O_3 phase, which has the corundum crystal structure (space group $R\bar{3}C$)[857], [859], [860]. Further Ga_2O_3 polymorphs are also known:

namely the γ-Ga_2O_3 phase, which has a defect-spinel structure; the δ-Ga_2O_3 phase, which has the bixbyite structure although there is evidence from neutron-diffraction experiments that data suggesting this structure has been misinterpreted[861]; and the ε-Ga_2O_3 phase, which was originally thought to be orthorhombic[859], [862], but in fact appears to be a hexagonal structure[861]. An orthorhombic analogue to the κ-Al_2O_3 is also present as the κ-Ga_2O_3[861].

This chapter will initially critique the literature of photoemission on β-Ga_2O_3 single crystals and the nature of the surface band bending on these crystals, before describing the photoemission experiments performed on a Sn-doped β-Ga_2O_3 single crystal, with a $(\bar{2}01)$ surface. The valence band measured by both monochromatic and synchrotron photoemission will then be compared with the densities of states predicted by DFT and the differences between them discussed. Natural band alignments of numerous TCO candidate materials will be given and compared.

The second part of this chapter will then discuss the photoemission of epitaxial Ga_2O_3 films grown on sapphire substrates by atomic layer deposition (ALD).

6.1 Photoemission of a b-Ga_2O_3 Single Crystal and the surface carrier density

In contrast to In_2O_3, β-Ga_2O_3 has previously been reported as exhibiting depletion of charge carriers at the vacuum interface in several previous reports[863]–[866].

To understand the fundamental surface properties of β-Ga_2O_3, a Sn-doped single crystal was acquired from the Tamura Corporation (Tokyo, Japan). This single crystal has surface termination $(\bar{2}01)$ and was grown by the floating zone technique. Confirmation of the single crystal nature of the sample was made by XRD. The resulting diffractogram is shown in Figure 6.2, which shows only the $(\bar{2}01)$ lattice plane and the reflections of this plane.

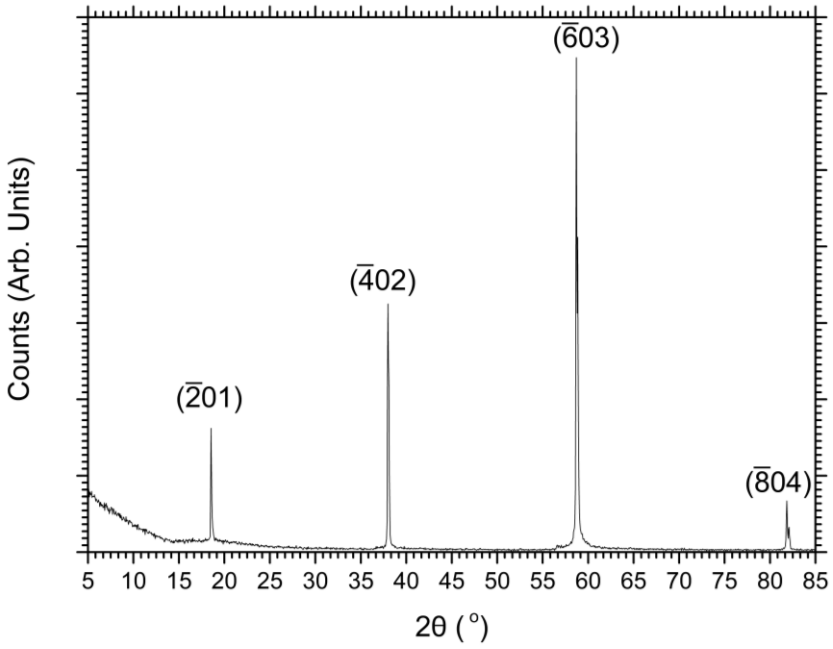

Figure 6.2 - The diffractogram from a commercial $(\bar{2}01)$ β-Ga_2O_3 single crystal.

Hall effect measurements in the van der Pauw mode[461] found the electron density to be $n = (3.51 \pm 0.02 \times 10^{18})$cm^{-3}. The corresponding Fermi-level is found to be at 5.52meV above the CBM, within the limits of the α-approximation. This value is comparable to that found by Peelaers *et al*. although, they find the Fermi-level to be slightly below the CBM[867]. The dispersion around the CBM can then be approximated by the α-approximation, giving the dispersion relation in equation (6.1).

$$E(1 + \alpha E) = \frac{\hbar^2 k^2}{2m_\Gamma^*} \qquad (6.1)$$

Where $\alpha = \frac{1}{E_g}$, the band gap is taken to be $E_g = 4.75$ eV[868], the effective mass is $m_\Gamma^* = 0.28m_e$ [867], [869], and the static and high-frequency dielectric constants to be $\epsilon_{st} = 9.93$[870] and $\epsilon_\infty = 3.57$[870] respectively. Peelaers *et al.* found that the electron effective mass is constant for carrier densities up to 1.1×10^{19}cm^{-3}, and that anisotropic effects on the effective mass only contribute at carrier densities above this[867].

Prior to PES measurements, the sample was annealed at 700°C for 20 minutes to remove surface contamination. Figure 6.3 shows the C 1s spectrum prior to, and after annealing. After annealing, the intensity of the C 1s peak is clearly reduced. The remaining carbon is likely due to impurities within the sample, rather than adventitious carbon. As such it is not appropriate to use this level for charge calibration. Instead, as the sample is conducting it is reasonable to assume that no charging occurs. The O 1s peak is observed to occur at 531.85 ± 0.05eV, which is comparable to that obtained by Michling and Schmeißer[871].

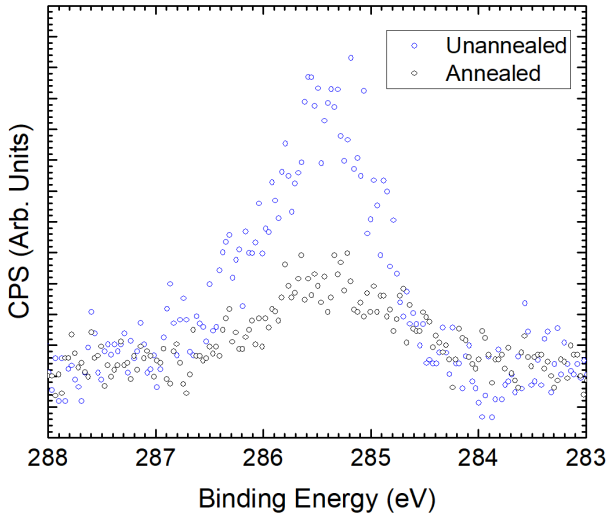

Figure 6.3 - Shown is the C 1s spectrum prior to and after annealing at 700°C for 20 minutes.

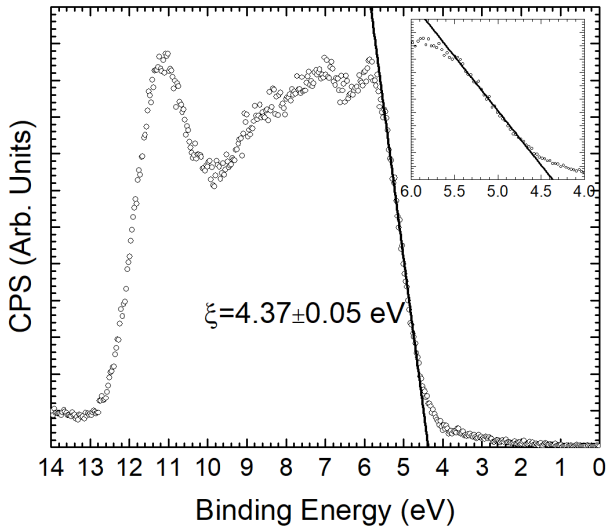

Figure 6.4 - XPS-VB after annealing of the Ga_2O_3 single crystal with the corresponding linear extrapolation to obtain the VBM-FL separation.

Figure 6.4 shows the XPS-VB from the Ga_2O_3 single crystal after it had been annealed. By way of linear extrapolation to the background, the VBM-FL is found to be $\xi = 4.37 \pm 0.05$eV. This is comparable to that found by Navarro-Quezada on a β-Ga_2O_3 (100) single crystal, with a comparable carrier density after annealing at 800°C[864].

Prior to comparison with the XPS-VB, the DFT PDoS need to be corrected for the photoionisation cross-sections. A comparison of the PDoS before and after this correction are shown in Figure 6.5. Surprisingly, the overall shape of the valence band does not change after cross-section correction, but the states that contribute the most DoS do. Before correction, the VB is dominated by O 2s and O 2p states, however after the correction, Ga 3d states are dominant.

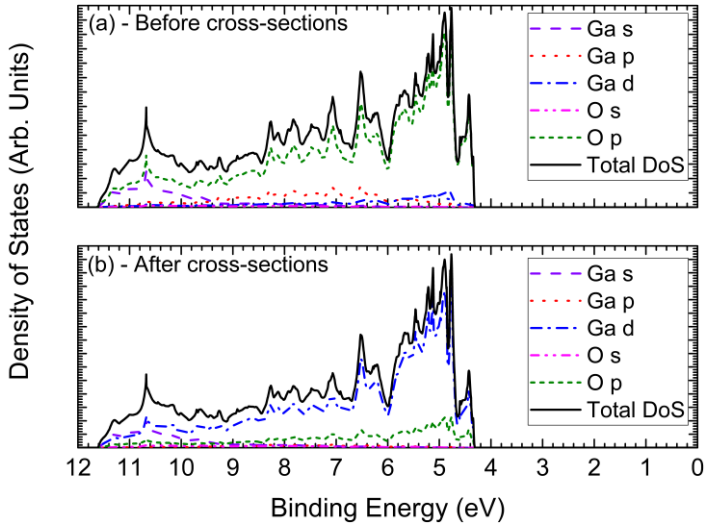

Figure 6.5 - PDoS predicted by DFT (a) before cross-section correction and (b) after cross-section correction

To compare the DFT-predicted TDoS shown in Figure 6.5(b), the Fermi-Dirac function was convoluted with a Gaussian of variable FWHM as described in section 2.6. The TDoS was then convoluted by the same Gaussian function to obtain a broadened TDoS, however lifetime effects still need to be considered. Hence, the broadened TDoS were then convoluted with a Lorentzian of variable FWHM. Figure 6.6 shows the XPS-VB and compares it with the convoluted TDoS for several Lorentzian FWHM values, by comparison with the leading edge of the VB, the FWHM is found to be 0.75 eV.

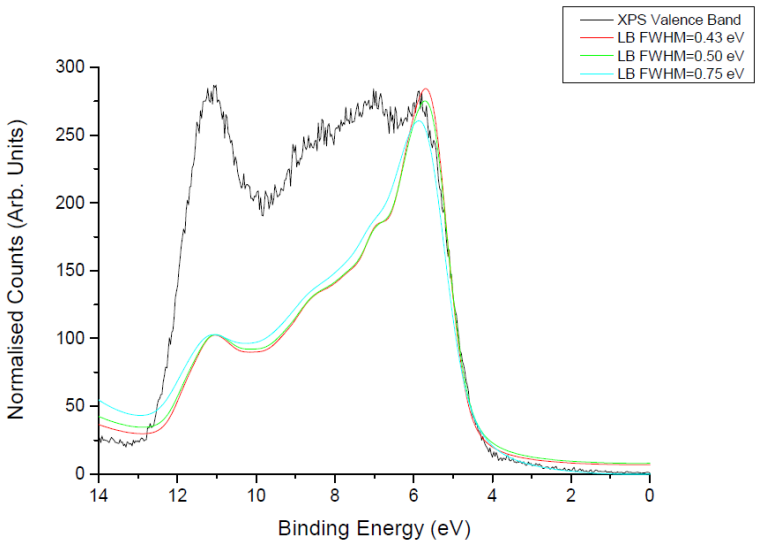

Figure 6.6 - A figure showing the XPS-VB and comparisons with broadened Gaussian-Lorentzian convoluted TDoS predicted by DFT. The FWHM of the Lorentzian was allowed to vary to obtain a best fit.

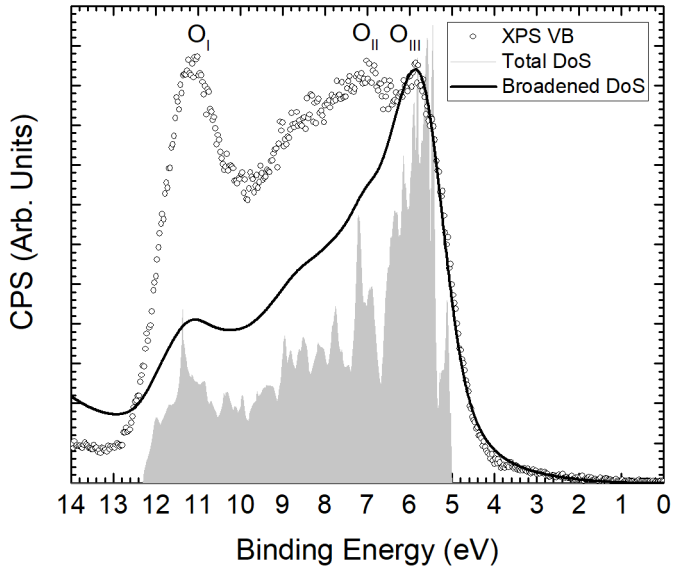

Figure 6.7 - Comparisons between the XPS-VB, the cross-section corrected TDoS and the broadened corrected TDoS.

Figure 6.7 shows a comparison between the XPS-VB, the cross-section corrected TDoS and the Gaussian-Lorentzian broadened TDoS. The low binding energy side of the VB fits reasonably well up to the feature labelled O_{III}, however, the intensity of the features labelled O_{II} and O_{III} are in poor agreement, although the binding energy positions are in good agreement. This is in contradiction to the VB presented by Li *et al*.[866]. However, Li *et al*. arbitrarily choose to use the Ge 4p cross-section as the Ga 4p cross-section is not tabulated for the photon energy used, and include 7 times the DoS of the Ga 4p to fit the experimental data. That they then claim the fact that their arbitrary choice of cross-section and DoS fits the experimental data, justifies this particular choice is neither here nor there, as if one chooses to multiply the density of states by some number, and then use the wrong cross-section, to fit the experimental data, then obviously the data will fit. The logic is obviously circular.

In fact the Ga 4p cross-section is tabulated by Scofield[472] for the Al K_α source used for this measurement, and from Figure 6.7 it is clear that the DFT model fails to match the experimental data. Hence, the approach in Li *et al*. is clearly not justified as the DFT model is fundamentally incorrect, and hence should not reproduce the HAXPES-VB correctly, particularly as the cross-sections are, in fact tabulated for the 8000 eV photons used, in Scofield's 1973 report for the US Atomic Energy Commission[872].

Li *et al.* also present the cross-section corrected DoS for a XPS experiment, and compare the results with the XPS spectrum presented by Michling and Schmeißer[871]. However,

they again use the cross-section for Ge 4p in place of the Ga 4p, which again is questionable.

Figure 4 of Navarro-Quezada *et al.*[865] shows similar discrepancies between the DFT TDoS and the XPS-VB, to that seen in Figure 6.7, although they falsely claim that there is 'good agreement between theory and experiment.'

It should also be noted that in Figure 6.6, the DFT TDoS has to be translated by 5eV in order to align with the VBM, in contrast to the value of $\xi = 4.37 \pm 0.05$eV obtained by the linear extrapolation method shown in Figure 6.4. This suggests that the linear extrapolation method is underestimating the VBM-FL separation by a considerable amount. In_2O_3 also shows this, due to the sharp onset of the VBM[699], [723], [873], [874]. Klein[873], Gassenbauer[723] and King[874] use the linear extrapolation method and underestimate the VBM-FL position, resulting in them suggesting surface depletion. However, by comparison with DFT, King later shows in Figure 3 of Ref [699] that the linear extrapolation method is incorrect as the experimental broadening on the VBM is considerably larger than the dispersion of the VBM. Hence, the experimental VBM is dominated by the experimental broadening and not the band edge.

From Figure 6.7, we can see that the experimental onset of the VBM is considerably broader than the DFT TDoS before experimental broadening, suggesting that the linear extrapolation will similarly underestimate the VBM-FL separation in this case.

Since the band gap of β-Ga_2O_3 is only 4.75eV, a VBM-FL separation of $\xi = 5.00 \pm 0.05$eV would suggest that the surface exhibits downwards band bending, resulting in the Fermi-level being considerably above the CBM at the surface. Similar VBM-FL separations are observed in high-resolution(HR) angle-resolved photoemission spectra (ARPES)[875]–[877], such as those shown in Figure 6.8, where the VBM-FL separation is found to be $\xi = 4.90 \pm 0.02\ \mathrm{eV}$. Since the energy resolution of HR-ARPES is considerably smaller than that of XPS (of the order of $10\ \mathrm{meV}$ or less[876], [878]–[880] in comparison to approximately $400\ \mathrm{meV}$ determined for XPS here), the experimental broadening will also necessarily be smaller, thus the value obtained for the VBM-FL is more likely to be correct than that obtained by

linear extrapolation of the valence band edge from XPS. Likewise, lower resolution ARPES such as that in Lovejoy *et al*. obtains a reduced VBM-FL separation.

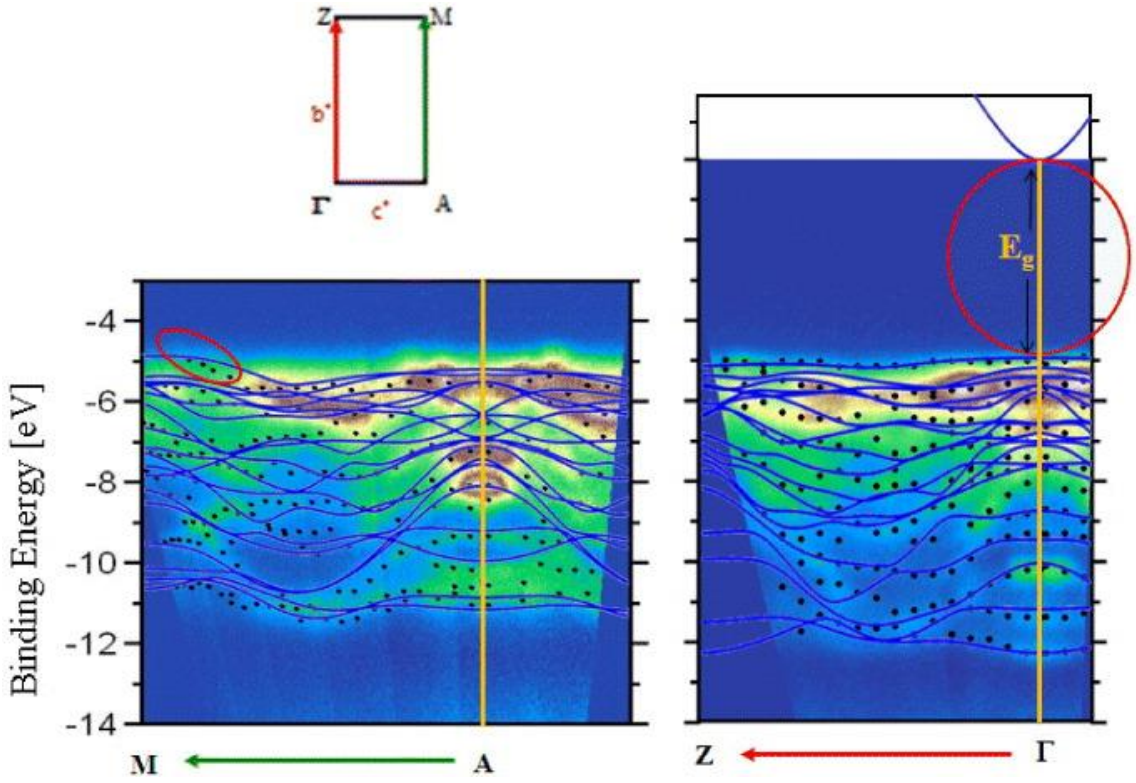

Figure 6.8 – Angle-resolve photoemission spectra of Ga_2O_3 single crystals along different symmetry directions. Figure is reproduced from ref. [876] *under a Creative Commons Attribution-NonCommercial-ShareAlike 3.0 Unported (CC BY-NC-SA version 3.0) licence.*

Figure 5 of Ref. [864] and Figure 2a of Ref. [865] both display a valence band similar to that observed in Figure 6.7, with three features labelled O_I, O_{II} and O_{III} which has been copied in Figure 6.7, and claim that these features are due to the inequivalent oxygen sites within the monoclinic crystal structure, citing Michling and Schmeißer[871].

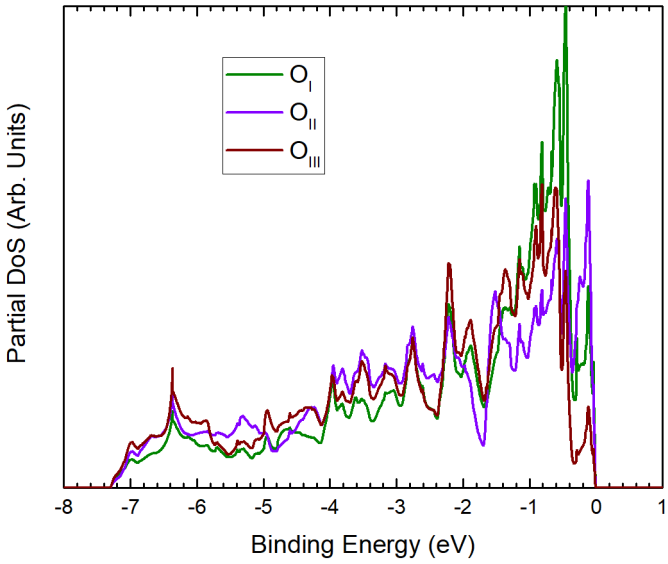

Figure 6.9 - The PDoS for the inequivalent oxygen sites in the β-Ga_2O_3 lattice. Energies are given with respect to the valence band maximum.

However, when compared with the DFT PDoS for each inequivalent oxygen site presented in Figure 6.9, it is clear that this is not justified, as each oxygen site clearly contribute PDoS throughout the valence band. Figure 6.9 clearly shows that whilst the inequivalent sites do contribute a different PDoS at each energy, these differences are not pronounced enough to justify the labelling in Refs. [864], [865].

By solving the Poisson equation given in equation (6.2), the nature of the surface charge at the vacuum interface can be determined.

$$\frac{d^2V}{dz^2} = \frac{e}{\varepsilon_{st}\varepsilon_0}[N_D^+ - N_A^- - n(z) + p(z)] \tag{6.2}$$

Here, ε_{st} is the static dielectric constant for Ga_2O_3, N_D^+ and N_A^- Thus, by using the value for the VBM-FL separation, obtained from XPS, to determine the band bending at the vacuum interface, and the van der Pauw measurements to determine the bulk Fermi level from the carrier density, initial conditions can be found for the Poisson equation, which are given in equations (6.3) and (6.4), which can then be solved numerically.

$$\left.\frac{dV}{dz}\right|_{z=0} = \frac{e}{\varepsilon_{st}\varepsilon_0}N_{SS} \tag{6.3}$$

$$\lim_{z\to\infty} V(z) = 0 \tag{6.4}$$

Where N_{SS} is the surface state density. The resulting band bending and carrier density profiles are shown in Figure 6.10. These profiles were calculated within the modified Thomas-Fermi approximation, using a non-parabolic conduction band. Close to the surface,

there is a large maximum in carrier density, corresponding to surface accumulation of charge, contrary to previous reports[863]–[866].

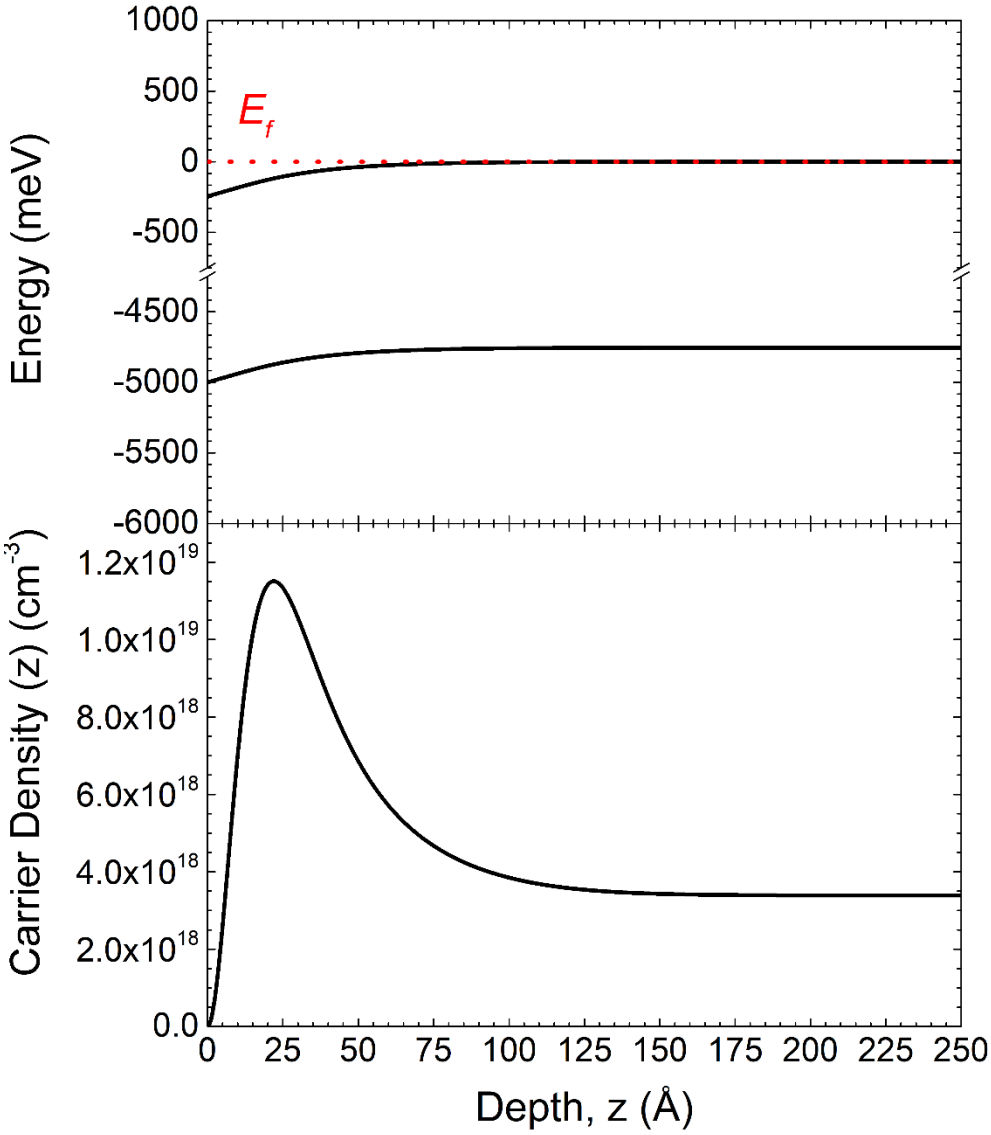

Figure 6.10 – Band bending and carrier density profiles of the Ga_2O_3 single crystal, calculated within the modified Thomas-Fermi approximation, with a non-parabolic conduction band. The energies are referenced to the Fermi level, which is found to occur at 5.52 meV above the bulk CBM.

This result is further supported by experiments involving exposure of the Ga_2O_3 single crystal to O_2 *in situ*. The sample was dosed with O_2 gas of 99.998% purity by volume at a partial pressure of 1×10^{-7} mbar for 5 mins. Once the pressure had recovered to the base pressure, XPS measurements were repeated. The valence band shown in Figure 6.11 was found to have moved to lower binding energy by 0.15 ± 0.05 eV, indicating a change in the position of the Fermi-level, resulting in a sample that is, in effect, less *n*-type in nature. This corresponds to oxygen physadsorbing to the Ga_2O_3 substrate and accepting an electron to for the commonly observed O_2^- ion. Thus, the carrier density at the surface would be

reduced, suggesting a mechanism for the gas-sensing properties of Ga_2O_3. A similar mechanism is proposed for ZnO gas-sensing[881], [882], where surface accumulation is also observed under some circumstances[624], [883], [884].

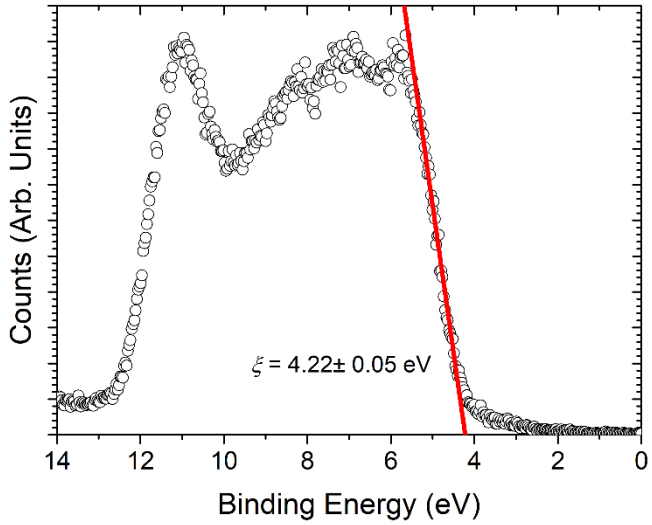

Figure 6.11 – VB-XPS spectrum of the Ga_2O_3 valence band after 5 minutes exposure to $5x10^{-7}$ mbar of O_2.

Figure 6.12 shows the VB of the β-Ga_2O_3 single crystal as measured by HAXPES, with a nominal photon energy of $(h\nu = 6450\text{eV})$ at the I09 beamline at the Diamond Light Source. The inset shows the same data magnified by a factor of x20 (blue) and x200 (red). The overall structure observed is similar to that seen by Li *et al*.[866], who measured the HAXPES-VB at a nominal photon energy of $(h\nu = 8000\text{eV})$.

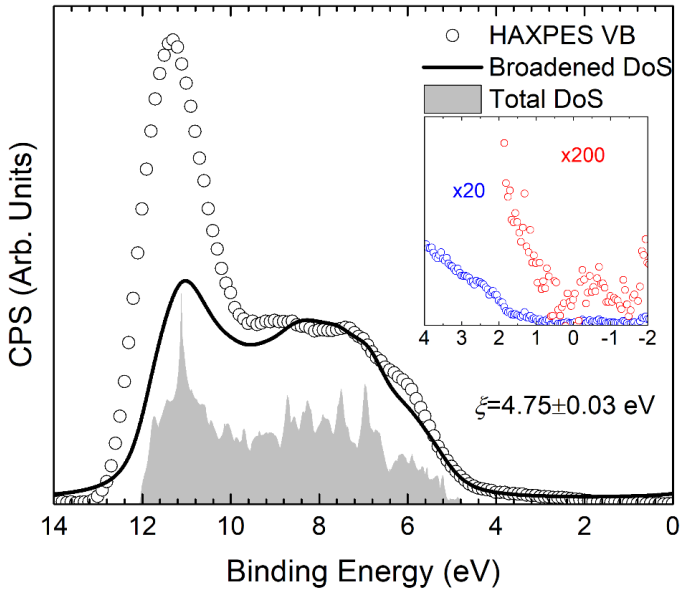

Figure 6.12 - The HAXPES-VB of the β-Ga_2O_3 single crystal. Inset is a magnified version of the region close to the Fermi-level. Intensity is still present up to the Fermi level. Also shown are the total-cross section corrected DoS and the experimentally broadened DoS.

At the low binding energy side of the VB, a tail is seen which does not go to zero until beyond the Fermi-level. A similar tail is also seen by Michling and Schmeißer[871], who attribute it to sub-gap states. Another similar feature is observed by King *et al*.[699], [885] and Zhang *et al.*[886] in In_2O_3, which exhibits electron accumulation at its surface. King also observes a small feature close to the Fermi-level which is assigned to photoemission from the conduction band. A similar, weaker feature centred on approximately -1 eV, is also observed in the inset figure at x200 magnification. This may support the hypothesis that this single crystal exhibits accumulation rather than depletion at the vacuum interface. However, the intensity of the feature is comparable to the signal-to-noise ratio, even after many scans with a high-intensity source, so an origin cannot be conclusively assigned. Equally, the results from the Poisson simulations suggest a surface carrier density that is considerably smaller than reported for In_2O_3, and as such, the conduction band emission in this crystal would also be expected to be considerably smaller. Similar results are obtained by Janowitz *et al*.[876] who do not see conduction band emission in HR-ARPES after long measurement times, even though their Fermi-level sits above the CBM, which they suggest is due to the low dopant density used.

The Ga 4p photoionisation cross-sections are, in fact, tabulated up to photon energies of $1500\ \mathrm{keV}$ by Scofield in his report for the US Atomic Energy Commission[872], which is comparable to the kinetic energies of the photoelectrons here. Thus, the PDoS presented in Figure 6.5(a) can be similarly corrected for the photoionisation cross-sections to obtain a theoretical band structure to compare with the experimental structure in Figure 6.12. The resulting theoretical band structure is presented in Figure 6.13.

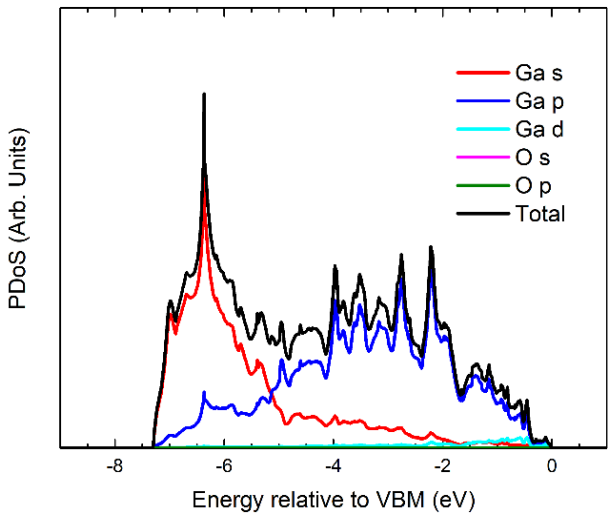

Figure 6.13 – Simulated valence band structures after correction for the photoionisation cross-sections at 6000 eV[872].

It is clear that the theoretical band structure fails, once again to match the intensity at the back of the valence band. Interestingly in both Figure 6.5(b) and Figure 6.13 the back of the valence band is dominated by Ga *s*-like states, which only contribute a small intensity throughout the rest of the valence-band. As it is this set of states which appears to contribute heavily to the back of the valence band, it appears to be that states of a nature similar to the Ga 4*s* are, for some reason, undercounted in the DFT calculations.

It should be noted that the VBM from the HAXPES data does not occur at the same binding energy position as the monochromatic XPS. This can be explained by considering the depth sensitivity of the two techniques. The IMFP of an electron with a kinetic energy of 1500eV, comparable to that of an electron from the VBM in monochromatic XPS, is approximately 2 nm, whereas for an electron at 6000eV the IMFP is approximately 4nm, assuming the universal curve for the IMFP holds[886]. I.e. the HAXPES measurements are considerably more sensitive to the bulk like properties of the material, and hence is less sensitive to the band bending.

Similarly, the VB presented by Michling and Schmeißer[871] uses a photon energy $h\nu = 150$eV, which would have an IMFP of the order of 7Å, rendering it more sensitive to the surface band bending, thus explaining why the value from their linear extrapolation is considerably larger than obtained here. The values of the IMFP calculated for these kinetic energies from equation (2.1) are given in Table 6.1.

Electron Kinetic Energy (eV)	**Inelastic Mean Free Path (Å)**
150	7
1500	21
6000	41

Table 6.1 - A table of the inelastic mean free paths for a range of electron kinetic energies

Thus, by comparison of the calculated IMFPs in Table 6.1 with the band bending simulations presented in Figure 6.10, we can see that the HAXPES is much less sensitive to the region where the band bending is occurring than the soft XPS is. This is also reflected in the energy by which the DFT weighted-DOS has to be moved to align with the features in the experimental band. The soft XPS weighted-DoS is moved by 5 eV, showing its sensitivity to the band bending, whereas the HAXPES weighted-DoS is translated by only 4.75 eV, which is entirely consistent with no band bending being detected and the Fermi-level being 5 meV above the CBM as suggested by the simulations above.

The next obvious question to ask is why do the TCOs exhibit accumulation at the surface when most *n*-type semiconductors exhibit depletion? The answer lies in the size and electronegativity mismatch in these materials and the resulting band structure. In the case of the TCOs the conduction band minimum is low-lying, close to the Γ-point (usually corresponding to a large electron affinity), thus the charge neutrality level (i.e. the mid-gap energy averaged across the full Brillouin zone), can occur within the conduction band of the material. The charge neutrality level is equivalent to the energy level at which native defects, surface states and hydrogen change from donors to acceptors, such that if the Fermi level is greater than the charge neutrality level, then these defects will act as acceptors; if it is below this level, the defects will be donors. The nature of defects and the lack of experimental sensitivity to hydrogen render probing of them difficult, however by using the light-isotope analogue of hydrogen, muonium, the nature of the hydrogen defects can be ascertained. In fact, results from muon spectroscopy techniques suggest muonium, and hence hydrogen is a shallow donor in Ga_2O_3[887], which would support the finding of surface accumulation.

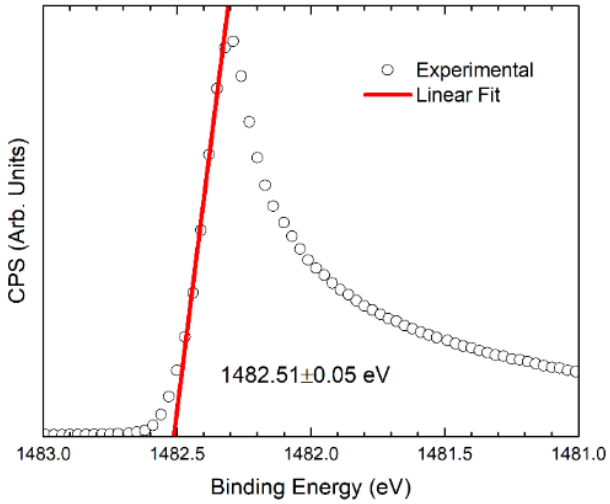

Figure 6.14 – The secondary electron cut-off of the Ga_2O_3 single crystal.

Using Figure 6.4 and Figure 6.14, the ionisation potential can be found, which is evaluated to be $V_{IP} = 9.04 \pm 0.05$ eV, which, when combined with a band gap of 4.75 eV, results in an electron affinity of $\chi = 4.34 \pm 0.05$ eV, considerably below that of most semiconductors. Figure 3.18, Figure 6.15 and Figure 6.16 show equivalent spectra for ZnO, In_2O_3 and SnO_2 single crystals respectively.

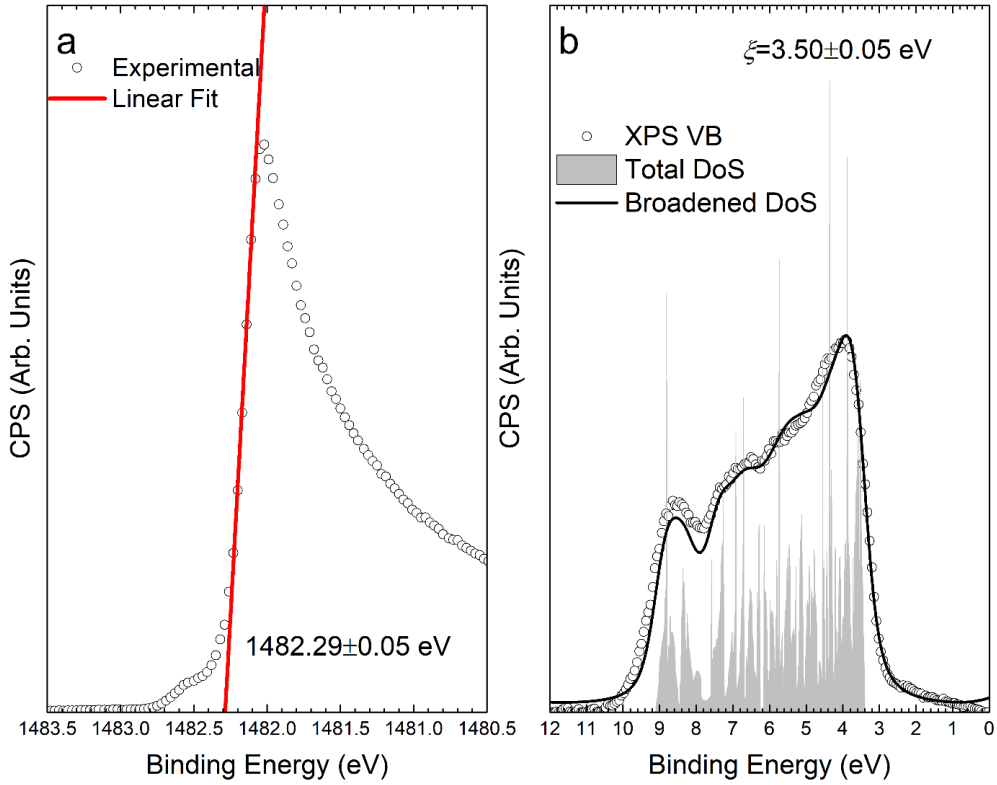

Figure 6.15 – PES Spectra of an In_2O_3 single crystal. (a) shows the secondary electron cut off, whilst (b) shows the VB-XPS. Also shown in (b) the total weighted DoS and the broadened DoS for In_2O_3

Figure 6.15(a) shows the secondary electron cut off for a bixbyite In_2O_3 single crystal, which is found to be 1482.29 ± 0.05 eV. Figure 6.15(b) shows the valence band spectrum as measured by XPS. As mentioned above, the linear extrapolation method to determine the VBM-FL separation also fails for In_2O_3, thus to determine this, PDoS from ref. [699] are cross-section corrected and broadened to compare with the XPS valence band. Thus, the VBM-FL separation is found to be $\xi = 3.50 \pm 0.05$ eV, resulting in an ionisation potential, $V_{IP} = 7.81 \pm 0.05$ eV and an electron affinity of $\chi = 4.88 \pm 0.05$ eV, assuming a band gap of $E_g = 2.93$ eV[699]. The ionisation potential and electron affinities obtained earlier for a ZnO single crystal were found to be $V_{IP} = 7.50 \pm 0.05$ eV and $\chi = 4.13 \pm 0.05$ eV respectively.

Figure 6.16(a) shows the secondary electron cut-off of a SnO_2 single crystal, which is determined to be 1481.99 ± 0.05 eV. Figure 6.16(b) shows the valence band and conduction bands as observe by XPS and IPES respectively. By linear extrapolation of the band edges to the baseline, the band gap of the SnO_2 single crystal is found to be $E_g = 3.52 \pm 0.14$ eV, consistent with the 3.6 eV band gap previously reported in literature[462], [713], [716].

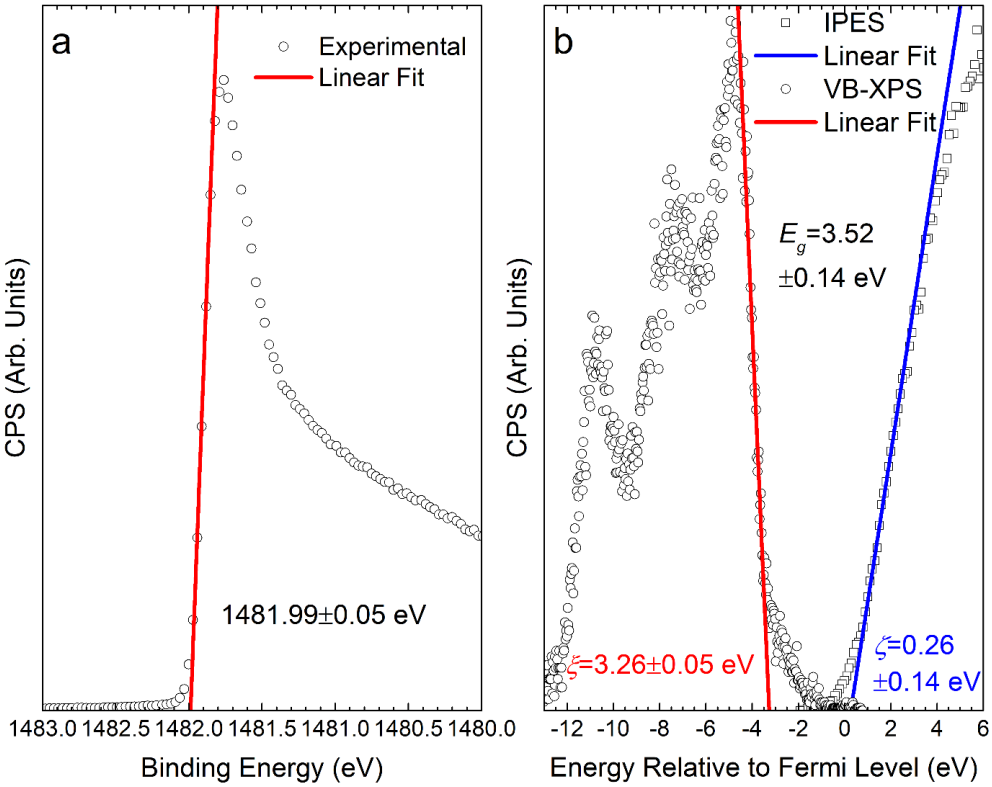

Figure 6.16 – PES Spectra of a SnO_2 single crystal. (a) shows the secondary electron cut-off and (b) shows the VB-XPS and IPES results, allowing for the determination of the band gap.

Thus, the ionisation potential and electron affinity of the SnO_2 single crystal are determined to be $V_{IP} = 7.87 \pm 0.05$ eV and $\chi = 4.35 \pm 0.05$ eV respectively. The ionisation potentials and electron affinities found in this work for the TCOs are summarised in Table 6.2.

	V_{IP} (eV)	E_g (eV)	χ (eV)
Ga_2O_3	9.04	4.75	4.34
In_2O_3	7.81	2.93	4.88
SnO_2	7.87	3.52	4.35
ZnO	7.50	3.37	4.13

Table 6.2 – A table summarising the ionisation potentials, band gaps and electron affinities of the TCOs considered in this work.

From Table 6.2, we can see that the valence bands of the TCOs occur at particularly large values, partially explaining the difficulty of doping a TCO to be a *p*-type semiconductor. The electron affinities are, likewise, large values compared to standard semiconductors. For In_2O_3, the electron affinity is especially deep, due to the relatively small band gap of In_2O_3. Thus, the charge neutrality level in almost all cases, will sit inside the conduction band. Hence, for reasonable doping concentrations, the Fermi-level will be below the CNL and the surface states will act as donors, as observed with muonium[888], thus resulting in surface

accumulation to result in a net, neutral charge. Similarly, accumulation is reported for SnO_2[889]. In contrast, accumulation and depletion layers have been reported for ZnO, depending on surface preparation, which can be understood as the CBM occurs at an energy closer to the vacuum level, thus for some carrier densities, the Fermi level will be above the CNL in some cases, rendering the surface states acceptors, resulting in depletion. Ga_2O_3 has a similar electron affinity to that of SnO_2, and as such would be expected to behave in a similar way.

In the next section, we will consider the different phases of Ga_2O_3 and how they can be distinguished by photoemission.

6.2 Epitaxial Ga_2O_3 on Sapphire

Atomic layer deposition (ALD) is a material growth method similar to chemical vapour deposition (CVD), in that the precursor chemicals are allowed into a vacuum chamber in pulses. Typically, ALD results in amorphous or polycrystalline films being deposited due to the low substrate temperatures used, however by careful choice of a suitable substrate, the growth of epitaxial films can be achieved. This is commonly known as atomic layer epitaxy.

Deposition of Ga_2O_3 films was carried out using an Oxford Instruments OpAL plasma enhanced atomic layer deposition reactor with the baffle plate removed from above the chamber, thus giving a direct line-of-sight from the remote plasma to the substrates. The depositions utilised an inductively coupled plasma system located approximately 60cm above the deposition chamber. Aduct-grade Triethylgallium (TEGa) from Epichem was used as the gallium source and dry, research grade O_2 from BOC was used as the oxygen source. Argon from BOC was used for chamber purges and as the precursor carrier gas. Research-grade materials were used for all process gases. The TEGa source was kept at 30°C with line temperatures into the reactor chamber held at 80°C and 90°C. For the lowest temperature deposition (120°C substrate) the chamber walls were held at 125°C, while the chamber walls were set at 150°C for all other growths. For each growth run, multiple c-plane sapphire samples with a miscut of 0.25±0.10° towards $(11\bar{2}0)$ were positioned centrally in the reaction chamber alongside Si(100) pieces. 500 PEALD cycles were used for the growth of each film. Initial ALD growth parameters were taken from Shih *et al.*[890], in which saturated growth and linear growth per cycle was found using 0.1 s TEGa dose time and 5 s O_2 plasma exposure.

Each PEALD cycle for the varying temperature series consisted of: 0.1s TEGa dose with 100sccm Ar carrier gas / 5 s, 100 sccm Ar purge / 3 s, 20 sccm O_2 + 5 sccm Ar flow stabilisation / 5 s, 300 W, 20 sccm O_2 + 5 sccm Ar plasma / 5 s, 100sccm Ar purge. The substrates temperatures used were 120°C, 150°C and then increasing 50°C increments up to 450°C.

The PEALD cycles for the series with varying O_2 flow consisted of: 0.1s TEGa dose with 100 sccm Ar carrier gas / 5 s, 100 sccm Ar purge / 3 s, O_2 + 5 sccm Ar flow stabilisation / 5 s, 300 W, O_2 + 5 sccm Ar plasma / 5 s, 100 sccm Ar purge. The O_2 flows used during the flow stabilisation and plasma steps were 10 sccm, 20 sccm, 40 sccm, 60 sccm and 100 sccm, whilst the substrate temperature was kept constant at 250°C.

In the final, variable plasma power series, each PEALD cycle used: 0.1s TEGa dose with 100 sccm Ar carrier gas / 5 s, 100 sccm Ar purge / 3 s, 20 sccm O_2 + 5 sccm Ar flow stabilisation / 5 s, 20 sccm O_2 + 5 sccm Ar plasma / 5 s, 100 sccm Ar purge. Substrate temperatures were similarly kept at 250°C while the plasma powers used in each cycle were chose to be 25 W, 50 W, 100 W, 200 W and 300 W respectively.

The base pressure in the chamber (with no process gases flowing) was found to be approximately 10 mTorr. During the deposition processes the chamber pressure varied between 80 mTorr (during the plasma steps) and 160 mTorr (during the TEGa dose).

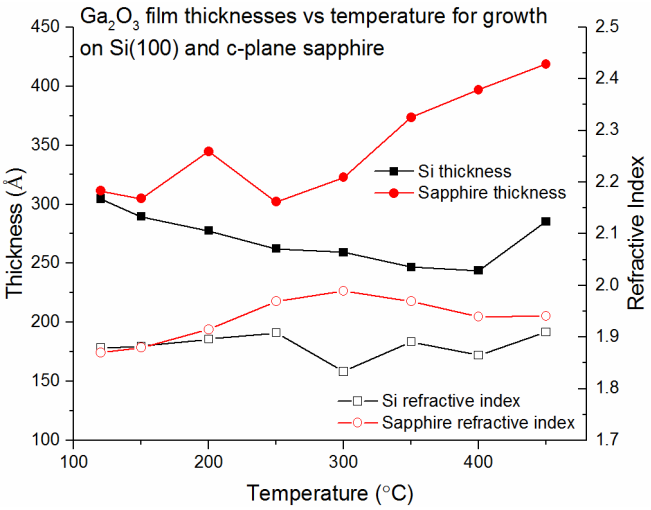

Figure 6.17 - Ga_2O_3 film thicknesses and refractive indices (at 632nm) against substrate temperature during growth

Figure 6.17 shows the results from fitting of spectroscopic ellipsometry data for Ga_2O_3 films grown on the sapphire and Si substrates against increasing substrate temperatures. The ellipsometry data is fitted with a Ga_2O_3 based Cauchy model, based on that found in ref.

[412]. For the films deposited on sapphire, average values from the three samples used in each run are shown. Standard deviations for the thickness and refractive index values were calculated to be 18 Å and 0.01, respectively. At 120°C, films grown on both the sapphire and Si substrates showed similar thicknesses and refractive indices at 30 nm and 1.89 respectively. With increasing substrate temperature, the films grown on Si showed a near linear decrease in thickness to a minimum of 25 nm at 400°C, while the refractive index of the films remained fairly constant. Growth rates determined from ellipsometry were found to range from 0.61 Å/cycle at 120°C to 0.49 Å/cycle at 400°C. The thickness for the films grown on Si at 450°C showed a marked increase compared to the thickness at 400°C which may indicate the decomposition of TEGa molecules in the reactor chamber. All films grown on Si were found to be amorphous, in agreement with previous ALD studies by other groups[891], [892]. Films grown on sapphire substrates showed a different response to increasing substrate temperature. At temperatures of 150°C and below the film thicknesses were similar to those seen on the Si substrates. The x-ray diffractograms shown in Figure 6.18 demonstrated that that these films were amorphous, with no observable lattice plane peaks between 2θ values of 37° to 44°.

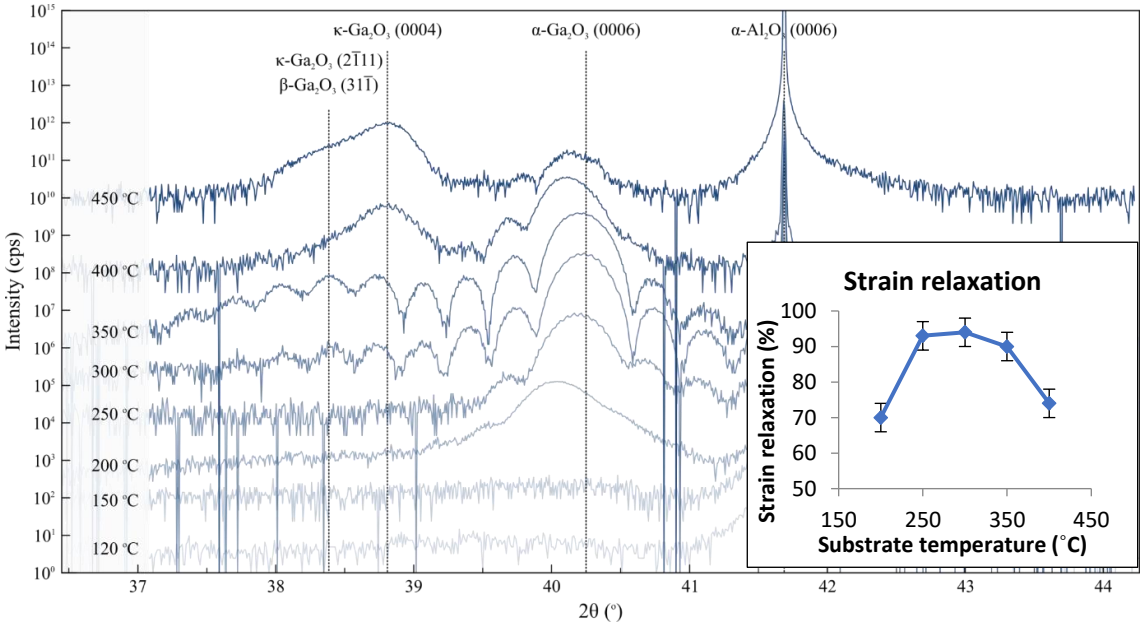

Figure 6.18 - XRD of Ga_2O_3 films grown on sapphire with varying substrate temperatures. INSET – strain relaxation calculated from the α-Ga_2O_3 (0006) peak

At 200°C a spike in the growth rate was observed, corresponding with the appearance of a strained α-Ga_2O_3 (0006) peak. Between 200°C and 300°C the growth rate dropped back to around 0.62Å/cycle and the α-Ga_2O_3 (0006) peak approached a more strain-relaxed value, as shown in the inset of Figure 6.18. At 350°C and above, XRD showed the appearance of

two peaks at lower 2θ values, corresponding to κ-Ga_2O_3 (0004) and κ-Ga_2O_3 $(2\bar{1}11)$ or β-Ga_2O_3 $(31\bar{1})$. There is also a decrease in the relative strength of the α-Ga_2O_3 peak and an increase in its associated strain. The thickness of the films increased significantly, reaching a maximum growth rate of 0.84Å/cycle at 450°C. The XRD peaks seen in Figure 6.18 are well-correlate with the refractive indices calculated from the ellipsometry data. The low temperature films (120°C to 200°C) show values around 1.9, corresponding to the amorphous phase[413], [890]–[892], medium temperature films (250°C to 350°C) show values approaching 2.0 which can be attributed to the higher refractive index of α-Ga_2O_3[893]–[895], whilst the higher temperature films (400°C and 450°C) show intermediate refractive index values of around 1.95, in agreement with values found by other groups for β-Ga_2O_3[412], [892], [893], [895]–[898].

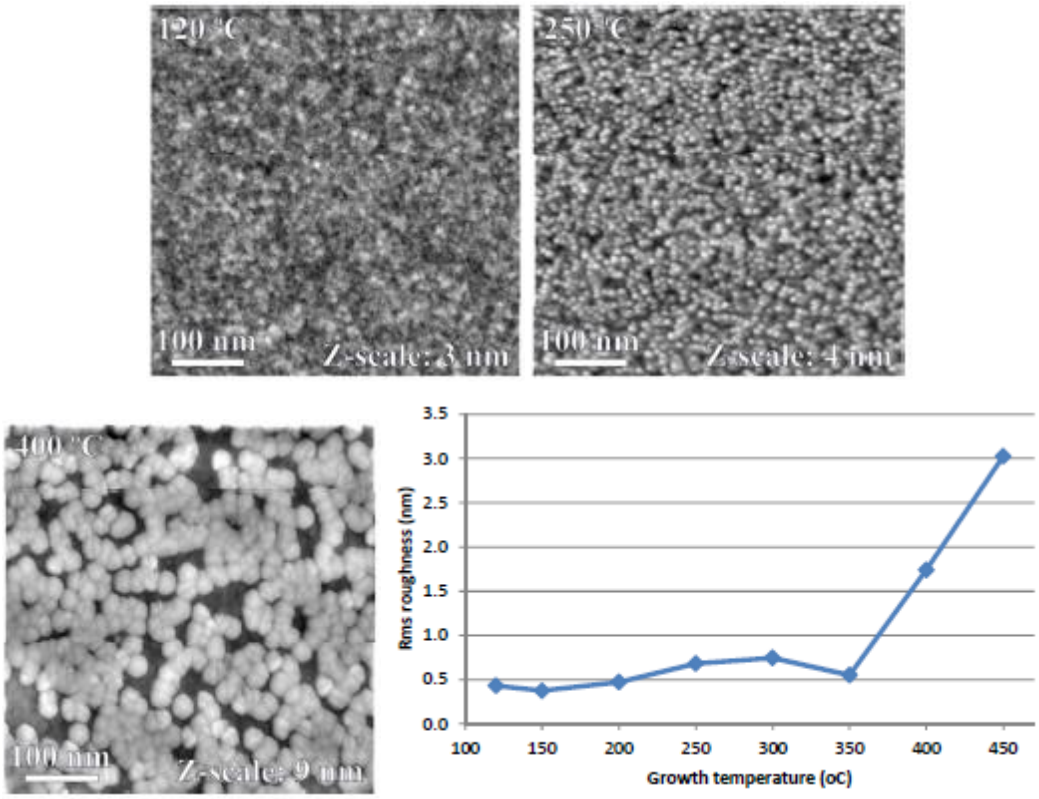

Figure 6.19 - Selected AFM images showing (a) Amorphous Ga_2O_3 film surface grown at 120°C, (b) α-Ga_2O_3 film surface grown at 250°C, (c) mixed β- κ-Ga2O3 film surface grown at 400°C and (d) RMS roughness vs growth temperature. (a) – (c) images shown are 1μm x 1μm.

Figure 6.19 shows selected AFM images of Ga_2O_3 films grown at 120°C, 250°C and 400°C. At 150°C and below, the AFM results show an amorphous surface with no apparent structure and RMS roughness values below 0.5nm, indicating a very uniform, conformal deposition, consistent with an amorphous film as observed by XRD. Between 200°C and 350°C, the

films show a small increase in roughness (to between 0.5nm and 0.7 nm), likely due to the formation of crystallites, confirmed by the presence of grain-like structures of the order of around 10 nm. The RMS roughnesses are measured over a 0.5 µm x 0.5 µm area. In previous work investigating the structure of 130 nm thick Ga_2O_3 films, it was observed by scanning electron diffraction that the structure of the 70 nm of Ga_2O_3 material adjacent to the substrate was dominated by α-phase columns with a diameter of 2-23nm[899]. The grain-like structures observed here by AFM thus, likely correspond to the upper-most surface of the α-Ga_2O_3 columns. Above 350°C, the surface roughness increases dramatically by one order of magnitude up to a maximum of 3.0 nm at 450°C. The surface of the films at these temperatures is dominated by larger, less densely packed circular features approximately 30 nm across and 5 nm high for the sample grown at 400°C and 45 nm across and 8 nm high for the sample grown at 450°C. Given that these large features appear in the samples where multiple phase cohabit, as shown in Figure 6.18, and increase in size with temperature, it may be reasonable to assume that these correspond to grains in the ε- or β-phase (rather than the α-phase).

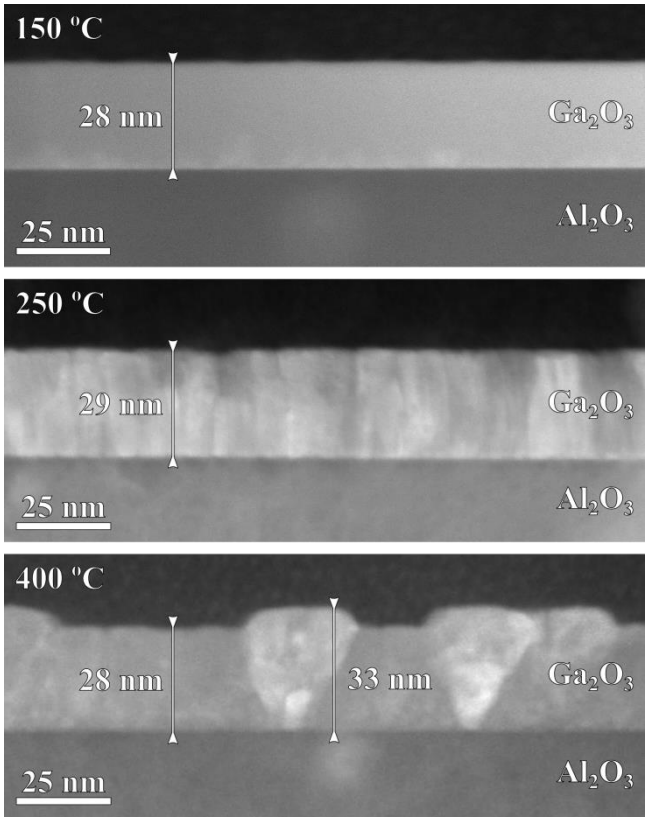

Figure 6.20 – Cross sectional TEM images for Ga_2O_3 films grown on sapphire. Top – Amorphous Ga_2O_3 grown at 150°C, Middle – α-Ga_2O_3 grown at 250°C, Bottom – Mixed phase Ga_2O_3 film grown at 400°C

Figure 6.20 shows cross sectional TEM images of Ga_2O_3 films grown on mis-cut c-plane sapphire. The images shown display representative cross sections of the Ga_2O_3 films grown

at various temperatures (150°C, 250°C and 400°C). As can be seen, the top film grown at 150 °C shows a uniform contrast, indicating its amorphous nature, and a smooth upper surface. The TEM image is in agreement with both the XRD (showing no Ga_2O_3 peaks) and the AFM data, which shows an average surface roughness of below 0.5nm. The middle image shows Ga_2O_3 grown at 250°C. Distinct columns of crystalline Ga_2O_3 can be seen running through the full thickness of the films. Comparison with Figure 6.18, indicates that the dominant phase is α-Ga_2O_3 while the lack of a distinct β- or other Ga_2O_3 polymorph peaks indicates that the secondary phase is amorphous. It can be seen that, in comparison with the top image, there is a slight increase in surface roughness brought about by the grain boundaries where neighbouring α-Ga_2O_3 columns touch. This is also in agreement with the AFM data from Figure 6.19. The bottom image shows a cross section of the Ga_2O_3 film grown at 400°C. The morphology of the film is different to the first two images with large, widely-spaced, triangular crystallites visible, and the space between them filled with seemingly amorphous regions. From the XRD in Figure 6.18, these can be identified as β-Ga_2O_3 crystallites. The surface roughness of the film, obtained from Figure 6.19, is an order of magnitude higher than that of the lower deposition temperatures and can be explained by a difference in growth rate between the apparently amorphous region and β-phases, with the β-phase growth higher than that of the amorphous material, once it has nucleated. For the growth temperatures shown here, the thicknesses measured by TEM (28 nm and 29 nm) are in agreement with those calculated from the spectroscopic ellipsometry model (~30nm ±10%). For the higher temperature film, the ellipsometry calculated thickness are inconsistent with that seen by TEM, beyond the normal expected error. This shows a deficiency in the ellipsometric model used. This discrepancy is likely due to a combination of the assumption of zero surface roughness in the ellipsometry model and the differences in the optical properties of the two phases present in the real film, whereas the model assumes a uniform single-phase film.

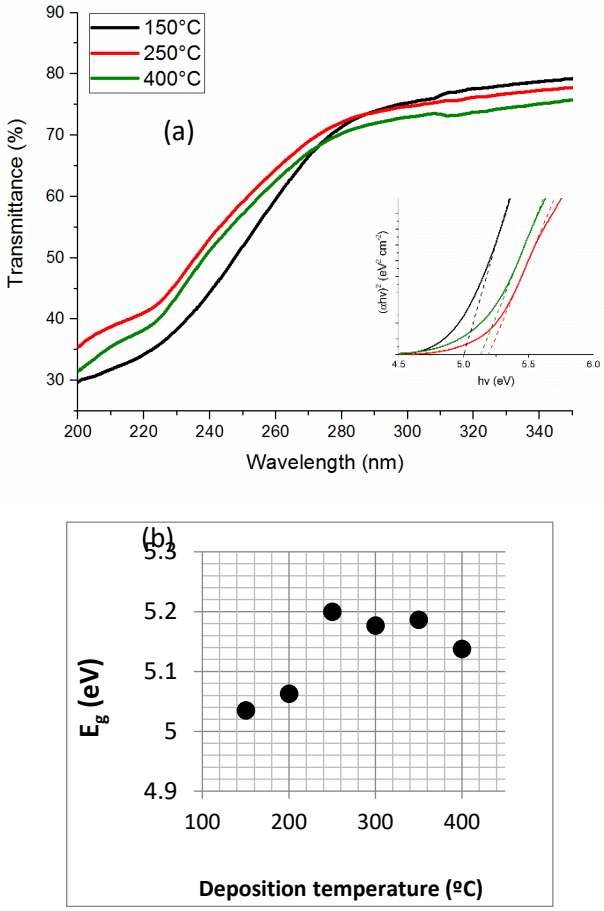

Figure 6.21 - (a) UV-vis transmittance for selected Ga_2O_3 films grown on sapphire (INSET – Tauc plot) and (b) Optical bandgaps for Ga_2O_3 films calculated from (a), assuming indirect bandgap.

Figure 6.21(a) shows the transmittance against wavelength for Ga_2O_3 films grown on sapphire. In the visible range, all films showed similar transmittances at around 80%. The amorphous films grown at 150°C and below show the lowest UV transmittance of the films considered. Beginning at around 280 nm the transmittance decreases smoothly reaching 40% at approximately 240 nm. The mixed β-Ga_2O_3 films showed the next lowest transmittance with the decrease starting around 270 nm and reaching 40% at around 230 nm. The α-Ga_2O_3 films show the best deep-UV transmittance. The decrease starts at the same wavelength as seen in the β-phase films but reaches 40% transmittance at a shorter wavelength, approximately 220 nm. The transmittance plots for both the 250°C and 400°C films show changes in the rate of decrease of transmittance at roughly 240 nm and 225 nm whilst there is a further change in the gradient at 210 nm for the 400°C film and another at close to 200 nm for the 250°C film. These changes in gradient may indicate that either the films are mixed-phase, and that each of the slopes corresponds to the band structure of each of the phases present. This would be plausible for the films grown at 400°C, where the

XRD data shown in Figure 6.18 confirmed that there are at least 3 Ga_2O_3 phases present. However, the XRD data also shows that the film grown at 250°C consists of α-Ga_2O_3, with no other peaks visible, similarly no second phase is observed in the TEM image in Figure 6.20. The changes in gradient seen here in Figure 6.21 appear to occur at very similar values, indicating that the origin is likely the same for both films. This would rule out the "multiple-phases" interpretation. Another possibility is that the changes in gradient are caused by the poly-crystallinity of the films. Incoherent or semi-coherent grain boundaries can introduce significant numbers of trap states into the bandgap, thus changing its apparent value. The TEM data in Figure 6.20 confirms that the films grown above 200°C are polycrystalline.

Many studies on monoclinic β-Ga_2O_3 use the assumption of a direct bandgap material[415], [891], [897], [900], [901]. This is strictly incorrect, as the fundamental bandgap (located on the I-L line in reciprocal-space) is indirect with a magnitude of 4.84eV, according to DFT simulations and experimental results by other groups. However, several studies have also shown that the direct bandgap (located at Γ) is only 0.04eV larger, with a bandgap of 4.88eV [877], [902], [903]. In this work, the direct bandgap assumption is used, due to the small difference between the two. The inset in Figure 6.21(a) shows a Tauc plot for the same films, assuming a direct band gap, from which the bandgaps can be obtained by linear extrapolation to the baseline.

Investigations of the band structure of α-Ga_2O_3 are less common than those on β-Ga_2O_3, which may be due to the lack of high quality single crystals of the material. Several reports do exist however. Choi *et al.*, simulated doping of various materials into α-Ga_2O_3 using HSE and found that for the undoped oxide, the bandgap was indirect with a value of 4.70 eV, whilst the nearest direct bandgap was 0.21 eV higher at 4.91eV [904].

Figure 6.21(b) shows the calculated optical bandgaps of the deposited films against deposition temperature. The observed bandgaps match well with the previous data, with the lower temperature amorphous films showing bandgaps at around 5.05eV, the α-Ga_2O_3 films (250°C-350°C) showing bandgaps closer to 5.2eV and the mixed β-film showing an intermediate bandgap of approximately 5.15eV. The band gaps of each phase are largely in good agreement with previously reported values[395], [905]. The nature of the band gaps is further complicated as there is considerable asymmetries in the band structure of the Ga_2O_3 phases.

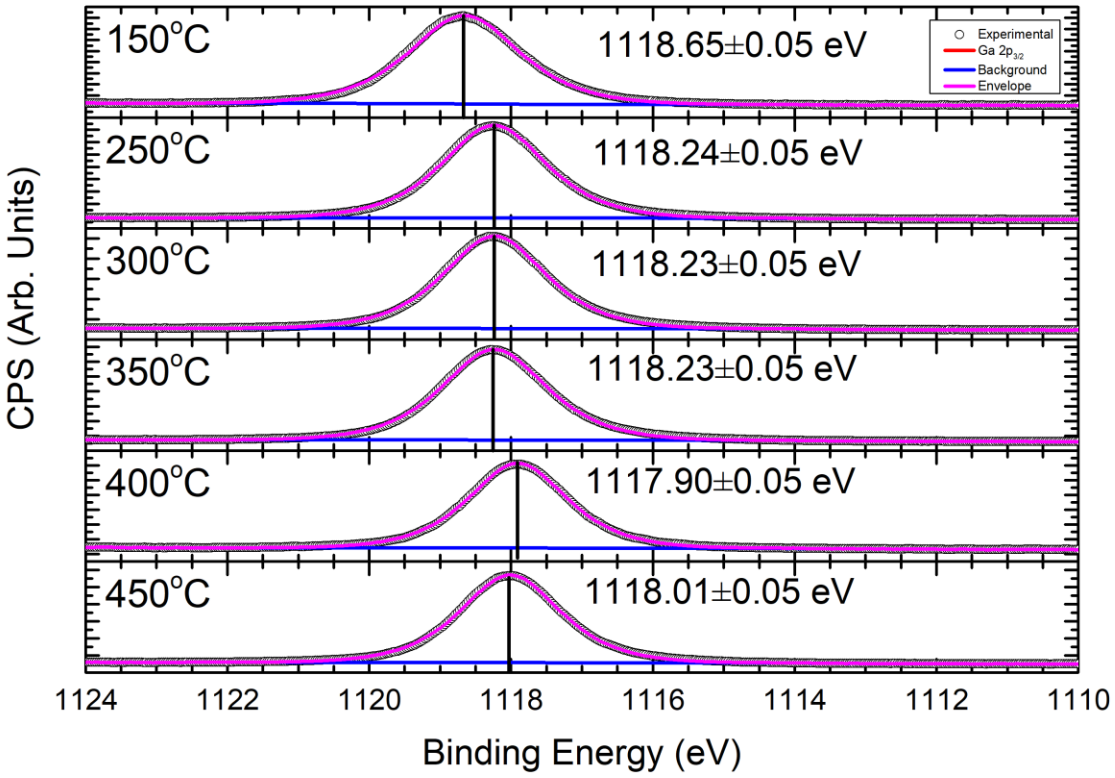

Figure 6.22 – Ga $2p_{3/2}$ core-levels for the samples synthesised between 150°C and 450°C

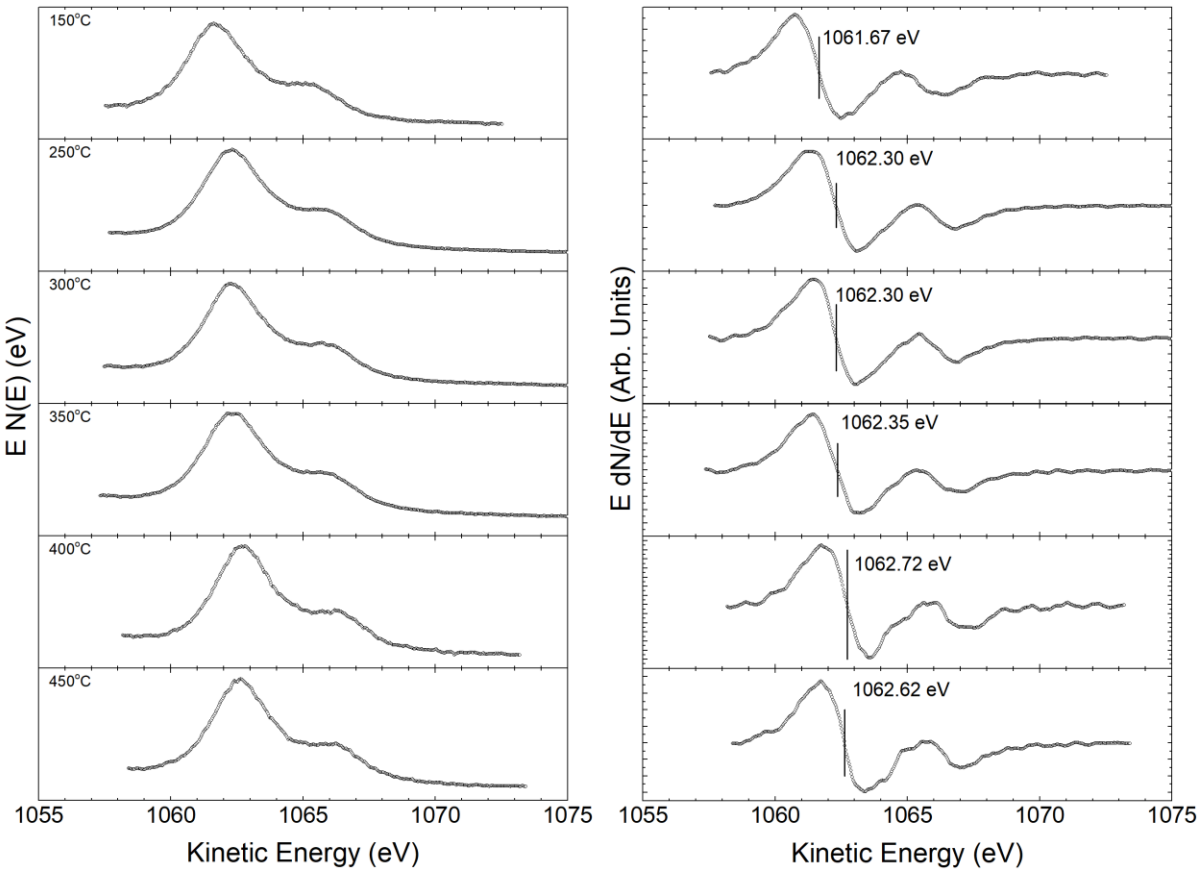

Figure 6.23 - This Figure shows the Ga $L_3M_{45}M_{45}$ Auger peaks for the synthesised Ga_2O_3 samples.

Figure 6.22 shows the Ga $2p_{3/2}$ core-level whilst Figure 6.23 shows the Ga $L_3M_{45}M_{45}$ Auger feature for the various Ga_2O_3 samples. As the peak is clearly asymmetric due to the nature of the Auger process, the energy of the Auger feature is found by numerically differentiating the line shape and multiplying the resulting shape by the kinetic energy. A linear fit can then be used to find the point at which the curve intercepts the x-axis. This point necessarily coincides with the maximum of the Auger feature; hence, the kinetic energy of the x-intercept is used as the position of the Auger peak.

Substrate Temperature (°C)	Ga $2p_{3/2}$ Binding Energy (eV)	Ga $L_3M_{45}M_{45}$ Kinetic Energy (eV)	Modified Auger Parameter (eV)
150	1118.65	1061.67	2180.32
250	1118.24	1062.30	2180.54
300	1118.23	1062.30	2180.53
350	1118.23	1062.35	2180.58
400	1117.90	1062.72	2180.62
450	1118.01	1062.62	2180.63
β-Ga_2O_3 single crystal	1118.00	1062.87	2180.87
Ga (Elemental)[906]	1116.3±0.2	1068.3	2184.6
Ga_2O_3[906]	1118.1±0.2	1062.6	2180.7

Table 6.3 - This table shows the Ga $2p_{3/2}$ binding energy, the kinetic energy of the Ga $L_3M_{45}M_{45}$ Auger peak, and the resulting modified Auger parameter for these peaks.

Table 6.3 shows the modified Auger parameter of the samples considered in this section alongside literature values for elemental Ga and Ga_2O_3 from Schön[906]. The modified Auger parameter for the samples deposited between $250 - 350$ °C are consistent with each other, and in the diffractograms shown in Figure 6.18 exhibit strong α-Ga_2O_3 (0006) peaks. The modified Auger parameter found for the sample deposited at 350 °C is slightly increased compared to those at 250 °C and 300 °C, which is due to the presence of secondary polymorphs within the sample as seen in the XRD data. With further increasing temperatures, the modified Auger parameter increases further, towards the value obtained for β-Ga_2O_3. The modified Auger parameter does not actually reach this value however, due to the continued presence of the α and other polymorphs. Here we can clearly see that the modified Auger parameter is dependent on the polymorph of the sample, despite the fact that the chemical states of the Ga and O ions are nominally the same, hence the Auger parameter could be used to determine the dominant polymorph of a Ga_2O_3 sample.

Elemental Ga was not measured as part of the work contained within this thesis as the system used did not have a cooled sample stage, required due to the low melting point of elemental Ga. However, as both the binding energy of the Ga $2p_{3/2}$ and the Auger parameter measured for Ga_2O_3 presented by Schön[906], are consistent with that measured for the β-Ga_2O_3 single crystal, it is reasonable to assume that similar values would be obtained for elemental Ga as those given by Schön[906]. Hence, the elemental values can be used to obtain the shifts in the photoelectron binding energy, the Auger electron kinetic energy and the initial state contributions and the relaxation energies for the samples considered here using the equations given in section 2.3.1.4. These values are presented in Table 6.4.

Substrate Temp (°C)	ΔE_b (eV)	ΔE_k (eV)	$\Delta\alpha'$ (eV)	$\Delta\varepsilon$ (eV)	ΔR (eV)
Ga Elemental[906]	0	0	0	0	0
Ga_2O_3[906]	1.8	-5.7	-3.9	0.15	-1.95
β-Ga_2O_3 single crystal	1.7	-5.43	-3.73	0.165	-1.865
150	2.35	-6.63	-4.28	-0.21	-2.14
250	1.94	-6	-4.06	0.09	-2.03
300	1.93	-6	-4.07	0.105	-2.035
350	1.93	-5.95	-4.02	0.08	-2.01
400	1.6	-5.58	-3.98	0.39	-1.99
450	1.71	-5.68	-3.97	0.275	-1.985

Table 6.4 - This table shows the differences in binding energies of the Ga $2p_{3/2}$ core-levels, the Auger electron kinetic energies and the modified Auger parameters. Also shown are the calculated differences in the initial state contributions and the relaxation energies for each sample. The values are referenced to those given for elemental Ga by Schön[906].

Thus, it is observed that the relaxation energies of the crystalline samples only vary by approximately 0.1 eV. Instead, most of the difference between the samples is due to the initial state effects, likely due to the different co-ordinations and bond lengths of the ions in each sample.

Figure 6.24 shows the bandgaps of films grown at 150°C, 250°C, 300°C, 350°C, 400°C and 450°C, measured from composite data obtained by XPS-IPES. The left of each graph (below 0 eV) shows the XPS scans at energies close to the Fermi level (at 0 eV), whilst to the right of the fermi level, the IPES data is presented. A natural question to ask is why do the band gaps obtained from XPS-IPES shown in Figure 6.24 and UV-Vis spectrometry, shown in Figure 6.21 disagree by so much? Several possible effects are plausible: firstly, the XPS-IPES gap necessarily probes the electronic gap, rather than optical gap, thus it is sensitive to any

dipole-forbidden transitions that may be present, whereas UV-Vis will probe the optical gap; Secondly, XPS-IPES will find the surface band gap, thus if there is downwards band bending with a quantised accumulation layer, the band extrema may be bent by different amounts, resulting in a surface band gap smaller than the bulk band gap[907]; thirdly, similarly to what was observed for the β-Ga_2O_3 phase above, the other phases observed here, may similarly have a rapid onset of the valence band, and thus the linear extrapolation method would underestimate the VBM-FL separation, resulting in a smaller band gap; finally, the density of states close to the CBM may be small, and hence the optical transitions from the VBM to the CBM may have a relatively small cross-section.

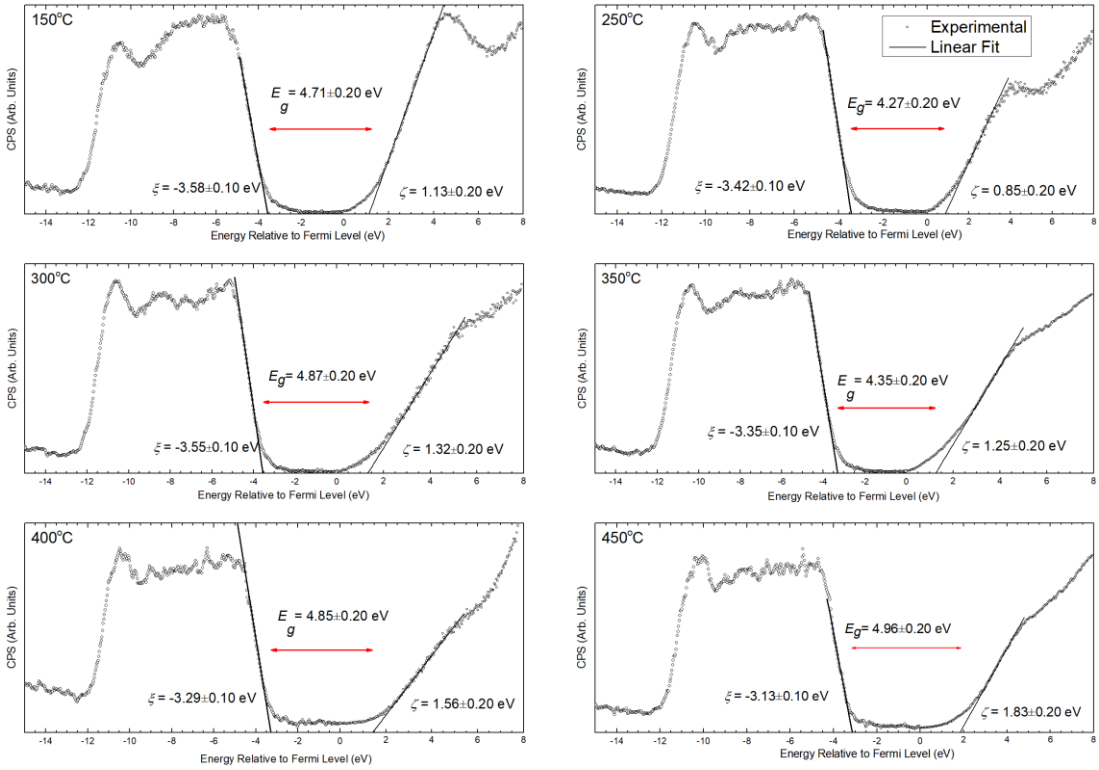

Figure 6.24 - XPS-IPES bandgaps for (A) amorphous Ga_2O_3 on sapphire grown at 150°C, (B) α-Ga_2O_3 grown on sapphire at 250°C, (C) α-Ga_2O_3 grown on sapphire at 300°C, (D) α-Ga_2O_3 grown on sapphire at 350°C, (E) α-Ga_2O_3 grown on sapphire at 400°C, and (F) α-Ga_2O_3 grown on sapphire at 450°C,

The first explanation, cannot be discounted, however, there are no reports of a dipole-forbidden band gap for α-Ga_2O_3, unlike In_2O_3. The second explanation, is unlikely as the VBM-FL separations reported in Figure 6.24 are consistent with a surface depletion layer, even if the experimental broadening of the valence band is accounted for. The samples also required the use of a low-energy electron flood gun to compensate the charge lost through the photoemission process, whereas, had surface accumulation been present, the charge lost would have been replenished through the upper contact.

To test the third and fourth explanations requires looking at the densities of states close to the valence and conduction band extrema. Figure 6.25 shows the partial and total density of states for a bulk α-Ga_2O_3 single crystal[908], from which two clear features of interest can be seen: firstly, the onset of the valence band is rapid as in β-Ga_2O_3; secondly the density of states near the conduction band maximum is small, thus both the third and fourth explanations of the increased band gap from optical measurements compared to photoemission are plausible. In fact, DFT calculations suggest that the rapid onset of the valence band and the low density of states close to the CBM are properties of all known crystalline phases of Ga_2O_3[909].

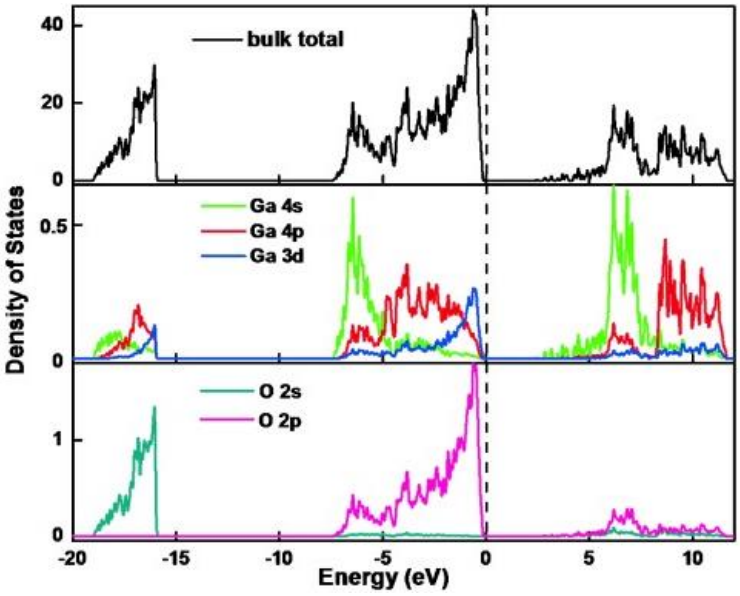

Figure 6.25 – PDoS and Total DoS of the valence and conduction bands of α-Ga_2O_3. Reproduced with permission from Ref. [908]*, Copyright 2014, Wiley-VCH Verlag GmbH & Co.*

Thus, linear extrapolation of the leading edge of the valence band will underestimate the VBM-FL separation, as in β-Ga_2O_3 and In_2O_3, whereas optical methods are sensitive to the joint matrix element between the DoS close to the VBM and CBM, which are small. Hence, with an already low-probability transition due to the indirect-nature of the gap[909], optical methods may in fact overestimate the band gap, particularly where a direct band gap is assumed.

6.3 Summary and Conclusions

This chapter began by considering the question of whether the transparent conducting oxide β-Ga_2O_3 single crystals exhibit charge accumulation or depletion at the vacuum interface, as previous literature has only reported depletion, despite the fact that the other related TCOs all show accumulation, at least under some conditions.

We find that, in fact, due to the sharp onset of the density of states at the top of the valence band, most previous authors have misinterpreted their data, causing linear their extrapolation of the valence band edge to underestimate the valence band maximum to Fermi level separation by approximately 0.6 eV. In contrast, by considering the orbital-resolved density of states predicted by first principle calculations, and broadening them by experimental parameters, we obtain a VBM-Fermi level separation consistent with electron accumulation at the surface. Intriguingly, even after correction for the photoionisation cross sections of each orbital, it is found that although the binding energy positions of the features in the valence band align, the intensities of the features disagree significantly.

The observation of surface accumulation is supported by the possible observation of weak conduction band emission in HAXPES data. ARPES data from the literature observes the valence band edge occurring at a similar value as that obtained by our lab-based XPS, which further supports our findings. Surface electron accumulation also explains properties such as the oxygen sensitivity of Ga_2O_3 gas sensors, which is shown by in *in situ* exposure of the annealed single crystal to oxygen. The presence of surface accumulation is then explained by considering the band positions relative to the vacuum level, alongside those of several other single crystal TCOs.

The second part of this chapter then discusses the growth and characterisation of epitaxial films of Ga_2O_3 grown on single crystal Al_2O_3 ingots. At temperatures between $250 - 350$ ℃, the α polymorph is found, below this range, the film is amorphous whereas for temperatures above 350 ℃, there are multiple polymorphs present. From this, it is shown that the crystal polymorph of Ga_2O_3 can be obtained by considering the modified Auger parameter, α'.

Similar to the β-polymorph, it is also demonstrated that linear extrapolation of the valence band edge to determine the VBM-FL separation for α-Ga_2O_3 is inappropriate, due to the sharp onset of the valence band. The valence band structure of other polymorphs of Ga_2O_3 also have sharp onsets, suggesting that for all crystalline forms of Ga_2O_3, the VBM-FL separation will be underestimated by the linear extrapolation method. Instead, convoluting the cross-section corrected DFT density of states with Gaussian and Lorentzian functions, representing the experimental broadening, should be used to evaluate the VBM-FL separation.

In the next chapter, we will review the conclusions of this thesis and discuss the future of kesterite photovoltaics.

7 CONCLUSIONS AND FURTHER DISCUSSIONS

In this chapter, we collate the findings distributed throughout the thesis. We then use these findings to suggest a potential route to commercially-viable, kesterite-based photovoltaics.

7.1 CHAPTER SUMMARIES

Each chapter has considered a different aspect of the kesterite photovoltaic cell. Band alignments, and interfaces were found to have a considerable impact upon the ultimate efficiency achieved by the photovoltaic device.

7.1.1 Chapter 3

In Chapter 3, kesterite materials are synthesised by two different synthetic routes. Characterisation of sputtered kesterite materials is described, before and after sulphurisation in a closed-space sublimation chamber. Considerable variations of the surface composition are observed by x-ray photoelectron spectroscopy, which can be explained by the different vapour pressures of the composite elements.

The photoelectron spectroscopy of thin-films of CZTS and CZTSSe synthesised from nanoparticle inks is described. The band alignments of the characterised materials with ZnO, ZnS, ZnSe, SnS_2 and In_2S_3 are determined using the Anderson electron affinity rule. It is shown that CdS is a poor material choice for a buffer layer as the conduction band offset is found to be cliff-like. Of the other materials considered, In_2S_3 is found to be the most ideal absorber, resulting in a spike-like, positive conduction band offset, which is sufficiently small to allow excitation above the potential barrier. ZnS and SnS_2 are also found to be potentially interesting alternative buffer materials for kesterite photovoltaics.

7.1.2 Chapter 4

In Chapter 4, we consider the band alignments of ZnO/CdS/CZTSSe and ZnO/In_2S_3/CZTSSe device-like stacks, by the Kraut method and compared to the results of the previous chapter, as the Anderson electron affinity rule fails to account for surface states or band bending at the interface. The band alignments of the absorber/buffer interface are found to be cliff-like and spike-like in agreement with the previous chapter.

The experimental band alignments as determined in Chapter 4 are then used in conjunction with the SCAPS software to investigate the effect of the alignments upon the simulated

device efficiency. The open-circuit voltage deficit of both simulated devices if found to be less than that of the record CZTSSe device, with the open-circuit voltage of the device with an In_2S_3 buffer layer being larger than that of the record CIGS device. Thus, changing the buffer layer used will likely have a considerable beneficial effect on the open-circuit voltage deficit observed in kesterite photovoltaics. The simulated device with an In_2S_3 buffer layer shows improved device statistics compared to that with a CdS buffer layer, consistent with what would be expected from the band alignment. The role of the *i*-ZnO layer in the record CZTSSe device is also discussed.

7.1.3 Chapter 5

In Chapter 5, the effect of the MoX_2 layer at the back contact was investigated by Ar^+ ion etching of monocrystalline samples. With increasing ion doses, MoS_2 and $MoSe_2$ are found to become more *p*-type in nature, as identified by the relative change of the core-level binding energies. This is explained as the effect of increasing densities of chalcogen vacancies.

In contrast $MoTe_2$ is found to become more *n*-type with increasing ion dosages, in contrast to what is observed for MoS_2 and $MoSe_2$. Also observed is a second Te component, at higher binding energy relative to that due to $MoTe_2$, which is identified as metallic Te. In STM studies of $MoTe_2$, adsorbed Te is found to result in *n*-type doping of $MoTe_2$, thus the increasing *n*-type nature of the $MoTe_2$ multilayer after etching is found to be due to the formation of metallic Te regions within the multilayer.

Hence, to avoid the formation of high-quality, *n*-type MoX_2 layers at the back contact of photovoltaics devices, deposition should be performed under chalcogen-poor conditions. For kesterite thin-films, deposition is almost always a two-step process, the second of which is an anneal in a chalcogen-rich environment. Thus, the $Mo(S,Se)_2$ layer in kesterite devices is almost always *n*-type. In contrast, CdTe deposition is usually a single-step process, with no anneal in a Te-rich environment. Therefore, the $MoTe_2$ layer would typically be low-quality and *p*-type, thus explaining why it does not have the same effect as $Mo(S,Se)_2$ does in kesterite photovoltaics. Further research is, however, required to fully understand the nature of elemental vacancies in this interesting class of materials.

7.1.4 Chapter 6

In Chapter 6, the final layer of a photovoltaic device, the window layer, is investigated by considering the properties of an alternative transparent conducting oxide, Ga_2O_3.

The chapter began by considering the surface properties of a β-Ga_2O_3 single crystal with $(\bar{2}01)$ surface termination. We show through a combination of XPS, HAXPES and calculations that, contrary to previous reports, Ga_2O_3, exhibits charge accumulation at the vacuum interface, rather than depletion as previously reported. For other TCOs, accumulation has frequently been reported. It is shown that the previous reports of depletion are based on a misinterpretation of the experimental data, due to the linear extrapolation of the valence band leading edge. In contrast, when alignment with the broadened, cross-section corrected densities of states obtained from density functional theory, a considerably larger valence band to Fermi level separation is obtained, resulting in charge accumulation.

The second part of the chapter considered the photoemission spectroscopy of epitaxial Ga_2O_3 thin-films deposited on sapphire. At very low temperatures, the films are found to be amorphous in nature, whereas at high-temperatures multiple polymorphs are observed. However, at intermediate temperatures, phase-pure α-Ga_2O_3 is produced. It is thus shown that the modified Auger parameter can be used to determine the phase of Ga_2O_3 present.

7.2 The Future of Kesterite Photovoltaics

In this final chapter, we have identified numerous issues that limit the efficiency of kesterite-based photovoltaics, So, how are they going to reach the 15% or so efficiency required to become commercially viable?

Due to the difficulty in synthesising high-quality kesterite absorber layers from one-step processes, device synthesis will likely still require a high temperature anneal in a chalcogen-rich atmosphere, which will lead to the formation of a *n*-type MoX_2 layer, resulting in a diode opposed to the main photodiode. Thus, high-efficiency devices will likely require the insertion of a thin chalcogen diffusion barrier, such as Al_2O_3 between the absorber and the back-contact, to limit the formation of the MoX_2 layer. The thickness of this layer will have to be of the order of 1 nm, to allow the holes to tunnel through efficiently. Otherwise an alternative, less reactive, high work-function back-contact, such as MoO_3 could be used.

The absorber layer itself may be composed of multiple alloy systems to inhibit the formation of so-called ‘killer’ defects, (Ag,Cu), (Cd,Zn) or (M,Zn) alloys could be used to prevent these defects, where M is one of a number of transition metals.

Alternative buffer layers are likely to offer a significant improvement in efficiencies, even though the efficiencies have been relatively poor to date. The poor efficiency is likely due

to the comparably poor understanding of the deposition of the alternative layer compared to CdS, which has been widely adopted for CIGS- and CdTe-based photovoltaics. These alternative buffer layers are likely to be Zn-chalcogenides, SnS_2 or In_2S_3 due to the positive conduction band offsets these are likely to give. Although In would still be used in the case of In_2S_3, the thickness of the buffer layer is small compared to the absorber and window layers, thus the cost of implementation is relatively small.

The choice of window layer is limited by the materials with sufficiently large band gaps and dopability. The current standards are fluorine-doped tin dioxide (FTO), tin-doped indium oxide (ITO) and aluminium-doped zinc oxide (AZO). However, each has considerable issues: in the case of FTO, the dopant is self-compensating, which limits the maximum achievable carrier density; with ITO, the main component of the TCO (In) is scarce and expensive due other technological applications; and AZO is not of particular interest to industry due to the difficulty of making ohmic contacts. Thus, an alternative TCO is likely to be required. These may be produced from existing dopants such as in molybdenum-doped indium oxide (IMO), or from oxides with an alternative cation such as CdO, TiO_2 or Ga_2O_3. An alternative would be a high-mobility 2D material such as graphene, however this is also limited by the difficulty of synthesising large, high quality sheets of the material.

Hence, the kesterites can still be considered a promising, earth-abundant, non-toxic materials for photovoltaics. Several potential avenues of research for improving the efficiency of kesterite-based photovoltaics have been identified, however considerable effort (and funding) is likely to be required for kesterite-based photovoltaics to become commercially viable. This effort and funding should be invested due to the sheer environmental and societal necessity to develop carbon-neutral forms of energy.

8 APPENDIX A

```
%Define and input for constants

h=6.626069e-34; %Planck constant in SI units
hbar=h/(2*pi); %Reduced Planck constant in SI units
m_e=9.109382e-31; %Electron rest mass in kg
c=299792451; %Speed of light
bman=8.61733e-5;  %Boltzmann Constant in ints of eV/K
q=1.602e-19; % Electron charge
n=1; %Counting variable
bmanSI=1.38064e-23; %Boltzmann constant in SI units
AM=1e-10; %Conversion between angstroms and metres
m = 0.28; %input('Enter the ratio of the effective mass of the charge carrier to the free electron rest mass: ');
%Set carrier effective mass
Eg = 4.63; %('Enter the bandgap of the material in units of electronvolts: '); %Set carrier band gap
kmax = 0.2; %input('Enter the maximum magnitude of the wavevector in 1/Angstroms: ');% Set maximum value
of k to be considered
temp= 273; %input('Enter the absolute temperature of the semiconductor: '); %Set temperature for Fermi-Dirac
distribution
num= 1000; % input('Enter the number of points to be considered when plotting: ');% Set the length of the
vector of k values
kmax=kmax/AM; %Convert 1/angstroms to 1/metres

%Band Structure Consideration
Emax=(hbar^2)*kmax^2/(2*m*m_e); %Sets maximum energy for axis
k=linspace(-1*kmax, kmax, num); %Set up k values to be plotted
E=(hbar^2)*k.^2/(2*m*m_e);  %Calculate Energy from wavevector
alpha=1/(q*Eg)*1/((1-m)^2); %Define alpha for alpha approximation
beta=-2/((q*Eg^2)); %Define beta (Not used)
Ea=(-1+sqrt(1+4*alpha.*E))/(2*alpha);%Energy value resulting from the positive root of the quadratic from the
alpha approximation
k=k*AM; %Convert wavevector back to 1/angstroms
E2=E/q; %Convert Energy from parabolic approximation to eV
E2a=Ea/q; %Convert Energy from alpha approximation to eV


fid = fopen('BandStructure.dat', 'w'); %Export data to external file
for i = 1:num
   fprintf(fid,'%d %d %d\n',k(i),E2(i),E2a(i)); %Prints the ith component of k,E2,E2a to the external file
end
fclose(fid);

figure %Figure 1
plot(k,E2,'k-',k,E2a,'b-')%Plot E vs wave vector
axis([-kmax*AM kmax*AM 0 Emax/q]) %Set values on axes
xlabel('Wave Vector (1/Å)') % Set title of x-axis
ylabel('Energy(eV)')   %Set title of y-axis
legend('Parabolic Approximation','\alpha -approximation','Location','north')
title('Band Diagram') %Title of graph


%Density of States Consideration


E=linspace(0, Emax, num); %Set up new variable for energy
g_E=q*1e-6*(8*pi*sqrt(2)/((h)^3))*((m*m_e)^(3/2)).*sqrt(E);%Density of States for simple quadratic case
g_Ea=q*1e-6*((1+2*alpha.*E)/((pi^2)*(hbar^2))).*sqrt(((2*m*m_e)/((hbar^2)))*E.*(1+alpha*E))*m*m_e;
%Density of states for alpha approximation
```

```
g_Eamax=q*1e-
6*((1+2*alpha.*Emax)/((pi^2)*(hbar^2))).*sqrt(((2*m*m_e)/((hbar^2))).*Emax.*(1+alpha*Emax))*m*m_e;%M
aximum value for DoS axis
E=E/q; %Convert energy to eV

fid = fopen('DOS.dat', 'w');%Output data to external file
for i = 1:num
   fprintf(fid,'%d %d %d\n',E(i),g_E(i),g_Ea(i));%Prints the ith component of E,g_E,g_Ea to the external file
end
fclose(fid);

figure %Figure 2
semilogy(E,g_E,'k-',E,g_Ea,'b-') %y-axis has a logarithmic scale
axis([0 Emax/q 0 g_Eamax]) %Set values on axes
xlabel('Energy (eV)') % Set title of x-axis
ylabel('Density of states (1/(cm^3 eV))')   %Set title of y-axis
legend('Parabolic Approximation','\alpha -approximation','Location','southeast')
title('Density of States vs Energy') %Title of graph


% Carrier Concentration Consideration
ni=linspace(0,0,num);
nia=linspace(0,0,num);
Efermi=linspace(-Emax/q,Emax/q,num); %Set up array for Fermi energies ranging from zero to Emax, since the
density of states is in units 1/(eV cm^3) the energy is in eV
for n=1:num
   Ef=Efermi(n); %Choose a Fermi energy from the array
   f_E=1./(exp((E-Ef)/(bman*temp))+1); %Fermi-Dirac Distribution
   fg_E=f_E.*g_E; %Fermi-Dirac x DoS Parabolic
   fg_Ea=f_E.*g_Ea; %Fermi-Dirac x DoS alpha
   ni(n)=trapz(E,fg_E);%Integrated with trapezium rule
   nia(n)=trapz(E,fg_Ea);%Integrated with trapezium rule
end
   g_Ejd=2e-6*(2*pi*m*m_e*bmanSI*temp/(h^2))^(3/2); %Effective DoS
   njd=linspace(0,g_Eamax,num); %Variable to find Fermi Energies
   Efjd=bman*temp.*(log(njd./g_Ejd)+(1/sqrt(8))*(njd./g_Ejd)-(3/16-sqrt(3)/9)*(njd./g_Ejd).^2); %Joyce-Dixon
Approximation for Degenerate semiconductors
   Efnd=bman*temp.*(log(njd./g_Ejd)); %Non-Degenerate semiconductors

figure %Figure 3
semilogy(Efermi,ni,'k-',Efermi,nia,'b-',Efjd,njd,'r-',Efnd,njd,'g-') %y-axis has a logarithmic scale
axis([-0.2*Emax/q Emax/q 1e16 g_Eamax]) %Set values on axes
xlabel('Fermi Energy (eV)') % Set title of x-axis
ylabel('Concentration of Carriers (1/(cm^3)')   %Set title of y-axis
legend('Parabolic Approximation','\alpha Approximation','Joyce-Dixon Approximation','Non-Degenerate
Semiconductor','Location','southeast')
title('Carrier Concentration vs Energy') %Title of graph

fid = fopen('CarrierConcentration.dat', 'w'); %Output data to external file
for i = 1:num
   fprintf(fid,'%e %e %e\n',Efermi(i),ni(i),nia(i));%Prints the ith component of Fermi energy, and the two carrier
densities to the external file
end
fclose(fid);
fid = fopen('JoyceDixonApprox.dat', 'w'); %Output data to external file
for i = 1:num
   fprintf(fid,'%e %e %e\n',njd(i),Efnd(i),Efjd(i));%Prints the ith component of the carrier density and the Fermi
energies in the non-degenerate and Joyce-Dixon approximation
end
fclose(fid);

%nim=[7.696e17 2.569e18 3.512e18 5.780e18]
%Efm=
```

9 REFERENCES

[1] S. KC and W. Lutz, "The human core of the shared socioeconomic pathways: Population scenarios by age, sex and level of education for all countries to 2100," *Glob. Environ. Chang.*, vol. 42, pp. 181–192, 2017.

[2] B. Lanz, S. Dietz, and T. Swanson, "Global Population Growth, Technology, and Malthusian Constraints: a Quantitative Growth Theoretic Perspective," *Int. Econ. Rev. (Philadelphia).*, vol. 58, no. 3, pp. 973–1006, 2017.

[3] K. Riahi, D. P. van Vuuren, E. Kriegler, J. Edmonds, B. C. O'Neill, S. Fujimori, N. Bauer, K. Calvin, R. Dellink, O. Fricko, W. Lutz, A. Popp, J. C. Cuaresma, S. KC, M. Leimbach, L. Jiang, T. Kram, S. Rao, J. Emmerling, K. Ebi, T. Hasegawa, P. Havlik, F. Humpenöder, L. A. Da Silva, S. Smith, E. Stehfest, V. Bosetti, J. Eom, D. Gernaat, T. Masui, J. Rogelj, J. Strefler, L. Drouet, V. Krey, G. Luderer, M. Harmsen, K. Takahashi, L. Baumstark, J. C. Doelman, M. Kainuma, Z. Klimont, G. Marangoni, H. Lotze-Campen, M. Obersteiner, A. Tabeau, and M. Tavoni, "The Shared Socioeconomic Pathways and their energy, land use, and greenhouse gas emissions implications: An overview," *Glob. Environ. Chang.*, vol. 42, pp. 153–168, 2017.

[4] O. Y. Edelenbosch, K. Kermeli, W. Crijns-Graus, E. Worrell, R. Bibas, B. Fais, S. Fujimori, P. Kyle, F. Sano, and D. P. van Vuuren, "Comparing projections of industrial energy demand and greenhouse gas emissions in long-term energy models," *Energy*, vol. 122, pp. 701–710, 2017.

[5] D. P. van Vuuren, E. Stehfest, D. E. H. J. Gernaat, J. C. Doelman, M. van den Berg, M. Harmsen, H. S. de Boer, L. F. Bouwman, V. Daioglou, O. Y. Edelenbosch, B. Girod, T. Kram, L. Lassaletta, P. L. Lucas, H. van Meijl, C. Müller, B. J. van Ruijven, S. van der Sluis, and A. Tabeau, "Energy, land-use and greenhouse gas emissions trajectories under a green growth paradigm," *Glob. Environ. Chang.*, vol. 42, pp. 237–250, 2017.

[6] P. de Almeida and P. D. Silva, "The peak of oil production-Timings and market recognition," *Energy Policy*, vol. 37, no. 4, pp. 1267–1276, 2009.

[7] R. A. Kerr, "Peak Oil Production May Already Be Here," *Sci. Mag*, vol. 331, no. March, pp. 1510–1511, 2011.

[8] I. Chapman, "The end of Peak Oil? Why this topic is still relevant despite recent denials," *Energy Policy*, vol. 64, pp. 93–101, 2014.

[9] R. J. Kuhns and G. H. Shaw, "Peak Oil and Petroleum Energy Resources," in *Navigating the Energy Maze*, Springer, 2018, pp. 53–63.

[10] P. J. Crutzen and E. F. Stoermet, "The 'Anthropocene,'" *IGBP Newsl.*, vol. 41, pp. 17–18, 2000.

[11] P. J. Crutzen, "Geology of mankind," vol. 415, no. January, p. 2002, 2002.

[12] B. D. Smith and M. A. Zeder, "The onset of the Anthropocene," *Anthropocene*, vol. 4, pp. 8–13, 2013.

[13] J. Zalasiewicz, C. N. Waters, M. Williams, A. D. Barnosky, A. Cearreta, P. Crutzen, E. Ellis, M. A. Ellis, I. J. Fairchild, J. Grinevald, P. K. Haff, I. Hajdas, R. Leinfelder, J. McNeill, E. O. Odada, C. Poirier, D. Richter, W. Steffen, C. Summerhayes, J. P. M. Syvitski, D. Vidas, M. Wagreich, S. L. Wing, A. P. Wolfe, Z. An, and N. Oreskes, "When did the Anthropocene begin? A mid-twentieth century boundary level is stratigraphically optimal," *Quat. Int.*, vol. 383, pp. 196–203, 2015.

[14] S. L. Lewis and M. A. Maslin, "Defining the Anthropocene," *Nature*, vol. 519, no. 7542, pp. 171–180, 2015.

[15] A. P. Wolfe, W. O. Hobbs, H. H. Birks, J. P. Briner, S. U. Holmgren, Ó. Ingólfsson, S. S. Kaushal, G. H. Miller, M. Pagani, J. E. Saros, and R. D. Vinebrooke, "Stratigraphic expressions of the Holocene-Anthropocene transition revealed in sediments from remote lakes," *Earth-Science Rev.*, vol. 116, no. 1, pp. 17–34, 2013.

[16] A. Frank, J. Carroll-Nellenback, M. Alberti, and A. Kleidon, "The Anthropocene Generalized: Evolution of Exo-Civilizations and Their Planetary Feedback," *Astrobiology*, vol. 18, no. 5, pp. 503–518, 2018.

[17] UNFCCC, "Paris Agreement," *Conf. Parties its twenty-first Sess.*, no. December, p. 32, 2015.

[18] R. Monastersky, "Global carbon dioxide levels near worrisome milestone," *Nature*, vol. 497, no. 7447, pp. 13–14, 2013.

[19] G. Bala, "Digesting 400 ppm for global mean CO2 concentration," *Curr. Sci.*, vol. 104, no. 11, pp. 10–11, 2013.

[20] Y. G. Zhang, M. Pagani, Z. Liu, S. M. Bohaty, R. Deconto, P. T. R. S. A, Y. G. Zhang, M. Pagani, Z. Liu, S. M. Bohaty, and R. Deconto, "A 40-million-year history of atmospheric CO 2 A 40-million-year history of atmospheric CO 2," *Philos. Trans. R. Soc. London. Ser. A, Math. Phys. Eng. Sci.*, vol. 371, 2013.

[21] M. A. Martínez-Botí, G. L. Foster, T. B. Chalk, E. J. Rohling, P. F. Sexton, D. J. Lunt, R. D. Pancost, M. P. S. Badger, and D. N. Schmidt, "Plio-Pleistocene climate sensitivity evaluated using high-resolution CO2 records," *Nature*, vol. 518, pp. 49–54, 2015.

[22] A. P. Ballantyne, Y. Axford, G. H. Miller, B. L. Otto-Bliesner, N. Rosenbloom, and J. W. C. White, "The amplification of Arctic terrestrial surface temperatures by reduced sea-ice extent during the Pliocene," *Palaeogeogr.*

Palaeoclimatol. Palaeoecol., vol. 386, pp. 59–67, 2013.

[23] D. J. Lunt, A. M. Haywood, G. L. Foster, and E. J. Stone, "The Arctic cryosphere in the Mid-Pliocene and the future," *Philos. Trans. R. Soc. A Math. Phys. Eng. Sci.*, vol. 367, no. 1886, pp. 49–67, 2009.

[24] B. A. Keisling, I. S. Castañeda, and J. Brigham-Grette, "Hydrological and temperature change in Arctic Siberia during the intensification of Northern Hemisphere Glaciation," *Earth Planet. Sci. Lett.*, vol. 457, pp. 136–148, 2017.

[25] D. M. Etheridge, L. P. Steele, R. L. Langenfelds, R. J. Francey, J. M. Barnola, and V. I. Morgan, "Natural and anthropogenic changes in atmospheric CO2 over the last 1000 years from air in Antarctic ice and firn," *J. Geophys. Res.*, vol. 101, no. D2, pp. 4115–4128, 1996.

[26] N. Lang and E. W. Wolff, "Interglacial and glacial variability from the last 800 ka in marine, ice and terrestrial archives," *Clim. Past*, vol. 7, no. 2, pp. 361–380, 2011.

[27] P. Tans, R. Keeling, S. J. Walker, S. C. Piper, and A. F. Bollenbacher, "Mauna Loa Annual Mean Data," *NOAA*, 2018. [Online]. Available: https://www.esrl.noaa.gov/gmd/ccgg/trends/data.html. [Accessed: 08-Jul-2018].

[28] The Committee for Climate Change, "Reducing UK emissions – 2018 Progress Report to Parliament," no. June, 2018.

[29] N. Hicks, U. Vik, P. Taylor, E. Ladoukakis, J. Park, F. Kolisis, and K. S. Jakobsen, "Using Prokaryotes for Carbon Capture Storage," *Trends Biotechnol.*, vol. 35, no. 1, pp. 22–32, 2017.

[30] M. Mondal, S. Goswami, A. Ghosh, G. Oinam, O. N. Tiwari, P. Das, K. Gayen, M. K. Mandal, and G. N. Halder, "Production of biodiesel from microalgae through biological carbon capture: a review," *3 Biotech*, vol. 7, no. 2, pp. 1–21, 2017.

[31] G. Gao, A. S. Clare, C. Rose, and G. S. Caldwell, "Ulva rigida in the future ocean: potential for carbon capture, bioremediation and biomethane production," *GCB Bioenergy*, vol. 10, no. 1, pp. 39–51, 2018.

[32] A. Arasto, E. Tsupari, J. Kärki, M. Sihvonen, and J. Lilja, "Costs and potential of carbon capture and storage at an integrated steel mill," *Energy Procedia*, vol. 37, pp. 7117–7124, 2013.

[33] D. Leeson, N. Mac Dowell, N. Shah, C. Petit, and P. S. Fennell, "A Techno-economic analysis and systematic review of carbon capture and storage (CCS) applied to the iron and steel, cement, oil refining and pulp and paper industries, as well as other high purity sources," *Int. J. Greenh. Gas Control*, vol. 61, pp. 71–84, 2017.

[34] M. Pang, L. Zhang, S. Liang, G. Liu, C. Wang, Y. Hao, Y. Wang, and M. Xu, "Trade-off between carbon reduction benefits and ecological costs of biomass-based power plants with carbon capture and storage (CCS) in China," *J. Clean. Prod.*, vol. 144, pp. 279–286, 2017.

[35] C. Lausselet, F. Cherubini, G. D. Oreggioni, G. del Alamo Serrano, M. Becidan, X. Hu, P. K. Rørstad, and A. H. Strømman, "Norwegian Waste-to-Energy: Climate change, circular economy and carbon capture and storage," *Resour. Conserv. Recycl.*, vol. 126, no. July, pp. 50–61, 2017.

[36] D. Archer, M. Eby, V. Brovkin, A. Ridgwell, L. Cao, U. Mikolajewicz, K. Caldeira, K. Matsumoto, G. Munhoven, A. Montenegro, and K. Tokos, "Atmospheric Lifetime of Fossil Fuel Carbon Dioxide," *Annu. Rev. Earth Planet. Sci.*, vol. 37, no. 1, pp. 117–134, 2009.

[37] Nuclear Decommisioning Authority, "Nuclear Provision: the cost of cleaning up Britain's historic nuclear sites," 2018. [Online]. Available: https://www.gov.uk/government/publications/nuclear-provision-explaining-the-cost-of-cleaning-up-britains-nuclear-legacy/nuclear-provision-explaining-the-cost-of-cleaning-up-britains-nuclear-legacy. [Accessed: 24-Jul-2018].

[38] P. Brown, "N-waste leak at Sellafield," *Guard.*, vol. 18 Apr, 2002.

[39] HSE - Health and Safety Executive, "Report of the investigation into the leak of dissolver product liquor at the Thermal Oxide Reprocessing Plant (THORP), Sellafield , notified to HSE on 20 April 2005," no. February, pp. 1–28, 2007.

[40] J. Vidal and R. Edwards, "Photographs of Sellafield nuclear plant prompt fears over radioactive risk," *Guard.*, vol. 29 Oct, 2014.

[41] F. Pearce, "Shocking state of world's riskiest nuclear waste site," *New Sci.*, vol. 21 Jan, 2015.

[42] S. Osborne, "Sellafield: Nuclear accident fears exposed by whistleblower in Panorama investigation," *Indep.*, vol. 5 Sept, 2016.

[43] R. L. Thompson, J. R. Ramler, and S. M. Stevenson, "STUDY OF EXTRATERRESTRIAL DISPOSAL OF RADIOACTIVE WASTES," *NASA Tech. Memo.*, 1974.

[44] R. E. Burns, W. E. Causey, W. E. Galloway, and R. W. Nelson, "Nuclear Waste Disposal in Space," *NASA Tech. Pap. 1225*, 1978.

[45] R. Salkeld and R. Beichel, "Nuclear waste disposal in space: Implications of advanced space transportation," *Acta Astronaut.*, vol. 7, no. 12, pp. 1373–1387, 1980.

[46] H. Kim, C. Park, and O. J. Kwon, "Conceptual design of the space disposal system for the highly radioactive component of the nuclear waste," *Energy*, vol. 115, pp. 155–168, 2016.

[47] M. R. Berkowitz, "Public health considerations of launching nuclear waste to the sun," *PCOM Sch. Pap.*, p. 281, 2013.

[48] National Research Council, “Societal Issues in Radioactive Waste Management,” in *Disposition of High-Level Waste and Spent Nuclear Fuel: The Continuing Societal and Technical Challenges*, Washington, DC: The National Academies Press, 2001.

[49] Department for Business Energy & Industrial Strategy and Nuclear Decommisioning Authority, “Radioactive Wastes in the UK: A Summary of the 2016 Inventory,” 2017. [Online]. Available: https://ukinventory.nda.gov.uk/the-2016-inventory/2016-inventory-reports/. [Accessed: 24-Jul-2017].

[50] BBC News Cumbria, “Nuclear waste disposal: Where in Cumbria to bury it?,” *BBC News*, vol. 8 Oct, 2012.

[51] M. Wainwright, “‘Nuclear waste? No thanks,’ say Lake District national park tourism chiefs,” *Guard.*, vol. 16 Jan, 2013.

[52] M. Boycott-Owen, “Campaigners slam £1m incentive to store nuclear waste,” *Obs.*, vol. 12 May, 2018.

[53] R. Morison, “Heat Wave in France Starts Cutting into Nuclear Power Production,” *Bloom. News*, vol. 25 July, 2018.

[54] ITER, “Is ITER Running Behind Schedule?,” 2018. [Online]. Available: http://www.iter.org/faq#Is_ITER_running_behind_schedule. [Accessed: 03-Jul-2018].

[55] F. Romanelli, “Fusion Electricity: A roadmap to the realisation of fusion energy,” *EFDA*, vol. November, pp. 1–75, 2012.

[56] J. W. Lund and T. L. Boyd, “Direct utilization of geothermal energy 2015 worldwide review,” *Geothermics*, vol. 60, no. 3, pp. 66–93, 2016.

[57] G. Larsen, M. T. Gudmundsson, and H. Björnsson, “Eight centuries of periodic volcanism at the center of the Iceland hotspot revealed by glacier tephrostratigraphy,” *Geology*, vol. 26, no. 10, pp. 943–946, 1998.

[58] R. van den Broek, A. Faaij, and A. van Wijk, “Biomass combustion for power generation,” *Biomass and Bioenergy*, vol. 11, no. 4, pp. 271–281, 1996.

[59] Y. Alipour, P. Henderson, and P. Szakálos, “The effect of a nickel alloy coating on the corrosion of furnace wall tubes in a waste wood fired power plant,” *Mater. Corros.*, vol. 65, no. 2, pp. 217–225, 2014.

[60] J. Kirkland, “Bioenergy From Forests: The Power Potential of Woody Biomass,” *PNW Sci. Find.*, no. 174, 2015.

[61] L. Rey-Salgueiro, B. Omil, A. Merino, E. Martínez-Carballo, and J. Simal-Gándara, “Organic pollutants profiling of wood ashes from biomass power plants linked to the ash characteristics,” *Sci. Total Environ.*, vol. 544, pp. 535–543, 2016.

[62] P. Weiland, “Biogas production: Current state and perspectives,” *Appl. Microbiol. Biotechnol.*, vol. 85, no. 4, pp. 849–860, 2010.

[63] P. Bohutskyi and E. Bouwer, “Biogas Production from Algae and Cyanobacteria Through Anaerobic Digestion: A Review, Analysis, and Research Needs,” in *Advanced Biofuels and Bioproducts*, J. W. Lee, Ed. New York: Springer Science+Business Media, 2013, p. 975.

[64] M. E. Montingelli, S. Tedesco, and A. G. Olabi, “Biogas production from algal biomass: A review,” *Renew. Sustain. Energy Rev.*, vol. 43, pp. 961–972, 2015.

[65] J. Van Gerpen, “Biodiesel processing and production,” *Fuel Process. Technol.*, vol. 86, no. 10, pp. 1097–1107, 2005.

[66] Y. Chisti, “Biodiesel from microalgae beats bioethanol,” *Trends Biotechnol.*, vol. 26, no. 3, pp. 126–131, 2008.

[67] T. M. Mata, A. A. Martins, and N. S. Caetano, “Microalgae for biodiesel production and other applications: A review,” *Renew. Sustain. Energy Rev.*, vol. 14, no. 1, pp. 217–232, 2010.

[68] M. Strack, Ed., *Peatlands and Climate Change*. International Peat Society, 2008.

[69] D. Keeney and C. Nanninga, *Biofuel and Global Biodiversity*. Minnepolis: Institute for Agriculture and Trade Policy, 2008.

[70] J. Tait, M. Adcock, G. C. Barker, S. Caney, J. Cataway, R. Gill, J. Hutton, O. Leyser, N. Mortimer, C. Raines, I. Smale, and J. Watson, *Biofuels: ethical issues*, vol. 44, no. April 2011. London: Nuffield Council on Bioethics, 2011.

[71] P. Thompson, “The Agricultural Ethics of Biofuels: The Food vs. Fuel Debate,” *Agriculture*, vol. 2, no. 4, pp. 339–358, 2012.

[72] C. Berman, “Impasses and controversies of hydroelectricity,” *Estud. Avançados*, vol. 21, no. 59, pp. 139–154, 2007.

[73] B. Verduzco Chávez and A. S. Bernal, “Planning hydroelectric power plants with the public: A case of organizational and social learning in Mexico,” *Impact Assess. Proj. Apprais.*, vol. 26, no. 3, pp. 163–176, 2008.

[74] J. Abbink, “Dam controversies: Contested governance and developmental discourse on the Ethiopian Omo River dam,” *Soc. Anthropol.*, vol. 20, no. 2, pp. 125–144, 2012.

[75] W. Kitchen and M. Ronayne, “The Ilisu Dam in Southeast Turkey: Archaeology at risk,” *Antiquity*, vol. 75, no. 287, pp. 37–38, 2001.

[76] M. Ronayne, “Archaeology against cultural destruction : the case of the Ihsu dam in the Kurdish region of Turkey,” *Public Archaeol.*, vol. 5187, pp. 223–236, 2002.

[77] I. Hodder, “Cultural Heritage Rights: From Ownership and Descent to Justice and Well-being,” *Anthropol. Q.*, vol. 83, no. 4, pp. 861–882, 2010.

[78] H. Hafsaas-Tsakos, “Ethical implications of salvage archaeology and dam building: The clash between archaeologists and local people in Dar al-Manasir, Sudan,” *J. Soc. Archaeol.*, vol. 11, no. 1, pp. 49–76, 2011.

[79] M. C. Blumm, “Hydropower vs. Salmon: The Struggle of the Pacific Northwest’s Anadromous Fish Resources for a Peaceful Coexistence with the Federal Columbia River Power System,” *Environ. Law*, vol. 11, p. 211, 1981.

[80] E. B. Thorstad, F. Økland, F. Kroglund, and N. Jepsen, “Upstream migration of Atlantic salmon at a power station on the River Nidelva, Southern Norway,” *Fish. Manag. Ecol.*, vol. 10, no. 3, pp. 139–146, 2003.

[81] M. J. Kuby, W. F. Fagan, C. S. ReVelle, and W. L. Graf, “A multiobjective optimization model for dam removal: An example trading off salmon passage with hydropower and water storage in the Willamette basin,” *Adv. Water Resour.*, vol. 28, no. 8, pp. 845–855, 2005.

[82] R. S. Waples, R. W. Zabel, M. D. Scheuerell, and B. L. Sanderson, “Evolutionary responses by native species to major anthropogenic changes to their ecosystems: Pacific salmon in the Columbia River hydropower system,” *Mol. Ecol.*, vol. 17, no. 1, pp. 84–96, 2008.

[83] M. Larinier, “Fish passage experience at small-scale hydro-electric power plants in France,” *Hydrobiologia*, vol. 609, no. 1, pp. 97–108, 2008.

[84] C. Durif, P. Elie, C. Gosset, and J. Rives, “Behavioral Study of Downstream Migrating Eels by Radio-telemetry at a Small Hydroelectric Power Plant,” *Am. Fish. Soc. Symp.*, no. January 2003, pp. 1–14, 2002.

[85] J. Behrmann-Godel and R. Eckmann, “A preliminary telemetry study of the migration of silver European eel (Anguilla anguilla L.) in the River Mosel, Germany,” *Ecol. Freshw. Fish*, vol. 12, pp. 196–202, 2003.

[86] H. V. Winter, H. M. Jansen, and M. C. M. Bruijs, “Assessing the impact of hydropower and fisheries on downstream migrating silver eel, Anguilla anguilla, by telemetry in the River Meuse,” *Ecol. Freshw. Fish*, vol. 15, no. 2, pp. 221–228, 2006.

[87] O. Calles, I. C. Olsson, C. Comoglio, P. S. Kemp, L. Blunden, M. Schmitz, and L. A. Greenberg, “Size-dependent mortality of migratory silver eels at a hydropower plant, and implications for escapement to the sea,” *Freshw. Biol.*, vol. 55, no. 10, pp. 2167–2180, 2010.

[88] IUCN, “Anguilla anguilla (European Eel),” *IUCN Red List*, 2014. [Online]. Available: http://www.iucnredlist.org/details/60344/0. [Accessed: 04-Jul-2018].

[89] P. Devine-Wright, “Beyond NIMBYism: Towards an integrated framework for understanding public perceptions of wind energy,” *Wind Energy*, vol. 8, no. 2, pp. 125–139, 2005.

[90] E. Devlin, “Factors Affecting Public Acceptance of Wind Turbines in Sweden,” *Wind Eng.*, vol. 29, no. 6, pp. 503–511, 2009.

[91] J. Meyerhoff, C. Ohl, and V. Hartje, “Landscape externalities from onshore wind power,” *Energy Policy*, vol. 38, no. 1, pp. 82–92, 2010.

[92] G. J. W. Van Bussel and M. B. Zaaijer, “Reliability , Availability and Maintenance aspects of large-scale offshore wind farms , a concepts study,” *MAREC 2001 Mar. Renew. Energies Conf.*, vol. 113, pp. 119–126, 2001.

[93] S. Butterfield, W. Musial, and J. Jonkman, “Engineering Challenges for Floating Offshore Wind Turbines,” in *2005 Copenhagen Offshore Wind Conference*, 2005, pp. 1–13.

[94] X. Liu and S. Islam, “Reliability issues of offshore wind farm topology,” *Probabilistic Methods Appl. to Power …*, 2008.

[95] J. J. Nielsen and J. D. Sørensen, “On risk-based operation and maintenance of offshore wind turbine components,” *Reliab. Eng. Syst. Saf.*, vol. 96, no. 1, pp. 218–229, 2011.

[96] I. Smales, “Fauna Collisions with Wind Turbines: Effect and Impacts, Individuals and Populations. What Are We Trying to Assess?,” in *Wind and Wildlife*, no. March, C. Hull, E. Bennett, E. Stark, I. Smales, J. Lau, and M. Venosta, Eds. Dordrecht: Springer, 2014, pp. 23–40.

[97] A. L. Drewitt and R. H. W. Langston, “Assessing the impacts of wind farms on birds,” *Ibis (Lond. 1859).*, vol. 148, pp. 29–42, 2006.

[98] T. Markvart and L. Castañer, *Principles of Solar Cell Operation*. Elsevier Ltd, 2012.

[99] S. J. Fonash, *Material Properties and Device Physics Basic to Photovoltaics*. 2010.

[100] A. da Rosa, *Photovoltaic Converters*. 2013.

[101] Y. Tian and C. Y. Zhao, “A review of solar collectors and thermal energy storage in solar thermal applications,” *Appl. Energy*, vol. 104, pp. 538–553, 2013.

[102] O. Behar, A. Khellaf, and K. Mohammedi, “A review of studies on central receiver solar thermal power plants,” *Renew. Sustain. Energy Rev.*, vol. 23, pp. 12–39, 2013.

[103] V. Siva Reddy, S. C. Kaushik, K. R. Ranjan, and S. K. Tyagi, “State-of-the-art of solar thermal power plants - A review,” *Renew. Sustain. Energy Rev.*, vol. 27, pp. 258–273, 2013.

[104] M. Ni, M. K. H. Leung, D. Y. C. Leung, and K. Sumathy, “A review and recent developments in photocatalytic water-splitting using TiO2for hydrogen production,” *Renew. Sustain. Energy Rev.*, vol. 11, no. 3, pp. 401–425, 2007.

[105] O. K. Varghese, M. Paulose, T. J. Latempa, C. A. Grimes, S. U. V, U. V Park, and V. Pennsyl, “High-Rate Solar Photocatalytic Conversion of CO 2 and Water Vapor to Hydrocarbon Fuels 2009,” *Nano Lett.*, vol. 9, no. 2, pp. 731–737,

2009.

[106] Q. Liu, Y. Zhou, J. Kou, X. Chen, Z. Tian, J. Gao, S. Yan, and Z. Zou, "High-yield synthesis of ultralong and ultrathin Zn2GeO4 nanoribbons toward improved photocatalytic reduction of CO2 into renewable hydrocarbon fuel.," *J. Am. Chem. Soc.*, vol. 132, no. 41, pp. 14385–14387, 2010.

[107] A. A. Ismail and D. W. Bahnemann, "Photochemical splitting of water for hydrogen production by photocatalysis: A review," *Sol. Energy Mater. Sol. Cells*, vol. 128, pp. 85–101, 2014.

[108] A. E. Becquerel, "Recherches sur les effets de la radiation chimique de la lumiere solaire au moyen des courants electriques," *Comptes Rendus L'Academie des Sci.*, vol. 9, pp. 145–149, 1839.

[109] A. E. Becquerel, "Memoire sur les effects d'electriques produits sous l'influence des rayons solaires," *Ann. der Physick und Chemie*, vol. 54, pp. 35–42, 1841.

[110] M. Iqbal, "An Introduction to Solar Radiation," in *An Introduction to Solar Radiation*, M. Iqbal, Ed. Academic Press, 1983.

[111] American Society for Testing and Materials, "Reference Solar Spectral Irradiance: Air Mass 1.5." [Online]. Available: http://rredc.nrel.gov/solar/spectra/am1.5/. [Accessed: 26-Feb-2018].

[112] A. Polizzotti, I. L. Repins, R. Noufi, S. H. Wei, and D. B. Mitzi, "The state and future prospects of kesterite photovoltaics," *Energy Environ. Sci.*, vol. 6, no. 11, pp. 3171–3182, 2013.

[113] L. Vegard, "Die Konstitution der Mischkristalle und die Raumfüllung der Atome," *Zeitschrift für Phys.*, vol. 5, no. 1, pp. 17–26, 1921.

[114] C. G. Van de Walle, M. D. McCluskey, C. P. Master, L. T. Romano, and N. M. Johnson, "Large and composition-dependent band gap bowing in $In_xGa_{1-x}N$ alloys," *Mater. Sci. Eng.*, vol. 59, pp. 274–278, 1999.

[115] Y. K. Kuo, B. T. Liou, S. H. Yen, and H. Y. Chu, "Vegard's law deviation in lattice constant and band gap bowing parameter of zincblende $In_xGa_{1-x}N$," *Opt. Commun.*, vol. 237, no. 4–6, pp. 363–369, 2004.

[116] S. Aminorroaya Yamini, V. Patterson, and R. Santos, "Band-Gap Nonlinearity in Lead Chalcogenide (PbQ, Q = Te, Se, S) Alloys," *ACS Omega*, vol. 2, no. 7, pp. 3417–3423, 2017.

[117] W. Shockley and H. J. Queisser, "Detailed Balance Limit of Efficiency of p-n Junction Solar Cells," *J. Appl. Phys.*, vol. 32, no. 3, p. 510, Jun. 1961.

[118] J. H. Guo, P. J. Cousins, and J. E. Cotter, "Investigations of parasitic shunt resistance in n-type buried contact solar cells," *Prog. Photovoltaics Res. Appl.*, vol. 14, no. 2, pp. 95–105, 2006.

[119] O. Kunz, J. Wong, J. Janssens, J. Bauer, O. Breitenstein, and A. G. Aberle, "Shunting Problems Due to Sub-Micron Pinholes in Evaporated Solid-Phase Crystallised Poly-Si Thin-Film Solar Cells on Glass," *Prog. Photovolt Res. Appl.*, vol. 17, pp. 35–46, 2009.

[120] N. E. Gorji, "Degradation sources of CdTe thin film PV: CdCl2residue and shunting pinholes," *Appl. Phys. A Mater. Sci. Process.*, vol. 116, no. 3, pp. 1347–1352, 2014.

[121] M. Wolf and H. Rauschenbach, "Series resistance effects on solar cell measurements," *Adv. Energy Convers.*, vol. 3, no. 2, pp. 455–479, 1963.

[122] M. Bashahu and A. Habyarimana, "Review and test of methods for determination of the solar cell series resistance," *Renew. Energy*, vol. 6, no. 2, pp. 129–138, 1995.

[123] W. Shockley, "The Theory of p-n Junctions in Semiconductors and p-n Junction Transistors," *Bell Syst. Tech. J.*, vol. 28, no. 3, pp. 435–489, 1949.

[124] N. Santakrus Singh, A. Jain, and A. Kapoor, "Determination of the solar cell junction ideality factor using special trans function theory (STFT)," *Sol. Energy Mater. Sol. Cells*, vol. 93, no. 8, pp. 1423–1426, 2009.

[125] M. A. Hamdy and R. L. Call, "The effect of the diode ideality factor on the experimental determination of series resistance of solar cells," *Sol. Cells*, vol. 20, no. 2, pp. 119–126, 1987.

[126] M. K. El-Adawi and I. A. Al-Nuaim, "A method to determine the solar cell series resistance from a single I-V. Characteristic curve considering its shunt resistance - New approach," *Vacuum*, vol. 64, no. 1, pp. 33–36, 2001.

[127] K. Bouzidi, M. Chegaar, and A. Bouhemadou, "Solar cells parameters evaluation considering the series and shunt resistance," *Sol. Energy Mater. Sol. Cells*, vol. 91, no. 18, pp. 1647–1651, 2007.

[128] G. M. M. W. Bissels, J. J. Schermer, M. A. H. Asselbergs, E. J. Haverkamp, P. Mulder, G. J. Bauhuis, and E. Vlieg, "Theoretical review of series resistance determination methods for solar cells," *Sol. Energy Mater. Sol. Cells*, vol. 130, pp. 605–614, 2014.

[129] M. B. H. Rhouma, A. Gastli, L. Ben Brahim, F. Touati, and M. Benammar, "A simple method for extracting the parameters of the PV cell single-diode model," *Renew. Energy*, vol. 113, pp. 885–894, 2017.

[130] W. Smith, "Effect of Light on Selenium During the Passage of An Electric Current," *Nature*, vol. 7, no. 173. pp. 303–303, 1873.

[131] W. G. Adams, "On the Action of Light on Tellurium and Selenium," *Proc. R. Soc. London*, vol. 24, pp. 163–164, 1875.

[132] W. G. Adams and R. E. Day, "The Action of Light on Selenium," *Phil. Trans. R. Soc. Lond. 1877*, vol. 167, p. 313, 1877.

[133] C. E. Fritts, "On a new form of selenium cell, and some electrical discoveries made by its use," *Am. J. Sci.*, vol. s3-26, no. 156, pp. 465–472, 1883.

[134] C. E. Fritts, *On the Fritts Selenium Cells and Batteries*. 1885.

[135] W. Siemens, "On the electromotive action of illuminated selenium, discovered by Mr. Fritts of New York," *London, Edinburgh, Dublin Philos. Mag. J. Sci.*, vol. 19, no. 119, pp. 315–316, 1885.

[136] American Physical Society, "This Month in Physics History," *APS News*, vol. 18, no. 4, 2009.

[137] J. Perlin, *Let It Shine: The 6,000-Year Story of Solar Energy*. New World Library, 2013.

[138] L. O. Grondahl, "The copper-cuprous-oxide rectifier and photoelectric cell," *Rev. Mod. Phys.*, vol. 5, no. 2, pp. 141–168, 1933.

[139] L. Bergmann, "Uber eine neue Selen-Sperrschicht Photozelle," *Phys. Zeitschrift*, vol. 32, pp. 286–289, 1931.

[140] F. C. Nix and A. W. Treptow, "A Thallous Sulphide Photo-e.m.f. Cell," *J. Opt. Soc. Am.*, vol. 29, no. 11, pp. 457–462, Nov. 1939.

[141] L. L. Tobin, T. O'Reilly, D. Zerulla, and J. T. Sheridan, "Characterising dye-sensitised solar cells," *Optik (Stuttg).*, vol. 122, no. 14, pp. 1225–1230, 2011.

[142] C. J. Cleveland and C. Morris, "Photovoltaics," in *Handbook of Energy*, vol. II, no. 1963, Elsevier Inc., 2014, pp. 287–302.

[143] N. Raval and A. K. Gupta, "Historic Developments, Current Technologies and Potential of Nanotechnology to Develop Next Generation Solar Cells with Improved Efficiency," *Int. J. Renew. Energy Dev.*, vol. 4, no. 2, pp. 77–93, 2015.

[144] G. Abbe and H. Smith, "Technological development trends in Solar-powered Aircraft Systems," *Renew. Sustain. Energy Rev.*, vol. 60, pp. 770–783, 2016.

[145] M. A. Green, "Third generation photovoltaics: Ultra-high conversion efficiency at low cost," *Prog. Photovoltaics Res. Appl.*, vol. 9, no. 2, pp. 123–135, 2001.

[146] D. M. Chapin, C. S. Fuller, and G. L. Pearson, "A New Silicon p - n Junction Photocell for Converting Solar Radiation into Electrical Power," *J. Appl. Phys.*, vol. 25, p. 676, 1954.

[147] F. A. Shirland, "The history, design, fabrication and performance of CdS thin film solar cells," *Adv. Energy Convers.*, vol. 6, no. 4, pp. 201–221, 1966.

[148] K. W. Böer and A. Rothwarf, "Materials for Solar Photovoltaic Energy Conversion," *Annu. Rev. Mater. Sci.*, vol. 6, p. 303, 1976.

[149] J. L. Shay, S. Wagner, and H. M. Kasper, "Efficient $CuInSe_2$/CdS solar cells," *Appl. Phys. Lett.*, vol. 27, no. 2, p. 89, 1975.

[150] J. D. Major, R. E. Treharne, L. J. Phillips, and K. Durose, "A low-cost non-toxic post-growth activation step for CdTe solar cells," *Nature*, vol. 511, no. 7509, pp. 334–337, 2014.

[151] A. A. Yaroshevsky, "Abundances of chemical elements in the Earth's crust," *Geochemistry Int.*, vol. 44, no. 1, pp. 48–55, 2006.

[152] G. Conibeer, "Third-generation photovoltaics," *Mater. Today*, vol. 10, no. 11, pp. 42–50, 2007.

[153] A. B. F. Martinson, S. C. Riha, E. Thimsen, J. W. Elam, and M. J. Pellin, "Structural, optical, and electronic stability of copper sulfide thin films grown by atomic layer deposition," *Energy Environ. Sci.*, vol. 6, no. 6, p. 1868, May 2013.

[154] H. Jia, S. Cheng, H. Zhang, J. Yu, and Y. Lai, "Band alignment at the Cu_2SnS_3/In_2S_3 interface measured by X-ray photoemission spectroscopy," *Appl. Surf. Sci.*, vol. 353, pp. 414–418, Oct. 2015.

[155] A. C. Lokhande, R. B. V. Chalapathy, M. He, E. Jo, M. Gang, S. A. Pawar, C. D. Lokhande, and J. H. Kim, "Development of Cu_2SnS_3 (CTS) thin film solar cells by physical techniques: A status review," *Sol. Energy Mater. Sol. Cells*, vol. 153, pp. 84–107, 2016.

[156] A. W. Welch, L. L. Baranowski, F. W. De Souza Lucas, E. S. Toberer, C. A. Wolden, and A. Zakutayev, "Copper antimony chalcogenide thin film PV device development," *2015 IEEE 42nd Photovolt. Spec. Conf. PVSC 2015*, pp. 3–6, 2015.

[157] T. J. Whittles, T. D. Veal, C. N. Savory, A. W. Welch, F. W. De Souza Lucas, J. T. Gibbon, M. Birkett, R. J. Potter, D. O. Scanlon, A. Zakutayev, and V. R. Dhanak, "Core Levels, Band Alignments, and Valence-Band States in $CuSbS_2$ for Solar Cell Applications," *ACS Appl. Mater. Interfaces*, vol. 9, no. 48, pp. 41916–41926, 2017.

[158] J. Zhong, W. Xiang, Q. Cai, and X. Liang, "Synthesis, characterization and optical properties of flower-like Cu_3BiS_3 nanorods," *Mater. Lett.*, vol. 70, pp. 63–66, 2012.

[159] M. V Yakushev, P. Maiello, T. Raadik, M. J. Shaw, P. R. Edwards, J. Krustok, A. V Mudryi, I. Forbes, and R. W. Martin, "Investigation of the Structural , Optical and Electrical Properties of Cu_3BiS_3 Semiconducting Thin Films," *Energy Procedia*, vol. 60, no. May, pp. 166–172, 2014.

[160] C. Yan, E. Gu, F. Liu, Y. Lai, J. Li, and Y. Liu, "Colloidal synthesis and characterizations of wittichenite copper bismuth sulphide nanocrystals †," *Nanoscale*, no. 1, pp. 1789–1792, 2013.

[161] T. Minemoto and M. Murata, "Theoretical analysis on effect of band offsets in perovskite

solar cells," *Sol. Energy Mater. Sol. Cells*, vol. 133, pp. 8–14, 2015.

[162] W.-C. Lai, K.-W. Lin, T.-F. Guo, P. Chen, and Y.-T. Wang, "Conversion efficiency improvement of inverted $CH_3NH_3PbI_3$ perovskite solar cells with room temperature sputtered ZnO by adding the C60 interlayer," *Appl. Phys. Lett.*, vol. 107, no. 25, p. 253301, 2015.

[163] X. Zhou, X. Li, Y. Liu, F. Huang, and D. Zhong, "Interface electronic properties of co-evaporated $MAPbI_3$ on ZnO(0001): In situ X-ray photoelectron spectroscopy and ultraviolet photoelectron spectroscopy study," *Appl. Phys. Lett.*, vol. 108, no. 12, p. 121601, 2016.

[164] P. Sinsermsuksakul, K. Hartman, S. Bok Kim, J. Heo, L. Sun, H. Hejin Park, R. Chakraborty, T. Buonassisi, and R. G. Gordon, "Enhancing the efficiency of SnS solar cells via band-offset engineering with a zinc oxysulfide buffer layer," *Appl. Phys. Lett.*, vol. 102, no. 5, 2013.

[165] T. J. Whittles, L. A. Burton, J. M. Skelton, A. Walsh, T. D. Veal, and V. R. Dhanak, "Band Alignments, Valence Bands and Core Levels in the Tin Sulfides SnS, SnS_2 and Sn_2S_3: Experiment and Theory," *Chem. Mater.*, vol. 28, no. 11, p. 3718, 2016.

[166] H. C. Sansom, G. F. S. Whitehead, M. S. Dyer, M. Zanella, T. D. Manning, M. J. Pitcher, T. J. Whittles, V. R. Dhanak, J. Alaria, J. B. Claridge, and M. J. Rosseinsky, "AgBiI4 as a Lead-Free Solar Absorber with Potential Application in Photovoltaics," *Chem. Mater.*, vol. 29, no. 4, pp. 1538–1549, 2017.

[167] T. D. Veal, N. Feldberg, N. F. Quackenbush, W. M. Linhart, D. O. Scanlon, L. F. J. Piper, and S. M. Durbin, "Band Gap Dependence on Cation Disorder in $ZnSnN_2$ Solar Absorber," *Adv. Energy Mater.*, vol. 5, no. 24, pp. 1–5, 2015.

[168] C. Navío, M. J. Capitán, J. Álvarez, F. Yndurain, and R. Miranda, "Intrinsic surface band bending in Cu_3N (100) ultrathin films," *Phys. Rev. B - Condens. Matter Mater. Phys.*, vol. 76, no. 8, pp. 1–8, 2007.

[169] M. Birkett, C. N. Savory, A. N. Fioretti, P. Thompson, C. A. Muryn, A. D. Weerakkody, I. Z. Mitrovic, S. Hall, R. Treharne, V. R. Dhanak, D. O. Scanlon, A. Zakutayev, and T. D. Veal, "Atypically small temperature-dependence of the direct band gap in the metastable semiconductor copper nitride Cu_3N," *Phys. Rev. B*, vol. 95, no. 11, pp. 1–10, 2017.

[170] D. Lan and M. A. Green, "Equivalent circuit analysis of radiative coupling in monolithic tandem solar cells," *Appl. Phys. Lett.*, vol. 106, no. 26, p. 263902, Jun. 2015.

[171] N. Song, M. Young, F. Liu, P. Erslev, S. Wilson, S. P. Harvey, G. Teeter, Y. Huang, X. Hao, and M. A. Green, "Epitaxial Cu_2ZnSnS_4 thin film on Si (111) 4° substrate," *Appl. Phys. Lett.*, vol. 106, no. 25, p. 252102, Jun. 2015.

[172] R. T. Ross and A. J. Nozik, "Efficiency of hot-carrier solar energy converters," *J. Appl. Phys.*, vol. 53, no. 5, p. 3813, 1981.

[173] M. A. Green, G. Conibeer, D. König, S. Shrestha, S. Huang, P. Aliberti, L. Treiber, R. Patterson, B. P. Veettil, A. Hsieh, Y. Feng, A. Luque, A. Marti, P. G. Linares, E. Cánovas, E. Antolín, D. F. Marrón, C. Tablero, E. Hernández, J. F. Guillemoles, L. Huang, A. Le Bris, T. Schmidt, R. Clad, and M. Tayebjee, "Hot carrier solar cells: Challenges and recent progress," *Conf. Rec. IEEE Photovolt. Spec. Conf.*, pp. 57–60, 2010.

[174] S. Saeed, E. M. L. D. De Jong, K. Dohnalova, and T. Gregorkiewicz, "Efficient optical extraction of hot-carrier energy," *Nat. Commun.*, vol. 5, pp. 1–5, 2014.

[175] J. A. R. Dimmock, S. Day, M. Kauer, K. Smith, and J. Hefferman, "Demonstration of a hot-carrier photovoltaic cell," *Prog. Photovoltaics Res. Appl.*, vol. 22, p. 151, 2014.

[176] J. H. Sung, S. Cha, H. Heo, S. Sim, J. Kim, H. Choi, and M. H. Jo, "Ultrafast Hot-Carrier Photovoltaics of Type-I Monolayer Heterojunctions in the Broad Spectral Ranges," *ACS Photonics*, vol. 4, no. 3, pp. 429–434, 2017.

[177] P. Chambadal, "Le choix du cycle thermique dans une usine generatrice nucleaire," *Rev. Gen. L'Electricite*, vol. 67, no. 6, pp. 332–345, 1958.

[178] I. I. Novikov, "The efficiency of atomic power stations (a review)," *J. Nucl. Energy*, vol. 7, no. 1–2, pp. 125–128, 1958.

[179] F. L. Curzon and B. Ahlborn, "Efficiency of a Carnot engine at maximum power output," *Am. J. Phys.*, vol. 43, no. 1, pp. 22–24, 1975.

[180] J. Chen, Z. Yan, G. Lin, and B. Andresen, "On the Curzon-Ahlborn efficiency and its connection with the efficiencies of real heat engines," *Energy Convers. Manag.*, vol. 42, no. 2, pp. 173–181, 2001.

[181] A. Bejan, "Entropy generation minimization: The new thermodynamics of finite-size devices and finite-time processes," *J. Appl. Phys.*, vol. 79, no. 3, pp. 1191–1218, 1996.

[182] S. Sieniutycz and A. De Vos, Eds., *Thermodynamic of Energy Conversion and Transport*. New York: Springer-Verlag, 2000.

[183] R. Brendel, J. H. Werner, and H. J. Queisser, "Thermodynamic efficiency limits for semiconductor solar cells with carrier multiplication," *Sol. Energy Mater. Sol. Cells*, vol. 41–42, pp. 419–425, 1996.

[184] A. Belghachi, "Theoretical Calculation of the Efficiency Limit for Solar Cells," in *Solar Cells - New Approaches and Reviews*, L. A. Kosyachenko, Ed. IntechOpen, 2015.

[185] A. Mondal and J. Radich, "Study of Charge Transfer Dynamics in Spray Deposited Cu_2ZnSnS_4 (CZTS) Photoelectrodes for Performance Improvement," *Meet. Abstr.*, vol. MA2017-01, no. 38, p. 1786, Apr. 2017.

[186] M. A. Green, Y. Hishikawa, E. D. Dunlop, D. H. Levi, J. Hohl-Ebinger, and A. W. Y. Ho-Baillie, "Solar cell efficiency tables (version 51)," *Prog. Photovoltaics Res. Appl.*, vol. 26, no. 1, pp. 3–12, 2018.

[187] H. Katagiri, N. Sasaguchi, S. Hando, S. Hoshino, J. Ohashi, and T. Yokota, "Preparation and evaluation of Cu_2ZnSnS_4 thin films by sulfurization of E-B evaporated precursors," *Sol. Energy Mater. Sol. Cells*, vol. 49, no. 1–4, pp. 407–414, 1997.

[188] P. A. Fernandes, P. M. P. Salomé, and A. F. da Cunha, "Study of polycrystalline Cu_2ZnSnS_4 films by Raman scattering," *J. Alloys Compd.*, vol. 509, no. 28, pp. 7600–7606, Jul. 2011.

[189] A. Khare, B. Himmetoglu, M. Johnson, D. J. Norris, M. Cococcioni, and E. S. Aydil, "Calculation of the lattice dynamics and Raman spectra of copper zinc tin chalcogenides and comparison to experiments," *J. Appl. Phys.*, vol. 111, no. 8, 2012.

[190] S. Siebentritt, "Why are kesterite solar cells not 20% efficient?," *Thin Solid Films*, vol. 535, pp. 1–4, May 2013.

[191] M. Kumar and C. Persson, "Cu_2ZnSnS_4 and $Cu_2ZnSnSe_4$ as Potential Earth-Abundant Thin-Film Absorber Materials: A Density Functional Theory Study," *Int. J. Theor. Appl. Sci.*, vol. 5, no. 1, pp. 1–8, 2013.

[192] M. Li, W. H. Zhou, J. Guo, Y. L. Zhou, Z. L. Hou, J. Jiao, Z. J. Zhou, Z. L. Du, and S. X. Wu, "Synthesis of pure metastable wurtzite CZTS nanocrystals by facile one-pot method," *J. Phys. Chem. C*, vol. 116, no. 50, pp. 26507–26516, 2012.

[193] U. V. Ghorpade, M. P. Suryawanshi, S. W. Shin, C. W. Hong, I. Kim, J. H. Moon, J. H. Yun, J. H. Kim, and S. S. Kolekar, "Wurtzite CZTS nanocrystals and phase evolution to kesterite thin film for solar energy harvesting," *Phys. Chem. Chem. Phys.*, vol. 17, no. 30, pp. 19777–19788, 2015.

[194] X. Zhang, Y. Xu, J. Zhang, S. Dong, L. Shen, and A. Gupta, "Synthesis of Wurtzite Cu_2ZnSnS_4 Nanosheets with Exposed High- Energy (002) Facets for Fabrication of Efficient Pt-Free Solar Cell Counter Electrodes," *Sci. Rep.*, vol. 8, no. 248, p. 1, 2018.

[195] P. Bonazzi, L. Bindi, G. P. Bernardini, and S. Menchetti, "A Model for the Mechanism of Incorporation of Cu, Fe, and Zn in the Stannite-Kesterite Series, Cu_2FeSnS_4 - Cu_2ZnSnS_4," *Can. Mineral.*, vol. 41, pp. 639–647, 2003.

[196] L. Choubrac, A. Lafond, C. Guillot-Deudon, Y. Moëlo, and S. Jobic, "Structure flexibility of the Cu_2ZnSnS_4 absorber in low-cost photovoltaic cells: From the stoichiometric to the copper-poor compounds," *Inorg. Chem.*, vol. 51, no. 6, pp. 3346–3348, 2012.

[197] L. O. Brockway, "The crystal structure of stannite, Cu_2FeSnS_4," *Zeitschrift für Krist. Mater.*, vol. 89, no. 1–6, pp. 434–441, 1934.

[198] L. Kaplan, G. Leitus, V. Lyakhovitskaya, F. Frolow, H. Hallak, and D. Cahen, "Synchrotron X-ray Diffraction Evidence for Native Defects in the Photovoltaic Semiconductor $CuInSe_2$," *Adv. Mater.*, vol. 12, no. 5, pp. 366–370, 2000.

[199] S. Chen, X. G. Gong, A. Walsh, and S.-H. H. Wei, "Crystal and electronic band structure of $Cu_2ZnSn\ X_4$ (X=S and Se) photovoltaic absorbers: First-principles insights," *Appl. Phys. Lett.*, vol. 94, no. 4, pp. 2–5, Jan. 2009.

[200] S. Chen, A. Walsh, J.-H. Yang, X. G. Gong, L. Sun, P.-X. Yang, J.-H. Chu, and S.-H. Wei, "Compositional dependence of structural and electronic properties of $Cu_2\ ZnSn(S,Se)_4$," *Phys. Rev. B*, vol. 83, no. 12, p. 125201, 2011.

[201] S. Chen, X. G. Gong, and S. H. Wei, "Band-structure anomalies of the chalcopyrite semiconductors $CuGaX_2$ versus $AgGaX_2$ (X=S and Se) and their alloys," *Phys. Rev. B - Condens. Matter Mater. Phys.*, vol. 75, no. 20, pp. 1–9, 2007.

[202] S. H. Wei and A. Zunger, "Band offsets and optical bowings of chalcopyrites and Zn-based II-VI alloys," *J. Appl. Phys.*, vol. 78, no. 6, pp. 3846–3856, 1995.

[203] A. Kanevce, I. Repins, and S.-H. Wei, "Impact of bulk properties and local secondary phases on the $Cu_2(Zn,Sn)Se_4$ solar cells open-circuit voltage," *Sol. Energy Mater. Sol. Cells*, vol. 133, pp. 119–125, Feb. 2015.

[204] Z. Yuan, S. Chen, H. Xiang, X. Gong, A. Walsh, J. Park, I. Repins, and S.-H. Wei, "Engineering Solar Cell Absorbers by Exploring the Band Alignment and Defect Disparity: The Case of Cu- and Ag-Based Kesterite Compounds," *Adv. Funct. Mater.*, pp. 6733–6743, 2015.

[205] A. Jacob, G. Larramona, C. Moisan, A. Lafond, F. Donatini, G. Rey, S. Siebentritt, A. Walsh, G. D. X. Xx, S. Bourdais, C. Choné, B. Delatouche, A. Jacob, G. Larramona, C. Moisan, A. Lafond, F. Donatini, G. Rey, S. Siebentritt, A. Walsh, and G. Dennler, "Is the Cu / Zn Disorder the Main Culprit for the Voltage Deficit in Kesterite Solar Cells ?," *Adv. Energy Mater.*, vol. 1502276, pp. 1–21, 2016.

[206] J. Kim, S. Park, S. Ryu, J. Oh, and B. Shin, "Improving the open-circuit voltage of $Cu_2ZnSnSe_4$ thin fi lm solar cells via interface passivation," *Prog. Photovoltaics Res. Appl.*, 2017.

[207] J. J. Scragg, J. T. Wätjen, M. Edoff, T. Ericson, T. Kubart, and C. Platzer-Björkman, "A detrimental reaction at the molybdenum back contact in $Cu_2ZnSn(S,Se)_4$ thin-film solar cells.," *J. Am. Chem. Soc.*, vol. 134, no. 47, pp. 19330–3, Nov. 2012.

[208] J. J. Scragg, T. Kubart, J. T. Wätjen, T. Ericson, M. K. Linnarsson, and C. Platzer-Björkman, "Effects of Back Contact Instability on Cu_2ZnSnS_4 Devices and Processes," *Chem. Mater.*, vol. 25, no. 15, pp. 3162–3171, Aug. 2013.

[209] S. W. Shin, K. V. Gurav, C. W. Hong, J. Gwak, H. R. Choi, S. A. Vanalakar, J. H. Yun, J. Y. Lee, J. H. Moon, and J. H. Kim, "Phase segregations and thickness of the Mo(S,Se) layer in $Cu_2ZnSn(S,Se)_4$ solar cells at different sulfurization temperatures," *Sol. Energy Mater. Sol. Cells*, vol. 143, pp. 480–487, 2015.

[210] O. Gunawan, T. Gokmen, and D. B. Mitzi, "Suns-VOC characteristics of high performance kesterite solar cells," *J. Appl. Phys.*, vol. 116, no. 8, 2014.

[211] T. Gershon, T. Gokmen, O. Gunawan, R. Haight, S. Guha, and B. Shin, "Understanding the relationship between $Cu_2ZnSn(S,Se)_4$ material properties and device performance," *MRS Commun.*, vol. 4, no. 4, pp. 159–170, 2014.

[212] F. Liu, J. Huang, K. Sun, C. Yan, Y. Shen, J. Park, A. Pu, F. Zhou, X. Liu, J. A. Stride, M. A. Green, and X. Hao, "Beyond 8% ultrathin kesterite Cu_2ZnSnS_4 solar cells by interface reaction route controlling and self-organized nanopattern at the back contact," *NPG Asia Mater.*, vol. 9, no. 7, 2017.

[213] T. Schnabel and E. Ahlswede, "On the interface between kesterite absorber and Mo back contact and its impact on solution-processed thin-film solar cells," *Sol. Energy Mater. Sol. Cells*, vol. 159, pp. 290–295, 2017.

[214] G. Altamura, L. Grenet, C. Roger, F. Roux, V. Reita, R. Fillon, H. Fournier, S. Perraud, and H. Mariette, "Alternative back contacts in kesterite $Cu_2ZnSn(S_{1-x}Se_x)_4$ thin film solar cells," *J. Renew. Sustain. Energy*, vol. 6, no. 1, p. 011401, Jan. 2014.

[215] S. Oueslati, G. Brammertz, M. Buffière, H. ElAnzeery, D. Mangin, O. ElDaif, O. Touayar, C. Köble, M. Meuris, and J. Poortmans, "Study of alternative back contacts for thin film $Cu_2ZnSnSe_4$-based solar cells," *J. Phys. D. Appl. Phys.*, vol. 48, no. 3, p. 035103, Jan. 2015.

[216] F. Z. Boutebakh, M. L. Zeggar, N. Attaf, and M. S. Aida, "Electrical properties and back contact study of CZTS/ZnS heterojunction," *Optik (Stuttg).*, vol. 144, pp. 180–190, 2017.

[217] P. K. Sarswat and M. L. Free, "Demonstration of a sol-gel synthesized bifacial CZTS photoelectrochemical cell," *Phys. status solidi*, vol. 208, no. 12, pp. 2861–2864, Dec. 2011.

[218] P. K. Sarswat, S. Kar, and M. L. Free, "Bifacial photodetector using CZTS absorber material," in *2012 International Conference on Emerging Electronics*, 2012, pp. 1–3.

[219] J. Ge, J. Chu, J. Jiang, Y. Yan, and P. Yang, "Characteristics of In-Substituted CZTS Thin Film and Bifacial Solar Cell," *ACS Appl. Mater. Interfaces*, vol. 6, no. 23, pp. 21118–21130, Dec. 2014.

[220] P. K. Sarswat and M. L. Free, "A Comparative Study of Co-electrodeposited Cu2ZnSnS4 Absorber Material on Fluorinated Tin Oxide and Molybdenum Substrates," *J. Electron. Mater.*, vol. 41, no. 8, pp. 2210–2215, Apr. 2012.

[221] A. Ismail, J. W. Cho, S. J. Park, Y. J. Hwang, and B. K. Min, "Synthesis of solution-processed $Cu_2ZnSnSe_4$ thin films on transparent conducting oxide glass substrates," *Bull. Korean Chem. Soc.*, vol. 35, no. 7, pp. 1985–1988, 2014.

[222] Z. Wang, J. Tao, W. Xiao, T. Xu, X. Zhang, D. Hu, and Z. Ma, "Influence of deposition potential on Cu_2ZnSnS_4 thin–film solar cells co–electrodeposited on fluorine–doped tin oxide substrates," *J. Alloys Compd.*, vol. 701, pp. 465–473, 2017.

[223] M. R. Rajesh Menon, D. R. Deepu, K. G. Deepa, C. Sudha Kartha, and K. P. Vijayakumar, "Effect of sulfurization on the properties of Cu_2ZnSnS_4 thin films deposited using chemical spray pyrolysis over ITO substrates," *Sol. Energy*, vol. 157, no. June, pp. 390–396, 2017.

[224] J. Ge, J. Chu, J. Jiang, Y. Yan, and P. Yang, "The Interfacial Reaction at ITO Back Contact in Kesterite CZTSSe Bifacial Solar Cells," *ACS Sustain. Chem. Eng.*, vol. 3, no. 12, pp. 3043–3052, 2015.

[225] J. Ge, J. Chu, Y. Yan, J. Jiang, and P. Yang, "Co-electroplated kesterite bifacial thin-film solar cells: A study of sulfurization temperature," *ACS Appl. Mater. Interfaces*, vol. 7, no. 19, pp. 10414–10428, 2015.

[226] J. Ge, Y. Yu, and Y. Yan, "Co-electroplated kesterite bifacial thin film solar cells," *2015 IEEE 42nd Photovolt. Spec. Conf. PVSC 2015*, pp. 1–6, 2015.

[227] J.-S. Kim, J.-K. Kang, and D.-K. Hwang, "High efficiency bifacial $Cu_2ZnSnSe_4$ thin-film solar cells on transparent conducting oxide glass substrates," *APL Mater.*, vol. 4, no. 9, p. 096101, 2016.

[228] P. K. Sarswat, M. L. Free, and A. Tiwari, "A study of increased resistivity of FTO back contact for CZTS based absorber material grown by electrodeposition-annealing route," *Mater. Res. Soc. Symp. Proc.*, vol. 1315, pp. 83–88, 2011.

[229] J. Ge, Y. Yu, W. Ke, J. Li, X. Tan, Z. Wang, J. Chu, and Y. Yan, "Improved performance of electroplated CZTS thin-film solar cells with bifacial configuration," *ChemSusChem*, vol. 9, no. 16, pp. 2149–2158, 2016.

[230] I. Bouchama and S. Ali-Saoucha, "Effect of wide band-gap TCO properties on the bifacial CZTS thin-films solar cells performances," *Optik (Stuttg).*, vol. 144, pp. 370–377, 2017.

[231] M. Espindola-Rodriguez, D. Sylla, Y. Sánchez, F. Oliva, S. Grini, M. Neuschitzer, L. Vines, V. Izquierdo-Roca, E. Saucedo, and M. Placidi, "Bifacial Kesterite Solar Cells on FTO Substrates," *ACS Sustain. Chem. Eng.*, vol. 5, no. 12, pp. 11516–11524, 2017.

[232] P. Termsaithong, R. Munprom, A. Shah, and A. Rodchanarowan, "Pulsed current co-

electrodeposition of kesterite Cu_2ZnSnS_4 absorber material on fluorinated tin oxide (FTO) glass substrate," *Surf. Coatings Technol.*, 2018.

[233] S. S. Mali, P. S. Shinde, C. A. Betty, P. N. Bhosale, Y. W. Oh, and P. S. Patil, "Synthesis and characterization of Cu_2ZnSnS_4 thin films by SILAR method," *J. Phys. Chem. Solids*, vol. 73, no. 6, pp. 735–740, Jun. 2012.

[234] R. P. Scott, A. C. Cullen, C. Fox-Lent, and I. Linkov, "Can Carbon Nanomaterials Improve CZTS Photovoltaic Devices? Evaluation of Performance and Impacts Using Integrated Life-Cycle Assessment and Decision Analysis," *Risk Anal.*, vol. 36, no. 10, pp. 1916–1935, 2016.

[235] Z. Shi and A. H. Jayatissa, "The impact of graphene on the fabrication of thin film solar cells: Current status and future prospects," *Materials (Basel).*, vol. 11, no. 1, 2017.

[236] K. H. L. Zhang, K. Xi, M. G. Blamire, and R. G. Egdell, "*P* -type transparent conducting oxides," *J. Phys. Condens. Matter*, vol. 28, no. 38, p. 383002, 2016.

[237] N. Sarmadian, R. Saniz, B. Partoens, and D. Lamoen, "Easily doped p-type, low hole effective mass, transparent oxides," *Sci. Rep.*, vol. 6, no. January, pp. 1–9, 2016.

[238] S. Englund, V. Paneta, D. Primetzhofer, Y. Ren, O. Donzel-Gargand, J. K. Larsen, J. Scragg, and C. Platzer Björkman, "Characterization of TiN back contact interlayers with varied thickness for $Cu_2ZnSn(S,Se)_4$ thin film solar cells," *Thin Solid Films*, vol. 639, pp. 91–97, 2017.

[239] B. Shin, Y. Zhu, N. A. Bojarczuk, S. J. Chey, and S. Guha, "High efficiency Cu2ZnSnSe4 solar cells with a TiN diffusion barrier on the molybdenum bottom contact," in *2012 38th IEEE Photovoltaic Specialists Conference*, 2012, pp. 000671–000673.

[240] B. Shin, Y. Zhu, N. A. Bojarczuk, S. Jay Chey, and S. Guha, "Control of an interfacial $MoSe_2$ layer in $Cu_2ZnSnSe_4$ thin film solar cells: 8.9% power conversion efficiency with a TiN diffusion barrier," *Appl. Phys. Lett.*, vol. 101, no. 5, p. 053903, Jul. 2012.

[241] H. T. Kim, C. Kim, C. duk Kim, and C. Park, "Formation of a Mo_2N skin layer in columnar-structural Mo films using NH_3 plasma nitridation as the Se diffusion-barrier layer," *Surf. Coatings Technol.*, vol. 302, pp. 463–467, 2016.

[242] F. Liu, K. Sun, W. Li, C. Yan, H. Cui, L. Jiang, X. Hao, and M. A. Green, "Enhancing the Cu_2ZnSnS_4 solar cell efficiency by back contact modification: Inserting a thin TiB_2 intermediate layer at Cu_2ZnSnS_4/Mo interface," *Appl. Phys. Lett.*, vol. 104, no. 5, p. 051105, Feb. 2014.

[243] W. Li, J. Chen, H. Cui, F. Liu, and X. Hao, "Inhibiting MoS_2 formation by introducing a ZnO intermediate layer for Cu_2ZnSnS_4 solar cells," *Mater. Lett.*, vol. 130, pp. 87–90, Sep. 2014.

[244] M. Vishwakarma, N. Thota, O. Karakulina, J. Hadermann, and B. R. Mehta, "Role of graphene inter layer on the formation of the MoS_2-CZTS interface during growth," *AIP Conf. Proc.*, vol. 1953, 2018.

[245] S. Ranjbar, G. Brammertz, B. Vermang, A. Hadipour, S. Cong, K. Suganuma, T. Schnabel, M. Meuris, A. F. da Cunha, and J. Poortmans, "Improvement of kesterite solar cell performance by solution synthesized MoO_3 interfacial layer," *Phys. Status Solidi Appl. Mater. Sci.*, vol. 214, no. 1, pp. 1–6, 2017.

[246] F. Zhou, F. Zeng, X. Liu, F. Liu, N. Song, C. Yan, A. Pu, J. Park, K. Sun, and X. Hao, "Improvement of J_{SC} in a Cu_2ZnSnS_4 Solar Cell by Using a Thin Carbon Intermediate Layer at the Cu_2ZnSnS_4/Mo Interface," *ACS Appl. Mater. Interfaces*, vol. 7, no. 41, pp. 22868–22873, 2015.

[247] Z. Tong, K. Zhang, K. Sun, C. Yan, F. Liu, L. Jiang, Y. Lai, X. Hao, and J. Li, "Modification of absorber quality and Mo-back contact by a thin Bi intermediate layer for kesterite Cu_2ZnSnS_4 solar cells," *Sol. Energy Mater. Sol. Cells*, vol. 144, pp. 537–543, 2016.

[248] H. Cui, C. Y. Lee, W. Li, X. Liu, X. Wen, and X. Hao, "Improving efficiency of evaporated Cu_2ZnSnS_4 thin film solar cells by a thin Ag intermediate layer between absorber and back contact," *Int. J. Photoenergy*, vol. 2015, 2015.

[249] S. Lopez-Marino, M. Espíndola-Rodríguez, Y. Sánchez, X. Alcobé, F. Oliva, H. Xie, M. Neuschitzer, S. Giraldo, M. Placidi, R. Caballero, V. Izquierdo-Roca, A. Pérez-Rodríguez, and E. Saucedo, "The importance of back contact modification in $Cu_2ZnSnSe_4$ solar cells: The role of a thin MoO_2 layer," *Nano Energy*, vol. 26, pp. 708–721, 2016.

[250] S. Lopez-Marino, M. Placidi, A. Perez-Tomas, J. Llobet, V. Izquierdo-Roca, X. Fontane, A. Fairbrother, M. Espindola-Rodriguez, D. Sylla, A. Perez-Rodriguez, and E. Saucedo, "Inhibiting the absorber/Mo-back contact decomposition reaction in Cu2ZnSnSe4 solar cells: the role of a ZnO intermediate nanolayer," *J. Mater. Chem. A*, vol. 1, no. 29, pp. 8338–8343, 2013.

[251] S. Gao, Y. Zhang, J. Ao, S. Lin, Z. Zhang, X. Li, D. Wang, Z. Zhou, G. Sun, F. Liu, and Y. Sun, "Tailoring $Mo(S,Se)_2$ structure for high efficient $Cu_2ZnSn(S,Se)_4$ solar cells," *Sol. Energy Mater. Sol. Cells*, vol. 176, pp. 302–309, 2018.

[252] J. Park, J. Huang, K. Sun, Z. Ouyang, F. Liu, C. Yan, H. Sun, A. Pu, M. Green, and X. Hao, "The effect of thermal evaporated MoO_3 intermediate layer as primary back contact for kesterite Cu_2SnSnS_4 solar cells," *Thin Solid Films*, vol. 648, no. October 2017, pp. 39–45, 2018.

[253] F. Zeng, K. Sun, L. Gong, L. Jiang, F. Liu, Y. Lai, and J. Li, "Back contact-absorber interface modification by inserting carbon intermediate layer and conversion efficiency improvement in

$Cu_2ZnSn(S,Se)_4$ solar cell," *Phys. status solidi - Rapid Res. Lett.*, vol. 9, no. 12, pp. 687–691, 2015.

[254] M. Placidi, M. Espindola-Rodriguez, S. Lopez-Marino, Y. Sanchez, S. Giraldo, L. Acebo, M. Neuschitzer, X. Alcobé, A. Pérez-Rodríguez, and E. Saucedo, "Effect of rapid thermal annealing on the Mo back contact properties for $Cu_2ZnSnSe_4$ solar cells," *J. Alloys Compd.*, vol. 675, pp. 158–162, 2016.

[255] H. Cui, X. Liu, N. Song, N. Li, F. Liu, and X. Hao, "Impact of rapid thermal annealing of Mo coated soda lime glass substrate on device performance of evaporated Cu_2ZnSnS_4 thin film solar cells," *Mater. Lett.*, vol. 125, pp. 40–43, 2014.

[256] X. Liu, H. Cui, C. Kong, X. Hao, Y. Huang, F. Liu, N. Song, G. Conibeer, and M. Green, "Rapid thermal annealed Molybdenum back contact for Cu2ZnSnS4 thin film solar cells," *Appl. Phys. Lett.*, vol. 106, no. 13, p. 131110, Mar. 2015.

[257] M. G. Sousa, A. F. Da Cunha, P. A. Fernandes, J. P. Teixeira, R. A. Sousa, and J. P. Leitão, "Effect of rapid thermal processing conditions on the properties of Cu2ZnSnS4thin films and solar cell performance," *Sol. Energy Mater. Sol. Cells*, vol. 126, pp. 101–106, 2014.

[258] X. Liu, H. Cui, C. Kong, X. Hao, Y. Huang, F. Liu, N. Song, G. Conibeer, and M. Green, "Rapid thermal annealed Molybdenum back contact for Cu_2ZnSnS_4 thin film solar cells," *Appl. Phys. Lett.*, vol. 106, no. 13, p. 131110, 2015.

[259] I. D. Olekseyuk, I. V. Dudchak, and L. V. Piskach, "Phase equilibria in the Cu2S–ZnS–SnS2 system," *J. Alloys Compd.*, vol. 368, no. 1–2, pp. 135–143, Apr. 2004.

[260] L. A. Burton and A. Walsh, "Band alignment in SnS thin-film solar cells: Possible origin of the low conversion efficiency," *Appl. Phys. Lett.*, vol. 102, no. 13, p. 132111, 2013.

[261] M. Bär, B. A. Schubert, B. Marsen, R. G. Wilks, S. Pookpanratana, M. Blum, S. Krause, T. Unold, W. Yang, L. Weinhardt, C. Heske, and H. W. Schock, "Cliff-like conduction band offset and KCN-induced recombination barrier enhancement at the CdS/Cu2ZnSnS4 thin-film solar cell heterojunction," *Appl. Phys. Lett.*, vol. 99, no. 22, pp. 4–7, 2011.

[262] R. Haight, A. Barkhouse, O. Gunawan, B. Shin, M. Copel, M. Hopstaken, and D. B. Mitzi, "Band alignment at the Cu2 ZnSn (SxSe1-x) 4 /CdS interface," *Appl. Phys. Lett.*, vol. 98, no. 25, 2011.

[263] A. Santoni, F. Biccari, C. Malerba, M. Valentini, R. Chierchia, and A. Mittiga, "Valence band offset at the CdS/Cu 2 ZnSnS 4 interface probed by x-ray photoelectron spectroscopy," *J. Phys. D. Appl. Phys.*, vol. 46, no. 17, p. 175101, 2013.

[264] C. Yan, F. Liu, N. Song, B. K. Ng, J. A. Stride, A. Tadich, and X. Hao, "Band alignments of different buffer layers (CdS, Zn(O,S), and In 2S3) on Cu2ZnSnS4," *Appl. Phys. Lett.*, vol. 104, no. 17, pp. 2012–2016, 2014.

[265] Z. Y. Dong, Y. F. Li, B. Yao, Z. H. Ding, G. Yang, R. Deng, X. Fang, Z. P. Wei, and L. Liu, "An experimental and first-principles study on band alignments at interfaces of Cu2ZnSnS4/CdS/ZnO heterojunctions," *J. Phys. D. Appl. Phys.*, vol. 47, no. 7, 2014.

[266] K. Kataoka, S. Tajima, M. Umehara, N. Takahashi, N. Isomura, K. Kitazumi, and Y. Kimoto, "Band slope in CdS layer of ZnO:Ga/CdS/Cu2ZnSnS4 photovoltaic cells revealed by hard X-ray photoelectron spectroscopy," *Appl. Phys. Lett.*, vol. 109, no. 20, 2016.

[267] W. Xiao, J. N. Wang, J. W. Wang, G. J. Huang, L. Cheng, L. J. Jiang, and L. G. Wang, "Structural and electronic properties of the heterointerfaces for Cu_2ZnSnS_4 photovoltaic cells: a density-functional theory study," *Phys. Chem. Chem. Phys.*, vol. 18, no. 17, pp. 12029–12034, 2016.

[268] W. Bao and M. Ichimura, "First-principles study on influences of crystal structure and orientation on band offsets at the CdS/Cu2ZnSnS4 interface," *Int. J. Photoenergy*, vol. 2012, no. 001, 2012.

[269] S. Y. Kim, T. R. Rana, J. H. Kim, D. H. Son, K. J. Yang, J. K. Kang, and D. H. Kim, "Limiting effects of conduction band offset and defect states on high efficiency CZTSSe solar cell," *Nano Energy*, vol. 45, no. December 2017, pp. 75–83, 2018.

[270] S. Rondiya, A. Rokade, P. Sharma, M. Chaudhary, A. Funde, Y. Jadhav, S. Haram, H. Pathan, and S. Jadkar, "CZTS/CdS: interface properties and band alignment study towards photovoltaic applications," *J. Mater. Sci. Mater. Electron.*, vol. 29, no. 5, pp. 4201–4210, 2018.

[271] M. Bär, T. Schnabel, J.-H. Alsmeier, S. Krause, N. Koch, R. G. Wilks, and E. Ahlswede, "CdS/Low-Band-Gap Kesterite Thin-Film Solar Cell Absorber Heterojunction: Energy Level Alignment and Dominant Recombination Process," *ACS Appl. Energy Mater.*, vol. 1, p. acsaem.7b00071, 2018.

[272] J. Ge, P. Koirala, C. R. Grice, P. J. Roland, Y. Yu, X. Tan, R. J. Ellingson, R. W. Collins, and Y. Yan, "Oxygenated CdS Buffer Layers Enabling High Open-Circuit Voltages in Earth-Abundant Cu2BaSnS4 Thin-Film Solar Cells," *Adv. Energy Mater.*, vol. 7, no. 6, 2017.

[273] D. A. R. Barkhouse, R. Haight, N. Sakai, H. Hiroi, H. Sugimoto, and D. B. Mitzi, "Cd-free buffer layer materials on Cu2ZnSn(SxSe1-x)4: Band alignments with ZnO, ZnS, and In2S3," *Appl. Phys. Lett.*, vol. 100, no. 19, pp. 4–9, 2012.

[274] G. Yang, Y. F. Li, B. Yao, Z. H. Ding, R. Deng, J. M. Qin, F. Fang, X. Fang, Z. P. Wei, and L. Liu, "Band alignments at interface of Cu2ZnSnS4/ZnO heterojunction: An X-ray photoelectron spectroscopy and first-principles study," *J. Alloys Compd.*, vol. 628, pp. 293–297, 2015.

[275] M. Aftab Akram, S. Javed, M. Islam, M. Mujahid, and A. Safdar, "Arrays of CZTS sensitized ZnO/ZnS and ZnO/ZnSe core/shell nanorods for liquid junction nanowire solar cells," *Sol. Energy Mater. Sol. Cells*, vol. 146, pp. 121–128, 2016.

[276] A. Ghosh, R. Thangavel, and A. Gupta, "Solution-processed Cd free kesterite Cu2ZnSnS4thin film solar cells with vertically aligned ZnO nanorod arrays," *J. Alloys Compd.*, vol. 694, pp. 394–400, 2017.

[277] J. Y. Park, R. B. V. Chalapathy, A. C. Lokhande, C. W. Hong, and J. H. Kim, "Fabrication of earth abundant Cu2ZnSnSSe4(CZTSSe) thin film solar cells with cadmium free zinc sulfide (ZnS) buffer layers," *J. Alloys Compd.*, vol. 695, pp. 2652–2660, 2017.

[278] K. Sun, C. Yan, F. Liu, J. Huang, F. Zhou, J. A. Stride, M. Green, and X. Hao, "Over 9% Efficient Kesterite Cu2ZnSnS4Solar Cell Fabricated by Using Zn1–xCdxS Buffer Layer," *Adv. Energy Mater.*, vol. 6, no. 12, pp. 4–9, 2016.

[279] M. Kriisa, R. Sáez-Araoz, C.-H. Fischer, T. Köhler, E. Kärber, Y. Fu, F. Hergert, M. C. Lux-Steiner, and M. Krunks, "Study of Zn(O,S) films grown by aerosol assisted chemical vapour deposition and their application as buffer layers in Cu(In,Ga)(S,Se)2 solar cells," *Sol. Energy*, vol. 115, pp. 562–568, May 2015.

[280] A. L. Dadlani, O. Trejo, S. Acharya, J. Torgersen, I. Petousis, D. Nordlund, R. Sarangi, P. Schindler, and F. B. Prinz, "Exploring the local electronic structure and geometric arrangement of ALD Zn(O,S) buffer layers using X-ray absorption spectroscopy," *J. Mater. Chem. C*, vol. 3, no. 47, pp. 12192–12198, 2015.

[281] M. Guc, M. Neuschitzer, D. Hariskos, A. Bauer, W. Witte, W. Hempel, L. Calvo-Barrio, P. Pistor, A. Perez-Rodriguez, and V. Izquierdo-Roca, "Raman scattering quantitative assessment of the anion composition ratio in Zn(O,S) layers for Cd-free chalcogenide-based solar cells," *RSC Adv.*, vol. 6, no. 29, pp. 24536–24542, 2016.

[282] M. Neuschitzer, K. Lienau, M. Guc, L. C. Barrio, S. Haass, J. M. Prieto, Y. Sanchez, M. Espindola-Rodriguez, Y. Romanyuk, A. Perez-Rodriguez, V. Izquierdo-Roca, and E. Saucedo, "Towards high performance Cd-free CZTSe solar cells with a ZnS(O,OH) buffer layer: The influence of thiourea concentration on chemical bath deposition," *J. Phys. D. Appl. Phys.*, vol. 49, no. 12, 2016.

[283] A. L. Dadlani, S. Acharya, O. Trejo, F. B. Prinz, and J. Torgersen, "ALD Zn(O,S) Thin Films' Interfacial Chemical and Structural Configuration Probed by XAS," *ACS Appl. Mater. Interfaces*, vol. 8, no. 23, pp. 14323–14327, 2016.

[284] B. Opasanont, A. G. Kuba, E. G. Louderback, K. Roy Choudhury, and J. B. Baxter, "Relating deposition conditions to Zn(S,O,OH) thin film properties for photovoltaic buffer layers using a continuous flow microreactor," *Chem. Mater.*, vol. 26, no. 23, pp. 6674–6683, 2014.

[285] C. Platzer-Björkman, C. Frisk, J. K. Larsen, T. Ericson, S.-Y. Y. Li, J. J. S. S. Scragg, J. Keller, F. Larsson, and T. Törndahl, "Reduced interface recombination in Cu2ZnSnS4 solar cells with atomic layer deposition Zn1−xSnxOy buffer layers," *Appl. Phys. Lett.*, vol. 107, no. 24, p. 243904, 2015.

[286] S. Tajima, M. Umehara, and T. Mise, "Photovoltaic properties of Cu_2ZnSnS_4 cells fabricated using ZnSnO and ZnSnO/CdS buffer layers," *Jpn. J. Appl. Phys.*, vol. 55, no. 11, p. 112302, 2016.

[287] X. Li, Z. Su, S. Venkataraj, S. K. Batabyal, and L. H. Wong, "8.6% Efficiency CZTSSe solar cell with atomic layer deposited Zn-Sn-O buffer layer," *Sol. Energy Mater. Sol. Cells*, vol. 157, pp. 101–107, 2016.

[288] A. Crovetto, C. Yan, B. Iandolo, F. Zhou, J. Stride, J. Schou, X. Hao, and O. Hansen, "Lattice-matched Cu2ZnSnS4/CeO2 solar cell with open circuit voltage boost," *Appl. Phys. Lett.*, vol. 109, no. 23, p. 233904, 2016.

[289] T. Gan, Y. Li, X. Z. Wang, X. T. Wang, and C. W. Wang, "Cu2ZnSnS4@TiO2p-n heterostructured nanosheet arrays: Controllable hydrothermal synthesis and enhanced visible light-driven photocatalytic activity," *Appl. Surf. Sci.*, vol. 408, pp. 60–67, 2017.

[290] Z. Wang and G. P. Demopoulos, "Growth of Cu2ZnSnS4Nanocrystallites on TiO2Nanorod Arrays as Novel Extremely Thin Absorber Solar Cell Structure via the Successive-Ion-Layer-Adsorption-Reaction Method," *ACS Appl. Mater. Interfaces*, vol. 7, no. 41, pp. 22888–22897, 2015.

[291] Z. Wang, R. Gauvin, and G. P. Demopoulos, "Nanostructural and photo-electrochemical properties of solution spin-coated Cu2ZnSnS4–TiO2 nanorod forest films with an improved photovoltaic performance," *Nanoscale*, vol. 9, no. 22, pp. 7650–7665, 2017.

[292] J. Kim, H. Hiroi, T. K. Todorov, O. Gunawan, M. Kuwahara, T. Gokmen, D. Nair, M. Hopstaken, B. Shin, Y. S. Lee, W. Wang, H. Sugimoto, and D. B. Mitzi, "High efficiency Cu2ZnSn(S,Se)4 solar cells by applying a double In2S3/CdS emitter.," *Adv. Mater.*, vol. 26, no. 44, pp. 7427–31, Nov. 2014.

[293] L. Lin, J. Yu, S. Cheng, P. Lu, Y. Lai, S. Lin, and P. Zhao, "Band alignment at the In2S3/Cu2ZnSnS4 heterojunction interface investigated by X-ray photoemission spectroscopy," *Appl. Phys. A*, vol. 116, no. 4, pp. 2173–2177, 2014.

[294] H. Guo, C. Ma, K. Zhang, X. Jia, Y. Li, N. Yuan, and J. Ding, "The fabrication of Cd-free Cu2ZnSnS4-Ag2ZnSnS4heterojunction photovoltaic devices," *Sol. Energy Mater. Sol. Cells*, vol. 178, no. May 2017, pp. 146–153, 2018.

[295] A. Crovetto, M. Palsgaard, T. Gunst, T. Markussen, K. Stokbro, M. Brandbyge, and O.

Hansen, “Interface band gap narrowing behind open circuit voltage losses in Cu2ZnSnS4 solar cells,” *Appl. Phys. Lett.*, vol. 110, p. 083903, 2017.

[296] T. Minemoto, T. Matsui, H. Takakura, Y. Hamakawa, T. Negami, Y. Hashimoto, T. Uenoyama, and M. Kitagawa, “Theoretical analysis of the effect of conduction band offset of window/CIS layers on performance of CIS solar cells using device simulation,” *Sol. Energy Mater. Sol. Cells*, vol. 67, no. 1–4, pp. 83–88, 2001.

[297] M. Sugiyama, T. Shimizu, D. Kawade, K. Ramya, and K. T. Ramakrishna Reddy, “Experimental determination of vacuum-level band alignments of SnS-based solar cells by photoelectron yield spectroscopy,” *J. Appl. Phys.*, vol. 115, no. 8, 2014.

[298] B. Ananthoju, J. Mohapatra, M. K. Jangid, D. Bahadur, N. V. Medhekar, and M. Aslam, “Cation/Anion Substitution in Cu2ZnSnS4 for Improved Photovoltaic Performance,” *Sci. Rep.*, vol. 6, no. February, pp. 1–11, 2016.

[299] T. Gershon, Y. S. Lee, P. Antunez, R. Mankad, S. Singh, D. Bishop, O. Gunawan, M. Hopstaken, and R. Haight, “Photovoltaic Materials and Devices Based on the Alloyed Kesterite Absorber (AgxCu1- x)2ZnSnSe4,” *Adv. Energy Mater.*, p. 1502468, 2016.

[300] H. Cui, X. Liu, F. Liu, X. Hao, N. Song, and C. Yan, “Boosting Cu_2ZnSnS_4 solar cells efficiency by a thin Ag intermediate layer between absorber and back contact,” *Appl. Phys. Lett.*, vol. 104, no. 4, p. 041115, Jan. 2014.

[301] W. Li, X. Liu, H. Cui, S. Huang, and X. Hao, “The role of Ag in (Ag,Cu)2ZnSnS4thin film for solar cell application,” *J. Alloys Compd.*, vol. 625, pp. 277–283, 2015.

[302] J. Jia, Y. Li, B. Yao, Z. Ding, R. Deng, Y. Jiang, and Y. Sui, “Band offsets of $Ag_2ZnSnSe_4$ /CdS heterojunction: An experimental and first-principles study,” *J. Appl. Phys.*, vol. 121, no. 21, p. 215305, 2017.

[303] S. Bag, O. Gunawan, T. Gokmen, Y. Zhu, and D. B. Mitzi, “Hydrazine-processed Ge-substituted CZTSe solar cells,” *Chem. Mater.*, vol. 24, no. 23, pp. 4588–4593, 2012.

[304] C.-M. Fan, M. D. Regulacio, C. Ye, S. H. Lim, S. K. Lua, Q.-H. Xu, Z. Dong, A.-W. Xu, and M.-Y. Han, “Colloidal nanocrystals of orthorhombic Cu2ZnGeS4: phase-controlled synthesis, formation mechanism and photocatalytic behavior.,” *Nanoscale*, vol. 7, no. 7, pp. 3247–53, 2015.

[305] M. Neuschitzer, J. Marquez, S. Giraldo, M. Dimitrievska, M. Placidi, I. Forbes, V. Izquierdo-Roca, A. Pérez-Rodriguez, and E. Saucedo, “Voc Boosting and Grain Growth Enhancing Ge-Doping Strategy for Cu2ZnSnSe4 Photovoltaic Absorbers,” *J. Phys. Chem. C*, vol. 120, no. 18, pp. 9661–9670, 2016.

[306] D. B. Khadka, S. Y. Kim, and J. H. Kim, “Effects of Ge Alloying on Device Characteristics of Kesterite-Based CZTSSe Thin Film Solar Cells,” *J. Phys. Chem. C*, vol. 120, no. 8, pp. 4251–4258, 2016.

[307] J. Li, H. Shen, J. Chen, Y. Li, and J. Yang, “Growth mechanism of Ge-doped CZTSSe thin film by sputtering method and solar cells,” *Phys. Chem. Chem. Phys.*, vol. 18, no. 41, pp. 28829–28834, 2016.

[308] S. Wang, J. Zhang, F. Peng, and L. Shao, “Preparation of Cu2FeSnS4 Single Crystals by Molten Salt Method,” *Nanosci. Nanotechnol. Lett.*, vol. 7, no. 5, p. 398, 2015.

[309] B. Zhou, X. Yan, P. Li, L. Yang, and D. Yu, “Raman spectroscopy as a superior tool to understand the synthetic pathway of Cu_2FeSnS_4 nanoparticles,” *Eur. J. Inorg. Chem.*, vol. 2015, no. 16, pp. 2690–2694, 2015.

[310] J. Zhong, Q. Wang, D. Chen, L. Chen, H. Yu, H. Lu, and Z. Ji, “Biomolecule-assisted solvothermal synthesis of 3D hierarchical Cu_2FeSnS_4 microspheres with enhanced photocatalytic activity,” *Appl. Surf. Sci.*, vol. 343, pp. 28–32, 2015.

[311] G. Chen, J. Li, S. Chen, Z. Huang, M. Wu, J. Zhao, W. Wang, H. Lin, and C. Zhu, “Low cost oxide-based deposition of Cu2FeSnS4thin films for photovoltaic absorbers,” *Mater. Chem. Phys.*, vol. 188, pp. 95–99, 2017.

[312] H. J. Chen, S. W. Fu, S. H. Wu, T. C. Tsai, H. T. Wu, and C. F. Shih, “Structural and photoelectron spectroscopic studies of band alignment at the Cu2ZnSnS4/CdS heterojunction with slight Ni doping in Cu2ZnSnS4,” *J. Phys. D. Appl. Phys.*, vol. 49, no. 33, 2016.

[313] G. S. D. Babu, X. S. Shajan, A. George, P. Parameswaran, S. Murugesan, R. Divakar, E. Mohandas, S. Kumaresan, and G. M. Rao, “Low-cost hydrothermal synthesis and characterization of pentanary Cu2ZnxNi1−xSnS4nanoparticle inks for thin film solar cell applications,” *Mater. Sci. Semicond. Process.*, vol. 63, no. February, pp. 127–136, 2017.

[314] G. S. D. Babu, X. S. Shajan, S. Alwin, V. Ramasubbu, and G. M. Balerao, “Effect of Reaction Period on Stoichiometry, Phase Purity, and Morphology of Hydrothermally Synthesized Cu2NiSnS4Nanopowder,” *J. Electron. Mater.*, vol. 47, no. 1, pp. 312–322, 2018.

[315] M. Wei, Q. Du, R. Wang, G. Jiang, W. Liu, and C. Zhu, “Synthesis of New Earth-abundant Kesterite Cu_2MgSnS_4 Nanoparticles by Hot-injection Method,” *Chem. Lett.*, vol. 43, no. 7, pp. 1149–1151, 2014.

[316] V. Pavan Kumar, E. Guilmeau, B. Raveau, V. Caignaert, and U. V. Varadaraju, “A new wide band gap thermoelectric quaternary selenide Cu2MgSnSe4,” *J. Appl. Phys.*, vol. 118, no. 15, p. 155101, 2015.

[317] M. Vishwakarma, D. Varandani, S. M. Shivaprasad, and B. R. Mehta, “Structural, optical, electrical properties and energy band diagram of Cu_2ZnSiS_4 thin films,” *Sol. Energy Mater. Sol. Cells*, vol. 174, no. October 2017, pp. 577–583, 2018.

[318] C. Li, M. Cao, J. Huang, L. J. Wang, and Y. Shen, “Facile synthesis of ultra-long Cu2CdSnS4nanowires with wurtzite-derived structure,” *Mater. Lett.*, vol. 140, pp. 170–173, 2015.

[319] L. Chen, H. Deng, J. Tao, H. Cao, L. Sun, P. Yang, and J. Chu, “Strategic improvement of Cu2MnSnS4films by two distinct post-annealing processes for constructing thin film solar cells,” *Acta Mater.*, vol. 109, pp. 1–7, 2016.

[320] A. Ghosh, S. Palchoudhury, R. Thangavel, Z. Zhou, N. Naghibolashrafi, K. Ramasamy, and A. Gupta, “A new family of wurtzite-phase Cu_2ZnAS_{4-x} and $CuZn_2AS_4$ (A = Al, Ga, In) nanocrystals for solar energy conversion applications,” *Chem. Commun.*, vol. 52, no. 2, pp. 264–267, 2016.

[321] C. L. McCarthy and R. L. Brutchey, “Solution Deposited $Cu_2BaSnS_{4-x}Se_x$ from a Thiol–Amine Solvent Mixture,” *Chem. Mater.*, p. acs.chemmater.7b03931, 2018.

[322] A. Dalui, A. H. Khan, B. Pradhan, J. Pradhan, B. Satpati, and S. Acharya, “Facile synthesis of composition and morphology modulated quaternary CuZnFeS colloidal nanocrystals for photovoltaic application,” *RSC Adv.*, vol. 5, no. 118, pp. 97485–97494, 2015.

[323] H. Guo, Y. Li, X. Guo, N. Yuan, and J. Ding, “Effect of silicon doping on electrical and optical properties of stoichiometric Cu 2 ZnSnS 4 solar cells,” *Phys. B Condens. Matter*, vol. 531, no. October 2017, pp. 9–15, 2018.

[324] Y. Wu, Y. Zhang, Y. Sui, Z. Wang, S. Lv, M. Wei, Y. Sun, B. Yao, X. Liu, and L. Yang, “Bandgap engineering of Cu2InxZn1−xSn(S,Se)4alloy films for photovoltaic applications,” *Ceram. Int.*, vol. 44, no. 2, pp. 1942–1950, 2018.

[325] C. Yan, K. Sun, J. Huang, S. Johnston, F. Liu, B. P. Veettil, K. Sun, A. Pu, F. Zhou, J. A. Stride, M. A. Green, and X. Hao, “Beyond 11% Efficient Sulfide Kesterite Cu2ZnxCd1-xSnS4Solar Cell: Effects of Cadmium Alloying,” *ACS Energy Lett.*, vol. 2, no. 4, pp. 930–936, 2017.

[326] Y. Sui, Y. Wu, Y. Zhang, Z. Wang, M. Wei, and B. Yao, “Indium effect on structural, optical and electrical properties of Cu2InxZn1-xSnS4alloy thin films for solar cell,” *Superlattices Microstruct.*, vol. 111, pp. 579–590, 2017.

[327] J. M. Skelton, A. J. Jackson, M. Dimitrievska, S. K. Wallace, and A. Walsh, “Vibrational spectra and lattice thermal conductivity of kesterite-structured Cu2ZnSnS4 and Cu2ZnSnSe4,” *APL Mater.*, vol. 3, no. 4, p. 041102, Apr. 2015.

[328] L. L. Baranowski, P. Zawadzki, S. Lany, E. S. Toberer, and A. Zakutayev, “A review of defects and disorder in multinary tetrahedrally bonded semiconductors,” *Semicond. Sci. Technol.*, vol. 31, no. 12, 2016.

[329] S. Kim, J. S. Park, and A. Walsh, “Identification of Killer Defects in Kesterite Thin-Film Solar Cells,” *ACS Energy Lett.*, vol. 3, no. 2, pp. 496–500, 2018.

[330] C. J. Hages, A. Redinger, S. Levcenko, H. Hempel, M. J. Koeper, R. Agrawal, D. Greiner, C. A. Kaufmann, and T. Unold, “Identifying the Real Minority Carrier Lifetime in Nonideal Semiconductors: A Case Study of Kesterite Materials,” *Adv. Energy Mater.*, vol. 7, no. 18, pp. 1–10, 2017.

[331] S. Chen, X. G. Gong, A. Walsh, and S. H. Wei, “Defect physics of the kesterite thin-film solar cell absorber Cu 2 ZnSnS4,” *Appl. Phys. Lett.*, vol. 96, no. 2, pp. 4–7, 2010.

[332] D. Huang and C. Persson, “Band gap change induced by defect complexes in Cu2ZnSnS 4,” *Thin Solid Films*, vol. 535, no. 1, pp. 265–269, 2013.

[333] Y. Zhang, K. Tse, X. Xiao, and J. Zhu, “Controlling defects and secondary phases of CZTS by surfactant potassium,” *Phys. Rev. Mater.*, vol. 1, no. 4, p. 045403, 2017.

[334] M. Kumar, A. Dubey, N. Adhikari, S. Venkatesan, and Q. Qiao, “Strategic review of secondary phases, defects and defect-complexes in kesterite CZTS–Se solar cells,” *Energy Environ. Sci.*, vol. 8, no. 11, pp. 3134–3159, 2015.

[335] C. H. Ruan, C. C. Huang, Y. J. Lin, G. R. He, H. C. Chang, and Y. H. Chen, “Electrical properties of CuxZnySnS4films with different Cu/Zn ratios,” *Thin Solid Films*, vol. 550, pp. 525–529, 2014.

[336] J. Márquez, M. Neuschitzer, M. Dimitrievska, R. Gunder, S. Haass, M. Werner, Y. E. Romanyuk, S. Schorr, N. M. Pearsall, and I. Forbes, “Systematic compositional changes and their influence on lattice and optoelectronic properties of Cu2ZnSnSe4 kesterite solar cells,” *Sol. Energy Mater. Sol. Cells*, vol. 144, no. October, pp. 579–585, 2016.

[337] W. Xiao, J. N. Wang, X. S. Zhao, J. W. Wang, G. J. Huang, L. Cheng, L. J. Jiang, and L. G. Wang, “Intrinsic defects and Na doping in Cu2ZnSnS4: A density-functional theory study,” *Sol. Energy*, vol. 116, pp. 125–132, 2015.

[338] C. Malerba, F. Biccari, C. L. A. Ricardo, M. Valentini, R. Chierchia, M. Müller, A. Santoni, E. Esposito, P. Mangiapane, P. Scardi, and A. Mittiga, “CZTS stoichiometry effects on the band gap energy,” *J. Alloys Compd.*, vol. 582, pp. 528–534, 2014.

[339] G. Rey, G. Larramona, S. Bourdais, C. Choné, B. Delatouche, A. Jacob, G. Dennler, and S. Siebentritt, “On the origin of band-tails in kesterite,” *Sol. Energy Mater. Sol. Cells*, vol. 179, no. October 2017, pp. 142–151, 2018.

[340] C. R. Tilford, “Pressure and Vacuum Measurements,” in *Physical Methods of*

Chemistry, 2nd Editio., B. W. Rossiter and R. C. Baetzold, Eds. John Wiley & Sons, Ltd, 1992, p. 760.

[341] P. Hofmann, *Surface Physics: An Introduction*. 2016.

[342] D. P. Woodruff and T. A. Delchar, "Introduction," in *Core Techniques in Surface Science*, C. P. Woodruff, Ed. Cambridge University Press, 1994, pp. 1–8.

[343] A. H. McIlraith, "A Charged Particle Oscillator," *Nature*, vol. 212, p. 1422, 1966.

[344] A. H. McIlraith, "A charged particle oscillator," *J. Vac. Sci. Technol.*, vol. 9, no. 1, p. 209, 1971.

[345] G. J. Rushton, K. R. O'Sheat, and R. K. Fitch, "Modes of operation of an electrostatic ion gun," *J. Phys. D. Appl. Phys.*, vol. 6, no. 10, pp. 1167–1172, 1973.

[346] A. M. Ghander and R. K. Fitch, "An improved form of the oscillating electron electrostatic ion source for ion etching," *Vacuum*, vol. 24, no. 10, pp. 483–487, 1974.

[347] G. Padeletti and G. M. Ingo, "Factors determining preferential sputtering in InGaAs system: Angle-resolved small-area XPS investigation," *Surf. Interface Anal.*, vol. 34, no. 1, pp. 266–270, 2002.

[348] J. B. Malherbe, W. O. Barnard, I. L. R. Strydom, and C. W. Louw, "Preferential sputtering of GaAs," *Surf. Interface Anal.*, vol. 18, no. 7, pp. 491–495, 1992.

[349] J. B. Malherbe, S. Hofmann, and J. M. Sanz, "Preferential sputtering of oxides: A comparison of model predictions with experimental data," *Appl. Surf. Sci.*, vol. 27, no. 3, pp. 355–365, 1986.

[350] A. Einstein, "Über einen die Erzeugung und Verwandlung des Lichtes betreffenden heuristischen Gesichtspunkt," *Ann. Phys.*, vol. 322, no. 6, pp. 132–148, 1905.

[351] D. Ter Haar, *The Old Quantum Theory*. Oxford: Pergamon Press, 1967.

[352] The Nobel Foundation, "The Nobel Prize in Physics 1921," 1921. [Online]. Available: https://www.nobelprize.org/nobel_prizes/physics/laureates/1921/index.html. [Accessed: 07-Feb-2018].

[353] K. Siegbahn and K. Edvarson, "β-Ray Spectroscopy in the Precision Range of 1:10^5," *Nucl. Physic*, vol. 1, pp. 137–159, 1956.

[354] C. Nordling, E. Sokolowski, and K. Siegbahn, "Precision Method for Obtaining Absolute Values of Atomic Binding Energies," *Phys. Rev.*, vol. 105, no. 5, pp. 1676–1677, 1957.

[355] The Nobel Foundation, "The Nobel Prize in Physics 1981," 1981. [Online]. Available: https://www.nobelprize.org/nobel_prizes/physics/laureates/1981/. [Accessed: 07-Feb-2018].

[356] M. P. Seah and W. A. Dench, "Quantitative electron spectroscopy of surfaces: A standard data base for electron inelastic mean free paths in solids," *Surf. Interface Anal.*, vol. 1, no. 1, pp. 2–11, 1979.

[357] H. Tokutaka, K. Nishimori, and H. Hayashi, "The electron mean free path (applicable to quantitative electron spectroscopy)," *Surf. Sci.*, vol. 149, no. 2–3, pp. 349–365, 1985.

[358] H. Wiedemann, *Particle accelerator physics: Third edition*. 2007.

[359] R. Caciuffo, S. Melone, F. Rustichelli, and A. Boeuf, "Monochromators for X-ray synchrotron radiation," *Rev. Sect. Phys. Lett.*, vol. 152, no. 1, pp. 1–71, 1987.

[360] Z. Zhong, G. Le Duc, D. Chapman, T. W. C., and E. Fontes, "A tunable Laue/bent-Laue monochromator with fixed second crystal for synchrotron radiation," *AIP Adv.*, vol. 417, pp. 95–100, 1997.

[361] V. R. Kocharyan, A. S. Gogolev, A. A. Kiziridi, A. V. Batranin, and T. R. Muradyan, "Hard X-ray Laue monochromator," *IOP Conf. Ser. Mater. Sci. Eng.*, vol. 135, no. 1, 2016.

[362] X. Shi, W. Xu, A. Yakovenko, G. Halder, Z. Liu, C. Kurtz, L. Ribaud, K. Beyer, K. Chapman, and P. Chupas, "Bent Bragg-Laue monochromator for high-energy X-rays," *J. Appl. Crystallogr.*, vol. 50, pp. 1158–1164, 2017.

[363] J. F. Moulder, W. F. Stickle, P. E. Sobol, and K. D. Bomben, *Handbook of X-ray Photoelectron Spectroscopy*. Eden Prairie, Minnesota: Physical Electronics, Inc., 1995.

[364] B. Vincent Crist, *Vol 1 - XPS of Elements & Native Oxides.pdf*. Ames, Iowa: XPS International, 1999.

[365] B. Vincent Crist, *Vol 2 - XPS of Binary Oxides*. Ames, Iowa: XPS International, 2005.

[366] D. A. Shirley, "High-resolution x-ray photoemission spectrum of the valence bands of gold," *Phys. Rev. B*, vol. 5, no. 12, pp. 4709–4714, 1972.

[367] A. Proctor and P. M. A. Sherwood, "Data Analysis Techniques in X-ray Photoelectron Spectroscopy," *Anal. Chem.*, vol. 54, no. 1, pp. 13–19, 1982.

[368] J. Végh, "The Shirley background revised," *J. Electron Spectros. Relat. Phenomena*, vol. 151, no. 3, pp. 159–164, 2006.

[369] S. Tougaard, "Quantitative analysis of the inelastic background in surface electron spectroscopy," *Surf. Interface Anal.*, vol. 11, no. 9, pp. 453–472, 1988.

[370] S. Doniach and M. Šunjić, "Many-electron singularity i n x-ray photoemission andx-ray line spectra from metals," *J. Phys. C Solid State Phys.*, vol. 3, pp. 285–291, 1970.

[371] A. Müller, A. Borovik, T. Buhr, J. Hellhund, K. Holste, A. L. D. Kilcoyne, S. Klumpp, M. Martins, S. Ricz, J. Viefhaus, and S. Schippers,

"Observation of four-electron Auger processes," *J. Phys. Conf. Ser.*, vol. 635, no. 1, 2015.

[372] A. Müller, A. Borovik, T. Buhr, J. Hellhund, K. Holste, A. L. D. Kilcoyne, S. Klumpp, M. Martins, S. Ricz, J. Viefhaus, and S. Schippers, "Observation of a four-electron Auger process in near- K -edge photoionization of singly charged carbon ions," *Phys. Rev. Lett.*, vol. 114, no. 1, pp. 1–5, 2015.

[373] F. Zhou, Y. Ma, and Y. Qu, "Single, double, and triple Auger decay probabilities of C+(1s2s22p2 2D, 2P) resonances," *Phys. Rev. A*, vol. 93, no. 6, pp. 1–5, 2016.

[374] C. D. Wagner, "Auger Lines in X-Ray Photoelectron Spectrometry," *Anal. Chem.*, vol. 44, no. 6, pp. 967–973, 1972.

[375] S. W. Gaarenstroom and N. Winograd, "Initial and final state effects in the ESCA spectra of cadmium and silver oxides," *J. Chem. Phys.*, vol. 67, no. 8, pp. 3500–3506, 1977.

[376] C. D. Wagner, "Chemical shifts of Auger lines, and the Auger parameter," *Faraday Discuss. Chem. Soc.*, vol. 60, p. 291, 1975.

[377] G. Moretti, "Auger parameter and Wagner plot in the characterization of chemical states by X-ray photoelectron spectroscopy: a review," *J. Electron Spectros. Relat. Phenomena*, vol. 95, no. 2–3, pp. 95–144, 1998.

[378] C. D. Wagner and J. A. Taylor, "Contributions to screening in the solid state by electron systems of remote atoms: Effects to photoelectron and Auger transitions," *J. Electron Spectros. Relat. Phenomena*, vol. 28, no. 2, pp. 211–217, 1982.

[379] B. Richter, H. Kuhlenbeck, H. J. Freund, and P. S. Bagus, "Cluster core-level binding-energy shifts: The role of lattice strain," *Phys. Rev. Lett.*, vol. 93, no. 2, pp. 026805-1, 2004.

[380] J. G. Tao, J. S. Pan, C. H. A. Huan, Z. Zhang, J. W. Chai, and S. J. Wang, "Origin of XPS binding energy shifts in Ni clusters and atoms on rutile TiO2surfaces," *Surf. Sci.*, vol. 602, no. 16, pp. 2769–2773, 2008.

[381] J. S. Pan, J. G. Tao, C. H. A. Huan, S. Y. Chiam, Z. Zhang, D. T. H. Li, Y. Sun, J. W. Chai, S. J. Wang, and C. Q. Sun, "Determination of atomic Ni interaction with TiO2 by XPS," *Surf. Interface Anal.*, vol. 42, no. February, pp. 878–881, 2010.

[382] N. V Smith, "Inverse photoemission," *Rep. Progr. Phys.*, vol. 51, no. 9, p. 1227, 1988.

[383] V. Dose, "Ultraviolet Bremsstrahlung spectroscopy," *Prog. Surf. Sci.*, vol. 13, no. 3, pp. 225–283, 1983.

[384] D. P. Woodruff, P. D. Johnson, and N. V. Smith, "Inverse photoemission," *J. Vac. Sci. Technol. A Vacuum, Surfaces, Film. 1,* vol. 1, no. 2, p. 1104, 1983.

[385] J. B. Pendry, "Theory of inverse photoemission," *J. Phys. C Solid State Phys.*, vol. 14, no. 9, pp. 1381–1391, 1981.

[386] P. D. Johnson and S. L. Hulbert, "Inverse photoemission," *Rev. Sci. Instrum.*, vol. 61, no. 9, pp. 2277–2288, 1990.

[387] T. Fauster, D. Straub, J. J. Donelon, D. Grimm, A. Marx, and F. J. Himpsel, "Normal-incidence grating spectrograph with large acceptance for inverse photoemission," *Rev. Sci. Instrum.*, vol. 56, no. 6, pp. 1212–1214, 1985.

[388] V. Dose, "VUV isochromat spectroscopy," *Appl. Phys.*, vol. 14, no. 1, pp. 117–118, 1977.

[389] P. Vavassori and E. Puppin, "New calibration procedure for an inverse photoemission spectrograph," *Rev. Sci. Instrum.*, vol. 4469, no. 1992, pp. 4469–4470, 1992.

[390] M. Pedio, M. Grilli, and C. Ottaviani, "Inverse photoemission studies of C 60 on Au (110)," *J. electron …*, vol. 76, pp. 405–409, 1995.

[391] K. D. Tsuei and J. Y. Yuh, "Photoemission and photoabsorption study of adsorption on Cu(111) surfaces," *Phys. Rev. B - Condens. Matter Mater. Phys.*, vol. 56, no. 23, pp. 15412–15420, 1997.

[392] M. Pedio, K. Hevesi, N. Zema, M. Capozi, P. Perfetti, R. Gouttebaron, J. J. Pireaux, R. Caudano, and P. Rudolf, "C60/metal surfaces: adsorption and decomposition," *Surf. Sci.*, vol. 437, no. 1, pp. 249–260, 1999.

[393] R. L. Anderson, "Germanium-Gallium Arsenide Heterojunctions [Letter to the Editor]," *IBM J. Res. Dev.*, vol. 4, no. 3, pp. 283–287, 1960.

[394] E. A. Kraut, R. W. Grant, J. R. Waldrop, and S. P. Kowalczyk, "Precise Determination of the Valence-Band Edge in X-Ray Photoemission Spectra: Application to Measurement of Semiconductor Interface Potentials," *Phys. Rev. Lett.*, vol. 44, no. 24, pp. 1620–1623, Jun. 1980.

[395] J. T. Gibbon, L. Jones, J. W. Roberts, M. Althobaiti, P. R. Chalker, I. Z. Mitrovic, and V. R. Dhanak, "Band alignments at Ga2O3 heterojunction interfaces with Si and Ge," *AIP Adv.*, vol. 8, no. 6, p. 065011, 2018.

[396] J. Frank, M. Fleischer, and H. Meixner, "Electrical doping of gas-sensitive, semiconducting Ga2O3 thin films," *Sensors Actuators B Chem.*, vol. 34, no. 1–3, pp. 373–377, Aug. 1996.

[397] J. Frank, M. Fleischer, and H. Meixner, "Gas-sensitive electrical properties of pure and doped semiconducting Ga2O3 thick films," *Sensors Actuators B Chem.*, vol. 48, no. 1–3, pp. 318–321, May 1998.

[398] C. Baban, Y. Toyoda, and M. Ogita, "Oxygen sensing at high temperatures using Ga2O3 films," *Thin Solid Films*, vol. 484, no. 1–2, pp. 369–373, Jul. 2005.

[399] H. Kim, S.-J. Park, and H. Hwang, "Thermally oxidized GaN film for use as gate insulators," *J. Vac. Sci. Technol. B Microelectron. Nanom.*

Struct., vol. 19, no. 2, p. 579, Mar. 2001.

[400] T. Minami, Y. Nishi, and T. Miyata, "High-Efficiency Cu 2 O-Based Heterojunction Solar Cells Fabricated Using a Ga 2 O 3 Thin Film as N-Type Layer," *Appl. Phys. Express*, vol. 6, no. 4, p. 044101, 2013.

[401] J. Wen, L. Q. Guo, and J. Tao, "Ultrathin Passivation of P-type Sulicon Surface by Atomic Layer Deposited Gallium Oxide Thin Films," *IOP Conf. Ser. Mater. Sci. Eng.*, vol. 170, p. 012009, 2017.

[402] D. Guo, Z. Wu, P. Li, Y. An, H. Liu, X. Guo, H. Yan, G. Wang, C. Sun, L. Li, and W. Tang, "Fabrication of β-Ga2O3 thin films and solar-blind photodetectors by laser MBE technology," *Opt. Mater. Express*, vol. 4, no. 5, p. 1067, May 2014.

[403] X. Z. Liu, P. Guo, T. Sheng, L. X. Qian, W. L. Zhang, and Y. R. Li, "β-Ga2O3 thin films on sapphire pre-seeded by homo-self-templated buffer layer for solar-blind UV photodetector," *Opt. Mater. (Amst).*, vol. 51, pp. 203–207, 2016.

[404] X. C. Guo, N. H. Hao, D. Y. Guo, Z. P. Wu, Y. H. An, X. L. Chu, L. H. Li, P. G. Li, M. Lei, and W. H. Tang, "β-Ga2O3/p-Si heterojunction solar-blind ultraviolet photodetector with enhanced photoelectric responsivity," *J. Alloys Compd.*, vol. 660, pp. 136–140, 2016.

[405] A. Paskaleva, D. Spassov, and P. Terziyska, "Electric, dielectric and optical properties of Ga2O3 grown by metal organic chemical vapour deposition," *J. Phys. Conf. Ser.*, vol. 755, p. 011001, 2016.

[406] Z. Chen, K. Nishihagi, X. Wang, K. Saito, T. Tanaka, M. Nishio, M. Arita, and Q. Guo, "Band alignment of Ga2O3/Si heterojunction interface measured by X-ray photoelectron spectroscopy," *Appl. Phys. Lett.*, vol. 109, no. 10, pp. 1–5, 2016.

[407] L. K. Chu, T. D. Lin, M. L. Huang, R. L. Chu, C. C. Chang, J. Kwo, and M. Hong, "Ga2O3(Gd2O3) on Ge without interfacial layers: Energy-band parameters and metal oxide semiconductor devices," *Appl. Phys. Lett.*, vol. 94, no. 20, pp. 10–13, 2009.

[408] T. W. Pi, M. L. Huang, W. C. Lee, L. K. Chu, T. D. Lin, T. H. Chiang, Y. C. Wang, Y. D. Wu, M. Hong, and J. Kwo, "High-resolution core-level photoemission study of CF4-treated Gd2 O3 (Ga2 O3) gate dielectric on Ge probed by synchrotron radiation," *Appl. Phys. Lett.*, vol. 98, no. 6, pp. 2–5, 2011.

[409] Y. Huang, J. P. Xu, L. Liu, P. T. Lai, and W. M. Tang, "N2-Plasma-Treated Ga2O3(Gd2O3) as Interface Passivation Layer for Ge MOS Capacitor with HfTiON Gate Dielectric," *IEEE Trans. Electron Devices*, vol. 63, no. 7, pp. 2838–2843, 2016.

[410] S. H. Park, S. H. Kim, S. Y. Park, and C. Lee, "Synthesis and CO gas sensing properties of surface-nitridated Ga $_2$ O $_3$ nanowires," *RSC Adv.*, vol. 4, no. 108, pp. 63402–63407, 2014.

[411] J. Jeong and Y. Hong, "Debye length and active layer thickness-dependent performance variations of amorphous oxide-based TFTs," *IEEE Trans. Electron Devices*, vol. 59, no. 3, pp. 710–714, 2012.

[412] M. Rebien, W. Henrion, M. Hong, J. P. Mannaerts, and M. Fleischer, "Optical properties of gallium oxide thin films," *Appl. Phys. Lett.*, vol. 81, no. 2, pp. 250–252, 2002.

[413] M. Passlack, E. F. Schubert, W. S. Hobson, M. Hong, N. Moriya, S. N. G. Chu, K. Konstadinidis, M. L. Schnoes, G. J. Zydzik, J. P. Mannaerts, M. L. Schnoes, and G. J. Zydzik, "Ga2O3 films for electronic and optoelectronic applications," *J. Appl. Phys.*, vol. 77, no. 2, p. 686, Jan. 1995.

[414] M. D. Heinemann, J. Berry, G. Teeter, T. Unold, D. Ginley, M. D. Heinemann, J. Berry, G. Teeter, T. Unold, and D. Ginley, "Oxygen deficiency and Sn doping of amorphous Ga2O3," *Appl. Phys. Lett.*, vol. 108, no. 2, pp. 1–5, 2016.

[415] R. O'Donoghue, J. Rechmann, M. Aghaee, D. Rogalla, H.-W. Becker, M. Creatore, A. D. Wieck, and A. Devi, "Low temperature growth of gallium oxide thin films via plasma enhanced atomic layer deposition," *Dalt. Trans.*, vol. 46, pp. 16551–16561, 2017.

[416] T. Koida, Y. Kamikawa-Shimizu, A. Yamada, H. Shibata, and S. Niki, "Cu(In,Ga)Se2 Solar Cells With Amorphous Oxide Semiconducting Buffer Layers," *IEEE J. Photovoltaics*, vol. 5, no. 3, pp. 956–961, 2015.

[417] P. de Mierry, D. Ballutaud, and M. Aucouturier, "Effect of Surface Preparations on Electrical and Chemical Surface Properties of P-Type Silicon," *J. Electrochem. Soc.*, vol. 137, no. 9, p. 2966, 1990.

[418] M. H. Kibel and P. W. Leech, "X-ray photoelectron spectroscopy study of optical waveguide glasses," *Surf. interface Anal.*, vol. 24, no. 9, pp. 605–610, 1996.

[419] P. Gorostiza, R. Díaz, J. Servat, and F. Sanz, "Atomic Force Microscopy Study of the Silicon Doping Influence on the First Stages of Platinum Electroless Deposition," *J. Electrochem. Soc.*, vol. 144, no. 3, p. 909, 1997.

[420] A. Rifai, S. Maikap, and Y. Nakamura, "Energy band alignments of Al2O3–HfO2/Al2O3 nanolaminates–SiO2–p-type Si structures," *J. Vac. Sci. Technol. B*, vol. 33, no. 5, p. 051812, 2015.

[421] Q. Li, S. J. Wang, K. B. Li, A. C. H. Huan, J. W. Chai, J. S. Pan, and C. K. Ong, "Photoemission study of energy-band alignment for RuOx/HfO2/Si system," *Appl. Phys. Lett.*, vol. 85, no. 25, pp. 6155–6157, 2004.

[422] S. J. Wang, A. C. H. Huan, Y. L. Foo, J. W. Chai, J. S. Pan, Q. Li, Y. F. Dong, Y. P. Feng, and C. K. Ong, "Energy-band alignments at ZrO2/Si, SiGe, and Ge interfaces," *Appl. Phys. Lett.*, vol. 85, no. 19, pp. 4418–4420, 2004.

[423] M. Perego, G. Seguini, G. Scarel, M. Fanciulli, and F. Wallrapp, “Energy band alignment at TiO2/Si interface with various interlayers,” *J. Appl. Phys.*, vol. 103, no. 4, 2008.

[424] K. Kakushima, K. Okamoto, K. Tachi, J. Song, S. Sato, T. Kawanago, K. Tsutsui, N. Sugii, P. Ahmet, T. Hattori, and H. Iwai, “Observation of band bending of metal/high- k Si capacitor with high energy x-ray photoemission spectroscopy and its application to interface dipole measurement,” *J. Appl. Phys.*, vol. 104, no. 10, 2008.

[425] S. A. Chambers, Y. Du, R. B. Comes, S. R. Spurgeon, and P. V. Sushko, “The effects of core-level broadening in determining band alignment at the epitaxial SrTiO3(001)/p-Ge(001) heterojunction,” *Appl. Phys. Lett.*, vol. 110, no. 8, pp. 0–4, 2017.

[426] K. J. Hubbard and D. G. Schlom, “Thermodynamic stability of binary oxides in contact with silicon,” *J. Mater. Res.*, vol. 11, no. 11, pp. 2757–2776, 1996.

[427] D. G. Schlom and J. H. Haeni, “A Thermodynamic Approach to Selecting Alternative Gate Dielectrics,” *MRS Bull.*, no. March, pp. 198–204, 2002.

[428] G. B. Alers, D. J. Werder, Y. Chabal, H. C. Lu, E. P. Gusev, E. Garfunkel, T. Gustafsson, and R. S. Urdahl, “Intermixing at the tantalum oxide/silicon interface in gate dielectric structures,” *Appl. Phys. Lett.*, vol. 73, no. 11, pp. 1517–1519, 1998.

[429] H. Ono and K. I. Koyanagi, “Formation of silicon-oxide layers at the interface between tantalum oxide and silicon substrate,” *Appl. Phys. Lett.*, vol. 75, no. 22, pp. 3521–3523, 1999.

[430] T. M. Klein, D. Niu, W. S. Epling, W. Li, D. M. Maher, C. C. Hobbs, R. I. Hegde, I. J. R. Baumvol, and G. N. Parsons, “Evidence of aluminum silicate formation during chemical vapor deposition of amorphous Al2O3 thin films on Si(100),” *Appl. Phys. Lett.*, vol. 75, no. 25, pp. 4001–4003, 1999.

[431] M. Kundu, N. Miyata, and M. Ichikawa, “Study of ultrathin Al2O3/Si(001) interfaces by using scanning reflection electron microscopy and x-ray photoelectron spectroscopy,” *Appl. Phys. Lett.*, vol. 78, no. 11, pp. 2001–2003, 2001.

[432] R. Puthenkovilakam and J. P. Chang, “Valence band structure and band alignment at the ZrO2/Si interface,” *Appl. Phys. Lett.*, vol. 84, no. 8, pp. 1353–1355, 2004.

[433] Y. Kamata, Y. Kamimuta, T. Ino, and A. Nishiyama, “Direct comparison of ZrO2 and HfO2 on Ge substrate in terms of the realization of ultrathin high-κ gate stacks,” *Japanese J. Appl. Physics, Part 1 Regul. Pap. Short Notes Rev. Pap.*, vol. 44, no. 4 B, pp. 2323–2329, 2005.

[434] R. Zhang, P. C. Huang, J. C. Lin, M. Takenaka, and S. Takagi, “Atomic layer-by-layer oxidation of Ge (100) and (111) surfaces by plasma post oxidation of Al2O3/Ge structures,” *Appl. Phys. Lett.*, vol. 102, no. 8, pp. 1–5, 2013.

[435] G. Hollinger and F. J. Himpsel, “Oxygen chemisorption and oxide formation on Si(111) and Si(100) surfaces,” *J. Vac. Sci. Technol. A Vacuum, Surfaces, Film.*, vol. 1, no. 2, pp. 640–645, 1983.

[436] G. Hollinger and F. J. Himpsel, “Probing the transition layer at the SiO2Si interface using core level photoemission,” *Appl. Phys. Lett.*, vol. 44, p. 93, 1984.

[437] W. Ranke and Y. R. Xing, “ORIENTATION DEPENDENT SILICON CRYSTAL II. Oxygen,” *Surf. Sci.*, vol. 157, pp. 353–370, 1985.

[438] D. Schmeisser, R. D. Schnell, A. Bogen, F. J. Himpsel, D. Rieger, G. Landgren, and J. F. Morar, “Surface oxidation states of germanium,” *Surf. Sci.*, vol. 172, no. 2, pp. 455–465, 1986.

[439] J. M. Hill, D. G. Royce, C. S. Fadley, L. F. Wagner, and F. J. Grunthaner, “Properties of oxidized silicon as determined by angular-dependent X-ray photoelectron spectroscopy,” *Chem. Phys. Lett.*, vol. 44, no. 2, pp. 225–231, 1976.

[440] P. J. Cumpson, “The Thickogram - a method for easy film The Thickogram - a method for easy film.pdf,” *Surf. Interface Anal.*, vol. 29, no. April, pp. 403–406, 2000.

[441] C. J. Powell and A. Jablonski, “Progress in quantitative surface analysis by X-ray photoelectron spectroscopy: Current status and perspectives,” *J. Electron Spectros. Relat. Phenomena*, vol. 178–179, no. C, pp. 331–346, 2010.

[442] M. Dimitrievska, A. Fairbrother, E. Saucedo, X. Fontané, T. Jawhari, V. Izquierdo-Roca, E. Saucedo, and A. Pérez-Rodríguez, “Multiwavelength excitation Raman scattering study of polycrystalline kesterite Cu 2 ZnSnS 4 thin films,” *Appl. Phys. Lett.*, vol. 021901, no. 2, pp. 1–5, 2014.

[443] M. Guc, S. Levcenko, I. V. Bodnar, V. Izquierdo-Roca, X. Fontane, L. V. Volkova, E. Arushanov, and A. Pérez-Rodríguez, “Polarized Raman scattering study of kesterite type Cu2 ZnSnS4 single crystals,” *Sci. Rep.*, vol. 6, no. January, pp. 1–7, 2016.

[444] M. Guc, S. Levcenko, V. Izquierdo-Roca, X. Fontané, E. Arushanov, and A. Pérez-Rodríguez, “Polarized Raman scattering analysis of Cu $_2$ ZnSnSe $_4$ and Cu $_2$ ZnGeSe $_4$ single crystals,” *J. Appl. Phys.*, vol. 114, no. 19, p. 193514, 2013.

[445] A. V Stanchik, V. F. Gremenok, S. A. Bashkirov, M. S. Tivanov, R. L. Juškénas, G. F. Novikov, R. Giraitis, and A. M. Saad, “Microstructure and Raman Scattering of Cu 2 ZnSnSe 4 Thin Films Deposited onto Flexible Metal Substrates,” *Semiconductors*, vol. 52, no. 2, pp. 215–220, 2018.

[446] P. A. Fernandes, P. M. P. Salomé, and A. F. Da

Cunha, “A study of ternary Cu2SnS3 and Cu3SnS 4 thin films prepared by sulfurizing stacked metal precursors,” *J. Phys. D. Appl. Phys.*, vol. 43, no. 21, 2010.

[447] H. Guan, H. Shen, C. Gao, and X. He, “Structural and optical properties of Cu2SnS3 and Cu3SnS4 thin films by successive ionic layer adsorption and reaction,” *J. Mater. Sci. Mater. Electron.*, vol. 24, no. 5, pp. 1490–1494, 2013.

[448] W. G. Nilsen, “Raman spectrum of cubic ZnS,” *Phys. Rev.*, vol. 182, no. 3, pp. 838–850, 1969.

[449] Y. C. Cheng, C. Q. Jin, F. Gao, X. L. Wu, W. Zhong, S. H. Li, and P. K. Chu, “Raman scattering study of zinc blende and wurtzite ZnS,” *J. Appl. Phys.*, vol. 106, no. 12, 2009.

[450] L. S. Price, I. P. Parkin, A. M. E. Hardy, R. J. H. Clark, T. G. Hibbert, and K. C. Molloy, “Atmospheric Pressure Chemical Vapor Deposition of Tin Sulfides (SnS, Sn_2S_3, and SnS_2) on Glass,” *Chem. Mater.*, vol. 11, no. 7, pp. 1792–1799, 1999.

[451] J. M. Skelton, L. A. Burton, A. J. Jackson, F. Oba, S. C. Parker, and A. Walsh, “Lattice dynamics of the tin sulphides SnS2 , SnS and Sn2S 3 : vibrational spectra and thermal transport,” *Phys. Chem. Chem. Phys.*, vol. 19, no. 19, pp. 12452–12465, 2017.

[452] A. Isac, A. Duta, A. Kriza, A. Enesca, and M. Nanu, “The growth of CuS thin films by Spray Pyrolysis,” *J. Phys. Conf. Ser.*, vol. 61, no. 1, pp. 477–481, 2007.

[453] T. Hurma and S. Kose, “XRD Raman analysis and optical properties of CuS nanostructured film,” *Optik (Stuttg).*, vol. 127, no. 15, pp. 6000–6006, 2016.

[454] H. Li, Q. Zhang, C. C. R. Yap, B. K. Tay, T. H. T. Edwin, A. Olivier, and D. Baillargeat, “From bulk to monolayer MoS2: Evolution of Raman scattering,” *Adv. Funct. Mater.*, vol. 22, no. 7, pp. 1385–1390, 2012.

[455] K. Gołasa, M. Grzeszczyk, R. Bozek, P. Leszczyński, A. Wysmołek, M. Potemski, and A. Babiński, “Resonant Raman scattering in MoS2-From bulk to monolayer,” *Solid State Commun.*, vol. 197, pp. 53–56, 2014.

[456] R. Saito, Y. Tatsumi, S. Huang, X. Ling, and M. S. Dresselhaus, “Raman spectroscopy of transition metal dichalcogenides,” *J. Phys. Condens. Matter*, vol. 28, no. 35, 2016.

[457] X. Zhang, X.-F. Qiao, W. Shi, J.-B. Wu, D.-S. Jiang, and P.-H. Tan, “Phonon and Raman scattering of two-dimensional transition metal dichalcogenides from monolayer, multilayer to bulk material,” *Chem. Soc. Rev.*, vol. 44, pp. 2757–2785, 2015.

[458] H. Terrones, E. Del Corro, S. Feng, J. M. Poumirol, D. Rhodes, D. Smirnov, N. R. Pradhan, Z. Lin, M. A. T. Nguyen, A. L. Elías, T. E. Mallouk, L. Balicas, M. A. Pimenta, and M. Terrones, “New First Order Raman-active Modes in Few Layered Transition Metal Dichalcogenides,” *Sci. Rep.*, vol. 4, pp. 1–9, 2014.

[459] D. Nam, J.-U. Lee, and H. Cheong, “Excitation energy dependent Raman spectrum of MoSe2,” *Sci. Rep.*, vol. 5, no. 1, p. 17113, 2015.

[460] A. Arora, K. Nogajewski, M. R. Molas, M. Koperski, and M. Potemski, “Exciton band structure in layered MoSe2: from a monolayer to the bulk limit,” *Nanoscale*, vol. 7, pp. 20769–20775, 2015.

[461] L. J. van der Pauw, “A method of measuring the resistivity and hall coefficient of discs of arbitrary shape,” *Philips Res. Reports*, vol. 13, no. 1, pp. 1–9, 1958.

[462] J. E. N. Swallow, B. A. D. Williamson, T. J. Whittles, M. Birkett, T. J. Featherstone, N. Peng, A. Abbott, M. Farnworth, K. J. Cheetham, P. Warren, D. O. Scanlon, V. R. Dhanak, and T. D. Veal, “Self-Compensation in Transparent Conducting F-Doped SnO2 Films,” *Adv. Funct. Mater.*, vol. 1701900, pp. 1–10, 2017.

[463] P. Hohenberg and W. Kohn, “Inhomogeneous electron gas,” *Phys. Rev.*, vol. 136, no. 3B, p. 864, 1964.

[464] W. Kohn and L. J. Sham, “Self-consistent equations including exchange and correlation effects,” *Phys. Rev.*, vol. 140, no. 4A, 1965.

[465] The Nobel Foundation, “The Nobel Prize in Chemistry 1998,” 1998. [Online]. Available: https://www.nobelprize.org/nobel_prizes/chemistry/laureates/1998/. [Accessed: 16-Feb-2018].

[466] E. Fermi, “Un metodo statistico per la determinazione di alcune priorieta dell’atome,” *Rend. Accad. Naz. Lincei*, vol. 6, no. 602–607, p. 32, 1927.

[467] L. H. Thomas, “The calculation of atomic □elds,” *Math. Proc. Cambridge Philos. Soc.*, vol. 23, no. 5, pp. 542–548, 1927.

[468] Y. Hinuma, A. Grüneis, G. Kresse, and F. Oba, “Band alignment of semiconductors from density-functional theory and many-body perturbation theory,” *Phys. Rev. B*, vol. 90, no. 15, p. 155405, 2014.

[469] X. Hai, J. Tahir-Kheli, and W. A. Goddard, “Accurate band gaps for semiconductors from density functional theory,” *J. Phys. Chem. Lett.*, vol. 2, no. 3, pp. 212–217, 2011.

[470] D. Bagayoko, “Understanding Density Functional Theory (DFT) and Completing It in Practice,” *AIP Adv.*, vol. 4, no. 127104, p. 1, 2014.

[471] D. Bagayoko, “Understanding the Relativistic Generalization of Density Functional Theory (DFT) and Completing It in Practice,” *J. Mod. Phys.*, vol. 07, no. 09, pp. 911–919, 2016.

[472] J. H. Scofield, “Hartree-Slater subshell photoionization cross-sections at 1254 and 1487 eV,” *J. Electron Spectros. Relat.*

Phenomena, vol. 8, no. 2, pp. 129–137, Jan. 1976.

[473] J. J. Yeh and I. Lindau, "Atomic subshell photoionization cross sections and asymmetry parameters: $1 \leqslant Z \leqslant 103$," *At. Data Nucl. Data Tables*, vol. 32, no. 1, pp. 1–155, Jan. 1985.

[474] I. M. Band, Y. I. Kharitonov, and M. B. Trzhaskovskaya, "Photoionization cross sections and photoelectron angular distributions for x-ray line energies in the range 0.132-4.509 keV targets: $1 \leq Z \leq 100$," *At. Data Nucl. Data Tables*, vol. 23, no. 5, pp. 443–505, 1979.

[475] M. B. TRZHASKOVSKAYA, V. I. NEFEDOV, and V. G. YARZHEMSKY, "PHOTOELECTRON ANGULAR DISTRIBUTION PARAMETERS FOR ELEMENTS Z=1 TO Z=54 IN THE PHOTOELECTRON ENERGY RANGE 100–5000 eV," *At. Data Nucl. Data Tables*, vol. 77, no. 1, pp. 97–159, Jan. 2001.

[476] M. B. TRZHASKOVSKAYA, V. I. NEFEDOV, and V. G. YARZHEMSKY, "PHOTOELECTRON ANGULAR DISTRIBUTION PARAMETERS FOR ELEMENTS Z=55 to Z=100 IN THE PHOTOELECTRON ENERGY RANGE 100–5000 eV," *At. Data Nucl. Data Tables*, vol. 82, no. 2, pp. 257–311, Nov. 2002.

[477] M. B. Trzhaskovskaya, V. K. Nikulin, V. I. Nefedov, and V. G. Yarzhemsky, "Non-dipole second order parameters of the photoelectron angular distribution for elements Z=1–100 in the photoelectron energy range 1–10keV," *At. Data Nucl. Data Tables*, vol. 92, no. 2, pp. 245–304, Mar. 2006.

[478] M. Leskelä and M. Ritala, "Atomic layer deposition (ALD): From precursors to thin film structures," in *Thin Solid Films*, 2002, vol. 409, no. 1, pp. 138–146.

[479] R. W. Johnson, A. Hultqvist, and S. F. Bent, "A brief review of atomic layer deposition: From fundamentals to applications," *Mater. Today*, vol. 17, no. 5, pp. 236–246, 2014.

[480] M. Ritala and M. Leskelä, "Atomic layer deposition," in *Handbook of Thin Films*, vol. 1, 2002, pp. 103–159.

[481] S. M. George, "Atomic layer deposition: an overview.," *Chem. Rev.*, vol. 110, no. 1, pp. 111–31, Jan. 2010.

[482] J. W. Elam, D. Routkevitch, P. P. Mardilovich, and S. M. George, "Conformal coating on ultrahigh-aspect-ratio nanopores of anodic alumina by atomic layer deposition," *Chem. Mater.*, vol. 15, no. 18, pp. 3507–3517, 2003.

[483] R. G. Gordon, D. Hausmann, E. Kim, and J. Shepard, "A Kinetic Model for Step Coverage by Atomic Layer Deposition in Narrow Holes or Trenches**," *Chem. Vap. Depos.*, vol. 9, no. 2, pp. 73–78, 2003.

[484] S. K. Karuturi, L. Liu, L. T. Su, Y. Zhao, H. J. Fan, X. Ge, S. He, and A. T. I. Yoong, "Kinetics of stop-flow atomic layer deposition for high aspect ratio template filling through photonic band gap measurements," *J. Phys. Chem. C*, vol. 114, no. 35, pp. 14843–14848, 2010.

[485] I. W. Boyd, "Thin film growth by pulsed laser deposition," *Ceram. Int.*, vol. 22, no. 5, pp. 429–434, 1996.

[486] R. Wood, J. Leboeuf, D. Geohegan, A. Puretzky, and K. Chen, "Dynamics of plume propagation and splitting during pulsed-laser ablation of Si in He and Ar," *Phys. Rev. B - Condens. Matter Mater. Phys.*, vol. 58, no. 3, pp. 1533–1543, 1998.

[487] P. R. Willmott and J. R. Huber, "Pulsed laser vaporization and deposition," *Rev. Mod. Phys.*, vol. 72, no. 1, pp. 315–328, 2000.

[488] M. N. R. Ashfold, F. Claeyssens, G. M. Fuge, and S. J. Henley, "Pulsed laser ablation and deposition of thin films," *Chem. Soc. Rev.*, vol. 33, no. 1, p. 23, 2004.

[489] H. Adachi and K. Wasa, "Thin Films and Nanomaterials," *Handb. Sputter Depos. Technol. Fundam. Appl. Funct. Thin Film. Nano-Materials MEMS Second Ed.*, no. Dlc, pp. 3–39, 2012.

[490] H. Adachi, T. Hata, and K. Wasa, "Basic Process of Sputtering Deposition," *Handb. Sputter Depos. Technol. Fundam. Appl. Funct. Thin Film. Nano-Materials MEMS Second Ed.*, no. Lcd, pp. 295–359, 2012.

[491] D. Depla, S. Mahieu, and J. E. Greene, "Sputter Deposition Processes," in *Handbook of Deposition Technologies for Films and Coatings*, Third Edit., Elsevier Ltd., 2010, pp. 253–296.

[492] D. M. Mattox, "Physical Sputtering and Sputter Deposition (Sputtering)," in *Handbook of Physical Vapor Deposition (PVD) Processing*, 2010, pp. 237–286.

[493] K. Wasa, *Sputtering Systems*, Second Edi. Elsevier Inc., 2012.

[494] S. C. Riha, B. A. Parkinson, and A. L. Prieto, "Solution-Based Synthesis and Characterization of Cu 2 ZnSnS 4 Nanocrystals," *J. Am. Chem. Soc.*, vol. 131, no. 34, pp. 12054–12055, 2009.

[495] S. C. Riha, "Tuning optoelectronic properties and understanding charge transport in nanocrystal thin films of earth abundant semiconducting materials," Colorado State University, 2011.

[496] M. Cao and Y. Shen, "A mild solvothermal route to kesterite quaternary Cu2ZnSnS 4 nanoparticles," *J. Cryst. Growth*, vol. 318, no. 1, pp. 1117–1120, 2011.

[497] C. Zou, L. Zhang, D. Lin, Y. Yang, Q. Li, X. Xu, X. Chen, and S. Huang, "Facile synthesis of Cu2ZnSnS4 nanocrystals," *CrystEngComm*, vol. 13, no. 10, p. 3310, 2011.

[498] W. Wang, H. Shen, F. Jiang, X. He, and Z. Yue, "Low-cost chemical fabrication of Cu2ZnSnS4 microparticles and film," *J. Mater. Sci. Mater. Electron.*, vol. 24, no. 6, pp. 1813–1817, 2013.

[499] M. P. Suryawanshi, S. W. Shin, U. V. Ghorpade, K. V. Gurav, C. W. Hong, G. L. Agawane, S. A. Vanalakar, J. H. Moon, J. H. Yun, P. S. Patil, J. H. Kim, and A. V. Moholkar, "Improved photoelectrochemical performance of Cu2ZnSnS4 (CZTS) thin films prepared using modified successive ionic layer adsorption and reaction (SILAR) sequence," *Electrochim. Acta*, vol. 150, pp. 136–145, 2014.

[500] W. Zhao, G. Wang, Q. Tian, Y. Yang, L. Huang, and D. Pan, "Fabrication of Cu $_2$ ZnSn(S,Se) $_4$ Solar Cells via an Ethanol-Based Sol–Gel Route Using SnS $_2$ as Sn Source," *ACS Appl. Mater. Interfaces*, vol. 6, no. 15, pp. 12650–12655, 2014.

[501] Vanalakar, Agwane, Gang, Patil, and Kim, "A mild hydrothermal route to synthesis of CZTS nanoparticle inks for solar cell applications," *Phys. Status Solidi Curr. Top. Solid State Phys.*, vol. 12, no. 6, pp. 500–503, 2015.

[502] Y. Zhao, W.-H. Zhou, J. Jiao, Z.-J. Zhou, and S.-X. Wu, "Aqueous synthesis and characterization of hydrophilic Cu2ZnSnS4 nanocrystals," *Mater. Lett.*, vol. 96, pp. 174–176, 2013.

[503] G. Gordillo, M. F. Hurtado, R. A. Becerra, S. D. Cruz, E. A. Ramirez, J. S. Oyola, and I. Lauermann, "Comparison Study of Czts Thin Films Grown Using Vacuum and Solution Based Methods," in *29th European Photovoltaic Solar Energy Conference and Exhibition*, 2015, p. 1704.

[504] P. Dai, X. Shen, Z. Lin, Z. Feng, H. Xu, and J. Zhan, "Band-gap tunable (Cu2Sn)x/3Zn1−xS nanoparticles for solar cells," *Chem. Commun.*, vol. 46, no. 31, p. 5749, 2010.

[505] S. S. Mali, B. M. Patil, C. A. Betty, P. N. Bhosale, Y. W. Oh, S. R. Jadkar, R. S. Devan, Y. R. Ma, and P. S. Patil, "Novel synthesis of kesterite Cu 2ZnSnS 4 nanoflakes by successive ionic layer adsorption and reaction technique: Characterization and application," *Electrochim. Acta*, vol. 66, pp. 216–221, 2012.

[506] H. Jiang, P. Dai, Z. Feng, W. Fan, and J. Zhan, "Phase selective synthesis of metastable orthorhombic Cu2ZnSnS4," *J. Mater. Chem.*, vol. 22, no. 15, p. 7502, 2012.

[507] B. T. Jheng, K. M. Huang, S. F. Chen, and M. C. Wu, "Effects of substrate temperature on the Cu2ZnSnS4films deposited by radio-frequency sputtering with single target," *Thin Solid Films*, vol. 564, pp. 345–350, 2014.

[508] D. R. Deepu, V. G. Rajeshmon, C. S. Kartha, and K. P. Vijayakumar, "XPS depth profile study of sprayed CZTS thin films," *AIP Conf. Proc.*, vol. 1591, pp. 1666–1668, 2014.

[509] D. Tang, Q. Wang, F. Liu, L. Zhao, Z. Han, K. Sun, Y. Lai, J. Li, and Y. Liu, "An alternative route towards low-cost Cu2ZnSnS4 thin film solar cells," *Surf. Coatings Technol.*, vol. 232, pp. 53–59, 2013.

[510] N. Thota, M. Gurubhaskar, A. C. Kasi Reddy, G. Hema Chandra, B. R. Mehta, A. Tiwari, and Y. P. Venkata Subbaiah, "Growth and properties of Cu2ZnSnS4 thin films prepared by multiple metallic layer stacks as a function of sulfurization time," *J. Mater. Sci. Mater. Electron.*, vol. 28, no. 16, pp. 11702–11711, 2017.

[511] V. T. Tiong, J. Bell, and H. Wang, "One-step synthesis of high quality kesterite Cu2ZnSnS4 nanocrystals - a hydrothermal approach," *Beilstein J. Nanotechnol.*, vol. 5, no. 1, pp. 438–446, 2014.

[512] X. Yu, A. Ren, F. Wang, C. Wang, J. Zhang, W. Wang, L. Wu, W. Li, G. Zeng, and L. Feng, "Synthesis and characterization of CZTS thin films by sol-gel method without sulfurization," *Int. J. Photoenergy*, vol. 2014, pp. 1–7, 2014.

[513] F. Liu, S. Shen, F. Zhou, N. Song, X. Wen, J. A. Stride, K. Sun, C. Yan, and X. Hao, "Kesterite Cu 2 ZnSnS 4 thin film solar cells by a facile DMF-based solution coating process," *J. Mater. Chem. C*, vol. 3, no. 41, pp. 10783–10792, 2015.

[514] C. A. M. Avendano, N. R. Mathews, M. Pal, F. P. Delgado, and X. Mathew, "Structural Evolution of Multilayer SnS/Cu/ZnS Stack to Phase-Pure Cu2ZnSnS4 Thin Films by Thermal Processing," *ECS J. Solid State Sci. Technol.*, vol. 4, no. 3, pp. P91–P96, 2015.

[515] A. Khalkar, K. Lim, and S. Yu, "Effect of Growth Parameters and Annealing Atmosphere on the Properties of Cu 2 ZnSnS 4 Thin Films Deposited by Cosputtering," *Int. J. Photoenergy*, vol. 2013, 2013.

[516] G. Gordillo, R. A. Becerra, and C. L. Calderón, "Novel Chemical Route for Deposition of Cu 2 ZnSnS 4 Photovoltaic Absorbers," *J. Braz. Chem. Soc.*, vol. 29, no. 3, pp. 649–658, 2018.

[517] G. Rajesh, N. Muthukumarasamy, E. P. Subramanian, M. R. Venkatraman, S. Agilan, V. Ragavendran, M. Thambidurai, S. Velumani, J. Yi, and D. Velauthapillai, "Solution-based synthesis of high yield CZTS (Cu2ZnSnS4) spherical quantum dots," *Superlattices Microstruct.*, vol. 77, no. January, pp. 305–312, 2015.

[518] G. Balaji, R. Balasundaraprabhu, S. Prasanna, N. Prabavathy, D. N. McIlroy, and M. D. Kannan, "Investigations of RF magnetron sputtered CZTS absorber layer thin films prepared using sulfur induced binary targets without sulfurization," *Opt. Mater. (Amst).*, vol. 75, pp. 56–60, 2018.

[519] J. P. Liu, K. L. Choy, M. Placidi, J. López-García, E. Saucedo, D. Colombara, and E. Robert, "Fabrication and characterization of kesterite Cu $_2$ ZnSnS $_4$ thin films deposited by electrostatic spray assisted vapour deposition method," *Phys. Status Solidi*, vol. 212, no. 1, pp. 135–139, 2015.

[520] Y. Qu, G. Zoppi, and N. S. Beattie, "The role of nanoparticle inks in determining the performance of solution processed Cu2ZnSn(S,Se)4thin film solar cells," *Prog. Photovoltaics Res. Appl.*, vol. 24, no. 6, pp. 836–

845, 2016.

[521] Q. Jiang, X. Chen, H. Gao, C. Feng, and Z. Guo, “Synthesis of Cu2ZnSnS4as Novel Anode material for Lithium-ion Battery,” *Electrochim. Acta*, vol. 190, pp. 703–712, 2016.

[522] B. S. Pawar, S. M. Pawar, S. W. Shin, D. S. Choi, C. J. Park, S. S. Kolekar, and J. H. Kim, “Effect of complexing agent on the properties of electrochemically deposited Cu2ZnSnS4(CZTS) thin films,” *Appl. Surf. Sci.*, vol. 257, no. 5, pp. 1786–1791, 2010.

[523] J. Wang, P. Zhang, X. Song, and L. Gao, “Surfactant-free hydrothermal synthesis of Cu_2ZnSnS_4 (CZTS) nanocrystals with photocatalytic properties,” *RSC Adv.*, vol. 4, no. 53, pp. 27805–27810, 2014.

[524] S. A. Vanalakar, S. W. Shin, G. L. Agawane, M. P. Suryawanshi, K. V. Gurav, P. S. Patil, and J. H. Kim, “Effect of post-annealing atmosphere on the grain-size and surface morphological properties of pulsed laser deposited CZTS thin films,” *Ceram. Int.*, vol. 40, no. 9 PART B, pp. 15097–15103, 2014.

[525] M. Hurtado, S. D. Cruz, R. a Becerra, C. Calderón, and G. Gordillo, “XPS analysis and structural characterization of CZTS thin films prepared using solution and vacuum based deposition techniques,” *Ieee Pvsc 40*, pp. 2–6, 2014.

[526] K. Kim, A. Razzaq, S. Sorcar, Y. Park, C. A. Grimes, and S.-I. In, “Hybrid mesoporous Cu2ZnSnS4 (CZTS)–TiO2 photocatalyst for efficient photocatalytic conversion of CO2 into CH4 under solar irradiation,” *RSC Adv.*, vol. 6, no. 45, pp. 38964–38971, 2016.

[527] S. J. Patil, V. C. Lokhande, D. W. Lee, and C. D. Lokhande, “Electrochemical impedance analysis of spray deposited CZTS thin film: Effect of Se introduction,” *Opt. Mater. (Amst).*, vol. 58, pp. 418–425, 2016.

[528] Y. Sun, Y. Zhang, H. Wang, M. Xie, K. Zong, H. Zheng, Y. Shu, J. Liu, H. Yan, M. Zhu, and W. Lau, “Novel non-hydrazine solution processing of earth-abundant Cu2ZnSn(S,Se)4 absorbers for thin-film solar cells,” *J. Mater. Chem. A*, vol. 1, no. 23, p. 6880, 2013.

[529] W. C. Liu, B. L. Guo, X. S. Wu, F. M. Zhang, C. L. Mak, and K. H. Wong, “Facile hydrothermal synthesis of hydrotropic Cu2ZnSnS4 nanocrystal quantum dots: band-gap engineering and phonon confinement effect,” *J. Mater. Chem. A*, vol. 1, no. 9, p. 3182, 2013.

[530] X. Yan, X. Hu, and S. Komarneni, “Solvothermal synthesis of CZTS nanoparticles in ethanol: Preparation and characterization,” *J. Korean Phys. Soc.*, vol. 66, no. 10, pp. 1511–1515, 2015.

[531] C. Sripan, V. E. Madhavan, A. K. Viswanath, and R. Ganesan, “Sulfurization and annealing effects on thermally evaporated CZTS films,” *Mater. Lett.*, vol. 189, no. October 2016, pp. 110–113, 2017.

[532] Q. Tang, H. Shen, H. Yao, W. Wang, Y. Jiang, and C. Zheng, “Synthesis of CZTS/RGO composite material as supercapacitor electrode,” *Ceram. Int.*, vol. 42, no. 8, pp. 10452–10458, 2016.

[533] Y. Zhao, W. Tao, J. Liu, and A. Wei, “Rapid synthesis of Cu2ZnSnS4 nanocrystalline thin films directly on transparent conductive glass substrates by microwave irradiation,” *Mater. Lett.*, vol. 148, pp. 63–66, 2015.

[534] Y. Wang and H. Gong, “Cu2ZnSnS4 synthesized through a green and economic process,” *J. Alloys Compd.*, vol. 509, no. 40, pp. 9627–9630, 2011.

[535] W. Xie, X. Jiang, C. Zou, D. Li, J. Zhang, J. Quan, and L. Shao, “Synthesis of highly dispersed Cu2ZnSnS4 nanoparticles by solvothermal method for photovoltaic application,” *Phys. E Low-dimensional Syst. Nanostructures*, vol. 45, pp. 16–20, 2012.

[536] S. A. Vanalakar, V. L. Patil, P. S. Patil, and J. H. Kim, “Controllable synthesis of stoichiometric Cu2ZnSnS4 nanoparticles by solvothermal method and its properties,” *AIP Conf. Proc.*, vol. 1665, p. 050061, 2015.

[537] S. Rondiya, A. Rokade, A. Jadhavar, S. Nair, M. Chaudhari, R. Kulkarni, A. Mayabadi, A. Funde, H. Pathan, and S. Jadkar, “Effect of calcination temperature on the properties of CZTS absorber layer prepared by RF sputtering for solar cell applications,” *Mater. Renew. Sustain. Energy*, vol. 6, no. 2, pp. 1–10, 2017.

[538] Y. Huang, G. Li, Q. Fan, M. Zhang, Q. Lan, X. Fan, Z. Zhou, and C. Zhang, “Facile solution deposition of Cu2ZnSnS4(CZTS) nano-worm films on FTO substrates and its photoelectrochemical property,” *Appl. Surf. Sci.*, vol. 364, pp. 148–155, 2016.

[539] D. Pareek, B. Kavaipatti, M. Vashistha, and P. Sharma, “Low cost synthesis of CZTS based absorber material for solar PV applications,” *Eco Revolut.*

[540] A. V. Moholkar, S. S. Shinde, A. R. Babar, K. U. Sim, H. K. Lee, K. Y. Rajpure, P. S. Patil, C. H. Bhosale, and J. H. Kim, “Synthesis and characterization of Cu2ZnSnS4thin films grown by PLD: Solar cells,” *J. Alloys Compd.*, vol. 509, no. 27, pp. 7439–7446, 2011.

[541] S. Das, R. M. Krishna, S. Ma, and K. C. Mandal, “Single phase polycrystalline Cu2ZnSnS4grown by vertical gradient freeze technique,” *J. Cryst. Growth*, vol. 381, pp. 148–152, 2013.

[542] H. Guo, C. Ma, K. Zhang, X. Jia, X. Wang, N. Yuan, and J. Ding, “Dual function of ultrathin Ti intermediate layers in CZTS solar cells: Sulfur blocking and charge enhancement,” *Sol. Energy Mater. Sol. Cells*, vol. 175, no. May 2017, pp. 20–28, 2018.

[543] W. Liu, B. Guo, C. Mak, A. Li, X. Wu, and F. Zhang, “Facile synthesis of ultrafine Cu2ZnSnS4nanocrystals by hydrothermal method for use in solar cells,” *Thin Solid Films*,

vol. 535, no. 1, pp. 39–43, 2013.

[544] B. Patro, S. Vijaylakshmi, and P. Sharma, “Rapid microwave-assisted solvothermal synthesis of Cu2ZnSnS4 (CZTS) nanocrystals for low-cost thin film photovoltaic: investigation of synthesis parameters and morphology control,” *J. Mater. Sci. Mater. Electron.*, vol. 29, no. 4, pp. 3370–3380, 2018.

[545] B. Long, S. Cheng, C. Yue, and L. Dong, “Modification of back electrode structure by a Mo intermediate layer for flexible CZTS thin film solar cells,” *Micro Nano Lett.*, vol. 13, no. 2, pp. 237–242, 2018.

[546] A. Santoni, F. Rondino, C. Malerba, M. Valentini, and A. Mittiga, “Electronic structure of Ar+ ion-sputtered thin-film MoS2: A XPS and IPES study,” *Appl. Surf. Sci.*, vol. 392, pp. 795–800, 2017.

[547] R. R. Thankalekshmi and A. C. Rastogi, “Studies on process induced optoelectronic and structural modifications of CdS/CZTS heterojunction interface affecting solar cell efficiency,” *2015 IEEE 42nd Photovolt. Spec. Conf. PVSC 2015*, 2015.

[548] F. Liu, C. Yan, J. Huang, K. Sun, F. Zhou, J. A. Stride, M. A. Green, and X. Hao, “Nanoscale Microstructure and Chemistry of Cu_2ZnSnS_4/CdS Interface in Kesterite Cu_2ZnSnS_4 Solar Cells,” *Adv. Energy Mater.*, vol. 6, no. 15, pp. 1–10, 2016.

[549] C. Yan, F. Liu, K. Sun, N. Song, J. A. Stride, F. Zhou, X. Hao, and M. Green, “Boosting the efficiency of pure sulfide CZTS solar cells using the In/Cd-based hybrid buffers,” *Sol. Energy Mater. Sol. Cells*, vol. 144, pp. 700–706, 2016.

[550] J. L. Johnson, H. Nukala, A. Bhatia, W. M. H. Oo, L. W. Rieth, M. A. Scarpulla, and E. A. Lund, “Effects of 2nd Phases, Stress, and Na at the Mo/Cu2ZnSnS4 Interface,” *MRS Proc.*, vol. 1268, no. January, pp. 1268-EE03-03, 2010.

[551] F. Jiang, H. Shen, and W. Wang, “Optical and Electrical Properties of Cu2ZnSnS4 Film Prepared by Sulfurization Method,” *J. Electron. Mater.*, vol. 41, no. 8, pp. 2204–2209, 2012.

[552] S. K. Verma, R. Verma, Y. Xie, D. Xiong, W. Chen, C. Hu, T. A. Emmanuel, M. Wang, and X. Zhao, “Heat-up and gram-scale synthesis of Cu-poor CZTS nanocrystals with controllable compositions and shapes,” *CrystEngComm*, vol. 19, no. 15, pp. 2013–2020, 2017.

[553] R. Nyholm, N. Martensson, A. Lebuglet, and U. Axelsson, “Auger and Coster-Kronig broadening effects in the 2p and 3p photoelectron spectra from the metals 22Ti-30Zn,” *J. Phys. F Met. Phys.*, vol. 11, no. 8, pp. 1727–1733, 1981.

[554] Y. A. Teterin, A. Y. Teterin, A. M. Lebedev, and K. E. Ivanov, “Secondary electronic processes and the structure of X-ray photoelectron spectra of lanthanides in oxygen-containing compounds,” *J. Electron Spectros. Relat. Phenomena*, vol. 137–140, no. SPEC. ISS., pp. 607–612, 2004.

[555] M. F. H. Morales, “XPS study for CZTS thin films growth by PVD co-evaporation method,” *Rev. Elem.*, vol. 4, pp. 87–95, 2014.

[556] M. Hurtado and J. Correa, “COMPOSITIONAL STUDY OF Cu2ZnSnS4 ABSORBER LAYERS FOR PHOTOVOLTAIC SOLAR CELL DEVICES,” *Rev. Colomb. Mater.*, vol. 5, pp. 171–176, 2014.

[557] L. Zhu, Y. H. Qiang, Y. L. Zhao, and X. Q. Gu, “Double junction photoelectrochemical solar cells based on Cu2ZnSnS4/Cu2ZnSnSe4thin film as composite photocathode,” *Appl. Surf. Sci.*, vol. 292, pp. 55–62, 2014.

[558] H. Zhou, T. Bin Song, W. C. Hsu, S. Luo, S. Ye, H. S. Duan, C. J. Hsu, W. Yang, and Y. Yang, “Rational defect passivation of Cu2ZnSn(S,Se)4photovoltaics with solution-processed Cu2ZnSnS4:Na nanocrystals,” *J. Am. Chem. Soc.*, vol. 135, no. 43, pp. 15998–16001, 2013.

[559] N. S. Kozhevnikova, A. S. Vorokh, O. I. Gyrdasova, I. V. Baklanova, A. N. Titov, and M. V. Kuznetsov, “Synthetic pathway of a Cu2ZnSnS4 powder using low temperature annealing of nanostructured binary sulfides,” *Nanosyst. Physics, Chem. Math.*, vol. 8, no. 6, pp. 787–792, 2017.

[560] W. Yang, H.-S. Duan, B. Bob, H. Zhou, B. Lei, C.-H. Chung, S.-H. Li, W. W. Hou, and Y. Yang, “Novel Solution Processing of High-Efficiency Earth-Abundant $Cu_2ZnSn(S,Se)_4$ Solar Cells,” *Adv. Mater.*, vol. 24, no. 47, pp. 6323–6329, 2012.

[561] W. B. Yang, H. S. Duan, B. Bob, B. Lei, S. H. Li, Y. Yang, and Ieee, “Novel Solution Processing of High Efficiency Earth Abundant CZTSSe Solar Cells,” *2012 38th Ieee Photovolt. Spec. Conf.*, pp. 2664–2667, 2012.

[562] M. Singh, J. Jiu, K. Suganuma, and J. H. Kim, “Non-toxic precursor solution route for fabrication of CZTS solar cell based on all layers solution processed,” *J. Alloys Compd.*, vol. 646, pp. 497–502, 2015.

[563] S. Exarhos, E. Palmes, R. Xu, and L. Mangolini, “Oxide-induced grain growth in CZTS nanoparticle coatings,” *RSC Adv.*, vol. 7, no. 41, pp. 25575–25581, 2017.

[564] J. Yu, Z. Zheng, L. Dong, S. Cheng, Y. Lai, Q. Zheng, H. Zhou, H. Jia, and H. Zhang, “Effect of deposited temperatures of the buffer layer on the band offset of CZTS/In_2S_3heterostructure and its solar cell performance,” *Chinese Phys. B*, vol. 26, no. 4, 2017.

[565] S. Huang, W. Luo, and Z. Zou, “Band positions and photoelectrochemical properties of Cu_2ZnSnS_4 thin films by the ultrasonic spray pyrolysis method,” *J. Phys. D. Appl. Phys.*, vol. 46, no. 23, p. 235108, 2013.

[566] S. Gupta, T. J. Whittles, Y. Batra, V. Satsangi, S. Krishnamurthy, V. R. Dhanak, and B. R. Mehta, “A low-cost, sulfurization free approach to control optical and electronic properties of Cu_2ZnSnS_4 via precursor variation,” *Sol. Energy*

Mater. Sol. Cells, vol. 157, pp. 820–830, 2016.

[567] T. J. Whittles, "Electronic Characterisation of Earth-Abundant Sulphides for Solar Photovoltaics," University of Liverpool, 2017.

[568] M. Aono, K. Yoshitake, and H. Miyazaki, "XPS depth profile study of CZTS thin films prepared by spray pyrolysis," *Phys. Status Solidi Curr. Top. Solid State Phys.*, vol. 10, no. 7–8, pp. 1058–1061, 2013.

[569] M. Danilson, M. Altosaar, M. Kauk, A. Katerski, J. Krustok, and J. Raudoja, "XPS study of CZTSSe monograin powders," *Thin Solid Films*, vol. 519, no. 21, pp. 7407–7411, 2011.

[570] R. Haight, X. Shao, W. Wang, and D. B. Mitzi, "Electronic and elemental properties of the Cu2ZnSn(S,Se)4 surface and grain boundaries," *Appl. Phys. Lett.*, vol. 104, no. 3, p. 033902, 2014.

[571] W. Li, J. Chen, C. Yan, and X. Hao, "The effect of ZnS segregation on Zn-rich CZTS thin film solar cells," *J. Alloys Compd.*, vol. 632, pp. 178–184, May 2015.

[572] M. Schmid, "Vapour Pressure Calculator," 2013. [Online]. Available: https://www.iap.tuwien.ac.at/www/surface/vapor_pressure. [Accessed: 29-Jul-2018].

[573] W. A. West and A. W. C. Menzies, "The Vapor Pressures of Sulphur between 100° and 550° with related Thermal Data," *J. Phys. Chem.*, vol. 33, no. 12, pp. 1880–1892, 1928.

[574] S. Campbell, Y. Qu, L. Bowen, P. Chapon, V. Barrioz, N. S. Beattie, and G. Zoppi, "Influence of OLA and FA ligands on the optical and electronic properties of Cu2ZnSn(S, Se)4 thin films and solar cells prepared from nanoparticle inks," *Sol. Energy*, vol. 175, no. February, pp. 101–109, 2018.

[575] J. Paier, R. Asahi, A. Nagoya, and G. Kresse, "Cu2 ZnSnS4 as a potential photovoltaic material: A hybrid Hartree-Fock density functional theory study," *Phys. Rev. B - Condens. Matter Mater. Phys.*, vol. 79, no. 11, pp. 1–8, 2009.

[576] N. B. Mortazavi Amiri and A. Postnikov, "Electronic structure and lattice dynamics in kesterite-type Cu2ZnSnSe4 from first-principles calculations," *Phys. Rev. B*, vol. 82, no. 20, p. 205204, 2010.

[577] Y. Du, J. Fan, W. Zhou, Z. Zhou, J. Jiao, and S. Wu, "One-Step Synthesis of Stoichiometric Cu 2 ZnSnSe 4 as Counter Electrode for Dye-Sensitized Solar Cells," *ACS Appl. Mater. Interfaces*, vol. 4, p. 1796, 2012.

[578] T. C. Liu and Y. Hu, "Preparation and characterization of CZTSe films through electrochemical deposition route," *Int. J. Electrochem. Sci.*, vol. 9, no. 6, pp. 2985–2992, 2014.

[579] H. Rupp and U. Weser, "X-ray photoelectron spectroscopy of some selenium containing amino acids.," *Bioinorg. Chem.*, vol. 5, no. 1, pp. 21–32, 1975.

[580] A. G. Shard, "Detection limits in XPS for more than 6000 binary systems using Al and Mg Kα X-rays," *Surf. Interface Anal.*, vol. 46, no. 3, pp. 175–185, 2014.

[581] L. A. Burton, T. J. Whittles, D. Hesp, W. M. Linhart, J. M. Skelton, B. Hou, R. F. Webster, G. O'Dowd, C. Reece, D. Cherns, D. J. Fermin, T. D. Veal, V. R. Dhanak, and A. Walsh, "Electronic and optical properties of single crystal SnS_2: an earth-abundant disulfide photocatalyst," *J. Mater. Chem. A*, vol. 4, no. 4, pp. 1312–1318, 2016.

[582] G. Ham, S. Shin, J. Park, J. Lee, H. Choi, S. Lee, and H. Jeon, "Engineering the crystallinity of tin disulfide deposited at low temperatures," *RSC Adv.*, vol. 6, no. 59, pp. 54069–54075, 2016.

[583] J. H. Ahn, M. J. Lee, H. Heo, J. H. Sung, K. Kim, H. Hwang, and M. H. Jo, "Deterministic Two-Dimensional Polymorphism Growth of Hexagonal n-Type SnS2and Orthorhombic p-Type SnS Crystals," *Nano Lett.*, vol. 15, no. 6, pp. 3703–3708, 2015.

[584] H. S. Song, S. L. Li, L. Gao, Y. Xu, K. Ueno, J. Tang, Y. B. Cheng, and K. Tsukagoshi, "High-performance top-gated monolayer SnS2field-effect transistors and their integrated logic circuits," *Nanoscale*, vol. 5, no. 20, pp. 9666–9670, 2013.

[585] J. Lee, J. Lee, G. Ham, S. Shin, J. Park, H. Choi, S. Lee, J. Kim, O. Sul, S. Lee, H. Jeon, J. Lee, J. Lee, G. Ham, S. Shin, J. Park, S. Lee, and H. Jeon, "Improved electrical properties of atomic layer deposited tin disulfide at low temperatures using ZrO2 layer," *AIP Adv.*, vol. 7, p. 025311, 2017.

[586] M. Mattinen, P. J. King, L. Khriachtchev, K. Meinander, J. T. Gibbon, V. R. Dhanak, J. Räisänen, M. Ritala, and M. Leskelä, "Low-Temperature Wafer-Scale Deposition of Continuous 2D SnS_2," *Small*, vol. 14, no. 21, p. 1800547, 2018.

[587] Y.-B. Yang, J. K. Dash, A. J. Littlejohn, Y. Xiang, Y. Wang, J. Shi, L. H. Zhang, K. Kisslinger, T.-M. Lu, and G.-C. Wang, "Large Single Crystal SnS_2 Flakes Synthesized from Coevaporation of Sn and S," *Cryst. Growth Des.*, vol. 16, no. 2, pp. 961–973, 2016.

[588] J. M. Gonzalez and I. I. Oleynik, "Layer-dependent properties of $SnS_{2\text{ and }SnSe2}$ two-dimensional materials," *Phys. Rev. B*, vol. 94, no. 12, pp. 1–10, 2016.

[589] D. L. Greenaway and R. Nitsche, "Preparation and optical properties of group IV–VI2 chalcogenides having the CdI2 structure," *J . Phys. Chem. Solids*, vol. 26, no. 8, p. 1445, 1965.

[590] G. Ye, Y. Gong, S. Lei, Y. He, B. Li, X. Zhang, Z. Jin, L. Dong, J. Lou, R. Vajtai, W. Zhou, and P. M. Ajayan, "Synthesis of large-scale atomic-layer SnS2 through chemical vapor deposition,"

Nano Res., vol. 10, no. 7, pp. 2386–2394, 2017.

[591] Y. Huang, E. Sutter, J. T. Sadowski, M. Cotlet, O. L. A. Monti, D. A. Racke, M. R. Neupane, D. Wickramaratne, R. K. Lake, B. A. Parkinson, and P. Sutter, "Tin disulfide-an emerging layered metal dichalcogenide semiconductor: Materials properties and device characteristics," *ACS Nano*, vol. 8, no. 10, pp. 10743–10755, 2014.

[592] D. W. Langer and C. J. Vesely, "Electronic core levels of zinc chalcogenides," *Phys. Rev. B*, vol. 2, no. 12, pp. 4885–4892, 1970.

[593] K. Laajalehto, I. Kartio, and P. Nowak, "XPS study of clean metal sulfide surfaces," *Appl. Surf. Sci.*, vol. 81, no. 1, pp. 11–15, 1994.

[594] J. F. Xu, W. Ji, J. Y. Lin, S. H. Tang, and Y. W. Du, "Preparation of ZnS nanoparticles by ultrasonic radiation method," *Appl. Phys. A Mater. Sci. Process.*, vol. 66, no. 6, pp. 639–641, 1998.

[595] B. Elidrissi, M. Addou, M. Regragui, A. Bougrine, A. Kachouane, and J. C. Bernède, "Structure, composition and optical properties of ZnS thin films prepared by spray pyrolysis," *Mater. Chem. Phys.*, vol. 68, no. 1–3, pp. 175–179, 2001.

[596] D. Barreca, A. Gasparotto, C. Maragno, and E. Tondello, "Nanostructured Cadmium Sulfide Thin Films by XPS," *Surf. Sci. Spectra*, vol. 9, no. 1, pp. 46–53, 2002.

[597] B. R. Strohmeier and D. M. Hercules, "Characterization of the Interaction Zinc Ions and y-Alumina," *J. Catal.*, vol. 86, pp. 266–279, 1984.

[598] V. Stevanović, S. Lany, D. S. Ginley, W. Tumas, and A. Zunger, "Assessing capability of semiconductors to split water using ionization potentials and electron affinities only," *Phys. Chem. Chem. Phys.*, vol. 16, no. 8, pp. 3706–3714, 2014.

[599] S. Larach, R. E. Shrader, and C. F. Stocker, "Anomalous variation of band gap with composition in zinc sulfo- and seleno-tellurides," *Phys. Rev.*, vol. 108, no. 3, pp. 587–589, 1957.

[600] K. R. Murali, A. Austine, and D. C. Trivedi, "Properties of ZnSe films brush plated on high temperature substrates," *Mater. Lett.*, vol. 59, pp. 2621–2624, 2005.

[601] K. R. Murali and M. Balasubramanian, "Properties of pulse plated ZnSe films," *Mater. Sci. Eng. A*, vol. 431, pp. 118–122, 2006.

[602] M. A. Haase, J. Qiu, J. M. DePuydt, and H. Cheng, "Blue-green laser diodes," *Appl. Phys. Lett.*, vol. 59, no. 11, pp. 1272–1274, 1991.

[603] G. J. Wagner, T. J. Carrig, R. H. Page, K. I. Schaffers, J. Ndap, X. Ma, and A. Burger, "Continuous-wave broadly tunable Cr 2+ :ZnSe laser," *Opt. Lett.*, vol. 24, no. 1, pp. 19–21, 1999.

[604] J. Ren, K. A. Bowers, B. Sneed, D. L. Dreifus, J. W. Cook, J. F. Schetzina, and R. M. Kolbas, "ZnSe light-emitting diodes," *Appl. Phys. Lett.*, vol. 57, no. 18, pp. 1901–1903, 1990.

[605] K. Katayama, H. Matsubara, F. Nakanishi, T. Nakamura, H. Doi, A. Saegusa, T. Mitsui, T. Matsuoka, M. Irikura, T. Takebe, S. Nishine, and T. Shirakawa, "ZnSe-based white LEDs," *J. Cryst. Growth*, vol. 214, pp. 1064–1070, 2000.

[606] Y. Ohtake, K. Kushiya, and M. Ichikawa, "Polycrystalline Cu (InGa) Se 2 thin-film solar cells with ZnSe buffer layers," *Jpn. J. Appl. Phys.*, vol. 34, pp. 5949–5955, 1995.

[607] M. Konagai, Y. Ohtake, T. Okamoto, and S. Mat Res, "Development of Cu(InGa)Se2 thin film solar cells with Cd-free buffer layers," in *Symposium on Thin Films for Photovoltaic and Related Device Applications, at the 1996 MRS Spring Meeting*, 1996, vol. 426, pp. 153–163.

[608] F. Engelhardt, L. Bornemann, M. Kontges, T. Meyer, J. Parisi, E. Pschorr-Schoberer, B. Hahn, W. Gebhardt, W. Riedl, and U. Rau, "Cu(In,Ga)Se2 solar cells with a ZnSe buffer layer: Interface characterization by quantum efficiency measurements," *Prog. Photovoltaics Res. Appl.*, vol. 7, no. 6, pp. 423–436, 1999.

[609] S. Siebentritt, T. Kampschulte, A. Bauknecht, U. Blieske, W. Harneit, U. Fiedeler, and M. Lux-Steiner, "Cd-free buffer layers for CIGS solar cells prepared by a dry process," *Sol. Energy Mater. Sol. Cells*, vol. 70, no. 4, pp. 447–457, 2002.

[610] S. Siebentritt, P. Walk, U. Fiedeler, I. Lauermann, K. Rahne, M. C. Lux-Steiner, T. P. Niesen, and F. Karg, "MOCVD as a dry deposition method of ZnSe buffers for Cu(In,Ga)(S,Se) 2 solar cells," *Prog. Photovoltaics Res. Appl.*, vol. 12, no. 5, pp. 333–338, 2004.

[611] S. T. Lakshmikumar and A. C. Rastogi, "Novel two-stage selenization process for the preparation of ZnSe films," *Thin Solid Films*, vol. 259, no. 2, pp. 150–153, 1995.

[612] R. Islam and D. R. Rao, "X-ray photoelectron spectroscopy of Zn1-xCdxSe thin films," *J. Electron Spectros. Relat. Phenomena*, vol. 81, no. 1, pp. 69–77, 1996.

[613] C. Wang, X. F. Qian, W. X. Zhang, X. M. Zhang, Y. Xie, and Y. T. Qian, "Preparation of ZnSe films through chemical solution reduction process," *Mater. Res. Bull.*, vol. 34, no. 10–11, pp. 1637–1641, 1999.

[614] B. Hyun, N. Xu, and J. Kwang, "Growth of crystalline ZnSe : N thin films by pulsed laser ablation deposition," *Vacuum*, vol. 64, pp. 145–151, 2002.

[615] A. C. Deshpande, S. B. Singh, M. K. Abyaneh, R. Pasricha, and S. K. Kulkarni, "Low temperature synthesis of ZnSe nanoparticles," *Mater. Lett.*, vol. 62, no. 23, pp. 3803–3805, 2008.

[616] K. R. Murali, S. Dhanapandiyana, and C. Manoharana, "Pulse electrodeposited Zinc

selenide films and their characteristics," *Chalcogenide Lett.*, vol. 6, no. 1, pp. 51–56, 2009.

[617] B. Nie, L. B. Luo, J. J. Chen, J. G. Hu, C. Y. Wu, L. Wang, Y. Q. Yu, Z. F. Zhu, and J. S. Jie, "Fabrication of p-type ZnSe:Sb nanowires for high-performance ultraviolet light photodetector application," *Nanotechnology*, vol. 24, no. 9, 2013.

[618] A. M. Chaparro, C. Maffiotte, M. T. Gutiérrez, and J. Herrero, "Morphological and compositional study of CBD-ZnSe thin films by microscopy techniques and angle resolved XPS," *Thin Solid Films*, vol. 358, no. 1, pp. 22–29, 2000.

[619] M. R. Islam, N. Kang, U. Bhanu, H. P. Paudel, M. Erementchouk, L. Tetard, M. N. Leuenberger, and S. I. Khondaker, "Tuning the electrical property via defect engineering of single layer MoS2by oxygen plasma," *Nanoscale*, vol. 6, no. 17, pp. 10033–10039, 2014.

[620] M. Z. Xue and Z. W. Fu, "Fabrication and electrochemical characterization of zinc selenide thin film by pulsed laser deposition," *Electrochim. Acta*, vol. 52, no. 3, pp. 988–995, 2006.

[621] M. Shenasa, S. Sainkar, and D. Lichtman, "XPS study of some selected selenium compounds," *J. Electron Spectros. Relat. Phenomena*, vol. 40, no. 4, pp. 329–337, 1986.

[622] J. Wang and M. Isshiki, "Wide-Bandgap II–VI Semiconductors: Growth and Properties," in *Springer Handbook of Electronic and Photonic Materials*, S. Kasap and P. Capper, Eds. 2006, pp. 1–21.

[623] V. Srikant and D. R. Clarke, "On the optical band gap of zinc oxide," *J. Appl. Phys.*, vol. 83, no. 10, pp. 5447–5451, 1998.

[624] M. W. Allen, C. H. Swartz, T. H. Myers, T. D. Veal, C. F. McConville, and S. M. Durbin, "Bulk transport measurements in ZnO: The effect of surface electron layers," *Phys. Rev. B*, vol. 81, no. 7, p. 075211, Feb. 2010.

[625] M. W. Allen, D. Y. Zemlyanov, G. I. N. Waterhouse, J. B. Metson, T. D. Veal, C. F. McConville, and S. M. Durbin, "Polarity effects in the x-ray photoemission of ZnO and other wurtzite semiconductors," *Appl. Phys. Lett.*, vol. 98, no. 10, p. 101906, Mar. 2011.

[626] Y. Chen, "Effects of annealing on structural, optical and electrical properties of Al-doped ZnO thin films," *Sci. China Ser. G Physics, Mech. Astron.*, vol. 47, no. 5, p. 588, 2004.

[627] A. Ray, M. Patel, B. Tripathi, and M. Kumar, "A study of the applicability of ZnO thin-films as anti-reflection coating on Cu2ZnSnS4 thin-films solar cell," in *INDIAN VACUUM SOCIETY SYMPOSIUM ON THIN FILMS: SCIENCE AND TECHNOLOGY*, 2012, vol. 1451, no. 1, pp. 97–99.

[628] R. L. Z. Hoye, K. P. Musselman, and J. L. MacManus-Driscoll, "Research Update: Doping ZnO and TiO2 for solar cells," *APL Mater.*, vol. 1, no. 6, p. 060701, Dec. 2013.

[629] B.-Y. Oh, M.-C. Jeong, T.-H. Moon, W. Lee, J.-M. Myoung, J.-Y. Hwang, and D.-S. Seo, "Transparent conductive Al-doped ZnO films for liquid crystal displays," *J. Appl. Phys.*, vol. 99, no. 12, p. 124505, 2006.

[630] S. Kwon, S. Bang, S. Lee, S. Jeon, W. Jeong, H. Kim, S. C. Gong, H. J. Chang, H. Park, and H. Jeon, "Characteristics of the ZnO thin film transistor by atomic layer deposition at various temperatures," *Semicond. Sci. Technol.*, vol. 24, no. 3, p. 035015, 2009.

[631] J. Jin, J. S. Wrench, J. T. Gibbon, D. Hesp, A. Shaw, I. Z. Mitrovic, S. Member, N. Sedghi, L. J. Phillips, J. Zou, V. R. Dhanak, P. R. Chalker, S. Hall, and S. Member, "Schottky Diodes on ZnO Thin Films Grown by Plasma-Enhanced Atomic Layer Deposition," *IEEE Trans. Electron Devices*, vol. 99, no. Xx, pp. 1–6, 2017.

[632] S. K. Pandey, V. Awasthi, B. S. Sengar, V. Garg, P. Sharma, S. Kumar, C. Mukherjee, and S. Mukherjee, "Band alignment and photon extraction studies of Na-doped MgZnO/Ga-doped ZnO heterojunction for light-emitter applications," *J. Appl. Phys.*, vol. 118, no. 16, p. 165301, 2015.

[633] M. Kunat, S. Gil Girol, T. Becker, U. Burghaus, and C. Wöll, "Stability of the polar surfaces of ZnO: A reinvestigation using He-atom scattering," *Phys. Rev. B*, vol. 66, no. 8, pp. 1–3, 2002.

[634] A. Önsten, D. Stoltz, P. Palmgren, S. Yu, M. Göthelid, and U. O. Karlsson, "Water adsorption on znO(0001): Transition from triangular surface structures to a disordered hydroxyl terminated phase," *J. Phys. Chem. C*, vol. 114, no. 25, pp. 11157–11161, 2010.

[635] J. Jin, J. S. Wrench, J. T. Gibbon, D. Hesp, A. Shaw, I. Z. Mitrovic, N. Sedghi, L. J. Phillips, J. Zou, V. R. Dhanak, P. R. Chalker, and S. Hall, "Schottky diodes on ZnO thin films grown by plasma-enhanced atomic layer deposition," *IEEE Trans. Electron Devices*, vol. 64, no. 3, p. 1225, 2017.

[636] H. Moormann, D. Kohl, and G. Heiland, "Work function and band bending on clean cleaved zinc oxide surfaces," *Surf. Sci.*, vol. 80, no. C, pp. 261–264, 1979.

[637] H. Moormann, D. Kohl, and G. Heiland, "Variations of work function and surface conductivity on clean cleaved zinc oxide surfaces by annealing and by hydrogen adsorption," *Surf. Sci.*, vol. 100, no. 2, pp. 302–314, 1980.

[638] R. Robles, N. Barreau, A. Vega, S. Marsillac, J. C. Bernède, and A. Mokrani, "Optical properties of large band gap β-In2S3−3xO3x compounds obtained by physical vapour deposition," *Opt. Mater. (Amst).*, vol. 27, no. 4, pp. 647–653, 2005.

[639] N. Barreau, S. Marsillac, J. C. Bernède, and L. Assmann, “Evolution of the band structure of β-In2S3−3xO3x buffer layer with its oxygen content,” *J. Appl. Phys.*, vol. 93, no. 9, pp. 5456–5459, 2003.

[640] N. Barreau, A. Mokrani, F. Couzinié-Devy, and J. Kessler, “Bandgap properties of the indium sulfide thin-films grown by co-evaporation,” *Thin Solid Films*, vol. 517, no. 7, pp. 2316–2319, 2009.

[641] R. Jayakrishnan, T. Sebastian, T. T. John, C. S. Kartha, and K. P. Vijayakumar, “Photoconductivity in sprayed B -In2 S3 thin films under sub-band-gap excitation of 1.96 eV,” *J. Appl. Phys.*, vol. 102, no. 4, 2007.

[642] K. Bouabid, A. Ihlal, A. Outzourhit, and E. L. Ameziane, “STRUCTURAL AND OPTICAL PROPERTIES OF In 2 S 3 THIN FILMS PREPARED BY FLASH EVAPORATION,” *Act. Passiv. Electron. Components*, vol. 27, no. December, pp. 207–214, 2004.

[643] N. B. Kindig and W. E. Spicer, “Band structure of cadmium sulfide-photoemission studies,” *Phys. Rev.*, vol. 138, no. 2A, 1965.

[644] M. Ozaki, D. Peebles, B. R. Weinberger, A. J. Heeger, and A. G. MacDiarmid, “Semiconductor properties of polyacetylene *p* -(CH) $_x$: *n* -CdS heterojunctions,” *J. Appl. Phys.*, vol. 51, no. 8, pp. 4252–4256, 1980.

[645] A. Niemegeers, M. Burgelman, and A. De Vos, “On the CdS/CuInSe2 conduction band discontinuity,” *Appl. Phys. Lett.*, vol. 67, no. 1995, p. 843, 1995.

[646] M. Burgelman, P. Nollet, and S. Degrave, “Modelling polycrystalline semiconductor solar cells,” *Thin Solid Films*, vol. 361, pp. 527–532, 2000.

[647] H. Hiroi, N. Sakai, T. Kato, and H. Sugimoto, “High voltage Cu2ZnSnS4 submodules by hybrid buffer layer,” *Conf. Rec. IEEE Photovolt. Spec. Conf.*, pp. 863–866, 2013.

[648] Y. Udaka, S. Takaki, K. Isowaki, T. Nagai, K. M. Kim, S. Kim, H. Tampo, H. Shibata, K. Matsubara, S. Niki, N. Sakai, T. Kato, H. Sugimoto, and N. Terada, “Electronic structure of Cu2ZnSn(SxSe1−x)4 surface and CdS/Cu2ZnSn(SxSe1−x)4 interface,” *Phys. Status Solidi Curr. Top. Solid State Phys.*, vol. 14, no. 6, pp. 1–5, 2017.

[649] N. Terada, S. Yoshimoto, K. Chochi, T. Fukuyama, M. Mitsunaga, H. Tampo, H. Shibata, K. Matsubara, S. Niki, N. Sakai, T. Katou, and H. Sugimoto, “Characterization of electronic structure of Cu2ZnSn(SxSe1 - X)4absorber layer and CdS/Cu2ZnSn(SxSe1 - X)4interfaces by in-situ photoemission and inverse photoemission spectroscopies,” *Thin Solid Films*, vol. 582, pp. 166–170, 2015.

[650] T. Nagai, Y. Udaka, S. Takaki, K. Isowaki, S. Kawamura, K. Kawasaki, H. Tampo, K. M. Kim, S. Kim, H. Shibata, K. Matsubara, S. Niki, and N. Terada, “Electronic structures of Cu 2 ZnSnSe 4 surface and CdS/Cu 2 ZnSnSe 4 heterointerface,” *Jpn. J. Appl. Phys.*, vol. 56, no. 6, p. 65701, 2017.

[651] P. D. C. King, T. D. Veal, A. Schleife, J. Zúñiga-Pérez, B. Martel, P. H. Jefferson, F. Fuchs, V. Muñoz-Sanjosé, F. Bechstedt, and C. F. McConville, “Valence-band electronic structure of CdO, ZnO, and MgO from x-ray photoemission spectroscopy and quasi-particle-corrected density-functional theory calculations,” *Phys. Rev. B*, vol. 79, no. 20, p. 205205, May 2009.

[652] T. D. Veal, P. D. C. King, and C. F. Mcconville, “Electronic Properties of Post-transition Metal Oxide Semiconductor Surfaces,” in *Functional Metal Oxide Nanostructures*, Springer, 2012, p. 127.

[653] G. Tang, H. Liu, and W. Zhang, “The variation of optical band gap for ZnO:In films prepared by sol-gel technique,” *Adv. Mater. Sci. Eng.*, vol. 2013, pp. 1–5, 2013.

[654] N. L. Marana, V. M. Longo, E. Longo, J. B. L. Martins, and J. R. Sambrano, “Electronic and Structural Properties of the (1010) and (1120) ZnO Surfaces,” *J Phys Chem A*, vol. 112, pp. 8958–8963, 2008.

[655] L. Li, W. Wang, H. Liu, X. Liu, Q. Song, and S. Ren, “First Principles Calculations of Electronic Band Structure and Optical Properties of Cr-Doped ZnO,” *J. Phys. Chem. C*, vol. 113, pp. 8460–8464, 2009.

[656] J. C. Conesa, “Modeling with hybrid density functional theory the electronic band alignment at the zinc oxide-anatase interface,” *J. Phys. Chem. C*, vol. 116, no. 35, pp. 18884–18890, 2012.

[657] E. A. Davis and E. L. Lind, “Physical Properties of Mixed Single Crystals of CdS and ZnS,” *J . Phys. Chem. Solids*, vol. 29, pp. 79–90, 1968.

[658] Y. J. Shin, S. K. Kim, B. H. Park, T. S. Jeong, H. K. Shin, T. S. Kim, and P. Y. Yu, “Photocurrent Study on the Splitting of the Valence Band for a CdS Single-Crystal Platelet,” *Phys. Rev. B*, vol. 44, no. 11, p. 5522, 1991.

[659] A. I. Oliva, O. Solís-Canto, R. Castro-Rodrígues, and P. Quintana, “Formation of the band gap energy on CdS thin films growth by two different techniques,” *Thin Solid Films*, vol. 391, no. 1, pp. 28–35, 2001.

[660] E. C. Ekuma, L. Franklin, G. L. Zhao, J. T. Wang, and D. Bagayoko, “Local Density Approximation Description of Electronic Properties of Wurtzite Cadmium Sulfide (w-CdS),” *Can. J. Phys.*, vol. 89, no. 3, 2010.

[661] J. C. Wu, J. Zheng, C. L. Zacherl, P. Wu, Z. K. Liu, and R. Xu, “Hybrid functionals study of band bowing, band edges and electronic structures of Cd1- xZnxS solid solution,” *J. Phys. Chem. C*, vol. 115, no. 40, pp. 19741–19748, 2011.

[662] N. Terada, R. T. Widodo, K. Itoh, S. H. Kong, H. Kashiwabara, T. Okuda, K. Obara, S. Niki, K.

Sakurai, A. Yamada, and S. Ishizuka, "Characterization of interface nature and band alignment in CBD-CdS/Cu(In,Ga)Se2 bi-layer structure by photoemission and inverse photoemission spectroscopy," *Thin Solid Films*, vol. 480–481, pp. 183–187, 2005.

[663] S. M. Sze and K. K. Ng, *Physics of Semiconductor Devices*. Wiley-Blackwell, 2006.

[664] M. A. Green, "Intrinsic concentration, effective densities of states, and effective mass in silicon," *J. Appl. Phys.*, vol. 67, no. 6, pp. 2944–2954, 1990.

[665] Y. S. Lee, T. Gershon, O. Gunawan, T. K. Todorov, T. Gokmen, Y. Virgus, and S. Guha, "Cu2ZnSnSe4 thin-film solar cells by thermal co-evaporation with 11.6% efficiency and improved minority carrier diffusion length," *Adv. Energy Mater.*, vol. 5, no. 7, pp. 2–5, 2015.

[666] L. Quang Phuong, M. Okano, Y. Yamada, A. Nagaoka, K. Yoshino, and Y. Kanemitsu, "Photocarrier localization and recombination dynamics in Cu_2ZnSnS_4 single crystals," *Appl. Phys. Lett.*, vol. 103, no. 19, p. 191902, 2013.

[667] L. Q. Phuong, M. Okano, Y. Yamada, A. Nagaoka, K. Yoshino, and Y. Kanemitsu, "Temperature-dependent photocarrier recombination dynamics in Cu_2ZnSnS_4 single crystals," *Appl. Phys. Lett.*, vol. 104, no. 8, p. 081907, 2014.

[668] S. G. Choi, T. J. Kim, S. Y. Hwang, J. Li, C. Persson, Y. D. Kim, S. H. Wei, and I. L. Repins, "Temperature dependent band-gap energy for Cu2ZnSnSe4: A spectroscopic ellipsometric study," *Sol. Energy Mater. Sol. Cells*, vol. 130, pp. 375–379, 2014.

[669] M. León, S. Levcenko, R. Serna, I. V. Bodnar, A. Nateprov, M. Guc, G. Gurieva, N. Lopez, J. M. Merino, R. Caballero, S. Schorr, A. Perez-Rodriguez, and E. Arushanov, "Spectroscopic ellipsometry study of $Cu_2ZnSnSe_4$ bulk crystals," *Appl. Phys. Lett.*, vol. 105, no. 6, p. 061909, 2014.

[670] A. Crovetto, A. Cazzaniga, R. B. Ettlinger, J. Schou, and O. Hansen, "Optical properties and surface characterization of pulsed laser-deposited Cu2ZnSnS4by spectroscopic ellipsometry," *Thin Solid Films*, vol. 582, pp. 203–207, 2015.

[671] S. Y. Li, C. Hägglund, Y. Ren, J. J. S. Scragg, J. K. Larsen, C. Frisk, K. Rudisch, S. Englund, and C. Platzer-Björkman, "Optical properties of reactively sputtered Cu2ZnSnS4solar absorbers determined by spectroscopic ellipsometry and spectrophotometry," *Sol. Energy Mater. Sol. Cells*, vol. 149, pp. 170–178, 2016.

[672] S. Ninomiya and S. Adachi, "Optical properties of wurtzite CdS," *J. Appl. Phys.*, vol. 78, no. 2, pp. 1183–1190, 1995.

[673] S. Marsillac, N. Barreau, H. Khatri, J. Li, D. Sainju, A. Parikh, N. J. Podraza, and R. W. Collins, "Spectroscopic ellipsometry studies of in2S3 top window and Mo back contacts in chalcopyrite photovoltaics technology," *Phys. Status Solidi Curr. Top. Solid State Phys.*, vol. 5, no. 5, pp. 1244–1248, 2008.

[674] E. C. Heltemes and H. L. Swinney, "Anisotropy in lattice vibrations of zinc oxide," *J. Appl. Phys.*, vol. 38, no. 5, pp. 2387–2388, 1967.

[675] B. Shin, O. Gunawan, Y. Zhu, N. A. Bojarczuk, S. Jay Chey, and S. Guha, "Thin film solar cell with 8.4% power conversion efficiency using an earth-abundant Cu2ZnSnS4 absorber," *Prog. Photovoltaics Res. Appl.*, vol. 21, pp. 72–76, 2013.

[676] J. Dresner and F. V. Shallcross, "Crystallinity and electronic properties of evaporated CdS films," *J. Appl. Phys.*, vol. 34, no. 8, pp. 2390–2395, 1963.

[677] W. Rehwald and G. Hweke, "ON THE CONDUCTION MECHANISM IN SINGLECRYSTAL BETA-INDIUM SULFIDE In2S3," *J. Phys. Chem. Solids*, vol. 26, pp. 1309–1324, 1965.

[678] A. Tsukazaki, A. Ohtomo, and M. Kawasaki, "High-mobility electronic transport in ZnO thin films," *Appl. Phys. Lett.*, vol. 88, no. 15, pp. 1–4, 2006.

[679] M. L. Lin, J. M. Huang, C. S. Ku, C. M. Lin, H. Y. Lee, and J. Y. Juang, "High mobility transparent conductive Al-doped ZnO thin films by atomic layer deposition," *J. Alloys Compd.*, vol. 727, pp. 565–571, 2017.

[680] D. M. Bishop, B. E. Mccandless, R. Haight, and R. Birkmire, "Fabrication and Optoelectronic Properties of CZTSe Single Crystals," *IEEE J. Photovoltaics*, vol. 5, no. 1, pp. 390–394, 2015.

[681] H. S. Sommers, R. E. Berry, and I. Sochard, "Photoelectromagnetic Effect in Insulating CdS," *Phys. Re*, vol. 101, no. 3, pp. 987–988, 1956.

[682] R. F. McCarthy, R. D. Schaller, D. J. Gosztola, G. P. Wiederrecht, and A. B. F. Martinson, "Photoexcited Carrier Dynamics of In2S3 Thin Films," *J. Phys. Chem. Lett.*, vol. 6, no. 13, pp. 2554–2561, 2015.

[683] F. X. Xiu, Z. Yang, L. J. Mandalapu, D. T. Zhao, J. L. Liu, and W. P. Beyermann, "High-mobility Sb-doped p-type ZnO by molecular-beam epitaxy," *Appl. Phys. Lett.*, vol. 87, no. 15, pp. 1–3, 2005.

[684] H. B. Ye, J. F. Kong, W. Z. Shen, J. L. Zhao, and X. M. Li, "Origins of shallow level and hole mobility in codoped p-type ZnO thin films," *Appl. Phys. Lett.*, vol. 90, no. 10, pp. 2005–2008, 2007.

[685] C. Persson, "Electronic and optical properties of Cu2ZnSnS4 and Cu2ZnSnSe4," *J. Appl. Phys.*, vol. 107, no. 5, p. 053710, 2010.

[686] O. Madelung, *Semiconductors: data handbook*. Springer Science & Business Media, 2012.

[687] Z. Zhao, Y. Cao, J. Yi, X. He, C. Ma, and J. Qiu, "Band-edge electronic structure of β-In 2S 3: The role of s or p orbitals of atoms at different

lattice positions," *ChemPhysChem*, vol. 13, no. 6, pp. 1551–1556, 2012.

[688] D. P. Norton, Y. W. Heo, M. P. Ivill, K. Ip, S. J. Pearton, M. F. Chisholm, and T. Steiner, "ZnO: Growth, doping & processing," *Mater. Today*, vol. 7, no. 6, pp. 34–40, 2004.

[689] S. Kose, F. Atay, V. Bilgin, I. Akyuz, and E. Ketenci, "Optical characterization and determination of carrier density of ultrasonically sprayed CdS:Cu films," *Appl. Surf. Sci.*, vol. 256, no. 13, pp. 4299–4303, 2010.

[690] M. Bedir and M. Öztas, "Effect of air annealing on the optical electrical and structural properties of In2S3 films," *Sci. China, Ser. E Technol. Sci.*, vol. 51, no. 5, pp. 487–493, 2008.

[691] E. M. Mkawi, K. Ibrahim, M. K. M. Ali, M. A. Farrukh, and A. S. Mohamed, "The effect of dopant concentration on properties of transparent conducting Al-doped ZnO thin films for efficient Cu2ZnSnS4 thin-film solar cells prepared by electrodeposition method," *Appl. Nanosci.*, vol. 5, no. 8, pp. 993–1001, 2015.

[692] S. K. Swami, A. Kumar, and V. Dutta, "Deposition of kesterite Cu2ZnSnS4 (CZTS) thin films by spin coating technique for solar cell application," *Energy Procedia*, vol. 33, pp. 198–202, 2013.

[693] W. Wang, M. T. Winkler, O. Gunawan, T. Gokmen, T. K. Todorov, Y. Zhu, and D. B. Mitzi, "Device characteristics of CZTSSe thin-film solar cells with 12.6% efficiency," *Adv. Energy Mater.*, vol. 4, no. 7, pp. 1–5, 2014.

[694] P. Jackson, R. Wuerz, D. Hariskos, E. Lotter, W. Witte, and M. Powalla, "Effects of heavy alkali elements in Cu(In,Ga)Se2 solar cells with efficiencies up to 22.6%," *Phys. Status Solidi - Rapid Res. Lett.*, vol. 10, no. 8, pp. 583–586, 2016.

[695] M. T. Winkler, W. Wang, O. Gunawan, H. J. Hovel, T. K. Todorov, and D. B. Mitzi, "Optical designs that improve the efficiency of $Cu_2ZnSn(S,Se)_4$ solar cells," *Energy Environ. Sci.*, vol. 7, no. 3, pp. 1029–1036, 2014.

[696] B. L. Williams, J. D. Major, L. Bowen, L. Phillips, G. Zoppi, I. Forbes, and K. Durose, "Challenges and prospects for developing CdS/CdTe substrate solar cells on Mo foils," *Sol. Energy Mater. Sol. Cells*, vol. 124, pp. 31–38, 2014.

[697] T. Liu, X. Zhang, J. Zhang, W. Wang, L. Feng, L. Wu, W. Li, G. Zeng, and B. Li, "Interface Study of ITO / ZnO and ITO / SnO 2 Complex Transparent Conductive Layers and Their Effect on CdTe Solar Cells," *Int. J. Photoenergy*, vol. 2013, no. 110, 2013.

[698] T. Liu, X. He, J. Zhang, L. Feng, L. Wu, W. Li, G. Zeng, and B. Li, "Effect of ZnO films on CdTe solar cells," *J. Semicond.*, vol. 33, no. 9, 2012.

[699] P. D. C. King, T. D. Veal, F. Fuchs, C. Y. Wang, D. J. Payne, A. Bourlange, H. Zhang, G. R. Bell, V. Cimalla, O. Ambacher, R. G. Egdell, F. Bechstedt, and C. F. McConville, "Band gap, electronic structure, and surface electron accumulation of cubic and rhombohedral In2O3," *Phys. Rev. B*, vol. 79, no. 20, p. 205211, May 2009.

[700] A. Walsh, J. L. F. Da Silva, S.-H. Wei, C. Körber, A. Klein, L. F. J. Piper, A. DeMasi, K. E. Smith, G. Panaccione, P. Torelli, D. J. Payne, A. Bourlange, and R. G. Egdell, "Nature of the Band Gap of In_2O_3 Revealed by First-Principles Calculations and X-Ray Spectroscopy," *Phys. Rev. Lett.*, vol. 100, no. 16, p. 167402, 2008.

[701] M. Feneberg, J. Nixdorf, C. Lidig, R. Goldhahn, Z. Galazka, O. Bierwagen, and J. S. Speck, "Many-electron effects on the dielectric function of cubic In_2O_3: Effective electron mass, band nonparabolicity, band gap renormalizati," *Phys. Rev. B*, vol. 93, no. 04, p. 045203, 2016.

[702] T. S. Moss, "The interpretation of the properties of indium antimonide," *Proc. Phys. Soc. B*, vol. 67, pp. 775–782, 1954.

[703] E. Burstein, "Anomalous optical absorption limit in InSb," *Phys. Rev.*, vol. 93, no. 3, pp. 632–633, 1954.

[704] J. A. Lahtinen, "Electroreflectance study of the Burstein-Moss shift in indium phosphide," *Phys. Rev. B*, vol. 33, no. 4, pp. 2550–2553, 1986.

[705] T. L. Tansley and C. P. Foley, "Optical band gap of indium nitride," *J. Appl. Phys.*, vol. 59, no. 9, pp. 3241–3244, 1986.

[706] P. K. Chakraborty, G. C. Datta, and K. P. Ghatak, "The simple analysis of the Burstein-Moss shift in degenerate n-type semiconductors," *Phys. B Condens. Matter*, vol. 339, no. 4, pp. 198–203, 2003.

[707] N. R. Yogamalar and A. Chandra Bose, "Burstein-Moss shift and room temperature near-band-edge luminescence in lithium-doped zinc oxide," *Appl. Phys. A Mater. Sci. Process.*, vol. 103, no. 1, pp. 33–42, 2011.

[708] K. G. Saw, N. M. Aznan, F. K. Yam, S. S. Ng, and S. Y. Pung, "New insights on the Burstein-Moss shift and band gap narrowing in indium-doped zinc oxide thin films," *PLoS One*, vol. 10, no. 10, pp. 1–17, 2015.

[709] N. Manjula, A. R. Balu, K. Usharani, N. Raja, and V. S. Nagarethinam, "Enhancement in some physical properties of spray deposited CdO:Mn thin films through Zn doping towards optoelectronic applications," *Optik (Stuttg).*, vol. 127, no. 16, pp. 6400–6406, 2016.

[710] Z. Lebens-Higgins, D. O. Scanlon, H. Paik, S. Sallis, Y. Nie, M. Uchida, N. F. Quackenbush, M. J. Wahila, G. E. Sterbinsky, D. A. Arena, J. C. Woicik, D. G. Schlom, and L. F. J. Piper, "Direct Observation of Electrostatically Driven Band Gap Renormalization in a Degenerate Perovskite Transparent Conducting Oxide," *Phys. Rev. Lett.*, vol. 116, no. 2, pp. 1–5, 2016.

[711] C. A. Pan and T. P. Ma, "Highly transparent conductive films of thermally evaporated In2O3

,” *J. Electron. Mater.*, vol. 10, no. 1, pp. 43–57, 1981.

[712] S. M. Rozati and Z. Bargebidi, “Characterization of molybdenum-doped indium oxide thin films by spray pyrolysis technique,” *Bull. Mater. Sci.*, vol. 36, no. 4, pp. 553–558, 2013.

[713] M. Batzill and U. Diebold, “The surface and materials science of tin oxide,” *Prog. Surf. Sci.*, vol. 79, no. 2–4, pp. 47–154, 2005.

[714] E. Y. Wang, “Determination of Electron Affinity of In[sub 2]O[sub 3] from Its Heterojunction Photovoltaic Properties,” *J. Electrochem. Soc.*, vol. 125, no. 8, p. 1328, 1978.

[715] C. A. Pan and T. P. Ma, “Work function of In_2O_3 film as determined from internal photoemission,” *Appl. Phys. Lett.*, vol. 37, no. 8, pp. 714–716, 1980.

[716] A. Klein, C. Körber, A. Wachau, F. Säuberlich, Y. Gassenbauer, S. P. Harvey, D. E. Proffit, and T. O. Mason, “Transparent conducting oxides for photovoltaics: Manipulation of fermi level,work function and energy band alignment,” *Materials (Basel).*, vol. 3, no. 11, pp. 4892–4914, 2010.

[717] J. Robertson and S. J. Clark, “Limits to doping in oxides,” *Phys. Rev. B - Condens. Matter Mater. Phys.*, vol. 83, no. 7, pp. 1–7, 2011.

[718] A. Myszkowski, L. E. Sansores, and J. Tagüeña-Martínez, “Tunneling solar cell under concentrated light illumination,” *J. Appl. Phys.*, vol. 52, no. 6, pp. 4288–4296, 1981.

[719] O. Lang, C. Pettenkofer, J. F. Sánchez-Royo, A. Segura, A. Klein, and W. Jaegermann, “Thin film growth and band lineup of In2O3on the layered semiconductor InSe,” *J. Appl. Phys.*, vol. 86, no. 10, pp. 5687–5691, 1999.

[720] A. Klein, “Electronic properties of In2O3 surfaces,” *Appl. Phys. Lett.*, vol. 77, no. 13, pp. 2009–2011, 2000.

[721] F. Rüggeberg and A. Klein, “The In2O3/CdTe interface: A possible contact for thin film solar cells?,” *Appl. Phys. A Mater. Sci. Process.*, vol. 82, no. 2, pp. 281–285, 2006.

[722] S. P. Harvey, T. O. Mason, Y. Gassenbauer, R. Schafranek, and A. Klein, “Surface versus bulk electronic/defect structures of transparent conducting oxides: I. Indium oxide and ITO,” *J. Phys. D. Appl. Phys.*, vol. 39, no. 18, pp. 3959–3968, 2006.

[723] Y. Gassenbauer, R. Schafranek, A. Klein, S. Zafeiratos, M. H??vecker, A. Knop-Gericke, and R. Schl??gl, “Surface states, surface potentials, and segregation at surfaces of tin-doped In2 O3,” *Phys. Rev. B - Condens. Matter Mater. Phys.*, vol. 73, no. 24, pp. 1–11, 2006.

[724] S. P. Harvey, T. O. Mason, C. Körber, Y. Gassenbauer, and A. Klein, “Evidence for surface dipole modifications in In2O3-based transparent conductors,” *Appl. Phys. Lett.*, vol. 92, no. 25, pp. 1–4, 2008.

[725] M. V. Hohmann, P. Goston, A. Wachau, T. J. M. Bayer, J. Brötz, K. Albe, and A. Klein, “Orientation dependent ionization potential of In2O3: A natural source for inhomogeneous barrier formation at electrode interfaces in organic electronics,” *J. Phys. Condens. Matter*, vol. 23, no. 33, 2011.

[726] S. Lany, A. Zakutayev, T. O. Mason, J. F. Wager, K. R. Poeppelmeier, J. D. Perkins, J. J. Berry, D. S. Ginley, and A. Zunger, “Surface origin of high conductivities in undoped In 2O 3 thin films,” *Phys. Rev. Lett.*, vol. 108, no. 1, pp. 2–6, 2012.

[727] L. Yang, S. Guo, Q. Yang, Y. Zhu, B. Dai, H. Yu, P. Lei, J. Han, Y. Hou, and J. Zhu, “Improved work function of preferentially oriented indium oxide films induced by the plasma exposure technique,” *Electron. Mater. Lett.*, vol. 11, no. 6, pp. 938–943, 2015.

[728] H. P. Song, G. L. Zheng, A. L. Yang, Y. Guo, H. Y. Wei, C. M. Li, S. Y. Yang, X. L. Liu, Q. S. Zhu, and Z. G. Wang, “The growth of ZnO on bcc-In2O3buffer layers and the valence band offset determined by X-ray photoemission spectroscopy,” *Solid State Commun.*, vol. 150, no. 41–42, pp. 1991–1994, 2010.

[729] T. C. Kaspar, T. Droubay, and J. E. Jaffe, “ZnO/Sn:In 2O 3 and ZnO/CdTe band offsets for extremely thin absorber photovoltaics,” *Appl. Phys. Lett.*, vol. 99, no. 26, pp. 10–13, 2011.

[730] T. C. Kaspar and T. C. Droubay, “Variation in band offsets at ZnO/Sn:In_2O_3 heterojunctions measured by x-ray photoelectron spectroscopy,” *J. Vac. Sci. Technol. A Vacuum, Surfaces, Film.*, vol. 30, no. 4, p. 04D112, 2012.

[731] A. Walsh, J. L. F. Da Silva, Y. Yan, M. M. Al-Jassim, and S.-H. Wei, “Origin of electronic and optical trends in ternary In2O3(ZnO)n transparent conducting oxides (n=1,3,5): Hybrid density functional theory calculations,” *Phys. Rev. B*, vol. 79, no. 7, p. 073105, 2009.

[732] D. Khim, Y. H. Lin, S. Nam, H. Faber, K. Tetzner, R. Li, Q. Zhang, J. Li, X. Zhang, and T. D. Anthopoulos, “Modulation-Doped In2O3/ZnO Heterojunction Transistors Processed from Solution,” *Adv. Mater.*, vol. 29, no. 19, 2017.

[733] V. Krishnakumar, K. Ramamurthi, A. Klein, and W. Jaegermann, “Band alignment of differently treated TCO/CdS interface,” *Thin Solid Films*, vol. 517, no. 7, pp. 2558–2561, 2009.

[734] Z.-Y. Xiao, Y.-F. Li, B. Yao, R. Deng, Z.-H. Ding, T. Wu, G. Yang, C.-R. Li, Z.-Y. Dong, L. Liu, L.-G. Zhang, and H.-F. Zhao, “Bandgap engineering of $Cu_2Cd_xZn_{1-x}SnS_4$ alloy for photovoltaic applications: A complementary experimental and first-principles study,” *J. Appl. Phys.*, vol. 114, no. 18, p. 183506, 2013.

[735] G. Sai Gautam, T. P. Senftle, and E. A. Carter, “Understanding the Effects of Cd and Ag Doping in Cu 2 ZnSnS 4 Solar Cells,” *Chem. Mater.*, vol. 30, pp. 4543–4555, 2018.

[736] Y. F. Tay, H. Kaneko, S. Y. Chiam, S. Lie, Q. Zheng, B. Wu, S. S. Hadke, Z. Su, P. S. Bassi, D.

Bishop, T. C. Sum, T. Minegishi, J. Barber, K. Domen, and L. H. Wong, “Solution-Processed Cd-Substituted CZTS Photocathode for Efficient Solar Hydrogen Evolution from Neutral Water,” *Joule*, vol. 2, pp. 1–12, 2018.

[737] C. H. Lui, A. J. Frenzel, D. V. Pilon, Y. H. Lee, X. Ling, G. M. Akselrod, J. Kong, and N. Gedik, “Trion-induced negative photoconductivity in monolayer MoS2,” *Phys. Rev. Lett.*, vol. 113, no. 16, pp. 1–5, 2014.

[738] Y. Wang, C. Cong, W. Yang, J. Shang, N. Peimyoo, Y. Chen, J. Kang, J. Wang, W. Huang, and T. Yu, “Strain-induced direct–indirect bandgap transition and phonon modulation in monolayer WS2,” *Nano Res.*, vol. 8, no. 8, pp. 2562–2572, 2015.

[739] G. Eda, T. Fujita, H. Yamaguchi, D. Voiry, M. Chen, and M. Chhowalla, “Coherent atomic and electronic heterostructures of single-layer MoS 2,” *ACS Nano*, vol. 6, no. 8, pp. 7311–7317, 2012.

[740] D. Yang, S. J. Sandoval, W. M. R. Divigalpitiya, J. C. Irwin, and R. F. Frindt, “Structure of single-molecular-layer MoS2,” *Phys. Rev. B*, vol. 43, no. 14, pp. 12053–12056, 1991.

[741] L. F. Mattheiss, “Band structures of transition-metal-dichalcogenide layer compounds,” *Phys. Rev. B*, vol. 8, no. 8, pp. 3719–3740, 1973.

[742] F. Wypych and R. Schollhorn, “1T-MoS2 , a New Metallic Modification of Molybdenum Disulfide,” *J. Chem. Soc., Chem. Commun.*, vol. 0, pp. 1386–1388, 1992.

[743] T. Boeker, R. Severin, A. Mueller, C. Janowitz, R. Manzke, D. Voss, P. Krueger, A. Mazur, and J. Pollmann, “Band structure of MoS_2, $MoSe_2$, and alpha-$MoTe_2$: Angle-resolved photoelectron spectroscopy and ab-initio calculations,” *Phys. Rev. B*, vol. 64, pp. 1–11, 2001.

[744] K. F. Mak, C. Lee, J. Hone, J. Shan, and T. F. Heinz, “Atomically thin MoS2: A new direct-gap semiconductor,” *Phys. Rev. Lett.*, vol. 105, no. 13, pp. 2–5, 2010.

[745] Y. Zhang, T. R. Chang, B. Zhou, Y. T. Cui, H. Yan, Z. Liu, F. Schmitt, J. Lee, R. Moore, Y. Chen, H. Lin, H. T. Jeng, S. K. Mo, Z. Hussain, A. Bansil, and Z. X. Shen, “Direct observation of the transition from indirect to direct bandgap in atomically thin epitaxial MoSe2,” *Nat. Nanotechnol.*, vol. 9, no. 2, pp. 111–115, 2014.

[746] C. Ruppert, O. B. Aslan, and T. F. Heinz, “Optical properties and band gap of single- and few-layer MoTe2 crystals,” *Nano Lett.*, vol. 14, no. 11, pp. 6231–6236, 2014.

[747] F. Grønvold and E. Røst, “The crystal structure of PdSe2 and PdS2,” *Acta Crystallogr.*, vol. 10, no. 4, pp. 329–331, 1957.

[748] C. Soulard, X. Rocquefelte, P.-E. Petit, M. Evain, S. Jobic, J.-P. Itié, P. Munsch, H.-J. Koo, and M.-H. Whangbo, “Experimental and Theoretical Investigation on the Relative Stability of the PdS_2 - and Pyrite-Type Structures of $PdSe_2$,” *Inorg. Chem.*, vol. 43, no. 6, pp. 1943–1949, 2004.

[749] Y. Wang, Y. Li, and Z. Chen, “Not your familiar two dimensional transition metal disulfide: structural and electronic properties of the PdS_2 monolayer,” *J. Mater. Chem. C*, vol. 3, no. 37, pp. 9603–9608, 2015.

[750] A. D. Oyedele, S. Yang, L. Liang, A. A. Puretzky, K. Wang, J. Zhang, P. Yu, P. R. Pudasaini, A. W. Ghosh, Z. Liu, C. M. Rouleau, B. G. Sumpter, M. F. Chisholm, W. Zhou, P. D. Rack, D. B. Geohegan, and K. Xiao, “PdSe2: Pentagonal Two-Dimensional Layers with High Air Stability for Electronics,” *J. Am. Chem. Soc.*, vol. 139, no. 40, pp. 14090–14097, 2017.

[751] J. Lin, S. Zuluaga, P. Yu, Z. Liu, S. T. Pantelides, and K. Suenaga, “Novel Pd2Se3 Two-Dimensional Phase Driven by Interlayer Fusion in Layered PdSe2,” *Phys. Rev. Lett.*, vol. 119, no. 1, pp. 1–6, 2017.

[752] B. Schönfeld, J. J. Huang, and S. C. Moss, “Anisotropic mean-square displacements (MSD) in single-crystals of 2H- and 3R-MoS2,” *Acta Crystallogr. Sect. B*, vol. 39, no. 4, pp. 404–407, Aug. 1983.

[753] S. S. Chou, N. Sai, P. Lu, E. N. Coker, S. Liu, K. Artyushkova, T. S. Luk, B. Kaehr, and C. J. Brinker, “Understanding catalysis in a multiphasic two-dimensional transition metal dichalcogenide,” *Nat. Commun.*, vol. 6, pp. 1–8, 2015.

[754] H. Terrones and M. Terrones, “Electronic and vibrational properties of defective transition metal dichalcogenide Haeckelites: New 2D semi-metallic systems,” *2D Mater.*, vol. 1, no. 1, 2014.

[755] Z. Y. Zhu, Y. C. Cheng, and U. Schwingenschlögl, “Giant spin-orbit-induced spin splitting in two-dimensional transition-metal dichalcogenide semiconductors,” *Phys. Rev. B - Condens. Matter Mater. Phys.*, vol. 84, no. 15, pp. 1–5, 2011.

[756] W. S. Yun, S. W. Han, S. C. Hong, I. G. Kim, and J. D. Lee, “Thickness and strain effects on electronic structures of transition metal dichalcogenides: 2H- MX_2 semiconductors (M=Mo, W; X=S, Se, Te),” *Phys. Rev. B*, vol. 85, no. 3, p. 033305, 2012.

[757] W. Jin, P. C. Yeh, N. Zaki, D. Zhang, J. T. Sadowski, A. Al-Mahboob, A. M. Van Der Zande, D. A. Chenet, J. I. Dadap, I. P. Herman, P. Sutter, J. Hone, and R. M. Osgood, “Direct measurement of the thickness-dependent electronic band structure of MoS2 using angle-resolved photoemission spectroscopy,” *Phys. Rev. Lett.*, vol. 111, no. 10, pp. 1–5, 2013.

[758] A. Splendiani, L. Sun, Y. Zhang, T. Li, J. Kim, C. Y. Chim, G. Galli, and F. Wang, “Emerging photoluminescence in monolayer MoS2,” *Nano Lett.*, vol. 10, no. 4, pp. 1271–1275, 2010.

[759] A. Castellanos-Gomez, J. Quereda, H. P. van der Meulen, N. Agraït, and G. Rubio-Bollinger,

"Spatially resolved optical absorption spectroscopy of single- and few-layer MoS 2 by hyperspectral imaging," *Nanotechnology*, vol. 27, no. 11, p. 115705, 2016.

[760] W. Zhao, Z. Ghorannevis, L. Chu, M. Toh, C. Kloc, P.-H. Tan, and G. Eda, "Evolution of Electronic Structure in Atomically Thin Sheets of WS 2 and WSe 2," *ACS Nano*, vol. 7, no. 1, pp. 791–797, 2013.

[761] I. G. Lezama, A. Arora, A. Ubaldini, C. Barreteau, E. Giannini, M. Potemski, and A. F. Morpurgo, "Indirect-to-Direct Band Gap Crossover in Few-Layer MoTe2," *Nano Lett.*, vol. 15, no. 4, pp. 2336–2342, 2015.

[762] C. H. Lee, E. C. Silva, L. Calderin, M. A. T. Nguyen, M. J. Hollander, B. Bersch, T. E. Mallouk, and J. A. Robinson, "Tungsten Ditelluride: A layered semimetal," *Sci. Rep.*, vol. 5, pp. 1–8, 2015.

[763] D. Di Sante, P. K. Das, C. Bigi, Z. Ergönenc, N. Gürtler, J. A. Krieger, T. Schmitt, M. N. Ali, G. Rossi, R. Thomale, C. Franchini, S. Picozzi, J. Fujii, V. N. Strocov, G. Sangiovanni, I. Vobornik, R. J. Cava, and G. Panaccione, "Three-Dimensional Electronic Structure of the Type-II Weyl Semimetal WTe2," *Phys. Rev. Lett.*, vol. 119, no. 2, pp. 1–6, 2017.

[764] R. Addou, L. Colombo, and R. M. Wallace, "Surface Defects on Natural MoS2," *ACS Appl. Mater. Interfaces*, vol. 7, no. 22, pp. 11921–11929, 2015.

[765] S. McDonnell, R. Addou, C. Buie, R. M. Wallace, and C. L. Hinkle, "Defect-Dominated Doping and Contact Resistance in MoS2," *ACS Nano*, vol. 8, no. 3, pp. 2880–2888, 2014.

[766] J. Su, N. Li, Y. Zhang, L. Feng, and Z. Liu, "Role of vacancies in tuning the electronic properties of Au-MoS 2 contact," *AIP Adv.*, vol. 5, no. 7, p. 077182, 2015.

[767] Y. Guo, D. Liu, and J. Robertson, "Chalcogen vacancies in monolayer transition metal dichalcogenides and Fermi level pinning at contacts," *Appl. Phys. Lett.*, vol. 106, no. 17, p. 173106, Apr. 2015.

[768] D. Kim, H. Du, T. Kim, S. Shin, S. Kim, M. Song, C. Lee, J. Lee, H. Cheong, D. H. Seo, and S. Seo, "The enhanced low resistance contacts and boosted mobility in two-dimensional p-type WSe2 transistors through Ar+ ion-beam generated surface defects," *AIP Adv.*, vol. 6, no. 10, 2016.

[769] T. Löher, Y. Tomm, A. Klein, D. Su, C. Pettenkofer, and W. Jaegermann, "Highly oriented layers of the three-dimensional semiconductor CdTe on the two-dimensional layered semiconductors MoTe2and WSe2," *J. Appl. Phys.*, vol. 80, no. 10, pp. 5718–5722, 1996.

[770] T. Löher, Y. Tomm, C. Petternkofer, A. Klein, and W. Jaegermann, "Structural dipoles at interfaces between polar II – VI semiconductors CdS and CdTe and non-polar layered transition metal dichalcogenide semiconductors MoTe 2 and WSe 2 T L oher," *Semicond. Sci. Technol.*, vol. 15, p. 514, 2000.

[771] J. . Bernède, C. Amory, L. Assmann, and M. Spiesser, "X-ray photoelectron spectroscopy study of MoTe2 single crystals and thin films," *Appl. Surf. Sci.*, vol. 219, no. 3–4, pp. 238–248, 2003.

[772] N. Dhar, P. Chelvanathan, K. S. Rahman, M. A. M. Bhuiyan, M. M. Alam, K. Sopian, and N. Amin, "Effect of n-type Transition Metal Dichalcogenide Molybdenum Ditelluride (n-MoTe 2) in Back Contact Interfacr of Cadmium Telluride Solar Cells From Numerical Analysis," *Chalcogenide Lett.*, vol. 11, no. 6, pp. 10–13, 2014.

[773] Z. Wang, W. Wang, Y. Yang, W. Li, L. Feng, J. Zhang, L. Wu, and G. Zeng, "The structure and stability of molybdenum ditelluride thin films," *Int. J. Photoenergy*, vol. 2014, 2014.

[774] N. Dhar, N. A. Khan, P. Chelvanathan, M. Akhtaruzzaman, M. M. Alam, Z. A. Alothman, K. Sopian, and N. Amin, "A Comprehensive Study on Mo/CdTe Metal-Semiconductor Interface Deposited by Radio Frequency Magnetron Sputtering," *J. Nanosci. Nanotechnol.*, vol. 15, no. 11, p. 9291, 2015.

[775] L. F. Schneemeyer and M. S. Wrighton, "Flat-Band Potential of n-Type Semiconducting Molybdenum Disulfide by Cyclic Voltammetry of Two-Electron Reductants: Interface Energetics and the Sustained Photooxidation of Chloride," *J. Am. Chem. Soc.*, vol. 101, no. 22, pp. 6496–6500, 1979.

[776] W. Kautek and H. Gerischer, "Photoelectrochemical Reactions and Formation of Inversion Layers at n-Type MoS2-, MoSe2-, and WSe2-Electrodes in Aprotic Solvents," *Berichte der Bunsengesellschaft für Phys. Chemie*, vol. 84, no. 7, pp. 645–653, 1980.

[777] W. Kautek and H. Gerischer, "Anisotropic photocorrosion of n-type MoS2MoSe2, and WSe2single crystal surfaces: the role 0f cleavage steps, line and screw dislocations," *Surf. Sci.*, vol. 119, no. 1, pp. 46–60, 1982.

[778] K. Dolui, I. Rungger, and S. Sanvito, "Origin of the n-type and p-type conductivity of MoS2 monolayers on a SiO2 substrate," *Phys. Rev. B - Condens. Matter Mater. Phys.*, vol. 87, no. 16, pp. 1–7, 2013.

[779] F. Meng, J. Li, S. K. Cushing, M. Zhi, and N. Wu, "Solar hydrogen generation by nanoscale p-n junction of p-type molybdenum disulfide/n-type nitrogen-doped reduced graphene oxide," *J. Am. Chem. Soc.*, vol. 135, no. 28, pp. 10286–10289, 2013.

[780] S. Chuang, C. Battaglia, A. Azcatl, S. McDonnell, J. S. Kang, X. Yin, M. Tosun, R. Kapadia, H. Fang, R. M. Wallace, and A. Javey, "MoS2 P-type transistors and diodes enabled by high work function MoOx contacts," *Nano Lett.*, vol. 14, no. 3, pp. 1337–1342, 2014.

[781] F. Xue, L. Chen, J. Chen, J. Liu, L. Wang, M. Chen, Y. Pang, X. Yang, G. Gao, J. Zhai, and Z. L. Wang, "P-Type MoS2 and n-Type ZnO Diode and Its Performance Enhancement by the Piezophototronic Effect," *Adv. Mater.*, vol. 28, no. 17, pp. 3391–3398, 2016.

[782] L. Feng, J. Su, and Z. Liu, "Effect of vacancies in monolayer MoS $_2$ on electronic properties of Mo–MoS $_2$ contacts," *RSC Adv.*, vol. 5, no. 26, pp. 20538–20544, 2015.

[783] H. J. Chuang, X. Tan, N. J. Ghimire, M. M. Perera, B. Chamlagain, M. M. C. Cheng, J. Yan, D. Mandrus, D. Tom??nek, and Z. Zhou, "High mobility WSe2 p - And n - Field-effect transistors contacted by highly doped graphene for low-resistance contacts," *Nano Lett.*, vol. 14, no. 6, pp. 3594–3601, 2014.

[784] J. A. Baglio, G. S. Calabrese, E. Kamieniecki, R. Kershaw, C. P. Kubiak, A. J. Ricco, A. Wold, M. S. Wrighton, and G. D. Zoski, "Characterization of n-Type Semiconducting Tungsten Disulfide Photoanodes in Aqueous and Nonaqueous Electrolyte Solutions: Photo-oxidation of Halides with High Efficiency ," *J. Electrochem. Soc.* , vol. 129, no. 7, pp. 1461–1472, Jul. 1982.

[785] J. A. Baglio, G. S. Calabrese, D. J. Harrison, E. Kamieniecki, A. J. Ricco, M. S. Wrighton, and G. D. Zoski, "Electrochemical Characterization of p-Type Semiconducting Tungsten Disulfide Photocathodes: Efficient Photoreduction Processes at Semiconductor/Liquid Electrolyte Interfaces," *J. Am. Chem. Soc.*, vol. 105, no. 8, pp. 2246–2256, 1983.

[786] N. S. McIntyre, P. A. Spevack, G. Beamson, and D. Briggs, "Effects of argon ion bombardment on basal plane and polycrystalline MoS2," *Surf. Sci.*, vol. 237, no. 1–3, 1990.

[787] J. R. Lince, P. D. Fleischauer, and M. M. Hills, "Chemical effects of Ne+ bombardmenton the MoS2(0001) surface studied by HR photoelectron spectroscopy," *Surf. Sci.*, vol. 210, pp. 387–405, 1989.

[788] J. Zhang, J. M. Soon, K. P. Loh, J. Yin, J. Ding, M. B. Sullivian, and P. Wu, "Magnetic molybdenum disulfide nanosheet films," *Nano Lett.*, vol. 7, no. 8, pp. 2370–2376, 2007.

[789] S. Tongay, S. S. Varnoosfaderani, B. R. Appleton, J. Wu, and A. F. Hebard, "Magnetic properties of MoS2: Existence of ferromagnetism," *Appl. Phys. Lett.*, vol. 101, no. 12, 2012.

[790] J. Luxa, O. Jankovský, D. Sedmidubský, R. Medlín, M. Maryško, M. Pumera, and Z. Sofer, "Origin of exotic ferromagnetic behavior in exfoliated layered transition metal dichalcogenides MoS 2 and WS 2," *Nanoscale*, vol. 8, no. 4, pp. 1960–1967, 2016.

[791] Y. Li, Z. Zhou, S. Zhang, and Z. Chen, "MoS 2 Nanoribbons: High Stability and Unusual Electronic and Magnetic Properties," *J. Am. Chem. Soc.*, vol. 130, no. 49, pp. 16739–16744, 2008.

[792] A. R. Botello-Méndez, F. López-Urías, M. Terrones, and H. Terrones, "Metallic and ferromagnetic edges in molybdenum disulfide nanoribbons," *Nanotechnology*, vol. 20, no. 32, 2009.

[793] R. Shidpour and M. Manteghian, "A density functional study of strong local magnetism creation on MoS2 nanoribbon by sulfur vacancy," *Nanoscale*, vol. 2, no. 8, p. 1429, 2010.

[794] C. Ataca, H. Şahin, E. Aktuörk, and S. Ciraci, "Mechanical and electronic properties of MoS2 nanoribbons and their defects," *J. Phys. Chem. C*, vol. 115, no. 10, pp. 3934–3941, 2011.

[795] Y. Zhou, P. Yang, H. Zu, F. Gao, and X. Zu, "Electronic structures and magnetic properties of MoS2 nanostructures: atomic defects, nanoholes, nanodots and antidots," *Phys. Chem. Chem. Phys.*, vol. 15, no. 25, p. 10385, 2013.

[796] S. Yang, C. Wang, H. Sahin, H. Chen, Y. Li, S. S. Li, A. Suslu, F. M. Peeters, Q. Liu, J. Li, and S. Tongay, "Tuning the optical, magnetic, and electrical properties of ReSe2 by nanoscale strain engineering," *Nano Lett.*, vol. 15, no. 3, pp. 1660–1666, 2015.

[797] X. Zhao, T. Wang, G. Wang, X. Dai, C. Xia, and L. Yang, "Electronic and magnetic properties of 1T-HfS2by doping transition-metal atoms," *Appl. Surf. Sci.*, vol. 383, pp. 151–158, 2016.

[798] C. Zhao, C. Jin, J. Wu, and W. Ji, "Magnetism in molybdenum disulphide monolayer with sulfur substituted by 3 d transition metals," *J. Appl. Phys.*, vol. 120, no. 14, pp. 1–8, 2016.

[799] X. Lin and J. Ni, "Charge and magnetic states of Mn-, Fe-, and Co-doped monolayer MoS2," *J. Appl. Phys.*, vol. 116, no. 4, 2014.

[800] J. Wang, F. Sun, S. Yang, Y. Li, C. Zhao, M. Xu, Y. Zhang, and H. Zeng, "Robust ferromagnetism in Mn-doped MoS2nanostructures," *Appl. Phys. Lett.*, vol. 109, no. 9, pp. 1–6, 2016.

[801] P. Tao, H. Guo, T. Yang, and Z. Zhang, "Strain-induced magnetism in MoS2 monolayer with defects," *J. Appl. Phys.*, vol. 115, p. 054305, 2014.

[802] H. Zheng, B. Yang, D. Wang, R. Han, X. Du, and Y. Yan, "Tuning magnetism of monolayer MoS2 by doping vacancy and applying strain," *Appl. Phys. Lett.*, vol. 104, no. 13, pp. 1–6, 2014.

[803] W. S. Yun and J. D. Lee, "Strain-induced magnetism in single-layer MoS2: Origin and manipulation," *J. Phys. Chem. C*, vol. 119, no. 5, pp. 2822–2827, 2015.

[804] S. Mathew, K. Gopinadhan, T. K. Chan, X. J. Yu, D. Zhan, L. Cao, A. Rusydi, M. B. H. Breese, S. Dhar, Z. X. Shen, T. Venkatesan, and J. T. L. Thong, "Magnetism in MoS $_2$ induced by proton irradiation," *Appl. Phys. Lett.*, vol. 101, no. 10, p. 102103, 2012.

[805] The RRUFF Project, "Molybdenite R060124."

[Online]. Available: http://rruff.info/Molybdenite/R060124. [Accessed: 26-Jun-2018].

[806] B. Lafuente, R. T. Downs, H. Yang, and N. Stone, *The power of databases: The RRUFF project*. 2016.

[807] H. J. Conley, B. Wang, J. I. Ziegler, R. F. Haglund, S. T. Pantelides, and K. I. Bolotin, "Bandgap engineering of strained monolayer and bilayer MoS2," *Nano Lett.*, vol. 13, no. 8, pp. 3626–3630, 2013.

[808] Z.-Y. Zhao and Q.-L. Liu, "Study of the layer-dependent properties of MoS2 nanosheets with different crystal structures by DFT calculations," *Catal. Sci. Technol.*, vol. 8, pp. 1867–1879, 2018.

[809] V. Buck, "Preparation and properties of different types of sputtered MoS2 films," *Wear*, vol. 114, no. 3, pp. 263–274, 1987.

[810] N. M. D. Brown, N. Cui, and A. Mckinley, "An XPS study of the surface modification of natural MoS 2 following treatment in an RF-oxygen plasma," *Appl. Surf. Sci.*, vol. 134, pp. 11–21, 1998.

[811] P. D. Fleischauer and J. R. Lince, "Comparison of oxidation and oxygen substitution in MoS2solid film lubricants," *Tribol. Int.*, vol. 32, no. 11, pp. 627–636, 1999.

[812] J. R. Lince and P. P. Frantz, "Anisotropic oxidation of MoS2 crystallites studied by angle-resolved X-ray photoelectron spectroscopy," *Tribol. Lett.*, vol. 9, no. 3–4, pp. 211–218, 2001.

[813] J. Yang, S. Kim, W. Choi, S. H. Park, Y. Jung, M. H. Cho, and H. Kim, "Improved growth behavior of atomic-layer-deposited high- k dielectrics on multilayer MoS2 by oxygen plasma pretreatment," *ACS Appl. Mater. Interfaces*, vol. 5, no. 11, pp. 4739–4744, 2013.

[814] D. Ganta, S. Sinha, and R. T. Haasch, "2-D Material Molybdenum Disulfide Analyzed by XPS," *Surf. Sci. Spectra*, vol. 21, no. 1, pp. 19–27, 2014.

[815] N. Kang, H. P. Paudel, M. N. Leuenberger, L. Tetard, and S. I. Khondaker, "Photoluminescence quenching in single-layer MoS2via oxygen plasma treatment," *J. Phys. Chem. C*, vol. 118, no. 36, pp. 21258–21263, 2014.

[816] H. Nan, Z. Wang, W. Wang, Z. Liang, Y. Lu, Q. Chen, D. He, P. Tan, F. Miao, X. Wang, J. Wang, and Z. Ni, "Strong photoluminescence enhancement of MoS2through defect engineering and oxygen bonding," *ACS Nano*, vol. 8, no. 6, pp. 5738–5745, 2014.

[817] R. Kelly and J. B. Sanders, "On the role of recoil implantation in altering the stoichiometry of a bombarded solid," *Nucl. Instruments Methods*, vol. 132, pp. 335–343, 1976.

[818] B. Villepelet, F. Ferrieu, A. Grouillet, A. Golanski, J. P. Gailliard, and E. Ligeon, "Recoil Implantation of Oxygen from SiO2 Thin Films on Silicon," *Nucl. Instruments Methods*, vol. 183, pp. 137–141, 1981.

[819] I. P. Jain and G. Agarwal, "Ion beam induced surface and interface engineering," *Surf. Sci. Rep.*, vol. 66, no. 3–4, pp. 77–172, Mar. 2011.

[820] P. Sigmund, "Recoil implantation and ion-beam-induced composition changes in alloys and compounds," *J. Appl. Phys.*, vol. 50, no. 11, pp. 7261–7263, 1979.

[821] M. P. Suryawanshi, S. W. Shin, U. V. Ghorpade, K. V. Gurav, C. W. Hong, P. S. Patil, A. V. Moholkar, and J. H. Kim, "Improved solar cell performance of Cu2ZnSnS4(CZTS) thin films prepared by sulfurizing stacked precursor thin films via SILAR method," *J. Alloys Compd.*, vol. 671, pp. 509–516, 2016.

[822] J. Zhu, Z. Wang, H. Yu, N. Li, J. Zhang, J. Meng, M. Liao, J. Zhao, X. Lu, L. Du, R. Yang, D. Shi, Y. Jiang, and G. Zhang, "Argon Plasma Induced Phase Transition in Monolayer MoS 2," *J. Am. Chem. Soc.*, vol. 129, pp. 10216–10219, 2017.

[823] W. Hardaker, N. Schoeni, G. Chapuis, N. Casademont, and M. Sisto, "Crystallographic applets and simulations," *Laboratory of Crystallography, École polytechnique fédérale de Lausanne*, 2016. [Online]. Available: http://escher.epfl.ch/. [Accessed: 11-Jul-2018].

[824] P. B. James and M. T. Lavik, "The crystal structure of MoSe2," *Acta Crystallogr.*, vol. 16, no. 11, pp. 1183–1183, 1963.

[825] R. T. Downs and M. Hall-Wallace, "The American Mineralogist Crystal Structure Database," *Am. Mineral.*, vol. 88, pp. 247–250, 2003.

[826] S. Gražulis, D. Chateigner, R. T. Downs, A. F. T. Yokochi, M. Quirós, L. Lutterotti, E. Manakova, J. Butkus, P. Moeck, and A. Le Bail, "Crystallography Open Database {--} an open-access collection of crystal structures," *J. Appl. Crystallogr.*, vol. 42, no. 4, pp. 726–729, Aug. 2009.

[827] S. Gražulis, A. Daškevič, A. Merkys, D. Chateigner, L. Lutterotti, M. Quirós, N. R. Serebryanaya, P. Moeck, R. T. Downs, and A. Le Bail, "Crystallography Open Database (COD): an open-access collection of crystal structures and platform for world-wide collaboration," *Nucleic Acids Res.*, vol. 40, no. D1, pp. D420–D427, 2012.

[828] S. Gražulis, A. Merkys, A. Vaitkus, and M. Okulič-Kazarinas, "Computing stoichiometric molecular composition from crystal structures," *J. Appl. Crystallogr.*, vol. 48, no. 1, pp. 85–91, Feb. 2015.

[829] A. Merkys, A. Vaitkus, J. Butkus, M. Okulič-Kazarinas, V. Kairys, and S. Gražulis, "{\it COD::CIF::Parser}: an error-correcting CIF parser for the Perl language," *J. Appl. Crystallogr.*, vol. 49, no. 1, Feb. 2016.

[830] R. Bromley, R. Murray, and A. Yoffe, "The band

structures of some transition metal dichalcogenides : III. Group VI A: trigonal prism materials," *J. Phys. J. Phys. C Solid State Phys*, vol. 5, pp. 759–778, 1972.

[831] A. H. Reshak and S. Auluck, "Band structure and optical response of 2H-Mo X2 compounds (X=S, Se, and Te)," *Phys. Rev. B - Condens. Matter Mater. Phys.*, vol. 71, no. 15, pp. 1–6, 2005.

[832] W. A. Abdallah and A. E. Nelson, "Characterization of MoSe2(0001) and ion-sputtered MoSe2 by XPS," *J. Mater. Sci.*, vol. 40, no. 9–10, pp. 2679–2681, 2005.

[833] J. C. Bernede, "About the preferential sputtering of chalcogen from transition metal dichalcogenide compounds and the determination of compound stoichiometry from XPS peak positions," *Appl. Surf. Sci.*, vol. 171, no. 1–2, pp. 15–20, 2001.

[834] R. W. G. Wyckhoff, "MoTe2," in *Crystal Structures*, 2nd ed., New York: Interscience Publishers, 1963, pp. 280–281.

[835] L. Zhou, K. Xu, A. Zubair, A. D. Liao, W. Fang, F. Ouyang, Y. H. Lee, K. Ueno, R. Saito, T. Palacios, J. Kong, and M. S. Dresselhaus, "Large-Area Synthesis of High-Quality Uniform Few-Layer $MoTe_2$," *J. Am. Chem. Soc.*, vol. 137, no. 37, pp. 11892–11895, 2015.

[836] I. T. McGovern and R. H. Williams, "The partial densities of p and d states in α-MoTe2by photoemission using a synchrotron source," *J. Phys. C Solid State Phys.*, vol. 9, no. 13, 1976.

[837] I. T. McGovern and R. H. Williams, "The band structure of α-MoTe2 by photoelectron spectroscopy," *Nuovo Cim. B Ser. 11*, vol. 38, no. 2, pp. 241–247, 1977.

[838] I. T. McGovern, R. H. Williams, and A. W. Parke, "The electronic structure of MoS 2 and α-MoTe 2 by photoelectron spectroscopy using line and synchrotron sources," *J. Phys. C*, vol. 12, no. 13, pp. 2689–2704, 1979.

[839] W. G. Dawson and D. W. Bullett, "Electronic structure and crystallography of $MoTe_2$ and WTe_2," *J. Phys. C Solid State Phys.*, vol. 20, no. 36, pp. 6159–6174, 1987.

[840] Q. Wang, H. Zhu, C. Zhang, R. Addou, K. Cho, R. M. Wallace, and M. J. Kim, "In Situ Heating Study of 2H-MoTe2 to Mo6Te6 Nanowire Phase Transition," *Microsc. Microanal.*, vol. 23, no. S1, pp. 1764–1765, 2017.

[841] H. Zhu, Q. Wang, L. Cheng, R. Addou, J. Kim, M. J. Kim, and R. M. Wallace, "Defects and Surface Structural Stability of $MoTe_2$ Under Vacuum Annealing," *ACS Nano*, p. acsnano.7b04984, 2017.

[842] H. Zhu, Q. Wang, C. Zhang, R. Addou, K. Cho, R. M. Wallace, and M. J. Kim, "New Mo_6Te_6 Sub-Nanometer-Diameter Nanowire Phase from 2H-$MoTe_2$," *Adv. Mater.*, vol. 29, no. 18, p. 1606264, 2017.

[843] Y. Yu, G. Wang, Y. Tan, N. Wu, X.-A. Zhang, and S. Qin, "Phase-Controlled Growth of 1D Mo_6Te_6 Nanowires and 2D $MoTe_2$ Ultrathin Films Heterostructures," *Nano Lett.*, p. acs.nanolett.7b03058, 2017.

[844] M. K. Bahl, R. L. Watson, and K. J. Irgolic, "X-ray photoemission studies of tellurium and some of its compounds," *J. Chem. Phys.*, vol. 66, no. 12, pp. 5526–5535, 1977.

[845] F. D. Brandão, G. M. Ribeiro, P. H. Vaz, J. C. González, and K. Krambrock, "Identification of rhenium donors and sulfur vacancy acceptors in layered MoS2 bulk samples," *J. Appl. Phys.*, vol. 119, no. 23, p. 235701, Jun. 2016.

[846] J.-Y. Noh, H. Kim, and Y.-S. Kim, "Stability and electronic structures of native defects in single-layer ${\mathrm{MoS}}_{2}$," *Phys. Rev. B*, vol. 89, no. 20, p. 205417, May 2014.

[847] H. P. Komsa and A. V. Krasheninnikov, "Native defects in bulk and monolayer MoS2 from first principles," *Phys. Rev. B - Condens. Matter Mater. Phys.*, vol. 91, no. 12, pp. 1–17, 2015.

[848] C. P. Lu, G. Li, J. Mao, L. M. Wang, and E. Y. Andrei, "Bandgap, mid-gap states, and gating effects in MoS2," *Nano Lett.*, vol. 14, no. 8, pp. 4628–4633, 2014.

[849] L. P. Feng, J. Su, and Z. T. Liu, "Effect of vacancies on structural, electronic and optical properties of monolayer MoS2: A first-principles study," *J. Alloys Compd.*, vol. 613, pp. 122–127, 2014.

[850] L. P. Feng, J. Su, S. Chen, and Z. T. Liu, "First-principles investigations on vacancy formation and electronic structures of monolayer MoS2," *Mater. Chem. Phys.*, vol. 148, no. 1–2, pp. 5–9, 2014.

[851] Ü. Özgür, Y. I. Alivov, C. Liu, A. Teke, M. A. Reshchikov, S. Doğan, V. Avrutin, S. J. Cho, and H. Morkç, "A comprehensive review of ZnO materials and devices," *J. Appl. Phys.*, vol. 98, no. 4, pp. 1–103, 2005.

[852] L. Yao and W. Lixi, "Recent progress of ohmic contact on ZnO," *Proceedings, 2008 Int. Conf. Electron. Packag. Technol. High Density Packag. ICEPT-HDP 2008*, pp. 1–4, 2008.

[853] L. J. Brillson and Y. Lu, "ZnO Schottky barriers and Ohmic contacts," *J. Appl. Phys.*, vol. 109, no. 12, 2011.

[854] K. G. Saw, S. S. Tneh, G. L. Tan, F. K. Yam, S. S. Ng, and Z. Hassan, "Ohmic-rectifying conversion of Ni contacts on ZnO and the possible determination of ZnO thin film surface polarity," *PLoS One*, vol. 9, no. 1, 2014.

[855] S. J. Ikhmayies, N. M. Abu El-Haija, and R. N. Ahmad-Bitar, "A comparison between different ohmic contacts for ZnO thin films," *J. Semicond.*, vol. 36, no. 3, 2015.

[856] K. E. Jahromi, M. Hossein, M. Ara, S. S. Mousavi, and B. Efafi, "Investigation of a Reliable Ohmic Contact to n-Type ZnO Thin Films Prepared by Sol – Gel Method," *Ieee*

Electron Device Lett., vol. 37, no. 1, pp. 2015–2017, 2016.

[857] V. M. Goldschmidt, T. M. W. Barth, and G. Lunde, *Geochemische Verteilungsgesetze der Elemente: Isomorphie und Polymorphie der Sesquioxyde. Die Lanthaniden-Kontraktion und ihre Konsequenzen/von VM Goldschmidt, T. Barth u. G. Lunde*. Skrifter Norske Videnskaps-Akademi Oslo, 1925.

[858] S. Geller, "Crystal Structure of β-Ga2O3," *J. Chem. Phys.*, vol. 33, no. 3, p. 676, Aug. 1960.

[859] S. Yoshioka, H. Hayashi, A. Kuwabara, F. Oba, K. Matsunaga, and I. Tanaka, "Structures and energetics of Ga 2 O 3 polymorphs," *J. Phys. Condens. Matter*, vol. 19, no. 34, p. 346211, Aug. 2007.

[860] J. P. Remeika and M. Marezio, "Growth of alpha-Ga2O3 single crystals at 44 kbars," *Appl. Phys. Lett.*, vol. 8, no. 4, pp. 87–88, 1966.

[861] H. Y. Playford, A. C. Hannon, E. R. Barney, and R. I. Walton, "Structures of uncharacterised polymorphs of gallium oxide from total neutron diffraction," *Chem. - A Eur. J.*, vol. 19, no. 8, pp. 2803–2813, 2013.

[862] R. Roy, V. G. Hill, and E. F. Osborn, "Polymorphism of Ga $_2$ O $_3$ and the System Ga $_2$ O $_3$ —H $_2$ O," *J. Am. Chem. Soc.*, vol. 74, no. 3, pp. 719–722, 1952.

[863] T. C. Lovejoy, R. Chen, X. Zheng, E. G. Villora, K. Shimamura, H. Yoshikawa, Y. Yamashita, S. Ueda, K. Kobayashi, S. T. Dunham, F. S. Ohuchi, and M. a. Olmstead, "Band bending and surface defects in β-Ga2O3," *Appl. Phys. Lett.*, vol. 100, no. 18, p. 181602, May 2012.

[864] A. Navarro-Quezada, Z. Galazka, S. Alamé, D. Skuridina, P. Vogt, and N. Esser, "Surface properties of annealed semiconducting β-Ga2O3 (100) single crystals for epitaxy," *Appl. Surf. Sci.*, vol. 349, pp. 368–373, Sep. 2015.

[865] A. Navarro-Quezada, S. Alamé, N. Esser, J. Furthmüller, F. Bechstedt, Z. Galazka, D. Skuridina, and P. Vogt, "Near valence-band electronic properties of semiconducting β-Ga_2O_3 (100) single crystals," *Phys. Rev. B*, vol. 92, no. 19, p. 195306, 2015.

[866] G.-L. Li, F. Zhang, Y.-T. Cui, H. Oji, J.-Y. Son, and Q. Guo, "Electronic structure of β-Ga2O3 single crystals investigated by hard X-ray photoelectron spectroscopy," *Appl. Phys. Lett.*, vol. 107, no. 2, p. 022109, 2015.

[867] H. Peelaers and C. G. Van de Walle, "Sub-band-gap absorption in Ga 2 O 3," *Appl. Phys. Lett.*, vol. 111, no. 18, p. 182104, 2017.

[868] E. G. Víllora, K. Shimamura, K. Kitamura, and K. Aoki, "Rf-plasma-assisted molecular-beam epitaxy of β-Ga[sub 2]O[sub 3]," *Appl. Phys. Lett.*, vol. 88, no. 3, p. 031105, Jan. 2006.

[869] J. B. Varley, J. R. Weber, A. Janotti, and C. G. Van de Walle, "Oxygen vacancies and donor impurities in β-Ga[sub 2]O[sub 3]," *Appl. Phys. Lett.*, vol. 97, no. 14, p. 142106, Oct. 2010.

[870] M. Passlack, N. E. J. Hunt, E. F. Schubert, G. J. Zydzik, M. Hong, J. P. Mannaerts, R. L. Opila, and R. J. Fischer, "Dielectric properties of electron-beam deposited Ga2O3 films," *Appl. Phys. Lett.*, vol. 64, no. 20, p. 2715, May 1994.

[871] M. Michling and D. Schmeißer, "Resonant Photoemission at the O1s threshold to characterize β-Ga2O3 single crystals," *IOP Conf. Ser. Mater. Sci. Eng.*, vol. 34, p. 012002, 2012.

[872] J. H. Scofield, "Theoretical photoionization cross sections from 1 to 1500 keV.," U.S. Atomic Energy Commission, Jan. 1973.

[873] A. Klein, "Electronic properties of Electronic properties of In 2 O 3 surfaces," *Appl. Phys. Lett.*, vol. 77, no. 13, pp. 3–6, 2000.

[874] P. D. C. King, T. D. Veal, D. J. Payne, A. Bourlange, R. G. Egdell, and C. F. McConville, "Surface Electron Accumulation and the Charge Neutrality Level in In2O3," *Phys. Rev. Lett.*, vol. 101, no. 11, p. 116808, 2008.

[875] M. Mohamed, I. Unger, C. Janowitz, R. Manzke, Z. Galazka, R. Uecker, and R. Fornari, "The surface band structure of β-Ga2O3," *J. Phys. Conf. Ser.*, vol. 286, no. 1, 2011.

[876] C. Janowitz, V. Scherer, M. Mohamed, A. Krapf, H. Dwelk, R. Manzke, Z. Galazka, R. Uecker, K. Irmscher, R. Fornari, M. Michling, D. Schmeißer, J. R. Weber, J. B. Varley, and C. G. Van de Walle, "Experimental electronic structure of In 2 O 3 and Ga 2 O 3," *New J. Phys.*, vol. 13, no. 8, p. 085014, 2011.

[877] M. Mohamed, C. Janowitz, I. Unger, R. Manzke, Z. Galazka, R. Uecker, R. Fornari, J. R. Weber, J. B. Varley, and C. G. Van De Walle, "The electronic structure of β-Ga2O3," *Appl. Phys. Lett.*, vol. 97, no. 21, pp. 2–5, 2010.

[878] D. S. Dessau, P. H. Dickinson, J. Dicarlo, A. G. Loeser, W. E. Spicer, and A. J. Arko, "HIGH ENERGY RESOLUTION ARPES MEASUREMENTS OF THE NORMAL AND SUPERCONDUCTING STATES OF Bi2Sr2CaCu2O8+?," in *Mat Res. Soc. Symp. Proc.*, 1993, vol. 307, pp. 187–192.

[879] H. Iwasawa, E. F. Schwier, M. Arita, A. Ino, H. Namatame, M. Taniguchi, Y. Aiura, and K. Shimada, "Development of laser-based scanning μ-ARPES system with ultimate energy and momentum resolutions," *Ultramicroscopy*, vol. 182, pp. 85–91, 2017.

[880] Y. Ma, H. C. Diaz, J. Avila, C. Chen, V. Kalappattil, R. Das, M. H. Phan, T. Čadež, J. M. P. Carmelo, M. C. Asensio, and M. Batzill, "Angle resolved photoemission spectroscopy reveals spin charge separation in metallic MoSe 2 grain boundary," *Nat. Commun.*, vol. 8, 2017.

[881] H. Nanto, T. Minami, and S. Takata, "Zinc-oxide thin-film ammonia gas sensors with high sensitivity and excellent selectivity," *J. Appl. Phys.*, vol. 60, no. 2, pp. 482–484, 1986.

[882] H. S. Hassan, A. B. Kashyout, I. Morsi, A. A. A.

Nasser, and A. Raafat, “Fabrication and characterization of nano-gas sensor arrays,” *AIP Conf. Proc.*, vol. 1653, no. 2015, 2015.

[883] R. Heinhold, S. P. Cooil, D. A. Evans, and M. W. Allen, “Stability of the surface electron accumulation layers on the nonpolar (1010) and (1120) faces of ZnO,” *J. Phys. Chem. C*, vol. 118, no. 42, pp. 24575–24582, 2014.

[884] M. J. Al-Saadi, S. H. Al-Harthi, H. H. Kyaw, M. T. Z. Myint, T. Bora, K. Laxman, A. Al-Hinai, and J. Dutta, “Influence of Atomic Hydrogen, Band Bending, and Defects in the Top Few Nanometers of Hydrothermally Prepared Zinc Oxide Nanorods,” *Nanoscale Res. Lett.*, vol. 12, no. 1, 2017.

[885] P. D. C. King, T. D. Veal, and C. F. McConville, “Nonparabolic coupled Poisson-Schrödinger solutions for quantized electron accumulation layers: Band bending, charge profile, and subbands at InN surfaces,” *Phys. Rev. B*, vol. 77, no. 12, p. 125305, Mar. 2008.

[886] K. H. L. Zhang, D. J. Payne, R. G. Palgrave, V. K. Lazarov, W. Chen, A. T. S. Wee, C. F. McConville, P. D. C. King, T. D. Veal, G. Panaccione, P. Lacovig, and R. G. Egdell, “Surface Structure and Electronic Properties of In 2 O 3 (111) Single-Crystal Thin Films Grown on Y-Stabilized ZrO 2 (111),” *Chem. Mater.*, vol. 21, no. 19, pp. 4353–4355, Oct. 2009.

[887] P. D. C. King, I. McKenzie, and T. D. Veal, “Observation of shallow-donor muonium in Ga[sub 2]O[sub 3]: Evidence for hydrogen-induced conductivity,” *Appl. Phys. Lett.*, vol. 96, no. 6, p. 062110, Feb. 2010.

[888] P. D. C. King, R. L. Lichti, Y. G. Celebi, J. M. Gil, R. C. Vilão, H. V. Alberto, J. Piroto Duarte, D. J. Payne, R. G. Egdell, I. McKenzie, C. F. McConville, S. F. J. Cox, and T. D. Veal, “Shallow donor state of hydrogen in In 2 O 3 and SnO 2 : Implications for conductivity in transparent conducting oxides,” *Phys. Rev. B*, vol. 80, no. 8, p. 081201, Aug. 2009.

[889] S. K. Vasheghani Farahani, T. D. Veal, J. J. Mudd, D. O. Scanlon, G. W. Watson, O. Bierwagen, M. E. White, J. S. Speck, and C. F. McConville, “Valence-band density of states and surface electron accumulation in epitaxial SnO2 Films,” *Phys. Rev. B*, vol. 90, no. 15, p. 155413, 2014.

[890] H.-Y. Shih, F.-C. Chu, A. Das, C.-Y. Lee, M.-J. Chen, and R.-M. Lin, “Atomic Layer Deposition of Gallium Oxide Films as Gate Dielectrics in AlGaN/GaN Metal–Oxide–Semiconductor High-Electron-Mobility Transistors,” *Nanoscale Res. Lett.*, vol. 11, no. 1, p. 235, 2016.

[891] D. J. Comstock and J. W. Elam, “Atomic Layer Deposition of Ga 2 O 3 Films Using Trimethylgallium and Ozone,” *Chem. Mater.*, vol. 24, no. 21, pp. 4011–4018, Nov. 2012.

[892] I. Donmez, C. Ozgit-Akgun, and N. Biyikli, “Low temperature deposition of Ga $_2$ O $_3$ thin films using trimethylgallium and oxygen plasma,” *J. Vac. Sci. Technol. A Vacuum, Surfaces, Film.*, vol. 31, no. 1, p. 01A110, 2013.

[893] H. He, R. Orlando, M. A. Blanco, R. Pandey, E. Amzallag, I. Baraille, and M. Rérat, “First-principles study of the structural, electronic, and optical properties of Ga2 O3 in its monoclinic and hexagonal phases,” *Phys. Rev. B - Condens. Matter Mater. Phys.*, vol. 74, no. 19, pp. 1–8, 2006.

[894] A. Segura, L. Artús, R. Cuscó, R. Goldhahn, and M. Feneberg, “Band gap of corundum like α-Ga_2O_3 determined by absorption and ellipsometry,” *Phys. Rev. Mater.*, vol. 1, no. 2, p. 024604, 2017.

[895] F. Litimein, D. Rached, R. Khenata, and H. Baltache, “FPLAPW study of the structural, electronic, and optical properties of Ga2O3: Monoclinic and hexagonal phases,” *J. Alloys Compd.*, vol. 488, no. 1, pp. 148–156, 2009.

[896] W. Mu, Z. Jia, Y. Yin, Q. Hu, Y. Li, B. Wu, J. Zhang, and X. Tao, “High quality crystal growth and anisotropic physical characterization of β-Ga2O3single crystals grown by EFG method,” *J. Alloys Compd.*, vol. 714, pp. 453–458, 2017.

[897] S. Ghose, S. Rahman, L. Hong, J. S. Rojas-Ramirez, H. Jin, K. Park, R. Klie, and R. Droopad, “Growth and characterization of β-Ga $_2$ O $_3$ thin films by molecular beam epitaxy for deep-UV photodetectors,” *J. Appl. Phys.*, vol. 122, no. 9, p. 095302, 2017.

[898] T. Onuma, S. Saito, K. Sasaki, T. Masui, T. Yamaguchi, T. Honda, A. Kuramata, and M. Higashiwaki, “Spectroscopic ellipsometry studies on β-Ga 2 O 3 films and single crystal,” *Jpn. J. Appl. Phys.*, vol. 55, no. 12, p. 1202B2, 2016.

[899] J. W. Roberts, J. C. Jarman, D. N. Johnstone, P. A. Midgley, P. R. Chalker, R. A. Oliver, and F. C. P. Massabuau, “α-Ga2O3 grown by low temperature atomic layer deposition on sapphire,” *J. Cryst. Growth*, vol. 487, pp. 23–27, 2018.

[900] L. Kong, J. Ma, C. Luan, and Z. Zhu, “Structural and optical properties of Ga2O3:In films deposited on MgO (1 0 0) substrates by MOCVD,” *J. Solid State Chem.*, vol. 184, no. 8, pp. 1946–1950, 2011.

[901] D. Choi, K.-B. Chung, and J.-S. Park, “Low temperature Ga2O3 atomic layer deposition using gallium tri-isopropoxide and water,” *Thin Solid Films*, vol. 546, pp. 31–34, Nov. 2013.

[902] C. Janowitz, V. Scherer, M. Mohamed, A. Krapf, H. Dwelk, R. Manzke, Z. Galazka, R. Uecker, K. Irmscher, R. Fornari, M. Michling, D. Schmeißer, J. R. Weber, J. B. Varley, and C. G. Van de Walle, “Experimental electronic structure of In $_2$ O $_3$ and Ga $_2$ O $_3$,” *New J. Phys.*, vol. 13, no. 8, p. 085014, 2011.

[903] H. Peelaers and C. G. Van de Walle, “Brillouin zone and band structure of β-Ga2O3,” *Phys. Status Solidi Basic Res.*, vol. 252, no. 4, pp. 828–832, 2015.

[904] M. Choi and J. Son, “Doping-induced bandgap tuning of α-Ga2O3for ultraviolet lighting,” *Curr. Appl. Phys.*, vol. 17, no. 5, pp. 713–716, 2017.

[905] D. Shinohara and S. Fujita, “Heteroepitaxy of corundum-structured α-Ga2O3 thin films on α-Al2O3 substrates by ultrasonic mist chemical vapor deposition,” *Jpn. J. Appl. Phys.*, vol. 47, no. 9 PART 1, pp. 7311–7313, 2008.

[906] G. Schön, “Auger and direct electron spectra in X-ray photoelectron studies of zinc, zinc oxide, gallium and gallium oxide,” *J. Electron Spectros. Relat. Phenomena*, vol. 2, no. 1, pp. 75–86, 1973.

[907] P. D. C. King, T. D. Veal, C. F. McConville, J. Zúñiga-Pérez, V. Muñoz-Sanjosé, M. Hopkinson, E. D. L. Rienks, M. F. Jensen, and P. Hofmann, “Surface band-gap narrowing in quantized electron accumulation layers,” *Phys. Rev. Lett.*, vol. 104, no. 25, pp. 1–4, 2010.

[908] X. Zhou, E. J. M. Hensen, R. A. Van Santen, and C. Li, “DFT simulations of water adsorption and activation on low-index α-Ga2O3surfaces,” *Chem. - A Eur. J.*, vol. 20, no. 23, pp. 6915–6926, 2014.

[909] J. Furthmüller and F. Bechstedt, “Quasiparticle bands and spectra of Ga_2O_3 polymorphs,” *Phys. Rev. B*, vol. 93, no. 11, p. 115204, 2016.